Jet, Rocket, Nuclear, Ion and Electric Propulsion: Theory and Design

Jet, Rocket, Nuclear, Ion and Electric

Propulsion:

Theory and Design

Edited and authored by W. H. T. Loh

NORTH AMERICAN ROCKWELL CORPORATION

DOWNEY, CALIFORNIA

Preface

During the last decade, rapid growth of knowledge in the field of jet, rocket, nuclear, ion and electric propulsion has resulted in many advances useful to the student, engineer and scientist. The purpose for offering this course is to make available to them these recent advances in theory and design.

Accordingly, this course is organized into seven parts: Part 1 Introduction; Part 2 Jet Propulsion; Part 3 Rocket Propulsion; Part 4 Nuclear Propulsion; Part 5 Electric and Ion Propulsion; Part 6 Theory on Combustion, Detonation and Fluid Injection; Part 7 Advanced Concepts and Mission Applications. It is written in such a way that it may easily be adopted by other universities as a textbook for a one semester senior or graduate course on the subject. In addition to the undersigned who served as the course instructor and wrote Chapter 1, 2 and 3, guest lecturers included: DR. G. L. DUGGER who wrote Chapter 4 "Ram-jets and Air-Augmented Rockets," DR. GEORGE P. SUTTON who wrote Chapter 5 "Rockets and Cooling Methods," DR.. MARTIN SUMMERFIELD who wrote Chapter 6 "Solid Propellant Rockets," DR. HOWARD S. SEIFERT who wrote Chapter 7 "Hybrid Rockets," DR. CHANDLER C. ROSS who wrote Chapter 8 "Advanced Nuclear Rocket Design," MR. GEORGE H. McLAFFERTY who wrote Chapter 9 "Gaseous Nuclear Rockets," DR. S. G. FORBES who wrote Chapter 10 "Electric and Ion Propulsion," DR. R. H. BODEN who wrote Chapter 11 "Ion Propulsion," DR. ANDREW CHARWAT who wrote Chapter 12 "Interaction Flows Due to Steps, Notches and Secondary Jets," DR. A. K. OPPENHEIM who wrote Chapter 13 "Theory of Explosions and Its Relevance to Propulsion," DR. ANTONIO FERRI who wrote Chapter 14 "Supersonic Combustion Theory," DR. SIN-I CHENG who wrote Chapter 15 "Combustion Instability Theory," and Chapter 16 "Advanced Space Compulsion Techniques," DR. JOHN F. McCARTHY, JR. who wrote Chapter 17 "Zero 'G' Propulsion Problems," and DR. KRAFFT A. EHRICKE who wrote Chapter 18 "Propulsion Systems and Comparison for Space Missions."

W. H. T. LOH, *Course Instructor*

Los Angeles, California

Contents

PART ONE – INTRODUCTION

Chapter 1. Fundamentals of Thermodynamics and Aerodynamics

vii

PART TWO – JET PROPULSION

Chapter 2. Thermodynamic Cycle Analysis of Gas Turbines and Air-breathing Propulsion Systems

Chapter 3. Aerodynamic Design of Axial Flow Compressors and Turbines

Chapter 7. Hybrid Rocket Theory and Design

PART FOUR – NUCLEAR PROPULSION

Chapter 8. Nuclear Rocket Propulsion

Chapter 9. Radioisotope Propulsion

PART FIVE – ELECTRIC AND ION PROPULSION

Chapter 10. Electric and Ion Propulsion

Chapter 11. Ion Propulsion

PART SIX – THEORY ON COMBUSTION, DETONATION AND FLUID INJECTION

Chapter 12. Interaction Flows Due to Supersonic Secondary Jets

Chapter 13. Gasdynamics of Explosions

Chapter 14. Supersonic Combustion Technology

Chapter 15. Combustion Instability Theory

PART SEVEN – ADVANCED CONCEPTS AND MISSION APPLICATIONS

Chapter 16. An Advanced Space Propulsion Concept

Chapter 17. Zero g Propulsion Problems

Part One

Introduction

Fundamentals of Thermodynamics
and Aerothermodynamics

W. H. T. LOH, Manager
Science and Technology,
Space Division,
North American Rockwell Corporation
Downey, California.

[1-1] INTRODUCTION

The performance of a jet, rocket, nuclear, ion or electric propulsion system can always be analyzed by four fundamental parameters, i.e., pressure, temperature, density and velocity inside the system. However, instead of using three physical properties of gases (pressure, temperature, and density), three thermodynamic properties of gases (enthalpy, entropy, and internal energy) are often used for convenience of calculations. Therefore, analysis of propulsion problems can be made by the application of the fundamentals of thermodynamics and aerothermodynamics. In this chapter, these fundamentals of thermodynamics and aerothermodynamics which are particularly applicable to propulsion problems will be given briefly but adequately. Extensive treatment or discussion of these subjects should, of course, be referred to the separate textbooks of thermodynamics and aerothermodynamics.

[1-2] EQUATION OF STATE

It was first found through Charles and Boyle's experiment that there exists a relationship between pressure p, Volume V, Temperature T, and Weight W of a gas substance as:

$$\frac{pV}{WT} = \text{constant } R \text{ of the gas substance.} \qquad (1\text{-}1)$$

This relationship is known as the equation of state of the substance. If any three of the properties are fixed, the fourth is determined.

If specific volumes v, namely volume per unit weight $v = V/W$, is used, it simply becomes:

$$\frac{pv}{T} = \text{constant } R \text{ of the gas substance.} \tag{1-2}$$

Equation (1-2) is characteristic of an ideal gas or perfect gas [which is defined as a gas, with constant specific heats, conforming exactly to the Charles and Boyle's Law Eq. (1-2)], and it relates very well the properties of real gases under low pressures and high temperatures. When V in Eq. (1-1) is expressed in terms of volume per Mol of gas (one Mol of any substance is defined as a quantity whose weight W expressed in pounds is equivalent to its molecular weight M), Eq. (1-1) becomes:

$$\frac{pV}{T} = MR . \tag{1-3}$$

Let us define

$$MR = \mathcal{R} . \tag{1-4}$$

For one Mol of gas, the product MR or $\mathcal{R}$ approximates a constant 1545.33 ft.# per # Mole °R which is the so-called universal gas constant $\mathcal{R}$. If specific volume v, which is volume per unit weight, or, in this case, $v = V/M$, is used, the equation of state of an ideal or perfect gas becomes:

$$\frac{pv}{T} = \frac{\mathcal{R}}{M} = R , \tag{1-5}$$

or, in terms of density ρ,

$$\frac{p}{\rho} = RT . \tag{1-5a}$$

[1-2.1] Equation of State of Real Gases

Many equations of state for real gases have been proposed by means of statistical mechanics to describe the $p-V-T$ relationship more accurately than the equation of state of ideal gas. One useful form is the so-called "virial form of equation of state":

$$\frac{pv}{RT} = 1 + \frac{B(T)}{v} + \frac{C(T)}{v^2} + \frac{D(T)}{v^3} + \cdots \tag{1-6}$$

in which B, C, D, ... are the second, third, fourth, ... virial coefficients. For some purposes, it is also convenient to write this expression in terms of powers of the pressure:

$$\frac{pv}{RT} = 1 + B'(T)p + C'(T)p^2 + D'(T)p^3 + \cdots \qquad (1-7)$$

in which $B' = B/RT$, and $C' = (C - B^2)/(RT)^2$, etc.

The virial coefficients are functions of temperature only, and they are given as integrals which contain the inter-molecular potential function ϕ (energy of interaction between a pair of molecules). For angle-independent potentials functions, the second and third virial coefficients are given by:

$$B(T) = 2\pi\tilde{N} \int_0^\infty f_{12} r_{12}^2 \, dr_{12} \qquad (1-8)$$

$$C(T) = -\frac{8\pi\tilde{N}^2}{3} \iiint f_{12} f_{13} f_{23} r_{12} r_{13} r_{23} \, dr_{12} \, dr_{13} \, dr_{23} \qquad (1-9)$$

where

$$\tilde{N} = \text{Avogadro's number}$$
$$r = \text{inter-molecular distance}$$
$$k = \text{Boltzmann constant} = \mathcal{R}/\tilde{N}$$
$$f_{12} = \exp\left\{\left[-\phi(r_{12})/kT\right] - 1\right\}, \text{ etc.}$$

The second virial coefficient describes basically the deviations from the ideal gas law due to the molecular binary collisions, while the third virial coefficient describes basically the deviations due to molecular ternary collisions. Thus, as the density of a gas is increased, more virial coefficients are needed to account for the deviations. For an ideal or perfect gas, all inter-molecular forces are being neglected; therefore, all virial coefficients are zero. In this case, Eq. (1-7) reduces to Eq. (1-5).

[1-3] FIRST LAW OF THERMODYNAMICS

Briefly speaking, the first law of thermodynamics is a statement of conservation of energy. If a system undergoes a small thermodynamic change at near equilibrium conditions and if the quantity

of heat energy entering the system through the walls is dQ, while the volume is increased dv by doing external work dW against the external pressure p, the change in internal energy dE is:

$$dE = dQ - p\,dv \ . \qquad (1-10)$$

This is to say that the system exchanges its energy with its surroundings by taking in heat energy dQ and by doing external work dW which is equal to pdv. If the heat dQ is added at constant volume where $dv = 0$, no external work dW is done; all the heat added goes to increase the internal energy dE of the gas.

[1-3.1] Specific Heats

If heat dQ is added to a gas and the temperature rise dT is observed, the rate of heat addition per degree temperature rise, per unit mass of gas, is called specific heat. Its value will depend on the type of process of heat addition, *i.e.,* its path in the p-v diagram. In particular, it will have one value, c_v, if the heat is added under constant volume process; and another, c_p, if the heat is added at constant pressure process.

[1-3.2] Internal Energy

A relationship between specific heat at constant volume c_v and the internal energy E exists. It is from the first law of thermodynamics:

$$dE = dQ - p\,dv \ . \qquad (1-10)$$

Since internal energy E of a gas is a function of its state, and therefore it is of any two of the gas parameters (v, T, p), it can be written:

$$dE = \left(\frac{\partial E}{\partial v}\right)_T dv + \left(\frac{\partial E}{\partial T}\right)_v dT \ . \qquad (1-11)$$

Combining Eqs. (1-10) and (1-11), one obtains:

$$\left(\frac{\partial E}{\partial v}\right)_T dv + \left(\frac{\partial E}{\partial T}\right)_v dT = dQ - p\,dv \ . \qquad (1-12)$$

If heat is added under constant volume $dv = 0$, Eq. (1-12) becomes:

$$\left(\frac{\partial E}{\partial T}\right)_v = \left(\frac{\partial Q}{\partial T}\right)_v = c_v . \tag{1-13}$$

Therefore, the internal energy for a perfect gas can be written:

$$dE = c_v \, dT . \tag{1-14}$$

If C_v is a constant,

$$E = \int c_v \, dT + E_0 = c_v T + E_0 . \tag{1-15}$$

Here E_0 is a referenced ground zero energy. Equation (1-13) also shows that when heat is added under constant volume, all the head added goes into increasing the internal energy dE of the gas.

[1-3.3] Relationship Between Specific Heats c_p and c_v

The specific heat at constant pressure c_p can be obtained also by writing Eq. (1-10) into:

$$c_v \, dT = dQ - p \, dv + v \, dp - v \, dp$$

$$\therefore dQ = c_v \, dT + d(pv) - v \, dp . \tag{1-16}$$

If heat is added under constant pressure, $dp = 0$, so

$$\left(\frac{dQ}{dT}\right)_p = \left(\frac{\partial Q}{\partial T}\right)_p = c_p = c_v + \frac{d(pv)}{dT} . \tag{1-17}$$

For a perfect gas, $pv = RT$, thus

$$c_p = c_v + R \quad \text{or} \quad R = c_p - c_v . \tag{1-18}$$

The ratio of specific heats, k, is usually defined as:

$$k = \frac{c_p}{c_v} \quad c_p = R\left(\frac{k}{k-1}\right). \tag{1-19}$$

[1-3.4] Enthalpy

Another function, h, can be defined by letting

$$h = pv + E . \tag{1-20}$$

Under this definition, h represents the total heat content or total heat of the gas, and it is customarily referred to as the enthalpy of the gas. With enthalpy defined, Eq. (1-10) can be rewritten as:

$$dQ = dE + p \, dv = dE + d(pv) - v \, dp$$

$$dQ = dh - v \, dp \, .$$

$$(1-21)$$

Therefore, if heat is added under constant pressure, $dQ = dh$; that is, all the heat added goes into increasing its enthalpy. Therefore, Eq. (1-21) becomes:

$$\left(\frac{dQ}{dT}\right)_p = \left(\frac{\partial Q}{\partial T}\right)_p = c_p = \frac{dh}{dT} \qquad (1-22)$$

or

$$dh = c_p \, dT$$

When c_p is constant, Eq. (1-22) results in:

$$h = \int c_p \, dT + h_0 = c_p T + h_0 \, .$$

Here h_0 is a referenced ground zero enthalpy. (If the enthalpy is measured from its ground zero value at $T = 0$, $h = c_p T$.)

[1-3.5] Entropy

A mathematical property called entropy s has considerable use in thermodynamics. It is a combination of certain physical properties of gases in such a way that an equation containing Eqs. (1-10) or (1-21) can be integrated only as a function of the initial and final states of gases and not of the type of process from one state to another. This can be done for an ideal or perfect gas. Dividing Eq. (1-21) by temperature T and using $pv = RT$ relationship, Eq. (1-21) becomes:

$$\frac{dQ}{T} = c_p \frac{dT}{T} - R \frac{dp}{p} \, . \qquad (1-23)$$

The right-hand side of Eq. (1-23) can obviously be integrated immediately. So dQ/T is the combination of certain physical properties of gases which enables one to integrate Eq. (1-23) only as a function of initial and final state of gases and not of the type of process. This quantity, dQ/T, is called entropy, which is defined by:

$$ds = \frac{dQ}{T} \, . \qquad (1-24)$$

The entropy can be given as a function of p and T by integrating Eq. (1-23).

$$s - s_0 = c_p \ln\left(\frac{T}{T_0}\right) - R \ln\left(\frac{p}{p_0}\right).$$

(1-25)

The constant of integration s_0 establishes the datum from which entropy is measured.

[1-3.5.1] Reversible Process

A process is said to be reversible if, after completion of the process, the initial states of the system taking part in the process can be restored. This requires zero changer of entropy, *i.e.*, $s = s_0$.

[1-3.5.2] Adiabatic Process

An adiabatic process is one in which no external heat is taken in or given out of a system.

[1-3.5.3] Isentropic Process

A process which is both reversible and adiabatic is called an isentropic process. In other words, a process with no external heat addition from outside the system is called an adiabatic process. However, this does not necessarily mean that $dQ = 0$, because internal heat may arise from dissipation of kinetic energy into heat inside the gas by viscous effect. Therefore, a process of both adiabatic (external heat addition is zero) and reversible (internal heat addition is zero or a friction-free process or a process with zero change of entropy) is an isentropic process. Most processes occurring are adiabatic, but not all are isentropic.
For an isentropic process where $ds = 0$, Eq. (1-25) becomes

$$\left(\frac{T}{T_0}\right) = \left(\frac{p}{p_0}\right)^{R/c_p} = \left(\frac{p}{p_0}\right)^{(k-1)/k}$$

(1-26)

or

$$pv^k = p_0 v_0^k = \text{constant}$$

(1-27)

or

$$\frac{p}{\rho^k} = \frac{p_0}{\rho_0^k} = \text{constant} .$$

(1-28)

[1- 3.5.4] Polytropic Process

To broaden the isentropic (reversible–adiabatic) concept into any reversible process, a polytropic process can be defined as a reversible process which conforms the relationship of $pv^n = p_0 v_0^n = $ constant. Here, both mechanical and fluid friction, naturally, do not exist in the reversible process. At any point, the process can be reversed, returning on the same path and restoring all properties to their initial values. The exponent n is the characteristic which indicates the character of the reversible process. The four special cases of n are:

1) Constant volume process $\qquad\qquad\qquad\qquad n = \infty$
2) Constant pressure process $\qquad\qquad\qquad\; n = 0$
3) Isothermal process $\qquad\qquad\qquad\qquad\quad\; n = 1$
4) Isentropic process $\qquad\qquad\qquad\qquad\quad\; n = k$

Other values of n may be considered as the polytropic process in general. From $pv^n = p_0 v_0^n = $ constant, relationships similar to Eqs. (1-26) and (1-28) may be derived for polytropic process. They are:

$$\left(\frac{T}{T_0}\right) = \left(\frac{p}{p_0}\right)^{(n-1)/n} \tag{1-29}$$

$$\frac{p}{\rho^n} = \frac{p_0}{\rho_0^n} = \text{constant} . \tag{1-30}$$

[1- 3.5.4. 1] Work Done

The work done of a polytropic process (per unit mass) is determined from the integration of expression

$$\int_1^2 dW = \int_1^2 p \, dv . \tag{1-31}$$

Since $pv^n = p_1 v_1^n = p_2 v_2^n = $ constant, one obtains:

$$W_{1 \to 2} = p_1 v_1^n \int_1^2 v^{-n} \, dv = \frac{p_2 v_2 - p_1 v_1}{1 - n}$$

$$= \frac{R(T_2 - T_1)}{1 - n} \text{ ft.-\#} . \tag{1-32}$$

Substitution of corresponding values of n into Eq. (1-32) provides the work done for the special cases given above, with the exception

of the isothermal process for which $n = 1$ makes Eq. (1-32) indeterminate, and therefore $pv = p_1v_1 = p_2v_2 = $ constant (for the isothermal process) must be substituted directly into Eq. (1-31) for work done:

$$W_{1 \to 2} = p_1v_1 \int \frac{dv}{v} = p_1v_1\ln\left(\frac{v_2}{v_1}\right) = p_1v_1\ln\left(\frac{p_1}{p_2}\right) = RT\ln\left(\frac{v_2}{v_1}\right)$$

$$= RT\ln\left(\frac{p_1}{p_2}\right) \text{ ft.-\# .} \tag{1-33}$$

[1-3.5.4.1.1] Special Case for Isentropic Case where $n = k$

$$W_{1 \to 2} = \frac{R}{1 - k}(T_2 - T_1) = \frac{(c_p - c_v)}{1 - c_p/c_v}(T_2 - T_1) = c_v(T_1 - T_2) . \tag{1-34}$$

[1-3.5.4.1.2] Heat Added

Heat added, dQ, may be determined from the first law of thermodynamics, Eq. (1-10):

$$dQ = dE + p\,dv = c_v\,dt + p\,dv . \tag{1-10}$$

If a polytropic process is assumed,

$$pv^n = p_1v_1^n = \text{constant} . \tag{1-35}$$

Substituting Eq. (1-35) into Eq. (1-10), one obtains the heat addition, Q, from state 1 to state 2:

$$Q_{1 \to 2} = \left[c_v + \frac{R}{1 - n}\right](T_2 - T_1) . \tag{1-36}$$

Substitution of corresponding values of n into Eq. (1-36) provides the heat addition for the special cases given previously ($n = \infty$, for constant volume process; $n = 0$, for constant pressure process; $n = k$, for isentropic process), with the exception of the isothermal process for which $n = 1$ makes Eq. (1-34) indeterminate, and, therefore, $p_1v_1 = p_2v_2 = pv = $ constant (for isothermal process) must be substituted into Eq. (1-10) directly, which results in a heat addition Q from state 1 to state 2 equal to:

$$Q_{1 \to 2} = RT\ln\left(\frac{p_1}{p_2}\right) = RT\ln\left(\frac{v_2}{v_1}\right). \tag{1-37}$$

[1-3.6] Mixture of Gases

Dalton's law states that the total pressure p of a mixture of gases is equal to the sum of the partial pressures $p_1, p_2, p_3, \ldots$ of the gas constituents $1, 2, 3, \ldots$ when each gas constituent occupies the same volume V of the mixture at the same temperature T as that of the gas mixture. Mathematically speaking, Dalton's law says that:

$$p = p_1 + p_2 + p_3 \cdots$$

Here $p_1 V = m_1 R_1 T$
$$p_2 V = m_2 R_2 T$$
$$p_3 V = m_3 R_3 T$$
$$\cdot$$
$$\cdot$$
$$\cdot$$

and $m_1, m_2, m_3, \ldots$ are the mass of the gas constituent $1, 2, 3, \ldots$ and $R_1, R_2, R_3, \ldots$ are the gas constant of the gas constituent. Combining the above expressions, one may write:

$$\left(\sum p_i\right) V = \left(\sum m_i R_i\right) T .$$

If one defines an equivalent gas constant R for the mixture of gas as

$$R = \frac{\sum m_i R_i}{\sum m_i} = \frac{\sum m_i R_i}{m} , \tag{1-38}$$

we have

$$pV = mRT , \tag{1-39}$$

which has the same form as the equation of state of a single gas. The only difference here is that:

$$m = m_1 + m_2 + m_3 + \cdots = \text{total mass of the mixture of gases}$$
$$p = p_1 + p_2 + p_3 + \cdots = \text{total pressure of the mixture of gases} .$$

The mole fraction X_i of a constituent i of the mixture of gases is defined as the ratio of the number of moles N_i of that constituent i in the mixture to the total number of moles ΣN_i of all constituents of the mixture of gases; namely,

$$X_i = \frac{N_i}{\sum N_i} = \frac{N_i}{N} . \qquad (1\text{--}40)$$

Here N is the total number of moles of the mixture of gases.

$$N = N_1 + N_2 + N_3 + \cdots = \sum N_i \qquad (1\text{--}41)$$

Since the number of moles N_i of the constituent i is equal to the ratio of the mass m_i to the molecular weight M_i of the constituent, i we may write:

$$N_i = \frac{m_i}{M_i} . \qquad (1\text{--}42)$$

Substituting Eq. (1–40) into Eq. (1–42), one obtains:

$$NX_i = \frac{m_i}{M_i} . \qquad (1\text{--}43)$$

We may now define an equivalent molecular weight. M of the mixture of gases as:

$$M = \frac{\sum m_i}{\sum N_i} = \frac{\sum X_i M_i}{\sum N_i} = \frac{m}{N} . \qquad (1\text{--}44)$$

Similarly, the total internal energy mE of a mixture of gases is equal to the sum of the partial internal energy m_iE_i of the constituent gases:

$$mE = m_1E_1 + m_2E_2 + m_3E_3 + \cdots = \sum m_iE_i . \qquad (1\text{--}45)$$

Here $E_i = \displaystyle\int c_{v_i}\, dT + E_{0_i} .$

Similarly, the total enthalpy mh of a mixture of gases is equal to the sum of the partial enthalpy m_ih_i of the constituent gases:

$$mh = m_1h_1 + m_2h_2 + m_3h_3 + \cdots = \sum m_ih_i \qquad (1\text{--}46)$$

Here $h_i = \displaystyle\int c_{p_i}\, dT + h_{0_i} .$

Similarly, the total entropy ms of a mixture of gases is equal to the sum of the partial entropy m_is_i of the constituent gases:

$$ms = m_1 s_1 + m_2 s_2 + m_3 s_3 + \cdots = \sum m_i s_i \,. \qquad (1\text{-}47)$$

Here

$$s_i = \int c_{p_i} \frac{dT}{T} - R_i \int \frac{dp_i}{p_i} + s_{0_i} \,.$$

From Eqs. (1-45) and (1-46) one obtains the equivalent specific heats c_v and c_p of the mixture of gases:

$$c_v = \frac{1}{m} \sum m_i c_{v_i} \qquad (1\text{-}48)$$

$$c_p = \frac{1}{m} \sum m_i c_{p_i} \,. \qquad (1\text{-}49)$$

It is to be noted here that once the equivalent thermodynamic properties of a gas mixture are determined in terms of the properties of the constituents, the mixture itself may be treated as if it is a single gas.

[1-3.7] Entropy-Enthalpy Diagram

The state of a gas can be fully described by three physical properties (pressure, temperature, and density or specific volume) and three thermodynamic properties (entropy, enthalpy, and internal energy) of the gas. Among these six properties or variables (pressure variable p, temperature variable T, density variable ρ, or specific volume variable v, entropy variable s, enthalpy variable h, and internal energy variable E), only two (any two of the six) are independent variables. Once the numerical values of any two variables are assigned, the numerical values of the rest of the four variables are determined. This is because we have the following four equations for the above-mentioned six unknowns.

1) Equation of State

$$\frac{p}{\rho} = RT \qquad (1\text{-}5)$$

2) Enthalpy

$$h = \int_{T_0}^{T} c_p \, dT + h_0 \qquad (1\text{-}22)$$

3) Internal Energy

$$E = \int_{T_0}^{T} c_v \, dT + E_0 \qquad (1\text{-}14)$$

4) Entropy

$$s = \int \frac{dQ}{T} = \int_{T_0}^{T} c_p \frac{dT}{T} - \int_{T_0}^{T} R \frac{dp}{p} + s_0 \qquad (1\text{-}23)$$

In thermodynamic analysis, it is usually convenient to use entropy s and enthalpy h as the two independent variables. Thermodynamic charts based on variable specific heats using temperature T or enthalpy h as ordinate and entropy s as abscissa, can accordingly be plotted for various gases or mixture of gases. Specific heats c_p and/or c_v versus temperature T are usually known either experimentally from measurement or theoretically from statistical thermodynamics for the gas or mixture of gases concerned. Under ordinary conditions, c_p and c_v are functions of temperature T only (except at very high temperatures where c_p and c_v are slightly pressure dependent):

$$c_p = f_1(T) \qquad (1\text{-}50)*$$

$$c_v = f_2(T) \qquad (1\text{-}51)*$$

Here c_p and c_v as a function of T could be either in the form of a curve or in the form of a mathematical series of T (such as power series, etc.). Substituting Eq. (1-50) into Eq. (1-22) and Eq. (1-51) into Eq. (1-14), one obtains:

$$h = \int_{T_0}^{T} f_1(T) \, dT + h_0 \qquad (1\text{-}52)$$

$$E = \int_{T_0}^{T} f_2(T) \, dT + E_0 \,. \qquad (1\text{-}53)$$

Eqs. (1-52) and (1-53) may be integrated either graphically or numerically. The results give h and E as a function of T. They may be presented in the form of a table such as the air table and gas table of Keenan and Kaye or they may be plotted as a chart or diagram, such as the so-called h-s diagram. However, in order

---

*For an ideal or perfect gas with constant specific heats (independent of temperature T), c_p and c_v are related by Eq. (1-18).

to calculate h and E as functions of temperature T, there is no need to know both c_p and c_v. If, knowing c_p, h may be integrated by Eq. (1-53), E may be calculated from Eq. (1-20) when rewritten as $E = h - RT$. Similarly, if c_v is known, E may be integrated from Eq. (1-53) and h may be calculated from $h = RT + E$. Usually h and E are plotted with T as ordinate (but in different scales) in an h-s diagram. Each value of T corresponds to one value of h and one value of E. For a constant pressure process, say $p_1 = a$ curve, where $dp = 0$, Eq. (1-23) reduces to:

$$s - s_1 = \int_{T_0}^{T} f_1(T) \frac{dT}{T} . \tag{1-54}$$

Eq. (1-54) may be integrated either graphically or numerically from one temperature T_1 to another temperature T for plotting the constant pressure curve on the h-s diagram. The value p is related to the abscissa entropy s, Eq. (1-23), by:

$$s - 0 = \int_{T_0}^{T} \frac{c_p dT}{T} - R \ln\left(\frac{p_1}{14.7}\right).$$

Here temperature T_0 and pressure $14.7 \#/\square''$ are usually arbitrarily chosen as the datum or "zero entropy" point. Any value of temperature and pressure may be chosen as the zero entropy point. By doing this, it changes the absolute value of entropy but does not change the entropy difference between any two states which is our only concern.

Similarly, for a constant specific volume, say $v_1 = b$ curve, Eq. (1-23) may be written into another form as:

$$s - s_1 = \int_{T_1}^{T_2} c_v \frac{dT}{T} + R \int_{v_1}^{v_2} \frac{dv}{v} \tag{1-55}$$

for constant specific volume process, $dv = 0$, one obtains:

$$s - s_1 = \int_{T_1}^{T_2} c_v \frac{dT}{T} . \tag{1-56}$$

The value of v_1 is again related to abscissa s_1 by:

$$s_1 = \int_{T_0}^{T_1} \frac{c_v dT}{T} + R \ln\left(\frac{v_1}{v_0}\right)$$

since zero entropy is chosen at T_0 and $p_0 = 14.7 \#/\square''$, so v_0 at zero entropy point is $v_0 = RT_0/(14.7 \times 144)$.

Equation (1–56) may again be integrated out graphically or numerically and plotted on the *h-s* diagram usually as dotted curves. This completes the basic method of constructing an *h-s* diagram or basic method to construct tables such as the air table or gas table for various gases or mixture of gases.

For an isentropic process, $ds = 0$, one obtains:

$$0 = \int_{T_1}^{T} \frac{c_p \, dT}{T} - R \int_{p_1}^{p} \frac{dp}{p}$$

or

$$\ln\left(\frac{p}{p_1}\right) = \frac{1}{R} \int_{T_1}^{T} \frac{c_p \, dT}{T} .$$

Therefore, for an isentropic process, all the pressure ratios between the two temperatures T_1 and T are always equal.

[1- 3.7.1] Remarks on Entropy- Enthalpy Diagram

It is to be cautioned here that, in general, enthalpy h is a function of temperature T only. In such cases, temperature T is always plotted alongside of h and E (because T is independent of s) in an *h-s* diagram. However, for cases where c_p is a function of both temperature T and pressure p (for example, under high temperature where dissociations occur or where it involves a mixture of gases and vapors, etc.), h becomes a function of both T and p. In such cases, temperature T should be plotted out separately (because T is now a function of h and s) on the *h-s* diagram in a similar manner as the p and v curves are plotted.

[1- 3.8] The Ideal (Reversible) Cycles

Typical engine cycles include: (1) Carnot Cycle which consists of two isothermal processes and two isentropic processes, (2) Otto Cycle which consists of two constant volume processes and two isentropic processes, and (3) Brayton Cycle which consists of two constant pressure processes and two isentropic processes.

[1- 3.9] Cycle Work, Cycle Heat Added, and Cycle Efficiency

Briefly speaking, cycle work is the net summation of the work done to outside by the process or processes concerned. Cycle heat

added is the summation of the heat supplied from outside by the process or processes concerned. Cycle efficiency is the ratio of the cycle work to cycle heat added. Here it is to be remembered that the work done by a process is different for "non-flow" type (such as piston type compression or expansion) from "continuous flow" type (such as continuous flow axial or centrifugal compression or expansion). This may best be illustrated through Eqs. (1-34) and (1-61).

Equation (1-34) gives the isentropic work for "non-flow" or piston type compression or expansion as:

$$W_{1 \to 2} = c_v(T_1 - T_2) \qquad (1\text{-}34)$$

while Eq. (1-61) gives the isentropic work for "continuous flow" or axial or centrifugal flow type compression or expansion as:

$$W_{1 \to 2} = c_p(T_1 - T_2) \ . \qquad (1\text{-}61)$$

The ratio of work done by Eq. (1-34) to work done by Eq. (1-61) is $1/k$. The compression or expansion work from one temperature T_1 to another temperature T_2 is different by the ratio of $1/k$ from piston type compression or expansion to axial or centrifugal flow type compression or expansion.

[1-4] STEADY FLOW ENERGY EQUATION

Assume a device through which there is a steady flow of fluid mass, m. Heat, mQ, is supplied to the device, and mechanical work mW, is done by the device. The fluid enters at an elevation of Z_1 with a velocity V_1 under a pressure p_1; it leaves at an elevation Z_2 with a velocity V_2 at a pressure p_2. The fluid enters the device against a pressure p_1 inside the device. The work done by the fluid inside the device on the entering fluid is $p_1 v_1$ per unit mass. The network done by the system, while a mass flows m into and out of the device, is therefore:

$$m(p_2 v_2 - p_1 v_1)$$

where v_1 and v_2 are the specific volumes (volume per unit mass) occupied by the mass on entering and leaving. The increase in internal energy of its mass is

$$m(E_2 - E_1)$$

where E_1 and E_2 are the internal energy per unit mass at entrance and exit respectively. In addition to the change in internal energy, the kinetic energy of the fluid has changed by

$$\frac{1}{2} m \left(V_2{}^2 - V_1{}^2 \right)$$

and its potential energy has changed by:

$$mg(Z_2 - Z_1)$$

where g is the local acceleration of gravity.

Equating the net energy supplied to the fluid to the net change in the total energy of the fluid, one obtains:

$$mQ - mW - m(p_2 v_2 - p_1 v_1) = m(E_2 - E_1)$$
$$+ \frac{1}{2} m \left(V_2{}^2 - V_1{}^2 \right) + mg(Z_2 - Z_1) \ .$$

Or, dividing through by m and rearranging terms, one obtains:

$$\left(E_1 + p_1 v_1 + \frac{1}{2} V_1{}^2 + gZ_1 \right) - \left(E_2 + p_2 v_2 + \frac{1}{2} V_2{}^2 + gZ_2 \right) - W + Q = 0$$

since $(E_1 + p_1 v_1)$ and $(E_2 + p_2 v_2)$ are respectively the enthalpies h_1 and h_2 at the entrance and exit, so finally:

$$\left(h_1 + \frac{1}{2} V_1{}^2 + gZ_1 \right) - \left(h_2 + \frac{1}{2} V_2{}^2 + gZ_2 \right) - W + Q = 0 \ . \quad (1\text{-}57)$$

Equation (1-57) is the steady flow energy equation. In most propulsion system work, the change in elevation is rather insignificant, so the energy equation becomes:

$$\left(h_1 + \frac{1}{2} V_1{}^2 \right) - \left(h_2 + \frac{1}{2} V_2{}^2 \right) - W + Q = 0 \ . \quad (1\text{-}58)$$

[1-4.1] Stagnation Enthalpy or Total Enthalpy, H

Stagnation enthalpy or total enthalpy H is defined as the enthalpy where the velocity is equal to zero, or, mathematically speaking,

$$H = h + \frac{1}{2} V^2 \ . \quad (1\text{-}59)$$

Using stagnation enthalpies at entrance and exit, Eq. (1-58) reduces to

$$H_1 - H_2 - W + Q = 0 \ . \quad (1\text{-}60)$$

[1-4.2] Application of Steady Flow Energy Equation to Compressor
and Turbine Analysis

The heat loss Q to its surrounding is generally very small,
and, therefore it can be neglected. Thus,

$$W = H_1 - H_2 \qquad (1\text{-}61)$$

when c_p is treated as a constant, Eq. (1-61) becomes:

$$W = c_p(T_1 - T_2) \ .$$

The shaft work given out by a turbine (or the negative work which
is the work supplied to a compressor) per unit mass of flow there-
fore is the total enthalpy difference between its inlet and outlet.

$$W_{\text{turbine}} = H_1 - H_2$$

$$W_{\text{compressor}} = H_2 - H_1$$

[1-5] ONE-DIMENSIONAL STEADY FLOW ANALYSIS

Many propulsion problems may be studied by a one-dimensional
steady flow system. A steady flow system whose cross-sectional
area is changing very slowly and whose axis of flow has a very
small change of curvature along the system is considered a one-
dimensional steady flow system. In a one-dimensional steady flow
system, the variation of all parameters across the cross-section
of the flow may be neglected, and all parameters are therefore a
function only of the coordinate along the axis of the flow, say x.
Many flows which are not exactly one-dimensional in this sense
can be approximated by a one-dimensional flow in which the veloc-
ities, pressures and densities are taken to be the proper averages
of those in the real flow.

[1-5.1] One-Dimensional Energy Equation

For a steady flow in the absence of heat dQ and mechanical
work dW, Eq. (1-60) reduces to

$$H_1 = H_2 = \text{constant} \qquad (1\text{-}62)$$

or

$$\frac{V_1{}^2}{2} + h_1 = \frac{V_2{}^2}{2} + h_2 = H_1 = H_2 \ . \qquad (1\text{-}63)$$

For constant c_p Eqs. (1-62) and (1-63) may be rewritten as:

$$c_p T_1 = c_p T_2 \tag{1-64}$$

$$\frac{1}{2} V_1{}^2 + c_p t_1 = \frac{1}{2} V_2{}^2 + c_p t_2 = \frac{1}{2} V^2 + c_p t = c_p T = \text{constant} \tag{1-65}$$

or, written in differential form,

$$V dV + c_p dt = 0 \ .$$

Here T indicates stagnation temperature, while t indicates static temperature. Using Eqs. (1-5) and (1-18), Eq. (1-65) may be rewritten as:

$$\frac{1}{2} V^2 + \frac{k}{k-1} \frac{p}{\rho} = \frac{k}{k-1} \frac{P}{\bar{\rho}} \ . \tag{1-66}$$

Here P and $\bar{\rho}$ are the stagnation pressure and density, respectively.

1-5.2 One-Dimensional Continuity Equation

Conservation of mass requires that

$$\rho_1 V_1 A_1 = \rho_2 V_2 A_2 = \rho V A = \text{constant} \ . \tag{1-67}$$

Equation (1-67) may be written into its differential form:

$$\frac{d\rho}{\rho} + \frac{dV}{V} + \frac{dA}{A} = 0 \ . \tag{1-68}$$

[1-5.3] One-Dimensional Momentum Equation Without Fluid Shearing or Friction Losses

Writing Newton's law as it applies to a fluid particle moving along a stream tube in one-dimensional flow, one obtains:

$$\rho A V dV + A dp = 0 \tag{1-69}$$

or

$$\rho V dV + dp = 0 \ .$$

[1- 5.3. 1] One-Dimensional Momentum Equation With Fluid Shearing or Friction Losses

The frictional shearing force dF may be defined as:

$$dF = f \frac{1}{2} \rho V^2 dA_w = f \frac{1}{2} \rho V^2 y dx \ .$$

Here F = frictional shearing force, f = frictional coefficient which is usually referred to as the Fanning friction factor, A_w = wetted area, and y = perimeter of the cross-section. If we define a hydraulic diameter D of a duct of any shape as four times the ratio of cross-sectional area A to the perimeter y (the hydraulic diameter equals to the actual diameter if the cross-section is a circle), we have:

$$dF = f \frac{1}{2} \rho V^2 \left(\frac{4A}{4A}\right) y dx = \frac{1}{2} \rho V^2 A \left(\frac{4f}{D}\right) dx \ .$$

Therefore, the net force on the fluid element becomes:

$$-Adp - A \frac{1}{2} \rho V^2 \ \frac{4f}{D} \ dx \ .$$

Since the rate of change of momentum is $\rho AVdV$, from Newton's law, we have:

$$\rho AVdV = -Adp - A \frac{1}{2} \rho V^2 \left(\frac{4f}{D}\right) dx$$

$$\rho VdV + dp + \frac{1}{2} \rho V^2 \left(\frac{4f}{D}\right) dx = 0 \ . \tag{1-69a}$$

[1- 5.4] Speed of Sound

Assume that a steady flow at velocity V, pressure p and density ρ suddenly encounters a discontinuity surface. After passing through the discontinuity surface, the flow has acquired increments in velocity, pressure, and density of dV, dp, and $d\rho$, respectively. The equations which the increments must satisfy are then:

$$\rho VdV + dp = 0$$

$$\frac{dV}{V} + \frac{d\rho}{\rho} = 0 \tag{1-69}$$

$$VdV + c_p dt = 0 \ . \tag{1-68}$$

From Eqs. (1-69) and (1-68) one obtains:

$$\frac{dp}{\rho} = c_p dt = \frac{c_p}{R} d\left(\frac{p}{\rho}\right) = \frac{k}{k-1} d\left(\frac{p}{\rho}\right) \ .$$

This solution gives $p =$ constant ρ^k, so the change of state through this small discontinuity or small wave must be isentropic. If ρdV is eliminated from the above three equations, one obtains:

$$V^2 = \frac{dp}{d\rho} \ . \tag{1-70}$$

Therefore, for a stationary discontinuity or disturbance to exist in a one-dimensional steady flow, the flow can have only one velocity V. If a uniform velocity V in the opposite direction is now imposed on the steady flow, the discontinuity will appear as a wave advancing at speed V in an undisturbed fluid. A sound wave is an example of such a small wave, and the quantity,

$$a = \sqrt{\frac{dp}{d\rho}} \ , \tag{1-71}$$

is called the local speed of sound. The ratio $dp/d\rho$ can be evaluated as follows:

$$p = \text{constant } \rho^k$$

$$\frac{dp}{d\rho} = \frac{kp}{\rho} = kgRt \tag{1-72}$$

or

$$a = \sqrt{kgRt} \ . \tag{1-73}$$

[1-5.5] Mach Number

Mach number M is defined as:

$$M = \frac{V}{a} \ . \tag{1-74}$$

[1-5.6] Another Form of Energy Equation

The energy equation can now be written in several equivalent forms, using the definition of the speed of sound, Eq. (1-73),

$$\frac{1}{2}V^2 + \frac{k}{k-1}\frac{p}{\rho} = \frac{1}{2}V^2 + \frac{1}{k-1}a^2 = \frac{1}{k-1}a_0^2 \qquad (1\text{-}75)$$

where a_0 is stagnation speed of sound, which is equal to $\sqrt{kgRt}$. Using the fact that $a/a_0 = t/T$ and Eq. (1-24), Eq. (1-75) can be written as:

$$\left(\frac{T}{t}\right) = \left[1 + \frac{k-1}{2}M^2\right] \qquad (1\text{-}76)$$

[1-5.7] Isentropic Flow Equations

If the flow is isentropic, the pressure, density, and temperature may be written into the following forms:

$$\left(\frac{T}{t}\right) = \left(\frac{P}{p}\right)^{\frac{k-1}{k}} = \left(\frac{\bar{\rho}}{\rho}\right)^{k-1} . \qquad (1\text{-}77)$$

Therefore

$$\left(\frac{P}{p}\right) = \left[1 + \frac{k-1}{2}M^2\right]^{\frac{k}{k-1}} \qquad (1\text{-}78)$$

$$\left(\frac{\bar{\rho}}{\rho}\right) = \left[1 + \frac{k-1}{2}M^2\right]^{\frac{1}{k-1}} . \qquad (1\text{-}79)$$

For an isentropic flow in a channel of varying cross-section A, the momentum equation may be rewritten, using $dp/d\rho = a^2$:

$$VdV + a^2\frac{d\rho}{\rho} = 0 . \qquad (1\text{-}80)$$

Eliminating $d\rho/\rho$ from the continuity equation, one obtains:

$$\frac{dV}{V}\left(\frac{V^2}{a^2} - 1\right) - \frac{dA}{A} = 0 \qquad (1\text{-}81)$$

or

$$\frac{dV}{V}(1 - M^2) = -\frac{dA}{A} . \qquad (1\text{-}82)$$

This equation gives the relation between a change in channel cross-section area A and the resulting change in speed V. At subsonic speeds, a decrease in area (dA less than zero) produces an increase in speed. When density changes are small or negligible, this must obviously be the case. When the Mach number M exceeds 1, however, the situation is reversed. At these speeds the density decreases so rapidly for a given speed increase that the channel must actually expand as the speed rises. This can be seen by the momentum equation,

$$\frac{d\rho}{\rho} = -M^2 \frac{dV}{V},$$ (1-83)

from which it is apparent that the higher the M, the greater the density ρ change for a given speed change.

From Eqs. (1-68), (1-72), (1-74) and (1-82) the changes in Mach number, density, pressure and temperature with area change may be obtained.

$$\frac{dM}{M} = -\frac{1 + \frac{k-1}{2}M^2}{1 - M^2} \frac{dA}{A}$$ (1-84)

$$\frac{d\rho}{\rho} = \frac{M^2}{1 - M^2} \frac{dA}{A}$$ (1-85)

$$\frac{dp}{p} = \frac{kM^2}{1 - M^2} \frac{dA}{A}$$ (1-86)

$$\frac{dt}{t} = \frac{(k-1)M^2}{1 - M^2} \frac{dA}{A}$$ (1-87)

$$\frac{dV}{V} = -\frac{1}{1 - M^2} \frac{dA}{A}$$ (1-82)

If, in terms of Mach number M, the above equations may be rewritten as:

$$\frac{dA}{A} = -\frac{1 - M^2}{2\left[1 + \frac{k-1}{2}M^2\right]} \frac{dM^2}{M^2}$$ (1-88)

$$\frac{d\rho}{\rho} = \frac{-M^2}{2\left[1 + \frac{k-1}{2}M^2\right]} \frac{dM^2}{M^2}$$ (1-89)

$$\frac{dp}{p} = - \frac{kM^2}{2\left[1 + \dfrac{k-1}{2}M^2\right]} \frac{dM^2}{M^2} \qquad (1\text{-}90)$$

$$\frac{dt}{t} = - \frac{(k-1)M^2}{2\left[1 + \dfrac{k-1}{2}M^2\right]} \frac{dM^2}{M^2} \qquad (1\text{-}91)$$

$$\frac{dV}{V} = \frac{1}{2\left[1 + \dfrac{k-1}{2}M^2\right]} \frac{dM^2}{M^2} \qquad (1\text{-}92)$$

The equations may be integrated between any two sections, A_1 and A_2. For example, integrating Eq. (1-84) or (1-88) gives:

$$\frac{A_1}{A_2} = \frac{M_2}{M_1}\left[\frac{1 + \dfrac{k-1}{2}M_1^2}{1 + \dfrac{k-1}{2}M_2^2}\right]^{\frac{k+1}{2(k-1)}} \qquad (1\text{-}93)$$

If the integration is carried out between one section where $M = 1$ and $A = A^*$ (throat section) and any other section where $M = M$ and $A = A$, we have

$$\frac{A}{A^*} = \frac{1}{M}\left[\frac{1 + \dfrac{k-1}{2}M^2}{\dfrac{k+1}{2}}\right]^{\frac{k+1}{2(k-1)}} \qquad (1\text{-}94)$$

Similarly, we have

$$\frac{\rho_1}{\rho_2} = \left[\frac{1 + \dfrac{k-1}{2}M_2^2}{1 + \dfrac{k-1}{2}M_1^2}\right]^{\frac{1}{k-1}} \qquad (1\text{-}95)$$

$$\frac{\rho}{\rho^*} = \left[\frac{\dfrac{k+1}{2}}{1 + \dfrac{k-1}{2}M^2}\right]^{\frac{1}{k-1}} \tag{1-96}$$

$$\frac{p_1}{p_2} = \left[\frac{1 + \dfrac{k-1}{2}M_2^2}{1 + \dfrac{k-1}{2}M_1^2}\right]^{\frac{k}{k-1}} \tag{1-97}$$

$$\frac{p}{p^*} = \left[\frac{\dfrac{k+1}{2}}{1 + \dfrac{k-1}{2}M^2}\right]^{\frac{k}{k-1}} \tag{1-98}$$

$$\frac{t_1}{t_2} = \left[\frac{1 + \dfrac{k-1}{2}M_2^2}{1 + \dfrac{k-1}{2}M_1^2}\right] \tag{1-99}$$

$$\frac{t}{t^*} = \left[\frac{\dfrac{k+1}{2}}{1 + \dfrac{k-1}{2}M^2}\right] \tag{1-100}$$

$$\frac{V_1}{V_2} = \frac{M_1}{M_2}\left[\frac{1 + \dfrac{k-1}{2}M_2^2}{1 + \dfrac{k-1}{2}M_1^2}\right]^{\frac{1}{2}} \tag{1-101}$$

$$\frac{V}{V^*} = M\left[\frac{\dfrac{k+1}{2}}{1 + \dfrac{k-1}{2}M^2}\right]^{\frac{1}{2}} \tag{1-102}$$

The ratios of pressure, density, and temperature at the throat to those in the reservoir (stagnation value) are of particular interest. These ratios, sometimes called the critical ratios, are obtained from Eqs. (1-77), (1-78), and (1-79) by inserting $M = 1$.

$$\frac{\rho^*}{\bar{\rho}} = \left(\frac{2}{k + 1}\right)^{\frac{1}{k - 1}} \qquad \frac{p^*}{P} = \left(\frac{2}{k + 1}\right)^{\frac{k}{k - 1}} \qquad \frac{t^*}{T} = \left(\frac{2}{k + 1}\right)$$

$$(1\text{-}103)$$

For air, with $k = 1.4$, these become:

$$\frac{\rho^*}{\bar{\rho}} = 0.634 \qquad \frac{p^*}{P} = 0.528 \qquad \frac{t^*}{T} = 0.833$$

$$(1\text{-}104)$$

Let us now derive a useful relation between the flow per unit area and stagnation temperature, stagnation pressure and Mach number. Starting with the equation of continuity, one obtains:

$$\frac{w}{A} = \rho V = \frac{p}{Rt} V = \frac{pV}{\sqrt{gkRt}} \sqrt{\frac{kg}{R}} \sqrt{\frac{T}{t}} \frac{1}{\sqrt{T}}$$

$$= \sqrt{\frac{kg}{R}} \frac{p}{\sqrt{T}} M \sqrt{1 + \frac{k - 1}{2} M^2} \qquad (1\text{-}105)$$

If we now put p in terms of P, one obtains:

$$\frac{w}{A} = \sqrt{\frac{kg}{R}} \frac{P}{\sqrt{T}} \frac{M}{\left[1 + \dfrac{k - 1}{2} M^2\right]^{\frac{k + 1}{2(k - 1)}}} \qquad (1\text{-}106)$$

or

$$\frac{W\sqrt{T}}{PA} = \sqrt{\frac{kg}{R}} \frac{M}{\left[1 + \dfrac{k - 1}{2} M^2\right]^{\frac{k + 1}{2(k - 1)}}} \qquad (1\text{-}106a)$$

Differentiating Eq. (1-106) with respect to M and setting it equal to zero, one finds that the maximum value of (w/A) occurs at $M = 1$. Therefore, the cross-sectional area A, for isentropic flow, passes

through a minimum value at a Mach number equal to unity. $(w/A)_{max}$, which occurs at $M = 1$, is equal to

$$\left(\frac{w}{A}\right)_{max.} = \left(\frac{w}{A^*}\right) = \sqrt{\frac{kg}{R}\left(\frac{2}{k+1}\right)^{\frac{k+1}{k-1}}} \quad \frac{P}{\sqrt{T}}$$

(1-107)

When we use A^* (where $M = 1$) as a reference area, we have

$$\frac{A}{A^*} = \frac{\left(\frac{w}{A^*}\right)}{\left(\frac{w}{A}\right)} = \frac{1}{M}\left[\frac{1 + \frac{k-1}{2}M^2}{\frac{k+1}{2}}\right]^{\frac{k+1}{2(k-1)}}$$

(1-108)

Here A^* is the throat area. The area ratio is always greater than unity, and for any given value of A/A^* there always correspond two values of M, *i.e.,* one for subsonic flow, the other for supersonic flow.

[1-6] NORMAL SHOCK WAVES AND RAYLEIGH AND FANNO LINES

Assume air in a channel at pressure p_1, density ρ_1, and velocity V_1, suddenly encounters a stationary discontinuity. Such a discontinuity, if it exists, is called a shock wave, since the velocity and pressure changes through it will occur discontinuously as a jump or shock. When the discontinuity is normal to the flow, it is called a normal shock wave. The momentum equation states that the increase in momentum of the gas per unit time equals the net force acting on the gas in the same direction. In the present case, this is

$$\rho_2 V_2{}^2 - \rho_1 V_1{}^2 = p_1 - p_2$$

(1-60)

The continuity equation is

$$\rho_1 V_1 = \rho_2 V_2$$

(1-67)

The energy equation is

$$\frac{V_1{}^2}{2} + \frac{k}{k-1}\frac{p_1}{\rho_1} = \frac{V_2{}^2}{2} + \frac{k}{k-1}\frac{p_2}{\rho_2} = c_p T_1 = c_p T_2$$

(1-66)

The equation of state is

$$\frac{p_1}{\rho_1} = Rt_1 \qquad\qquad \frac{p_2}{\rho_2} = Rt_2 \qquad\qquad (1\text{-}6)$$

There are four equations with four unknowns, V_2, ρ_2, p_2 and t_2; therefore, they can be solved. Dividing the momentum equation by the continuity equation and multiplying by $(V_1 + V_2)$, one obtains:

$$\left(V_2{}^2 - V_1{}^2\right) = (p_1 - p_2)\left(\frac{1}{\rho_1} + \frac{1}{\rho_2}\right)$$

Substituting into the energy equation, one obtains, after simplification,

$$\frac{p_2}{p_1} = \frac{\dfrac{k+1}{k-1}\dfrac{\rho_2}{\rho_1} - 1}{\dfrac{k+1}{k-1} - \dfrac{\rho_2}{\rho_1}} \qquad\qquad (1\text{-}109)$$

or

$$\frac{\rho_2}{\rho_1} = \frac{V_1}{V_2} = \frac{1 + \dfrac{k+1}{k-1}\dfrac{p_2}{p_1}}{\dfrac{k+1}{k-1}\dfrac{p_2}{p_1}} \qquad\qquad (1\text{-}110)$$

Equations (1-109) and (1-110) are called Rankine and Hugoniot relationship, and they are different from the isentropic relationship between pressure and density changes. The velocity change across the shock can be found by writing the momentum equation as:

$$V_1 - V_2 = \frac{p_2}{\rho_2 V_2} - \frac{p_1}{\rho_1 V_1} \qquad\qquad (1\text{-}111)$$

By using the energy equation in the form of Eq. (1-75), p/ρ may be eliminated, giving

$$(V_1 - V_2) = (V_1 - V_2)\left[\left(\frac{1}{k}\right)\frac{a_0{}^2}{V_1 V_2} + \frac{k-1}{2k}\right] \qquad\qquad (1\text{-}112)$$

One obvious solution is

$$V_1 - V_2 = 0$$

The other solution is

$$1 = \left(\frac{1}{k}\right) \frac{a_0^2}{V_1 V_2} + \frac{k-1}{2k} \qquad (1\text{-}113)$$

or

$$V_1 V_2 = \frac{a_0^2}{\left(\dfrac{k+1}{2}\right)}$$

This is the basic equation for the velocity change across a normal shock. Therefore, it is possible for a discontinuity to exist in the flow with speed, pressure, and density changes as given by Eqs. (1-109), (1-110), and (1-113). Since Mach number is a function of the speed ratio V/a, the relation between Mach number before and after the shock becomes:

$$M_2^2 = \frac{1 + \dfrac{k-1}{2} M_1^2}{k M_1^2 - \dfrac{k-1}{2}} \qquad (1\text{-}114)$$

The pressure change across the shock wave can be written also in terms of initial Mach number:

$$\frac{p_2}{p_1} = \frac{2k}{k+1} M_1^2 - \frac{k-1}{k+1} \qquad (1\text{-}115)$$

$$\frac{P_1}{P_2} = \left[\frac{2k}{k+1} M_1^2 - \frac{k-1}{k+1}\right]^{\frac{1}{k-1}} \left[\frac{(k-1)M_1^2 + 2}{(k+1) M_1^2}\right]^{\frac{k}{k-1}}$$

$$\qquad (1\text{-}115a)$$

$$T_2 = T_1 \qquad (1\text{-}66a)$$

The above normal shock solution is based on constant specific heats. For normal shock solution of variable specific heats, the following graphical method may be used:

1) Equation of continuity gives

$$\rho V = \rho_1 V_1 = \rho_2 V_2 = \text{constant "}C_1\text{"} \qquad (1\text{-}67)$$

2) Momentum equation gives

$$p + \rho V^2 = p_1 + \rho_1 V_1^2 = p_2 + \rho_2 V_2^2 = \text{constant "}C_2\text{"} \qquad (1\text{-}69)$$

3) Energy equation gives

$$\frac{V^2}{2} + h = \frac{V_1^2}{2} + h_1 = \frac{V_2^2}{2} + h_2 = \text{constant "}C_3\text{"} \qquad (1\text{-}63)$$

4) Equation of state gives

$$\frac{p}{\rho t} = \frac{p_1}{\rho_1 t_1} = \frac{p_2}{\rho_2 t_2} = \text{constant "}R\text{"} \qquad (1\text{-}6)$$

5) h and t relationship is given by "h–s" diagram or gas table or Eq. (1-52).

There are five equations with five unknowns $(p_2, \rho_2, t_2, h_2, V_2)$; therefore, they are completely solved numerically or graphically. The shock is characterized by the four constants, C_1, C_2, C_3 and R. Solving the equation of continuity for V and substituting the expression in the momentum and energy equations, one obtains:

$$p + \frac{C_1^2}{\rho} = C_2 \qquad (1\text{-}116)$$

$$h + \frac{1}{2}\frac{C_1^2}{\rho^2} = C_3 \qquad (1\text{-}117)$$

The state of the flow on opposite sides of the shock must satisfy both Eqs. (1-116) and (1-117). Equations (1-116) and (1-117) each represent a curve in the h–s diagram (which is a function of Eqs. (1-6) and (1-52)). The former is called the Rayleigh line and the latter the Fanno line. These lines intersect at two points, whose coordinates satisfy both equations and, therefore, correspond to the state of the flow on opposite sides of the shock. Figure 1-1 shows typical forms of these two curves. The Rayleigh and Fanno lines are plotted as follows. When conditions on the upstream side of the shock are given, the constants C_1, C_2, and C_3 can be computed. We may first assign arbitrary values to p and compute ρ from Eq. (1-116). From the equation of state, the
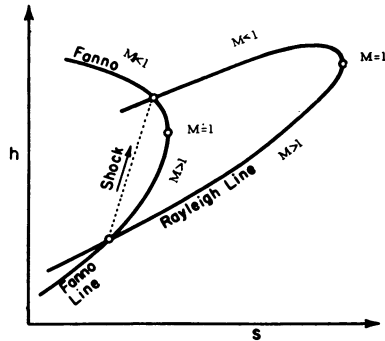
Fig. 1-1

the temperature t can be calculated. Consequently, the enthalpy h and the entropy s can be obtained from temperature t and, therefore, a graph of h versus s gives the Rayleigh line. Similarly, we can assign values to h and compute ρ from Eq. (1-117). Then t and s can be determined and a second graph of h versus s gives the Fanno line. Note that the entropy s passes through a maximum in both curves. Calculations also show that $M < 1$ on the upper branch of both curves, $M > 1$ on the lower branches, and $M = 1$ at the points of maximum entropy. Since entropy can only increase, it follows that point 1 corresponds to the upstream side of the shock and point 2 to the downstream side and that velocity can only change from supersonic to subsonic by crossing a shock. For very weak shocks, points 1 and 2 approach the point of maximum entropy on the Fanno line and the change in entropy approaches zero. That is, a sound wave is a limiting case of a weak shock.

[1-7] OBLIQUE SHOCK WAVES

Similar to normal shock, the basic equations for oblique shock are:

1) State:

$$\frac{p_1}{\rho_1 t_1} = \frac{p_2}{\rho_2 t_2} = R \qquad (1\text{-}6)$$

2) Continuity:

$$\rho_1 V_{n_1} = \rho_2 V_{n_2} \qquad (1\text{-}67)$$

3) Momentum in tangential direction:

$$\left(\rho_1 V_{n_1}\right)V_{t_1} = \left(\rho_2 V_{n_2}\right)V_{t_2} \quad \therefore \quad V_{t_1} = V_{t_2} \tag{1-118}$$

4) Momentum in normal direction:

$$p_1 - p_2 = \rho_2 V_{n_2}^2 - \rho_1 V_{n_1}^2 \tag{1-69}$$

5) Energy:

$$\frac{V_{n_1}^2 + V_{t_1}^2}{2} + c_p t_1 = \frac{V_{n_2}^2 + V_{t_1}^2}{2} + c_p t_2 \tag{1-65}$$

6) Mach number definition:

$$M_1 = \frac{\sqrt{V_{n_1}^2 + V_{t_1}^2}}{\sqrt{kgRt_1}} \qquad M_2 = \frac{\sqrt{v_{n_2}^2 + V_{t_1}^2}}{\sqrt{kgRt_2}} \tag{1-74}$$

Since state (1) is known $(\rho_1,\ p_1,\ t_1,\ V_{n_1},\ V_{t_1},\ M_1)$ ahead of oblique shock, through the Mach number (or velocity) and oblique shock angle (or wedge angle), state (2) may be solved out completely from the six equations (1-6), (1-67), (1-118), (1-69), (1-65), and (1-74) for the six unknowns $(\rho_2,\ p_2,\ t_2,\ V_{n_2},\ V_{t_2},\ M_2)$. Remember that V_{n_1} and V_{t_1} determine the shock angle, β, while V_{n_2} and V_{t_2} determine the wedge angle, or the flow turning angle, θ. Solving these six equations simultaneously, one obtains, after much simplification:

$$\frac{p_2}{p_1} = \frac{2k}{k+1} M_1^2 \sin^2\beta - \frac{k-1}{k+1} \tag{1-119}$$

$$M_2^2 = \frac{1 + \dfrac{k-1}{2} M_1^2}{kM_1^2 \sin^2\beta - \dfrac{k-1}{2}} + \frac{M_1^2 \cos^2\beta}{1 + \dfrac{k-1}{2} M_1^2 \sin^2\beta} \tag{1-120}$$

$$\frac{\rho_2}{\rho_1} = \frac{\dfrac{k+1}{k-1}\left(\dfrac{p_2}{p_1}\right) + 1}{\dfrac{k+1}{k-1} + \left(\dfrac{p_2}{p_1}\right)} \tag{1-121}$$

$$t_2 = \frac{p_2}{\rho_2 R} \tag{1-122}$$

$$a_2 = \sqrt{k \frac{p_2}{\rho_2}} = \sqrt{kgRt_2} \tag{1-123}$$

$$\frac{1}{M_1^2} = \sin^2\beta - \left(\frac{k+1}{2}\right) \frac{\sin\beta \sin\theta}{\cos(\beta - \theta)} \tag{1-124}$$

$$\frac{\tan\beta}{\tan(\beta - \theta)} = \frac{p_2}{p_1} \tag{1-125}$$

$$\tan(\beta - \theta) = \left(\frac{V_{n_2}}{V_{t_2}}\right) = \left(\frac{V_{n_2}}{V_{t_1}}\right) \tag{1-126}$$

$$V_2 = M_2 \sqrt{k \frac{p_2}{\rho_2}} \tag{1-127}$$

$$\frac{P_1}{P_2} = \left[\frac{2k}{k+1} M_1^2 \sin^2\beta - \frac{k-1}{k+1}\right]^{\frac{1}{k-1}} \left[\frac{(k-1)M_1^2 \sin^2\beta + 2}{(k+1)M_1^2 \sin^2\beta}\right]^{\frac{k}{k-1}} \tag{1-128}$$

However, these relations are valid only for constant specific heats. Considerable error may be introduced in oblique shock calculations based on constant specific heats, if the temperature change across the shock is very large. In such cases, oblique shock based on variable specific heats must be calculated. The method of determining oblique shock based on variable specific heats can be obtained through the use of normal shock method already discussed in the preceding section.

Oblique shock can be treated by superimposing on the normal shock picture V_{n_1} a uniform tangential velocity V_t parallel to the shock front; this would be the picture apparent to an observer moving in the shock front direction with the speed equal to the superimposed uniform tangential velocity V_t. Then the relations between two sides of oblique shock may be obtained through those relations already obtained for normal shock. Remember here that the static properties such as temperature t, pressure p, density ρ, speed of sound a, and entropy s, are not changed by the motion of the observer while the velocity V, consequently the Mach number M, and stagnation properties such as stagnation temperature T and stagnation pressure P, are changed by the superimposed

tangential component V to the normal shock picture V_{n_1}. Here two independent variables V_{n_1} and V_t, determine an oblique shock, while only one independent variable V determines a normal shock.

Once the conditions in front of the shock are given (such as the velocity V_1, the shock angle β, the altitude or ambient condition p_1 and t_1), the "normal shock picture" may be obtained as in Fig. 1-2.

To a stationary observer   To a moving observer   The speed of a moving observer
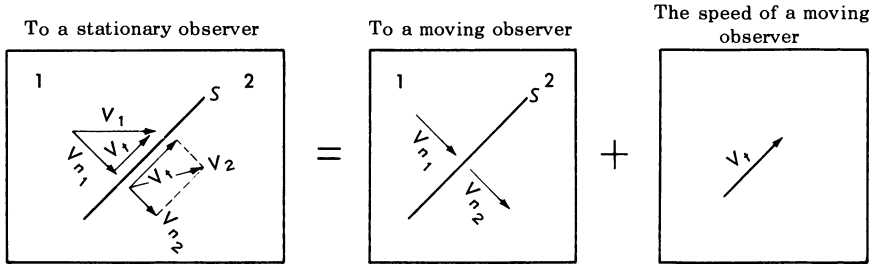
	Actual field	Fictitious normal field upstream of shock (an apparent field to an observer moving in the direction of shock with speed V_t)	Superimposed uniform tangential velocity V_t (the observer's velocity and direction)
Static properties not affected by moving observer	p_1 t_1 ρ_1 $h_1 = f(t_1)$ Eq. (52)	p_1 t_1 ρ_1 h_1	Motion only (no static properties are involved here)
Velocity and stagnation properties affected by moving observer	$V_1 = \sqrt{V_{n_1}^2 + V_t^2}$	$V_{n_1} = V_1 \sin\beta$	$V_t = V_1 \cos\beta$

Fig. 1-2

With the fictitious normal field (upstream a normal shock) known $(p_1,\ \rho_1,\ t_1,\ h_1,\ V_{n_1})$, the fictitious normal field downstream of a normal shock $(p_2,\ \rho_2,\ t_2,\ h_2,\ V_{n_2})$ may be obtained for the case of variable specific heats method, according to the procedures already given. With fictitious normal field downstream of a normal shock calculated $(p_2,\ \rho_2,\ t_2,\ h_2,\ V_{n_2})$, the velocity and stagnation properties in the actual field may be obtained as in Fig. 1-3.
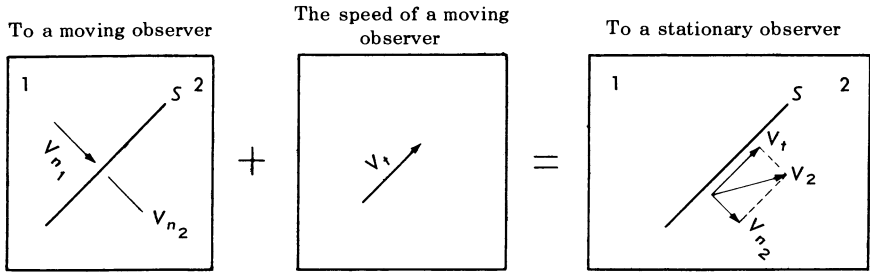
	Fictitious normal field downstream of shock (an apparent field to an observer moving in the direction of shock front with speed V_t)	Superimposed uniform tangential velocity V_t (the observer's velocity and direction)	Actual field downstream of an oblique shock
Static properties not affected by moving observer	p_2 t_2 ρ_2 $h_2 = f(t_2)$	Motion only (no static properties are involved here)	p_2 ρ_2 t_2 h_2
Velocity and stagnation properties affected by moving observer	V_{n_2}	$V_t = V_1 \cos \beta$	$V_2 = \sqrt{V_{n_2}^2 + V_t^2}$

Fig. 1-3

With the conditions downstream of an oblique shock known (p_2, ρ_2, t_2, h_2, V_2), other properties may be calculated according to the following equations:

$$a_2 = \sqrt{kgRt_2} = \sqrt{k\frac{p_2}{\rho_2}}$$

$$M_2 = \frac{V_2}{a_2}$$

$$H_2 = h_2 + \frac{V_2^2}{2}$$

$$p_2 = f(h_2, H_2) \qquad \text{from} \quad h\text{--}s \quad \text{diagram or gas table.}$$

From the geometry of Fig. 1-3, one obtains:

$$\tan(\beta - \theta) = \frac{V_{n_2}}{V_t}.$$

The basic method presented above, together with the basic method presented for constructing the h-s diagram in Sec. 1-3.7, enables one to calculate normal and oblique shock solutions with variable specific heats for any kind of gases. Since, in many cases, such information is not available, the basic method is presented here so that anyone who needs such information may obtain it himself either by hand calculations or by IBM machine calculations.

[1-8] ONE-DIMENSIONAL CONVERGENT - DIVERGENT NOZZLE FLOW

In one-dimensional flow, changes of pressure, temperature, density, velocity, and Mach number with changes of nozzle cross-sectional area are given by Eqs. (1-93), (1-95), (1-97), (1-99), and (1-101). For illustrative purposes, let us discuss pressure and Mach number curves only. In Fig. 1-4, when the exit pressure p_e is slightly less than the stagnation pressure at entrance P_o, say at p_a, the pressure and Mach number curves are shown by curve a. A reduction of exit pressure to p_b moves pressure and Mach number curve to curve b. Notice that both curves a and b have a throat Mach number less than "unity," and subsonic flows are in both convergent and divergent sections of the nozzle. Further reduction of exit pressure to p_c where throat Mach number reaches unity, moves pressure and Mach number curve to curve c. Notice here that curve c is similar to curves a and b except that the throat Mach number is now unity, $M_t = M^* = 1$ and, from Eq. (1-103) throat pressure becomes:

$$p_t = p^* = \left[\frac{P_o}{\left(\frac{k+1}{2} \right)^{\frac{k}{k-1}}} \right]$$

and subsonic flow still prevails in the divergent section of the nozzle. This exit pressure p_c, which makes Mach number unity at the throat and shock free flow in both convergent and divergent sections of the nozzle, is determined by solving Eqs. (1-94) and (1-98) simultaneously:
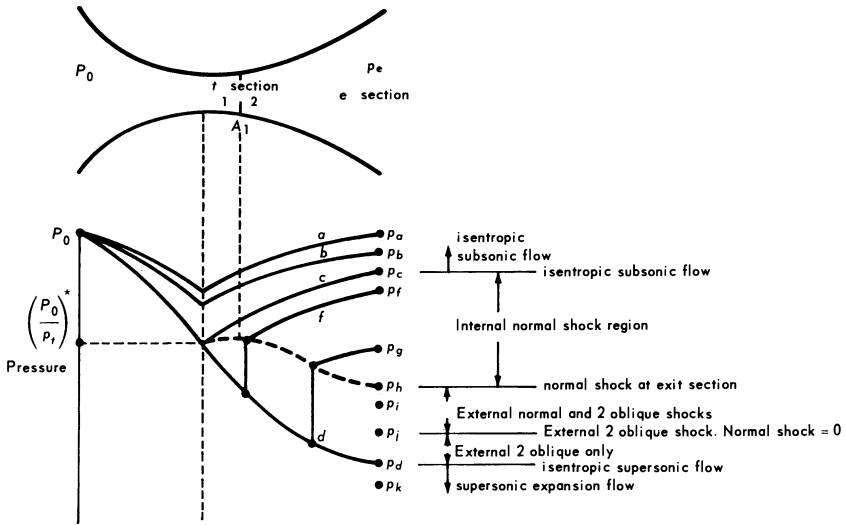
Fig. 1-4

$$\frac{A_e}{A^*} = \frac{1}{M_e} \left[\frac{1 + \dfrac{k-1}{2} M_e^2}{\left(\dfrac{k+1}{2}\right)} \right]^{\frac{k+1}{2(k-1)}}$$ (1-94)

$$\frac{p_e}{p^*} = \frac{p_e}{\dfrac{P_o}{\left[\left(\dfrac{k+1}{2}\right)^{\frac{k}{k-1}}\right]}} = \left[\frac{\left(\dfrac{k+1}{2}\right)}{1 + \dfrac{k-1}{2} M_e^2} \right]^{\left(\frac{k}{k-1}\right)}$$ (1-98)

With P_o and $A_e/A_t = A_e/A^*$ known, both p_e and M_e may be solved from Eqs. (1-94) and (1-98). However, Eqs. (1-94) and (1-98) have two solutions: one is the p_c and M_c solution just discussed, which gives shock-free subsonic flow in the divergent section of the nozzle, and the other is the p_d and M_d solution which gives a shock-free supersonic flow in the divergent section of the nozzle. The latter solution is often referred to as the "design pressure ratio P_o/p_d" of the supersonic flow nozzle. Therefore, for curves a, b,

and c, the pressure first decreases then increases along the nozzle (Fig. 1-4), while the velocity or Mach number first increases and then decreases along the nozzle. Further reduction of exit pressure below p_c, the throat condition

$$p_t = p^* = \left[\frac{P_o}{\left(\dfrac{k+1}{2}\right)^{\frac{k}{k-1}}}\right] \quad \text{and} \quad M_t = M^* = 1$$

and the subsonic flow preceding the throat in the convergent section of the nozzle will be the same as that of curve c and remain unchanged afterwards. When the exit pressure is exactly at the design pressure p_d, the pressure decreases continuously, beyond the throat, along the divergent section of the nozzle, while the Mach number increases continuously beyond the throat, into supersonic flow along the divergent section of the nozzle. This condition corresponds to curve d. For a given stagnation pressure P_o and a given exit area to throat area ratio (A_e/A^*), p_c and p_d are determined from Eqs. (1-94) and (1-98). When the exit pressure p_e is greater than or equal to p_c, the flow is shock-free subsonic in the divergent section of the nozzle. When the exit pressure p_e is less than or equal to p_d, the flow is again shock-free but supersonic, in the divergent section of the nozzle. When the exit pressure p_e is between p_c and p_d, shock wave exists in the flow but after the throat section. This is because no flow solution fulfilling the conditions of isentropic one-dimensional flow can be found. No mathematical solution fulfilling isentropic flow conditions can be found for exit pressures between p_c and p_d. The only mathematical solution satisfying equations of continuity, momentum, energy and state are solutions with normal shock in the divergent section or normal and oblique shock in the exhaust flow immediately behind the exit section. This is also what actually happens. These phenomena can best be illustrated in the following. When p_e is reduced below p_c, the variations in pressure and Mach number along the nozzle are shown in curve f. A normal shock wave becomes established in the divergent portion of the nozzle as shown. This condition can be determined from Eqs. (1-94), (1-98),(1-93), (1-97), (1-115) and (1-114). Referring to Fig. 1-4, one may write the following isentropic relations between sections t and 1 and between sections 2 and e. Normal shock relations exist between sections 1 and 2.

$$\frac{A_1}{A_t} = \frac{A_1}{A^*} = \frac{1}{M_1}\left[\frac{1 + \dfrac{k-1}{2}M_1^2}{\left(\dfrac{k+1}{2}\right)}\right]^{\frac{k+1}{2(k-1)}} \tag{1-94}$$

$$\frac{p_1}{p_t} = \frac{p_1}{p^*} = \left[\frac{\dfrac{k+1}{2}}{1 + \dfrac{k-1}{2} M_1^2}\right]^{\frac{k}{k-1}} \tag{1-98}$$

$$\frac{p_2}{p_1} = \left(\frac{2k}{k+1}\right) M_1^2 - \frac{k-1}{k+1} \tag{1-115}$$

$$M_2^2 = \frac{1 + \dfrac{k-1}{2} M_1^2}{kM_1^2 - \dfrac{k-1}{2}} \tag{1-114}$$

$$\frac{p_2}{p_e} = \left[\frac{1 + \dfrac{k-1}{2} M_e^2}{1 + \dfrac{k-1}{2} M_2^2}\right]^{\frac{k}{k-1}} \tag{1-97}$$

$$\frac{A_2}{A_e} = \frac{A_1}{A_e} = \frac{M_e}{M_2}\left[\frac{1 + \dfrac{k-1}{2} M_2^2}{1 + \dfrac{k-1}{2} M_e^2}\right]^{\frac{k+1}{2(k-1)}} \tag{1-93}$$

Since $A_t = A^*$, $p^* = p_t = \dfrac{P_o}{\left(\dfrac{k+1}{2}\right)^{\frac{k}{k-1}}}$, A_e, $p_e = p_f$ are known. There

are six unknowns, M_1, M_2, A_1, p_1, p_2, M_e, in the six equations (1-94),
(1-98), (1-115), (1-114), (1-97) and (1-93). They may be solved
simultaneously. Thus, the solution gives the location of shock A_1
in the divergent portion of the nozzle and the pressure and Mach
number variation from sections t to 1, to 2 to e as shown by curve f.
Curve f indicates that the static pressure across the shock de-
creases and the Mach number which is supersonic at the left of
the shock decreases and becomes subsonic at the right of the shock.
Since after the shock Mach number is less than 1, the velocity de-
creases and static pressure increases in the divergent section
behind the shock which is in contrast to the divergent section in
front of the shock, where the Mach number increases continuously

from unity at the throat to a supersonic Mach number M_1, and static pressure decreases continuously from p^* to p_1. When p_e is further reduced from p_f to p_g, the normal shock moves to the right as shown by curve g. In the flow represented by curve h, the normal shock stands at the nozzle exit section and the pressure immediately behind the shock equals p_h. This value of p_h, at which normal shock attaches at the exit section, can be determined from Eqs. (1-94), (1-98), and (1-115).

$$\left(\frac{A_e}{A_t}\right) = \left(\frac{A_1}{A^*}\right) = \frac{1}{M_1}\left[\frac{1 + \frac{k-1}{2}M_1^2}{\frac{k+1}{2}}\right]^{\frac{k+1}{2(k-1)}}$$

Use M > 1 solution here because it is in front of shock

$$(1-94)$$

$$\frac{p_1}{p^*} = \frac{\dfrac{p_1}{P_o}}{\left(\dfrac{k+1}{2}\right)^{\frac{k}{k-1}}} = \left[\frac{\frac{k+1}{2}}{1 + \frac{k-1}{2}M_1^2}\right]^{\frac{k}{k-1}} \qquad (1-98)$$

$$\left(\frac{p_2}{p_1}\right) = \left(\frac{p_h}{p_1}\right) = \left(\frac{2k}{k+1}\right)M_1^2 - \frac{k-1}{k+1} \qquad (1-115)$$

Here there are three unknowns, M_1, p_1, p_h, in three equations; therefore, they may be solved. Further reduction below p_h results in pushing the shock out of the nozzle. Therefore, we may say: (1) that for exit pressure between p_c and p_h, a normal shock exists in the divergent portion of the nozzle, and (2) that for exit pressure between p_h and p_d, normal and oblique shock pattern exists in the flow immediately behind the exit section. This may further be illustrated as follows. When p_e is reduced further below p_h, say at p_i, the normal shock at the nozzle exit turns into two strong oblique shocks but still with a portion of normal shock in the center portion as shown in Fig. 1-5. The two strong oblique shocks producing the required pressure rise may be determined in the following way. Referring to Fig. 1-5, one may write the following equations for the following flow regions:

1) Region e at nozzle exit but in front of the shock pattern. Applying isentropic relations between throat sections and exit sections, one obtains:

$$\frac{A_e}{A_t} = \frac{A_e}{A^*} = \frac{1}{M_e} \left[\frac{1 + \frac{k-1}{2} M_e^2}{\frac{k+1}{2}} \right]^{\frac{k+1}{2(k-1)}} \qquad (1\text{-}94)$$

$$\frac{p_e}{p_t} = \frac{p_e}{p^*} = \frac{p_e}{\frac{P_o}{\left(\frac{k+1}{2}\right)^{\frac{k}{k-1}}}} = \left[\frac{\frac{k+1}{2}}{1 + \frac{k-1}{2} M_e^2} \right]^{\left(\frac{k}{k-1}\right)} \qquad (1\text{-}98)$$

Since the only unknowns are M_e and p_e, they may be solved from Eqs. (1-94) and (1-98).

2) Region "1" where the pressure is p_i, the known exit pressure. Applying oblique shock relations between region e and 1, one obtains:

$$\frac{p_i}{p_e} = \frac{2k}{k+1} M_e^2 \sin^2 \beta_e - \frac{k-1}{k+1} \qquad (1\text{-}119)$$

$$M_1^2 = \frac{1 + \frac{k-1}{2} M_e^2}{k M_e^2 \sin^2 \beta_e - \frac{k-1}{k+1}} + \frac{M_e^2 \cos^2 \beta_e}{1 + \frac{k-1}{2} M_e^2 \sin^2 \beta_e} \qquad (1\text{-}120)$$

$$\frac{1}{M_e^2} = \sin^2 \beta_e - \frac{k+1}{2} \frac{\sin \beta_e \sin \theta_e}{\cos (\beta_e - \theta_e)} \qquad (1\text{-}124)$$

Since M_e and p_e are known from Step (1) above, the shock angle β_e, flow deflection angle θ_e, and Mach number M_1 may be determined from Eqs. (1-119), (1-120), and (1-124).

3) Region 2 where the center section flow passes through a normal shock. Applying normal shock relations between sections e and 2, one obtains:

$$M_2{}^2 = \frac{1 + \dfrac{k-1}{2} M_e{}^2}{k M_e{}^2 - \dfrac{k-1}{2}} \tag{1-114}$$

$$\frac{p_2}{p_1} = \frac{2k}{k+1} M_e{}^2 - \frac{k-1}{k+1} \tag{1-115}$$

Since M_e and p_e are known from Step (1), M_2 and p_2 may be determined from Eqs. (1-114) and (1-115).

4) Region 3. The gas which has passed through strong oblique shocks will have experienced an entropy change which is different from that of the gas crossing the normal shock at the center section. Therefore, there must exist a slip stream s, separating regions 2 and 3, across which there is a density, temperature and velocity gradient, while the static pressure remains equal, i.e., $p_2 = p_3$. From oblique shock relations, we have

$$\frac{p_3}{p_i} = \frac{p_2}{p_i} = \frac{2k}{k+1} M_1{}^2 \sin^2\beta_1 - \frac{k-1}{k+1} \tag{1-119}$$

$$M_3{}^2 = \frac{1 + \dfrac{k-1}{2} M_1{}^2}{k M_1{}^2 \sin^2\beta_1 - \dfrac{k-1}{2}} + \frac{M_1{}^2 \cos^2\beta_1}{1 + \dfrac{k-1}{2} M_1{}^2 \sin^2\beta_1} \tag{1-124}$$

$$\frac{1}{M_1{}^2} = \sin^2\beta_1 - \frac{k+1}{2} \frac{\sin\beta_1 \sin\theta_1}{\cos(\beta_1 - \theta_1)} \tag{1-120}$$

Since $p_3 = p_2$, p_i, M_1 are known from Steps (1), (2), and (3) above, the reflected shock angle β_1, flow deflection angle θ_1, and Mach number M_3, may be determined. Since flow direction across the slip stream S, must be parallel, i.e., $V_2 \| V_3$, and since V_3 as solved out from the straight-line pattern of normal-and-oblique-shocks as given in the procedures above, may not be exactly parallel, the normal and oblique shocks must actually be curved near the intersection as shown by the dotted line in Fig. 1-6, so that changes of gas properties should be gradual rather than discrete. However, the straight-line shock pattern gives a good approximation except near slip-stream regions. As the exit reduces gradually below p_i, the strong oblique shocks become weaker and the normal shock portion becomes smaller and moves farther away from the nozzle exit section and normal shock finally disappears, as shown in Fig. 1-7. Further reduction in exit pressure results in weaker oblique shocks until they completely
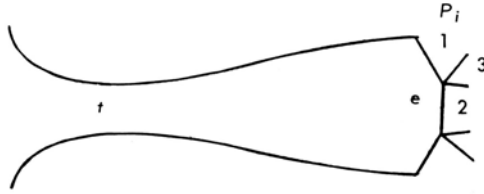
Fig. 1-5
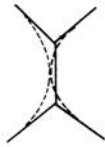
Fig. 1-6
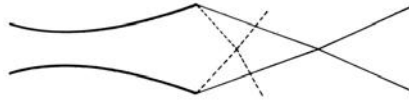
Fig. 1-7

disappear as the exit pressure approaches p_d where the flow becomes completely isentropic and shock-free. Further reduction of exit pressure below p_d, say at p_k, the flow remains supersonic to the exit of the nozzle. It then undergoes an expansion around the corner of the exit in order to drop to the lower exit pressure p_k. This expansion will take place through expansion waves of the Prandtl-Meyer type as shown in Fig. 1-8. The expansion wave angle θ may be calculated from

$$\frac{p_e}{p_k} = \left[\frac{1 + \dfrac{k-1}{2} M_k{}^2}{1 + \dfrac{k-1}{2} M_e{}^2}\right]^{\frac{k}{k-1}} \tag{1-97}$$

$$\theta = -\left[\sqrt{\frac{k-1}{k+1}} \tan^{-1} \sqrt{\frac{k-1}{k+1}(M_e{}^2 - 1)} - \tan^{-1}\sqrt{M_e{}^2 - 1}\right]$$

$$+ \left[\sqrt{\frac{k-1}{k+1}} \tan^{-1}\sqrt{\frac{k-1}{k+1}(M_k{}^2 - 1)} - \tan^{-1}\sqrt{M_k{}^2 - 1}\right] \tag{1-129}$$

Here p_e and M_e are known from Step (1) and p_k is the given ambient pressure; M_k and θ may be determined from Eqs. (1-97) and (1-129). Note here that the mass rate of flow and the throat pressure remain
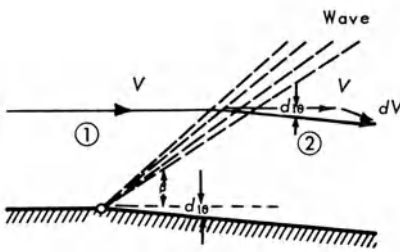
Fig. 1-8
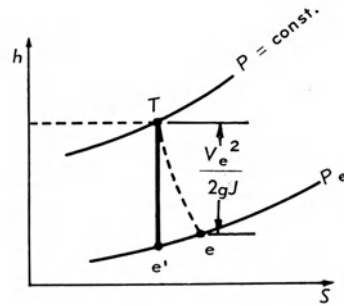
Fig. 1-9
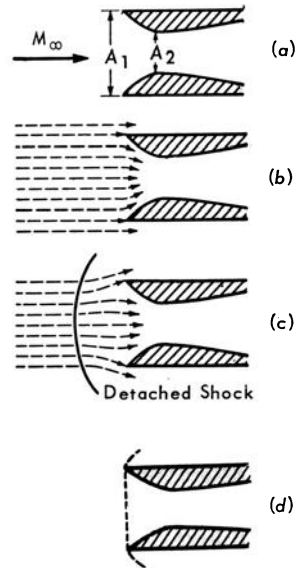
Fig. 1-10
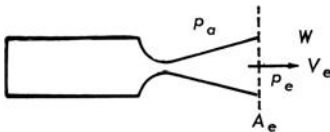
Fig. 1-11

constant for all values of p_e less than that corresponding to curve c, and that the flow within the nozzle is the same for all pressures less than that corresponding to curve h. The exit pressure equals the back pressure for all values of p_e down to curve h and also when it equals the design pressure as in curve d.

[1-8.1] Nozzle Efficiency

Consider a nozzle (Fig. 1-9) supplied with gas at stagnation pressure and stagnation temperature P and T respectively. The gas expands adiabatically but with increasing entropy, to state e.

If it had expanded without friction to the same final pressure p_e, the end state would have been e'. We now define the nozzle efficiency as the ratio of the exit kinetic energy to the exit kinetic energy which would be obtained in a frictionless nozzle expanding the gas to the same final pressure p_e.

$$\eta_N = \frac{H - h_e}{H - h_{e'}} = \frac{c_p(T - t_e)}{c_p(T - t_{e'})} = \frac{(V_e^2/2)}{c_p(T - t_{e'})}$$

$$= \frac{\left(\dfrac{V_e^2}{2}\right)}{c_p T \left[1 - \left(\dfrac{t_{e'}}{T}\right)\right]} \tag{1-130}$$

$$= \frac{\left(\dfrac{V_e^2}{2}\right)}{c_p T \left[1 - \left(\dfrac{p_e}{P}\right)^{\frac{k-1}{k}}\right]}$$

[1-8.2] Nozzle Thrust

Consider a nozzle (Fig. 1-10) which generates gas steadily at stagnation pressure P, and stagnation temperature T. The nozzle, with a throat area A_t and an exit area A_e, discharges w pounds of gas per second into an ambient pressure p_a. Applying the momentum equation to the control volume of Fig. 1-10, we find the thrust is

$$F = \text{thrust} = \frac{w}{g} V_e + A_e(p_e - p_a). \tag{1-131}$$

[1-9] SUPERSONIC INLET

Now consider the inlet of air-breathing propulsion engines when operating at supersonic Mach number M_∞. Figure 1-11a shows a converging-diverging inlet which has an inlet area A_1 and a throat area A_2. If there is no shock in front of the inlet at supersonic speeds, the free-stream supersonic flow corresponding

to the cross-sectional area A_1 must enter the inlet completely (Fig. 1-11b). If the inlet cannot pass this amount of free-stream supersonic flow, a detached shock will appear in front of the inlet (Fig. 1-11c), as then the flow behind the shock becomes subsonic and may spill out. The lower curve of Fig. 1-12 shows the maximum contraction possible when there is no shock. It comes from the isentropic area relationships, Eq. (1-94):

$$\left(\frac{A_1}{A_2}\right) = \left(\frac{A_1}{A^*}\right) = \frac{1}{M_\infty}\left[\frac{1 + \dfrac{k-1}{2}M_\infty^2}{\dfrac{k+1}{2}}\right]^{\frac{k+1}{2(k-1)}} \tag{1-94}$$

The upper curve shows the maximum contraction possible for the case where a normal shock attaches at lip (Fig. 1-11d), thus forcing all the free stream supersonic air through the engine at lower stagnation pressure. It comes from the following relationships:

Applying Eq. (1-106a) in front of the shock, one obtains;

$$\frac{w\sqrt{T_\infty}}{P_\infty A_1} = \sqrt{\frac{k}{R}}\left[\frac{M_\infty}{\left[1 + \dfrac{k-1}{2}M_\infty^2\right]^{\frac{k+1}{2(k-1)}}}\right] \tag{1-106a}$$

Applying Eq. (1-10) at the throat section, one obtains;

$$\frac{w\sqrt{T_2}}{P_2 A_2} = \frac{w\sqrt{T^*}}{P^* A^*} = \sqrt{\frac{k}{R}}\frac{1}{\left(\dfrac{k+1}{2}\right)^{\frac{k+1}{2(k-1)}}} \tag{1-107}$$

Since the stagnation pressure ratio across a normal shock is given by Eq. (1-115a),

$$\frac{P_1}{P_2} = \frac{P_\infty}{P^*} = \left[\frac{2k}{k+1}M_\infty^2 - \frac{k-1}{k+1}\right]^{\frac{1}{k-1}}\left[\frac{(k-1)M_\infty^2 + 2}{(k+1)M_\infty^2}\right]^{\frac{k}{k-1}} \tag{1-115a}$$

and since stagnation temperature ratio across a normal shock is given by Eq. (1-66a),

$$T_\infty = T_2 \tag{1-66a}$$

Dividing Eq. (1-107) by Eq. (1-106a) and eliminating (T_∞/T) and (P_∞/P) by using Eqs. (1-66a) and (115a), one obtains;

$$\frac{A_2}{A_1} = \frac{M_\infty \left[\dfrac{k+1}{2}\right]^{\frac{k+1}{2(k-1)}}}{\left[1 + \dfrac{k-1}{2} M_\infty^2\right]^{\frac{k+1}{2(k-1)}}} \left[\frac{2k}{k+1} M_\infty^2 - \frac{k-1}{k+1}\right]^{\frac{1}{k-1}} \left[\frac{(k-1) M_\infty^2 + 2}{(k+1) M_\infty^2}\right]^{\frac{k}{k-1}}$$

$$\tag{1-132}$$

Equation (1-132) is plotted as the upper curve in Fig. 1-12. It gives the maximum contraction possible when normal shock attaches at the inlet lip (Fig. 1-11d).
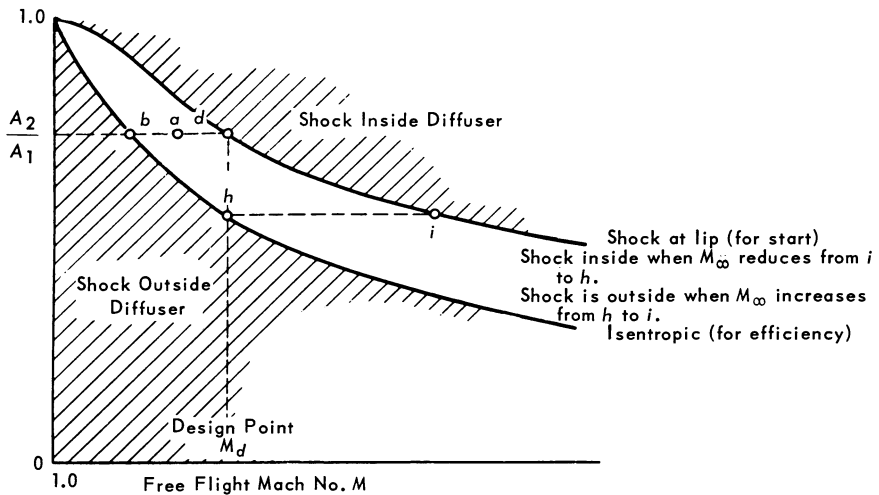
Fig. 1-12

[1-9.1] Constant Geometry Supersonic Inlet

Figure 1-13 shows various stages during a supersonic inlet starting. In Fig. 1-13a, Free flight Mach number M_a is less than the designed Mach number M_d; a detached shock is in the front of the inlet (point a of Fig. 1-12). When the speed is slightly greater than the designed Mach number M_d, the shock moves into the inlet.

The equilibrium position of the shock in the divergent section of the inlet depends on the back pressure resulted from matching characteristics of the engine behind the inlet. When shock is too far downstream of the divergent section (Fig. 1-13c), it gives poor diffusion efficiency. Figure 1-13d shows the farthest upstream position (at the throat section) for which the flow is still stable. However, a slight disturbance in the flow pattern of Fig. 1-13d will move the shock out of the inlet. Such a diffuser possesses the so-called hysteresis effect. During acceleration, the shock will not be swallowed until the speed M_d (Fig. 1-12) is reached. Once swallowed, the shock will not be pushed out upon deceleration until the speed M_b (Point b of Fig. 1-12) is reached. Therefore, it is possible to eliminate the shock of a fixed-geometry inlet when overspeeded. Assume another inlet designed for the speed M_d and containing a higher contraction ratio $(A_2/A_1)_h$ instead of $(A_2/A_1)_d$. By first overspeeding to M_i (Point i of Fig. 1-12), the shock is swallowed, and then decelerating to the design Mach number M_d where an isentropic inlet prevails (further decrease below M_d will push the shock out of the inlet).

[1-9.2] Variable-Geometry Supersonic Inlet

The shock may also be eliminated by a variable-geometry inlet. Let us consider the inlet designed for the speed M_d and having in Fig. 1-12 a contraction ratio $(A_2/A_1)_h$. At the start, the throat area is too small, corresponding to point h of Fig. 1-12; a detached shock will appear in front of the inlet. When the throat area (A_2/A_1) is increased, the shock moves toward the inlet. When point $(A_2/A_1)_d$ of Fig. 1-12 is reached, the shock is swallowed. The throat area may now be decreased without pushing the shock out until point $(A_2/A_1)_h$ of Fig. 1-12 is again reached. When the exhaust pressure is properly adjusted, the inlet may be made free of shock.

[1-9.3] Inlet Diffuser Efficiency

Assuming the velocity leaving the inlet diffuser to be negligibly small, one may define, from Fig. 1-14:

$$\eta_D = \frac{H_2' - h_1}{H_2 - h_1} \qquad (1-133)$$

where state (1) is the actual state entering the inlet, state (2) is the actual state leaving the inlet, and state (2') is a fictitious state at the actual leaving pressure but at the entering entropy.
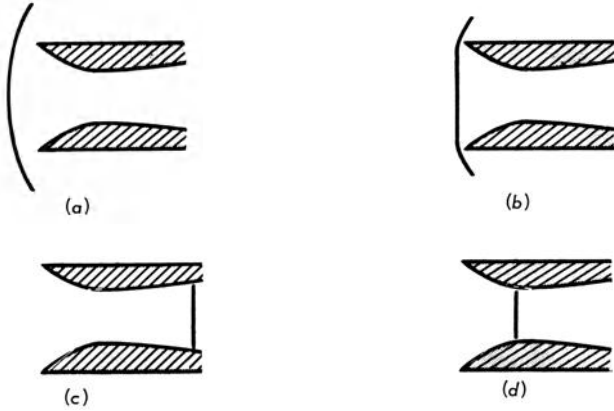
Fig. 1-13
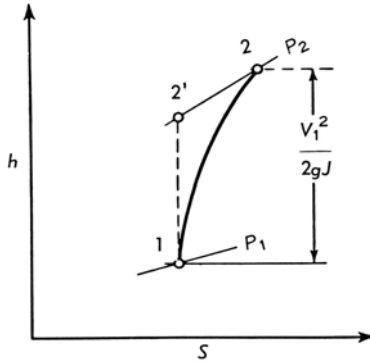
Fig. 1-14

For a perfect gas, using Eqs. (1-63), (1-22), and (1-26), one may rewrite Eq. (1-133) to:

$$\eta_D = \frac{c_p t_1 \left[\left(\dfrac{T_2'}{t_1} \right) - 1 \right]}{\dfrac{V_1^2}{2}} = \frac{\left(\dfrac{P_2}{p_1} \right)^{\frac{k-1}{k}} - 1}{\dfrac{k-1}{2} M_1^2} \tag{1-134}$$

Since $\left(\dfrac{P_2}{p_1} \right) = \left(\dfrac{P_2}{P_1} \right)\left(\dfrac{P_1}{p_1} \right)$

and for normal shock, we have:

$$\left(\frac{P_2}{P_1}\right) = \left[\frac{2k}{k+1}M^2 - \frac{k-1}{1-k}\right]^{\frac{1}{1-k}} \left[\frac{(k-1)M_1^2 + 2}{(k+1)M_1^2}\right]^{\frac{k}{1-k}}$$

$$(1\text{-}115a)$$

$$\left(\frac{P_1}{p_1}\right) = \left[1 + \frac{k-1}{2}M_1^2\right]^{\frac{k}{k-1}} \qquad (1\text{-}78)$$

Substituting Eqs. (1-115a) and (1-78) into Eq. (1-134), one obtains:

$$\eta_D = \frac{\left[1 + \frac{k-1}{2}M_1^2\right]\left[\frac{2k}{k+1}M_1^2 - \frac{k-1}{k+1}\right]^{\frac{1}{1-k}}\left[\frac{(k-1)M_1^2 + 2}{(k+1)M_1^2}\right]^{\frac{k}{1-k}} - 1}{\frac{k-1}{2}M_1^2}$$

$$(1\text{-}135)$$

Equation (1-135) gives diffuser efficiency versus Mach number for a normal shock diffuser.

[1-10] ONE-DIMENSIONAL FLOW ANALYSIS WITH AREA CHANGE, FRICTION AND HEAT ADDITION

The following equations are applicable:

1) Equation of State

$$\frac{p}{\rho} = RT \qquad (1\text{-}5)$$

or, in its differential form,

$$\frac{dp}{p} = \frac{d\rho}{\rho} + \frac{dt}{t} \qquad (1\text{-}136)$$

2) Equation of Continuity

$$\frac{d\rho}{\rho} + \frac{dA}{A} + \frac{dV}{V} = 0 \qquad (1\text{-}68)$$

or

$$\frac{d\rho}{\rho} + \frac{dA}{A} + \frac{1}{2} \frac{dV^2}{V^2} = 0 \qquad (1\text{-}137)$$

3) Equation of Energy

$$\frac{T}{t} = 1 + \frac{k-1}{2} M^2 \qquad (1\text{-}76)$$

or, in its differential form,

$$\frac{dT}{T} = \frac{dt}{t} + \frac{\frac{k-1}{2}M^2}{1 + \frac{k-1}{2} M^2} \frac{dM^2}{M^2} \qquad (1\text{-}138)$$

4) Mach number definition

$$M^2 = \frac{V^2}{a^2} = \frac{V^2}{k\frac{p}{\rho}} = \frac{V^2}{kRt} \qquad (1\text{-}139)$$

or, in its differential form,

$$\frac{dM^2}{M^2} = \frac{dV^2}{V^2} - \frac{dt}{t} \qquad (1\text{-}140)$$

5) Equation of Momentum

$$VdV + dp + \frac{1}{2} V^2 \left(\frac{4f}{D}\right) dx = 0 \qquad (1\text{-}69\text{a})$$

or, in terms of Mach number,

$$\frac{dp}{p} + \frac{k}{2} M^2 \frac{dV^2}{V^2} + \frac{k}{2} M^2 4f \frac{dx}{D} = 0 \qquad (1\text{-}141)$$

In order to derive a useful expression with involved independent variables, *i.e.,* (1) area change A, (2) friction factor f, and (3) stagnation temperature change T due to heat addition, we perform the following:

Eliminating $(d\rho/\rho)$ from Eqs. (1-136) and (1-137), one obtains:

$$\frac{dp}{p} - \frac{dt}{t} + \frac{1}{2}\frac{dV^2}{V^2} + \frac{dA}{A} = 0 \qquad (1\text{-}142)$$

Eliminating (dV^2/V^2) from Eqs. (1-140) and (1-142), one obtains:

$$\frac{dp}{p} - \frac{dt}{t} + \frac{1}{2}\left(\frac{dM^2}{M^2} + \frac{dt}{t}\right) + \frac{dA}{A} = 0 \qquad (1\text{-}143)$$

Eliminating (dV^2/V^2) from Eqs. (1-140) and (1-141), one obtains:

$$\frac{dp}{p} + \frac{1}{2}k\,M^2\left(\frac{dM^2}{M^2} + \frac{dt}{t}\right) + \frac{k}{2}\,M^2\,4f\,\frac{dx}{D} = 0 \qquad (1\text{-}144)$$

Eliminating (dp/p) from Eqs. (1-143) and (1-144), one obtains:

$$\left(\frac{1}{2} + \frac{kM^2}{2}\right)\frac{dt}{t} + \left(\frac{kM^2}{2} - \frac{1}{2}\right)\frac{dM^2}{M^2} - \frac{dA}{A} + \frac{kM^2}{2}\left(4f\,\frac{dx}{D}\right) = 0$$

$$(1\text{-}145)$$

Eliminating (dt/t) from Eqs. (1-138) and (1-145), one obtains, after simplification:

$$\frac{dM^2}{M^2} = -\frac{2\left(1 + \dfrac{k-1}{2}\,M^2\right)}{1 - M^2}\frac{dA}{A} + \frac{(1 + kM^2)\left(1 + \dfrac{k-1}{2}\,M^2\right)}{1 - M^2}\frac{dT}{T}$$

$$+ \frac{kM^2\left(1 + \dfrac{k-1}{2}\,M^2\right)}{1 - M^2}\left(4f\,\frac{dx}{D}\right)$$

$$(1\text{-}146)$$

This is the basic equation for one-dimensional flow with area change, friction and heat addition. In order to solve Eq. (1-146), numerical integration should be used. However, for the following three special cases, analytical solutions are available:

   1) Heat addition in a duct of constant cross-section without friction. Here A = constant, and $f = 0$; Eq. (1-146) reduces to

$$\frac{dM^2}{M^2} = \frac{(1 + kM^2)\left(1 + \dfrac{k-1}{2} M^2\right)}{1 - M^2} \frac{dT}{T} \tag{1-147}$$

Equation (1-147) may be integrated to give

$$\frac{T_2}{T_1} = \frac{M_2^2\left(1 + \dfrac{k-1}{2} M_2^2\right)\left(1 + kM_1^2\right)^2}{M_1^2\left(1 + \dfrac{k-1}{2} M_1^2\right)\left(1 + kM_2^2\right)^2} \tag{1-148}$$

$$\left(\frac{P_2}{P_1}\right) = \left(\frac{1 + kM_1^2}{1 + kM_2^2}\right)\left[\frac{1 + \dfrac{k-1}{2} M_2^2}{1 + \dfrac{k-1}{2} M_1^2}\right]^{\frac{k}{k-1}} \tag{1-148a}$$

This is the so-called "Rayleigh Line." A maximum value of (T_2/T_1), $(T_2/T_1)_{max}$, exits at $M_2 = 1$ (thermal choking). Heat addition in excess of $(T_2/T_1)_{max}$ will force the adjustment (lowering when $M_1 < 1$ and increasing when $M_1 > 1$) of incoming M_1 value.

2) Area change without heat addition and without friction. Here T = constant, and $f = 0$. Equation (1-146) reduces to

$$\frac{dM^2}{M^2} = -\frac{2\left(1 + \dfrac{k-1}{2} M^2\right)}{1 - M^2} \frac{dA}{A} \tag{1-149}$$

Equation (1-149) may be integrated to give

$$\frac{A_2}{A_1} = \frac{M_1}{M_2}\left[\frac{1 + \dfrac{k-1}{2} M_2^2}{1 + \dfrac{k-1}{2} M_1^2}\right]^{\frac{k+1}{2(k-1)}} \tag{1-150}$$

This is the so-called "isentropic line." A minimum value of (A_2/A_1), $(A_2/A_1)_{min}$, exits at $M = 1$ (throat choking). Area ratio smaller than $(A_2/A_1)_{min}$ will force the adjustment (lowering when $M_1 < 1$ and increasing when $M_1 > 1$) of incoming M_1 value.

3) Flow in duct of constant cross-sectional area with friction but without external heat addition. Here T = constant and A = constant; Eq. (1-146) reduces to

$$\frac{dM^2}{M^2} = \frac{kM^2\left(1 + \frac{k-1}{2}M^2\right)}{1 - M^2} \; 4f \; \frac{dx}{D} \qquad (1\text{-}151)$$

Equation (1-151) may be integrated to give

$$4f\left(\frac{L}{D}\right) = \frac{1}{k}\left\{ \frac{1}{M_1^2} - \frac{1}{M_2^2} + \frac{k+1}{2}\ln\left[\frac{M_1^2\left(1 + \frac{k-1}{2}M_2^2\right)}{M_2^2\left(1 + \frac{k-1}{2}M_1^2\right)}\right] \right\}$$

$$(1\text{-}152)$$

$$\left(\frac{P_2}{P_1}\right) = \frac{M_1}{M_2}\left[\frac{1 + \frac{k-1}{2}M_2^2}{1 + \frac{k-1}{2}M_1^2}\right]^{\frac{k+1}{2(k-1)}} \qquad (1\text{-}152a)$$

This is the so-called "Fanno Line." A maximum value of $(4f\,L/D)$, $(4f\,L/D)_{\max}$, exits at $M = 1$ (friction choking). $(4f\,L/D)$ in excess of $(4f\,L/D)_{\max}$ will force the adjustment (lowering when $M_1 < 1$ and increasing when $M_1 > 1$) of incoming M_1 value.

   4) Step-by-step numerical or graphical integrations of the basic equation (1-146). Equation (1-146) may be rewritten as

$$dM^2 = -\frac{2M^2\left(1 + \frac{k-1}{2}M^2\right)}{1 - M^2}\frac{dA}{A} + \frac{M^2(1 + kM^2)\left(1 + \frac{k-1}{2}M^2\right)}{1 - M^2}$$

$$+ \frac{kM^4\left(1 + \frac{k-1}{2}M^2\right)}{1 - M^2}\; 4f\;\frac{dx}{D}$$

$$(1\text{-}153)$$

Equation (1-153) can now be integrated approximately in finite difference form over a short interval between Secs. 1 and 2, the approximation being that the coefficients of (dA/A), (dT/T), and (dx/D) are constants (at their mean value) during the short interval. Evaluate the influence coefficients (function of Mach number themselves) of (dA/A), (dT/T), and (dx/D) as constants which are

calculated according to an average Mach number, $\overline{M} = (M_1 + M_2)/2$. Therefore, Eq. (1-153) becomes:

$$M_2{}^2 - M_1{}^2 = - \frac{2\overline{M}^2\left(1 + \frac{k-1}{2}\overline{M}^2\right)}{1 - \overline{M}^2} \frac{(A_2 - A_1)}{\left(\dfrac{A_2 + A_1}{2}\right)}$$

$$+ \frac{\overline{M}^2(1 + k\overline{M}^2)\left(1 + \frac{k-1}{2}\overline{M}^2\right)}{1 - \overline{M}^2} \frac{(T_2 - T_1)}{\left(\dfrac{T_2 + T_1}{2}\right)}$$

$$+ \frac{k\overline{M}^4\left(1 + \frac{k-1}{2}\overline{M}^2\right)}{1 - \overline{M}^2} \, 4f\left(\dfrac{\Delta x}{\dfrac{D_1 + D_2}{2}}\right)$$

$$(1\text{-}154)$$

$$M_2{}^2 - M_1{}^2 = F_A(\overline{M}) \frac{(A_2 - A_1)}{\left(\dfrac{A_2 + A_1}{2}\right)} + F_Q(\overline{M}) \frac{(T_2 - T_1)}{\left(\dfrac{T_2 + T_1}{2}\right)} + F_f(\overline{M}) 4f \frac{\Delta x}{\left(\dfrac{D_1 + D_2}{2}\right)}$$

$$(1\text{-}155)$$

Here $F_A(\overline{M})$, $F_Q(\overline{M})$ and $F_f(\overline{M})$ are called influence coefficients, and they are:

$$F_A(\overline{M}) = - \frac{2\overline{M}^2\left(1 + \frac{k-1}{2}\overline{M}^2\right)}{1 - \overline{M}^2} \qquad (1\text{-}156)$$

$$F_Q(\overline{M}) = \frac{\overline{M}^2(1 + k\overline{M}^2)\left(1 + \frac{k-1}{2}\overline{M}^2\right)}{1 - \overline{M}^2} \qquad (1\text{-}157)$$

$$F_f(\overline{M}) = \frac{k\overline{M}^4\left(1 + \frac{k-1}{2}\overline{M}^2\right)}{1 - \overline{M}^2} \qquad (1\text{-}158)$$

$$\bar{M} = \left(\frac{M_1 + M_2}{2}\right) \qquad (1\text{-}159)$$

The following procedure is suggested: (a) assume M_2; (b) calculate $\bar{M}$ from Eq. (1-159); (c) calculate $F_A(\bar{M})$, $F_Q(\bar{M})$ and $F_f(\bar{M})$ from Eqs. (1-156), (1-157), and (1-158); (d) calculate M_2 from Eq. (1-155); (e) if the calculated value of M_2 from Eq. (1-155) checks with the assumed value of M_2, the assumed M_2 is the solution. Otherwise, reiterate it until it checks (usually three or four trials will yield the correct solution).

[1-10.1] One-Dimensional Flow Analysis with Area Change, Friction and Heat Addition (Additional Analysis)

As discussed in the previous section, the case of area change, friction and heat addition cannot be solved analytically. A numerical method must be used. However, instead of using area A as one of the three independent variables (they are area A, friction f, and heat addition T, which are independent of each other) like the case just discussed in Sec. (1-10), one may also analyze the case where area A is a dependent variable (such as making area A a function of temperature T, due to heat addition or friction or both). In such cases, there are only two independent variables, *i.e.*, temperature T and friction f, although the flow still involves area change A. Let us use area change A as a function of static pressure change p as an illustrative example. There are many ways of expressing mathematically the variation of pressure p with flow area A. The example that has been chosen for this analysis, because of its simplicity, is from L. Crocco and is represented by

$$p = \text{constant } A^{\frac{\epsilon}{1-\epsilon}} \qquad (1\text{-A-}1)$$

or, in its differential form,

$$\frac{dp}{p} = \left(\frac{\epsilon}{1-\epsilon}\right)\frac{dA}{A} \qquad (1\text{-A-}2)$$

Special cases of interest include: (1) $\epsilon = 1$ for flow of constant cross-sectional area and (2) $\epsilon = 0$ for flow of constant static pressure.

Now considering an infinitesimal length of duct dx, the rate of heat transfer to the fluid is approximately

$$\bar{h}\pi D dx\, (T_w - T)$$

Here $\bar{h}$ = heat transfer coefficient, and T_w = wall temperature. Using the energy balance, we have

$$\bar{h}\pi D dx (T_w - T) = \rho\left(\frac{\pi}{4}D^2\right)V \, c_p dT$$

or

$$\frac{dT}{T_w - T} = \frac{4\bar{h}}{\rho V c_p} \frac{dx}{D} \qquad\qquad (1\text{-}A\text{-}3)$$

From the Reynolds analogy,

$$\frac{\bar{h}}{\rho V c_p} = \frac{f}{2} \qquad\qquad (1\text{-}A\text{-}4)$$

we may write Eq. (1-A-3) to:

$$\frac{dT}{T_w - T} = 2f \frac{dx}{D} \qquad\qquad (1\text{-}A\text{-}5)$$

Equations of state, Eqs. (1-136); continuity, Eq. (1-137); energy, Eq. (1-138); Mach number, Eq. (1-140); and momentum, Eq. (1-141) are valid. Substituting Eq. (1-A-5) into the equation of momentum (Eq. 1-141), we have:

$$\frac{dp}{p} + \frac{kM^2}{2}\frac{dV^2}{V^2} + kM^2\left(\frac{dT}{T_w - T}\right) = 0 \qquad\qquad (1\text{-}A\text{-}6)$$

Eliminating $(d\rho/\rho)$ from equations of continuity and state, we have:

$$\frac{dp}{p} - \frac{dt}{t} + \frac{1}{2}\frac{dV^2}{V^2} + \frac{dA}{A} = 0 \qquad\qquad (1\text{-}142)$$

Eliminating (dV^2/V^2) from Eqs. (1-140), (1-142), and (1-A-2), we have:

$$\frac{dp}{p} - \frac{\epsilon}{2}\frac{dt}{t} + \frac{\epsilon}{2}\frac{dM^2}{M^2} = 0 \qquad\qquad (1\text{-}A\text{-}7)$$

Eliminating dV^2/V^2 from Eqs. (1-140) and (1-A-6), we have:

$$\frac{dp}{p} + \frac{1}{2}kM^2\left(\frac{dM^2}{M^2} + \frac{dt}{t}\right) + kM^2\frac{dT}{T_w - T} = 0 \qquad\qquad (1\text{-}A\text{-}8)$$

Eliminating (dp/p) from Eqs. (1-A-7) and (1-A-8), we have:

$$(\epsilon + kM^2)\,\frac{dt}{t} + (kM^2 - \epsilon)\,\frac{dM^2}{M^2} + 2kM^2\,\frac{dT}{T_w - T} = 0$$

$$(1\text{-}A\text{-}9)$$

Eliminating dt/t from Eqs. (1-138) and (1-A-9), we have, after simplification:

$$\frac{dM^2}{M^2} = \frac{(\epsilon + kM^2)\left(1 + \dfrac{k-1}{2}M^2\right)}{\epsilon(1 - M^2) - (1 - \epsilon)kM^2}\,\frac{dT}{T}$$

$$(1\text{-}A\text{-}10)$$

$$+ \frac{2kM^2\left(1 + \dfrac{k-1}{2}M^2\right)}{\epsilon(1 - M^2) - (1 - \epsilon)kM^2}\,\frac{dT}{T_w - T}$$

The following special cases will be discussed first:

1) Heat addition in non-constant area duct without friction. Here $f = 0$. Consequently, from Eq. (1-A-5):

$$\left(\frac{dT}{T_w - T}\right) = 2f\frac{dx}{D} = 0 \qquad (1\text{-}A\text{-}5a)$$

Therefore, Eq. (1-A-10) reduces to

$$\frac{dM^2}{M^2} = \frac{(\epsilon + kM^2)\left(1 + \dfrac{k-1}{2}M^2\right)}{\epsilon(1 - M^2) - (1 - \epsilon)kM^2}\,\frac{dT}{T} \qquad (1\text{-}A\text{-}10a)$$

Equation (1-A-10a) may be integrated to give

$$\left(\frac{T}{T_1}\right) = \frac{M^2\left(1 + \dfrac{k-1}{2}M^2\right)\left(\epsilon + kM_1^2\right)^2}{M_1^2\left(1 + \dfrac{k-1}{2}M_1^2\right)\left(\epsilon + kM^2\right)^2} \qquad (1\text{-}A\text{-}10b)$$

From the energy equation $c_p(T - T_1) = q$, we have

$$\left(\frac{T}{T_1}\right) = 1 + \left(\frac{q}{c_p T_1}\right) \qquad (1\text{-}A\text{-}10c)$$

Here q = heat addition in B.T.U. per pound of flow. There exists a critical maximum value of (T_c/T_1) which may be obtained by:

$$\frac{d(T/T_1)}{dM^2} = 0 \qquad (1\text{-}A\text{-}11)$$

The result of Eq. (1-A-11) gives the critical Mach number as:

$$M_c{}^2 = \left[\frac{k}{\epsilon} - (k - 1)\right]^{-1} \qquad (1\text{-}A\text{-}12)$$

Consequently, the critical (maximum) temperature becomes:

$$1 + \left(\frac{q}{c_p T_1}\right) = \left(\frac{T_c}{T_1}\right) = \frac{M_c{}^2 \left(1 + \frac{k-1}{2} M_c{}^2\right)\left(\epsilon + kM_1{}^2\right)^2}{M_1{}^2 \left(1 + \frac{k-1}{2} M_1{}^2\right)\left(\epsilon + kM_c{}^2\right)^2}$$

$$(1\text{-}A\text{-}13)$$

(T_c/T_1) is the condition of thermal choking in a duct of variable cross-section. For the special case of flow of constant cross-sectional area where $\epsilon = 1$, Eq. (1-A-12) shows that M_c becomes unity, which is the well-known condition of thermal choking at $M_c = 1$ for heat addition in a duct of constant cross-section. However, for a duct of variable cross-section, M_c is subsonic (less than unity), when $\epsilon < 1$, and M_c is supersonic (greater than unity) when $\epsilon > 1$. Equation (1-A-12) indicates that when ϵ varies from 0 to $k/k-1$, M_c varies from 0 to ∞. This is the range of interest. In general, for a given value of ϵ, there exist two solutions, *i.e.*, one subcritical solution and one supercritical solution. Heat addition in excess of (T_c/T_1) is impossible at the given value of M_1. Actually, for heat addition in excess of (T_c/T_1), the incoming Mach number M_1 will be forced to adjust to such a value so that with the given heat addition q and duct configuration ϵ, Eq. (1-A-13) is satisfied. (Critical Mach number M_c at the exit is maintained).

When the relationship of Eq. (1-A-10b) is plotted on the h–s diagram or T–s diagram (Fig. 1-A-1), it gives the generalized Rayleigh line. Here each value of ϵ corresponds to one generalized Rayleigh line. The upper branches of the lines delineate a subcritical heat addition where Mach number increases with heat addition (finally reaching the critical condition M_c at the maximum entropy point, behind which heat addition is impossible for the given ϵ and the given M_1), while the lower branches correspond to supercritical heat addition where Mach number decreases with
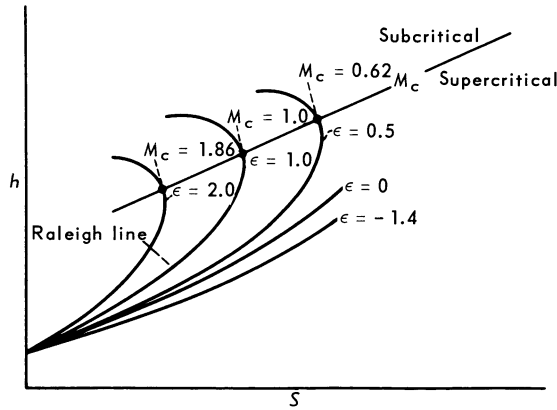
Fig. 1-A-1. (After A. Doborowolski, NASA TND 3626).

heat addition (finally reaching the critical Mach number M_c at the maximum entropy point, beyond which heat addition is impossible for the given ϵ and the given M_1). The curve $\epsilon = 1$ is the conventional Rayleigh line where $M_c = 1$. It will be shown later that the minimum stagnation pressure loss of the supercritical burning for given heat addition q and given configuration ϵ occurs when the incoming Mach number M_1 is shown such that the critical condition M_c is reached at the exit.

Similarly, for a given entrance supercritical Mach number M_1, a given entrance stagnation temperature T_1, and a given heat addition q, one may calculate the required duct configuration ϵ which will yield a critical Mach number M_c at the exit in order to achieve minimum stagnation pressure losses. The required value ϵ may be calculated directly from Eq. (1-A-13), when Eq. (1-A-12) is substituted into Eq. (1-A-13) for M_c and Eq. (1-A-10c) is substituted into Eq. (1-A-13) for (T_c/T_1).

Stagnation Pressure Ratio. The stagnation pressure ratio (an indication of total pressure losses) is important. This may be obtained as follows:

Eliminating dt/t from Eqs. (1-A-7) and (1-A-8), one obtains:

$$(\epsilon + kM^2)\frac{dp}{p} + \epsilon k dM^2 = 0 \qquad \text{(1-A-14)}$$

Integrating Eq. (1-A-14), one obtains:

$$\left(\frac{p}{p_1}\right) = \left[\frac{\epsilon + kM_1^2}{\epsilon + kM^2}\right]^\epsilon \qquad \text{(1-A-15)}$$

Putting into the stagnation pressure P, one obtains:

$$\left(\frac{P}{P_1}\right) = \left(\frac{p}{p_1}\right) \left[\frac{1 + \dfrac{k-1}{2} M^2}{1 + \dfrac{k-1}{2} M_1^{\,2}}\right]^{\frac{k}{k-1}}$$

(1-A-16)

$$= \left[\frac{\epsilon + kM_1^{\,2}}{\epsilon + kM^2}\right]^{\epsilon} \left[\frac{1 + \dfrac{k-1}{2} M^2}{1 + \dfrac{k-1}{2} M_1^{\,2}}\right]^{\frac{k}{k-1}}$$

For the special case of constant cross-section where $\epsilon = 1$, Eq. (1-A-16) reduces to Eq. (1-148a).

In order to be able to judge the merit of one particular ϵ (the advantage of one particular duct configuration ϵ for the given initial flow conditions) and one particular heat addition, the influence of ϵ (Fig. 1-A-2) on the stagnation pressure loss during burning has to be considered.

Figure 1-A-3 shows the stagnation pressure ratio achieved during burning initiated at M_1 and ending at M_c. The stagnation pressure ratio of the process ending at any other Mach number is equal to the ratio of the pressure ratios corresponding to the initial and final Mach numbers since $P_2/P_1 = (P_c/P_1)/(P_c/P_2)$. The relation between M_1 and M_2 is found by applying the ϵ expression of the preceding section for a particular inlet stagnation enthalpy (function of flight Mach number) and heat addition (function of fuel type and fuel-air ratio). Figure 1-A-4 shows the stagnation pressure ratio for several ϵ values and supercritical burning for the specific case of flight Mach number $M_0 = 20$ and stoichiometric
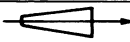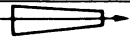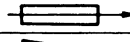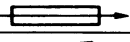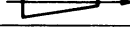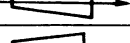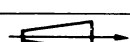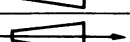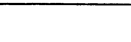
ϵ	Subcritical	Supercritical
$\epsilon > 1$		
$\epsilon = 1$		
$0 < \epsilon < 1$		
$\epsilon = 0$		
$\epsilon < 0$		

Fig. 1-A-2 (After A. Doborowolski, NASA TND 3626).
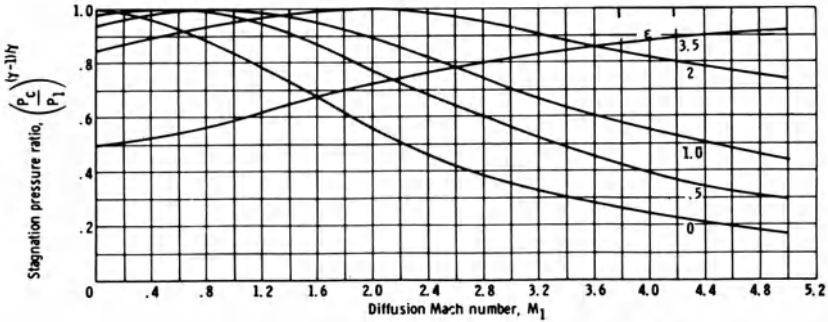
Fig. 1-A-3 Stagnation pressure ratio due to burning that changes flow from diffusion to critical Mach number. (After A. Doborowolski, NASA TND 3626).
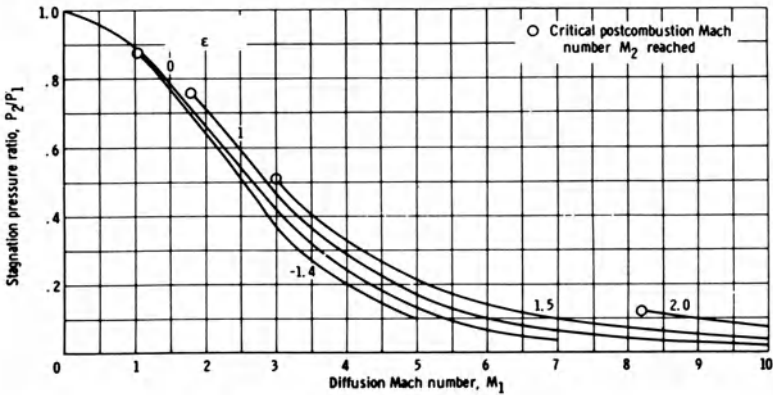
Fig. 1-A-4 Stoichiometric hydrogen combustion stagnation pressure ratio as function of diffusion Mach number for flight Mach number of 20. (After A. Doborowolski, NASA TND 3626).

combustion of hydrogen. It is seen that given a series of ϵ ducts with the supercritical flows at the same initial Mach number M_1 and subjected to the same heat addition, the larger the ϵ, the smaller the stagnation pressure loss. From Fig. 1-A-2, where the shapes of the ducts are noted, this would imply, for example, that a convergent duct is superior to a constant area duct for the same M_1.

Given a series of ϵ ducts with the supercritical flows of the same stagnation enthalpy at different initial Mach numbers M_1, such that each duct reaches a critical condition after the same heat addition, the larger the positive ϵ, the larger the stagnation pressure loss (circled points in Fig. 1-A-4). This implies that a constant area duct is superior to a convergent duct if a critical condition is reached in both ducts. (The shapes of duct are noted from Fig.

1-A-2.) Thus, diffusing the flow (without losses) sufficiently for the subsequent heat addition in the constant area duct to reach a critical condition will yield a better stagnation pressure ratio than direct use of a critically convergent duct. A diverging, critical, constant Mach number duct ($\epsilon = -1.4$) is still better. Best of all is the constant pressure case ($\epsilon = 0$); however, heat addition in this case requires the flow to pass smoothly from supersonic to subsonic. This condition may not be achievable in practice.

2) Heat addition in non-constant area duct with friction and $(T_w/T) = Constant.$ In this case, Eq. (1-A-10) becomes:

$$\frac{dM^2}{M^2} = \frac{(\epsilon + kM^2)\left(1 + \dfrac{k-1}{2}M^2\right) + 2kM^2\left(1 + \dfrac{k-1}{2}M^2\right)\left[\dfrac{1}{(T_w/T)-1}\right]}{\epsilon(1-M^2) - (1-\epsilon)kM^2}\left(\frac{dT}{T}\right)$$

(1-A-17)

Equation (1-A-17) may be integrated. Once M in terms of M_1 is known, (P/P_1) may be obtained from Eq. (1-106a) by ratioing the two sections concerned.

3) Flow with friction in non-constant area duct without heat addition. In this case, $dT = 0$, so Eq. (1-A-5a) must be substituted back into Eq. (1-A-10) which gives:

$$\frac{dM^2}{M^2} = \frac{kM^2\left(1 + \dfrac{k-1}{2}M^2\right)}{\epsilon(1-M^2) - (1-\epsilon)kM^2}\,4f\,\frac{dx}{D}$$

(1-A-18)

since $\dfrac{\pi}{4}D^2 = A$

$$D = \frac{2A^{1/2}}{\sqrt{\pi}} = \frac{2}{\sqrt{\pi}}\left(\frac{p}{p_1}\right)^{\frac{1-\epsilon}{2\epsilon}}A_1^{\frac{1}{2}}$$

Eliminating (dt/t) from Eqs. (1-A-7) and (1-38) for the case of $dT = 0$, one obtains after simplification:

$$p = \left[\frac{1 + \dfrac{k-1}{2}M_1^2}{1 + \dfrac{k-1}{2}M^2}\right]^{\frac{\epsilon}{2}}\left(\frac{M_1}{M}\right)^{\epsilon}p_1$$

(1-A-19)

Therefore

$$D = \frac{2}{\sqrt{\pi}} \left(\frac{p}{p_1}\right)^{\frac{1-\epsilon}{2\epsilon}} A^{\frac{1}{2}}$$

$$= \frac{2}{\sqrt{\pi}} \left[\left(\frac{1 + \frac{k-1}{2} M_1^2}{1 + \frac{k-1}{2} M^2} \right)^{\frac{1}{2}} \left(\frac{M_1}{M}\right) \right]^{\frac{1-\epsilon}{2}} A^{\frac{1}{2}}$$

Let

$$c_2 = \left(\frac{2}{\sqrt{\pi}}\right) A^{\frac{1}{2}} p_1 \left[\left(1 + \frac{k-1}{2} M_1^2\right)^{\frac{1}{2}} M_1 \right]^{\frac{1-\epsilon}{2}}$$

$$\therefore D = c_2 \left[\left(1 + \frac{k-1}{2} M^2\right)^{\frac{1}{2}} M \right]^{\frac{\epsilon-1}{2}} \qquad (1\text{-}A\text{-}20)$$

Substituting Eq. (1-A-20) into Eq. (1-A-18), one may integrate Eqs. (1-A-18) in the form of M as a function of x. This is the generalized Fanno line. For the special case of constant cross-section area where $\epsilon = 1$, Eq. (1-A-20) reduces to constant D and the result reduces to Eq. (1-152), the conventional Fanno line.

4) Constant Mach number heat addition in non-constant area duct with friction. Here $M =$ constant Eq. (1-A-10) becomes:

$$(\epsilon + kM^2)\frac{dT}{T} = 2kM^2 \frac{dT}{T - T_w} = -kM^2 \, 4f \frac{dx}{D}$$

$$(\epsilon + kM^2) \frac{dT}{T} = -kM^2 \, 4f \frac{dx}{\left[\left(1 + \frac{k-1}{2} M^2\right)^{\frac{1}{2}} M \right]^{\frac{\epsilon-1}{2}}}$$

$$-\frac{(\epsilon + kM^2)\left[\left(1 + \frac{k-1}{2} M^2\right)^{\frac{1}{2}} M \right]^{\frac{\epsilon-1}{2}}}{M^2} \frac{dT}{T} = \left(\frac{k4f}{c_2}\right) dx. \qquad (1\text{-}A\text{-}21)$$

Since M = constant, Eq. (1-A-21) may be integrated to give:

$$-\frac{\left[\left(1 + \frac{k-1}{2} M^2\right)^{\frac{1}{2}} M\right]^{\frac{\epsilon-1}{2}} (\epsilon + kM^2)}{M^2} \ln \frac{T}{T_1} = \frac{k4f}{c_2} (x - x_1)$$

$$-\ln\left(\frac{T}{T_1}\right) = \left(\frac{k4f}{c_2}\right) \frac{M^2 x}{(\epsilon + kM^2)\left[\left(1 + \frac{k-1}{2} M^2\right)^{\frac{1}{2}} M\right]^{\frac{\epsilon-1}{2}}}$$

$$\left(\frac{T_1}{T}\right) = \exp\left\{\left(\frac{k4f}{c_2}\right)x\right\}\left\{(\epsilon + kM^2)^{-1}\left[\left(1 + \frac{k-1}{2} M^2\right)^{\frac{1}{2}} M\right]^{\frac{1-\epsilon}{2}}\right\} \quad (1-A-22)$$

[1-10.2] Mixing of Two Flows in a Non-Constant Area Duct

The analysis of ducted fan, ducted rocket, etc., requires a knowledge of the mixing of two flows of different temperature, pressure and velocity. Sometimes subsequent heating of the mixed flow may be realized if one of the two flows is fuel riched. Let us again use a duct whose cross-sectional area A varies with pressure p by the prescribed relationship:

$$\left(\frac{p}{p_1}\right) = \left(\frac{A}{A_1 + A_2}\right)^{\frac{\epsilon}{1-\epsilon}} \quad \text{or} \quad (A_1 + A_2)\left(\frac{p}{p_1}\right)^{\frac{1-\epsilon}{\epsilon}} = A$$

$$(1-A-23)$$

1) Continuity

$$m_1 + m_2 = m_3 \quad (1-A-24)$$

$$\rho_1 V_1 A_1 + \rho_2 V_2 A_2 = \rho_3 V_3 A_3 \quad (1-A-25)$$

2) Momentum

$$\rho V dV + dp = 0 \quad (1-A-26)$$

Equation (1-A-26) can be written as

$$\rho A V dV + d(pA) - p dA = 0 \quad (1-A-27)$$

Applying Eq. (1-A-27) between sections 3 and 1+2, one obtains:

$$\rho_1 A_1 V_1 (V_3 - V_1) + \rho_2 A_2 V_2 (V_3 - V_2) + p_3 A_3 - (p_1 A_1 + p_2 A_2)$$

$$- \int_{(A_1 + A_2)}^{A_3} p_1 \left(\frac{A}{A_1 + A_2} \right)^{\frac{\epsilon}{1-\epsilon}} dA = 0 \qquad \text{(1-A-28)}$$

Here

$$\int_{(A_1 + A_2)}^{A_3} p_1 \left(\frac{A}{A_1 + A_2} \right)^{\frac{\epsilon}{1-\epsilon}} dA = (1 - \epsilon) \left[p_3 A_3 - p_1 (A_1 + A_2) \right].$$

$$\text{(1-A-29)}$$

Substituting Eq. (1-A-29) into Eq. (1-A-28), one obtains:

$$\rho_3 A_3 V_3^2 - \left(\rho_1 V_1^2 A_1 + \rho_2 A_2 V_2^2 \right) + \epsilon p_3 A_3 - \epsilon p_1 A_1$$

$$- p_2 A_2 + p_1 A_2 - \epsilon p_1 A_2 = 0.$$

Rearranging terms, one obtains:

$$A_3 \left[\rho_3 V_3^2 + \epsilon p_3 \right] = A_1 \left[\rho_1 V_1^2 + \epsilon p_1 \right]$$

$$+ A_2 \left\{ \rho_2 V_2^2 + \left[\epsilon + \left(1 - \frac{p_1}{p_2} \right)(1 - \epsilon) \right] p_2 \right\}$$

$$\text{(1-A-30)}$$

since $\rho V^2 = k p M^2$, we have

$$p_3 A_3 \left[k_3 M_3^2 + \epsilon \right] = p_1 A_1 \left[k_1 M_1^2 + \epsilon \right]$$

$$+ p_2 A_2 \left\{ k_2 M_2^2 + \left[\epsilon + \left(1 - \frac{p_1}{p_2} \right)(1 - \epsilon) \right] \right\}$$

$$\text{(1-A-31)}$$

Substituting Eq. (1-A-23) into Eq. (1-A-31), one obtains:

$$p_3 \, (A_1 + A_2) \left(\frac{p_3}{p_1}\right)^{\frac{1-\epsilon}{\epsilon}} \left[k_3 M_3^2 + \epsilon\right] = p_1 A_1 \left[k_1 M_1^2 + \epsilon\right]$$

$$+ \, p_2 A_2 \left\{ k_2 M_2^2 + \left[\epsilon + \left(1 - \frac{p_1}{p_2}\right)(1 - \epsilon)\right] \right\}$$

Since $P_3 = p_3 \left[1 + \frac{k-1}{2} M_3^2\right]^{\frac{k}{k-1}}$, we have

$$\left\{ \left(\frac{P_3}{P_1}\right) \frac{\left[1 + \frac{k_1 - 1}{2} M_1^2\right]^{\frac{k_1}{k_1 - 1}}}{\left[1 + \frac{k_3 - 1}{2} M_3^2\right]^{\frac{k_3}{k_3 - 1}}} \right\}^{\frac{1}{\epsilon}} \left[k_3 M_3^2 + \epsilon\right] = \left(\frac{A_1}{A_1 + A_2}\right) \left[k_1 M_1^2 + \epsilon\right]$$

$$+ \left(\frac{p_2}{p_1}\right) \left(\frac{A_2}{A_1 + A_2}\right) \left\{ k_2 M_2^2 + \left[\epsilon + \left(1 - \frac{p_1}{p_2}\right)(1 - \epsilon)\right] \right\}$$

$$(1-A-32)$$

Using the continuity equation, we have

$$\rho_1 A_1 V_1 + \rho_2 A_2 V_2 = \rho_3 A_3 V_3 \qquad\qquad (1-A-25)$$

Since $\rho AV = \dfrac{pA}{R\sqrt{t}} \dfrac{\sqrt{kR}}{\sqrt{kR}} \dfrac{V}{\sqrt{t}} = \sqrt{\dfrac{k}{Rt}} \; pAM$, we have

$$\sqrt{\frac{k_1}{R_1}} \frac{A_1 M_1}{(A_1 + A_2)} + \sqrt{\frac{k_2 t_1}{R_2 t_2}} \left(\frac{p_2}{p_1}\right) \frac{A_2 M_2}{(A_1 + A_2)} = \sqrt{\frac{k_3}{R_3 t_3}} \frac{p_3 A_3 M_3}{(A_1 + A_2)} \left(\frac{t_1}{p_1}\right)$$

$$= \sqrt{\frac{k_3 t_1}{R_3 t_3}} \; M_3 \left(\frac{p_3}{p_1}\right)^{\frac{1}{\epsilon}}$$

$$(1-A-33)$$

$$\left[\sqrt{\frac{k_1}{R_1}}\left(\frac{A_1 M_1}{A_1 + A_2}\right) + \sqrt{\frac{k_2}{R_2}}\left(\frac{A_2 M_2}{A_1 + A_2}\right)\left(\frac{t_1}{t_2}\right)^{\frac{1}{2}}\right] = \sqrt{\frac{k_3}{R_3}}\ M_3 \left(\frac{t_1}{t_3}\right)^{\frac{1}{2}}\left(\frac{p_3}{p_1}\right)^{\frac{1}{\epsilon}}$$

(1-A-34)

or

$$\frac{t_3}{t_1} = \left\{\frac{\sqrt{\dfrac{k_3}{R_3}}\ M_3 \left(\dfrac{p_3}{p_1}\right)^{\frac{1}{\epsilon}}}{\sqrt{\dfrac{k_1}{R_1}}\left(\dfrac{A_1}{A_1 + A_2}\right) M_1 + \sqrt{\dfrac{k_2}{R_2}}\left(\dfrac{A_2}{A_1 + A_2}\right) M_2 \left(\dfrac{t_1}{t_2}\right)^{\frac{1}{2}}}\right\}^2$$

or

$$\left(\frac{T_3}{T_1}\right)\left[\frac{1 + \dfrac{k-1}{2} M_1^{\ 2}}{1 + \dfrac{k-1}{2} M_3^{\ 2}}\right] = \left\{\sqrt{\frac{k_3}{R_3}}\ M_3 \right.$$

$$\times \left\{\frac{\left(\dfrac{A_1}{A_1 + A_2}\right)(\epsilon + kM_1^{\ 2}) + \left(\dfrac{p_2}{p_1}\right)\left(\dfrac{A_2}{A_1 + A_2}\right)\left\{k_2 M_2^{\ 2} + \left[\epsilon + \left(1 - \dfrac{p_1}{p_2}\right)(1 - \epsilon)\right]\right\}}{k_3 M_3^{\ 2} + \epsilon}\right.$$

$$\left. \div \left\{\sqrt{\frac{k_1}{R_1}}\left(\frac{A_1}{A_1 + A_2}\right) M_1 + \sqrt{\frac{k_2}{R_2}}\left(\frac{A_2}{A_1 + A_2}\right) M_2 \left(\frac{t_1}{t_2}\right)^{\frac{1}{2}}\right\}^2\right.$$

$$\left(\frac{T_3}{T_1}\right) = \left\{ \frac{\sqrt{\frac{k_3}{R_3}} M_3 \left[\frac{\left[\left(\frac{A_1}{A_1 + A_2}\right)(\epsilon + k_1 M_1^2) + \left(\frac{p_2}{p_1}\right)\left(\frac{A_2}{A_1 + A_2}\right)\left\{ k_2 M_2^2 + \left[\epsilon + \left(1 - \frac{p_1}{p_2}\right)(1 - \epsilon)\right]\right\}\right]}{k_3 M_3^2 + \epsilon}\right]^2}{\sqrt{\frac{k_1}{R_1}}\left(\frac{A_1}{A_1 + A_2}\right) M_1 + \sqrt{\frac{k_2}{R_2}}\left(\frac{A_2}{A_1 + A_2}\right) M_2 \left(\frac{t_1}{t_2}\right)^{\frac{1}{2}}} \right\}$$

$$\times \left[\frac{1 + \dfrac{k_3 - 1}{2} M_3^2}{1 + \dfrac{k - 1}{2} M_1^2}\right]$$

(1-A-35)

From the energy equation, we have

$$(m_1 + m_2) c_{p_3} T_3 - \left[m_1 c_{p_1} T_1 + m_2 c_{p_2} T_2\right] = 0$$

or

$$\left(\frac{T_3}{T_1}\right) = \left(\frac{m_1}{m_1 + m_2}\right)\left(\frac{c_{p_1}}{c_{p_3}}\right) + \left(\frac{m_2}{m_1 + m_2}\right)\left(\frac{c_{p_2}}{c_{p_3}}\right)\left(\frac{T_2}{T_1}\right) \quad \text{(1-A 36)}$$

If burning occurs after or during mixing, the energy equation becomes:

$$(m_1 + m_2) c_{p_3} T_3 - \left[m_1 c_{p_1} T_1 + m_2 c_{p_2} T_2\right]$$

$$= (m_1 + m_2) q = (m_1 + m_2) \eta_b f h^*$$

or

$$\left(\frac{T_3}{T_1}\right) = \left(\frac{m_1}{m_1 + m_2}\right)\left(\frac{c_{p_1}}{c_{p_3}}\right) + \left(\frac{m_2}{m_1 + m_2}\right)\left(\frac{c_{p_2}}{c_{p_3}}\right)\left(\frac{T_2}{T_1}\right) + \left(\frac{\eta_b f h^*}{c_{p_3} T_1}\right) \quad \text{(1-A-37)}$$

Here

$$f = \text{fuel-air-ratio} = \frac{\text{pounds of fuel}}{\text{pounds of unburned air in } m_3}$$

Here we have three equations: (1-A-32), (1-A-35), and (1-A-37) with three unknowns (P_3, T_3, M_3) so they may be solved.

The following special cases are of particular interest.

1) Constant area mixing. For constant area mixing when $\epsilon = 1$, Eqs. (1-32), (1-A-35) and (1-A-37) reduce to:

$$\left(\frac{P_3}{P_1}\right)\left[\frac{\left[1 + \dfrac{k_1 - 1}{2}M_1^2\right]^{\frac{k_1}{k_1-1}}}{\left[1 + \dfrac{k_3 - 1}{2}M_3^2\right]^{\frac{k_3}{k_3-1}}}\right]\left(k_3 M_3^2 + 1\right)$$

$$= \left(\frac{A_1}{A_1 + A_2}\right)\left(1 + k_1 M_1^2\right) + \left(\frac{p_2}{p_1}\right)\left(\frac{A_2}{A_1 + A_2}\right)\left(1 + k_2 M_2^2\right)$$

$$\tag{1-A-32a}$$

$$\left(\frac{T_3}{T_1}\right) = \left\{\sqrt{\frac{k_3}{R_3}}\,M_3\right.$$

$$\times \left\{\frac{\left(\dfrac{A_1}{A_1 + A_2}\right)\left(1 + k_1 M_1^2\right) + \left(\dfrac{p_2}{p_1}\right)\left(\dfrac{A_2}{A_1 + A_2}\right)\left[k_2 M_2^2 + 1\right]}{\left(1 + k_3 M_3^2\right)}\right\}$$

$$\div \left\{\sqrt{\frac{k_1}{R_1}}\left(\frac{A_1}{A_1 + A_2}\right)M_1 + \sqrt{\frac{k_2}{R_2}}\left(\frac{A_2}{A_1 + A_2}\right)M_2\left(\frac{t_1}{t_2}\right)^{\frac{1}{2}}\right\}^2 \times$$

$$\tag{1-A-35a}$$

$$\times \quad \left[\frac{1 + \dfrac{k_3 - 1}{2} M_3^2}{1 + \dfrac{k_1 - 1}{2} M_1^2} \right]$$

$$\text{(1-A-35a cont.)}$$

Here Eq. (1-A-37) remains the same.

When specific heats are constant, *i.e.*, $k_1 = k_2 = k_3$, $R_1 = R_2 = R_3$, $c_{p_1} = c_{p_2} = c_{p_3}$ Eqs. (1-A-32), (1-A-35), and (1-A-37) further reduce to:

$$\left(\frac{P_3}{P_1} \right) \left[\frac{1 + \dfrac{k - 1}{2} M_1^2}{1 + \dfrac{k - 1}{2} M_3^2} \right]^{\frac{k}{k-1}} \quad \left(k M_3^2 + 1 \right)$$

$$= \left(\frac{A_1}{A_1 + A_2} \right) \left(1 + k M_1^2 \right) + \left(\frac{p_2}{p_1} \right) \left(\frac{A_2}{A_1 + A_2} \right) \left(1 + k M_2^2 \right)$$

$$\text{(1-A-32b)}$$

$$\left(\frac{T_3}{T_1} \right) = \left\{ \frac{M_3 \left[\left(\dfrac{A_1}{A_1 + A_2} \right) \left(1 + k M_1^2 \right) + \left(\dfrac{p_2}{p_1} \right) \left(\dfrac{A_2}{A_1 + A_2} \right) \left(1 + k M_2^2 \right) \right]}{\left(1 + k M_3^2 \right) \left[\left(\dfrac{A_1}{A_1 + A_2} \right) M_1 + \left(\dfrac{A_2}{A_1 + A_2} \right) M_2 \left(\dfrac{t_1}{t_2} \right)^{\frac{1}{2}} \right]} \right\}^2 \left[\frac{1 + \dfrac{k - 1}{2} M_3^2}{1 + \dfrac{k - 1}{2} M_1^2} \right]$$

$$\text{(1-A-35b)}$$

$$\left(\frac{T_3}{T_1} \right) = \left(\frac{m_1}{m_1 + m_2} \right) = \left(\frac{m_2}{m_1 + m_2} \right) \left(\frac{T_2}{T_1} \right) + \left(\frac{\eta_b f h^*}{c_p T_1} \right)$$

$$\text{(1-A-37b)}$$

When mixing without burning at constant specific heats, Eqs. (1-A-37), (1-A-32), and (1-A-35) further reduce to:

$$\left(\frac{T_3}{T_1} \right) = \left(\frac{m_1}{m_1 + m_2} \right) + \left(\frac{m_2}{m_1 + m_2} \right) \left(\frac{T_2}{T_1} \right)$$

$$\text{(1-A-37c)}$$

(1-A-32b) remains the same. (1-A-35b) remains the same. When mixing without burning and $p_1 = p_2$ Eqs. (1-A-32), (1-A-35), and (1-A-37) reduce to:

$$\left(\frac{P_3}{P_1}\right)\left[\frac{1 + \frac{k-1}{2}M_1^2}{1 + \frac{k-1}{2}M_3^2}\right]^{\frac{k}{k-1}}\left(1 + kM_3^2\right) = \left(\frac{A_1}{A_1+A_2}\right)\left(1 + kM_1^2\right) + \left(\frac{A_2}{A_1+A_2}\right)\left(1 + kM_2^2\right)$$

$$(1\text{-}A\text{-}32d)$$

$$\left(\frac{T_3}{T_1}\right) = \left\{\frac{M_3\left[\left(\frac{A_1}{A_1+A_2}\right)\left(1 + kM_1^2\right) + \left(\frac{A_2}{A_1+A_2}\right)\left(1 + kM_2^2\right)\right]}{\left(1 + kM_3^2\right)\left[\left(\frac{A_1}{A_1+A_2}\right)M_1 + \left(\frac{A_2}{A_1+A_2}\right)M_2\left(\frac{t_1}{t_2}\right)\right]^{\frac{1}{2}}}\right\}^2\left[\frac{1 + \frac{k-1}{2}M_3^2}{1 + \frac{k-1}{2}M_1^2}\right]$$

$$(1\text{-}A\text{-}35d)$$

Equation (1-A-37c) remains the same.

2) *Constant pressure mixing.* For constant pressure mixing where $\epsilon = 0$, Eqs. (1-A-32), (1-A-35), and (1-A-37) reduce to:

$$A_3k_3M_3^2 = A_1k_1M_1^2 + A_2k_2M_2^2 \qquad (1\text{-}A\text{-}32e)$$

$$\left(\frac{T_3}{T_1}\right) = \left\{\frac{\sqrt{\frac{k_3}{R_3}}\left[\left(\frac{A_1}{A_1+A_2}\right)k_1M_1^2 + \left(\frac{A_2}{A_1+A_2}\right)k_2M_2^2\right]}{k_3M_3\left[\sqrt{\frac{k_1}{R_1}}\left(\frac{A_1}{A_1+A_2}\right)M_1 + \sqrt{\frac{k_2}{R_2}}\left(\frac{A_2}{A_1+A_2}\right)M_2\sqrt{\frac{t_1}{t_2}}\right]}\right\}^2\left[\frac{1 + \frac{k_3-1}{2}M_3^2}{1 + \frac{k_1-1}{2}M_1^2}\right]$$

$$(1\text{-}A\text{-}35e)$$

(1-A-37) remains the same.

When the specific heats are constants, *i.e.*, $k_1 = k_2 = k_3$, $R_1 = R_2 = R_3$, $c_{p_1} = c_{p_2} = c_{p_3}$, Eqs. (1-A-32), (1-A-37), and (1-A-35) reduce to:

$$A_3M_3^2 = A_1M_1^2 + A_2M_2^2 \qquad (1\text{-}A\text{-}32f)$$

$$\left(\frac{T_3}{T_1}\right) = \left\{\frac{\left[\left(\frac{A_1}{A_1+A_2}\right)M_1^2 + \left(\frac{A_2}{A_1+A_2}\right)M_2^2\right]}{M_3\left[\left(\frac{A_1}{A_1+A_2}\right)M_1 + \left(\frac{A_2}{A_1+A_2}\right)M_2\left(\frac{t_1}{t_2}\right)\right]^{\frac{1}{2}}}\right\}^2\left[\frac{1 + \frac{k-1}{2}M_3^2}{1 + \frac{k-1}{2}M_1^2}\right]$$

$$(1\text{-}A\text{-}35f)$$

$$\left(\frac{T_3}{T_1}\right) = \left(\frac{m_1}{m_1 + m_2}\right) + \left(\frac{m_2}{m_1 + m_2}\right)\left(\frac{T_2}{T_1}\right) + \left(\frac{\eta_b\, fh}{c_p T_1}\right)^*$$

(1-A-37f)

When mixing without burning at constant specific heats, Eqs. (1-A-32), (1-A-35), and (1-A-37) reduce to:

$$\left(\frac{T_3}{T_1}\right) = \left(\frac{m_1}{m_1 + m_2}\right) + \left(\frac{m_2}{m_1 + m_2}\right)\left(\frac{T_2}{T_1}\right)$$

(1-A-37g)

(1-A-32f) remains the same. (1-A-35f) remains the same.

[1-11] THERMODYNAMIC CYCLE ANALYSIS

The thermodynamic performance of a gas turbine or jet propulsion engine can be analyzed through the use of thermodynamic cycle analysis. Thermodynamic cycle analysis is usually carried out, based on one unit mass flow per second. With this understanding in mind, the following unit process per unit mass may be described through the use of entropy-enthalpy diagram.

[1-11.1] Ram Compression and Ram Pressure Recovery

The performance of aircraft propulsion is often considered as the aircraft remains stationary while the air approaches it with the aircraft speed V_0. Therefore, in Fig. 1-15, point 0 (at a temperature equal to ambient temperature t_0, and at a pressure equal to ambient pressure p_0) represents the ambient state. From energy equation

$$h_0 + \frac{V_0^2}{2gJ} = H_0 = H_1$$

(1-63)

the total enthalpy should rise to H_1, the state at the exit of the diffuser. For an ideal isentropic process (s = constant) with full recovery from the speed V_0 effect, the stagnation pressure would rise to P_1, as shown in Fig. 1-15. However, with full pressure recovery impossible (through a diffuser), the stagnation pressure is actually P_1, a value less than P_1', due to pressure losses, as shown in Fig. 1-15. Therefore, ram pressure recovery may be defined as:

$$\eta_r = \frac{\text{actual pressure rise}}{\text{isentropic pressure rise}} = \frac{P_1 - p_0}{P_1' - p_0}.$$

(1-160)

It is to be noted here that, although P_1 is less than P_1', H_1 is equal to H_1'. For constant specific heats, Eq. (1-160) may be written as follows:

$$\eta_r = \frac{\left(\dfrac{P_1}{p_0}\right) - 1}{\left(\dfrac{P_1'}{p_0}\right) - 1} = \frac{\left(\dfrac{P_1}{p_0}\right) - 1}{\left[1 + \dfrac{V_0^2}{2gJc_p t_0}\right]^{\frac{k}{k-1}} - 1} \qquad (1\text{-}161)$$

$$\frac{V_0^2}{2gJ} + c_p t_0 = c_p T_1. \qquad (1\text{-}162)$$

Therefore, for constant specific heats, the stagnation pressure P_1 and stagnation temperature T_1 can be calculated when ambient temperature t_0, ambient pressure p_0, ram pressure recovery η_r and airplane velocity V_0 are known from Eqs. (1-161) and (1-162). For more accurate calculation with variable specific heats, one may use either the h–s diagram or the air table of Keenan and Kaye.

1) Use of h–s diagram. Point 0 may be determined from ambient pressure p_0 and ambient temperature t_0. Ambient enthalpy h_0 may now be read directly from the h–s diagram. H_1 and H_1' may be obtained from Eq. (1-63),

$$h_0 + \frac{V_0^2}{2gJ} = H_1 = H_1'. \qquad (1\text{-}63)$$

Point P_1' may be determined from the value of H_1' and the known value of entropy s (vertically above point 0). Point 1 may be determined by H_1 and P_1 where P_1 may be calculated from ram pressure recovery η_r which is given.

2) Use of air table or gas table. Air table gives h and p_r as a function of T.

Point	T	h	p_r	p
0	t_0	h_0	p_{r_0}	p_0
1'	T_1'	H_1'	p_{r_1}	P_1'
1	T_1	H_1		P_1

a) At point 0, t_0 is known, so h_0 and p_{r_0} may be read directly from the air table.

b) $H_1{}'$ may be determined from $H_1 = h_0 + V_0{}^2/2gJ$ and then read correspondingly $T_1{}'$ and p_{r_1} ,from the air table.

c) From point 0 to point 1', it is an isentropic process, so we have:

$$\frac{p_{r_0}}{p_{r_1}} = \frac{p_0}{P_1}$$

Here relative pressure relation
is valid for isentropic process
only (see air table or gas table).

Therefore, $P_1{}'$ may be calculated from the above equation.

d) With ram pressure recovery η_r known, p_1 may be calculated from

$$\eta_r = \frac{P_1 - p_0}{P_1' - p_0} .$$

e) Since $H_1 = H_1{}'$, read T correspondingly to H_1 from the air table.

This gives both stagnation pressure p_1 and stagnation temperature T_1 as shown in the table above.

[1-11.2] Compressor Compression and Compressor Work

In thermodynamic cycle analysis of compressor, turbine, intercooling, reheating, regeneration, etc., stagnation pressure, stagnation temperature and stagnation enthalpy are often used. Therefore, for steady flow compression, Eq. (1-61) gives

$$W_{compressor} = H_2 - H_1. \tag{1-61}$$
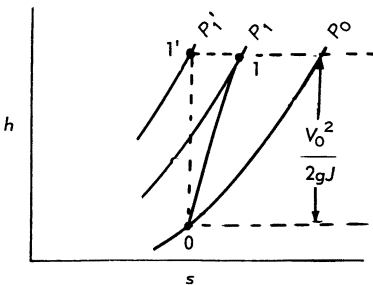
Fig. 1-15
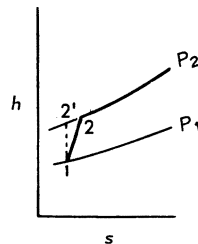
Fig. 1-16

In Fig. 1-16, point 1 represents the thermodynamic state ahead of the compressor (stagnation temperature T_1, stagnation pressure P_1,

stagnation enthalpy H_1). Dotted vertical line 1–2' represents isentropic compression (zero entropy change) between stagnation pressures P_1 and P_2', respectively, at compressor inlet and outlet. Due to friction in actual compression which causes an increase of entropy, actual compression always follows solid line 1–2. For the same compression pressure rise from pressure P_1 to P_2 (which is equal to P_2'), more energy or shaft work is required for actual compression than isentropic compression. Therefore, a compressor efficiency may be defined as:

$$\eta_c = \frac{\text{Isentropic compressor work } W_{c_i}}{\text{Actual compressor work } W_{c_a}} = \frac{H_2' - H_1}{H_2 - H_1}. \qquad (1\text{-}163)$$

For constant specific heats, Eq. (1-163) may be written as:

$$\eta_c = \frac{c_p(T_2' - T_1)}{c_p(T_2 - T_1)} = \frac{\left(\dfrac{T_2'}{T_1}\right) - 1}{\left(\dfrac{T_2}{T_1}\right) - 1} = \frac{\left(\dfrac{P_2'}{P_1}\right)^{\frac{k-1}{k}}}{\left(\dfrac{T_2}{T_1}\right) - 1} = \frac{\left(\dfrac{P_2}{P_1}\right)^{\frac{k-1}{k}} - 1}{\left(\dfrac{T_2}{T_1}\right) - 1}.$$

$$(1\text{-}164)$$

From Eq. (1-61), actual compressor work per pound of air flow per second is represented by the solid line 1–2 or

$$W_{c_a} = H_2 - H_1. \qquad (1\text{-}61)$$

For constant specific heats, one obtains from Eq. (1-164):

$$W_{c_a} = c_p(T_2 - T_1) = c_p T_1 \left[\left(\frac{T_2}{T_1}\right) - 1\right] = \frac{c_p T_1}{\eta_c}\left[\left(\frac{P_2}{P_1}\right)^{\frac{k-1}{k}} - 1\right].$$

$$(1\text{-}165)$$

Here, compressor work is in terms of compressor inlet temperature T_1, compressor efficiency η_c, and compression ratio (P_2/P_1). It is to be noted here that, for the same compression ratio (P_2/P_1) and the same compressor efficiency η_c, the lower the inlet temperature T_1, the less the compressor work W_{c_a}. Therefore, a jet engine operating at high altitude or cold ambient temperature requires less compressor work and consequently more power output

when everything else remains the same. The compressor outlet temperature T_2 can be calculated from Eq. (1-164).

$$\left(\frac{T_2}{T_1}\right) = 1 + \frac{1}{\eta_c}\left[\left(\frac{P_2}{P_1}\right)^{\frac{k-1}{k}} - 1\right] \qquad (1\text{-}166)$$

For more accurate calculation with variable specific heats, one may use either the $h-s$ diagram or the air table or gas table of Keenan and Kaye.

1) $h-s$ diagram. Point 1 is determined by the known values of stagnation temperature T_1 and stagnation pressure P_1. Read H_1 from the $h-s$ diagram for the corresponding value of T_1. The compressor outlet pressure P_2 (known value) and entropy s (going vertically upwards for isentropic compression process) determines point $H_2{}'$, and consequently determines H_2 from Eq. (1-163). With H_2 and P_2 known, point 2 is determined. Therefore, T_2 becomes known. The compressor work W_{c_a} may then be calculated from Eq. (1-61).

2) Air table or gas table.

Point	T	h	p_r	P
1	T_1	$\underline{H_1}$	p_{r_1}	P_1
2'	$\underline{T_2{}'}$	$\underline{H_2{}'}$	$p_{r_2}{}'$	$P_2{}'$
2	$\underline{T_2}$	T_2		P_2

a) T_1 and P_1 are given values. Read p_{r_1} and H_1 from air table.
b) Since $P_2{}' = P_2$ which is given, $p_{r_2}{}'$ may be calculated from

$$\left(\frac{p_{r_2}{}'}{p_{r_1}}\right) = \left(\frac{P_2}{P_1}\right)$$

c) $T_2{}'$ and $H_2{}'$ are read from the air table from the known value of $p_{r_2}{}'$.
d) With the known compressor efficiency η_c, H_2 may be calculated from Eq. (1-163). Then T_2 may be read from the air table corresponding to H_2.
e) Compressor work W_{c_a} may then be calculated from Eq. (1-61).

[1-11.3] Combustion and Burner Efficiency

Because of the very low value of fuel-air ratio (around 0.01 to 0.03) associated with the gas turbine or jet propulsion engine, constant pressure combustion in the gas turbine or jet engine burner may sometimes be approximated, for quick calculation purposes, by constant pressure heating of air from combustion inlet temperature T_1 to combustion outlet temperature T_2. If the thermodynamic properties of fuel-air mixture (products of combustion) can be approximated by the thermodynamic properties of hot air, the calculation process can be greatly shortened. The error introduced is usually in the order of 3 to 5 percent. Therefore, if we treat combustion as heating, we have from Eq. (1-60) and from the $h-s$ diagram:

$$Q = H_2 - H_1.$$

Heat supplied to the combustion chamber is Q which is equal to $fh^*\eta_b$, the product of fuel-air ratio f (pound of fuel consumed per pound of air), heating value of the fuel h^* (heat generated in Btu per pound of fuel consumed), and combustion or burner efficiency η_b. For constant specific heats, we have

$$Q = fh^*\eta_b = c_p(T_2 - T_1). \tag{1-167}$$

Equation (1-167) gives the fuel-air ratio f required to raise stagnation temperature from T_1 to T_2, the combustion chamber inlet and outlet temperature, respectively.

For more accurate calculations, instead of using the hot air approximation, thermodynamic properties of gases or combustion products must be used. This can be done as follows.

[1-11.3.1] Combustion
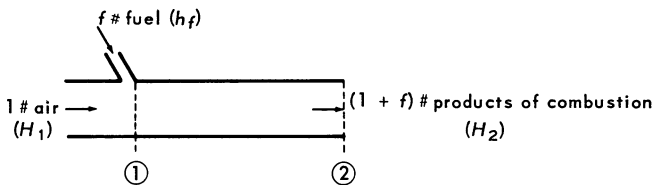
Fig. 1-17

In Fig. 1-17, at Sec. (1) one pound of air enters at air temperature T_1 and f pound of fuel enters at fuel temperature T_f. At Sec. (2), $(1 + f)$ pound of products of combustion leaves at temperature T_2.

Between Secs. (1) and (2), chemical reaction of fuel with air results in a release of Q Btu of heat which is equal to $fh^*\eta_b$. Assuming no heat loss to the outside, the energy equation gives:

$$H_1 + fh_f + Q = (1 + f)H_2. \tag{1-168}$$

Here

H_1 = stagnation enthalpy of entering air at temperature T_1, Btu/#air.

f = fuel-air ratio or pound of fuel per pound air.

h_f = stagnation enthalpy of entering fuel at temperature T_f, Btu/#-fuel.

Q = chemical heat released in combustion chamber = $fh^*\eta_b$, Btu/#fuel.

h^* = heating value of fuel, Btu/#fuel.

η_b = combustion or burner efficiency.

H_2 = stagnation enthalpy of gas or products of combustion at temperature T_2, Btu/#products of combustion.

For gas turbine or jet propulsion engine analysis, the fh_f term is usually very small in comparison with the H_1 and Q term, so it could be neglected. (See analysis on page 110 when the fh_f term is not being neglected). Therefore, we have:

$$(1 + f)H_2 - H_1 = Q = fh^*\eta_b \tag{1-169}$$

or

$$f = \frac{(1 + f)H_2 - H_1}{h^*\eta_b} \tag{1-169a}$$

or approximately

$$f = \frac{H_2 - H_1}{h^*\eta_b}. \tag{1-169b}$$

Here H_1 and H_2 as a function of temperature T_1 and T_2 and fuel air ratio may be obtained directly from the gas table of Keenan and Kaye.

On the other hand, Pinkel has produced a convenient burner or combustion chart (Fig. 1-18) for easy use. Based on the required stagnation temperature rise $(T_2 - T_1)$ and the burner outlet temperature T_2, one may read the effective fuel-air ratio $\eta_b f$ directly from Fig. 1-18.
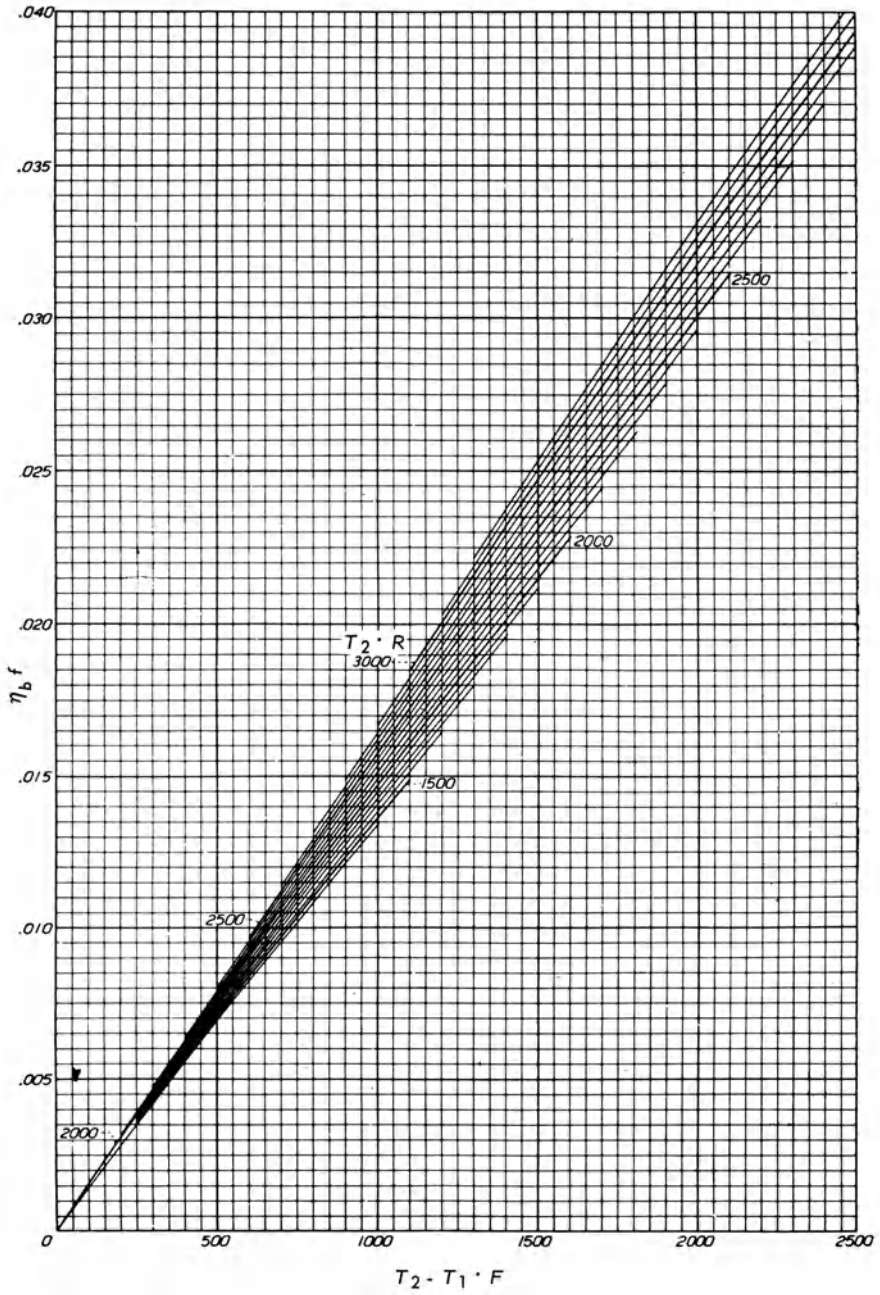
Fig. 1-18 (After B. Pinkel and I. M. Karp, NACA TR 114).

[1-11.4] Turbine Expansion and Turbine Work

For steady flow expansion, Eq. (1-61) gives:

$$w_{\text{turbine}} = w_T = H_1 - H_2. \qquad (1\text{-}61)$$

In Fig. 1-19, point 1 represents the thermodynamic state ahead of the turbine (stagnation temperature T_1, stagnation pressure P_1, and stagnation enthalpy H_1). Vertical dotted line 1–2' represents isentropic expansion (zero entropy change) between stagnation pressures P_1 and P_2, respectively, at turbine inlet and outlet. Due to friction in actual expansion which causes an increase of entropy, actual expansion always follows the solid line 1–2. For the same expansion from pressure P_1 to P_2 (which is equal to P_2'), less energy or shaft work is delivered by the actual turbine expansion than the ideal turbine expansion. Therefore, a turbine efficiency η_T may be defined as:

$$\eta_T = \frac{\text{actual turbine work } w_{T_a} \text{ or } w_T}{\text{isentropic turbine work } w_{T_i}} = \frac{H_1 - H_2}{H_1 - H_2'}. \qquad (1\text{-}170)$$

For constant specific heats, Eq. (1-170) may be written as:

$$\eta_T = \frac{c_p(T_1 - T_2)}{c_p(T_1 - T_2')} = \frac{1 - \left(\dfrac{T_2}{T_1}\right)}{1 - \left(\dfrac{T_2'}{T_1}\right)} = \frac{1 - \left(\dfrac{T_2}{T_1}\right)}{1 - \left(\dfrac{P_2}{P_1}\right)^{\frac{k-1}{k}}}. $$

$$(1\text{-}171)$$

From Eq. (1-61), actual turbine work per pound of air flow is represented by the solid line 1–2 or

$$w_T = H_1 - H_2.$$

For constant specific heats, one obtains from Eq. (1-171):

$$w_T = c_p(T_1 - T_2) = c_p T_1 \left[1 - \left(\frac{T_2}{T_1}\right)\right] = c_p T_1 \eta_T \left[1 - \left(\frac{P_2}{P_1}\right)^{\frac{k-1}{k}}\right].$$

$$(1\text{-}172)$$

Here turbine work is in terms of turbine inlet temperature T_1, turbine efficiency η_T, and turbine expansion ratio (P_1/P_2). It is to be noted that for the same turbine expansion ratio and the same turbine efficiency, the higher the turbine inlet temperature is, the more the turbine work output. Therefore, it is always desirable to raise turbine inlet temperature for higher specific power output.

The turbine outlet temperature T_2 can be calculated from Eq. (1-171):

$$\left(\frac{T_2}{T_1}\right) = 1 - \eta_T \left[1 - \left(\frac{P_2}{P_1}\right)^{\frac{k-1}{k}} \right]. \qquad (1\text{-}173)$$

For more accurate calculations with variable specific heats, one may again either use h–s diagram or the air table.

1) h–s diagram. Point 1 is determined by the known values of stagnation temperature T_1 and stagnation pressure P_1. Read H_1 from the h–s diagram for the corresponding value of T_1 and P_1. In general, either turbine outlet stagnation pressure P_2 or turbine work w_T is known. If P_2 is known, one may determine H_2' by going vertically downward from H_1 until he hits the P_2 line (isentropic expansion process) as shown in Fig. 1-19. With the turbine efficiency η_T known, one may determine H_2 from Eq. (1-170). With H_2 and P_2 known, point 2 is determined. Therefore T_2 becomes known by reading directly from the h–s diagram. Turbine work w_T may then be calculated from Eq. (1-61). If, instead of P_2 being known, w_T is known, we may calculate H_2' from Eq. (1-170), because here w_T ($= H_1 - H_2$) is known. Calculate H_2 from

$$H_2 = H_1 - w_T = H_1 - (H_1 - H_2). \qquad (1\text{-}174)$$

Once H_2 is known, T_2 may be obtained directly from the h–s diagram.

2) Air table or gas table

Point	T	h	p_r	P
1	$\underline{T_1}$	$\underline{H_1}$	$\underline{p_{r_1}}$	P_1
2'	$\underline{T_2'}$	$\underline{H_2'}$	$p_{r_2'}$	P_2'
2	$\underline{T_2}$	H_2		P_2
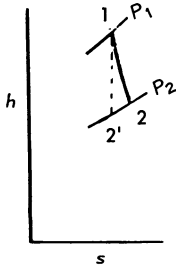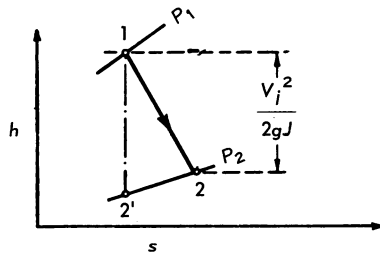
Fig. 1-19   Fig. 1-20

a) T_1 and P_1 are given values. Read p_{r_1} and H_1 from the air table or gas table (use the gas table of the correct fuel–air ratio or interpolate between two fuel air ratios).

b) If $P_2 (= P_2')$ is given, p_{r_2}' may be calculated from

$$\left(\frac{p_{r_2}'}{p_{r_1}}\right) = \left(\frac{P_2'}{P_1'}\right)$$

c) T_2' and H_2' are read from the air table or gas table from known values of p_{r_2}'.

d) With the known value of turbine efficiency η_T, H_2 may be calculated from Eq. (1-170). Then T_2 may be read from the air table or gas table corresponding to H_2.

e) Turbine work w_T may then be calculated from Eq. (1-61).

If, instead of P_2 being known, w_T is known, we start from step (b) as follows:

Point	T	h	p_r	P
1	T_1	H_1	p_{r_1}	P_1
2'	T_2'	H_2'	p_{r_2}'	P_2'
2	T_2	H_2		P_2

a) Same as step (a) above.

b) Calculate H_2' from Eq. (1-170).

c) Read corresponding T_2' and p_{r_2}' from the air table or gas table. Calculate P_2 from

$$\left(\frac{p_{r_1}}{p_{r_2}'}\right) = \left(\frac{P_1}{P_2'}\right)$$

d) Since $P_2' = P_2$, write P_2 down in the table. Calculate H_2 from Eq. (1-174). Read T_2 from the air table or gas table.

One is to be cautioned here that since the enthalpy of the gas table is made on the basis of one pound-mole of gas, one should always transfer the enthalpy from one pound-mole basis to one pound basis by dividing the enthalpy H of the gas table by the molecular weight R of the gas.

[1-11.5] Nozzle Expansion and Nozzle Efficiency

The nozzle is used to expand high pressure gas into high velocity stream in order to produce thrust. In Fig. 1-20, point 1 represents the inlet state, *i.e.*, the stagnation pressure P_1 and stagnation temperature T_1 of the nozzle inlet. For an isentropic expansion (where s = constant), P_1 expands vertically down to the static pressure p_2' (which is usually the ambient or exhaust pressure). However, due to friction, nozzle expansion always follows solid line 1-2 instead of the ideal case, dotted line, 1-2'. Therefore, a nozzle efficiency η_N may be defined as;

$$\eta_N = \frac{H_1 - h_2}{H_1 - h_2'} . \qquad (1\text{-}175)$$

For constant specific heats,

$$\eta_N = \frac{c_p(T_1 - T_2)}{c_p(T_1 - T_2')} = \frac{1 - \left(\dfrac{t_2}{T_1}\right)}{1 - \left(\dfrac{t_2'}{T_1}\right)} = \frac{1 - \left(\dfrac{t_2}{T_1}\right)}{1 - \left(\dfrac{p_2'}{P_1}\right)^{\frac{k-1}{k}}}$$

$$\qquad (1\text{-}175a)$$

$$= \frac{1 - \left(\dfrac{t_2}{T_1}\right)}{1 - \left(\dfrac{p_2}{P_1}\right)^{\frac{k-1}{k}}} .$$

The exhaust temperature t_2 may be calculated now as

$$\left(\frac{t_2}{T_1}\right) = 1 - \eta_N \left[1 - \left(\frac{p_2}{P_1}\right)^{\frac{k-1}{k}} \right]. \qquad (1\text{-}176)$$

From Eq. (1-59), nozzle exit or jet velocity V_j may be determined from the actual enthalpy drop from stagnation pressure P_1 to static pressure p_2 (which is equal to p_2'). Applying Eq. (1-59) in this case, we have:

$$H_1 - h_2 = \frac{V_j^2}{2gJ} = \eta_N (H_1 - h_2'). \qquad (1\text{-}177)$$

For constant specific heats, we may write Eq. (1-177) to:

$$\frac{V_j^2}{2gJ} = H_1 - h_2 = \eta_N (H_1 - h_2') = \eta_N c_p (T_1 - t_2')$$

$$= \eta_N c_p T_1 \left[1 - \left(\frac{t_2'}{T_1}\right) \right] = \eta_N c_p T_1 \left[1 - \left(\frac{p_2'}{P_1}\right)^{\frac{k-1}{k}} \right]$$

$$= \eta_N c_p T_1 \left[1 - \left(\frac{p_2}{P_1}\right)^{\frac{k-1}{k}} \right] \qquad (1\text{-}178)$$

or

$$V_j = \sqrt{ 2gJ\, c_p T_1 \eta_N \left[1 - \left(\frac{p_2}{P_1}\right)^{\frac{k-1}{k}} \right] }. \qquad (1\text{-}178a)$$

For more accurate calculation with variable specific heats, one may again use the $h\text{-}s$ diagram or air or gas table.

1) Use of h–s diagram.

a) Point 1 is determined by the known value of the inlet stagnation pressure P_1 and stagnation temperature T_1. Therefore, H_1 can be read from the h–s diagram.

b) Point 2' is determined from p_2 and s (vertically down from H_1). Note $p_2' = p_2 =$ ambient pressure or exhaust pressure. Now h_2' may be read.

c) From nozzle efficiency η_N and h_2', one may determine h_2 from Eq. (1–175):

$$\eta_N = \frac{H_1 - h_2}{H - h_2'}.$$

(1–175)

d) Calculate V_j from Eq. (1–59):

$$\frac{V_j^2}{2gJ} = H_1 - h_2.$$

(1–179)

2) Use of air table or gas table

Point	T	h	p_r	p
1	T_1	H_1	p_{r_1}	P_1
2'	t_2'	h_2'	p_{r_2}'	p_2'
2	t_2	h_2		p_2

a) From T_1, read the corresponding H_1 and p_{r_1} from the air table or gas table.

b) Since 1 to 2' is isentropic, one may calculate p_{r_2}' from

$$\frac{p_{r_2}'}{p_{r_1}} = \frac{p_2'}{P_1}$$

remembering that p_2' is equal to p_2 by definition.

c) Read corresponding t_2' and h_2' from the air table or gas table at p_{r_2}'.

d) Calculate h_2 from Eq. (1–175):

$$\eta_N = \frac{H_1 - h_2}{H_1 - h_2'}.$$

(1–175)

e) Calculate V_j from Eq. (1-59):

$$\frac{V_j^2}{2gJ} = H_1 - h_2 \qquad\qquad (1\text{-}179)$$

[1-12] VARIATIONS OF BASIC GAS TURBINE OR JET ENGINE CYCLES

Basic gas turbine or jet propulsion cycle consists of (1) ram compression, (2) compressor compression, (3) combustion or heat addition, (4) turbine expansion, and (5) nozzle expansion. The unit process of (1), (2), (3), (4), and (5) was given in the previous section (1-11). However, basic gas turbine or jet engine cycle may be modified by the addition of (1) intercooling, (2) reheat, (3) regeneration, (4) after-burning, and (5) water injection. The following sections will be used to describe these unit processes.

[1-12.1] Intercooling

As mentioned in Sec. 1-11.2, the compressor work is reduced when the compressor inlet temperature is reduced. Therefore, an intercooling process sometimes may be used in order to reduce the compressor work. This situation can best be seen through the $h-s$ diagram (Fig. 1-21). For example, instead of compressor compression from P_1 directly to P_2 which requires a compressor work $(H_2 - H_1)$, one may first compress the air to an intermediate pressure P_a (at enthalpy H_a and temperature T_a) and then cool the T_a temperature back down to T_1 by a perfect interstage air cooler before compressing it again from the intermediate pressure P_a to the final required pressure P_2. From Fig. 1-16 the compressor work w_c for compression from P_1 to P_a is $(H_a - H_1)$., and the compressor work w_{c_2} for compression from P_a to P_2 after cooling T_a to T_1 is $(H_c - H_1)$. Therefore, the total compressor work is

$$w_c = w_{c_1} + w_{c_2} = (H_a - H_1) + (H_c - H_1)$$

which, from the $h-s$ diagram, is obviously less than $w_c = H_2 - H_1$. It may also be proved numerically from the analytical expression as follows:

$$\frac{c_p T_1}{\eta_c}\left[\left(\frac{P_2}{P_1}\right)^{\frac{k-1}{k}} - 1\right] > \frac{c_p T_1}{\eta_c}\left[\left(\frac{P_a}{P_1}\right)^{\frac{k-1}{k}} - 1\right] + \frac{c_p T_1}{\eta_c}\left[\left(\frac{P_2}{P_a}\right)^{\frac{k-1}{k}} - 1\right]$$

Compressor work of one-stage com-   Compressor work of two stage com-
sion without intercooling.   pression with intercooling. Here P_a
                                      could be any intermediate pressure
                                      between P_1 and P_2.

Each value of P_a will yield one value of total compressor work. The minimum total compressor work may be obtained by differentiating the total compressor work with respect to P_a and setting the result equal to zero.* This condition gives:

$$\frac{P_a}{P_1} = \frac{P_2}{P_a}$$

or

$$P_a = \sqrt{P_1 P_2} \qquad \text{or} \qquad \left(\frac{P_a}{P_1}\right) = \sqrt{\frac{P_2}{P_1}}$$

(1–180)

In other words, Eq. (1–180) says that dividing the two-stage into two equal pressure ratios yields the minimum total compressor work which is equal to:

$$w_{c_1} + w_{c_2} = \frac{c_p T_1}{\eta_c}\left[\left(\frac{P_a}{P_1}\right)^{\frac{k-1}{k}} - 1\right] + \frac{c_p T_1}{\eta_c}\left[\left(\frac{P_2}{P_a}\right)^{\frac{k-1}{k}} - 1\right]$$

$$= 2\,\frac{c_p T_1}{\eta_c}\left[\left(\frac{P_2}{P_1}\right)^{\frac{k-1}{2k}} - 1\right].$$

(1–181)

*Instead of intercooling for minimum compressor work which occurs as $P_a = \sqrt{P_1 P_2}$, one may obtain P_a for maximum cycle efficiency by differentiating cycle efficiency with respect to P_a.

Therefore, the decrease of compressor work due to intercooling is equal to

$$\Delta w_c = w_c - \left(w_{c_1} + w_{c_2} \right)$$

$$= \frac{c_p T_1}{\eta_c} \left[\left(\frac{P_2}{P_1} \right)^{\frac{k-1}{k}} - 1 \right] - 2 \frac{c_p T_1}{\eta_c} \left[\left(\frac{P_2}{P_1} \right)^{\frac{k-1}{k}} - 1 \right].$$

$$(1\text{-}182)$$

Similarly, instead of two-stage compression with one intercooling in between the two stages, one may use three-stage compression with two intercooling for further reduction of compressor work (Fig. 1-22). One may likewise find that minimum compressor work occurs at

$$\left(\frac{P_a}{P_1} \right) = \left(\frac{P_b}{P_a} \right) = \left(\frac{P_2}{P_b} \right) = \sqrt[3]{\frac{P_2}{P_1}}. \qquad (1\text{-}183)$$

The decrease of compressor work is

$$\Delta w_c = w_c - \left(w_{c_1} + w_{c_2} + w_{c_3} \right)$$

$$= \frac{c_p T_1}{\eta_c} \left[\left(\frac{P_2}{P_1} \right)^{\frac{k-1}{k}} - 1 \right] - \frac{3 c_p T_1}{\eta_c} \left[\left(\frac{P_2}{P_1} \right)^{\frac{k-1}{3k}} - 1 \right].$$

$$(1\text{-}184)$$

Similarly, for n stage compression, at each stage compression ratio of $\sqrt[n]{(P_2/P_1)}$, with $(n-1)$ intercooling, the decrease of compressor work is
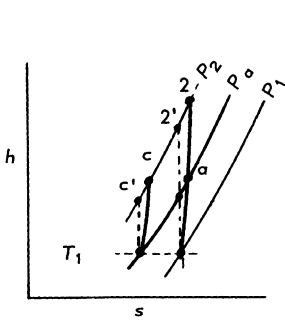
Fig. 1-21
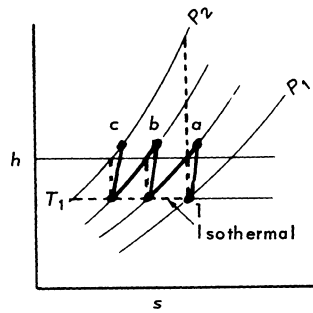
Fig. 1-22
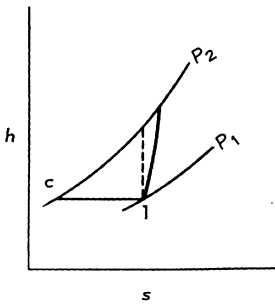
Fig. 1-23
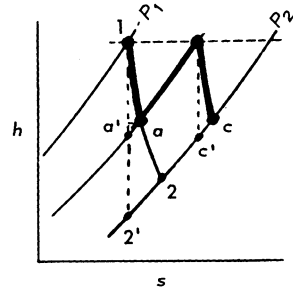
Fig. 1-24

$$\Delta w_c = \frac{c_p T_1}{\eta_c}\left[\left(\frac{P_2}{P_1}\right)^{\frac{k-1}{k}} - 1\right] - n\,\frac{c_p T_1}{\eta_c}\left[\left(\frac{P_2}{P_1}\right)^{\frac{k-1}{nk}} - 1\right].$$

$$(1\text{-}185)$$

The ultimate case is the infinite stage compressor compression with infinite intercooling or the case of isothermal compression (Fig. 1-23). In the ultimate case of isothermal compression, the decrease of compressor work is

$$\Delta w_c = \frac{c_p T_1}{\eta_c}\left[\left(\frac{P_2}{P_1}\right)^{\frac{k-1}{k}} - 1\right] - R\,T\ln\left(\frac{P_2}{P_1}\right).$$

$$(1\text{-}186)$$

Here

$$w_{c_{\text{isothermal}}} = R\,T\,\ln\!\left(\frac{P_2}{P_1}\right). \qquad (1\text{-}186a)$$

In the actual case, perfect intercooling to temperature T_1 can never be achieved, because it requires an intercooler with an infinite cooling surface. Therefore, an intercooler effectiveness may be defined as:

$$\eta_I = \frac{H_a - H_b}{H_a - H_1}. \qquad (1\text{-}187)$$

For constant specific heats, it reduces to:

$$\eta_I = \frac{T_a - T_b}{T_a - T_1} \qquad \text{or} \qquad T_b = T_a(1 - \eta_I) + \eta_I T_1. \qquad (1\text{-}187a)$$

Consequently, the total compressor work for a two-stage compression, at equal compression ratio $\sqrt{P_2/P_1}$ at the same η_c, with an intercooler of effectiveness η_I, is $w_{c_1} + w_{c_2}$.
But

$$w_{c_1} = \frac{c_p T_1}{\eta_c}\left[\left(\frac{P_2}{P_1}\right)^{\frac{k-1}{2k}} - 1\right]. \qquad (1\text{-}181)$$

From Eq. (1-166) we have

$$T_a = T_1\left\{1 + \frac{1}{\eta_c}\left[\left(\frac{P_2}{P_1}\right)^{\frac{k-1}{2k}} - 1\right]\right\} \qquad (1\text{-}166)$$

and from Eq. (1-187a) we have

$$T_b = T_a(1 - \eta_I) + \eta_I T_1$$

$$= T_1\left\{1 + \frac{1}{\eta_c}\left[\left(\frac{P_2}{P_1}\right)^{\frac{k-1}{2k}} - 1\right]\right\}(1 - \eta_I) + \eta_I T_1 \qquad (1\text{-}188)$$

w_{c_2} may be calculated from Eq. (1-165);

$$w_{c_2} = \frac{c_p T_b}{\eta_c} \left[\left(\frac{P_2}{P_1} \right)^{\frac{k-1}{2k}} - 1 \right]$$

$$= \frac{c_p}{\eta_c} \left\{ T_1 \left\{ \left[1 + \frac{1}{\eta_c} \left(\frac{P_2}{P_1} \right)^{\frac{k-1}{2k}} - 1 \right] \right\} (1 - \eta_I) + \eta_I T_I \right\} \left[\left(\frac{P_2}{P_1} \right)^{\frac{k-1}{2k}} - 1 \right].$$

(1-189)

Therefore, the total compressor work becomes $w_{c_1} + w_{c_2}$. The total compressor work is again in terms of compressor inlet temperature T_1, compressor efficiency η_c, total compression ratio (P_2/P_1) and intercooler effectiveness η_I. Because of the size and weight of intercooler and pressure drop through the intercooler, thermodynamic trade-off study must be made for application of intercooling process. For variable specific heat calculations, the process described in Sec. 1-11.2 may be used for each stage compression, while Eq. (1-187) should be used in conjunction with the air table or h–s diagram for temperature drop through the intercooler such as from $(T_a$ to $T_b)$.

[1-12.2] Reheat

As mentioned in Sec. 1-11.4, the turbine work is increased when the turbine inlet temperature is increased. Therefore, reheat process sometimes may be used in order to increase the turbine work. Reheat between turbine stages is similar to intercooling between compressor stages. One is for reducing compressor work, while the other is for increasing turbine work. This situation can again be seen through h–s diagram (Fig. 1-24). For example, instead of turbine expansion from P_1 directly to P_2 which delivers a turbine work of $(H_1 - H_2)$, one may first expand the gas to an intermediate pressure P_a (at enthalpy H_a and temperature T_a), and then heat the T_a temperature back up to T_1, as shown in Fig. 1-24, by a reheater (interstage burner) before expanding it again from the intermediate pressure P_a to the final pressure P_2. From Fig. 1-24, the turbine work w_{T_1} for expansion from P_1 to P_a is $(H_1 - H_a)$; and the turbine work w_{T_2} for expansion from P_a to P_2 after

reheating T_a back up to T_1 is $(H_1 - H_c)$. Therefore, the total turbine work is

$$w_{T_1} + w_{T_2} = (H_1 - H_a) + (H_1 - H_c) \qquad (1\text{-}190)$$

which, from the $h\text{-}s$ diagram, is obviously more than $w_T = H_1 - H_2$. Or it may be proved numerically from analytical expression as follows:

$$c_p T_1 \eta_T \left[1 - \left(\frac{P_2}{P_1}\right)^{\frac{k-1}{k}} \right] < c_p T_1 \eta_T \left[1 - \left(\frac{P_a}{P_1}\right)^{\frac{k-1}{k}} \right] + c_p T_1 \eta_T \left[1 - \left(\frac{P_2}{P_a}\right)^{\frac{k-1}{k}} \right].$$

Turbine work without reheat.   Turbine work with reheat. Here P_a could be any intermediate pressure between P_1 and P_2.

Each value of P_a will yield one value of total turbine work. The maximum total turbine work may be obtained by differentiating the total turbine work with respect to P_a and setting the result equal to zero.* This condition gives

$$\left(\frac{P_1}{P_a}\right) = \left(\frac{P_a}{P_2}\right) \qquad (1\text{-}191)$$

or

$$\left(\frac{P_1}{P_a}\right) = \left(\frac{P_2}{P_1}\right)^{\frac{1}{2}}. \qquad (1\text{-}192)$$

Dividing the two stages into equal expansion ratios yields the maximum total turbine work which is equal to

$$w_{T_1} + w_{T_2} = 2 c_p T_1 \eta_T \left[1 - \left(\frac{P_2}{P_1}\right)^{\frac{k-1}{2k}} \right]. \qquad (1\text{-}193)$$

*Instead of reheat for maximum turbine work which occurs at $P_a = \sqrt{P_1 P_2}$ one may obtain P_a for maximum cycle efficiency by differentiating cycle efficiency with respect to P_a.

Therefore the increase of turbine work due to reheat is equal to

$$\Delta w_T = \left(w_{T_1} + w_{T_2} \right) - w_T$$

$$= 2 c_p T_1 \eta_N \left[1 - \left(\frac{P_2}{P_1} \right)^{\frac{k-1}{2k}} \right] - c_p T_1 \eta_T \left[1 - \left(\frac{P_2}{P_1} \right)^{\frac{k-1}{k}} \right].$$

$$(1-194)$$

Similarly, instead of two-stage expansion with one reheat, one may use a three-stage expansion with two reheat for further increase of turbine work. One may similarly find the maximum turbine work occurs at:

$$\left(\frac{P_1}{P_a} \right) = \left(\frac{P_a}{P_b} \right) = \left(\frac{P_b}{P_2} \right) = \left(\frac{P_1}{P_2} \right)^{\frac{1}{3}}. \qquad (1-195)$$

The increase of turbine work is

$$\Delta w_T = \left(w_{T_1} + w_{T_2} + w_{T_3} \right) - w_T$$

$$= 3 c_p T_1 \eta_T \left[1 - \left(\frac{P_2}{P_1} \right)^{\frac{k-1}{3k}} \right] - 1 \, c_p T_1 \eta_T \left[1 - \left(\frac{P_2}{P_1} \right)^{\frac{k-1}{k}} \right].$$

$$(1-196)$$

Similarly, for n stage expansion with $(n-1)$ reheat, the increase of turbine work is

$$\Delta w_T = n c_p T_1 \eta_T \left[1 - \left(\frac{P_2}{P_1} \right)^{\frac{k-1}{nk}} \right] - c_p T_1 \eta_T \left[1 - \left(\frac{P_2}{P_1} \right)^{\frac{k-1}{k}} \right].$$

$$(1-197)$$

The ultimate case is the infinite stage expansion with infinite reheat or the ultimate case of isothermal expansion. In the case of isothermal expansion, the increase of turbine work is

$$\Delta w_T = R T \ln\left(\frac{P_1}{P_2}\right) - c_p T_1 \eta_T \left[1 - \left(\frac{P_2}{P_1}\right)^{\frac{k-1}{k}}\right].$$

$$(1\text{-}198)$$

Here

$$w_{T_{\text{isothermal}}} = R T \ln(P_1/P_2) \qquad (1\text{-}198a)$$

So far as the combustion or heating process of reheat is concerned, the unit process already described in Sec. 1-11.3 should be applied for accuracy. (Also see Sec. 1-12.4.) For isothermal reheat, the amount of heat added Q is equal to $R T \ln(P_1/P_2)$. $Q = \eta_b fh^* = R T \ln(P_1/P_2)$. Because of the size and weight of the reheater and the pressure drop through the reheater, trade-off study must be made for actual application of the reheat process.

For variable specific heats calculations, the methods already described in Sec. 1-11.4 could be applied to each stage of turbine expansion. No further discussion is really needed here.

[1-12.3] Regeneration

The energy contained in the exhaust gas in the form of heat can be recuperated into the incoming air of the combustion chamber in order to save part of the fuel which would otherwise be required, if no regeneration exists, as shown in Fig. 1-25. Figure 1-25 shows that fuel energy required is $H_3 - H_6$ with regeneration compared with $H_3 - H_2$ without regeneration. An ideal regeneration with infinite heat transfer surface can raise the burner air temperature from state 2 to state 6', the state of the exhaust inlet into regenerator. However, the actual regenerator (size and pressure loss, etc.) usually limits the air temperature from state 2 to state 6. Therefore, a regenerator effectiveness can be defined as:

$$\eta_x = \frac{H_6 - H_2}{H_{6'} - H_2} = \frac{H_6 - H_2}{H_4 - H_2}.\qquad (1\text{-}199)$$

When H_2, H_4 and η_x are known, H_6 may be calculated.
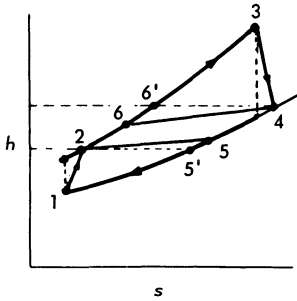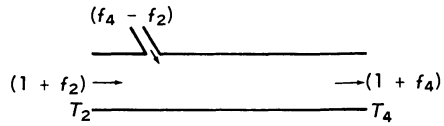
Fig. 1-25   Fig. 1-26

For constant specific heats, it reduces to:

$$\eta_x = \frac{T_6 - T_2}{T_{6'} - T_2} = \frac{T_6 - T_2}{T_4 - T_2}. \tag{1-200}$$

When T_2, T_4 and η_x are known, T_6 may be calculated. The temperature of the exhaust gas leaving the regenerator into the nozzle may be determined by energy balance *i.e.,*

$$H_4 - H_5 = \frac{H_6 - H_2}{(1 + f)}. \tag{1-201}$$

[1-12.4] After-burning

Turbine inlet temperature is usually limited by present metallurgical knowledge on turbine materials. The tail-pipe-burning method of thrust augmentation, or afterburning as it is sometimes designated, consists of introducing and burning fuel between the turbine and the exhaust nozzle of the engine. The increased temperature of the exhaust gases thus produced results in an increase in the jet velocity and hence an increase in the thrust.

When combustion occurs in a reheating burner or afterburner, the gas entering the combustion chamber is the product of a previous combustion. From Fig. 1-26, we can see that the temperature T_2 and the fuel-air ratio $\eta_b f_2$ at the inlet of the afterburner are known. These values can be used with Fig. 1-18 to obtain a fictitious initial temperature that would exist in a combustion chamber whose exit conditions are the same as the inlet conditions T_2 and $\eta_b f_2$ of the afterburner. If the temperature at the exit from this theoretical combustion chamber is increased, Fig. 1-18 gives the new value of $\eta_b f_4$ required to reach the new exit temperature T_4.

The difference between these two fuel-air ratios $\eta_b f_4 - \eta_b f_2 = \eta_b (f_4 - f_2)$ is the amount of fuel ideally required to change $(1 + f_2)$ pounds of gas from the state at the inlet of the afterburner to $(1 + f_4)$ pounds of gas at the required temperature at the exit from the afterburner. The total actual fuel-air ratio at this point 4 is expressed as (use different η_b value, if they are not equal)

$$f_4 = f_2 + \frac{\eta_b (f_4 - f_2)}{\eta_{A.B.}}.$$

Here

$$\eta_{A.B.} = \text{After-burning efficiency.}$$

A similar principle can be applied for the use of the gas table for afterburning.

[1-12.5] Water Injection

One method of augmenting the specific thrust of turbojet engines is to inject water or a nonfreezing mixture of water and alcohol into the air entering the compressor of the engine. The evaporation of this injected liquid extracts heat from the air and results, for the same compressor work input, in a higher compressor pressure ratio. This increased pressure ratio is reflected throughout the engine and increases both the mass flow of gases through the engine and the exhaust-jet velocity; both factors increase the specific thrust produced by the engine. An analysis of the evaporative cooling process can be conveniently divided into two phases: (1) the cooling occurring at constant pressure before the air enters the compressor, and (2) the additional cooling associated with further evaporation during the mechanical compression process. A specialized psychrometric chart by Wilcox and Trout that permits calculation of the first phase of the constant-pressure evaporation process and a Mollier diagram for air saturated with water vapor that permits calculation of the second phase of evaporation during compression are presented here.

The following numerical example is presented to illustrate the method of using the psychometric chart and the Mollier diagram to calculate the compressor-outlet conditions for a saturated compression process. Assume that a compressor having an adiabatic efficiency η_c of 0.80 and imparting an enthalpy rise $\bar{w}_{c_a}$ of 80 Btu per pound of air to the working fluid is operated with sufficient water injected at the compressor inlet to maintain saturation at all times. Further, assume that the inlet air has a relative humidity ϕ of 0.50 at a temperature T_a of 530° R and a

pressure P_a of 14.7 pounds per square inch and that it is desired to find the compressor outlet pressure P_2, outlet temperature T_2, outlet water vapor-air ratio X_2, and the amount of water evaporated during the process.

The conditions at the compressor inlet after saturation can be obtained from the psychrometric chart (Fig. 1-27). For the initial condition of ambient relative humidity ϕ of 0.50, temperature T_o of 530° R, and pressure P_o of 14.7 pounds per square inch, the water vapor-air ratio X_o is 0.0077 and the enthalpy H_o is 100 Btu per pound of air. After saturation at constant pressure, from Fig. 1-27, the temperature T_1 is 519° R, the water vapor-air ratio X_1 is 0.016, and the enthalpy H_1 is 100 Btu per pound of air.
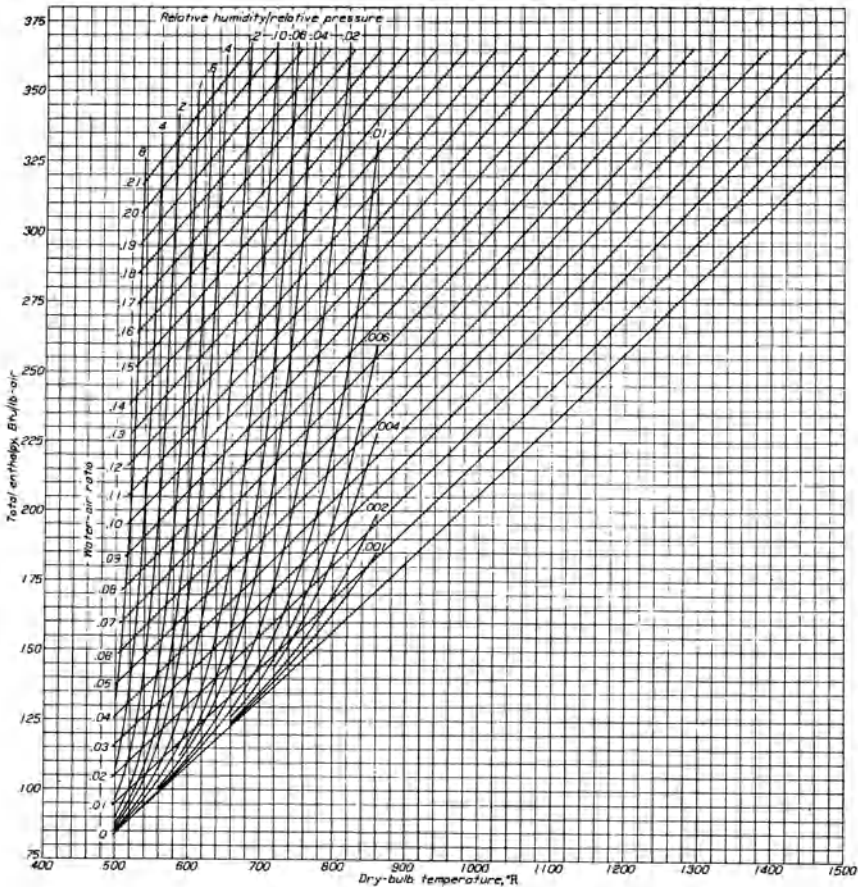
Fig. 1-27 (After E. C. Wilcox & A. M. Trout, NACA TR 1006).

From the Mollier diagram (Fig. 1-28), for a temperature T_1 of 519° R and a pressure P_1 of 14.7 pounds per square inch, the

entropy S_1 is 0.10 Btu/(lb.air) (° R). By increasing the enthalpy at constant entropy by an amount equal to the ideal work of compression, the actual pressure at the compressor outlet may be read from the diagram. The ideal work of compression is

$$w_{c_i} = \eta_c \, w_{c_a} = 0.80 \times 80 = 64 \, (\text{Btu}/\text{lb. air})$$

and

$$H_{2'} = H_1 + w_{c_i} = 100 + 64 = 164 \, (\text{Btu}/\text{lb. air}).$$

The value of pressure read from the diagram at an enthalpy of 164 Btu per pound of air and an entropy of 0.10 Btu/(lb. air) (° R) is

$$P_2 = 70.7 \, (\text{lb.}/\square'').$$

The enthalpy at the compressor outlet is equal to the enthalpy at the inlet plus the actual enthalpy change, or

$$H_2 = H_1 + w_{c_a} = 100 + 80 = 180 \, (\text{Btu}/\text{lb. air}).$$

From the Mollier diagram, at a pressure of 70.7 pounds per square inch and an enthalpy of 180 Btu per pound of air, the values of temperature and water vapor-air ratio at the compressor outlet are

$$T_2 = 630°R \qquad \text{and} \qquad X_2 = 0.0583.$$

The amount of water evaporated is

$$X_2 - X_0 = (X_1 - X_0) + (X_2 - X_1) = .0029 + 0.0477 = 0.0506 \, (\text{lb} \, H_2O/\text{lb. air}).$$

The amount of water vapor represented by $(X_1 - X_0)$ is that evaporated at the inlet prior to compression and the amount $(X_2 - X_1)$ represents that water evaporated during the mechanical compression process.

The fuel-air ratio f required for a given temperature rise is approximately the same as obtained when the air-water mixture is treated as pure air. However, since the thermodynamic properties of c_p, k and R are changed slightly by the presence of water vapor, the modified values of c_p, k, and R sometimes may be used in the turbine expansion and jet nozzle expansion equations. The small corner chart in Fig. 1-28 gives such change of thermodynamic properties at 1650°R. Although the actual values of c_p and k vary with temperature, the values given in Fig. 1-28 can be used for appreciable temperature range with neglibible error because of the compensating manner in which c_p and k enter the equations for an expansion process.
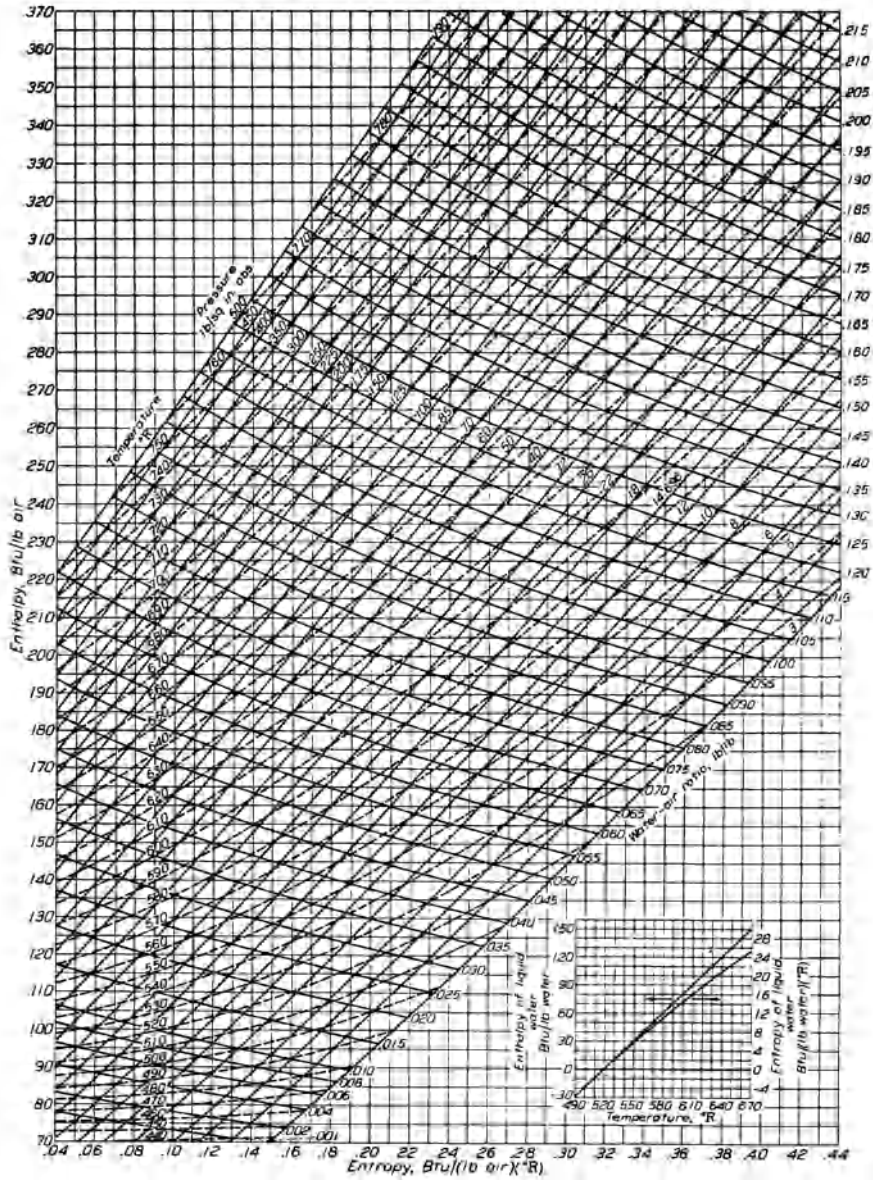
Fig. 1-28 (After E. C. Wilcox and A. M. Trout, NACA TR 1006).

[1-12.6] Pressure Loss in Various Components

1) Burner pressure loss. Burner momentum pressure loss can be calculated through Eq. (1-148a). However, for most applications

of gas turbine or jet engines calculations, a representative value of 3% of the burner inlet total pressure loss could be assumed, without the necessity of going through the calculations.

2) *Intercooler, reheater, and regenerator pressure loss*. Calculation of pressure loss in intercooler, reheater and regenerator depends on their respective configurations. Without a specific configuration, one may assume a loss of 3 to 5% of inlet total pressure in each component. It is to be remembered here that although total pressure is lost, total enthalpy always remains the same. For this reason, the thermodynamic states of "with" and "without" pressure loss are always "at the same enthalpy *H*". We will see the horizontal shift to a lower pressure line at the same enthalpy *H* (for actual intercooler, burner, reheater, regenerator, etc.) on all *h–s* diagrams with pressure losses.

[1-13.1] Output, Input and Thermal Efficiency

The net output w_{net} of a gas turbine engine per pound of working fluid (air) is equal to the difference between summation of all turbine work w_T and summation of all compressor work w_c, i.e.,

$$w_{net} = (1 + f)\, w_T - w_c. \tag{1-202}$$

Here f is the actual amount of fuel flow per pound of air flow. Since the energy input to the engine is equal to $\eta_b f h^*$, the thermal efficiency η becomes

$$\eta = \frac{Output}{Input} = \frac{w_{net}}{f h^*}. \tag{1-203}$$

[1-13.2] Jet Thrust

Jet thrust F_j, which is equal to the change in momentum of air passing through the engine, can be expressed, for nozzle of complete expansion, as:

$$\left(\frac{F_j}{W_a}\right) = \left(\frac{1 + f}{g}\right) V_j - \frac{1}{g}\, V_0 \tag{1-204}$$

and, for nozzle of partial expansion, as:

$$\left(\frac{F_j}{W_a}\right) = \frac{1 + f}{g}\, V_e + A_e\, (p_e - p_a) - \frac{1}{g}\, V_0. \tag{1-205}$$

Here

F_j = Jet thrust in pounds

W_a = Air flow in pounds per second

$\dfrac{F_j}{W_a}$ = Jet thrust per unit weight of working fluid (air)

f = Total fuel-air ratio of the engine, #fuel/#air

V_j = Jet velocity by complete expansion to ambient pressure p_a, in ft. per second.

V_0 = Aircraft speed, in ft. per second.

g = Gravity constant = 32.2 ft./sec^2.

V_e = Jet velocity at nozzle exit for a partial expansion nozzle, in ft./sec.

A_e = Exit area of partial expansion nozzle in ft^2.

p_e = Static pressure at nozzle exit of partial expansion nozzle in lb./ft^2.

p_a = Ambient pressure in lb./ft^2.

[1-13.3] Propeller Thrust

The thrust horsepower THP_p of a propeller is equal to propeller-turbine's brake-horsepower BHP_p times propeller and reduction gear efficiency η_p; namely,

$$THP_p = \eta_p BHP_p. \qquad (1\text{-}206)$$

The thrust horsepower THP_p is equal to:

$$THP_p = \frac{\text{Propeller Thrust } F_p \times \text{Airplane Velocity } V_0}{550} \qquad (1\text{-}207)$$

therefore, the propeller thrust F_p can be written as:

$$F_p = \frac{550 \, \eta_p \, BHP_p}{V_0}$$

and

$$\left(\frac{F_p}{W_a}\right) = \frac{550 \, \eta_p \, (\text{BHP}_p/W_a)}{V_0}. \qquad (1\text{-}208)$$

It is to be remembered here that the driving thrust for aircraft powered by turbine-propeller engine is developed mainly by the propeller thrust F_p plus an augmented jet thrust F_j from the

exhaust gases. Therefore, the total thrust F of a turbine-propeller engine is equal to:

$$\left(\frac{F}{W_a}\right) = \left(\frac{F_p}{W_a}\right) + \left(\frac{F_j}{W_a}\right). \tag{1-209}$$

[1-13.4] Specific Fuel Consumption

1) Thrust specific fuel consumption (T.S.F.C.) for jet propulsion engines is defined as the quotient of fuel flow (in pounds per hours) and thrust. It gives the fuel consumption in pounds per hour per pound of jet thrust produced. It can be expressed as:

$$\text{T.S.F.C.} = \frac{3600\ f}{(F_j/W_a)} \tag{1-210}$$

2) Brake specific fuel consumption (B.S.F.C.) of gas turbine engine is defined as the fuel consumption in pounds per hour per net brake horsepower output BHP of the engine.

$$\text{B.S.F.C.} = \frac{3600\ f}{(\text{BHP}/W_a)} = \frac{3600\ f}{W_{\text{Net}}(778/550)}. \tag{1-211}$$

Substituting Eq. (1-203) into Eq. (1-211), one obtains:

$$\text{B.S.F.C.} = \left(\frac{3600 \times 550}{778\ h^*}\right)\left(\frac{1}{\eta}\right). \tag{1-212}$$

Therefore, the higher the thermal efficiency, the lower the B.S.F.C.; one is inversely proportional to the other.

[1-14] VARIATIONS OF GAS TURBINE CYCLE AND TURBOJET CYCLE BY GAS TABLE METHOD

In order to give two typical numerical examples for illustration of the previously discussed unit processes, the gas table method was chosen for simplicity and convenience. Two examples will be given, one for the basic gas turbine cycle and one for the basic turbojet cycle.

[1-14.1] Gas Table

Thermodynamic calculations based on ideal or perfect gas with constant specific heats usually results in some errors when

temperature increases involved are large. To eliminate the use of variable specific heat equations for each individual calculation, Keenan and Kaye have tabulated in the book, Gas Table, the properties of air and certain combustion gas mixtures against temperature. A brief description of the derivation and the use of some of the tables are presented here.

The properties of gas given in *Gas Table* are based on the assumption that the specific heats, consequently the internal energy E and enthalpy H, are functions of temperature T and temperature T only. Hence, the presentation of these properties consists of a table with the single argument, temperature T. The base temperature T_0, for which enthalpy H is zero, is taken to be zero on the Rankine temperature scale. Entropies cannot simply be presented with temperature T alone as an argument, since entropy is a function of pressure P as well as temperature T. From Eq. (1-23) and (1-24), if the base temperature T_0 for which the entropy is zero is taken as zero on the Rankine temperature scale, one obtains:

$$ s = \int_0^T C_p \frac{dT}{T} - R \int_{P_0}^P \frac{dP}{P} = \int_0^T C_p \frac{dT}{T} - R \ln\left(\frac{P}{P_0}\right) $$

(1-213)

so change of entropy between any two states, say states 1 and 2, can be expressed as:

$$ s_2 - s_1 = \int_0^{T_2} C_p \frac{dT}{T} - \int_0^{T_1} C_p \frac{dT}{T} - R \ln\left(\frac{P_2}{P_1}\right). $$

(1-214)

The quantity

$$ \phi = \int_0^T C_p \frac{dT}{T} $$

(1-215)

is given in the gas table as a function of temperature. The change of entropy now may be written as:

$$ s_2 - s_1 = \phi_2 - \phi_1 - R \ln\left(\frac{P_2}{P_1}\right) $$

(1-216)

where the value of ϕ is obtained directly from the gas table and the quantity $R \ln(P_2/P_1)$ is computed.

For an isentropic process, one has:

$$\ln\left(\frac{P}{P_0}\right) = \frac{1}{R}\int_0^T C_P \frac{dT}{T} \tag{1-23}$$

$$\ln\left(\frac{v}{v_0}\right) = \ln\left(\frac{\rho_0}{\rho}\right) = -\frac{1}{R}\int_0^T C_v \frac{dT}{T} \tag{1-55}$$

from which it is seen that ratios (P/P_0) and (v/v_0) are a function of temperature only. The ratio $(P/P_0) = p_r$ is called the relative pressure, and the ratio $(v/v_0) = v_r$ is called the relative volume. They are given in the gas table as functions of temperature T only.

From Eqs. (1-23) and (1-55), one sees that the ratios (P_1/P_2) and (v_1/v_2) corresponding to the temperatures T_1 and T_2, respectively, along a particular isentropic process, are equal to the relative pressures P_{r_1} and P_{r_2} and the ratio of the relative volumes v_{r_1} and v_{r_2}, respectively, or

$$\left(\frac{P_1}{P_2}\right)_{S = \text{Const.}} = \left(\frac{P_{r_1}}{P_{r_2}}\right) \tag{1-217}$$

$$\left(\frac{v_1}{v_2}\right)_{s = \text{Const.}} = \left(\frac{v_{r_1}}{v_{r_2}}\right). \tag{1-218}$$

The gas table consists of six columns. The first column gives the temperature on the Rankine scale. The following columns give the corresponding values of enthalpy h in Btu/lb-m, relative pressure, internal energy (Btu/lb-m), relative volume, and the quantity ϕ in Btu/lb-m° R, in that order. The following two examples illustrate the use of the gas table. They are taken directly from the text of Gas Table by Keenan and Kaye.

[1-14.2] Example 1: Gas Turbine Analysis

Air is compressed isentropically in steady flow from 1 atm and 50 F abs to 5 atm. Liquid octane at 520 F abs is introduced into the stream of compressed air at such a rate that the resultant mixture contains 300% theoretical air. The octane burns completely at constant pressure, and the products of combustion expand isentropically to 1 atm. Find the efficiency.

1) Compressor compression. Let subscripts 1 and 2 refer to states at inlet and outlet of the compressor, respectively. Then from Table 1 of Keenan and Kaye we have

$$T_1 = 520°R, \quad h_1 = 124.27, \quad P_{r_1} = 1.2147$$

$$P_{r_2} = \frac{5}{1} \times 1.2147 = 6.074, \quad T_2 = 821.6°R, \quad h_2 = 197.07$$

Table 1-A. States in the Gas Turbine (Fig. 1-29)

State	Gas Table Number	T F abs	h Btu/lb	$\bar{h}$ Btu/lb-mole	P_r	P atm
1	1	520	124.27*	3,600.1*	1.2147	1
2	1	821.6	197.07*	5,709.1*	6.074	5
3	4, 7	794.7	192.23*	5,660.2		5
4	4, 7	2,308.9	609.71	17,610.4	365.4	5
5	4, 7	1,568.6	397.41	11,478.3	73.08	1

*Base state is a fuel-air mixture. Where values of these properties are not so marked, the base state is a mixture of air and products of complete combustion.

2) Mixing. Application of the first law of Thermodynamics to the adiabatic process of mixing liquid octane and air shows that the enthalpy of the resultant air-fuel mixture is equal to the sum of the enthalpies of the air and the fuel before mixing. To evaluate the temperature of the mixture of air and octane vapor, a common base state is selected from which the enthalpies of the mixture and of the components may be reckoned.

In Gas Table 1 of Keenan and Kaye, the enthalpy of air is zero at 0° F abs. Using an analogous convention, we may fix the enthalpy of octane vapor at zero at 0° F abs. Data relative to this base have been published by the Bureau of Standards for hydrocarbons. The enthalpy of liquid octane as obtained from these data is given with satisfactory precision over a range of temperatures centering on 500 F abs by the equation

$$h_f = 0.5\,T - 287 \text{ BTU/\#}$$

where h_f denotes the enthalpy of a pound of liquid octane at the temperature T° F abs. The effect of pressure on enthalpy may be safely ignored in problems involving combustion.

The theoretical fuel-air ratio for octane $(C_8 H_{18})$ is 0.06621 based on the composition of air used in constructing Gas Table 1 of Keenan and Kaye. Then for 300% theoretical air, each pound of fuel-air mixture contains 0.0216 lb. of fuel and 0.9784 lb. of air. The enthalpy of each pound of liquid fuel at 520 F abs based on vapor at 0° F abs is

$$h_f = 0.5 \times 520 - 287 = -27 \text{ BTU/lb}.$$
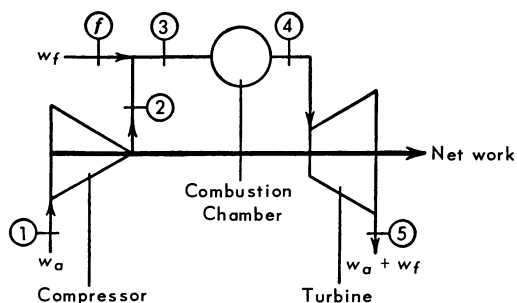
Fig. 1-29

The enthalpy of the fuel-air mixture based on a state having the same chemical aggregation is then

$$h_3 = 0.0216\,(-27) + 0.9784 \times 197.07 = 192.23 \text{ BTU/lb}$$

and

$$\bar{h}_3 = 192.23 \times 29.445 = 5660.2 \text{ BTU/lb-mole}$$

where subscript 3 refers to the state immediately after mixing and 29.445 is the molecular weight of the mixture. The temperature of this mixture is obtained by linear extrapolation, on the basis of percent of theoretical fuel, with the aid of Gas Tables 4 and 7 of Keenan and Kaye. From Table B on page 206 of Gas Table by Keenan and Kaye, a mixture of air and octane vapor for 28% theoretical fuel corresponds closely to a products table for 50% theoretical fuel. From the value of h_3 we get from Table 7 of Keenan and Kaye, for 28% theoretical fuel, $T_3 = 797.8$; from Table 4 of Keenan and Kaye, for 14% theoretical fuel, $T_3 = 805.9$. Hence, for 33.33% theoretical fuel, we have, by extrapolation,

$$T_3 = 797.8 + \frac{33.33 - 28}{28 - 14}\,(797.8 - 805.9) = 794.7°R.$$

3) Combustion. Application of the first law to the process of adiabatic combustion between states 3 and 4 (Fig. 1-29) results in the equation

$$h_3 = h_4$$

where h_3 and h_4 represent the enthalpy per pound for reactants and products of combustion, respectively. The base states for h_3 and h_4 must, of course, be the same.

The values of enthalpy used above in the calculation of the mixing process are based on an enthalpy of zero for gaseous reactants at 0° F abs. The values of enthalpy given in Tables 4

and 7 of Keenan and Kaye, on the other hand, are based on enthalpy of zero for gaseous products of combustion at 0° F abs. If the enthalpy of the reactants is to be reckoned from this latter or products base, the values on the reactants base must be augmented by the increase in enthalpy when products at 0° F abs are changed to reactants at 0° F abs. This quantity is the negative of the enthalpy of combustion at 0° F abs and is equal to the constant-pressure "heat of combustion" at 0° F abs.

For octane, the enthalpy of combustion per pound of fuel at 0° F abs, h_{RP_0}, is constant over the range from 0 to 100% theoretical fuel and is given by

$$h_{RP_0} = h_{P_0} - h_{R_0} = -19{,}328 \text{ BTU/lb. of octone}$$

where h_{R_0} and h_{P_0} denote the enthalpy at 0° F abs of the reactants and of the products, respectively, per pound of octane.

Values of the enthalpy per pound of reactants on the reactants base must therefore be augmented by the negative of h_{RP_0} multiplied by the fraction of a pound of octane in each pound of reactants, that is, by

$$-\frac{w_f h_{RP_0}}{w_a + w_f} = \left(\frac{1}{1 + f}\right) h_{RP_0}$$

where w_f and w_a denote the mass rate of fuel and air, respectively. Hence, the enthalpy of the fuel-air mixture before combustion at state 3, reckoned from the products base, is given by

$$h_3 = 192.23 + 0.0216 \times 19{,}328 = 609.71 \text{ BTU/lb.}$$

Since the enthalpies at states 3 and 4 are equal,

$$h_4 = 609.71 \text{ BTU/lb.}$$

where h_4 is reckoned from the products base state, then

$$\bar{h}_4 = 609.71 \times 28.883 = 17{,}610.4 \text{ BTU/lb.-mole}$$

where 28.883 is the molecular weight of the mixture found by interpolation from Table 9 of Keenan and Kaye. This value of h_4 and a table of enthalpies for products of combustion for 300% theoretical air will yield the temperature at state 4 at the exit of the combustion chamber, because there is no change in chemical aggregation for such a mixture between the products base state and state 4. Since, however, a table for products of combustion for 300% theoretical fuel, between Tables 4 and 7 of Keenan and Kaye, yields a value for the temperature as follows: from Table 4 of

Keenan and Kaye for 25% theoretical fuel, $T_4 = 2322.5$; from Table 7 of Keenan and Kaye for 50% theoretical fuel, $T_4 = 2281.7$. Hence, for 33.33% theoretical fuel, we get

$$T_4 = 2322.5 + \frac{33.33 - 25}{50 - 25}(2281.7 - 2322.5) = 2308.9°R.$$

Similarly, for the relative pressure at state 4, we get

$$p_{r_4} = 361 + \frac{33.35 - 25}{50 - 25}(374.3 - 361) = 365.4.$$

4) Expansion. For isentropic expansion from 5 atm to 1 atm, we find the relative pressure at state 5 from that at state 4:

$$p_{r_5} = p_{r_4} \times \frac{1}{5} = 73.08.$$

The temperature and enthalpy at state 5 are found by linear interpolation, with respect to the percentage of theoretical fuel, between Tables 4 and 7 of Keenan and Kaye. Thus for a value of p_{r_5} of 73.08, we get, from Table 4 of Keenan and Kaye for 25% theoretical fuel, $T_5 = 1577.7$; from Table 7 of Keenan and Kaye for 50% theoretical fuel, $T_5 = 1550.5$. Hence, for 33.33% theoretical fuel,

$$T_5 = 1577.7 + \frac{33.35 - 25}{50 - 25}(1550.5 - 15.77.7) = 1568.6.$$

A similar calculation for h_5 yields

$$h_5 = 397.41.$$

The shaft work of the turbine per pound of products is now

$$W_T = 609.71 - 397.41 = 212.30 \text{ BTU/lb.}$$

5) Performance. The shaft work of the compressor per pound of products is (from Table 1-A):

$$W_c = \left(\frac{1}{1+f}\right)(h_2 - h_1) = 0.9784 \times 72.80 = 71.23 \text{ BTU/lb.}$$

The net work of the gas turbine per pound of products is

$$W_N = 212.3 - 71.2 = 141.1 \text{ BTU/lb.}$$

since the work of compressing the liquid fuel is negligible. The heating value of the fuel supplied may be taken to be

$$-\left(\frac{1}{1+f}\right) h^* = -.0216\,(-19{,}256) = 415.9 \text{ BTU/lb.}$$

where 19,256 is an arbitrarily selected heat of combustion h^* for octane at 25 C. The effieicney of the gas turbine is then

$$\eta = \frac{141.1}{415.9} = 0.339$$

The mixing and combustion processes may be combined and analyzed as a single process between Secs. 1 and 2 on the one hand, and Sec. 4 on the other. Then the values for Sec. 3 need not be determined.

If the products of combustion were treated as air in this example, the calculations for combustion and expansion would have been greatly simplified. Table 1 of Keenan and Kaye would have been used in place of Tables 4 and 7 of Keenan and Kaye; no conversions to molal quantities and no interpolation between these tables would have been necessary. The temperature found at state 4 would have been 2374 F abs, an error of 65 degrees, and the efficiency would have been 0.349, an error of about 3%.

1-14.3 Example 2: Turbojet Analysis

A turbojet is to be designed for a speed of 400 mph at an altitude of 30,000 feet (Fig. 1-30). Air is diffused isentropically from a relative velocity of 400 mph at Sec. 1, the entrance to the diffuser, to zero velocity at Sec. 2, the exit of the diffuser. The air is then compressed isentropically in steady flow through a fourfold increase in pressure from Sec. 2 to Sec. 3. Liquid octane at 500 F abs is
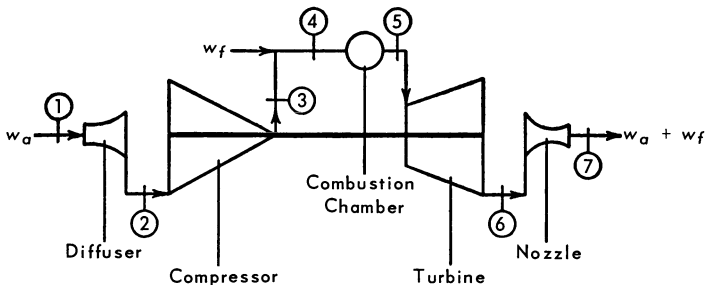
Fig. 1-30

introduced into the stream of compressed air at such a rate that the resultant homogeneous mixture at Sec. 4 contains 25% theoretical fuel. The octane burns completely at constant pressure, and the products of combustion leave the combustion chamber at Sec. 5. Next, the products expand isentropically through a turbine to that pressure at Sec. 6 which results in equality of power output from the turbine and power input to the compressor. Finally, the products expand reversibly and adiabatically through a nozzle to atmospheric pressure at Sec. 7.

Calculate the efficiency of the power plant. Solution.

Table 1-B. States in the Turbojet (Fig. 1-30)

State	Gas Table Number	T F abs	h Btu/lb.	$\bar{h}$ Btu/lb.-mole	p_r	p in. Hg	V ft./sec.
1	1	412	98.41	2,850.9	0.5386	8.88	586.7
2	1	440.73	105.28	3,050.1	0.6815	11.24	0
3	1	654.9	156.69	4,539.4	2.726	44.95	0
4	1, 4	640	153.54	4,502.7		44.95	0
5	4	1,832.3	468.26	13,534.5	133.86	44.95	0
6	4	1,651.1	417.69	12,072.8	87.70	29.45	0
7	4	1,215.8	300.40	8,682.8	26.45	8.88	2423.4

1) Diffusion. The air enters the diffuser with a velocity of 400 mph or 586.7 ft./sec., a temperature of 412 F abs, and a pressure of 8.88 in. Hg. For zero exit velocity, application of the first law results in

$$h_2 = H_2 = h_1 + \frac{V_1^2}{2g} = 98.41 + \frac{(586.7)^2}{2(32.174)(778.16)} = 105.28 \text{ BTU/lb.}$$

where the numerical value for h_1 is obtained from Table 1 of Keenan and Kaye at T_1. Table 1 of Keenan and Kaye at H_2 now gives

$$T_4 = 440.73°R, \qquad p_{r_2} = 0.6815 \quad \text{and} \quad p_2 = 11.2 .$$

These values are summarized here in Table 1-B of states of the turbojet.

2) Compression. The work of isentropic compression in steady flow is the increase in enthalpy across the compressor if the velocities are small. State 3 at the exit of the compressor is identified through the relative pressure (Table 1) of Keenan and Kaye.

$$p_{r_3} = 4 p_{r_2} = 4 \times 0.6815 = 2.726 .$$

Hence, T_3 is 654.93° R and h_3 is 156.69 Btu/lb. of air. The work of compression is given by

$$W_c = h_3 - h_2 = 51.40 \text{ BTU/lb. of air}$$

3) Mixing and combustion. The same technique is used here as in Example 1, on the gas turbine analysis. The results are given here in Table 1-B of the states of the turbojet.

4) Turbine expansion. The equality of compressor power and turbine power is given by

$$(h_3 - h_2) = \left(\frac{w_a + w_f}{w_a}\right)(h_5 - h_6) = (1 + f)(h_5 - h_6)$$

where w_f and w_a denote the mass rate of flow of fuel and air, respectively, and h_6 is the only unknown.

5) Nozzle expansion. For steady flow through the nozzle,

$$V_1^2 = 2g(h_6 - h_7).$$

Since the nozzle expansion is isentropic, the relative pressure (from Table 4) of Keenan and Kaye at the exit of the nozzle determines state 7 as follows:

$$p_{r_7} = p_{r_6} \frac{p_7}{p_5} \frac{p_5}{p_6} = 87.70 \frac{133.86}{87.70} \frac{8.88}{44.95} = 26.45$$

$$T_7 = 1215.8^\circ\text{R} \qquad h_7 = 300.4 \text{ BTU/lb.}$$

Hence the velocity V_7 leaving the nozzle is

$$V_7 = \sqrt{50{,}073(417.69 - 300.4)} = 2423.4 \text{ ft./sec.}$$

6) Performance. The thrust for a mass flow of one pound of air per second is given by the momentum equation in the form

$$\frac{T}{w_a} = \frac{(1+f)V_7}{g} - \frac{V_1}{g}.$$

The propulsive work for a mass flow of one pound of air per second is

$$\frac{W}{w_a} = \frac{T \times V_1}{w_a}.$$

The propulsive efficiency, the ratio of the propulsive work to the heating value of the fuel burned in the same period of time, is given by

$$\eta = \frac{W/w_a}{(w_f/w_a)(-h_{RP})} = \frac{V_1[(1+f)V_7 - V_1]}{gfh^*}$$

$$= \frac{586.7[(2423.4/0.9837) - 586.7]}{32.174[(0.01628/0.9837)(19{,}256)(778.16)]} = 0.138.$$

REFERENCES

1.   Shapiro, A.H.: Dynamics and Thermodynamics of Compress-Fluid, Ronald Press, 1954.
2.   Keenan, J.H.: Thermodynamics, John Wiley & Sons, 1941.
3.   Lee, J.F. and F.W. Sears: Thermodynamics, Addison-Wesley, 1955.
4.   Liepmann, H.W. and A.E. Puckett: Introduction to Aerodynamics of a Compressible Fluid, John Wiley & Sons, 1947.
5.   Keenan, J.H. and J. Kaye: Gas Tables, John Wiley & Sons, 1945.
6.   Condon, E.V. and H. Odishaw: Handbook of Physics, McGraw-Hill, 1958.
7.   Sorenson, H.A.: Gas Turbines, Ronald Press, 1951.
8.   Trout, Arthur M. and Eldon W. Hall: Method for Determining Optimum Division of Power Between Jet and Propeller for Maximum Thrust Power of a Turbine-Propeller Engine, NACA TN 2178, 1950.
9.   Hensley, Reece V.: Theoretical Augmentation of Turbine-Propeller Engine by Compressor-Inlet Water-injection, Tail-Pipe Burning, and Their Combination, NACA TN 2672, 1952.
10.   Dobrowolski, Andrzej: Analysis of Nonconstant Area Combustion and Mixing in Ramjet and Rocket-Ramjet Hybrid Engines, NASA TN D-3626, 1966.
11.   Inman, Robert M.: Theoretical Investigation of Turbulent Liquid-Metal Heat Transfer in Channels with Heat Sources in the fluid, 1966.
12.   Lundin, Bruce T.: Theoretical Analysis of Various Thrust-Augmentation Cycles for Turbojet Engines, NACA 981, 1950.
13.   Pinkel, Benjamin and Irving M. Karp: A Thermodynamic Study of the Turbine-Propeller Engine, NACA 1114, 1953.
14.   ———— and ————: A Thermodynamic Study of the Turbojet Engine, NACA 891, 1947.
15.   Wilcox, Clinton and Arthur M. Trout: Analysis of Thrust Augmentation of Turbojet Engines by Water Injection at Compressor Inlet Including Charts for Calculating Compression Processes with Water Injection, NACA 1006, 1951.
16.   Bittker, David A.: Comparison of Experimental and Kinetically Limited Theoretical Performance of the Hydrogen-Fluorine Propellant System, NASA TN D-3607.
17.   Allison, Dennis O.: Calculation of Thermodynamic Properties of Arbitrary Gas Mixtures with Modified Vibrational-Rotational Corrections, NASA TN D-3538.
18.   Newman, Perry A. and Dennis O. Allison: Direct Calculation of Specific Heats and Related Thermodynamic Properties of Arbitrary Gas Mixtures with Tabulated Results, NASA TN D-3540, 1966.
19.   Loh, W.H.T.: Analytical Solutions for Rotary Matrix Wire Screen Heat Exchangers, *Journal of the Franklin Institute*, 272:3, September 1961.

20.   ———: UCLA "Jet Propulsion" classnotes.
21.   ———: SMU "Advanced Propulsion Technology" classnotes.
22.   ———: Hydraulic Analogue for One Dimensional Unsteady Gas Dynamics, *Journal of the Franklin Institute*, 269: 1, January 1960.
23.   ———: Hydraulic Analogy for Two Dimensional and One Dimensional Flows, *Journal Aero-Space Sci.*, 26, pp. 389–390 (1959).
24.   ———: TCU "Jet Propulsion and Gas Turbine" classnotes.
25.   ———: "Advanced Lectures on Propulsion Series" given at Convair and Chance Vaught.

Part Two

Jet Propulsion

Thermodynamic Cycle Analysis of Gas Turbines

and Air-breathing Propulsion Systems

W.H.T. LOH, Manager
Science and Technology,
Space Division,
North American Rockwell Corporation
Downey, California

[2-1] INTRODUCTION
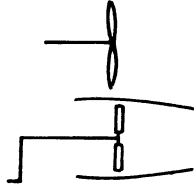
Air-breathing propulsion systems include turbojet, turboprop, ducted fan, ramjet, ducted rocket, nuclear jet, pulse jet, and their many variations with intercooling, reheat, regeneration, after-burning, and water injection. These air-breathing propulsion systems can best be analyzed through thermodynamic cycle analysis. The fundamentals of thermodynamic cycle analysis were already described in detail in Chapter 1 through the various unit processes and through the two illustrative examples using the gas table. However, in order to provide clarity in certain special cases when such clarity is required, the application of the unit processes to such propulsion systems will be given here, although detailed procedures within each unit process will still be omitted (here readers should refer to Chapter 1).

[2-2] SYMBOLS AND SKETCHES OF AIR-BREATHING PROPULSION SYSTEMS

In analyzing gas turbine and jet propulsion engines, it is convenient to use the following sketch and symbol for each engine component. In making calculations, it is always convenient to use the unit processes based on one pound of air flow per second through the system. Subscripts "a" and "i" indicate "actual" and "isentropic" process respectively. A number with a prime, such as 1', 2', 3', 4', etc., indicates the fictitious "isentropic" or "ideal" state of a gas, while a number without a prime such as 1, 2, 3, 4,

etc., indicates the corresponding "actual" state of gas. Capital letters such as T, P, $\bar{\rho}$, H, indicate stagnation properties of the gas, while small letters such as t, p, ρ, h, indicate static properties of the gas.

Component	Sketch	Symbol	Associated Terminology and Its Symbols
1. Diffuser or Inlet		D	Diffuser efficiency $$\eta_D = \frac{H_2{'} - h_1}{H_2 - h_1}$$ Diffuser total pressure loss $= \left(\dfrac{\Delta P}{P}\right)_D$
2. Compressor		C	Compression ratio $= C.R.$ Compressor efficiency $= \eta_c$ Compressor work $= W_c$
3. Intercooler		I	Intercooler effectiveness $= \eta_I$ Intercooler total pressure loss $= \left(\dfrac{\Delta P}{P}\right)_I$
4. Combusion Chamber or Burner		B	Combustion efficiency or burner efficiency $= \eta_b$ Fuel air ratio $= f$ Combustion chamber total pressure loss $= \left(\dfrac{\Delta P}{P}\right)_B$ Heating value of fuel $= h^*$ Heat supplied per pound of gas $= Q$

Component	Sketch	Symbol	Associated Terminology and Its Symbols
5. Turbine		T	Turbine Expansion Ratio = $E.R.$ Turbine efficiency = η_T Turbine work per pound of gas = W_T
6. Reheater or Burner		B	Same as burner
7. Regenerator		X	Regenerator effectiveness = η_x Regenerator total pressure loss $= \left(\dfrac{\Delta P}{P}\right)_x$
8. After burner		B	Same as burner
9. Nozzle or Jet		N	Nozzle efficiency = η_N Nozzle total pressure loss = $\left(\dfrac{\Delta P}{P}\right)_N$
10. Propeller or Ducted Fan		P F	Propeller efficiency = η_P Fan efficiency = η_F
11. Rocket		R	Primary Flow with subscript p Secondary Flow with subscript s

[2-3] GAS TURBINE CYCLES

Based on the above symbols and sketches, the following representations may be made on various gas turbine engine cycles.

Gas Turbine Configurations

Sketches

Symbols

h—s Diagram and Unit Process Required from One State to the Next
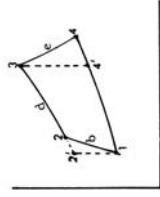
Basic Gas Turbines

Isentropic (CBT)$_i$

Actual (CBT)$_a$

One Intercooling Gas Turbine
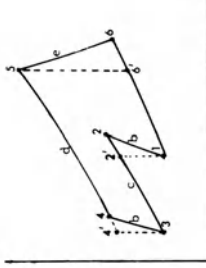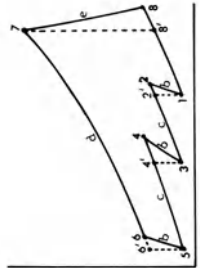
Isentropic (CICBT)$_i$

Actual (CICBT)$_a$

Two Intercooling Gas Turbine

Isentropic (CICICBT)$_i$

Actual (CICICBT)$_a$

Gas Turbine Configurations	Sketches	Symbols	h–s Diagram and Unit Process Required from One State to the Next
Isothermal Intercooling Gas Turbine		Isentropic $(CICI....CBT)_i$ Actual $(CICI....CBT)_a$	
One Reheating Gas Turbine		Isentropic $(CBTBT)_i$ Actual $(CBTBT)_a$	
Two Reheating Gas Turbine		Isentropic $(CBTBTBT)_i$ Actual $(CBTBTBT)_a$	
Isothermal Reheating Gas Turbine		Isentropic $(CBTBT....BT)_i$ Actual $(CBTBT....BT)_a$	
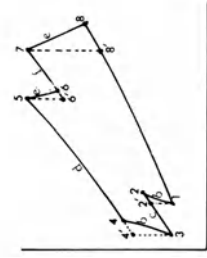
Gas Turbine Configurations	Sketches	Symbols	h–s Diagram and Unit Process Required from One State to the Next
One Intercooling and One Reheating Gas Turbine		Isentropic (CICBTBT)$_i$ Actual (CICBTBT)$_a$	
Two Intercooling and Two Reheating Gas Turbine		Isentropic (CICICBTBTBT)$_i$ Actual (CICICBTBTBT)$_a$	
Isothermal Intercooling and Isothermal Reheating Gas Turbine		Isentropic (CICIC....ICBTBT ....BT)$_i$ Actual (CKIC.....ICBTBT ....BT)$_a$	
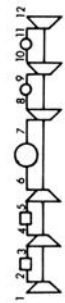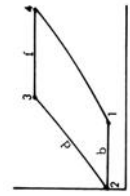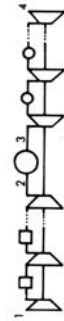
Gas Turbine Configurations	Sketches	Symbols	$h-s$ Diagrams and Unit Process Required from One State to the Next
Regeneration with Basic Gas Turbine		Isentropic $(CBTX)_i$ Actual $(CBTX)_a$	
Regeneration with One Intercooling Gas Turbine		Isentropic $(CICBTX)_i$ Actual $(CICBTX)_a$	
Regeneration with One Reheating Gas Turbine		Isentropic $(CBTBTX)_i$ Actual $(CBTBTX)_a$	
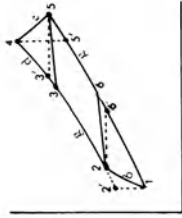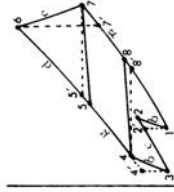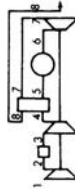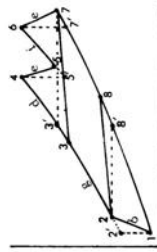
Gas Turbine Configurations	Sketches	Symbols	h–s Diagrams and United Process Required from One State to the Next
Regeneration with One Intercooling and One Reheating Gas Turbine		Isentropic $(CICBTBTX)_i$ Actual $(CICBTBTX)_a$	
Regeneration with Two Intercooling and Two Reheating Gas Turbine		Isentropic $(CICICBTBTBTX)_i$ Actual $(CICICBTBTBTX)_a$	
Regeneration with Isothermal Inter-cooling and Iso-thermal Reheating Gas Turbine		Isentropic $(CICI....CBTB....TX)_i$ Actual $(CICI....CBTB....TX)_a$	
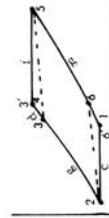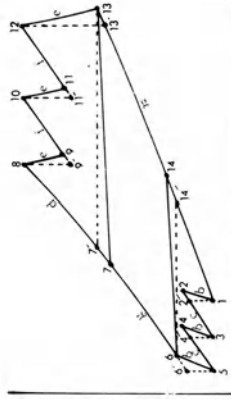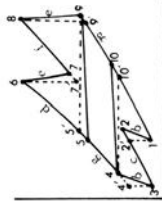
Pressure drop in burners, intercoolers, reheaters, regenerators, and after-burners is being neglected in the *h–s* diagrams for simplicity of illustration of basic thermodynamic processes involved. Dotted line indicates "isentropic," while solid line indicates "actual."

Unit process required to calculate from one state to the next is indicated by the following symbols marked in the middle of each process involved. Refer to these processes in Chapter 1 for methods of calculation.

- b = Compressor compression, pp. 75–77
- c = Intercooling, pp. 87–92
- d = Combustion, pp. 78–80
- e = Turbine expansion, pp. 81–84
- f = Reheating (including the amount of fuel required for reheat in the cycle analysis), pp. 92–95
- g = Regeneration, pp. 95–96
- h = After-burning, pp. 96–97
- j = Water injection, pp. 97–100
- m = Net work output W_{net}
- η = Thermal efficiency and B.S.F.C.

$$W_{net} = \Sigma [W_T (1 + f)] - \Sigma W_c$$

$$\eta = \frac{W_{net}}{\Sigma fh^*}$$

$$B.S.F.C. = \frac{3600 \, \Sigma f}{W_{net} \left(\dfrac{778}{550}\right)}$$

The results of thermodynamic cycle analysis were plotted in Figs. 2-1 and 2-2. Figure 2-1 shows thermal efficiency and *B.S.F.C.* (brake specific fuel consumption in fuel per hour per brake horsepower) of various gas turbine engines versus compression ratio, while Fig. 2-2 shows Net Work W_{net} (in Btu/lb. air per sec.) versus compression ratio. It is to be noticed that both η and W_{net} curves in Figs. 2-1 and 2-2 have peak values of η and W_{net}, occurring at certain values of compression ratio. This maximum thermal efficiency and maximum net work may be obtained analytically in the case of constant specific heat analysis by differentiating the thermal efficiency expression or net work expression (which should be put in terms of compression ratio) with respect to compression ratio and setting it equal to zero. For example, for $(CBT)_a$ systems, Fig. 2-3, the compressor work and compressor exit temperature are, respectively:

Fig. 2-1 Effect of compression ratio on thermal efficiency and brake specific fuel consumption for compressor-intercooler-burner-turbine-regenerator combination. Net work curves are same for with or without regeneration.
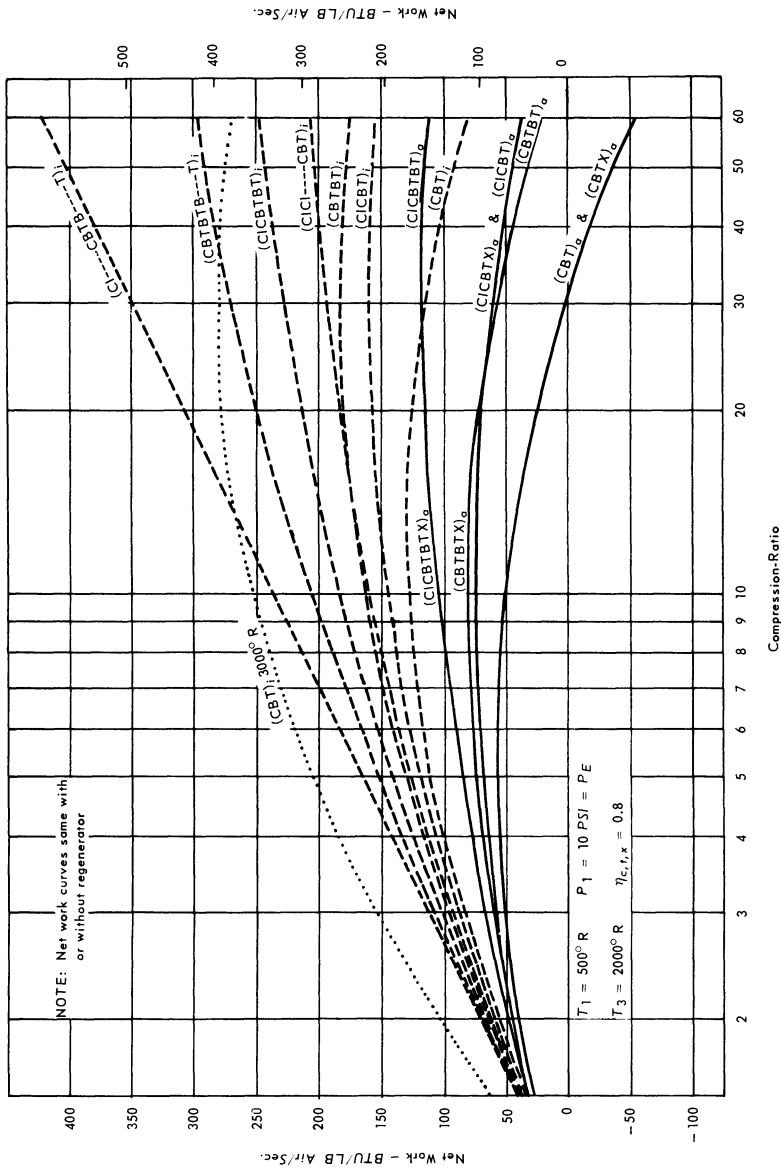
Fig. 2-2 Effect of compression ratio on net work and brake horsepower per pound air per sec, for compressor-intercooler-burner-turbine-regenerator combinations. In this set of curves the net work vs. compression ratio is the same with or without regeneration, *i.e.*, CBT is same as CBTX, etc.
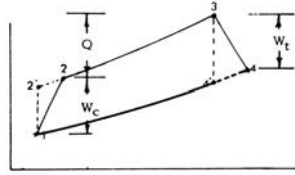
Fig. 2-3

$$W_c = \frac{c_p T_1}{\eta_c} \left[\left(\frac{P_2}{P_1} \right)^{\frac{k-1}{k}} - 1 \right]$$

$$T_2 = T_1 \left\{ 1 + \frac{1}{\eta_c} \left[\left(\frac{P_2}{P_1} \right)^{\frac{k-1}{k}} - 1 \right] \right\}.$$

The amount of heat added is

$$Q = \eta_b f h^* = c_p (T_3 - T_2)$$

$$= c_p T_3 - c_p T_1 \left\{ 1 + \frac{1}{\eta_c} \left[\left(\frac{P_2}{P_1} \right)^{\frac{k-1}{k}} - 1 \right] \right\}.$$

The turbine work is

$$W_T = c_p T_3 \eta_T \left[1 - \left(\frac{P_4}{P_3} \right)^{\frac{k-1}{k}} \right]$$

$$= c_p T_3 \eta_T \left[1 - \frac{1}{\left(\frac{P_2}{P_1} \right)^{\frac{k-1}{k}}} \right].$$

Therefore, the net work and thermal efficiency become:

$$W_{net} = W_T - W_c = c_p T_3 \eta_T \left[1 - \frac{1}{\left(\dfrac{P_2}{P_1}\right)^{\frac{k-1}{k}}} \right] - \frac{c_p T_1}{\eta_c} \left[\left(\frac{P_2}{P_1}\right)^{\frac{k-1}{k}} - 1 \right]$$

$$\eta = \frac{W_{net}}{Q} = \frac{c_p T_3 \eta_T \left[1 - \dfrac{1}{\left(\dfrac{P_2}{P_1}\right)^{\frac{k-1}{k}}} \right] - \dfrac{c_p T_1}{\eta_c} \left[\left(\dfrac{P_2}{P_1}\right)^{\frac{k-1}{k}} - 1 \right]}{c_p T_3 - c_p T_1 \left\{ 1 + \dfrac{1}{\eta_c} \left[\left(\dfrac{P_2}{P_1}\right)^{\frac{k-1}{k}} - 1 \right] \right\}} .$$

For constant T_1 (compressor inlet temperature), T_3 (turbine inlet temperature), η_c (compressor efficiency), η_T (turbine efficiency), both W_{net} and η are in terms of compression ratio (P_2/P_1). When differentiate W_{net}, for example, with respect to (P_2/P_1) and set equal to zero, one obtains:

$$\left(\frac{P_2}{P_1}\right)_{W_{net_{max.}}} = \left[\frac{\eta_c \eta_T T_3}{T_1} \right]^{\frac{k}{2(k-1)}} \qquad (2-1)$$

$$W_{net_{max.}} = c_p T_3 \eta_T \left[1 - \frac{1}{\left(\dfrac{\eta_c \eta_T T_3}{T_1}\right)^{\frac{1}{2}}} \right] - \frac{c_p T_1}{\eta_c} \left[\left(\frac{\eta_c \eta_T T_3}{T_1}\right)^{\frac{1}{2}} - 1 \right] . \qquad (2-2)$$

It is to be noticed here that the maximum net work and maximum thermal efficiency [consequently minimum specific fuel consumption; see Eq. (1-212)] occur at different compression ratios. Maximum net work occurs at a lower compression ratio than

maximum efficiency. Therefore, if a gas turbine is aimed at maximum net work rather than thermal efficiency or fuel economy, it should be designed in the neighborhood of $(P_2/P_1)_{W_{net_{max.}}}$. However, if it is aimed at maximum efficiency or fuel economy, it should be designed at a high compression ratio near $(P_2/P_1)_{\eta_{max.}}$

value. It is also to be noticed that because of the flat nature near the peak value of W_{net} and η, other factors such as weight, size, and compressor stages, may affect the selection of optimum compression ratio. Eqs. (2-1) and (2-2) give the locus of $(P_2/P_1)_{W_{net_{max.}}}$

and $W_{net_{max.}}$ for other values of T_3 or T_1. Increase of turbine inlet temperature T_3 or decrease of compressor inlet temperature T_1 increases both the W_{net} and η, and moves both $(P_2/P_1)_{W_{net_{max.}}}$ and

$(P_2/P_1)_{\eta_{max.}}$ toward a higher compression ratio. From Fig. 2-1, one sees that use of regeneration increases thermal efficiency and moves $(P_2/P_1)_{\eta_{max.}}$ to a lower value. Although Fig. 2-2 shows that

W_{net} is the same for systems with and without regeneration (because in this set of calculations, pressure losses through regenerators were neglected), actual systems with regeneration always have less W_{net} than systems without regeneration. Addition of

intercooling or reheat or both tend to increase, in general, the W_{net} and η, and tend to move $(P_2/P_1)_{W_{net_{max.}}}$ and $(P_2/P_1)_{\eta_{max.}}$ toward

high compression ratios. Increase of compressor efficiency η_c and turbine efficiency η_T increases both W_{net} and η and also moves

$(P_2/P_1)_{W_{net_{max.}}}$ and $(P_2/P_1)_{W_{net_{max.}}}$ toward high compression ratios.

When $\eta_c = 1$ and $\eta_T = 1$, the system becomes an isentropic system, and Figs. 2-1 and 2-2 show that both thermal efficiency and W_{net} increase with compression ratio (except those regeneration

systems which approach the Carnot Cycle efficiency $(T_3 - T_1)/T_3$. Figure 2-1 shows that η increases continuously with compression ratio, while W_{net} still reaches a $W_{net_{max.}}$ at a certain compression

ratio, beyond which W_{net} decreases even for the isentropic systems.

This situation can be seen for $(CBT)_i$ from W_{net} and η expressions.

When $\eta_c = 1$ and $\eta_T = 1$, W_{net} and η expressions reduce to:

$$W_{\text{NET}} = c_p T_3 \left[1 - \frac{1}{\left(\dfrac{P_2}{P_1}\right)^{\frac{k-1}{k}}} \right] - c_p T_1 \left[\left(\frac{P_2}{P_1}\right)^{\frac{k-1}{k}} - 1 \right]$$

$$\text{(2-3)}$$

$$\eta = 1 - \frac{1}{\left(\dfrac{P_2}{P_1}\right)^{\frac{k-1}{k}}} . \qquad \text{(2-4)}$$
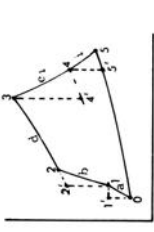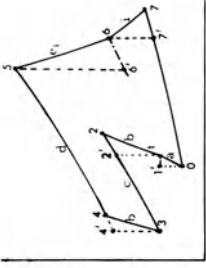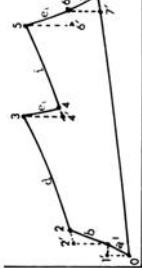
Equation (2-3) has a maximum at $(P_2/P_1)_{W_{\text{net}_{\text{max.}}}} = (T_3/T_1)^{k/2(k-1)}$ (because turbine work approaches a fixed value for a given T_3 while compression work increases continuously), while Eq. (2-4) shows η approaches 1 when (P_2/P_1) approaches infinity. A similar method can be applied to other gas turbine systems shown in Figs. 2-1 and 2-2 for determination of compressor compression ratio where $W_{\text{net}_{\text{max.}}}$ and $\eta_{\text{max.}}$ occur respectively.

[2-4] AIR-BREATHING PROPULSION SYSTEMS: TURBOJET, TURBO-PROP, DUCTED FAN, RAM JET AND DUCTED ROCKET

Based on the previously described symbols and sketches, the following representations may be made of various air breathing propulsion systems. Although many variations with intercooling, reheat, regeneration after-burning and water injection may be made to each "isentropic" and "actual" basic air breathing propulsion system similar to those already shown for the gas turbine cycles, only a few typical "actual" cycles will be shown in the following list as illustrative examples.

Propulsion Systems	Sketches	Symbols	$h-s$ Diagram and Unit Process Required for Calculation
Basic Turbo–Jet		$(DCBTJ)_a$	
Intercooling Turbo–Jet		$(DCICBTJ)_a$	
Reheating Turbo–Jet		$(DCBTBTJ)_a$	
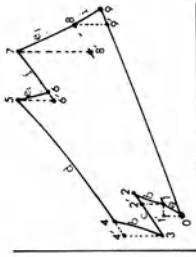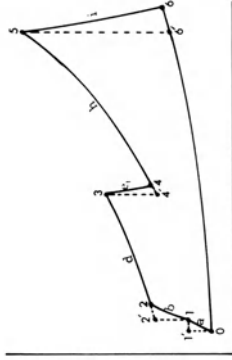
Propulsion Systems	Sketches	Symbols	h–s Diagram and Unit Process Required for Calculation
Intercooling and Reheating Turbo–Jet		$(DCICBTBTJ)_a$	
After-burning Turbo–Jet		$(DCBTBJ)_a$	
Intercooling and Reheating Turbo–Jet with After-burning		$(DCICBTBTBJ)_a$	
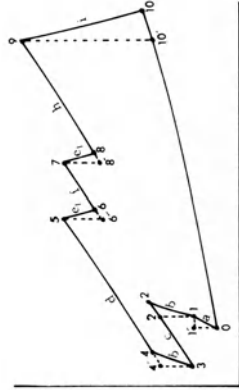
Propulsion Systems	Sketches	Symbols	h–s Diagram and Unit Process Required for Calculation
Basic Turbo-Prop		$(DCBTPJ)_a$	
Intercooling Turbo-Prop		$(DCICBTPJ)_a$	
Reheating Turbo-Prop		$(DCBTBTPJ)_a$	
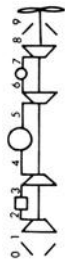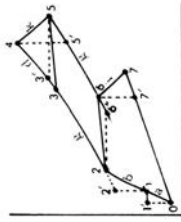
Propulsion Systems	Sketches	Symbols	h–s Diagram and Unit Process Required for Calculation
Intercooling and Reheating Turbo-Prop		$(DCICBTBTPJ)_a$	
Regeneration Turbo-Prop		$(DCBTPXJ)_a$	
Intercooling and Reheating Turbo-Prop with Regeneration		$(DCICBTBTPXJ)_a$	
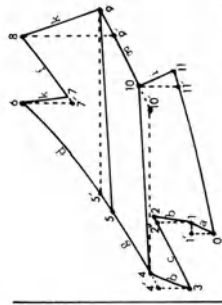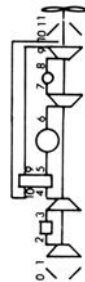
Propulsion Systems	Sketches	Symbols	*h–s* Diagram and Unit Process Required for Calculation
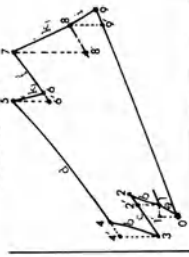
Propulsion Systems

Sketches

Symbols

h—s Diagram and Unit Process Required for Calculation
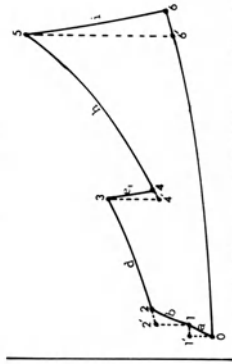
Ducted Fan with After-Burning

(DCBTFBJ)$_a$

Primary h—s

Secondary h—s

Propulsion Systems

Sketches

Symbols

h–s Diagram and Unit Process Required for Calculation

Air Loop

Liquid Metal Loop

(DBJ)$_a$

Basic Ram Jet

Liquid Metal Cycle Nuclear Turbo–Jet
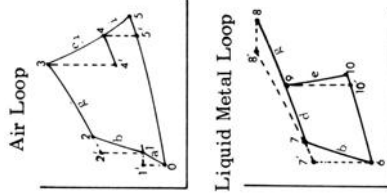
Propulsion Systems	Sketches	Symbols	h−s Diagram and Unit Process Required for Calculation
Liquid Metal Cycle Nuclear Turbo-Prop			Air Loop Liquid Metal Loop
Ducted Rocket		$(DRJ)_a$	Ducted rocket will be treated in Chapter 4. No further discussion will be given here.
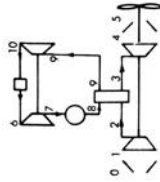
In addition to those symbols already shown for gas turbine cycles, the following which are involved in air breathing propulsion systems are added here.

a = ram compression, pp. 73-75

e_1 = turbine expansion required to yield $\Sigma W_c = \Sigma[(1+f)W_T]$

i = nozzle expansion and jet thrust, pp. 84-87

k = turbine expansion and propeller thrust, pp. 102-103

k_1 = turbine expansion and turbine work available to drive fan = $W_{T_F} = \Sigma[(1+f)W_T] - \Sigma W_c$

b_1 = fan compression work W_{c_F} to satisfy $W_{c_F} = W_{T_F}/W_{a_F}$, here W_{a_F} is the airflow through fan, pp. 75-77

i_1 = nozzle expansion for secondary air flow through fan and fan jet thrust (remembering that W_{a_F} pound fan air flow per pound of primary air flow), p. 101

a_1 = ran compression for air flow through fan (W_{a_F} pounds)

d_1 = combustion or heating of air flow through fan (W_{a_F} pounds secondary air flow for each pound of primary air flow)

The application of unit processes to the above jet propulsion cycles shown in the table should be straight forward (by using the unit process given in Chapter 1) except the following notes concerning application to turboprop and ducted fan cycles.

Note on application of unit processes to Turboprop cycles.   As pointed out in Chapter 1, the thrust F of a turboprop consists of two parts, *i.e.,* the thrust from propeller F_p and the thrust from the jet exhaust F_j.
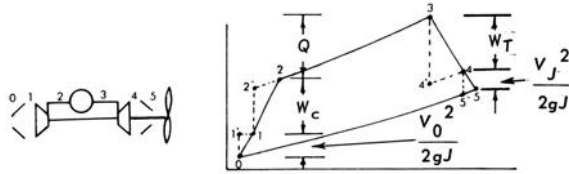
Fig. 2-4

From Fig. 2-4, the turbine work W_T and turbine exit temperature T_4 are, respectively,

$$W_T = c_p T_3 \eta_T \left[1 - \left(\frac{P_4}{P_3}\right)^{\frac{k-1}{k}} \right]$$

$$T_4 = T_3 \left\{ 1 - \eta_T \left[1 - \left(\frac{P_4}{P_3} \right)^{\frac{k-1}{k}} \right] \right\}.$$

The propeller work W_p is

$$W_p = (1 + f) W_T - W_c = (1 + f) c_p T_3 \eta_T \left[1 - \left(\frac{P_4}{P_3} \right)^{\frac{k-1}{k}} \right] - W_c.$$

The propeller shaft horsepower SHP_p is

$$SHP_p = W_p \times \frac{778}{550} \times \eta_m.$$

Here η_m is the mechanical efficiency of propeller-reduction gear. The propeller thrust horsepower THP_p is

$$THP_p = \eta_p SHP_p = \frac{778}{550} \eta_p \eta_m W_p.$$

Here η_p = propeller efficiency. Since the propeller thrust F_p is defined by

$$THP_p = \frac{F_p \times V_o}{550}$$

The propeller thrust F_p is

$$F_p = \frac{550 \, THP_p}{V_o} = \frac{778 \, \eta_p \eta_m W_p}{V_o}$$

$$= \frac{778}{V_o} \eta_p \eta_m \left\{ (1 + f) c_p T_3 \eta_T \left[1 - \left(\frac{P_4}{P_3} \right)^{\frac{k-1}{k}} \right] - W_c \right\}.$$

The jet thrust F_j is (note from point 4 to point 5 of Fig. 2-4):

$$F_j = \frac{1+f}{g} V_j - \frac{1}{g} V_o = \frac{1+f}{g} \sqrt{2gJ \eta_N c_p T_4 \left[1 - \left(\frac{p_o}{P_4}\right)^{\frac{k-1}{k}}\right]} - \frac{1}{g} V_o$$

therefore the total thrust of a turboprop is

$$F = F_p + F_j = \left\{(1+f)c_p T_3 \eta_T \left[1 - \left(\frac{P_4}{P_3}\right)^{\frac{k-1}{k}}\right] - W_c \right\} \frac{778}{V_o} \eta_p \eta_m$$

$$+ \left\{\frac{1+f}{g} \sqrt{2gJc_p\eta_N T_3 \left\{1 - \eta_T \left[1 - \left(\frac{P_4}{P_3}\right)^{\frac{k-1}{k}}\right]\right\}\left[1 - \left(\frac{p_0}{P_4}\right)^{\frac{k-1}{k}}\right]} - \frac{1}{g} V_o \right\}.$$

For a fixed turboprop design, each value of P_4 will yield one value of a total turboprop thrust. The maximum total turboprop thrust may be obtained by differentiating the total thrust F with respect to P_4 and setting the result equal to zero. This condition gives

$$V_{j_{\text{optimum}}} = \frac{\eta_N}{\eta_T \eta_p \eta_m} V_o .$$

The optimum division of turboprop thrust between jet thrust and propeller thrust for maximum total thrust occurs when jet velocity V_j equals to air plane velocity V_o times $(\eta_N / \eta_T \eta_p \eta_m)$. A simple derivation of the above expression may more easily be obtained in the following way by dividing the total isentropic energy into x and $(c-x)$ as shown in Fig. 2-5.
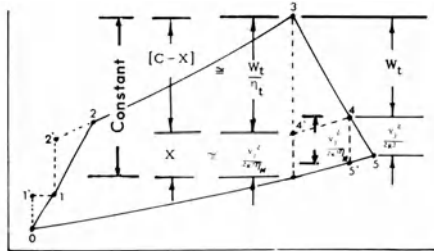
Fig. 2-5

From Fig. 2-5, the jet thrust becomes

$$F_j = \frac{1 + f}{g} \sqrt{2gJ \, \eta_N \, x} - \frac{1}{g} V_o.$$

The propeller thrust becomes

$$F_p = \frac{778}{V_o} \eta_p \eta_m \left\{ (1 + f)(c - x) \eta_T - W_c \right\}.$$

The total thrust F becomes

$$F = \left(\frac{1 + f}{g} \right) \sqrt{2gJ \, \eta_N x} - \frac{1}{g} V_o + \frac{778}{V_o} \eta_p \eta_m \left\{ (1 + f) \eta_T (c - x) - W_c \right\}.$$

Differentiating F with respect to x and setting it equal to zero, one obtains:

$$x^{\frac{1}{2}} = \sqrt{\frac{\eta_N}{2gJ} \frac{V_o}{\eta_T \, \eta_p \, \eta_m}}$$

or

$$V_{j_{\text{optimum}}} = \left(\frac{\eta_N}{\eta_T \, \eta_p \, \eta_m} \right) V_o.$$

Therefore, for all turboprop cycle analysis, the optimum thrust distribution as given above is used. Similar derivation for maximum thrust may be obtained for turboprop cycle with and without intercooling, reheat and/or regeneration.

Note on ducted fan cycle analysis. Referring to Fig. 2-6 and its corresponding primary and secondary h–s diagrams, one may write:

Primary System   Secondary System
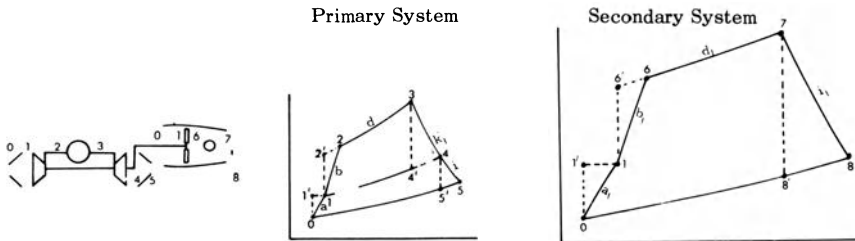
Fig. 2-6

The fan compression work per pound of air flow in the primary system is

$$W_{c_F} = W_{a_F}(H_6 - H_1).$$

Here W_{c_F} = fan compression work per pound of air flow in the primary system. W_{a_F} = secondary air flow in pounds per second through the fan for each pound of air flow through the primary system.

H_6 = total enthalpy after fan
H_1 = total enthalpy before fan

The turbine work available to drive the fan is

$$W_{T_F} = (1 + f) W_T - W_c .$$

Here W_{T_F} = turbine work available to drive the fan per pound of air flow in the primary system

W_c = compression work in the primary system.
f_p = fuel air ratio in the primary system.

It is necessary that $W_{T_F} = W_{c_F}$ be satisfied. The primary jet thrust F_{j_p} is

$$F_{j_p} = \frac{1 + f_p}{g} V_{j_p} - \frac{1}{g} V_o .$$

The secondary jet thrust F_{j_s} is

$$F_{j_s} = \left\{ \frac{1 + f_s}{g} V_{j_s} - \frac{1}{g} V_o \right\} W_{a_F} .$$

The total thrust per pound of primary air flow is

$$F_j = F_{j_p} + F_{j_s} = \left(\frac{1 + f_p}{g} V_{j_p} - \frac{1}{g} V_o \right) + \left\{ \frac{1 + f_s}{g} V_{j_s} - \frac{1}{g} V_o \right\} W_{a_F} .$$

The specific thrust per pound of total air flow (both primary and secondary) is

$$\text{Specific Thrust} = \frac{F_j}{1 + W_{a_F}} .$$

The fuel flow in pounds per hour is equal to

$$f_p \times 3600 \times 1 + f_s \times 3600 \times W_{a_F} .$$

The thrust specific fuel consumption (T.S.F.C.) is

$$\text{T.S.F.C.} = \frac{f_p \times 3600 \times f_s \times 3600 \times W_{a_F}}{F_j} .$$

It is to be noted that sometimes primary and secondary flow may be mixed before exhaust through a common jet nozzle. In such cases, equations of mixing as given on p. 65 to p. 73 may be used. After mixing, the analysis can be made in the normal way.

[2-4.1] Turbojet Cycles

A schematic diagram of the turbojet engine considered is shown in Fig. 2-7. Air enters the inlet duct and passes to the compressor inlet. The air is further compressed passing through the compressor and enters the combustion chamber where fuel is injected and burned. The products of combustion then pass through the turbine nozzles and blades where an appreciable drop in pressure occurs and finally are discharged rearwardly through the exhaust nozzle to provide thrust.
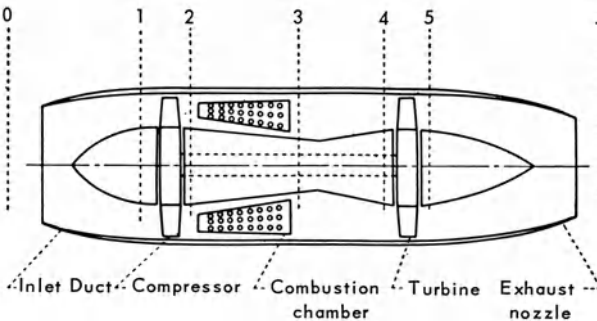
Fig. 2-7 (After B. Pinkel and I. M. Karp, NACA TR 891).

Design-point engines. For the purpose of illustrating the manner in which the thrust per unit mass rate of air flow and the specific fuel consumption are influenced by compressor pressure ratio, combustion-chamber-outlet temperature, flight speed, and ambient-air temperature, the following fixed parameters are assumed:

Compressor efficiency η_c	0.85
Turbine efficiency η_T	0.90
Combustion efficiency η_b	0.96
Exhaust-nozzle efficiency η_N	0.97
Heating value of fuel, h^*, Btu/lb.	18,900

Fig. 2-8   (After B. Pinkel and I. M. Karp, NACA TR 891).
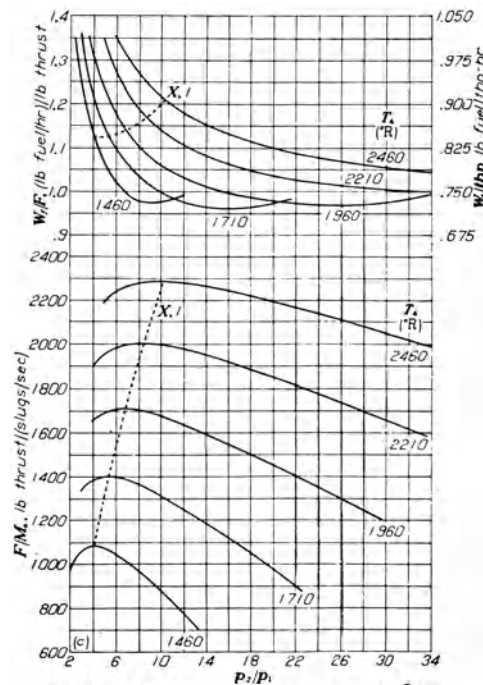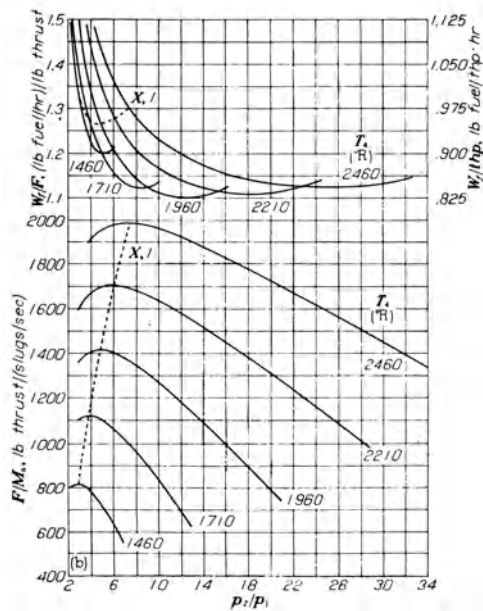
(b) V_o, 733 feet per second; T_o, 519° R.

(c) V_o, 733 feet per second; T_o, 412° R.

The specific fuel consumption and the thrust per unit mass rate of air flow plotted against the compressor pressure ratio for various values of combustion-chamber-outlet temperature are shown in Fig. 2-8 for several combinations of ambient temperature and airplane velocity. A line for compressor pressure ratios giving maximum thrust per unit mass rate of air flow is also included in the illustration.

It is shown in Fig. 2-8 that the minimum specific fuel consumption occurs at a higher compressor pressure ratio than maximum thrust per unit mass rate of air flow. When high thrust per unit mass rate of air flow rather than low specific fuel consumption is the primary consideration, it is apparent from Fig. 2-8 that high combustion-chamber-outlet temperatures should be used. High thrust is the more important consideration in take-off, climb, and maximum-speed operation.

As the combustion-chamber-outlet temperature is increased from the minimum value required to produce a thrust, the thrust per unit mass rate of air flow increases and the specific fuel consumption decreases until reaching the temperature giving minimum specific fuel consumption. Increasing the temperature further results in both increased thrust per unit mass rate of air flow and specific fuel consumption.

Effect of turbine inlet temperature and compression ratio. In general, an increase of turbine inlet temperature increases specific thrust almost lineraly. The maximum specific thrust which can be obtained at a certain turbine inlet temperature increases as the turbine inlet temperature is increased. The maximum values are obtained at higher compression ratios as turbine inlet temperature is increased. At high compression ratios, the specific thrust falls off rapidly for low turbine inlet temperature. The effect of increasing turbine inlet temperature at any given compression ratio has in general, the effect of increasing specific fuel consumption.

Effect of compressor and turbine efficiency. An increase of compressor and turbine efficiency increases the specific thrust and decreases specific fuel consumption. Both the maximum specific thrust point and minimum specific fuel consumption point move toward high compression ratio as the compressor and turbine efficiency is increased. At higher compressor and turbine efficiency, compression ratio 10 to 15 engine would be desirable. This is because the rapid drop of specific fuel consumption and negligible drop of specific thrust between compression ratio 10 to 15 would result.

Effect of flight speed. In general, the optimum compression ratio either for maximum specific thrust or for minimum specific fuel consumption would be decreased as the flight speed increases.

Effect of intercooling. Turbojet intercooling usually iccreases specific fuel consumption. For example, at compression ratio 8, intercooling could result in a 15% increase of specific thrust and a 10% increase of specific fuel consumption. At compression ratio 12, the corresponding values could be 22.5% and 11.5%.

Effect of reheat. Turbojet reheat usually increases specific thrust, particularly at high compression ratios. Although reheat slightly increases specific fuel consumption at low compression ratios, the amount of increase becomes negligible at high compression ratios. For example, at compression ratio 8, reheat could result in a 24% increase of specific thrust with a 5% increase of specific fuel consumption. The corresponding values at compression ratio 12 could be 38.5% and 2.5%. Another feature of reheat is that the specific thrust falls off rapidly above about compression ratio 5 for engines without reheat, but only small changes in specific thrust occur between compression 5 and 16 when reheat is used.

Effect of intercooling and reheat. At a given compression ratio, intercooling and reheat considerably increase specific thrust (especially at high CR) and specific fuel consumption. Typical comparison of engine performance would show that a turbojet engine of about compression ratio 5 without intercooling and reheat could have the same specific fuel consumption as one of compression ratio 22 with intercooling and reheat, but latter could have about 23% more thrust.

Effect of after-burning. A 70% increase of thrust at an expense of 60% increase of specific fuel consumption could result from after-burning to $3000°R$ in a compression ratio 5 engine. The corresponding increases could increase to about 110% and 76% respectively in a compression ratio 12 engine. An increase of airplane speed increases the gain of thrust increase and reduces the penalty of fuel consumption.

[2-4.2] Turboprop Cycles

A schematic diagram of the turbine-propeller engine considered is shown in Fig. 2-9. Air enters the inlet duct and passes to the compressor inlet. The air is further compressed in passing through the compressor and enters the combustion chamber where fuel is injected and burned. The products of combustion then pass through the turbine nozzles and blades, where an appreciable drop in pressure occurs, and finally are discharged rearwardly through the exhaust nozzle to provide jet thrust. The turbine shown in Fig. 2-9 may consist of a single turbine driving both the compressor
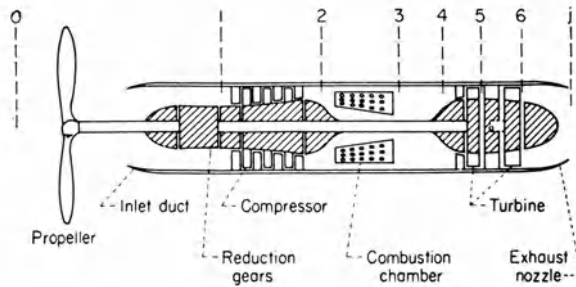
Fig. 2-9 Schematic diagram of turbine-propeller engine. (After B. Pinkel and I. M. Karp, NACA TR 1114).

and the propeller or a combination of two turbines, one driving the compressor and another driving the propeller. When engine performance is evaluated, the combination of the two turbines is considered as a single turbine having the combined power output and over-all turbine efficiency of the two. The total thrust horsepower of the engine is the sum of the jet-thrust horsepower and propeller-thrust horsepower. For the engine operating at a given set of conditions, an optimum division of power between the exhaust jet and the propeller exists for which the total thrust horsepower and efficiency of the system are maximum. The jet velocity for this optimum condition is given very closely by:

$$ V_j = \frac{\eta_N}{\eta_T \, \eta_p \, \eta_m} \; V_o \; . $$

It is to be noted that the jet velocity can vary appreciably from this optimum value with only a small effect on the total thrust horsepower and engine efficiency.

Design point engines. For the purpose of illustrating the manner in which the thrust horsepower per unit mass rate of air flow and specific fuel consumption are influenced by compressor pressure ratio, combustion-chamber-outlet temperature, flight speed, and ambient-air temperature, the following fixed parameters are assumed:

Compressor efficiency η_c	0.85
Turbine efficiency η_T	0.90
Combustion efficiency η_b	0.96
Propeller efficiency η_p	0.85
Exhaust-nozzle efficiency η_N	0.97
Heating value of fuel, h^*, Btu/lb.	18,900
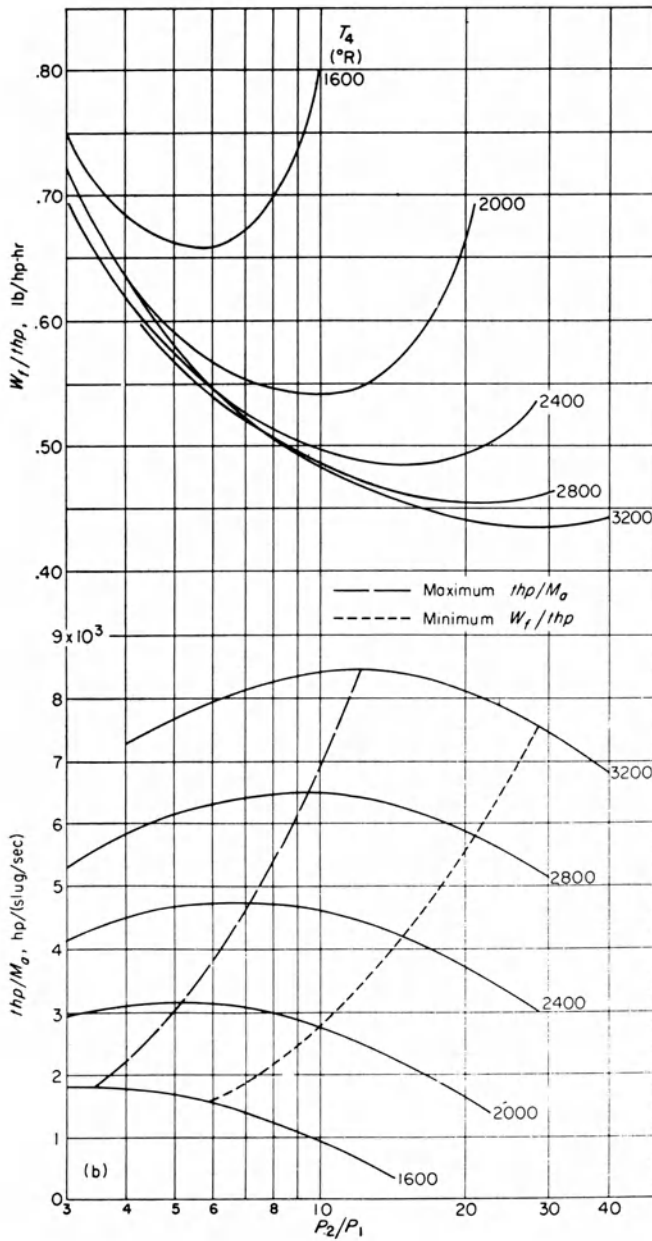
(b) V_o, 733 feet per second; t_o, 519° R; V_i, 902 feet per second; η_p, 0.85.

Fig. 2-10   (After B. Pinkel and I. M. Karp, NACA TR 1114).

The performance of the system is presented in Fig. 2-10. The thrust horsepower per unit mass rate of air flow and the specific fuel consumption are plotted against compressor pressure ratio for various values of combustion-chamber-outlet temperature at several combinations of airplane velocity and ambient-air temperature. The range of turbine inlet temperature T_4 investigated was from 1600° to 3200° R, and the compressor pressure ratios ranged up to 40. Lines for compressor pressure ratios giving maximum thrust horsepower per unit mass rate of air flow and for minimum specific fuel consumption at any temperature T_4 are included in the figure.

The curves of Fig. 2-10 show that with no limitation on compressor pressure ratio, higher THP/M_a and lower specific fuel consumption can be obtained by increasing the T_4. At any given T_4 there is an optimum (P_2/P_1) for maximum thrust (THP/M_a) and an optimum (P_2/P_1) for minimum specific fuel consumption. The compressor pressure ratio for the latter is greater than that required for maximum thrust. (Here M_a = air flow in slugs/sec).

The effects of flight speed and ambient-air temperature on the performance of the turbine-propeller system at a given combustion-chamber-outlet temperature of 1960° R are shown in Fig. 2-11. In Fig. 2-11a, the THP/M_a and fuel consumption are plotted against ambient-air temperatures at V_o of 367 and 733 feet per second for the following cases: (a) compressor pressure ratio chosen to give maximum THP/M_a and (b) compressor pressure ratio chosen to give minimum fuel consumption. At each flight speed, the corresponding optimum jet velocity is used. This figure shows that t_o has an important effect on the performance values: the THP/M_a decreases and the specific fuel consumption increases appreciably as t_o increases.

[2-4.3] Ducted Fan Cycles

The ducted-fan type of turbojet engine represents an attempt to combine the fuel economy of a propeller-type engine with the light weight of the turbojet engine. A ducted-fan turbojet engine may be considered a modification of the turbojet engine which requires the installation of a more powerful turbine to drive a relatively small-diameter multibladed propeller in addition to the normal compressor. All or part of the air (depending on the configuration) that is handled by the propeller, or fan, is passed through a separate duct. Burners are installed in the separate duct to augment the thrust when necessary. These engines are designated ducted-fan engines. A schematic diagram of this type of engine is presented in Fig. 2-12.

For economy operation, the ducted-fan engine is intended to handle a greater mass of air at lower jet velocities (unheated
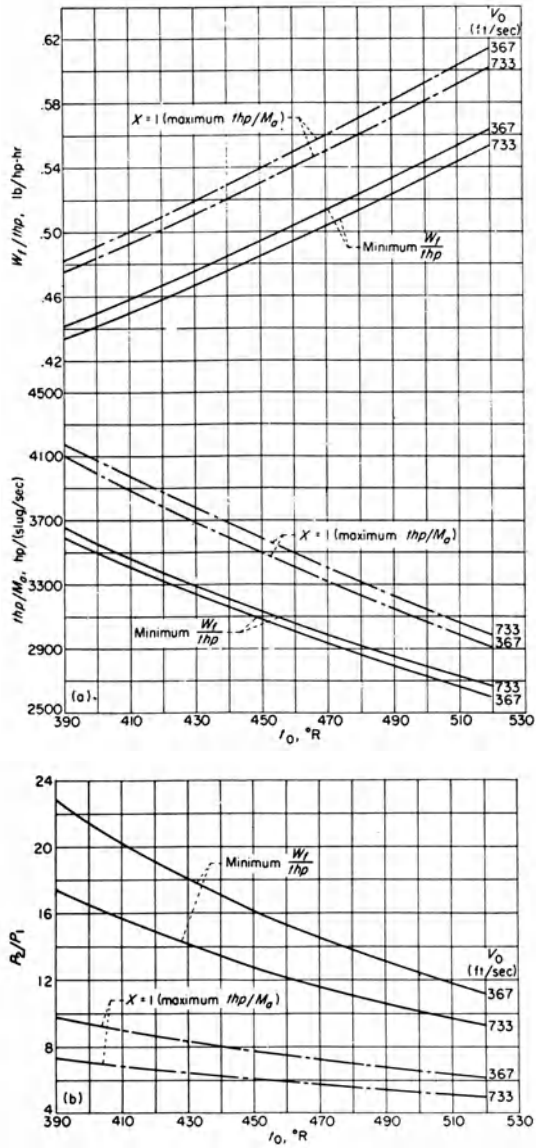
Fig. 2-11   Effects of flight speed and ambient-air temperature on performance at compressor pressure ratios for minimum specific fuel consumption and for maximum thrust horsepower per unit mass rate of air flow; T_4, 1960° R; η_c, 0.85; η_t, 0.90; η_p, 0.85; η_b, 0.96; (a) Specific fuel consumption and thrust horsepower per unit mass rate of air flow. (b) Compressor pressure ratios for minimum W_f/thp and maximum thp/M_a. (After B. Pinkel and I. M. Karp, NACA TR 114).

(a)

(b)
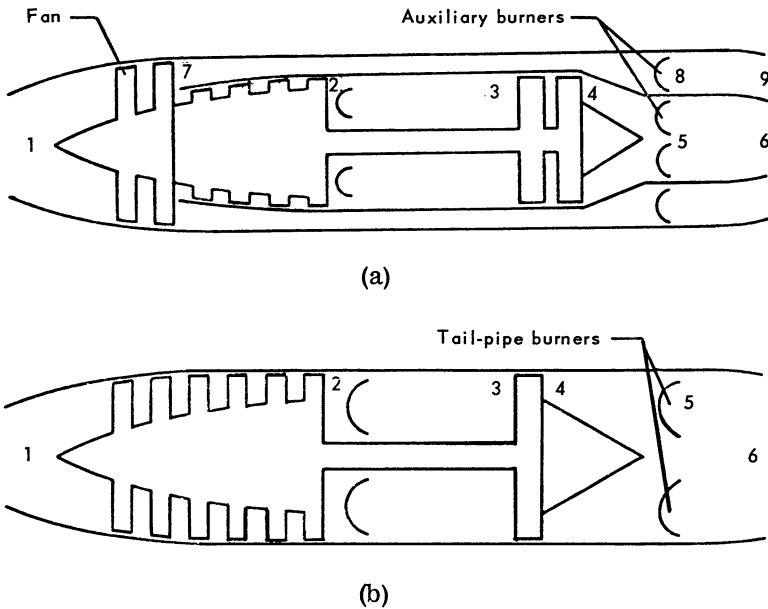
Fig. 2-12 Schematic diagrams of ducted-fan engine (a) and turbojet engine (b), including auxiliary burners. Station: 0 ambient atmosphere; 1 compressor and fan inlet; 2 compressor outlet; 3 turbine inlet; 4 turbine outlet; 5 tail-pipe- and auxiliary-burner inlet; 6 jet nozzle throat; 7 fan outlet; 8 auxiliary-burner inlet (secondary burner); 9 jet-nozzle throat (secondary jet). (After R. B. Parisen, J. C. Armstrong, and S. C. Huntley, NACA TN 1745).

outer-duct air) and hence attain a higher propulsive efficiency than a turbojet engine of equal thrust. The higher propulsive efficiency appears in the form of a lower specific fuel consumption. If the thrust per unit frontal area of the ducted-fan engine were made equal to that of the turbojet engine, it would be necessary to increase the air-handling capacity per unit frontal area of the ducted-fan engine beyond that of the turbojet engine.

Because of the fact that if an increased air flow per unit area were possible for a ducted-fan engine it would also be possible for the turbojet engine, the ducted-fan engine actually has a lower specific fuel consumption and a lower thrust per unit frontal area than a comparable turbojet engine.

Ducted fan engines may be designed for obtaining maximum net thrust per pound of air handled, maximum economy or maximum range. The engines with thrust augmentation by auxiliary burning (simultaneous operation of all auxiliary burners) are used for obtaining maximum thrust; those without auxiliary burning are used for achieving maximum economy or maximum range.

Design point engines. The following assumptions are made:

Compressor efficiency	0.85
Burner efficiency	0.95
Heating value of fuel h^* 18,500 Btu per pound	
Turbine efficiency	0.9
Tail-pipe-burner efficiency	0.9
Nozzle efficiency	0.94
Fan efficiency	0.85

The effect of the ratio of the power to the fan to the available fan power $\emptyset$ and the ratio of secondary air flow to primary air flow W_r on net thrust per pound of air handled by ducted-fan engines with auxiliary burning at a Mach number of 0.3 is illustrated in Fig. 2-13. The corresponding change in net-thrust specific fuel consumption is also shown. The curve indicates that the maximum net thrust per pound of air handled is obtained by reducing $\emptyset$ and W_r to zero. The ducted-fan engine with auxiliary burning therefore evolves into a turbojet engine with tail-pipe burning. A calculation of maximum net thrust per pound of air handled at a flight Mach number of 0.9 gave similar results. It can also be seen (Fig. 2-13) that ducted-fan engines with auxiliary burning not only develop a lower net thrust per pound of air handled but show an increase in net-thrust specific fuel consumption as compared to a turbojet engine with tail-pipe burning. The optimum compressor pressure ratio for maximum thrust of the ducted-fan engine with auxiliary burning is about the same as that of the turbojet engine with tail-pipe burning.

The approximate compressor pressure ratio for obtaining maximum net thrust per pound of air handled is plotted in Fig. 2-14 against the Mach number for turbojet engines with tail-pipe burning. The decrease of compressor pressure ratio with flight speed is such that the product of compressor pressure ratio and ram pressure ratio is approximately constant over the speed range. This constancy is coincidental inasmuch as the compressor pressure ratio decreases with Mach number for the condition of maximum thrust as a result of the decreasing ratio of turbine-inlet to compressor-inlet temperatures. The compressor pressure ratios shown in Fig. 2-14 tend to produce the maximum propulsive jet velocity.

The variation of minimum obtainable net-thrust specific fuel consumption and corresponding net thrust per pound of air handled with flight Mach number is shown in Fig. 2-15 for ducted-fan and turbojet engines. Values of net-thrust specific fuel consumption are also shown for the turbine-propeller engine but are not necessarily minimums because the engine is of constant pressure ratio. These values do, however, demonstrate the capacity of the turbine propeller engine to operate at substantially lower values of net thrust specific fuel consumption below a flight Mach number of approximately 0.85 than ducted-fan and turbojet enginer.
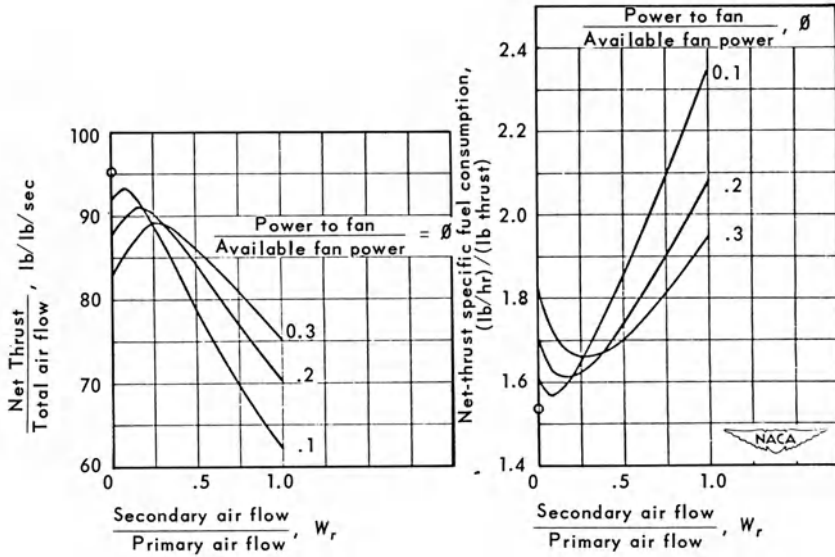
Fig. 2-13 Effect of varying ratio of secondary air flow to primary air flow and ratio of power to fan to available fan power with net thrust per pound of air and net-thrust specific fuel consumption for ducted-fan engines with auxiliary burning. Mach number, 0.3; altitude, 30,000 feet. o Turbojet with tail-pipe burning (maximum thrust). —— Ducted fan with auxiliary burning. (After Parisen, Armstrong, Huntley, NACA TN1745).
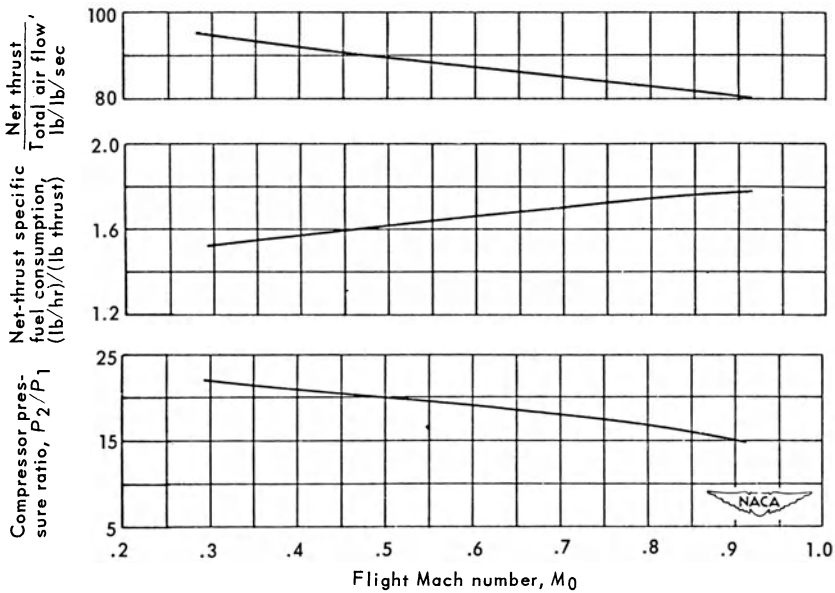
Fig. 2-14 Net thrust per pound of air, net-thrust specific fuel consumption, and compressor pressure ratio for maximum-thrust turbojet engines with tail-pipe burning (optimum configuration of ducted-fan engine with auxiliary burning) at various flight Mach numbers, Altitude, 30,000 feet. (After Parisen, Armstrong, and Huntley, NACA TN 1745).
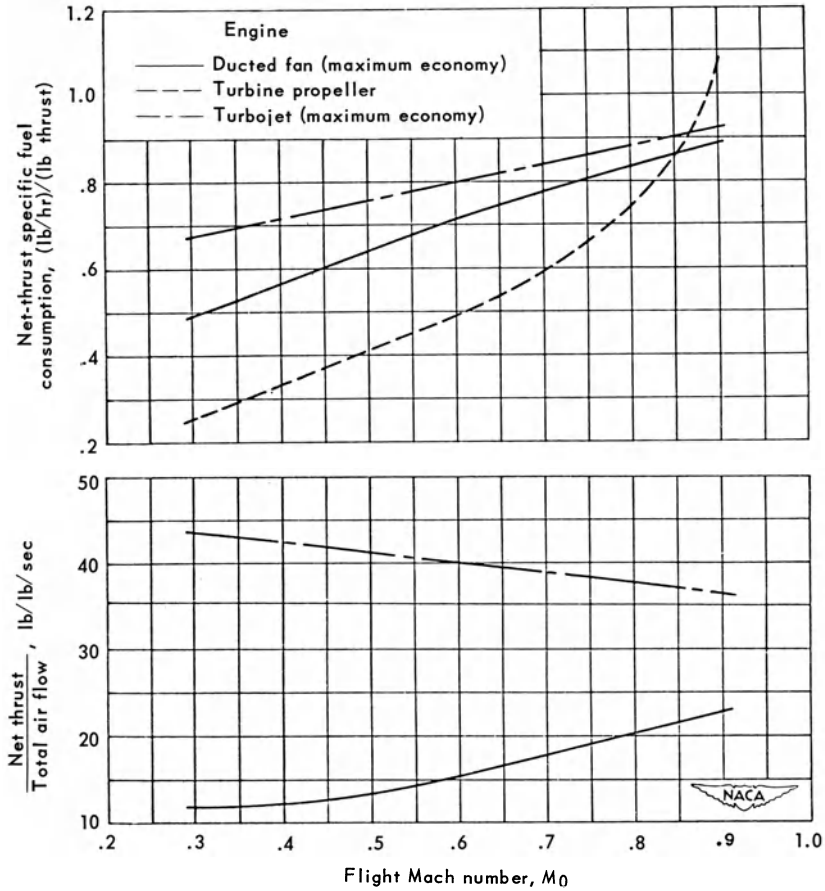
Fig. 2-15   Net thrust per pound of air and net-thrust specific fuel consumption for maximum-economy ducted-fan and turbojet engines at various flight Mach numbers. (Net-thrust specific fuel consumption also shown for turbine-propeller engine.) Altitude, 30,000 feet. (After Parisen, Armstrong, and Huntley, NACA TN 1745).

At a Mach number of 0.3, the net-thrust specific fuel consumption of a ducted-fan engine is about 27% lower than that of a turbojet engine. This difference diminishes to approximately 4% at a Mach number of 0.9. The low net-thrust specific fuel consumption is accompanied, however, by low values of net thrust per pound of air. These values are only 27 to 64% (depending on the flight Mach number) of the net thrust per pound of air produced by turbojet engines. A plot of the net thrust per pound of air handled by the turbine-propeller engine is omitted because of lack of a comparable basis of presentation.

The values of fan pressure ratio P_7/P_1, $\emptyset$ and W_r required to obtain minimum net-thrust specific fuel consumption over the range of Mach numbers considered are presented in Fig. 2-16. The fan pressure ratio increases with increasing Mach number, whereas both the power input to the fan and the secondary air flow decrease with increasing Mach number. The increasing fan pressure ratio is the result of the secondary air flow decreasing at a greater rate than the fan power input. The approximate compressor pressure ratios necessary to provide minimum obtainable net-thrust specific fuel consumption are also shown in Fig. 2-16 for ducted-fan and turbojet engines for the range of flight Mach numbers considered.
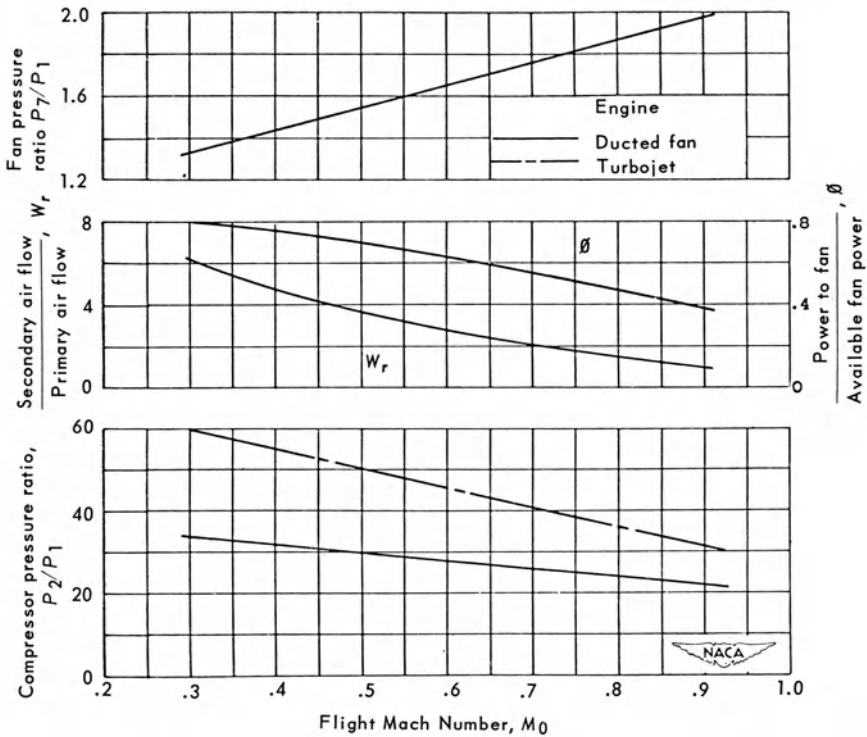
Fig. 2-16   Approximate variation with flight Mach number of fan pressure ratio, ratio of power to fan to available fan power, ratio of secondary air flow to primary air flow, and compressor pressure ratio necessary to permit ducted-fan engines to operate with maximum economy. (Required compressor pressure ratios also shown for turbojet engine operating at maximum economy.)   Altitude, 30,000 feet. (After Parisen, Armstrong, and Huntley, NACA TN 1745).

The convergence of the curves of Figs. 2-15 and 2-16 indicate the conversion of the ducted-fan engine into a turbojet engine at a

flight Mach number greater than 0.9. A separate calculation locates the end point of this trend at a flight Mach number of approximately 1.2.

In order to determine the applications of various airplane–engine configurations, it is necessary to know the values of three important engine parameters: specific fuel consumption sfc, jet thrust F_j, and engine weight W_e.

A low specific fuel consumption turbojet engine requires a high compressor pressure ratio, or greater engine weight, and produces a low thrust per pound of air, which results in an extremely high specific engine weight W_e/F_j.

A maximum–thrust type turbojet engine, although possessing a low specific engine weight, is unable to operate at a sufficiently low value of specific fuel consumption. A compromise is therefore necessary.

One of the anticipated advantages of a ducted–fan engine is a low specific weight relative to turbojet engines. If ducted–fan engines are compared to turbojet engines of equal air–handling capacity per unit frontal area, however, a lower specific weight will not be indicated.

If flight speeds do not exceed a flight Mach number of approximately 0.6, the turbine–propeller engine should offer the most favorable performance. If, however, higher flight Mach numbers are desired, the turbojet engine with tail–pipe burner (operating for maximum thrust and non–operative for achieving greater range) should provide the greatest flexibility.

[2- 4.4] Off-Design Point Engines

Sections 2–4.1, 2–4.2, and 2–4.3 discussed design point (at design altitude and design airplane speed) turbojet, turboprop, and ducted–fan engines. Engines operating at off–design point will result in different compressor compression ratios and different engine–air flows. In order to calculate engine performance at off–design point, the determination of compressor compression ratio and engine air flow of turbojet, turboprop, and ducted–fan are important. The variation of compressor compression ratio and engine air flow with altitude and airplane speed (really variation with compressor inlet temperature) are functions of compressor–turbine design and nozzle characteristics. However, without knowing specific compressor–turbine and nozzle characteristics, a generalized compressor compression ratio and engine air flow variation with altitude and air speed (really variation with compressor inlet temperature) are given here. These variations are calculated according to the following semi–empirical derivations. Such variations have been checked with many actual turbojet, turboprop, and ducted–fan engines and were found to be very

satisfactory, providing the nozzle does not limit the compressor operation. The error introduced without knowing a specific compressor is usually within a few percent.

[2-4.4.1] Compression Ratio Variation with Altitude and Air Speed (Variation with Compressor Inlet Temperature) at Constant Compressor Speed

From Eq. (3-8) of Chapter 3, we have

$$\left(\frac{P_2}{P_1}\right)_{T_a} = (C.R.)_{T_a} = \left[1 + \frac{u\omega r}{c_p \overline{T}_a Jg}\right]^{\frac{k}{k-1}} .$$

Since $u\omega r$ is the same under different inlet temperatures, we have

$$\left(\frac{P_2}{P_1}\right)_{T_b} = (C.R.)_{T_b} = \left\{1 + \frac{\left[(C.R.)_{T_a}^{\frac{k-1}{k}} - 1\right]}{\left(\dfrac{\overline{T}_b}{\overline{T}_a}\right)}\right\}^{\frac{k}{k-1}}$$

From compressor efficiency Eq. (1-164) and compressor exit temperature, Eq. (1-166), we have

$$\overline{T}_a = \frac{T_{1_a} + T_{2_a}}{2} = T_{1_a}\left\{1 + \frac{1}{2\eta_c}\left[(C.R.)_{T_a}^{\frac{k-1}{k}} - 1\right]\right\}$$

and

$$\overline{T}_b = \frac{T_{1_b} + T_{2_b}}{2} = T_{1_b}\left\{1 + \frac{1}{2\eta_c}\left[(C.R.)_{T_b}^{\frac{k-1}{k}} - 1\right]\right\} .$$

Here we assume that the compressor efficiency variation due to compressor inlet temperature is small in comparison with

compression ratio variation. *C.R.* = compression ratio. For the meaning of u, ωr, c_p, J and g, see symbols of Chapter 3. P_1 and P_2, T_1 and T_2 are compressor inlet and exit stagnation pressure and temperature, respectively. Subscripts a and b indicate the compressor operating at compressor inlet temperature a and b, respectively (under two different inlet temperatures).

Substituting T_a and T_b expressions into $(P_2/P_1)_{T_b}$, we have

$$(C.R.)_{T_b} = \left\{ 1 + \frac{\left[(C.R.)_{T_a}^{\frac{k-1}{k}} - 1 \right] T_{1_a} \left\{ 1 + \frac{1}{2\eta_c} \left[(C.R.)_{T_a}^{\frac{k-1}{k}} - 1 \right] \right\}}{T_{1_b} \left\{ 1 + \frac{1}{2\eta_c} \left[(C.R.)_{T_b}^{\frac{k-1}{k}} - 1 \right] \right\}} \right\}^{\frac{k}{k-1}}$$

This is the variation of compression ratio with compressor inlet temperature which is plotted as Fig. 2-17 for convenient use.

[2-4.4.2] Air Flow Variation with Altitude and Airplane Speed at Constant Compressor Speed

Without a specific compressor, the following approximation may be made. The compressor operating at different altitude and different airplane speed results approximately in a constant volume flow into the compressor when the compressor rotational speed is maintained the same. This means that the axial velocity of the air flow into the compressor is the same at two different inlet temperature conditions. Use this assumption, the air flow variation with altitude and speed are plotted in Fig. 2-18. Such variations have been checked with many turbojet, turboprop, and ducted-fan engines and were found to be satisfactory. The error introduced (without knowing a specific compressor) is usually within a few percent.

Once the compression ratio and engine air flow variation with altitude and airplane speed are known, the cycle analysis (based on one pound air flow per second) may be performed. Consequently, the engine performance under different altitude and airplane speeds can be calculated (off-design point engine performance), and complete engine performance may be estimated approximately for all altitude and airplane speeds (for a fixed design point engine).
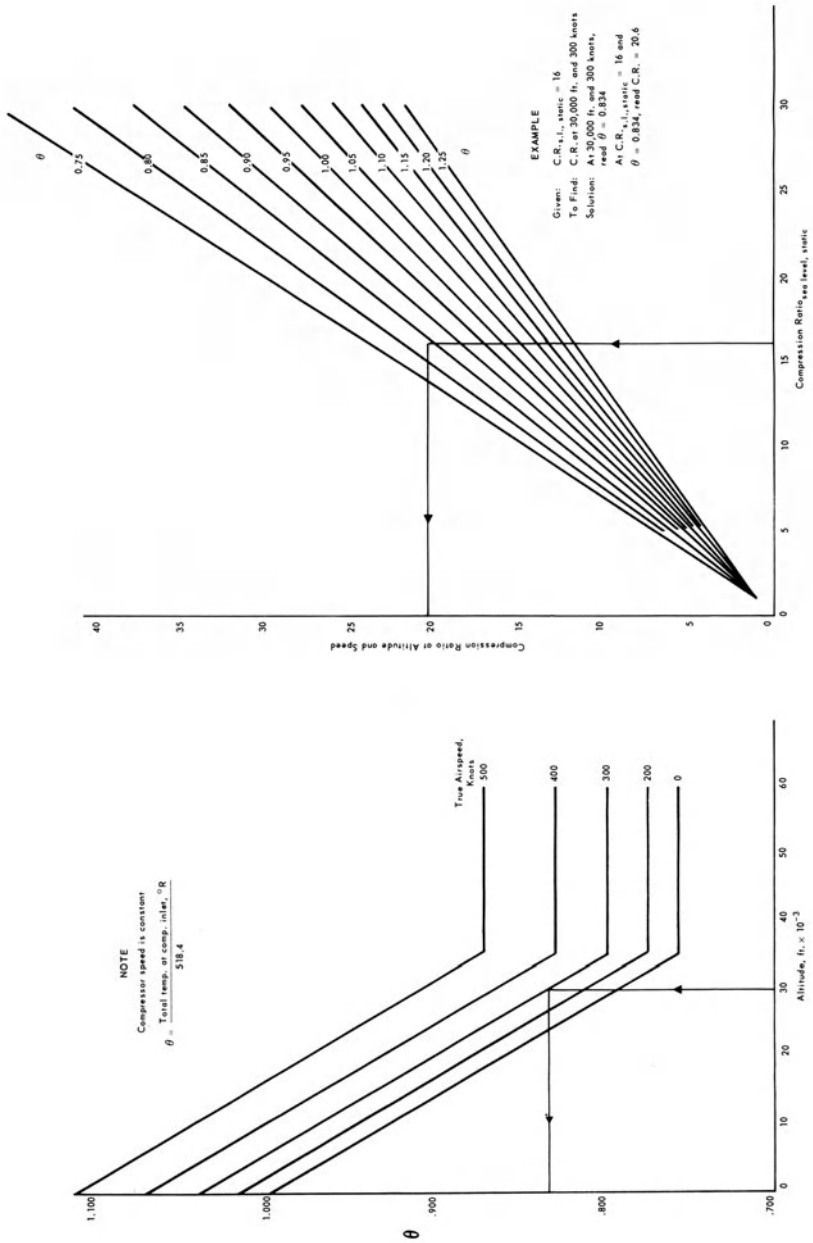
Fig. 2-17 Generalized chart, variation of compressor compression ratio with altitude and speed, NACA Day.
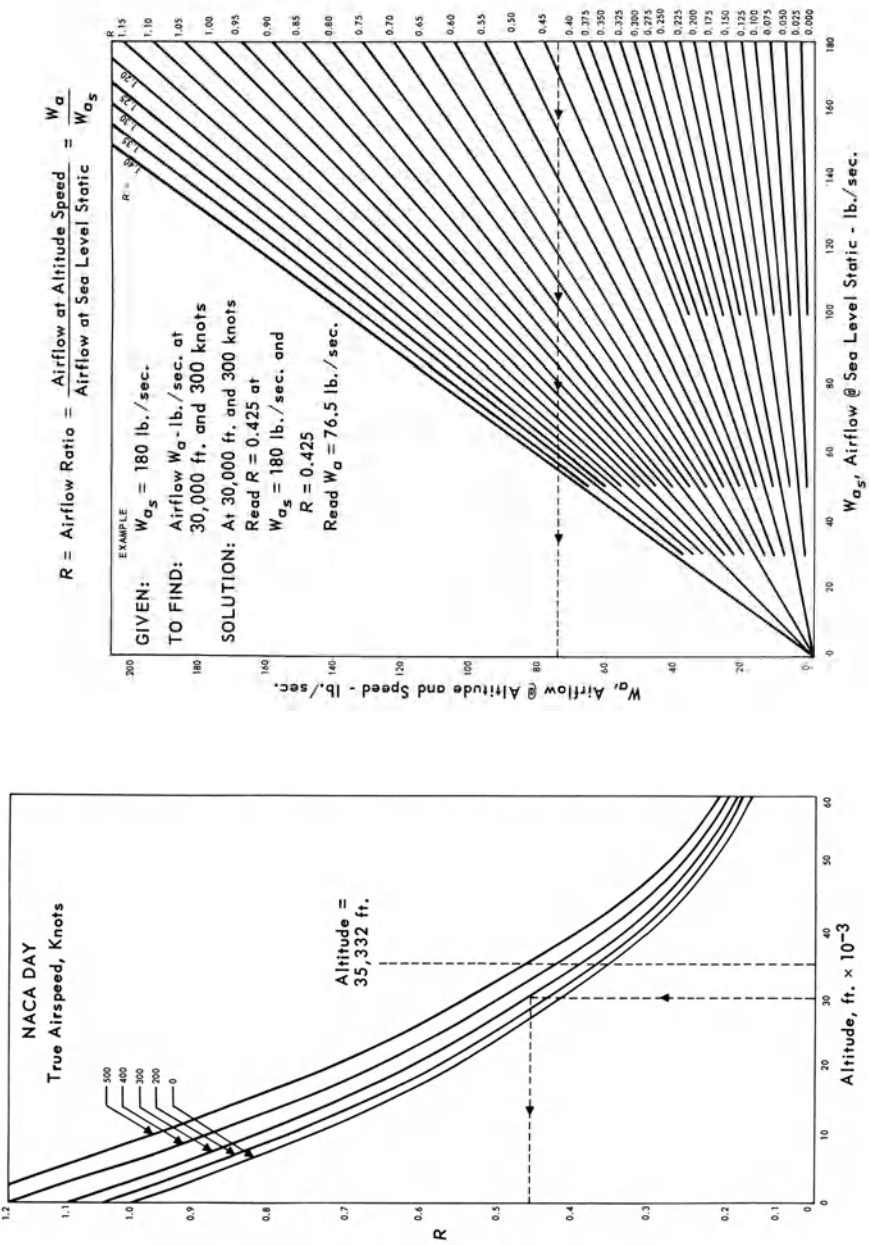
Fig. 2-18 Generalized chart, approximate variation of airflow with altitude and speed (at constant engine speed).

[2-5] ROTARY MATRIX REGENERATOR FOR TURBOPROP APPLICATIONS

In addition to the conventional regenerator (plate-fin type), a unique regenerator suitable for turboprop adoption because of its weight and size advantages is described below. This regenerator is the Loh Rotary Matrix Regenerator. Performance of this regenerator, based on quantitative analysis, has been compared with conventional heat exchangers.

Development of this unit as a regenerator for gas turbine power plants would remove one of the big obstacles in the optimum utilization of the turbo-propeller engine by improving operating efficiency. This achievement would thus provide additional incentive for the application of turbo-powered aircraft transports.

By virtue of it's compatible configuration, the regenerator may be incorporated directly into the engine, either in one unit or as several smaller units. It possesses the unique features of light core weight and small core volume plus the inherent feature of compatible configuration, a design principle important in the field of gas turbine regeneration.

[2-5.1] Discussion

The function of a regenerator is to transfer heat from one fluid stream to another and thus preheat the air entering the combustion chamber. Past efforts have been directed toward heat transfer through tubes or similar channels accomplished by directing one fluid inside and the other around the outside of the channels. Compactness is gained by increasing the ratio of heat transfer surface to overall volume. This is usually accomplished by a reduction in the size of flow passages or the addition of surface irregularities to produce turbulence. It is thus apparent that achievement of compactness eventually reaches the point of diminishing returns from mounting pressure loss. Additional compactness must then evolve from some new concept for a heat transfer media. The Loh Rapid Transfer Heat Exchanger is based on a different concept not subject to the pressure loss limitations inherent in the use of conventional design criteria. Heat transfer is effected by a moving heat conveyor heated in the hot stream and cooled in the cold stream. This effect is accomplished by rotating a screened disc or cone matrix through the two fluid streams. Quantitative analysis shows exceptionally high heat transfer capacity at very low pressure loss. Massiveness and weight penalties imposed by conventional tubular or corrugated fin plate surface construction are thus avoided.

To determine the significance of the Loh Heat Regenerator as applied to the gas turbine, a comparative study of a regenerator unit for a 10,000 shaft horsepower gas turbine engine was made.

A regenerator is employed to increase cycle efficiency by extract-
ing heat from exhaust gas and transferring such heat to the intake
air stream, thus heat-changing or preheating this air prior to its
entrance into the combustion chamber. The most advanced con-
ventional regenerative heat exchanger, developed by London and
Kays, was selected for comparison. Table 2-1 shows the results of
this comparison, although to date no such unit has been success-
fully applied as an airborne regenerator because of the prohibitive
size, weight and shape dictated by the design criteria developed.

Table 2-1

	Core Volume	Core Weight
	(ft.^{3}/1000 SHP)	(lbs./1000 SHP)
Existing most-compact plate-louvered fin surface heat exchanger	9.1	861
Loh rotating wire screen heat exchanger	0.51	45.3

All figures are for heat transfer surfaces only and therefore are
exclusive of shell, headers, and other accessories.

Of compelling interest is the effect of the regenerator cycle on
fuel consumption. For example, a 10,000 s.h.p. turbine-propeller
engine requires approximately 0.48 pound of fuel per brake horse-
power per hour, whereas the same engine equipped with a regen-
erator of 72% effectiveness requires only 0.35 pound of fuel per
brake horsepower hour, a reduction of over 25% in fuel consumption.

Figure 2-19 shows the principal parts of the Loh Heat Exchanger.
The upper sketch shows one type of construction utilizing a disc
to contain the screen wire elements. The disc is rotated either by
airflow acting against curved sides of the screen compartments or
by the application of external power. The entrance and exit ducts
are divided into two passages to accommodate the hot and cold
streams. Alternate heating and cooling of the wire screen con-
stitutes the means of heat transfer. Separation of the two streams
at the two faces of the screen disc is achieved by dividing the screen
disc into pie-shaped segments and making the separating partition
of the ducts equal to or slightly larger than the screen segments.
Consequently, when a screen segment passes from one stream to
the other, the flow of gas is blocked. A minute amount of gas will
be trapped in the screen segment and carried to the opposing
stream. However, calculations show that this constitutes a very
small percentage of the total flow.

When the number of layers of screen results in prohibitive
pressure loss, increased heat transfer capacity may be obtained
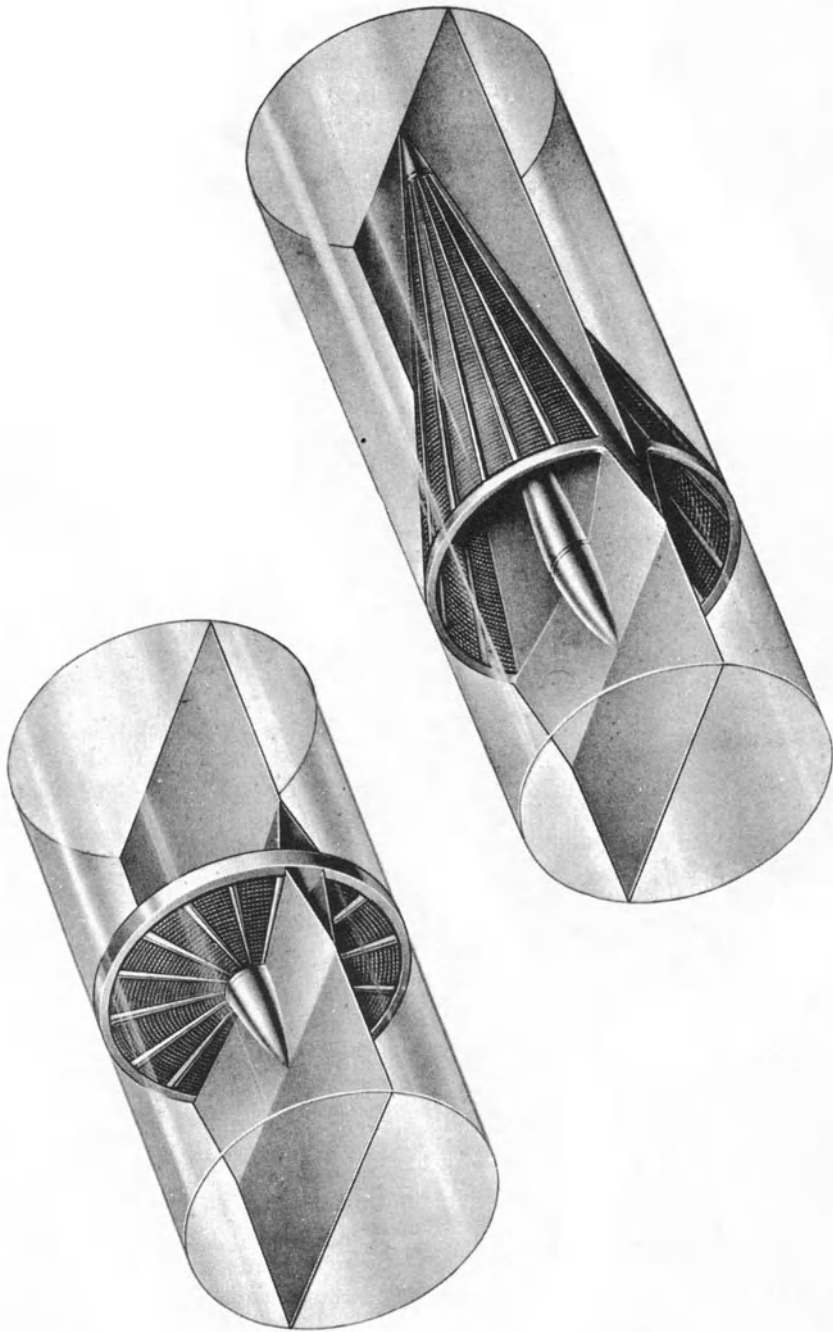
Fig. 2-19   The Loh Heat Exchanger.   (Top) Cylindrical; (Bottom) Conical.

by substituting a rotating cone for a disc. This design, while less compact than the disc design, is still far superior to the more advanced conventional designs.

The adaptability of this type of heat exchanger to the gas turbine engine as a regenerator is easily visualized. Three factors, all of which are influential in aricraft design, make this unit attractive. These are: (1) light core weight, (2) small core volume, and (3) shape adaptability (circular). The application of the gas turbine engine is perhaps most ideal in aircraft use. Other applications may be used to replace conventional heat exchangers in many instances, but the advantages appear primarily at high heat loads and high temperatures. It is conceivable that a rather large saving in-weight of a small unit might not be worthwhile.

[2-5.2] Operating Principles

In the case of the conventional heat exchanger, heat is transferred through the walls separating the two fluids. Various means are adopted for increasing the effectiveness of these units, such as the introduction of turbulence and the use of fins. According to most textbooks, heat flow takes place largely through convection, since conduction through the metal walls has such a small effect. Heat exchanger size is governed, for illustration purposes, by the following combination of variables: $Q/\Delta T_m = UA$.

Where:

Q = Amount of heat being transferred, Btu/sec.
ΔT_m = Log mean temperature difference between hot and cold fluids, degrees R
U = Overall heat transfer coefficient, $Btu/\text{sec.}/\text{ft.}^2/°R$
A = Heat transfer surface area, sq. ft.

Equations such as this state that the amount of heat being transferred per unit time per unit temperature difference is equal to the product of the heat transfer coefficient and the surface area. This means that if the value of A is increased, for the same temperature differential, the rate of heat transfer will also be increased. To survey the factors controlling A with regard to volume, or area to volume ratio, examine the geometry of a tube:

$$\text{Surface Area} = \pi dl$$

$$\text{Volume} = \frac{\pi d^2 l}{4}$$

$$\frac{A}{V} = \frac{\pi dl}{\frac{\pi}{4} d^2 l} = \frac{4}{d}$$

$$b = 1.0 \quad \frac{W_h}{W_c} = 1.0$$

$$\eta_s = \frac{1}{\beta} \sum_1^\infty \frac{\frac{1}{\zeta\beta}}{1 + \left(\frac{n}{\zeta\beta}\right)^2}$$

$$n = 1, 3, 5, 7, 9 \dots$$

When β very small $\eta_s = 1.1838\zeta$

$$b = 1.0 \quad \frac{W_h}{W_c} = 1.0$$

$$\frac{\Delta T_w}{T_h - T_c} = \frac{T_{w\pi} - T_{w0}}{T_h - T_c} = \frac{4}{\pi} \sum_1^\infty \frac{\left(\frac{1}{\zeta\beta}\right)}{1 + \left(\frac{n}{\zeta\beta}\right)^2}$$

$$n = 1, 3, 5, 7, 9 \dots$$

Fig. 2-20

COUNTER FLOW

NO. OF SCREENS IN PARALLEL

$$\eta_1 = \eta_s$$

$$\eta_2 = \eta_1 \left(\frac{1-\eta_s}{1-\eta_s\eta_1} \right) + \eta_s \left(\frac{1-\eta_1}{1-\eta_s\eta_1} \right)$$

$$\eta_3 = \eta_2 \left(\frac{1-\eta_s}{1-\eta_s\eta_2} \right) + \eta_s \left(\frac{1-\eta_2}{1-\eta_s\eta_2} \right)$$

$$\eta_4 = \eta_3 \left(\frac{1-\eta_s}{1-\eta_s\eta_3} \right) + \eta_s \left(\frac{1-\eta_3}{1-\eta_s\eta_3} \right)$$

$$\eta_5 = \eta_4 \left(\frac{1-\eta_s}{1-\eta_s\eta_4} \right) + \eta_s \left(\frac{1-\eta_4}{1-\eta_s\eta_4} \right)$$

$$\eta_n = \eta_{n-1} \left(\frac{1-\eta_s}{1-\eta_s\eta_{n-1}} \right) + \eta_s \left(\frac{1-\eta_{n-1}}{1-\eta_s\eta_{n-1}} \right)$$

Here $\eta_1, \eta_2, \eta_3, \ldots \eta_n$ = Overall effectiveness of 1, 2, 3, ... n screens all together.

η_s = single screen effectiveness of each individual screen.

η η_s
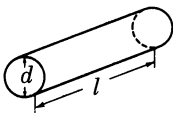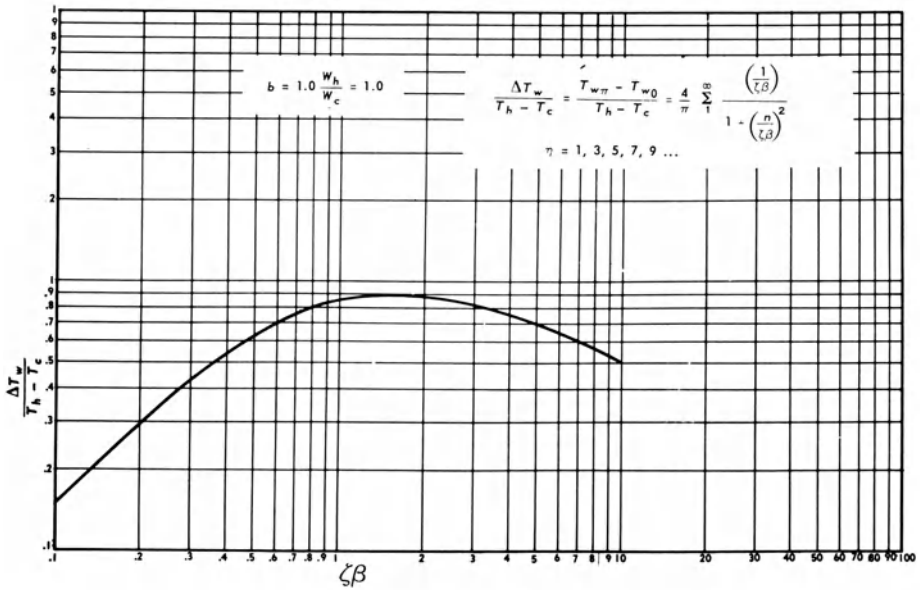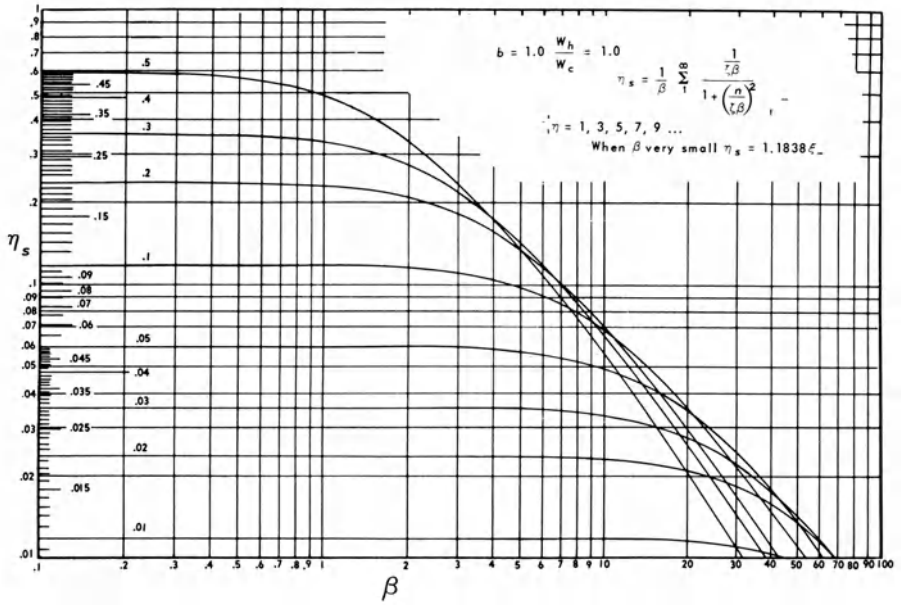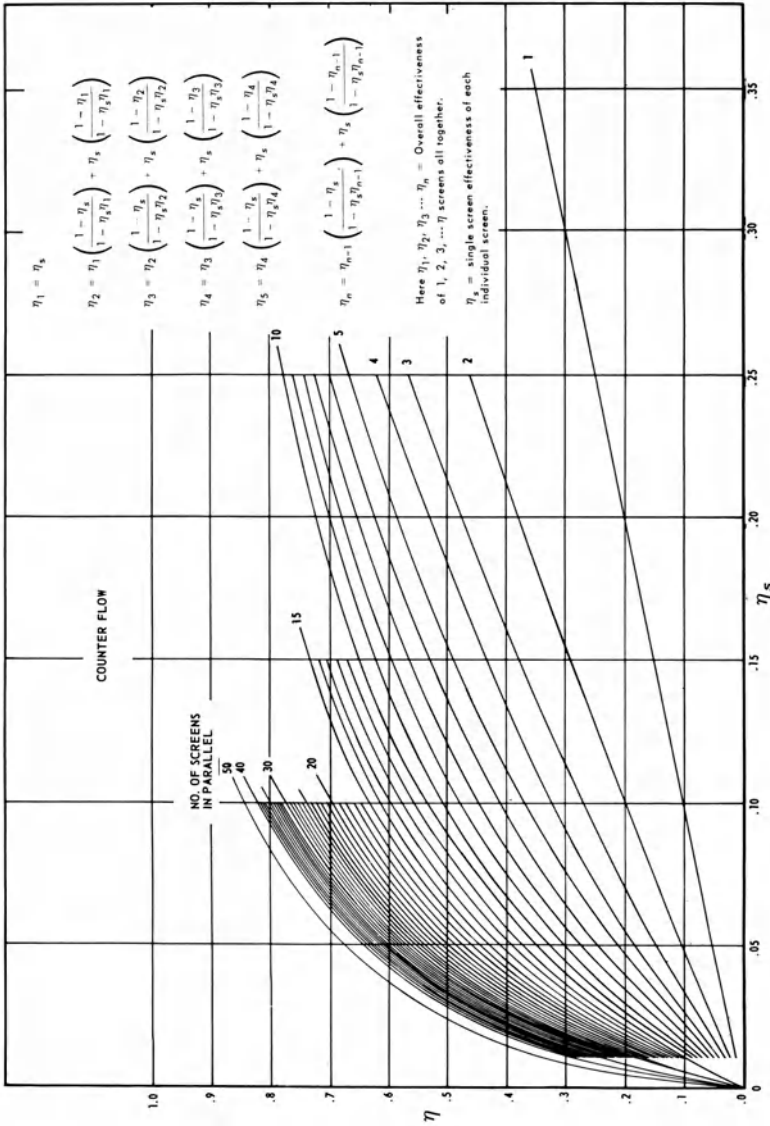
Fig. 2-21

This shows that as the diameter decreases, the surface to volume ratio increases. (Similar equations may be written for other flow passages by substituting the term equivalent diameter or hydraulic diameter for the tube diameter.) This equation harbors a very important, though not readily perceived, factor, *i.e.,* what happens when the tube diameter is decreased? Increased pressure drop occurs which ultimately reaches a point of diminishing returns, thus prohibiting further gains in this direction.

The second variable U is defined in the following manner:

$$\frac{1}{U} = \frac{1}{h_1} + \frac{1}{h_2} + \frac{x}{k}$$

Where:

$1/U$ = The total resistance to heat transfer
$1/h_1$ = Film resistance on the tube inside
$1/h_2$ = Film resistance on the tube outside
$1/k$ = Resistance due to thermal conductivity of the tube wall
      (usually this term is so small that it may be neglected.)
   x = Wall thickness of conductor

For the conventional heat exchanger, U may be increased by promoting turbulence or by reducing the hydraulic diameter. The scrubbing action of the fluid during turbulent flow reduces the boundary layer resistance $(1/h)$. Reductions in hydraulic diameter result in reduced Reynolds number and high heat transfer, other factors remaining constant. But note that both of these factors also increase pressure loss, and again compactness is gained only at the expense of pressure loss.

Therefore, something new must be added. The Loh regenerator does this. In this design, the hydraulic diameter, which controls both area-to-volume ratio and Reynolds number, may be further reduced without prohibitive pressure losses. Whereas tube diameters must be maintained fairly large to accommodate flow inside, wire diameters can be reduced to values in the range of .01 inch or smaller without the same flow restrictions, because both the hot and cold stream flow is external. The value of U is further increased by virtue of the fact that $1/U$ is no longer equal to the sum $1/h_1$ and $1/h_2$ but equal to $1/h_1$ alone while the screen is in one stream. Consider, as an illustration, h_1 and h_2 both being equal to 2. In the conventional heat exchanger, U would be equal to 1 because $1/U = 1/2 + 1/2$ or $1/U = 1$; $U = 1$; whereas, in the new design, $1/U = 1/2$ or $U = 2$. Because of these factors, the product of UA may be increased 20 to 30 times per unit core volume for the same pressure loss as a conventional heat exchanger or, in terms of size and weight, 1/20 to 1/30 of that of the most compact conventional heat exchanger known. (Wire dia/Tube dia $\leqslant$.1 or .05).

[2-5.3] Theory and Design

Based on an analytical study (see Sec. 2-6), the performance of a rotating wire screen heat exchanger, when applied as a gas turbine regenerator, is a function of only two non-dimensional parameters. These are speed-wire property parameter β and heat transfer geometry parameter ζ.

$$\beta = \frac{1}{2}\left(\frac{\rho c_p}{\rho_w c_{p_w}}\right)\frac{s}{d}\left(\frac{V_a}{Nd}\right)\left(\frac{1 - \dfrac{m\alpha}{2\pi}}{m}\right)$$

$$\zeta = \frac{8}{\pi}\left(\frac{h}{G_{\max} c_p}\right)\left[\frac{\left(\dfrac{d}{s}\right)}{\left(1 - \dfrac{d}{s}\right)^2}\right]$$

and

ρ = density of gas in lbs./ft.^{3}
ρ_w = density of wire material in lbs./ft.^{3}
c_p = specific heat of gas in Btu/lb. °R
c_{p_w} = specific heat of wire material in Btu/lb. °R
V_a = axial velocity of gas in ft./sec.
N = revolutions of rotating wire screen rotor per second
d = wire diameter in feet or inches
s = transverse pitch between wire in feet or inches
m = total number of hot and cold sections in duct
α = angle in degrees or radians which prevents mixing of hot and cold gases during passage through rotating wire screen rotor
h = heat transfer film coefficient between gas and wire in Btu/sec. ft.^{2} °R
$G_{\max}$ = maximum mass flow velocity per unit area in lbs./sec.ft.^{2}
ΔT_w = wire temperature rise in °R during passage of the wire through the hot section
T_h = total temperature of hot gas in °R
T_c = total temperature of cold gas in °R
η_s = temperature effectiveness of each individual wire screen
η = overall temperature effectiveness of rotating wire screen heat exchanger

For detailed design procedures, see Section 2-6.

[2-6] ANALYTICAL SOLUTIONS FOR ROTARY MATRIX, WIRE SCREEN HEAT EXCHANGERS

The rotary matrix heat exchanger, developed in early 1922, embodies a moving heat conveyor heated in the hot stream and cooled in the cold stream. Heat is thus transferred by rotating the conveyor through the two streams. The heat conveyor originally proposed was a rotary matrix made of plain metal plate surfaces. Improvements in heat transfer were effected through the use of corrugated plate-fin-type surfaces. Further improvements may be obtained by using multi-layer individual wire screen as the conveyor. This was conceived by Loh.

Analytical studies relating to rotating heat exchangers have been made by Nussett, Hausen, Boestad, Saunders and many others.
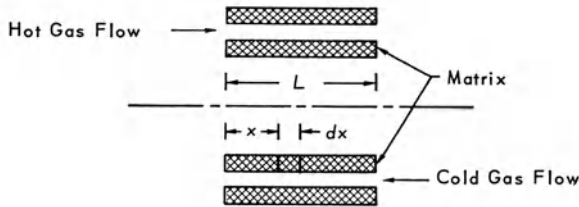
Fig. 2-22   Flow passage length for generalized rotary matrix.

However, these authors have concentrated on the solution of the partial differential equation which was derived primarily for the generalized rotary matrix along the lines of the original proposed arrangements. This type of arrangement has a flow passage length (L) as shown in Fig. 2-22.

It can be seen that the temperature (T) is a function of both time (t) and space (x), and that the only equation describing this type of matrix is partial differential equation

$$WC_p \frac{\partial T}{\partial x} + \rho A_f C_p \frac{\partial T}{\partial t} = -\frac{M_r C_{pr}}{L} \frac{\partial T_r}{\partial t} = -\frac{hA}{L}(T - T_r).$$

Because of mathematical complexities, solutions were generally obtained either by graphical or numerical methods, since no analytical closed form solution has been found. The present analysis takes a different approach. This approach, primarily for multi-layer rotary matrix, starts with a single screen (see Fig. 2-23).

It can be seen that the temperature (T) is a function of time (t) only. Therefore, an ordinary differential equation was developed, resulting in an exact and closed form solution. The multi-layer screen system was then developed by an energy balance of each
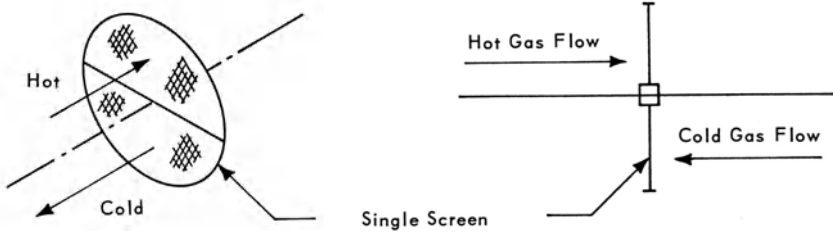
Fig. 2-23 Flow passage length for single screen $= L \cong 0$.

individual single screen. Since this approach led to a closed form analytical solution for the rotating multilayer wire screen heat exchanger, it was then possible to develop design charts for this type of heat exchangers.

Assumptions

1. Gas and material properties such as ρ, C_p, k, μ, P_r, etc. are treated as constants.

2. Heat transfer through conduction and radiation is small compared with heat transfer through convection; conduction and radiation heat transfer is, therefore, neglected.

3. Variations in the gas temperature ahead of each individual screen are small when compared with the gas temperature itself, hence the gas temperature ahead of each screen is treated as uniform, as is the gas temperature after each screen.

4. The size of wire is so small that it may be treated as a point for gas flow across it.

Analysis

Equal Mass Flow for Hot and Cold Streams

Equal mass flow in equal cross-sectional areas results in equal values of G, and consequently, equal values of h in both hot and cold streams.

1. Wire Temperature vs. Time

For a cross-wire screen element as shown in Fig. 2-24, the energy equation gives

$$\frac{dT_w}{dt} + \left(\frac{4h}{\rho_w C_{p_w} d}\right) T_w = \left(\frac{4h}{\rho_w C_{p_w} d}\right) T. \qquad (2\text{-}5)$$
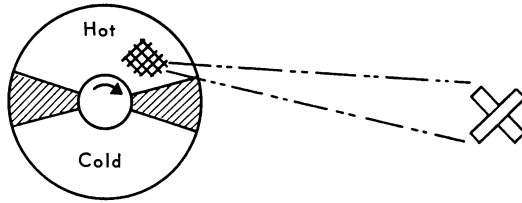
Fig. 2-24 Cross-wire screen element.

As the wire element rotates from hot stream to cold stream, the surrounding gas temperature (T), shown in Fig. 2-25, can be expressed by the Fourier series

$$T = \sum_{t=\text{odd}}^{\infty} \frac{2}{\pi} \left(\frac{T_h - T_c}{n} \right) \sin n\omega t + \left(\frac{T_h + T_c}{2} \right). \qquad (2\text{-}6)$$

Solving Eqs. (2-5) and (2-6) gives

$$T_w = \left\{ T_{w_i} - b_0 + \sum_{n=\text{odd}}^{\infty} a_n \left[\frac{(n\omega/c)}{1 + (n\omega/c)^2} \right] \right\} e^{-ct}$$

$$+ \left\{ b_0 + \sum_{n=\text{odd}}^{\infty} a_n \left[\frac{1}{\sqrt{1 + (n\omega/c)^2}} \right] \sin (n\omega t - \phi_n) \right\}.$$

$$(2\text{-}7)$$

Equation (2-7) describes the complete time history of the wire temperature from the very start to steady state cyclic operations. Since the transient portion becomes negligibly small after an elapsed time approximately equal to $(3/c)$ seconds from the very start of the operation, only the steady state portion of the complete solution is really needed. This steady state solution in non-dimensional form is

$$\frac{T_w - b_0}{T_h - T_c} = \sum_{n=\text{odd}}^{\infty} \left[\left(\frac{2}{\pi} \right) \frac{1}{n \sqrt{1 + (n\omega/c)^2}} \right] \sin (n\omega t - \phi_n).$$

$$(2\text{-}8)$$

Equation (2-8) describes the complete wire element steady state cyclic temperature variations in terms of wire geometry, wire material properties, hot and cold stream temperatures, heat transfer coefficients, and revolutions per second of the wire screen rotor.
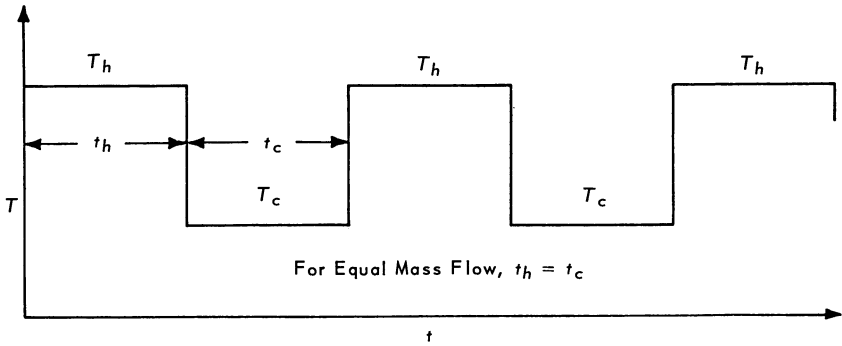
Fig. 2-25   Gas temperature in rotating wire element.

2. Cyclic Wire Temperature Rise

After steady state heat transfer is attained, the zero time $(t = 0)$ can be set at the instant that the wire element enters the hot stream. The wire element leaves the hot stream at $t = t_h$. If T_{w_0} indicates the wire element temperature in $°F.$ at $t = 0$ and T_{w_π} indicates the wire element temperature in $°F.$ at $t = t_h,$ from Eq. (2-8) the values of T_{w_0} and T_{w_π} can be calculated as:

$$\frac{T_{w_0} - b_0}{T_h - T_c} = \sum_{n=\text{odd}}^{\infty} \mu_n \sin(-\phi_n) = -\sum_{n=\text{odd}}^{\infty} \mu_n \sin \phi_n \qquad (2\text{-}9)$$

$$\frac{T_{w_\pi} - b_0}{T_h - T_c} = \sum_{n=\text{odd}}^{\infty} \mu_n \sin(n\pi - \phi_n) = \sum_{n=\text{odd}}^{\infty} \mu_n \sin \phi_n$$

$$\mu_n = \left(\frac{2}{\pi}\right) \frac{1}{n\sqrt{1 + (n\omega/c)^2}} \qquad \phi_n = \tan^{-1}\left(\frac{n\omega}{c}\right). \qquad (2\text{-}10)$$

Consequently, the wire temperature rise ΔT_w from T_{w_0} to T_{w_π} during the passage of the wire element through the hot stream section is

$$\frac{\Delta T_w}{T_h - T_c} = \frac{T_{w_\pi} - T_{w_0}}{T_h - T_c} = \sum_{n=\text{odd}}^{\infty} 2\mu_n \sin \phi_n. \qquad (2\text{-}11)$$

3. Temperature Effectiveness of a Single Rotating Wire Screen

The temperature effectiveness η_s of a single rotating wire screen is defined as

$$\eta_s = \frac{T_h - T_{h_e}}{T_h - T_c}.$$ (2-12)

Using the energy equation, one obtains:

$$W_w C_{p_w}(T_{w_\pi} - T_{w_0}) = W_h C_{p_h}(T_h - T_{h_e}).$$ (2-13)

From geometry and the equation of continuity, one obtains:

$$W_w = \left\{ \frac{\frac{\pi}{4}(D_0)^2 \left[1 - \left(\frac{D_i}{D_0}\right)^2\right]}{s^2} \right\} \left[2\left(\frac{\pi}{4} d^2\right) s\right] \rho_w N$$ (2-14)

$$W_h = \frac{1}{m} \left\{ \frac{\pi}{4}(D_0)^2 \left[1 - \left(\frac{D_i}{D_0}\right)^2\right]\left[1 - \frac{m\alpha}{2\pi}\right] \right\} \rho V_a$$ (2-15)

$$G = G_{\max}\left(1 - \frac{d}{s}\right)^2.$$ (2-16)

Substituting Eqs. (2-11, (2-13), (2-14), (2-15), and (2-16) into Eq. (2-12) and simplifying, one obtains:

$$\eta_s = \frac{1}{\beta} \sum_{n=\text{odd}}^{\infty} \frac{1/\zeta\beta}{1 + (n/\zeta\beta)^2}.$$ (2-17)

Here

$$\zeta = \frac{8}{\pi}\left(\frac{h}{G_{\max}C_p}\right)\left[\frac{d/s}{(1 - d/s)^2}\right]$$ (2-18)

$$\beta = \frac{1}{2}\left(\frac{\rho C_p}{\rho_w C_{p_w}}\right)\left(\frac{s}{d}\right)\left(\frac{V_a}{Nd}\right)\left(\frac{1 - m\alpha/2\pi}{m}\right).$$ (2-19)

ζ may be called the "heat transfer geometry parameter," and β may be called the "gas flow geometry parameter." These two nondimensional parameters alone determine the temperature effectiveness of the single layer wire screen. It should be noted that, when the gas flow geometry parameter, β, is small or approaches zero, the temperature effectiveness approaches 1.184ζ.

4. Temperature Effectiveness of a Multilayer Rotating Wire Screen Heat Exchanger

For a single layer wire screen rotor, the results of the expression of temperature effectiveness are the same for both parallel flow and counter flow heat exchangers. However, the results for parallel flow and counter flow are different for multi-layer rotating wire screens. These results are derived separately as follows:

a. Parallel Flow

Figure 2-26 illustrates a typical arrangement of a multi-layer rotating wire screen heat exchanger having n individual screens.

By definition,

$$\eta_{s_1} = \frac{T_{h_1} - T_{h_2}}{T_{h_1} - T_{c_1}} \qquad \eta_1 = \frac{T_{h_1} - T_{h_2}}{T_{h_1} - T_{c_1}}$$

$$\eta_{s_2} = \frac{T_{h_2} - T_{h_3}}{T_{h_2} - T_{c_2}} \qquad \eta_2 = \frac{T_{h_1} - T_{h_3}}{T_{h_1} - T_{c_1}}$$

$$\eta_{s_3} = \frac{T_{h_3} - T_{h_4}}{T_{h_3} - T_{c_3}} \qquad \eta_3 = \frac{T_{h_1} - T_{h_4}}{T_{h_1} - T_{c_1}} \qquad (2\text{-}20)$$

$$\eta_{s_n} = \frac{T_{h_n} - T_{h_{n+1}}}{T_{h_n} - T_{c_n}} \qquad \eta_n = \frac{T_{h_1} - T_{h_{n+1}}}{T_{h_1} - T_{c_1}}$$

therefore,

$$\eta_1 = \eta_{s_1} \qquad (2\text{-}21)$$

$$\eta_2 = \frac{T_{h_1} - T_{h_3}}{T_{h_1} - T_{c_1}} = \left(\frac{T_{h_1} - T_{h_2}}{T_{h_1} - T_{c_1}}\right) + \left(\frac{T_{h_2} - T_{h_3}}{T_{h_2} - T_{c_2}}\right)\left(\frac{T_{h_2} - T_{c_2}}{T_{h_1} - T_{c_1}}\right)$$

$$(2\text{-}22)$$
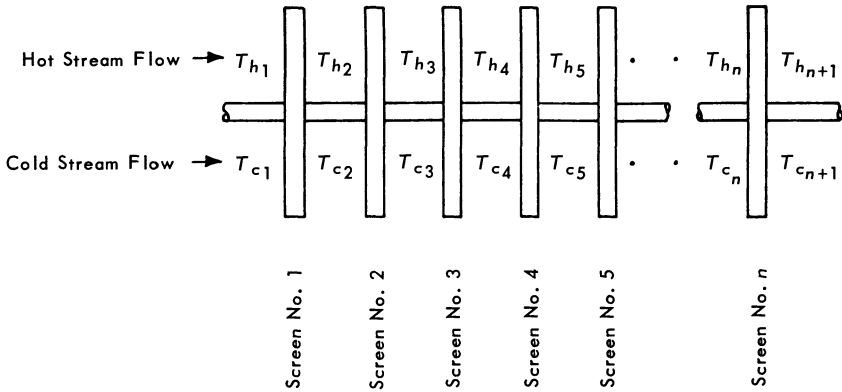
Fig. 2-26 Typical multi-layer rotating wire screen heat exchanger having n individual screens, parallel flow.

but

$$T_{h_2} = T_{h_1} - \eta_1(T_{h_1} - T_{c_1}) \qquad (2\text{-}23)$$

$$T_{c_2} = T_{c_1} + \eta_1(T_{h_1} - T_{c_1}). \qquad (2\text{-}24)$$

Substituting Eqs. (2-23) and (2-24) into Eq. (2-22), one obtains:

$$\eta_2 = \eta_1 + \eta_{s_2}(1 - 2\eta_1). \qquad (2\text{-}25)$$

Similarly,

$$\eta_3 = \eta_2 + \eta_{s_3}(1 - 2\eta) \qquad (2\text{-}26)$$

$$\eta_n = \eta_{n-1} + \eta_{s_n}(1 - 2\eta_{n-1}). \qquad (2\text{-}27)$$

For the special case of $\eta_{s_1} = \eta_{s_2} = \eta_{s_3} = \eta_{s_n} = \eta_s$, Eqs. (2-21), (2-25), (2-26), and (2-27) reduce to

$$\left.\begin{aligned}
\eta_1 &= \eta_s \\
\eta_2 &= \eta_1 + \eta_s(1 - 2\eta_1) \\
\eta_3 &= \eta_2 + \eta_s(1 - 2\eta_2) \\
&\vdots \\
\eta_n &= \eta_{n-1} + \eta_s(1 - 2\eta_{n-1})
\end{aligned}\right\} \qquad (2\text{-}28)$$
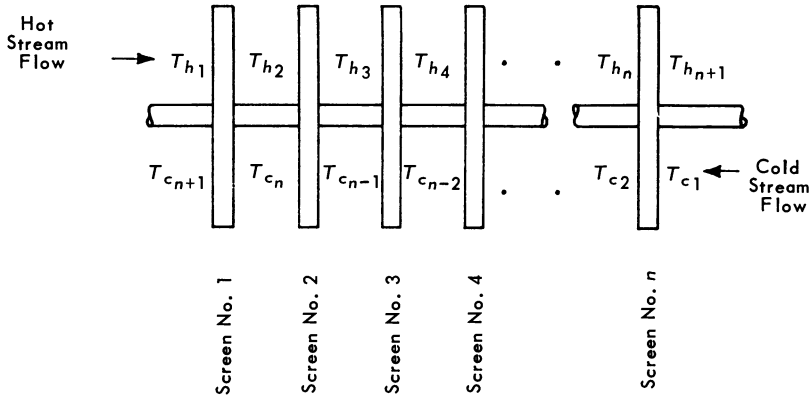
Fig. 2-27   Typical multi-layer rotating wire screen heat exchanger having n individual screens, counter flow.

b. Counter Flow

Figure 2-27 illustrates a typical arrangement of a multi-layer rotating wire screen heat exchanger having n screens. By definition,

$$\eta_{s_1} = \frac{T_{h_1} - T_{h_2}}{T_{h_1} - T_{c_n}} \qquad \eta_1 = \frac{T_{h_1} - T_{h_2}}{T_{h_1} - T_{c_n}}$$

$$\eta_{s_2} = \frac{T_{h_2} - T_{h_3}}{T_{h_2} - T_{c_{n-1}}} \qquad \eta_2 = \frac{T_{h_1} - T_{h_3}}{T_{h_1} - T_{c_{n-1}}}$$

$$\eta_{s_3} = \frac{T_{h_3} - T_{h_4}}{T_{h_3} - T_{c_{n-2}}} \qquad \eta_3 = \frac{T_{h_1} - T_{h_4}}{T_{h_1} - T_{c_{n-2}}} \qquad (2\text{-}29)$$

$$\eta_{s_n} = \frac{T_{h_n} - T_{h_{n+1}}}{T_{h_n} - T_{c_1}} \qquad \eta_n = \frac{T_{h_1} - T_{h_{n+1}}}{T_{h_1} - T_{c_1}}$$

Therefore,

$$\eta_1 = \eta_{s_1} \qquad\qquad (2\text{-}30)$$

$$\eta_2 = \eta_1 \left(\frac{T_{h_1} - T_{c_n}}{T_{h_1} - T_{c_{n-1}}} \right) + \eta_{s_2} \left(\frac{T_{h_2} - T_{c_{n-1}}}{T_{h_1} - T_{c_{n-1}}} \right) \qquad (2\text{-}31)$$

but

$$T_{h_2} = T_{h_1} - \eta_1 (T_{h_1} - T_{c_n}) \qquad\qquad (2\text{-}32)$$

$$T_{c_n} = T_{c_{n-1}} + \eta_{s_2}(T_{h_2} - T_{c_{n-1}}). \tag{2-33}$$

Using Eqs. (2-32) and (2-33), it is easy to prove that

$$\frac{T_{h_1} - T_{c_n}}{T_{h_1} - T_{c_{n-1}}} = \frac{1 - \eta_{s_2}}{1 - \eta_{s_2}\eta_1} \tag{2-34}$$

$$\frac{T_{h_2} - T_{c_{n-1}}}{T_{h_1} - T_{c_{n-1}}} = \frac{1 - \eta_1}{1 - \eta_{s_2}\eta_1}. \tag{2-35}$$

Substituting Eqs. (2-34) and (2-35) into Eq. (2-31) results in

$$\eta_2 = \eta_1 \left(\frac{1 - \eta_{s_2}}{1 - \eta_{s_2}\eta_1}\right) + \eta_{s_2}\left(\frac{1 - \eta_1}{1 - \eta_{s_2}\eta_1}\right). \tag{2-36}$$

Similarly,

$$\eta_3 = \eta_2 \left(\frac{1 - \eta_{s_3}}{1 - \eta_{s_3}\eta_2}\right) + \eta_{s_3}\left(\frac{1 - \eta_2}{1 - \eta_{s_3}\eta_2}\right) \tag{2-37}$$

$$\eta_n = \eta_{n-1} \left(\frac{1 - \eta_{s_n}}{1 - \eta_{s_n}\eta_{n-1}}\right) + \eta_{s_n}\left(\frac{1 - \eta_{n-1}}{1 - \eta_{s_n}\eta_{n-1}}\right). \tag{2-38}$$

For the special case of $\eta_{s_1} = \eta_{s_2} = \eta_{s_3} = \eta_{s_n} = \eta_s$, Eqs. (2-30), (2-36), (2-37) and (2-38) reduce to

$$\left.\begin{array}{l} \eta_1 = \eta_s \\[2ex] \eta_2 = \eta_1 \left(\dfrac{1 - \eta_s}{1 - \eta_s\eta_1}\right) + \eta_s\left(\dfrac{1 - \eta_1}{1 - \eta_s\eta_1}\right) \\[3ex] \eta_3 = \eta_2 \left(\dfrac{1 - \eta_s}{1 - \eta_s\eta_2}\right) + \eta_s\left(\dfrac{1 - \eta_2}{1 - \eta_s\eta_2}\right) \\[3ex] \eta_4 = \eta_3 \left(\dfrac{1 - \eta_s}{1 - \eta_s\eta_3}\right) + \eta_s\left(\dfrac{1 - \eta_3}{1 - \eta_s\eta_3}\right) \\[3ex] \quad\vdots \\[2ex] \eta_n = \eta_{n-1} \left(\dfrac{1 - \eta_s}{1 - \eta_s\eta_{n-1}}\right) + \eta_s\left(\dfrac{1 - \eta_{n-1}}{1 - \eta_s\eta_{n-1}}\right) \end{array}\right\} \tag{2-39}$$

Unequal Mass Flow for Hot and Cold Streams

For unequal mass flows, the same value of G in both hot and cold streams may be obtained by designing the ratio of the cross-sectional area of one stream to that of the other so that it is equal to the corresponding mass flow ratio of the two streams. This results in the same values of h in both hot and cold streams.

1. Wire Temperature vs. Time

Equation (2-5) is also valid for unequal mass flows. The surrounding gas temperature (T) shown in Fig. 2-28, however, becomes

$$T = b_0' + \sum_{n=1}^{\infty} a_n' \sin n\omega t + \sum_{n=1}^{\infty} b_n' \cos n\omega t$$

$$\left. \begin{array}{l} a_n' = \dfrac{T_h - T_c}{n\pi} (1 - \cos nb\pi) \\[3mm] b_n' = \dfrac{T_h - T_c}{n\pi} (\sin nb\pi) \\[3mm] b_0' = \dfrac{b}{2} (T_h - T_c) + T_c \end{array} \right\} . \qquad \textbf{(2-40)}$$

The solution of Eqs. (2-5) and (2-40) is

$$T_w = A_a' e^{-ct} + b_0' + \sum_{n=1}^{\infty} c_n \left[\frac{1}{\sqrt{1 + (n\omega/c)^2}} \right] \sin (n\omega t + \psi_n - \phi_n).$$

$$\textbf{(2-41)}$$

Here

$$c_n = \sqrt{2} \left(\frac{T_h - T_c}{n\pi} \right) \sqrt{1 - \cos nb\pi}$$

$$\phi_n = \tan^{-1} \left(\frac{n\omega}{c} \right) \qquad \psi_n = \tan^{-1} \left[\frac{\sin nb\pi}{1 - \cos nb\pi} \right]. \qquad \textbf{(2-42)}$$

The value of the arbitrary constant A_a' can be determined by setting $t = 0$ and $T_w = T_{w_i}$ in Eq. (2-41):

$$A_a' = T_{w_i} - b_0' + \sum_{n=1}^{\infty} c_n \left[\frac{1}{\sqrt{1 + (n\omega/c)^2}} \right] \sin(\psi_n - \phi_n).$$

(2-43)

$$\text{For Unequal Mass Flow, } t_h \neq t_c$$
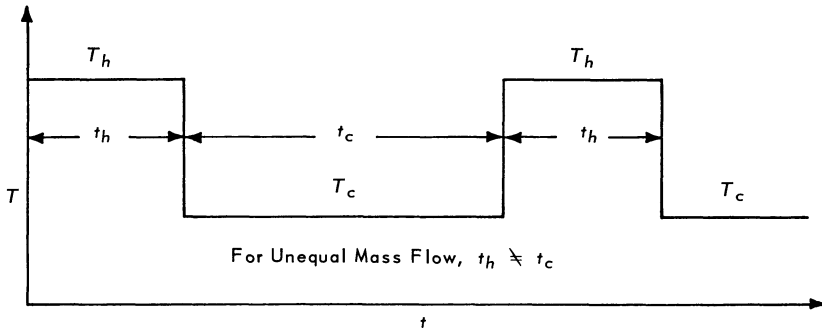
Fig. 2-28

After an elapsed time equal to $(3/c)$ seconds from the very start of the operation, the transient state portion becomes negligibly small. Therefore, for practical purposes, only the steady state portion is needed. This solution in nondimensional form is

$$\frac{T_w - b_0'}{T_h - T_c} = \sum_{n=1}^{\infty} \left\{ \frac{2}{\pi} \left[\frac{1}{n\sqrt{1 + (n\omega/c)^2}} \right] \left[\sqrt{\frac{1}{2} - \frac{\cos nb\pi}{2}} \right] \right\} \sin(n\omega t + \psi_n - \phi_n).$$

(2-44)

Equation (2-44) reduces to Eq. (2-8) when $b = 1$, for equal mass flows.

2. Cyclic Wire Temperature Rise

By employing a procedure similar to the one described for the corresponding portion of equal mass flows, one obtains the wire temperature rise:

$$\frac{\Delta T_w}{T_h - T_c} = \frac{T_{w_{b\pi}} - T_{w_0}}{T_h - T_c} = \sum_{n=1}^{\infty} \left[\frac{1}{2} - \frac{\cos nb\pi}{2} \right] 2\mu_n \sin \phi_n.$$

(2-45)

For equal mass flows, Eq. (2-45) reduces to Eq. (2-11) when $b = 1$.

3. *Temperature Effectiveness of a Single Layer Rotating Wire Screen*

By employing a procedure similar to the one described for the corresponding portion of equal mass flows, one obtains

$$\eta_s = \frac{1}{b}\left(\frac{1}{\beta}\right)\sum_{n=1}^{\infty}\left[\frac{1}{2} - \frac{\cos nb\pi}{2}\right]\left[\frac{1/\zeta\beta}{1 + (n/\zeta\beta)^2}\right]. \qquad (2\text{-}46)$$

For equal mass flows, Eq. (2-46) reduces to Eq. (2-17) when $b = 1$. When $\beta \cong 0$

$$\eta_s \cong \frac{\zeta}{b}\sum_{n=1}^{\infty}\left[\frac{1}{2} - \frac{\cos nb\pi}{2}\right]\left[\frac{1}{n^2}\right]. \qquad (2\text{-}47)$$

4. *Temperature Effectiveness of a Multi-layer Rotating Wire Screen Heat Exchanger*

a. *Parallel Flows*

A procedure similar to that employed for equal mass flows yields

$$\left.\begin{aligned}
\eta_1 &= \eta_{s_1}\\[2mm]
\eta_2 &= \eta_1 + \eta_{s_2}\left[1 - 2\eta_1\left(\frac{1}{2} + \frac{f}{2}\right)\right]\\[2mm]
\eta_3 &= \eta_2 + \eta_{s_3}\left[1 - 2\eta_2\left(\frac{1}{2} + \frac{f}{2}\right)\right]\\[2mm]
\eta_4 &= \eta_3 + \eta_{s_4}\left[1 - 2\eta_3\left(\frac{1}{2} + \frac{f}{2}\right)\right]\\[2mm]
&\ \ \vdots\\[2mm]
\eta_n &= \eta_{n-1} + \eta_{s_n}\left[1 - 2\eta_{n-1}\left(\frac{1}{2} + \frac{f}{2}\right)\right]
\end{aligned}\right\}. \qquad (2\text{-}48)$$

Where

$$f = \frac{W_h}{W_c} = \frac{b}{2-b}.$$

For the special case of $\eta_{s_1} = \eta_{s_2} = \eta_{s_3} = \eta_{s_n} = \eta_s$, Eq. (2-48) reduces to

$$\left. \begin{array}{l} \eta_1 = \eta_s \\[2ex] \eta_2 = \eta_1 + \eta_s \left[1 - 2\eta_1 \left(\frac{1}{2} + \frac{f}{2} \right) \right] \\[3ex] \eta_3 = \eta_2 + \eta_s \left[1 - 2\eta_2 \left(\frac{1}{2} + \frac{f}{2} \right) \right] \\[3ex] \eta_4 = \eta_3 + \eta_s \left[1 - 2\eta_3 \left(\frac{1}{2} + \frac{f}{2} \right) \right] \\[3ex] \vdots \\[2ex] \eta_n = \eta_{n-1} + \eta_s \left[1 - 2\eta_{n-1} \left(\frac{1}{2} + \frac{f}{2} \right) \right] \end{array} \right\} . \qquad (2\text{-}49)$$

b. *Counter Flows*

A procedure similar to that employed for equal mass flows yields

$$\left. \begin{array}{l} \eta_1 = \eta_{s_1} \\[3ex] \eta_2 = \eta_1 \left(\dfrac{1 - \eta_{s_2} f}{1 - \eta_{s_2} \eta_1 f} \right) + \eta_{s_2} \left(\dfrac{1 - \eta_1}{1 - \eta_{s_2} \eta_1 f} \right) \\[4ex] \eta_3 = \eta_2 \left(\dfrac{1 - \eta_{s_3} f}{1 - \eta_{s_3} \eta_2 f} \right) + \eta_{s_3} \left(\dfrac{1 - \eta_2}{1 - \eta_{s_3} \eta_2 f} \right) \\[4ex] \eta_n = \eta_{n-1} \left(\dfrac{1 - \eta_{s_n} f}{1 - \eta_{s_n} \eta_{n-1} f} \right) + \eta_{s_n} \left(\dfrac{1 - \eta_{n-1}}{1 - \eta_{s_n} \eta_{n-1} f} \right) \end{array} \right\} . \qquad (2\text{-}50)$$

For the special case of $\eta_{s_1} = \eta_{s_2} = \eta_{s_3} = \eta_s$, Eq. (2-50) reduces to

$$
\left.
\begin{aligned}
\eta_1 &= \eta_s \\[2ex]
\eta_2 &= \eta_1 \left(\frac{1 - \eta_s f}{1 - \eta_s \eta_1 f}\right) + \eta_s \left(\frac{1 - \eta_1}{1 - \eta_s \eta_1 f}\right) \\[2ex]
\eta_3 &= \eta_2 \left(\frac{1 - \eta_s f}{1 - \eta_s \eta_2 f}\right) + \eta_s \left(\frac{1 - \eta_2}{1 - \eta_s \eta_2 f}\right) \\[2ex]
\eta_4 &= \eta_3 \left(\frac{1 - \eta_s f}{1 - \eta_s \eta_3 f}\right) + \eta_s \left(\frac{1 - \eta_3}{1 - \eta_s \eta_3 f}\right) \\[2ex]
&\;\;\vdots \\[2ex]
\eta_n &= \eta_{n-1} \left(\frac{1 - \eta_s f}{1 - \eta_s \eta_{n-1} f}\right) + \eta_s \left(\frac{1 - \eta_{n-1}}{1 - \eta_s \eta_{n-1} f}\right)
\end{aligned}
\right\}
. \quad (2\text{-}51)
$$

Equations developed in the Analysis Section may be readily plotted as design charts to establish design criteria. This was done (see Figs. 2-29 to 2-32) for equal mass flows. For unequal mass flows, similar plots may be readily prepared, using the equations for unequal mass flows. These plots are not shown here, but are left to the individual designer to prepare to suit his own applications. For purpose of illustration, the general design procedure is given below:

Given: T_h, T_c, P_h, P_c, W_h, W_c, C_{p_h}, C_{p_c}.
Required: To design a heat exchanger to attain an effectiveness η.
Procedures:

1. Arbitrarily select the following quantities: m, α, n_s, d, s, counter flow or parallel flow, and wire material which determine $\rho_w C_{p_w}$.
2. Read η_s in Fig. 2-29 or 2-30 from known values of η and n_s.
3. Select ζ and β in Fig. 2-31 from known value of η_s. (It is always desirable to have β as close to maximum as possible and ζ as close to minimum as possible.)
4. Calculate $(h/G_{\max} C_p)$ from Eq. (2-18) and read $(d G_{\max}/\mu)$ in Fig. 2-32 from known value of $(h/G_{\max} C_p)$.
5. Calculate G from Eq. (2-16), N from Eq. (2-19).
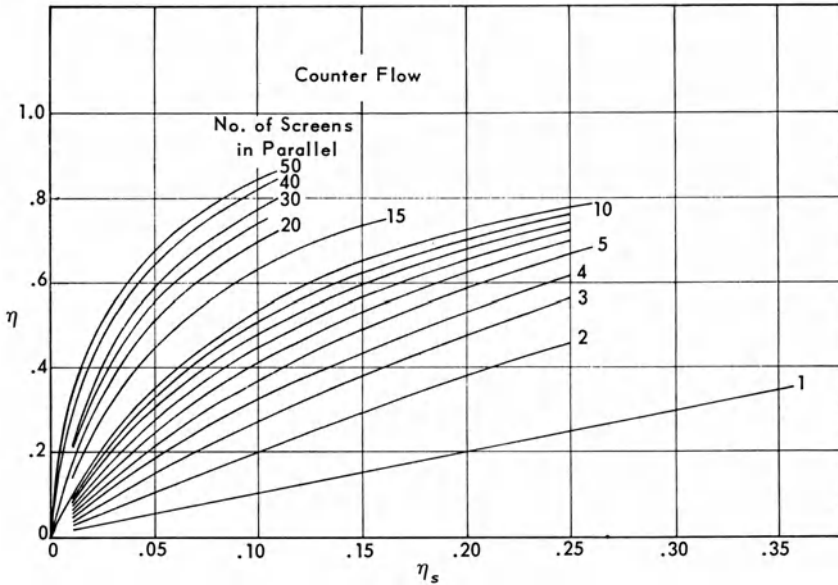
Fig. 2-29

6. Calculate free flow area A_f for either hot or cold gas from $A_f = W_h/G_h = W_c/G_c$, and calculate the outside diameter of the wire screen rotor using

$$A_f = \frac{\pi}{4} (D_0)^2 \left[1 - \left(\frac{D_i}{D_0} \right)^2 \right] \left(\frac{1 - m\alpha/2\pi}{m} \right).$$

NOTE: (D_i/D_0) may be arbitrarily selected but is usually from 0.1 to 0.3.

7. Calculate the total wire screen core weight W_w using

$$W_w = \frac{\pi}{4} (D_0)^2 \left[1 - \left(\frac{D_i}{D_0} \right)^2 \right] \left(\frac{\pi}{4} \right) \left(\frac{d}{s} \right)^2 2 s \rho_w n_s,$$

8. Calculate the core thickness of the wire screen layers l using

$$l = (n_s - 1) p + d \quad \text{(in inches)}$$

9. Calculate the core volume using

$$\text{Core Volume} = \frac{\pi}{4} (D_0)^2 \left[1 - \left(\frac{D_i}{D_0} \right)^2 \right] \left(\frac{l}{12} \right).$$
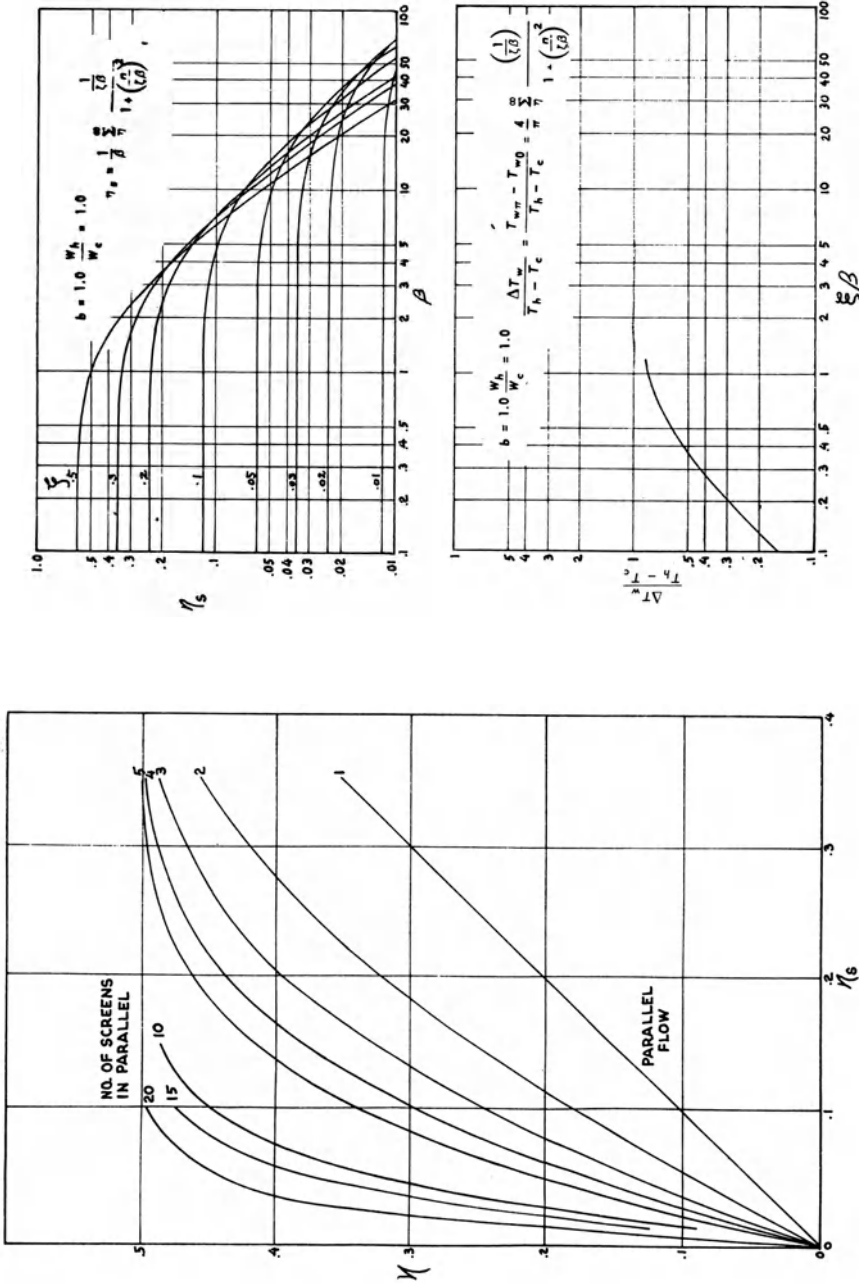
Fig. 2-31

Fig. 2-30
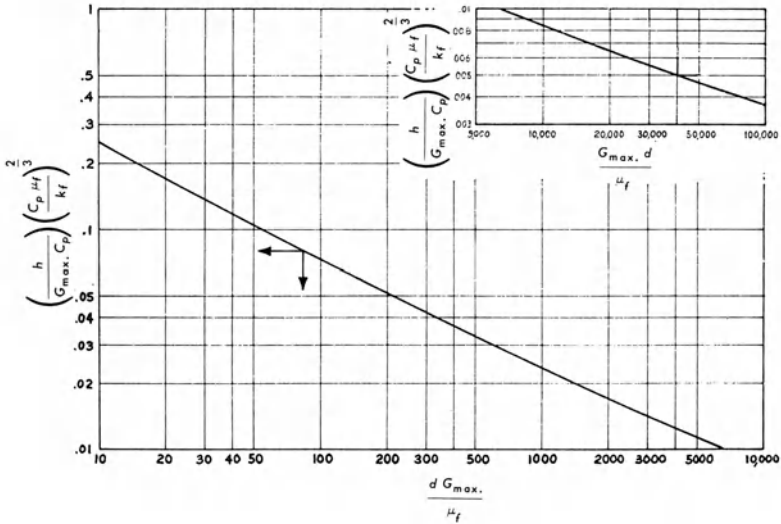
Fig. 2-32

For a given rotating wire screen heat exchanger, the performance can also be calculated from the charts in a similar but reverse manner. Knowing the values of V_a, N, etc., the value of η may readily be calculated for the given heat exchanger under the given operating conditions.

SYMBOLS

A_f = free flow area in sq. ft.

C_p = specific heat of gas in Btu/lb. °R.

C_{p_w} = specific heat of wire material in Btu/lb. °R.

c = Constant = $(4h/\rho_w C_{p_w} d)$

D_i = inside diameter of rotating wire screen rotor in ft.

D_0 = outside diameter of rotating wire screen rotor in ft.

d = wire diameter in ft. or inches

f = W_h/W_c

G = mass flow velocity per unit area in lb./sec. ft.^{2} = ρV

$G_{max.}$ = maximum mass flow velocity per unit area in lbs./sec. ft.^{2}

g = acceleration of gravity in ft./sec.^{2}

h = heat transfer film coefficient between gas and wire in Btu/sec. ft.^{2} °R.

k = thermal conductivity of the wire in Btu/sec. ft.^{2} °R./ft.

l = thickness of the rotating wire screen rotor in ft. or inches (thickness of multi-layer screen part only)

M = Mach number = $\left(V_a/\sqrt{\gamma g R t_s}\right)$

m = total number of hot and cold sections in duct (see Fig. 2-33)

N = revolutions of rotating wire screen rotor per second

n = integral number = n^{th} harmonic in a Fourier Series
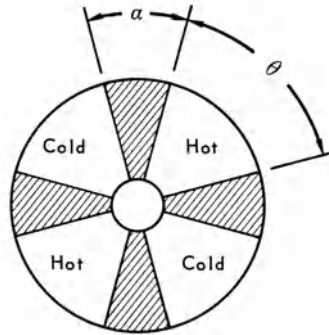
Fig. 2-33 $m = 4$.

n_s = number of screens in parallel in a rotating wire screen rotor

P = total pressure in lb./in.^{2} or lb./ft.^{2}

P_r = Prandtl number

R = gas constant in ft./°R. = 53.3 (for air)

s = Transverse pitch between wires in ft. or inches

T = total temperature in °R

T_{h_0} = total temperature of hot gas leaving the wire in °R.

T_w = instantaneous wire element temperature in °R.

ΔT_w = wire temperature rise in °R. during passage of the wire through the hot section = $T_{w_\pi} - T_{w_0}$

t = time in seconds

V_a = axial velocity of gas in ft./sec.

W = weight flow of gas in lb./sec.

W_w = total wire weight in lbs.

α = angle in degrees or radians which prevents mixing of hot and cold gases during passage through rotating wire screen rotor

β = $1/2(\rho C_p/\rho_w C_{p_w})[1/(d/s)](V_a/Nd)[1 - (m\alpha/2\pi)/m]$

γ = ratio of specific heats of gases

ζ = $8/\pi(h/G_{\max.}C_p)[(d/s)/(1 - d/s)^2]$

η = over-all temperature effectiveness of rotating wire screen heat exchanger

η_s = temperature effectiveness of an individual wire screen

$\eta_1, \eta_2, \eta_3, \cdots \eta_n$ = temperature effectiveness of one, two, three, four . . . n wire screens in parallel

$\eta_{s_1}, \eta_{s_2}, \eta_{s_3}, \cdots \eta_{s_n}$ = temperature effectiveness of first, second, third, fourth . . . n^{th} individual wire screen

θ = angle in degrees or radians in hot or cold section of the duct

ρ = density of gas in lb./ft.^{3}

σ = screen solidity = $2(d/s) - (d/s)^2$

ω = equivalent angular frequency in radians per second = $mN\pi/[1 - (m\alpha/2\pi)]$

GENERAL SUBSCRIPTS

c indicates cold gas

h indicates hot gas

i indicates initial

n indicates n^{th} harmonic in a Fourier Series

o indicates steady state time wire element entering hot section

s indicates single wire screen

w indicates wire or wire screen

π or $b\pi$ indicates steady state time wire element leaving hot section

[2-7] PULSE JET

Figure 2-34 gives a schematic diagram for illustrating pulse jet operations. Pulse jet operates on a periodic cycle controlled by the opening and closing of the inlet valve. The phenomenon may best be demonstrated through the following pressure-time history. When the inlet valve opens, the inlet air under ram pressure enters the combustion chamber where the pressure rises from ambient or neat ambient p_a to the ram pressure P_1, depending on ram efficiency [see Eq. (1-160)], as shown from point a to point b. This is called the inlet charging process. The time required for charging is t_c. At the end of point b where the inlet valve closes, combustion takes place and raises the temperature and, consequently, the pressure, to a maximum point c. The time required for combustion is t_b. Discharge starts at point a and ends at point c where the pressure becomes ambient or near ambient again. This completes one cycle. The frequency is equal to (Fig. 2-35)

$$f = \frac{1}{t_c + t_b + t_d} .$$

It is to be remembered that since there is no exhaust valve, discharge takes place continuously during the charging and combustion process as well as during the discharging process.
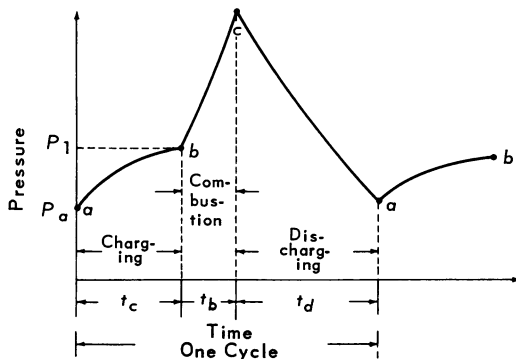
Fig. 2-34   Fig. 2-35

[2-7.1] Discharging from Point c to Point a

When the inlet valve is in the closed position, the situation may be represented by Fig. 2-36. Let m, P, T and ρ represent the mass, pressure, temperature and density, respectively, of gas inside the chamber, at any instant t. Let V_0 and A_2 represent, respectively, the effective volume of the chamber which is a constant and the exit nozzle throat area. Use sub 0 to indicate the initial condition when
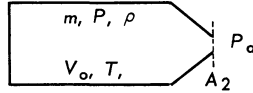
Fig. 2-36

discharge starts at point c. Assume the expansion inside the chamber during the discharging process follows the isentropic pressure temperature relationship (which is a good assumption and is very close to actual cases).

$$m = V_0 \rho$$

$$\because \frac{P}{\rho^k} = \frac{P_0}{\rho_0{}^k} = c_1 \qquad \therefore \rho = \left(\frac{P}{c_1}\right)^{\frac{1}{k}}$$

$$m = V_0 \left(\frac{P}{c_1}\right)^{\frac{1}{k}} \tag{2-52}$$

$$\frac{dm}{dt} = \frac{V_0}{kC_1{}^{\frac{1}{k}}} P^{\left(\frac{1-k}{k}\right)} \frac{dP}{dt}$$

Here dm/dt is the rate of change of mass of gas inside the chamber which must be equal to the rate of exhaust gas leaving the nozzle exit, W. Combining Eqs. (1-106) and (1-78), we have

$$w_2 = \frac{PA_2}{\sqrt{T}} \sqrt{\frac{kg}{R}} \sqrt{\frac{2}{k-1}} \sqrt{\left(\frac{p}{P}\right)^{\frac{2}{k}} \left[1 - \left(\frac{p}{P}\right)^{\frac{k-1}{k}}\right]} = -\frac{dm}{dt} . \tag{2-53}$$

Substituting Eq. (2-53) into Eq. (2-52), one obtains:

$$-\frac{PA_2}{\sqrt{T}} \sqrt{\frac{kg}{R}} \sqrt{\frac{2}{k-1}} \sqrt{\left(\frac{p}{P}\right)^{\frac{2}{k}} \left[1 - \left(\frac{p}{P}\right)^{\frac{k-1}{k}}\right]} \frac{kc_1{}^{\frac{1}{k}}}{V_0} = P^{\frac{1-k}{k}} \frac{dP}{dt} .$$

Since

$$\frac{P}{P_0} = \left(\frac{T}{T_0}\right)^{\frac{k}{k-1}}$$

we have

$$\sqrt{T} = \sqrt{T_0}\left(\frac{P}{P_0}\right)^{\frac{k-1}{2k}}. \qquad (2\text{-}54)$$

Substituting Eq. (2-54) into (2-53), one obtains:

$$-c_2 dt = \frac{P^{\frac{1-3k}{2k}} dP}{\sqrt{\left(\frac{p}{P}\right)^{\frac{2}{k}}\left[1 - \left(\frac{p}{P}\right)^{\frac{k-1}{k}}\right]}}. \qquad (2\text{-}55)$$

Here

$$c_2 = \frac{A_2}{\sqrt{T_0 \rho_0}} P_0^{\left(\frac{k-1}{2k}\right)} \sqrt{\frac{kg}{R}} \sqrt{\frac{2}{k-1}} \left(\frac{kP_0}{V_0}\right)^{\frac{1}{k}}. \qquad (2\text{-}56)$$

[2-7.1.1] Supercritical Discharging When $(P/p) \geq [(k+1)/2]^{k/(k-1)}$

For all pressure ratios greater than or equal to the critical pressure ratio

$$\left(\frac{P}{p}\right) \geq \left(\frac{k+1}{2}\right)^{\frac{k}{k-1}}$$

the throat is choked and the Mach number is one at the throat. Under this condition, (P/p) becomes a constant which is equal to $[(k+1)/2]^{k/(k-1)}$ Therefore, for super critical or critical flow, we have

$$-c_3 dt = P^{\frac{1-3k}{2k}} dP. \qquad (2\text{-}57)$$

Here

$$c_3 = c_2 \sqrt{\left(\frac{2}{k+1}\right)^{\frac{2}{k-1}} \left[1 - \frac{2}{k+1}\right]}. \tag{2-58}$$

Equation (2-57) may easily be integrated to give

$$t = \frac{1}{c_3}\left(\frac{2k}{k-1}\right)\left[P^{\frac{1-k}{2k}} - P_0^{\frac{1-k}{2k}}\right] \tag{2-59}$$

$$t = c_4\left[\left(\frac{P}{P_0}\right)^{\frac{1-k}{2k}} - 1\right]. \tag{2-60}$$

Here

$$c_4 = \frac{1}{c_3}\left(\frac{2k}{k-1}\right)P_0^{\left(\frac{1-k}{2k}\right)}. \tag{2-61}$$

With pressure versus time known, the temperature T, density ρ versus time may be known from the isentropic pressure-temperature, pressure-density relationships. They are:

$$t = c_4\left[\left(\frac{T_0}{T}\right)^{\frac{1}{2}} - 1\right] = c_4\left[\left(\frac{\rho_0}{\rho}\right)^{\frac{k-1}{2}} - 1\right]. \tag{2-62}$$

From Eqs. (2-53) and (2-54) and supercritical flow conditions where

$$\left(\frac{P}{p}\right) = \left(\frac{k+1}{2}\right)^{\frac{k}{k-1}}$$

one obtains:

$$\frac{dm}{dt} = -c_5 P^{\frac{k+1}{2k}}. \tag{2-63}$$

Here

$$c_5 = \frac{A_2}{\sqrt{T_0}} P_0^{\frac{k-1}{2k}} \sqrt{\frac{kg}{R}} \sqrt{\frac{2}{k-1}} \sqrt{\left(\frac{2}{k+1}\right)^{\frac{2}{k-1}}\left(\frac{k-1}{k+1}\right)}. \quad (2\text{-}64)$$

Substituting Eq. (2-59) into (2-64), one obtains:

$$\frac{dm}{dt} = -c_5(c_6 t + c_7)$$

$$\frac{dm}{dt} = -c_5 \left[(c_6 t + c_7)^{\frac{2k}{1-k}}\right]^{\frac{k+1}{2k}} = -c_5(c_6 t + c_7)^{\frac{k+1}{1-k}}. \quad (2\text{-}65)$$

Here

$$c_6 = \frac{c_3(k-1)}{2k}$$

$$c_7 = c_4 c_6.$$

Equation (2-65) may be integrated to obtain:

$$m - m_0 = -\left(\frac{c_5}{c_6}\right)\left(\frac{1-k}{2}\right)\left[(c_6 t + c_7)^{\frac{2}{1-k}} - c_7^{\frac{2}{1-k}}\right]. \quad (2\text{-}66)$$

[2-7.1.2] Subcritical Discharging When $(P/p) < [(k+1)/2]^{k/(k-1)}$

For subcritical flow $p = p_a$, so we may rewrite Eq. (2-55) as

$$-c_8 \, dt = \frac{\chi^{\left(\frac{1-3k}{2k}\right)} d\chi}{\sqrt{\left(\frac{1}{\chi}\right)^{\frac{2}{k}}\left[1 - \left(\frac{1}{\chi}\right)^{\frac{k-1}{k}}\right]}} = \frac{d\chi}{\sqrt{\chi^{3\left(\frac{k-1}{k}\right)} - \chi^{2\left(\frac{k-1}{k}\right)}}}.$$

$$(2\text{-}67)$$

Here

$$c_8 = \frac{c_2}{p_a^{\frac{1-k}{2k}}}$$

$$\chi = \left(\frac{P}{p_a}\right).$$

When $k = 1.4$, which is the case of usual interest, we have

$$-c_8\,dt = \frac{d\chi}{\sqrt{\chi^{\frac{6}{7}} - \chi^{\frac{4}{7}}}}. \tag{2-68}$$

Equation (2-68) may be integrated to give

$$t = -\frac{7}{c_8}\left\{ \chi_i^{\frac{3}{7}}\sqrt{\chi_i^{\frac{2}{7}} - 1} - \frac{3}{4}\chi_i^{\frac{1}{7}}\left(\chi_i^{\frac{2}{7}} - 1\right)^{\frac{3}{2}} - \frac{3}{8}\chi_i^{\frac{1}{7}}\left(\chi_i^{\frac{2}{7}} - 1\right)^{\frac{1}{2}} \right.$$

$$+ \frac{3}{8}\ln\left[\chi_i^{\frac{1}{7}} + \left(\chi_i^{\frac{2}{7}} - 1\right)^{\frac{1}{2}}\right] - \chi^{\frac{3}{7}}\sqrt{\chi^{\frac{2}{7}} - 1} + \frac{3}{4}\chi^{\frac{1}{7}}\left(\chi^{\frac{2}{7}} - 1\right)^{\frac{3}{2}}$$

$$\left. + \frac{3}{8}\chi^{\frac{1}{7}}\left(\chi^{\frac{2}{7}} - 1\right)^{\frac{1}{2}} - \frac{3}{8}\ln\left[\chi^{\frac{1}{7}} + \left(\chi^{\frac{2}{7}} - 1\right)^{\frac{1}{2}}\right]\right\}. \tag{2-69}$$

Here χ_i is the initial value of (P/p_a) at the start of subcritical flow and which is equal to $[(k + 1)/2]^{k/k-1}$. For the other value of k, Eq. (2-67) must be integrated graphically.

[2-7.2] Combustion from Point b to Point c

Combustion in pulse jet is neither a constant volume combustion nor a constant pressure combustion; it is in between. From Eq. (1-21) of Chapter 1, we have

$$dQ = dE + pdV = dh - vdp \ . \qquad (1\text{-}21)$$

From Eqs. (1-167) and (1-168) of Chapter 1, we have

$$dQ = \eta_b h^* \ \frac{df}{1+f} \ . \qquad (1\text{-}167)$$

The term $(1+f)$ is being added because the heat addition dQ is for heating $(1+f)$ pound of combustion products. Therefore, we may write Eq. (1-21) as

$$(1+f)\left(c_v \ \frac{dT}{dt} + \frac{pdv}{Jdt}\right) = \eta_b h^* \ \frac{df}{dt} \ . \qquad (2\text{-}70)$$

If the rate of fuel injection (df/dt) is constant or equal to its average rate during the combustion period t_c, i.e., $df/dt = f/t_c$. Here f = total pound of fuel injected per pound of air during combustion period t_c (which should be as short as possible for best efficiency):

t_c = combustion time period, in seconds.

Then Eq. (2-70) may be written as follows:

$$\frac{dT}{dt} + \frac{P}{Jc_v} \ \frac{dv}{dt} = \left(\frac{f}{1+f}\right) \eta_b h^* \ \frac{1}{t_c c_v} \qquad (2\text{-}71)$$

or

$$\frac{dT}{dt} + \frac{RT}{Jc_v V_o} \ \frac{dv}{dt} = c_9 \ . \qquad (2\text{-}72)$$

Here

$$c_9 = \left(\frac{f}{1+f}\right) \eta_b h^* \left(\frac{1}{t_c c_v}\right) . \qquad (2\text{-}73)$$

During the combustion process, the flow at the nozzle throat is usually critical, $M^* = 1$, so from Eq. (1-106), we have

$$\frac{dm}{dt} - -w_2 = -\sqrt{\frac{kg}{R}} \ \frac{A_2 P}{\left(\dfrac{k+1}{2}\right)^{\frac{k+1}{2(k-1)}} \sqrt{T}} \tag{2-74}$$

$$dm = -c_{10} \frac{\sqrt{T}}{V} \, dt \, . \tag{2-75}$$

Here

$$c_{10} = \sqrt{\frac{kg}{R}} \ \frac{A_2 R}{\left(\dfrac{k+1}{2}\right)^{\frac{k+1}{2(k-1)}}} \tag{2-76}$$

since

$$dm = V_0 \, d\rho = V_0 d\left(\frac{1}{v}\right) = -V_0 \frac{dv}{v^2} \, . \tag{2-77}$$

Equating Eqs. (2-75) and (2-77), one obtains:

$$\frac{c_{10} \sqrt{T}}{V_0} \, dt = \frac{dv}{v} \, . \tag{2-78}$$

Substituting Eq. (2-78) into (2-72), one obtains:

$$\frac{dT}{dt} + c_{11} T^{\frac{3}{2}} = c_9 \, . \tag{2-79}$$

Here

$$c_{11} = \left(\frac{Rc_{10}}{Jc_v V_0}\right) \, . \tag{2-80}$$

Equation (2-79) may be written

$$\frac{dT}{c_9 - c_{11} T^{\frac{3}{2}}} = dt \, . \tag{2-81}$$

Let $T^{1/2} = \chi$ so $(1/2)\, T^{-1/2}\, dT = d\chi$

so

$$\frac{dT}{c_9 - c_{11}\, T^{\frac{3}{2}}} = \frac{2\chi d\chi}{c_9 - c_{11}\chi^3} = dt. \tag{2-82}$$

Let $c_9 = a$, $-c_{11} = b$, $c_{12} = (a/b)^{1/3}$

Equation (2-82) may be integrated to give:

$$t = \frac{2}{3bc_{12}} \left\{ \frac{1}{2} \ln \left[\frac{c_{12}^2 - c_{12}\chi + \chi^2}{(c_{12} + \chi)^2} + \sqrt{3}\ \tan^{-1}\left(\frac{2\chi - c_{12}}{c_{12}\sqrt{3}}\right)\right] \right\}. \tag{2-83}$$

Therefore, we have

$$t = \frac{2}{3c_{11}c_{12}} \left[\frac{1}{2} \frac{\ln c_{12}^2 - c_{12}\sqrt{T} + T}{\left(c_{12} + \sqrt{T}\right)^2} \right.$$

$$\left. + \sqrt{3}\ \tan^{-1}\left(\frac{2\sqrt{T} - c_{12}}{c_{12}\sqrt{3}}\right)\right]. \tag{2-84}$$

Zero time or initial time is at the beginning of combustion or at point b where the temperature is equal to T_1 and pressure is equal to P_1. Since $pv = RT$, we have

$$\frac{dP}{P} = \frac{dT}{T} - \frac{dv}{v}. \tag{2-85}$$

Substituting Eq. (2-78) into (2-85), we have

$$\frac{dP}{P} = \frac{dT}{T} - \frac{c_{10}}{V_0}\sqrt{T}\ dt. \tag{2-86}$$

Substituting Eq. (2-81) into (2-86), we have

$$\frac{dP}{P} = \frac{dT}{T} - \frac{c_{10}}{V_0} \frac{T^{\frac{1}{2}} dT}{c_9 - c_{11} T^{\frac{3}{2}}} \qquad (2\text{-}87)$$

$$dT^{\frac{3}{2}} = \frac{3}{2} T^{\frac{1}{2}} dT$$

$$\int_{P_i}^{P} \frac{dP}{P} = \int_{T_i}^{T} \frac{dT}{T} + \frac{2c_{10}}{3c_{11}V_0} \int_{T_2}^{T} \frac{d\left(c_9 - c_{11}T^{\frac{3}{2}}\right)}{\left(c_9 - c_{11}T^{\frac{3}{2}}\right)}. \qquad (2\text{-}88)$$

Equation (2-88) may be integrated to give

$$\ln\left(\frac{P}{P_i}\right) = \ln\left(\frac{T}{T_i}\right) + \frac{2}{3}\left(\frac{c_{10}}{c_{11}V_0}\right) \ln\left[\frac{c_9 - c_{11}T^{\frac{3}{2}}}{c_9 - c_{11}T_i^{\frac{3}{2}}}\right]. \qquad (2\text{-}89)$$

Here the subscript i indicates the initial condition or conditions at point b where temperature is T_1 and pressure is P_1. Since T versus time is known from Eq. (2-84), pressure versus time may be known from Eqs. (2-89) and (2-84).

[2-7.3] Charging Process from Point a to Point b

The charging process may be represented from the following sketch:

A₁
Valve
Position

A₂
Nozzle Throat
Position
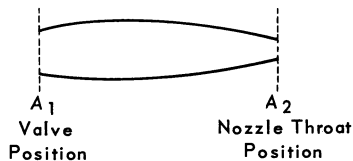
Here the rate of change of gas mass inside the chamber must be equal to

$$\frac{dm}{dt} = w_1 - w_2.$$ (2-90)

Again applying Eqs. (1-106) and (1-78) of Chapter 1 to the present case, we have

$$w_1 = \frac{P_1 A_1}{\sqrt{T_1}} \sqrt{\frac{kg}{R}} \sqrt{\frac{2}{k-1}} \sqrt{\left(\frac{P}{P_1}\right)^{\frac{2}{k}} \left[1 - \left(\frac{P}{P_1}\right)^{\frac{k-1}{k}}\right]}.$$ (2-91)

Here P is the pressure inside the chamber, P_1 and T_1 are ram pressure and ram temperature, respectively [Eq. (1-160)].

$$w_2 = \frac{PA_2}{\sqrt{T_1}} \sqrt{\frac{kg}{R}} \sqrt{\frac{2}{k-1}} \sqrt{\left(\frac{p_a}{P}\right)^{\frac{2}{k}} \left[1 - \left(\frac{p_a}{P}\right)^{\frac{k-1}{k}}\right]}.$$ (2-92)

Here p_a is the ambient pressure. Equations (2-91) and (2-92) may be rewritten as

$$w_1 = c_{13} \sqrt{\left(\frac{P}{P_1}\right)^{\frac{2}{k}} \left[1 - \left(\frac{P}{P_1}\right)^{\frac{k-1}{k}}\right]}.$$ (2-93)

Here

$$c_{13} = \frac{P_1 A_1}{\sqrt{T_1}} \sqrt{\frac{kg}{R}} \sqrt{\frac{2}{k-1}} = \text{constant}$$ (2-94)

$$w_2 = c_{14} \left(\frac{P}{p_a}\right) \sqrt{\left(\frac{p_a}{P}\right)^{\frac{2}{k}} \left[1 - \left(\frac{p_a}{P}\right)^{\frac{k-1}{k}}\right]}.$$ (2-95)

Here

$$c_{14} = \frac{A_2}{p_a \sqrt{T_1}} \sqrt{\frac{kg}{R}} \sqrt{\frac{2}{k-1}} . \qquad (2\text{-}96)$$

When the flow is critical, *i.e.*, Mach 1 at the throat section, when $(P_1/P) \geq [(k+1)/2]^{k/(k-1)}$ for w_1 flow and when $(P/p_a) \geq [(k+1)/2]^{k/(k-1)}$ for w_2 flow, Eqs. (2-93) and (2-95) become constant, *i.e.*,

$$w_1 = c_{13} \sqrt{\left(\frac{2}{k+1}\right)^{\frac{k}{k-1}} \left[\frac{k-1}{k+1}\right]}$$

$$= c_{15} = \text{constant} \qquad (2\text{-}93a)$$

$$w_2 = c_{14} \sqrt{\left(\frac{2}{k+1}\right)^{\frac{k}{k-1}} \left(\frac{k-1}{k+1}\right)} = c_{16} = \text{constant} .$$

$$(2\text{-}95a)$$

During the charging process for high-speed pulse jets where ram pressure over ambient pressure is above critical value, the charging process consists of three parts. When the inlet valve opens, the chamber pressure is near the ambient pressure p_a, while ram pressure is P_1 (a value higher than or equal to the critical pressure ratio), the charging process is "supercritical charging and subcritical discharging," as shown in Fig. 2-37. When the chamber pressure gradually builds up, the ratio P_1/P becomes $< [(k+1)/2]^{k/(k-1)}$, the charging process becomes "subcritical charging and subcritical discharging." Finally, the chamber pressure builds up so high that the chamber pressure P over the ambient pressure p_a exceeds the critical value $[(k+1)/2]^{k/(k-1)}$ and results in "subcritical charging and supercritical discharging" as shown in Fig. 2-37. The analysis may now be made in the following.

[2-7.3.1] Supercritical Charging and Subcritical Discharging

Combining Eqs. (2-90), (2-93a) and (2-95), one obtains:

$$\frac{dm}{dt} = c_{15} - c_{14} \left(\frac{P}{p_a}\right) \sqrt{\left(\frac{p_a}{P}\right)^{\frac{2}{k}} \left[1 - \left(\frac{p_a}{P}\right)^{\frac{k-1}{k}}\right]} . \qquad (2\text{-}97)$$

Substituting Eq. (2-52) into (2-97), one obtains:

(1) Supercritical charging subcritical discharging
(2) Subcritical charging subcritical discharging
(3) Subcritical charging supercritical discharging
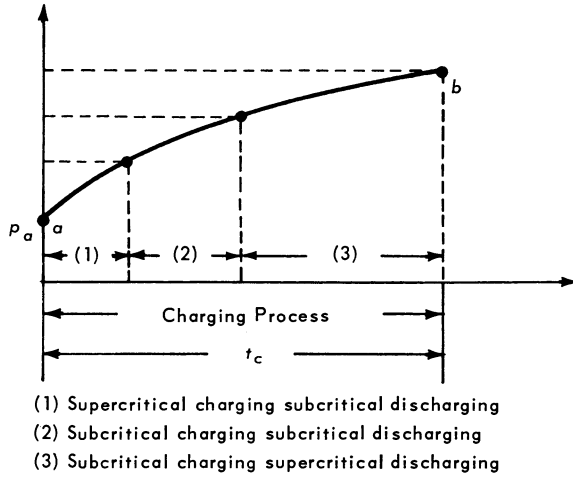
Fig. 2-37

$$
\frac{V_0}{kc_1^{\frac{1}{k}}} \, P^{\frac{1-k}{k}} \, \frac{dP}{dt} = c_{15} - c_{14} \left(\frac{P}{p_a}\right) \sqrt{\left(\frac{p_a}{P}\right)^{\frac{2}{k}} \left[1 - \left(\frac{p_a}{P}\right)^{\frac{k-1}{k}}\right]}
$$

(2-98)

or

$$
\int_{x_i}^{x} \frac{c_{17} \, \chi^{\frac{1-k}{k}} \, d\chi}{c_{15} - c_{14} \sqrt{\chi^{2\left(\frac{k-1}{k}\right)} - \chi^{\left(\frac{k-1}{k}\right)}}} = t \; .
$$

(2-99)

Here

$$
c_{17} = \frac{V_0}{kc_1^{\frac{1}{k}}} \, p_a^{\frac{1}{k}}
$$

(2-100)

$$
\chi = \left(\frac{P}{p_a}\right) .
$$

(2-101)

Equation (2-99) which gives pressure versus time may be integrated graphically.

[2-7.3.2] Subcritical Charging and Subcritical Discharging

Following the same procedure as was used in the previous section, one obtains:

$$\int \frac{c_{17}\, \chi^{\frac{1-k}{k}}\, d\chi}{c_{13}\sqrt{\left(\frac{p_a}{P_1}\right)^{\frac{2}{k}} \chi^{-\frac{2}{k}}\left[1 - \left(\frac{p_a}{P_1}\right)^{\frac{k-1}{k}} \chi^{\frac{1-k}{k}}\right] - c_{14}\sqrt{\chi^{\frac{2(k-1)}{k}} - \chi^{\left(\frac{k-1}{k}\right)}}}} = t\,.$$

$$(2\text{-}102)$$

[2-7.3.3] Subcritical Charging and Supercritical Discharging

Following the same procedure again, one obtains:

$$\int \frac{c_{17}\chi^{\frac{1-k}{k}}\, d\chi}{c_{13}\sqrt{\left(\frac{p_a}{P_1}\right)^{\frac{2}{k}} \chi^{-\frac{2}{k}}\left[1 - \left(\frac{p_a}{P_1}\right)^{\frac{k-1}{k}} \chi^{\frac{1-k}{k}}\right] - c_{16}}} = t\,.$$

$$(2\text{-}103)$$

Both Eq. (2-102) and (2-103) may be integrated graphically. Once pressure versus time is known, the temperature T, density ρ, Mass flow w_1 and w_2 versus time may also be obtained through pressure P. This is shown in the following:

$$\frac{T}{T_i} = \left(\frac{P}{P_i}\right)^{\frac{k-1}{k}}$$

$$\frac{\rho}{\rho_i} = \left(\frac{P}{P_i}\right)^{\frac{1}{k}}$$

m versus t may be obtained from Eq. (2-97) when P versus t is known. w_1 and w_2 versus t may be obtained from Eq. (2-93) and (2-95), respectively, when P versus t is known.

Jet velocity V_j versus t may be obtained through Eq. (1-178a).

$$V_j = \sqrt{2gJc_p\eta_N T \left[1 - \left(\frac{p_a}{P}\right)^{\frac{k-1}{k}}\right]} \qquad (1\text{-}178a)$$

when T and P versus t are known from the above, the gross thrust $F_g = (w_2/g)\,V_j$ is known when V_j and w_2 versus t are known. The net thrust F_N versus t may be obtained through $F_N = (w_2/g)\,V_j - (w_1/g)\,V_0$ when w_2, w_1 and V_j versus t are known from the above. This value may also be measured based on a weighted average value of one complete cycle.

REFERENCES

1. Keenan, J.H. and J. Kaye: Gas Tables, John Wiley & Sons, 1945.
2. Sorenson, H.A.: Gas Turbines, Ronald Press, 1951.
3. Trout, Arthur M. and Eldon W. Hall: Method for Determining Optimum Division of Power between Jet and Propeller for Maximum Thrust Power of a Turbine-Propeller Engine, NACA TN 2178, 1950.
4. Hensley, Reece V.: Theoretical Augmentation of Turbine-Propeller Engine by Compressor-Inlet Water Injection, Tail-Pipe Burning, and Their Combination, NACA TN 2672, 1952.
5. Lundin, Bruce T.: Theoretical Analysis of Various Thrust-Augmentation Cycles for Turbojet Engines, NACA 981, 1950.
6. Pinkel, Benjamin and Irving M. Karp: A Thermodynamic Study of the Turbine-Propeller Engine, NACA 1114, 1953.
7. —— and ——: A Thermodynamic Study of the Turbojet Engine, NACA 891, 1947.
8. Wilcox, Clinton and Arthur M. Trout: Analysis of Thrust Augmentation of Turbojet Engines by Water Injection at Compressor Inlet Including Charts for Calculating Compression Processes with Water Injection, NACA 1006, 1951.
9. Bittker, David A.: Comparison of Experimental and Kinetically Limited Theoretical Performance of the Hydrogen-Fluorine Propellant System, NASA TN D-3607.
10. Loh, W.H.T.: Analytical Solutions for Rotary Matrix Wire Screen Heat Exchangers, Journal of the Franklin Institute, 272: 3, September 1961.
11. ——: UCLA "Jet Propulsion" classnotes.

12. Loh, W.H.T.: SMU "Advanced Propulsion Technology" class-notes.
13. ——: Hydraulic Analogue for One Dimensional Unsteady Gas Dynamics, Journal of the Franklin Institute, 269: 1, January 1960.
14. ——: TCU "Jet Propulsion and Gas Turbine" classnotes.
15. ——: "Advanced Lectures on Propulsion Series" given at Convair and Chance Vaught.
16. ——: "Machine Design," May 1957.

Aerodynamic Design of Axial Flow Compressors and Turbines

W. H. T. LOH, Manager
Science and Technology,
Space Division,
North American Rockwell Corporation
Downey, California.

[3-1] INTRODUCTION

Fundamental aerothermodynamic equations derived in Chapter 1 may now be applied for aerodynamic design of axial flow compressors and turbines. A typical sketch of an axial flow compressor is shown in Fig. 3-1. The following symbols are conventionally used:
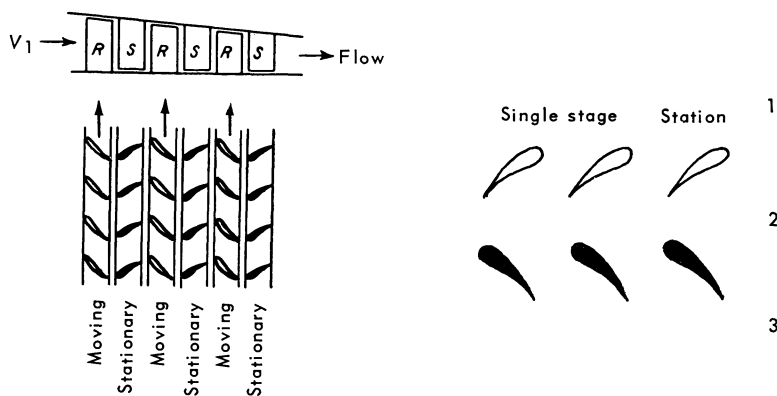
Fig. 3-1

V = absolute velocity
u = change of tangential velocity component
ω = angular velocity-rad/sec.
W = relative velocity

Subscripts

t = tangential
a = axial
o = average velocity

r = radius

ρ = density #/Ft^3

L = Lift

D = Drag

C_L = lift coefficient = $L/(\rho V^2/2)$

C_D = drag coefficient = $D/(\rho V^2/2)$

β = angle between average relative velocity (W_0) or average absolute velocity (V_0) and tangential direction

α = angle of attack measured between chord and incoming stream

W_0 = average relative velocity = $(W_{1a} + W_{2a})/2$

V_0 = average absolute velocity = $(V_{1a} + V_{2a})/2$

$\tan \epsilon$ = D/L

A = axial force

T = tangential force

σ = solidity = chord/spacing = c/s

c = blade chord

p = static pressure

s = blade spacing

B = number of blades

t = temperature

η_b = blade element efficiency

ϕ = angle between axial direction and W_1 direction (stagger angle)

[3-2] COMPRESSIBLE FLOW ANALYSIS

A typical stage of an axial flow compressor which consists of multi-stage bladed annulus is shown in Fig. 3-2.
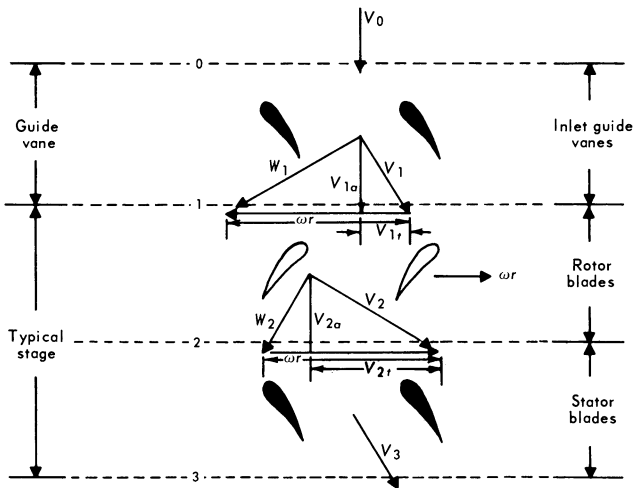
Fig. 3-2
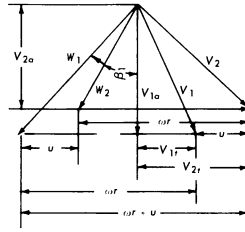
Fig. 3-3

For compressible flow across the guide vanes, Eq. (1-63) gives

$$\frac{V_0{}^2}{2\,gJ} + h_0 = \frac{V_1{}^2}{2\,gJ} + h_1. \tag{3-1}$$

For compressible flow across the rotor blades, one may again apply Eq. (1-63) when relative velocities W_1 and W_2 are used. (Treat the rotating blades as if they were stationary by using relative velocities W_1 and W_2 instead of absolute velocities V_1 and V_2.)

$$\frac{W_1{}^2}{2\,gJ} + h_1 = \frac{W_2{}^2}{2\,gJ} + h_2 \tag{3-2}$$

From the geometry of the velocity diagram, Fig. 3-3, one obtains:

$$h_2 - h_1 = \frac{W_1{}^2 - W_2{}^2}{2\,gJ} = \frac{1}{2\,gJ}\left[V_{1a}{}^2 + (\omega r - V_{1t})^2 - V_{2a}{}^2 - (\omega r - V_{2t})^2\right]. \tag{3-3}$$

The absolute values of total enthalpy "before" and "after" the rotor blades are, respectively, H_1 and H_2.

$$H_1 = h_1 + \frac{V_1{}^2}{2\,gJ} \tag{3-4}$$

$$H_2 = h_2 + \frac{V_2{}^2}{2\,gJ} \tag{3-5}$$

Therefore, the total enthalpy increase across the rotor blades is

$$H_2 - H_1 = h_2 + \frac{V_2{}^2}{2\,gJ} - h_1 - \frac{V_1{}^2}{2\,gJ}$$

$$= h_2 - h_1 + \frac{V_{2t}{}^2 + V_{2a}{}^2}{2\,gJ} - \frac{V_{1t}{}^2 + V_{1a}{}^2}{2\,gJ}$$

$$= \frac{1}{2\,gJ}\left[V_{1a}{}^2 + (\omega r)^2 - 2\omega r V_{1t} + V_{1t}{}^2 - V_{2a} - (\omega r)^2 + 2\omega r V_{2t}\right.$$

$$\left. - V_{2t}{}^2 + V_{2t}{}^2 + V_{2a}{}^2 - V_{1t}{}^2 - V_{1a}{}^2\right]$$

$$= \frac{1}{2\,gJ}\,(2\,u\omega r) = \frac{1}{gJ}\,u\omega r.$$

$$(3\text{-}6)$$

Here $u = (V_{2t} - V_{1t})$; see Fig. 3-3.

Equation (3-6) is the Euler's equation for compressors and turbines. It says that the total enthalpy increase (total energy increase) is equal to the rotating speed ωr times the change of tangential component u. Assume constant specific heats are valid for each stage, and Eq. (3-6) becomes

$$c_p(T_2 - T_1) = \frac{1}{gJ}\,u\omega r$$

or

$$\left(\frac{T_2}{T_1}\right) = \left(\frac{P_2}{P_1}\right)^{\frac{k-1}{k}} = 1 + \left(\frac{1}{gJc_p\,T_1}\right)u\omega r \qquad (3\text{-}7)$$

or

$$\frac{P_2 - P_1}{P_1} = \left[1 + \frac{1}{gJc_p\,T_1}\,u\omega r\right]^{\frac{k}{k-1}} - 1. \qquad (3\text{-}8)$$

If, for incompressible flow, $k = \infty$, $k/(k-1) = 1$, $R/c_p = (k-1)/k = 1$, Eq. (3-8) reduces to

$$P_2 - P_1 = \frac{1}{g}\,\rho u\omega r. \qquad (3\text{-}8a)$$

Equation (3-8) gives the pressure rise through a stage by compressible equation, while Eq. (3-8a) gives the pressure rise through a stage by incompressible flow equation.

[3-2.1] Radial Equilibrium

Figure 3-4 shows the flow along the radial direction and its corresponding radial equilibrium condition.
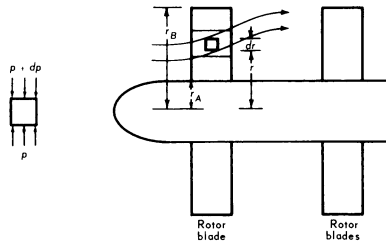
Fig. 3-4

For radial equilibrium, dp must be balanced by the centrifugal force $[(\rho/g)\,dr]\,\omega^2 r$. Therefore we have

$$dp = \left(\frac{\rho}{g}\,dr\right)\omega^2 r = \left(\frac{\rho}{g}\,dr\right)\frac{V_t^2}{r} \qquad (3\text{-}9)$$

or

$$\frac{dp}{dr} = \frac{\rho}{g}\frac{V_t^2}{r}. \qquad (3\text{-}10)$$

Equation (3-10) is the radial equilibrium condition which must be satisfied by fluid element. Now let us take a look at enthalpy change along the radial direction. Differentiating Eq. (3-6) with respect to r, one obtains:

$$\frac{1}{2}\frac{d}{dr}\left(2gJh_2 - 2gJh_1 + V_{2t}^2 + V_{2a}^2 - V_{1t}^2 - V_{1a}^2\right) = \frac{d}{dr}u\omega r$$

$$(3\text{-}11)$$

since

$$dh = c_p dt = \frac{c_p}{R} d\left(\frac{p}{\rho}\right) = \frac{c_p}{(c_p - c_v)J} d\left[p\left(\frac{c}{p}\right)^{1/k}\right]$$

$$\left(\text{here } \frac{p}{\rho^k} = c\right)$$

$$= \frac{1}{J}\left(\frac{k}{k-1}\right)(c)^{\frac{1}{k}} d\, p^{\frac{k-1}{k}} = \frac{1}{J}\left(\frac{k}{k-1}\right)\left(\frac{k-1}{k}\right)\frac{c^{1/k}}{p^{1/k}}\, dp$$

$$= \frac{1}{J\rho}\, dp. \tag{3-12}$$

Substituting Eq. (3-10) into (3-12), one obtains:

$$\frac{dh}{dr} = \frac{1}{Jg}\frac{V_t^2}{r}. \tag{3-13}$$

Substituting Eq. (3-13) into (3-11) and integrating from radius r_A to radius r_B, one obtains:

$$\int_{r_A}^{r_B} \frac{V_{2t}^2}{r}\, dr - \int_{r_A}^{r_B} \frac{V_{1t}^2}{r}\, dr + \int_{r_A}^{r_B} V_{2t}\, dV_{2t} + \int_{r_A}^{r_B} V_{2a}\, dV_{2a}$$

$$- \int_{r_A}^{r_B} V_{1t}\, dV_{1t} - \int_{r_A}^{r_B} V_{1a}\, dV_{1a} = \int_{r_A}^{r_B} d(u\omega r) = \int_{r_A}^{r_B} d(V_{2t} - V_{1t})\omega r \tag{3-14}$$

Referring to Fig. 3-5, one may write the following integration approximately as

$$\int_{r_A}^{r_B} \frac{V_{2t}^2}{r}\, dr = \text{shaded area in Fig. 3-5}$$

$$= \left\{ \frac{\dfrac{V_{2t_A}^2}{r_A} + \dfrac{V_{2t_B}^2}{r_B}}{2} \right\} (r_B - r_A) \tag{3-15}$$
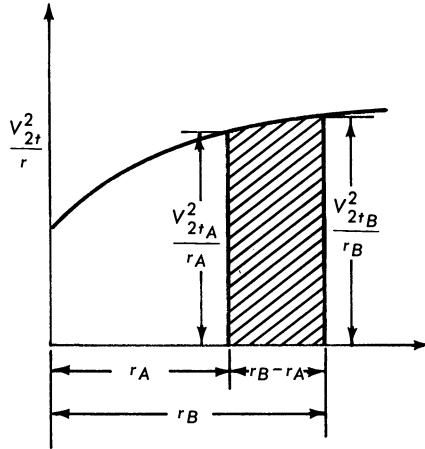
Fig. 3-5

With the approximation of Eq. (3-15), we may write Eq. (3-14) into

$$\frac{1}{2}\left(\frac{V_{2t_A}^2}{r_A} + \frac{V_{2t_B}^2}{r_B}\right)(r_B - r_A) - \frac{1}{2}\left(\frac{V_{1t_A}^2}{r_A} - \frac{V_{1t_B}^2}{r_B}\right)(r_B - r_A)$$

$$+ \frac{1}{2}V_{2t_B}^2 - \frac{1}{2}V_{2t_A}^2 + \frac{1}{2}V_{2a_B}^2 - \frac{1}{2}V_{2a_A}^2 - \frac{1}{2}V_{1t_B}^2 + \frac{1}{2}V_{1t_A}^2$$

$$- \frac{1}{2}V_{1a_B}^2 + \frac{1}{2}V_{1a_A}^2 = \left(V_{2t_B} - V_{1t_B}\right)\omega r_B - \left(V_{2t_A} - V_{1t_A}\right)\omega r_A.$$

$$(3\text{-}16)$$

We may rewrite Eq. (3-16) into

$$\frac{1}{2}V_{2t_A}^2\left(\frac{r_B}{r_A} - 1\right) - \frac{1}{2}V_{1t_A}^2\left(\frac{r_B}{r_A} - 1\right) - \frac{1}{2}V_{2a_A}^2 - \frac{1}{2}V_{2t_A}^2$$

$$+ \frac{1}{2}V_{1t_A}^2 + \frac{1}{2}V_{1a_A}^2 + \omega r_A\left(V_{2t_A} - V_{1t_A}\right)$$

$$= \frac{1}{2}V_{2t_B}^2\left(\frac{r_A}{r_B} - 1\right) - \frac{1}{2}V_{1t_B}^2\left(\frac{r_A}{r_B} - 1\right) - \frac{1}{2}V_{2t_B}^2 - \frac{1}{2}V_{2a_B}^2$$

$$+ \frac{1}{2}V_{1t_B}^2 + \frac{1}{2}V_{1a_B}^2 + \omega r_B\left(V_{2t_B} - V_{1t_B}\right).$$

$$(3\text{-}17)$$

Let F indicate the function at the left- or right-hand side of Eq. (3-17), and one can see immediately that

$$F_A = F_B.$$ (3-17a)

Equation (3-17a) indicates that for radial equilibrium condition F_A must be equal to F_B while points A and B are two points along the radial direction (while points 1 and 2 indicate the point before and after the rotor blades). Equation (3-17) is the same for both compressible or incompressible radial equilibrium analysis.

[3-2.2] Continuity Equation

The compressible continuity equation requires

$$\int_{r_{\text{hub}}}^{r_{\text{tip}}} \rho_2 V_{2a}\, 2\pi r dr = \int_{r_{\text{hub}}}^{r_{\text{tip}}} \rho_1 V_{1a}\, 2\pi r dr.$$ (3-18)

For incompressible flow, Eq. (3-18) simplifies to

$$\int_{r_{\text{hub}}}^{r_{\text{tip}}} V_{2a}\, dr^2 = \int_{r_{\text{hub}}}^{r_{\text{tip}}} V_{1a}\, dr^2.$$ (3-18a)

[3-2.3] Density Relationship

For constant specific heats, Eq. (3-3) may be rewritten as

$$c_p(t_2 - t_1) = \frac{1}{2\,gJ}\left[2u\omega r + V_{1a}^2 + V_{1t}^2 - V_{2a}^2 - V_{2t}^2\right]$$ (3-19)

$$\left(\frac{t_2}{t_1}\right) = 1 + \left(\frac{1}{2\,gJc_p t_1}\right)\left[2u\omega r + V_{1a}^2 + V_{1t}^2 - V_{2a}^2 - V_{2t}^2\right].$$ (3-20)

For isentropic or polytropic relationships, one obtains:

$$\left(\frac{t_2}{t_1}\right) = \left(\frac{p_2}{p_1}\right)^{\frac{k-1}{k}} = \left(\frac{\rho_2}{\rho_1}\right)^{k-1}$$

$$= 1 + \left(\frac{1}{2\,gJc_p t_1}\right)\left[2u\omega r + V_{1a}^2 + V_{1t}^2 - V_{2a}^2 - V_{2t}^2\right]$$ (3-20a)

or

$$\left(\frac{t_2}{t_1}\right) = \left(\frac{p_2}{p_1}\right)^{\frac{n-1}{n}} = \left(\frac{\rho_2}{\rho_1}\right)^{n-1}$$

$$= 1 + \left(\frac{1}{2\,gJc_p\,t_1}\right)\left[2\,u\omega r + V_{1a}^2 + V_{1t}^2 - V_{2a}^2 - V_{2t}^2\right].$$

(3-20b)

[3-2.4] Method of Calculation

1. Divide the blade into five sections, namely, a, b, c, d, e, as shown in Fig. 3-6.
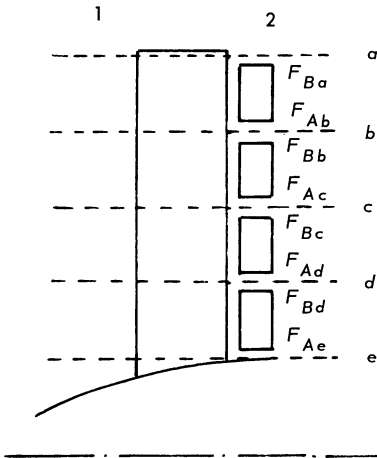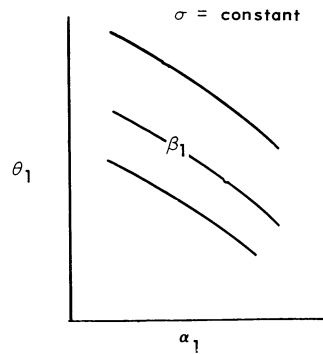
Fig. 3-6   Fig. 3-7

2. At each section, draw the blade velocity diagram as shown for the middle section c of Fig. 3-6.
3. At each section write down the airfoil section number (such as NACA airfoil four-digit series section), blade angle ϕ, blade chord c, blade solidity σ, blade radial location r, blade spacing s.
4. Assuming (for each section) five values of V_{2a} (such as $V_{2a} = V_{1a} - 50$, $V_{1a} - 100$, V_{1a}, $V_{1a} + 50$, $V_{1a} + 100$ Calculate β_1 by

$$\tan\beta_1 = \frac{(\omega r - V_{1t})}{V_{1a}}.$$

(3-21)
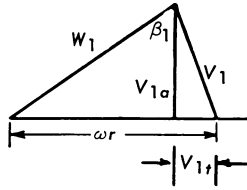
5. Calculate α_1 by

$$\alpha_1 = \phi + \beta_1 - 90°. \tag{3-22}$$
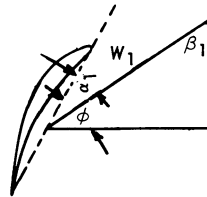
6. From $\beta_1, \alpha_1, \sigma$ airfoil section and its wind tunnel cascade characteristics, read the turning angle θ_1 (cascade characteristics are usually presented in NACA data as functions of β_1, α_1, and σ for the airfoil section concerned) as shown in Fig. 3-7.

7. Calculate V_{2t} by $V_{2t} = \omega r - V_{2a} \tan(\beta_1 - \theta_1)$. $\tag{3-23}$

8. Calculate V_2 by $V_2 = \sqrt{V_{2a}{}^2 + V_{2t}{}^2}$. $\tag{3-24}$

9. Calculate the values of F_A and F_B for each value of the five values assumed at each section for V_{2a} (calculate the left-hand side F_A and the right-hand side F_B of Eq. (3-17) separately) according to Eqs. (3-25) and (3-26):

$$F_A = \frac{1}{2} V_{2t_A}{}^2 \left(\frac{r_B}{r_A} - 1 \right) - \frac{1}{2} V_{1t_A}{}^2 \left(\frac{r_B}{r_A} - 1 \right) - \frac{1}{2} V_{2t_A}{}^2 - \frac{1}{2} V_{2a_A}{}^2$$

$$+ \frac{1}{2} V_{1t_A}{}^2 + \frac{1}{2} V_{1a_A}{}^2 + \omega r_A \left(V_{2t_A} - V_{1t_A} \right)$$

$$\tag{3-25}$$

$$F_B = \frac{1}{2} V_{2t_B}{}^2 \left(\frac{r_A}{r_B} - 1 \right) - \frac{1}{2} V_{1t_B}{}^2 \left(\frac{r_A}{r_B} - 1 \right) - \frac{1}{2} V_{2t_B}{}^2 - \frac{1}{2} V_{2a_B}{}^2$$

$$+ \frac{1}{2} V_{1t_B}{}^2 + \frac{1}{2} V_{1a_B}{}^2 + \omega r_B \left(V_{2t_B} - V_{1t_B} \right)$$

$$\tag{3-26}$$

10. Plot F_A and F_B versus five assumed values of V_{2a} for each section (*a, b, c, d, e*) of the five blade sections as shown in Fig. 3–8.
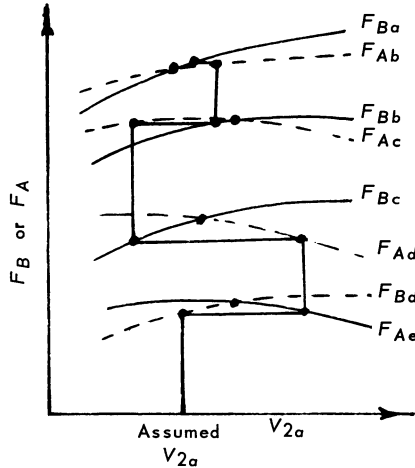
Fig. 3 -8

Since F_A must be equal to F_B for radial equilibrium, we must always satisfy the following chain solutions. Assume a value of V_{2a} at the hub section (section *e*) as shown by the straight lines in Fig. 3–8. This assumed value of V_{2a} at section *e* determines a chain of relations of V_{2a} at sections *d, c, b* and *a* (because at each section F_A must be equal to F_B as shown by the straight lines). This requirement determines V_{2a} variation along the radius from r_{hub} to r_{tip} for the assumed value of V_{2a} at the hub section. This requirement also gives a chain relation on the velocity diagram (because V_{2a}, in turn, determines the velocity diagram) on each blade section. The velocity diagram, in turn, determines the density ρ_2 according to Eq. (3–20a) or (3–20b). Therefore, for each assumed value of V_{2a} at section *e* (hub section), one determines the complete V_{2a} and ρ_2 variation along the radius direction from hub to tip. With V_{2a} and ρ_2 variation along the radius known (for each value of V_{2a} assumed for section *e*), one may graphically determine the total mass flow term m_2 after the rotor blades

$$m_2 = \int_{r_{hub}}^{r_{tip}} \rho_{2a} V_{2a} 2\pi r dr \qquad (3\text{-}27)$$

which must be equal to the mass flow term m_1 *before* the rotor blades

$$m_1 = \int_{r_{hub}}^{r_{tip}} \rho_{1a} V_{2a} 2\pi r \, dr. \qquad (3\text{-}28)$$

If m_2 does not check with m_1 which is known through graphic integration of Eq. (3-28), one must assume other values for V_{2a} at section e (hub section) until m_2 checks with m_1. When $m_2 = m_1$, the assumed value of V_{2a} and, therefore, its variations along the radii, are the corrected answers.

11. Once the right value of V_{2a} along the radii from hub to tip is known, the right velocity diagram at each section, a, b, c, d and e may be drawn. Consequently, the $H_2 - H_1$ at each section, a, b, c, d and e are known from Eq. (3-6).

$$H_2 - H_1 = \frac{1}{gJ} \omega r (V_{2t} - V_{1t}) \tag{3-6}$$

$$\frac{T_2}{T_1} = \left[1 + \frac{1}{gJc_p T_1} (V_{2t} - V_{1t}) \omega r \right] \tag{3-29}$$

$$\frac{P_2}{P_1} = \left[1 + \frac{1}{gJc_p T_1} (V_{2t} - V_{1t}) \omega r \right]^{\frac{k}{k-1}} \tag{3-30}$$

Calculate P_2 at each section a, b, c, d and e. Get p_1 from Eq. (1-78).

$$\frac{P_1}{p_1} = \left[1 + \frac{k-1}{2} \frac{V_1^2}{kgRt_1} \right]^{\frac{k}{k-1}} \tag{3-31}$$

To plot P_2 versus the radius r^2 from r_{hub} to r_{tip}, one may obtain the weighted average value of the pressure rise from hub to tip by graphic integration of

$$(P_2 - P_1)_{\text{ave}} = \frac{\displaystyle\int_{r_{\text{hub}}}^{r_{\text{tip}}} 2\pi r \rho_2 V_{2a} (P_2 - P_1)\, dr}{\displaystyle\int_{r_{\text{hub}}}^{r_{\text{tip}}} 2\pi r \rho_2 V_{2a}\, dr}. \tag{3-32}$$

12. The above analysis gives V_{2a}, V_{2t}, ρ_2, p_2, T_2, H_2, $(P_2 - P_1)$ and local mass flow distribution variation along the blade radius from hub to tip.

[3-3] TURBINE ANALYSIS

The turbine may be looked on as if it were a negative operation of a compressor; therefore, the analysis made in the previous

section applies also to the turbine analysis here. Figure 3-9 shows the velocity diagram of a turbine stage. Notice here that the turning angle of the turbine is usually much larger than that of the compressor. Because of the expansion through the cascade rather than compression through the cascade, the turbine can usually turn up to 150° without causing flow separation, while the flow separates in the compressor cascade if the turning angle is greater than 20° or 30°. This is because the expansion stream tends to fill the cascade passage suppressing separation, while the compression stream aggravates the flow separation. With the large turning angle possible for turbine operation, the expansion ratio is consequently much higher than the compression ratio. Applying the Euler's equation [Eq. (3-6)] to the turbine analysis, we have

$$H_1 - H_2 = \frac{u\omega r}{g}. \tag{3-6}$$

Referring to Fig. 3-9, when $W_1 = W_2$, $p_1 = p_2$, the turbine is called an impulse turbine, in which the velocity diagram is symmetrical and the static pressure is equal at the inlet and exit. The turbine analysis can best be illustrated by an example.

Given: Turbine horsepower = Y
Turbine RPM = N
Turbine gas flow = W lb./sec.
Turbine inlet temperature = $T°$R
Turbine inlet total pressure = P_1 (psi)
Turbine tip speed = n ft./sec.
Turbine inlet flow at pitch radius ϕ degrees with the horizontal

Solution

1. Turbine angular speed ω may be known from

$$\omega = \frac{\pi}{60} N. \tag{3-33}$$

2. Turbine radius r_{tip} may be known from

$$r_{\text{tip}} = \frac{n}{\omega}. \tag{3-34}$$

3. Turbine annular free flow area "$A_1 \sin\phi$" may be obtained from the application of Eq. (1-106a) to the annular area at pitch section as shown in Fig. 3-10.

$$\frac{W\sqrt{T_1}}{P_1(A_1 \sin\phi)} = \sqrt{\frac{kg}{R}} \frac{M_1}{\left[1 + \frac{k-1}{2}M_1^2\right]^{\frac{k+1}{2(k-1)}}}. \tag{3-106a}$$
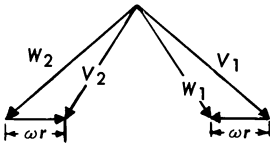
Fig. 3-9
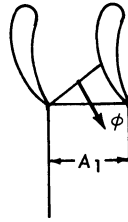
Fig. 3-10
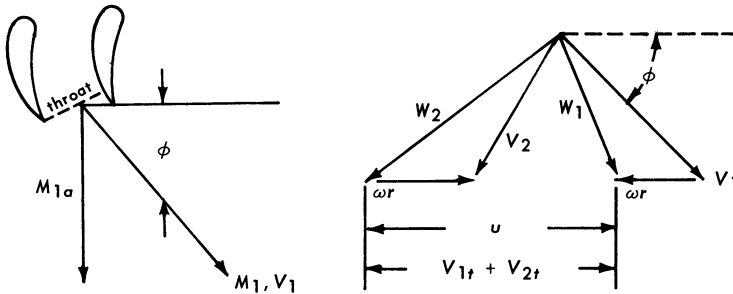
Fig. 3-11

Since the turbine throat is choked, $M_1 = 1$. Therefore, every quantity in Eq. (1-106a) is known except A_1, so A_1 may be solved from Eq. (1-106a).

4. The turbine hub radius r_{hub} may be solved from the following equation:

$$A_1 = \pi\left(r_{\text{tip}}^2 - r_{\text{hub}}^2\right). \qquad (3\text{-}35)$$

5. The turbine-required enthalpy drop $(H_1 - H_2)$ may be obtained from

$$(H_1 - H_2)\frac{778}{550}W = Y. \qquad (3\text{-}36)$$

Here W and Y are given. Therefore, $H_1 - H_2$ may be solved.

6. From Eq. (3-6), ur may be solved.

$$H_1 - H_2 = \frac{1}{g}u\omega r \qquad (3\text{-}6)$$

or

$$ur = (H_1 - H_2)\frac{g}{\omega}. \qquad (3\text{-}37)$$

A free vortex turbine is one in which ur is constant at any radii. Consequently, the pressure is constant at any radii and no radial flow results. The radial equilibrium condition derived in the previous section is not needed for the free vortex design of compressors or turbines, and ur is a constant. So u at tip, pitch, and hub may be solved from the known value of ur as follows:

Tip	Pitch	Hub
r_{tip}	r_{pitch}	r_{hub}
u_{tip}	u_{pitch}	u_{hub}

u is defined as the change of the tangential component between the inlet and exit. In the case of the turbine,

$$u = V_{2t} + V_{1t}.$$

(See Fig. 3-9.) We may now construct the velocity diagram at tip, pitch and hub as shown for pitch in Fig. 3-11.

7. With the velocity diagram drawn, the following may be calculated from the geometry of the velocity diagram:

$$W_1 \text{ from vector addition of } V_1 \text{ and } \omega r$$

$$M_{1a} = M_1 \sin \phi$$

$$V_{1a} = M_{1a}\sqrt{kgRt_1}$$

$$W_1 = \sqrt{V_{1a}^2 + (V_{1t} - \omega r)^2} \qquad (3\text{-}38)$$

$$W_2 = \sqrt{V_{2a}^2 + (u + \omega r - V_{1t})^2} \qquad (3\text{-}39)$$

$$V_2 = \sqrt{V_{2a}^2 + (u - V_{1t})^2} \qquad (3\text{-}40)$$

Because of the turbine expansion as shown in Fig. 3-12, V_a may be designed so that V_{2a} is slightly greater than V_{1a}, say, $V_{2a} = V_{1a} + 50$ ft./sec.

Since

$$V_{2t} + V_{1t} = u$$

$$W_{2t} + W_{1t} = u \qquad (3\text{-}41)$$
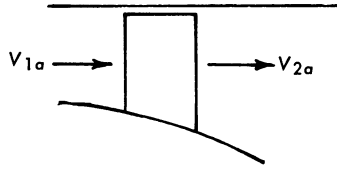
Fig. 3-12

we have

$$(V_{1t}r)_{\text{tip}} = (V_{1t}r)_{\text{pitch}} = (V_{1t}r)_{\text{hub}} \tag{3-42}$$

$$(V_{2t}r)_{\text{tip}} = (V_{2t}r)_{\text{pitch}} = (V_{2t}r)_{\text{hub}} \tag{3-43}$$

$$[(V_{2t} + V_{1t})r]_{\text{tip}} = [(V_{2t} + V_{1t})r]_{\text{pitch}} = [(V_{2t} + V_{1t})r]_{\text{hub}} \tag{3-44}$$

Using the pitch section as an illustrative example, the velocity diagram and *h-s* diagram shown in Fig. 3–13 may be drawn.
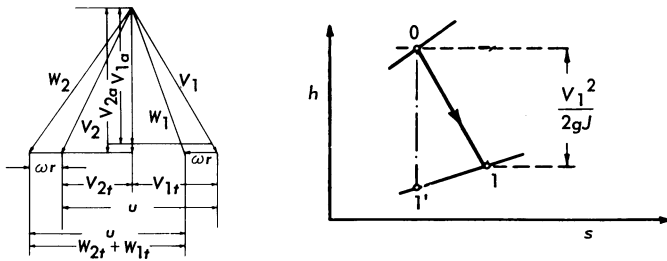
Fig. 3-13

With the velocity diagram, *h-s* diagram, and gas table, the gas properties $P, T, \bar{\rho}$ at each section may be calculated in a manner similar to that used to calculate the nozzle flow in Chapter 1.

Station	T	h	P_r	P
0	T_0	H_0	P_{r_0}	P_0
1´ (stator)	t_1'	h_1'	P_{r_1}'	p_1'
1 (based on absolute velocity V_1)		h_1	.	p_1
1 (based on relative velocity W_1)		h_{1_r}	P_{1_r}	p_1
2 (based on relative velocity W_2)	t_{2r}	h_{2r}		p_2
2´(based on relative velocity W_2)	t_2'	h_{2_r}'	P_{2_r}'	p_2
2 (based on absolute velocity V_2)	t_2	h_2		p_2

Here the prime indicates the fictitious isentropic state of the gas.
From Point 0 to Point 1.

$$H_0 - \frac{V_1^2}{2gJ} = h_1$$

$$\eta_N = \frac{H_0 - h_1}{H_0 - h_1'}$$

$$T_0 = T_1$$

$$H_0 = H_1$$

but

$$P_0 \neq P_1 \quad \text{(because of pressure loss here)}$$

From absolute to relative values

$$h_1 = h_{1r}$$

$$t_1 = t_{1r}$$

$$\frac{P_{r(H1)}}{p_{r(h1)}} = \frac{P_{(H1)}}{p_{(h1)}}$$

$$H_{1r} = h_{1r} + \frac{W_1^2}{2gJ} = h_1 + \frac{W_1^2}{2gJ}$$

$$H_{2r} = h_{2r} + \frac{W_2^2}{2gJ} = h_2 + \frac{W_2^2}{2gJ}$$

$$H_{1r} = H_{2r}$$

From relative to absolute values

$$H_2 = h_2 + \frac{V_2^2}{2gJ}$$

$$h_{2r} = h_2$$

$$t_{2r} = t_2$$

$$p_{2r} = p_2 = p_2'$$

Turbine expansion

$$\frac{P_2}{P_0} = \frac{P_{r(2')}}{P_{r(0)}}$$

Turbine efficiency

$$\eta_T = \frac{H_0 - H_2}{H_0 - H_2'}$$

All subscripts r indicate that the quantity is based on relative velocity W instead of absolute velocity V except P_r indicates relative pressure used conventionally in the gas table of Keenan and Kaye.

For two or three stages of turbine design, the analysis is the same as the one-stage design illustrated above. No repetition will be given here.

[3-4] APPENDIX: TWO-DIMENSIONAL INCOMPRESSIBLE COMPRESSOR DESIGN

Analysis of an Axial-flow Compressor Stage. Assumptions:

1. The density of the gas is constant throughout the stage. ρ = constant.
2. The axial velocity is constant throughout the stage. V_a = constant.
3. The gas velocities at entrance and exit of the stage are identical. $V_1 = V_3$.
4. There are no radial components of velocity in the stage.
5. Losses are due to profile drag only. Losses due to clearance leakage and to secondary flows are neglected.

Vector Diagrams. Figure 3-14 shows the blades of the rotor and stator developed on a cylinder of radius r. Figure 3-15 shows the velocity diagram for the blade-elements at the radius r. From assumption 3 it follows that $V_1 = V_3$. From assumption 2 it follows that $V_{1a} = V_{2a} = V_{3a} = V_a$. The geometry of the vector diagram indicates that $V_{2t} - V_{1t} = W_{2t} - W_{1t}$. The velocity W_r is the mean velocity of approach to the rotor blade; the tangential component of W_r is defined as the mean value between the tangential components of W_1 and W_2, respectively. The velocity V_s is the mean velocity of approach to the stator blade; the tangential component of V_s is the mean value between the tangential components of V_2 and V_3, respectively.

Figure 3-16 shows the forces acting on an element of the rotor blade of infinitesimal length dr. A similar diagram may be constructed for an element of the stator blade.
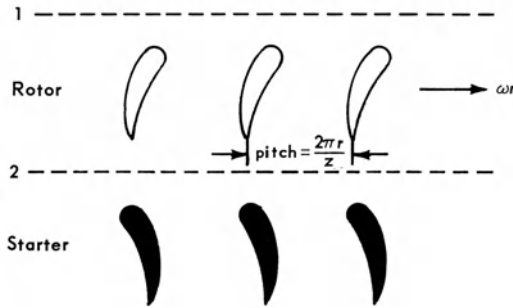
Fig. 3-14 Development of rotor and stator blades at radius r; t = chord; r = radius of blade element; z = number of blades; ω = angular velocity; σ = solidity ratio = chord/pitch = $t/(2\pi r/z) = tz/2\pi r$; subscript r refers to rotor; subscript s refers to stator.
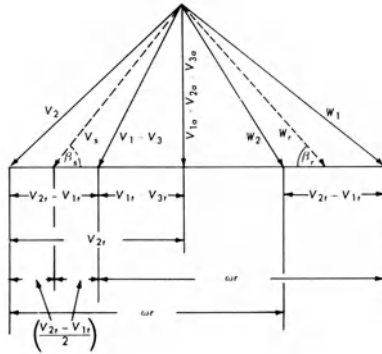
Fig. 3-15 Velocity-vector diagram for rotor and stator blades at radius r; V = velocity relative to stator or absolute velocity; W = velocity relative to rotor; subscript a refers to axial component of velocity; subscript t refers to tangential component of velocity; β is measured with respect to direction of motion of rotor blades.
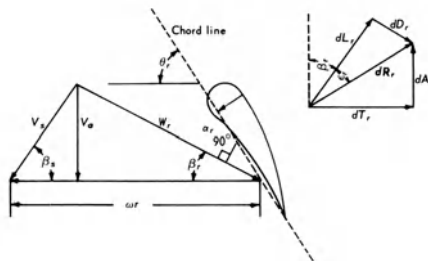
Fig. 3-16 Force-vector diagram for element of rotor blade of length dr; α = angle of attack; θ = blade-setting angle = $\alpha + \beta$; L = lift force; D = drag force; A = axial component of force on blade; T = tangential component of force on blade; $\epsilon = \tan^{-1}(D/L)$.

Analysis of Rotor. The subscript r is omitted from the symbols in this section with the understanding that all quantities refer to the rotor. The force-vector diagram of Fig. 3-16 indicates that

$$dT = dL \sin\beta + dD \cos\beta \qquad (3\text{-}45)$$

and

$$dA = dL \cos\beta - dD \sin\beta \qquad (3\text{-}46)$$

By definition, $\tan\epsilon = D/L$, and, since ϵ is usually much less than 0.1, we may write

$$\epsilon \simeq \frac{dD}{dL} \qquad (3\text{-}47)$$

Equations (3-45) and (3-46) may then be rearranged as follows:

$$dT = dL \sin\beta \left[1 + \left(\frac{\epsilon}{\tan\beta}\right)\right] \qquad (3\text{-}48)$$

and

$$dA = dL \cos\beta [1 - \epsilon \tan\beta] . \qquad (3\text{-}49)$$

The lift dL may be expressed in terms of the lift coefficient C_L as follows:

$$dL = C_L \frac{\rho}{2g_0} W_r^2 t\, dr. \qquad (3\text{-}50)$$

Application of the momentum equation in the axial direction to the flow through a control surface bounded by sections 1 and 2 and by cylinders of radii r and $(r + dr)$ results in the expression

$$Z dA = (p_2 - p_1)(2\pi r dr). \qquad (3\text{-}51)$$

After substitution of (3-49) and (3-50) into (3-51), we obtain

$$p_2 - p_1 = \sigma C_L \frac{\rho}{2g_0} W_r^2 \cos\beta (1 - \epsilon \tan\beta) \qquad (3\text{-}52)$$

where $\sigma = tZ/2\pi r$ and represents the "solidity" of the blading or the ratio of chord to pitch.

Application of the equation for angular momentum to the flow passing through the same control surface described above results in the expression

$$\frac{\rho V_a 2\pi r \, dr}{g} r(V_{2t} - V_{1t}) = Zr \, dT. \tag{3-53}$$

After substituting (3-48) and (3-50) into (3-53), we obtain

$$V_{2t} - V_{1t} = \frac{\sigma C_L}{2} \frac{W_r^2}{V_a} \sin\beta \left(1 + \frac{\epsilon}{\tan\beta}\right). \tag{3-54}$$

Now $$V_a = W_r \sin\beta$$

so that we may write

$$V_{2t} - V_{1t} = \frac{\sigma C_L}{2} W_r \left(1 + \frac{\epsilon}{\tan\beta}\right). \tag{3-55}$$

Analysis of Stator. Equations (3-45) through (3-55) apply to the stator as well as to the rotor, substituting V_s for W_r and employing the subscript s instead of the subscript r. Since there is no net change in tangential velocity between the entrance and exit of the stage, *i.e.*,

$$V_{2t} - V_{1t} = V_{2t} - V_{3t}$$

it follows from (3-55) that

$$\sigma_r C_{Lr} W_r \left(1 + \frac{\epsilon_r}{\tan\beta_r}\right) = \sigma_s C_{Ls} V_s \left(1 + \frac{\epsilon_s}{\tan\beta_s}\right). \tag{3-56}$$

Through a comparison of (3-56) with (3-52), we may derive the ratio of the pressure rise in the rotor to that in the stator. Neglecting the terms containing ϵ, we obtain

$$\frac{p_2 - p_1}{p_3 - p_2} \simeq \frac{\tan\beta_s}{\tan\beta_r}. \tag{3-57}$$

Thus, to obtain equal static-pressure rises in the rotor and stator, it is necessary to have a velocity diagram which is approximately symmetrical. With a nearly symmetrical diagram, $W_r = V_s$ and (3-56) indicates that the product of σC_L must be approximately the same for both rotor and stator.

Work and Power Input. The amount of power input to the rotor-blade elements between r and $(r + dr)$ is given by the expression

$$dP = Z_r r\omega \, dT_r \tag{3-58}$$

Introducing Eqs. (3-48) and (3-50), we obtain for dP the relation

$$dP = 2\pi\omega\,\sigma_r\,C_{Lr}\,\frac{\rho}{2g_0}\,W_r^2\,\sin\beta_r\left(1 + \frac{\epsilon_r}{\tan\beta_r}\right)r^2\,dr. \qquad (3\text{-}59)$$

Integration of (3-59) between the hub radius and casing radius gives the total shaft power supplied to the rotor.

The shaft work per unit mass of gas is given by

$$W_x = \frac{dP}{dw} = \frac{dP}{2\pi r\,V_a\,\rho\,dr}.$$

Substitution into this of (3-58) and (3-53) results in the expression

$$W_x = \frac{\omega r(V_{2t} - V_{1t})}{g}. \qquad (3\text{-}60)$$

If we assume no heat transfer between the gas and the compressor, we may equate W_x to the increase inenthalpy for the stage. Thus,

$$W_x = \Delta h = c_p\,\Delta T.$$

If the fluid is a perfect gas, the temperature rise for the stage is given by

$$T_3 - T_1 = \frac{\omega r(V_{2t} - V_{1t})}{J g C_p} \qquad (3\text{-}61)$$

where C_p is the average specific heat at constant pressure over the temperature range in question.

Efficiency. The blade-element efficiency for the stage η_b is defined as the ratio of the isentropic rise of enthalpy to the shaft work input for the rotor and stator elements of length dr, namely,

$$\eta_b = \frac{\Delta h_s}{W_x}.$$

From the thermodynamic relation, $Tds = dh - vdp$, it is evident that the efficiency equation becomes, for an incompressible fluid,

$$\eta_b = \frac{p_3 - p_1}{\rho W_x}. \qquad (3\text{-}62)$$

The efficiency of the entire stage η_s is defined as the ratio of the isentropic increase of enthalpy-flux to the power input, namely,

$$\eta_s = \frac{2\pi V_a \int (p_3 - p_1) r\, dr}{\rho \int dP} \qquad (3\text{-}63)$$

where the numerator is integrated between the hub and casing radii and $\int dP$ is found from (3-59).

Symmetrical Velocity Diagram. We shall assume now that at a particular radius the velocity diagram of Fig. 3-15 is symmetrical and that the rotor and stator blades at this section have the same profile and operate with the same values of σC_L and ϵ.
  Then $W_r = V_s$, and $\beta_r = \beta_s = \beta$.
  Also,

$$\tan \beta = \frac{2V_a}{\omega r}. \qquad (3\text{-}64)$$

It is evident from (3-55) that the conditions imposed above, *i.e.,* the same values of σ, C_L, W, ϵ and β for both rotor and stator elements, are compatible with the condition that there shall be no net change in tangential velocity for the stage. Also, it follows from (3-52) that the static-pressure rise in the rotor is identical with that in the stator.
  Equation (3-62) may now be rewritten as follows:

$$\eta_b \simeq 2\, \frac{p_2 - p_1}{\rho W_x}.$$

This expression, after substitution of (3-52), (3-60) and (3-55), may be written in the form

$$\rho_b \simeq \frac{1 - \epsilon \tan \beta}{1 + (\epsilon / \tan \beta)}. \qquad (3\text{-}65)$$

The maximum of η_b corresponding to a fixed value of ϵ is found by $\partial \eta_b / \partial (\tan \beta) = 0$. For the maximum efficiency, η_b^*, we get

$$\eta_b^* \simeq \frac{1 - \epsilon}{1 + \epsilon}. \qquad (3\text{-}66)$$

The corresponding value of β^* is given by
$$\tan \beta^* \simeq 1 - \epsilon. \qquad (3\text{-}67)$$

Preliminary design of axial-flow compressor under the follow-ing design conditions: pressure ratio = 4; flow rate = 64 lb./sec. of air; inlet temperature = 520 R; inlet pressure = 14.7 Psia. Design of the entire compressor at pitch radius. Assumptions:

1. A set of guide vanes forward of the first-stage rotor induces the proper amount of pre-rotation. The guide vanes are frictionless.
2. The stream leaving the last stage rotor is straightened and diffused to an axial velocity of 200 ft./sec. with an isentropic diffusion.
3. The velocity diagram for each stage is symmetrical at the pitch radius with a ratio of axial-to-wheel velocities of 0.5.
4. The pitch radius is the same for each stage.
5. The axial velocity is constant throughout the entire com-pressor.
6. The air velocities at entrance and exit of each stage are identical.
7. In calculating blade forces, the flow in each stage is treated as incompressible, with a density corresponding to the arithmetic means of the end pressures and temperatures for the stage.
8. The Mach number at the pitch radius of the first-stage rotor is 0.5 based on the mean velocity relative to the first-stage rotor and on the sound velocity corresponding to the undisturbed air entering the compressor. (This sound velocity is almost identical with the stagnation sound velocity corresponding to the mean rela-tive velocity.)
9. All stages have a solidity ratio (σ = chord/pitch) of 1 at the pitch radius.
10. All stages employ the NACA 2409-34 airfoil (refer to NACA Technical Report No. 492). The characteristics are chosen at an average Mach number of 0.4. A lift coefficient of 0.60 is used, corresponding to an angle of attack of 3.7° and a drag-lift ratio of 0.029.
11. The hub-casing diameter ratio at the entrance to the first-stage rotor is 0.75.

Calculation Procedure:
*1. Calculate the mean relative velocity W_r for the first rotor.
*2. Calculate the axial velocity V_a, wheel velocity ωr, tangential velocities V_{1t} and V_{2t}, and the velocities V_1 and V_2 for the first stage.
*3. Find the angle β_g at which the entrance guide vanes are to be set.
4. Compute the pressure and temperature upstream of the first rotor based on an isentropic expansion in the guide vanes. Treat the air as compressible for this process.
*5. Find the blade height and pitch diameter at the entrance to the first rotor, assuming that conditions at the pitch diameter

represent average conditions over the annulus. Calculate the rpm of the rotor.

6. Calculate the temperature rise $T_3 - T_1$ for the first stage.

7. Derive an expression for the pressure rise in any stage of the form

$$\frac{p_3}{p_1} = \frac{1 + (K/2)}{1 - (K/2)}$$

where K depends only on the average temperature for the stage. In forming this expression, note that σ, C_L, ϵ, and the mean velocities relative to the blades are the same not only for the rotor and stator of each stage but have identical values for all stages.

8. Find the value of K for the first stage. Calculate the pressure rise and the final pressure for the first stage.

*9. Compute the efficiency of the first stage based on conditions at the pitch diameter.

10. Repeat steps 1 to 8 for the second, third, ..., stages, performing the calculations in tabular form. Proceed until the final pressure is such that the pressured at the exit of the diffuser corresponds to an overall pressure ratio for the compressor of at least 4.

*11. Find the pressure and temperature at the diffuser exit and the cross-sectional area (ft.^{2}) of the exit duct for the compressor. Treat the air as compressible in analyzing the diffusion process.

*12. Find the over-all efficiency (Δh isentropic/Δh) of the portion of the compressor comprising rotor and stator elements.

13. Find the total shaft work (by summation of stage works).

*14. Calculate the over-all efficiency of the entire compressor based on the definition

$$\eta = \frac{\Delta h_{\text{isentropic}} + \left(V_f^2/2g\right)}{W_x}.$$

15. *Results:* (a) Tabulate for the entrance to each rotor the temperature (F abs.), pressure (psia), and radial height (inches). Present the same quantities for the exit of the last stator. (b) Summarize the values of all results for the items above marked with asterisks. Give velocities in ft./sec., temperatures in F abs, pressures in psia, angles in degrees, and lengths in inches.

Detailed design of the first stage. Assumptions:

1. The flow is incompressible, with a density corresponding to the mean density at the pitch radius based on the arithmetic means of the end temperatures and pressures at the pitch radius.

2. The value of $V_t r$ is the same at all radii for each section, *i.e.,* before and after the first rotor and after the first stator.

3. At any radius, the entering and leaving velocities for the stage are identical.

4. The same profile and same values of C_L, ϵ and σ are used at all radii.

6. There are 60 blades on the first rotor and the same number on the first stator.

Calculation Procedure:

1. Select five equally-spaced radii at which calculations will be made: the inside, outside, and pitch radii for the first rotor, and the two radii midway between the pitch and extreme radii. The following calculations are to be carried out in tabular form for each of these radii.

2. Find the values of V_{1t}, V_{2t}, ωr, W_r, V_s, β_g, β_r, β_s, θ_r, and θ_s.

3. Compute the values of σ_r and σ_s.

4. Calculate the chords t_r and t_s (inches).

5. Find $p_2 - p_1$, $p_3 - p_2$, and $p_3 - p_1$ (psi).

6. Compute the work W_x and the temperature rise $T_3 - T_1$.

7. Calculate the blade-element efficiency η_b.

8. Calculate the stage efficiency η_s.

9. *Results*: (a) Plot the following quantities versus the radius (inches): u_r and V_s (ft./sec.); σ_s and σ_r; t_r and t_s (inches); β_g, θ_r and θ_s (degrees); $p_2 - p_1$, $p_3 - p_2$, and $p_3 - p_1$ (psi) and η_b. (b) Draw velocity diagrams to scale for each of the five radii studied.

[3-4.1] Turning Angle θ as $f(C_L)$ and Derivation of Blade Efficiency η_b
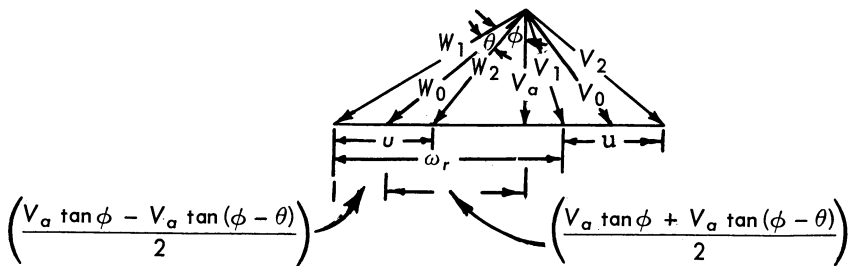
$$\left(\frac{V_a \tan\phi - V_a \tan(\phi - \theta)}{2}\right) \qquad\qquad \left(\frac{V_a \tan\phi + V_a \tan(\phi - \theta)}{2}\right)$$

Fig. 3-17

$$u = V_a \tan\phi - V_a \tan(\phi - \theta)$$

$$u = \frac{1}{2}\sigma C_L W_0 \left(\frac{1 + \epsilon}{\tan\beta}\right)$$

$$[\tan\phi - \tan(\phi - \theta)] = \frac{1}{2}\sigma C_L \frac{W_0}{V_a}\left(\frac{1 + \epsilon}{\tan\beta}\right)$$

$$W_0{}^2 = V_a{}^2 + \left[\frac{V_a \tan \phi - V_a \tan (\phi - \theta)}{2} \right]^2$$

$$\frac{W_0{}^2}{V_a{}^2} = 1 + \left[\frac{\tan \phi - \tan (\phi - \theta)}{2} \right]^2$$

$$\frac{W_0}{V_a} = \sqrt{1 + \left[\frac{\tan \phi - \tan (\phi - \theta)}{2} \right]^2}$$

$$\tan (\phi) - \tan (\phi - \theta) = \frac{1}{2} \sigma C_L \sqrt{1 + \left[\frac{\tan \phi - \tan (\phi - \theta)}{2} \right]^2 \left(\frac{1 + \epsilon}{\tan \beta} \right)}$$

$$u = \frac{1}{2} \sigma \epsilon W_0 \left(1 + \frac{2}{\tan \beta} \right)$$

$$\tan \beta - \frac{V_a}{[V_a \tan \phi + V_a \tan (\phi - \theta)]/2} = \frac{2}{\tan \phi + \tan (\phi - \theta)}$$

$$\sigma C_L = \frac{2[\tan \phi - \tan (\phi - \theta)]}{\sqrt{1 + \left[\frac{\tan \phi + \tan (\phi - \theta)}{2} \right]^2} (1 + \epsilon) \frac{[\tan \phi + \tan (\phi - \theta)]}{2}}$$

$$P_3 = p_3 + \frac{\rho V_3{}^2}{2g} \qquad \text{and} \qquad P_1 = p_1 + \frac{\rho V_1{}^2}{2g}$$

$$\text{if} \quad V_1 = V_3 \qquad P_3 - P_1 = p_3 - p_1$$

$$p_2 - p_1 = \frac{1}{2} \frac{\rho}{g} \sigma_r C_{L_r} W_0{}^2 \cos \beta_r (1 - \epsilon_r \tan \beta_r)$$

$$P_1 = p_1 + \frac{\rho V_1{}^2}{2g}$$

$$P_2 = p_2 + \frac{1}{2} \frac{\rho}{g} V_2{}^2$$

$$P_2 - P_1 = p_2 - p_1 + \frac{\rho}{2g} \left[V_2{}^2 - V_1{}^2 \right]$$

The stator acts as a diffuser to yield static pressure rise:

$$P_2 - P_1 = \frac{1}{2} \frac{\rho}{g} \sigma_r C_{L_r} W_0{}^2 \cos \beta_r (1 - \epsilon_r \tan \beta_r) + \frac{\rho}{2g} \left(V_2{}^2 - V_1{}^2 \right)$$

$$u = (V_{2t} - V_{1t}) = \frac{1}{2} \sigma_r C_{Lr} W_0 \left(1 + \frac{\epsilon_r}{\tan \beta_r}\right)$$

$$P_2 - P_1 = \frac{\rho}{g} u W_0 \cos \beta_r \left[\frac{1}{1 + (\epsilon_r/\tan \beta_r)}\right](1 - \epsilon_r \tan \beta_r)$$
$$+ \frac{\rho}{2g} \left(V_a{}^2 + V_{2t}{}^2 - V_a{}^2 - V_{1t}{}^2\right)$$

$$P_2 - P_1 = \frac{\rho}{g} \left\{ u \frac{(1 - \epsilon_r \tan \beta_r)}{[1 + (\epsilon_r/\tan \beta_r)]} W_0 \cos \beta_r + \frac{1}{2} \left(V_{2t}{}^2 - V_{1t}{}^2\right) \right\}$$

$$= \frac{\rho}{g} \left\{ u \left[\frac{1 - \epsilon_r \tan \beta_r}{1 + (\epsilon_r/\tan \beta_r)}\right] W_0 \cos \beta_r + \frac{1}{2} \left[(V_{1t} + u)^2 - V_{1t}{}^2\right] \right\}$$

$$= \frac{\rho}{g} \left\{ u \left[\frac{1 - \epsilon_r \tan \beta_r}{1 + (\epsilon_r/\tan \beta_r)}\right] W_0 \cos \beta_r + V_{1t} + \frac{u}{2} \right\}$$

$$= \frac{\rho}{g} u\omega r \left\{ \left[\frac{1 - \epsilon_r \tan \beta_r}{1 + (\epsilon_r/\tan \beta_r)}\right] \frac{W_0 \cos \beta_r}{\omega r} + \frac{[V_{1t} + (u/2)]}{\omega r} \right\}$$

Set $u = W_{1t} - W_{2t} = V_{1t} - V_{2t}$

$$\therefore P_2 - P_1 = \frac{\rho}{g} u\omega r \left[\frac{1 - \epsilon_r \tan \beta_r}{1 + (\epsilon_r/\tan \beta_r)}\right] \frac{W_0 \cos \beta_r}{\omega r} + \frac{\omega r - b - (u/2) + (u/2)}{\omega r}$$

$$P_2 - P_1 = \frac{\rho}{g} u\omega r \left\{ \left[\frac{1 - \epsilon_r \tan \beta_r}{1 + (\epsilon_r/\tan \beta_r)}\right] \frac{W_0 \cos \beta_r}{\omega r} + 1 - \frac{W_0 \cos \beta_r}{\omega r} \right\}$$

$$= \frac{\rho}{g} u\omega r \left\{ 1 - \left[1 - \frac{(1 - \epsilon_r \tan \beta_r)}{1 + (\epsilon_r/\tan \beta_r)}\right] \frac{W_0 \cos \beta_r}{\omega r} \right\} \quad \text{with losses}$$

$$P_2 - P_1 = \eta_b \frac{\rho}{g} u\omega r$$

$$\eta_b = \text{blade efficiency}$$

$$= \left\{ 1 - \left[1 - \frac{(1 - \epsilon_r \tan\beta_r)}{1 + (\epsilon_r/\tan\beta_r)} \right] \frac{W_0 \cos\beta_r}{\omega r} \right\}$$

REFERENCES

1. Taylor, E.S.: M.I.T. "Jet Propulsion and Gas Turbine" class-notes.
2. Loh, W.H.T.: UCLA "Jet Propulsion" classnotes.
3. _____ : SMU "Advanced Propulsion Technology" class notes.
4. _____ : TCU "Jet Propulsion and Gas Turbine" classnotes.
5. _____ : "Advanced Lectures on Propulsion Series" given at Convair and Chance Vaught.

Ramjets and Air-Augmented Rockets

Gordon L. Dugger
Supervisor, Hypersonic Propulsion
Applied Physics Laboratory
The Johns Hopkins University

For atmospheric flight at speeds above Mach 3, and even for $M < 3$ for unmanned vehicles, the most promising propulsion systems are ramjets and air-augmented rockets. Many ramjet-powered vehicles have been developed (see, *e.g.*, Refs. 1-3), including a successful experimental turbo-ramjet airplane [4]. Three operational ramjet missiles have been deployed: Talos (still in the United States Fleet), Bomarc, and the British Bloodhound. Air-augmented, solid-propellant rockets are simpler than ramjets and should be as good or better for some applications, and air-augmented liquid rockets offer versatility in thrust/specific-impulse tradeoffs during flight. Still simpler is the "external burning ramjet," which employs combustion over an external surface and could be used for range extension or side forces on simple bodies. For hypersonic propulsion, ramjets with internal supersonic combustion (scramjets) show great promise (see also Chapter 14).

This chapter emphasizes design and performance of ramjets for the Mach 2-6 regime. The first section discusses preliminary performance calculations and typical results for kerosene-fueled and hydrogen-fueled ramjets. The next section covers inlet (diffuser) design in some detail, since it is the inlet that primarily differentiates air-breathing engines from rockets. Combustor and nozzle design are covered more briefly, because combustor design tends to be an art, and nozzles are common to all propulsion systems. Some attention is given to vehicle configuration, *i.e.*, propulsion-airframe requirements. Air-augmented rockets are covered briefly in relation to the ramjet discussion. Finally, some work on external ramjets and scramjets is mentioned.

[4-1] PRELIMINARY PERFORMANCE CALCULATIONS

The "gross thrust" for a ramjet (Fig. 4-1) will be defined by
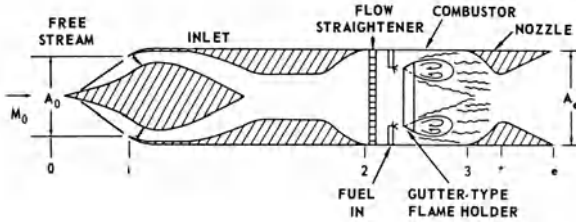
Fig. 4-1 Schematic of a typical supersonic ramjet for a surface-to-air missile.

$$F_g \equiv \mathfrak{I}_e - \mathfrak{I}_0 - P_0(A_e - A_0) = \dot{m}_e V_e + A_e(P_e - P_0) - \dot{m}_0 V_0$$

(4-1)

where $\mathfrak{I}$ is the "stream thrust,"

$$\mathfrak{I} \equiv \dot{m}V + PA = PA(1 + \gamma M^2),$$

(4-2)

P is static pressure, A is area, $\dot{m}$ is mass flow rate, V is velocity, γ is specific heat ratio, M is Mach number, and subscripts 0 and e refer to the free stream and the nozzle exit plane, respectively. Gross thrust coefficient and fuel specific impulse are defined as follows:

$$C_F \equiv F_g / q_0 A_{\text{ref}}$$

(4-3)

$$I_f \equiv F_g / \dot{m}_f g = F_g / \dot{w}_f$$

(4-4)

where q_0 is dynamic pressure, A_{ref} is a reference area (usually maximum engine cross-sectional area), and subscript f refers to fuel. (The foregoing equations do *not* account for external wave drag or friction drag on the engine, just as a quoted thrust coefficient or specific impulse for a rocket motor does not account for any vehicle drag. In ramjet-rocket comparisons, the specific configurations and inert weight fractions must be considered.) The basic continuity and energy equations are:

$$\dot{m}_e = \dot{m}_0 + \dot{m}_f \quad (\text{or} \quad \dot{w}_e = \dot{w}_a + \dot{w}_f)$$

(4-5)

$$(h_{t_0} + fh_{t_f})/(1 + f) = h_{t_e} = h_e + (V_e^2/2gJ)$$

(4-6)

where h and h_t are static and stagnation enthalpy, respectively, f is the fuel-air ratio $(\dot{m}_f/\dot{m}_0)$, $J \equiv 778$ ft.-lb./Btu, and h_{t_f} includes the heat of combustion. The first equality in Eq. (4-6) implies that the

system is adiabatic insofar as (non-regenerative) heat exchange between the flow and the hardware is concerned. Moreover, since the second equality usually is solved for one-dimensional flow in either shifting equilibrium or frozen composition through the nozzle, it does not account for combustion inefficiency, effects of chemical kinetics in the nozzle flow, or divergence or flow non-uniformities. Since a small mass flow of unburned fuel will not appreciably affect the results, it is often sufficient to apply a "combustion efficiency" η_c as a correction factor on I_f; *i.e.*, the result of Eq. (4-4) is multiplied by some η_c, say, 0.9. Thus, one assumes that the foregoing equations give the required η_b but $\dot{w}_f/0.9 = 1.11 \dot{w}_f$, or 11% more than the theoretical rate of fuel consumption was needed. Kinetic effects may be approximated by computing $\mathfrak{I}_e$ for both frozen and equilibrium flow beyond the throat and taking an intermediate result, *e.g.*, 2/3 of the way from the equilibrium to the frozen flow value. For cruising vehicles at $M_0 \leq 3$, sufficient accuracy is obtained by computing the equilibrium $\mathfrak{I}_*$ at the nozzle throat and assuming isentropic expansion at constant γ to compute $\mathfrak{I}_e/\mathfrak{I}_*$. Nozzle losses due to friction, heat transfer, flow distortions and divergence are often lumped into a "nozzle efficiency" η_n that is a multiplier on $\mathfrak{I}_e$ (typically 0.96 or 0.97).

To relate free-stream conditions to combustor conditions we still need the total pressure ratios across the diffuser $(\eta_d = P_{t_2}/P_{t_0})$ and burner $(\eta_b = P_{t_3}/P_{t_2})$, the Mach number M_2, and the fuel injection stream thrust, $\mathfrak{I}_{f_2}$. These parameters depend on detailed engine design and operating conditions. At low speeds, η_d is relatively high (*e.g.*, 0.95 at $M_0 = 2$ versus 0.3 at $M_0 = 5$), whereas F_g may be relatively low (*e.g.*, 0.8 for a "can" type flameholder at $M_0 = 2$ versus 0.99+ for a "gutter" type flameholder and lower M_b at $M_0 = 5$); M_2 is generally small enough to assume that $P_2 \sim P_{t_2}$. The "kinetic energy efficiency" of the diffuser is often used instead of η_d,* since it is relatively insensitive to M_0:

$$\eta_{KE} \equiv (V_2')^2/V_0{}^2 = (h_{t_2} - h_2')/(h_{t_0} - h_0) \qquad (4\text{-}7)$$

where $h_{t_2} = h_{t_0}$ for an adiabatic diffuser, and state 2' represents the hypothetical expansion of the diffused air back to P_0 (*i.e.*, $P_2' = P_0$), and η_{KE} and η_d are related by

$$\eta_d = \left[1 + (1 - \eta_{KE}) \frac{\bar{\gamma} - 1}{2} M_0{}^2 \right]^{-\bar{\gamma}/(\bar{\gamma}-1)} \qquad (4\text{-}8)$$

where $\bar{\gamma}$ is an "effective" specific heat ratio. Fortunately, Eq. (4-8) is not very sensitive to γ, so that $\bar{\gamma} = (\gamma_0 + \gamma_2)/2$ can

*Other diffuser efficiency definitions and their relationships are discussed in Ref. 5.

be assumed. In a constant-area combustor,

$$\mathfrak{I}_{a_2} + \mathfrak{I}_{f_2} = \mathfrak{I}_{m_2} \tag{4-9}$$

where $\mathfrak{I}_{a_2}$ is air stream thrust, and $\mathfrak{I}_{f_2}$ may be either positive or negative (upstream injection) but is generally negligible (as will be discussed in Section 4-5; however, $\mathfrak{I}_{f_2}$ is *not* negligible for an air-augmented rocket.)

Some typical results for kerosene-fueled ramjets [6a] were obtained as follows. Flight along various constant-q_0 trajectories was assumed; thus, $P_0 = 2q_0/\gamma_0 M_0^2$. This P_0 for any M_0 established the altitude Z and hence T_0 and h_0 for a standard atmosphere. For η_{KE}' of 0.90 and 0.94, values of h_2' (and hence s_2) were found from Eq. (4-7). Assuming that $\eta_b = P_{t_3}/P_{t_2}$ varied from 0.94 at $M_0 = 3$ to 1.0 at $M_0 \geq 5$, and using Eq. (4-6) to find $h_{t_3} = h_{t_e}$, the entropy s_e for the isentropic expansion was found. (The calculations across the combustor and nozzle were based on equilibrium chemistry.) For any P_e, an h_e could be found, and then V_e from Eq. (4-6). The A_e corresponding to P_e was found by continuity from Eq. (4-5) and the perfect gas law, $A_e = \dot{m}_0(1 + f)(R_e T_e/P_e V_e)$. Values of C_F and I_f were computed from Eqs. (4-1), (4-3) and (4-4), using various η_n's as multipliers on $\mathfrak{I}_e$, and $\eta_c = 0.95$ as a multiplier on I_f. From results for expansions to various P_e's, the results for $A_e/A_0 = 1.5$ were found by interpolation and plotted.

Figure 4-2a [6a] shows the effect of fuel-air equivalence ratio (ER $= f/f_{\text{stoichiometric}}$) and the envelope for I_f versus M_0 that theoretically could be obtained by operating a "rubber" engine at "optimum" ER for two values of η_{KE} (with $\eta_n = 0.96$). By a "rubber" engine we mean that the inlet always was "on-design," and the nozzle throat area A_* varied as required by $\dot{m}_0(M_0, q_0, A_0)$, η_{KE}, and ER. Of course, even a "rubber" engine would seldom operate at "optimum" ER because, *e.g.*, to cruise, one throttles the engine to obtain thrust = drag at an ER that usually is less than "optimum." Note that at $M_0 = 6$, η_e falls by 14% when η_{KE} falls from 0.94 to 0.90; at Mach 10, the loss is 40%. Practical considerations may reduce the effect of η_{KE} on system performance; *e.g.*, if boundary layer bleed were required to achieve the higher η_{KE}, the loss due to bleed might wipe out the apparent gain (see Section 4-2.5). Moreover, a lower design goal on η_{KE} permits a shorter and lighter inlet (and perhaps reduced combustor and nozzle weights), but use of 0.90-0.92 is reasonable for preliminary studies. It can be shown that a small change in η_n (applied to $\mathfrak{I}_e$) has about the same effect as the same change in η_{KE}.

Figure 4-2b shows how I_f and C_F curves shift with the specified q_0. If the abscissa were changed to V_0, the apparent effect of q_0 would be smaller. The lower q_0's represent higher altitudes (above the isothermal layer), hence higher T_0 and V_0 for a given M_0. However, keeping q_0 high enough to stay within the 390°R isothermal
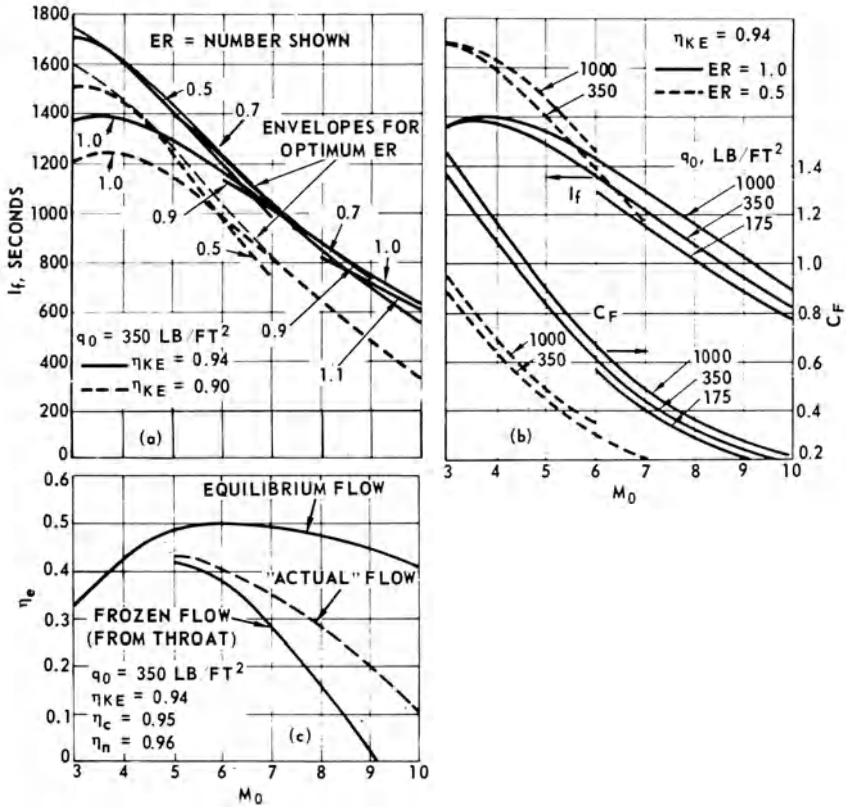
Fig. 4-2 Preliminary performance estimates for a kerosene-fueled ramjet with $\eta_c = 0.95$. Parts (a) and (b) are based on equilibrium exhaust flow [6a].

layer is favorable to I_f because of the lower T_2 and reduced dissociation in the combustor. In fact, q_0's of 1000–2000 psf are most frequently quoted in recent hypersonic vehicle studies.

At this point we note that many preliminary analyses such as the foregoing have been based on equilibrium chemistry that keeps pace with the P, T changes during expansion through the nozzle. This assumption can be grossly misleading, as shown by Fig. 4-2c [6a], where η_e is the "overall efficiency,"

$$\eta_e \equiv \frac{I_f V_0}{H + V_0^2/2g} \tag{4-10}$$

where H is the heating value of the fuel in ft.-lb./lb., and we add to it the kinetic energy required to accelerate the fuel to V_0 (for kerosene, $V_0^2/2g = 0.027 H$ at 5000 fps or 0.11 H at 10,000 fps). The

equilibrium curve corresponds to the optimum envelope in Fig. 4-2a. With "actual" flow based on realistic reaction rates, the maximum η_e occurs at lower flight speed $(M_0 \simeq 5)$, and η_e drops much more rapidly as M_0 is increased. It follows that operation at higher q_0 to keep the vehicle within the 390°R layer $(36 < Z < 83 \text{ k ft.})^*$ to minimize T_2 becomes more beneficial to I_f and η_e. Detailed trade-off studies and test data are required to set realistic M_0, Z design goals.
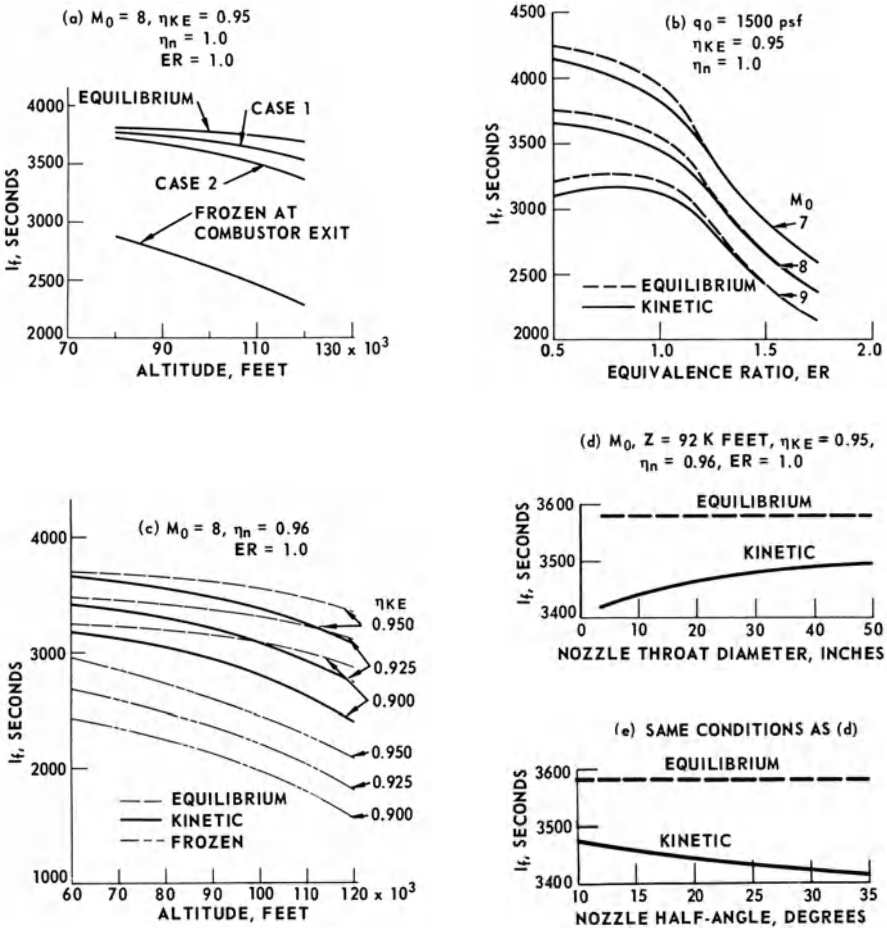
Fig. 4-3 Preliminary estimates for hydrogen-fueled ramjets with $\eta_c = 1.0$ and complete expansion $(P_e = P_0)$——effects of exhaust flow kinetics, ER, M_0, and nozzle size and cone angle [7].

*ICAO Std. Atm. used in Ref. [6a]; upper limit for U.S. Std. Atm. is 67 k ft.

A parametric study of hydrogen–fueled, subsonic combustion ramjets was done by Franciscus and Lezberg [7] who calculated I_f's for complete expansion, $P_e = P_0$. At $M_0 = 8$ there is only a small difference between equilibrium and "actual" kinetic cases for H_2. In Fig. 4–3a, Case 1 is for "fast" rate constants for the $H + H + M$ and $H + OH + M$ three–body recombination reactions, and Case 2 is for rates slower by a factor of 10. Figure 4–3b shows that the effect will be even smaller if fuel–rich operation is required to provide extra fuel for cooling. For a launch vehicle, this fuel–rich operation would not be as penalizing as it first appears, because $F_g \propto I_f \cdot ER$, and a higher F_g would give a greater acceleration capability, making it possible to reduce the time integrals of drag and gravitational losses. The ER for maximum I_f increases with M_0 (as it did for kerosene in Fig. 4–2a). Figure 4–3c shows that kinetic effects become more important with a less efficient inlet or at higher altitudes. As nozzle throat diameter (hence length or residence time) increases, more recombination can occur and $I_{f,\text{kinetic}}$ increases (Fig. 4–3d). The nozzle half–angle probably should be kept near 15° to keep the effects of kinetics (Fig. 4–3e) and the nozzle divergence (cosine effect) loss down without leading to excessive viscous loss due to nozzle length. Nozzle tailoring would be worthy of considerable development effort for a hypersonic aircraft application.

[4-2] DIFFUSER DESIGN

The diffuser decelerates the air, increasing P_2 and T_2 while decreasing the kinetic energy of the stream. This section emphasizes axisymmetric designs. Various other types [6b, 6d, 8, 9] enjoy advantages in certain applications; however, the principles of external–compression limitations, compression–surface design, and duct design in the vicinity of the cowl lip are fundamental and apply to any inlet type. Mass capture, η_d, and external drag must be considered simultaneously, since a gain in one is often at the expense of another. Many compromises may be made to achieve acceptable performance throughout a range of M_0's, Reynolds numbers, angles of attack (α), and atmospheric properties. For missiles, the best compromise in fixed geometry usually is sought. For aircraft or reusable launchers, a variable inlet may be worth its complexity and expense.

Figure 4-4 shows various inlet operating conditions. At the design Mach number, M_D, all of the flow approaching the cowl is captured (sketch a, $\dot{m}_0 = \dot{m}_i$; $A_0 = A_i$). Below this design speed (sketch b, $M_0 < M_D$), or when the normal shock is expelled due to excessive heat release in the combustor (sketch c, subcritical operation), $\dot{m}_0/\dot{m}_i = A_0/A_i < 1$. If $M_0 = M_D$ but too little heat is added in the combustor, full capture may be achieved, but reduced
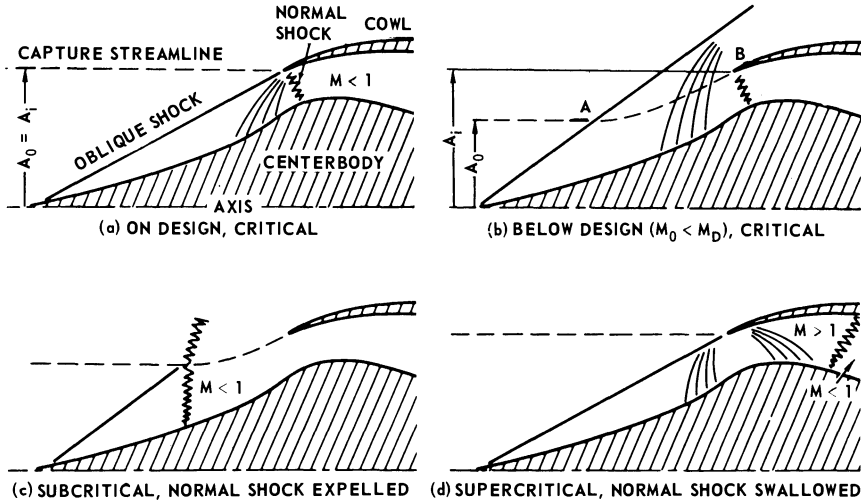
Fig. 4-4 Inlet operating conditions (illustrated for axisymmetric, external-compression inlet).

"back pressure" will allow the normal shock to be "swallowed," causing a loss in η_d (sketch d, supercritical operation). The total diffuser drag comprises wave drag (including drag due to any blunting of the cowl lip) skin-friction drag, and the "additive drag" D_A due to spill over when $A_0 < A_i$; D_A is the integral of the pressure forces acting parallel to the axis along the streamline AB in Fig. 4-4b. When $A_0 = A_i$, $D_A = 0$; D_A is usually kept relatively small in the supercritical regime (swallowed normal shock) by suitable diffuser design, but in the subcritical regime (expelled normal shock), it rises rapidly with increased spillover.

Theoretically, one could use a reversed de Laval (convergent-divergent) nozzle for all-internal, isentropic diffusion. However, such a diffuser would operate (without shocks) only at precisely M_D; at $M_0 < M_D$, a normal shock would be expelled, and at $M_0 > M_D$ the flow would still be at $M > 1$ at the throat and hence would reaccelerate supersonically downstream. However, we could not "start" the diffuser (establish the desired supersonic flow field in the convergent section) without opening the throat to allow the starting shock to pass through. The limiting A_t/A_i for starting (curve B in Fig. 4-5) is found by assuming the normal shock is on the lip, and $A_t/A_i = (A_*/A)_2$ is found from the Mach number behind a normal shock at M_0 [10b, 11]:

$$\left(\frac{A_t}{A_i}\right)_B = \left(\frac{A_*}{A}\right)_2 = \left(\frac{\gamma+1}{2}\right)^{\frac{-(\gamma+1)}{2(\gamma-1)}} \cdot \frac{\left(1 + \frac{\gamma-1}{2} M_0^2\right)^{\frac{1}{2}} \left(\gamma M_0^2 - \frac{\gamma-1}{2}\right)^{\frac{1}{\gamma-1}}}{M_0^{(\gamma+1)/(\gamma-1)}}$$

$$(4-11)$$
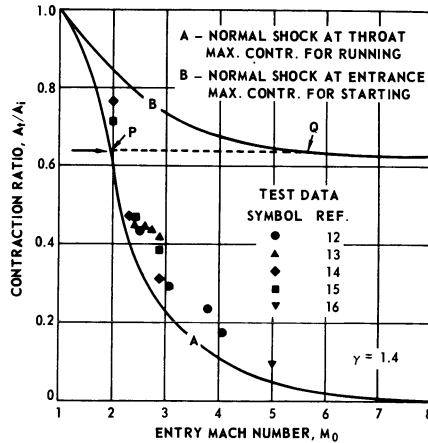
Fig. 4-5 Limit curves for internal contraction ratios for starting (A) and operating (B) [23].

Once the flow is started, the area may be reduced to that given by curve A in Fig. 4-5. To allow some operating margin, curve A represents design for an internal normal shock at $M > 1$ (but as near as practical to 1), which is stabilized in the divergent section downstream of the throat. If a ramjet with $A_t/A_i = 0.64$ is accelerating, the shock will not be swallowed until the M_0 of point Q on curve B is reached; upon deceleration, the shock will remain swallowed until point P on curve A is reached. (The differences between the theoretical curve A and experimental data [12–16] give estimates of the supersonic viscous losses; the required A_t exceeds the isentropic value by $\sim 20\%$ at $M_0 = 2$ and 100% at $M_0 = 5$.) To alleviate this area-ratio problem, many ways of varying A_t have been devised. For axisymmetric designs, a translating centerbody may be used [13]. In a two-dimensional design, flexible walls might be used, but they are heavy, and pressure recoveries are limited by the thick boundary layers that develop in the throat region [12]. Improvement in η_d can be achieved by bleeding off the boundary layer [15], but bleeding arrangements are complicated and cause losses themselves. These limitations have led to a greater interest in inlets that depend primarily on external compression, since a protruding centerbody (Fig. 4-4) eliminates the starting problem.

[4-2.1] Inviscid Design of External-Compression Diffusers

The simplest design uses a cone for the forward part of the centerbody. For such single-cone diffusers, theoretical η_d for inviscid flow has been calculated as a function of M_0 and θ_s, the cone half-angle [10b]. Properties of the conical flow field may be

found in tables [17]. There is an optimum θ_s for each M_0, but its value is not critical, so long as it is small enough to avoid shock detachment [18]. A double-cone inlet with two oblique shocks that meet at the cowl lip is more efficient. Kennedy [19] computed flow fields for several biconic bodies for a wide range of M_0's. Much development of double-cone inlets was pursued during the period 1950-1960 [18, 20].

For greatest external-compression efficiency, a spike may be designed (in theory) for isentropic (Prandtl-Meyer) compression, so that all shocks are reduced to Mach waves that coalesce at the cowl lip. In practice, a conical tip is used in conjunction with an isentropic compression surface (Fig. 4-6). For the conical tip,

$$\frac{P_{t_1}}{P_{t_0}} = \left[\frac{(\gamma + 1) M_0^2 \sin^2 \theta_w}{(\gamma - 1) M_0^2 \sin \theta_w + 2} \right]^{\frac{\gamma}{\gamma - 1}} \left[\frac{\gamma + 1}{2 \gamma M_0^2 \sin^2 \theta_w - \gamma + 1} \right]^{\frac{1}{\gamma - 1}}$$

$$(4\text{-}12)$$

Associated values of M_0, θ_w, and θ_s may be found from tables [10b, 21, 22]. The choice for θ_{s_1} depends upon mission requirements; $\theta_{s_1} \simeq 15$ deg is typical for supersonic missiles.
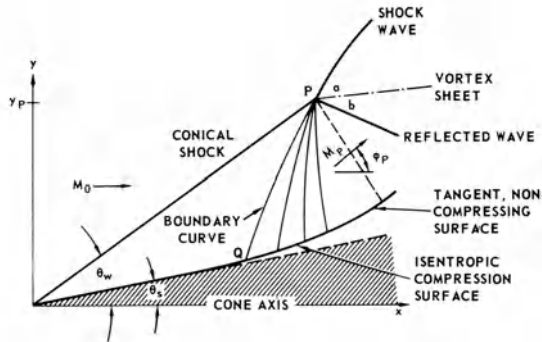
Fig. 4-6 External flow field for cone-tipped "isentropic spike" centerbody [23].

Two compression-limit design criteria relate to (1) the inner-body shock wave coalescence phenomenon and (2) shock waves and resulting drag associated with the cowl lip. From point P, a vortex sheet (running downstream) is generated and a wave usually is reflected toward the surface. The vortex sheet adjusts until the pressures and flow directions on its two sides are equal; P_a/P_0, as a function of M_0 and ϕ, is most easily obtained from graphs [22]. The limiting compression Mach number, M_P, and the limiting flow angle, ϕ_p, are shown versus M_0 for $\theta_{s_1} = 0$ and 15 degrees in
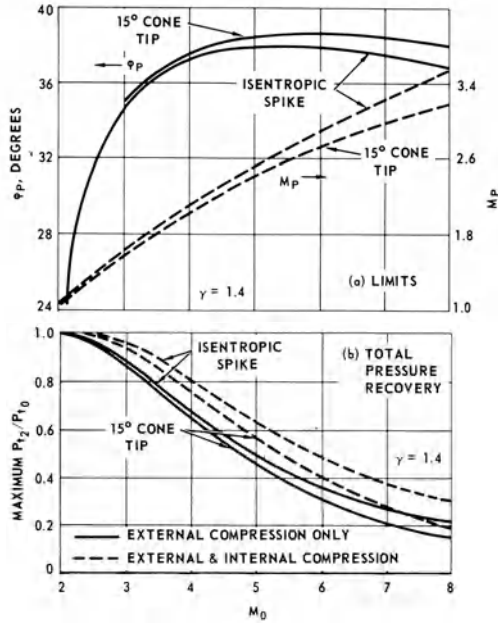
Fig. 4-7 Limits on compression flow angles and Mach numbers imposed by vortex-sheet criterion, and corresponding total pressure recoveries for pure isentropic spike and 15-deg-tipped isentropic spike [23].

Fig. 4-7a; corresponding maximum (inviscid) η_d's are shown in Fig. 4-7b for the cases of a normal shock occurring just inside the lip (external compression only) and at the minimum "starting" throat (curve B in Fig. 4-5). In a practical design, the cowl lip is often placed on the bow shock line (θ_w for $M_0 = M_D$) but slightly below point P to ensure that the vortex sheet does not enter the diffuser [23].

To design the inviscid isentropic compression surface, the method of characteristics [24] is used. Values of M and ϕ at P, as well as along all rays emanating from the cone tip, are listed in tables [17]. The left-running characteristic from P has an inclination of $(\phi_p + \mu_p + 180)$ degrees, where μ_p is the Mach angle at P. The upstream boundary curve, PQ, of the characteristics net is constructed in short segments whose end points lie on adjacent rays in the conical field. The inclination of each segment is made equal to the average of the inclinations of the two ends. This construction is continued until the characteristic line meets the cone surface at Q. Each subsequent characteristic line starts from P, has an arbitrary increment of turning, and is continued until it meets the streamline passing through Q. Behind the last characteristic line, $\phi \leq \phi_p$, where ϕ_p is given in Fig. 4-7a. The isentropic surface is followed by a length of tangent,

noncompressing surface. The increase in M along this surface and along all the streamlines of the non-compressing flow results in an approximately constant M along a line from P_i normal to the flow.

Next, the cowl lip angles (Fig. 4-8) [23] must be chosen. The shock caused by the incoming flow must not detach from the interior cowl lip surfaces. The minimum δ_i is evaluated at the lowest M_0 anticipated,

$$\delta_{i_{min}} = \phi_P - (\delta)_{M_P} \tag{4-13}$$

where $(\delta)_{M_P}$ is the limiting wedge angle for shock attachment at $M_P = M_P(M_0)$. For a given M_D, each value of M_P uniquely determines ϕ_P, $(\delta)_{M_P}$, and δ_i (curves A). Curve B gives the limiting value of M_P determined from the vortex-sheet criterion of Fig. 4-7a. Curve C indicates a small region at low M_0 where the shock detachment limit is more restrictive. Values of δ_i to the left of curve B and above curve C satisfy both the vortex-sheet and the attached-lip-shock criteria. Along any curve A, η_d will increase as M_P decreases (and hence the minimum δ_i increases), but a high δ_i means a high δ_e and high external drag. Upper limiting values of δ_e for attached shocks are of little interest since optimization of η_d and drag requires much lower angles; $(\delta_e - \delta_i)$ usually is defined by structural requirements as about 2 to 4 degrees. Since $\delta_e > \delta_i > 0$, there is always some minimum cowl drag for this type of diffuser; the optimum value depends also on the allowable geometry of the annular ducting.
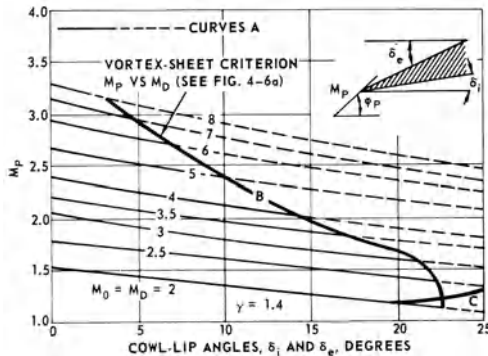
Fig. 4-8 Minimum cowl-lip angles determined by vortex-sheet criterion and shock attachment limits for various M_0's; 15-deg-tipped isentropic spike [23].

The flow must be turned to an axial direction inside the cowl while negotiating the "normal shock" system. The pressure gradient associated with the latter often causes separation of the boundary layer from the innerbody just upstream of this critical

turn; experimental evaluation usually is required. A slight contraction of the duct area gives increased η_d even under spillage conditions; the net gain (2-3%) results from reduced subsonic turning losses rather than decreased shock losses (A_t/A_i cannot be less than curve B in Fig. 4-5, of course). Downstream of the throat section, the area must be rapidly re-expanded; otherwise, the range of stable operation at high α's is reduced, because the effective throat then falls downstream of the geometric minimum area [23]. For a double-cone inlet with $M_D = 2.73$, it was found [23] that innerbody turning radius could be reduced to 2.8 times the annular duct height at the cowl lip with no appreciable loss in pressure recovery.

Transient aerodynamic heating effects become important for $M_0 > 3$, because differential expansions can cause large changes in air capture or internal contraction that may cause subsonic spillage and/or buzz.

[4-2.2] Off-Design Operation, Boundary Layer Problems, and Instabilities

Inlet performance at $M_O \neq M_D$ strongly affects the total worth of a vehicle. The characteristics curves of Fig. 4-6 do not coalesce in the off-design flow network. Figure 4-9 shows C_{D_A} and A_0/A_i versus M_D for various M_0's (from unpublished work by T. Konrad of the Applied Physics Laboratory). A diffuser designed to give maximum η_d at M_D may be severely limited in its acceleration capabilities due to low capture ratio and high D_A at $M_0 < M_D$. One means of increasing the off-design A_0/A_i without excessive D_A is to locate the cowl lip on θ_w at M_D but at $y < y_p$; some loss in η_d at M_D occurs, of course. Other methods are to use variable cowl vents or a translating spike at the expense of weight, volume and complexity.

Large α's during lateral maneuvers will tend to expel a strong bow shock on the leeward side of the inlet, which may induce a gross flow separation from the spike, resulting in large discontinuities in the external aerodynamic characteristics, and may cause engine flame-out. The α (separation) limits can be increased [23] by (a) moving the normal shock in the inlet by opening cowl vents or reducing heat release in the combustor, (b) moving the cowl-lip rearward, which reduces A_0/A_i, or (c) increasing nozzle throat area. Changing the characteristics of the bounday layer by use of trips or roughness or by bleeding or energization may be slightly beneficial. Variations of δ_i and θ_{s_1} have little effect, but flow alignment vanes in the annulus entrance reduce the internal cross-flow tendencies and slightly alleviate the separation [23].

Figure 4-10 shows off-design performance [23] for a volume-limited ramjet similar to Fig. 4-1 with $M_D \simeq 4.2$, $\delta_i \simeq 20°$, and a small internal contraction. The diffused air accelerates into
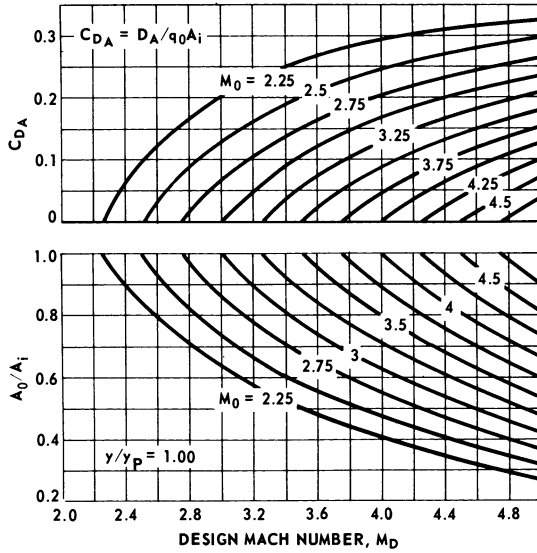
Fig. 4-9 Off-design performance for 15-deg-tipped isentropic spike inlets; theoretical additive drag coefficients and capture-area ratios when $M_0 < M_D$ [23].
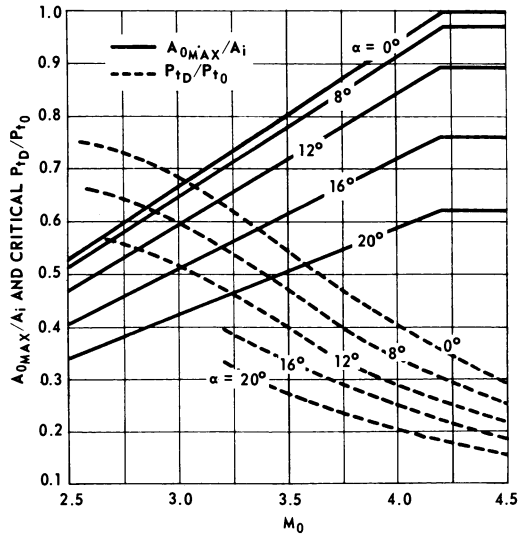
Fig. 4-10 Typical performance characteristics at various angles of attack for a Mach 2.8 to 4.5 ramjet [23].

the "thru-duct" ($M_{duct} \simeq 0.6$ at $M_0 = 2.5$) to maximize the volume of the surrounding annular fuel tank, then passes through a short subsonic diffuser and a flow-smoothing grid before it enters the

combustor. This design gives neither the highest η_d nor the lowest drag that one could obtain with complete freedom of inlet design, but it represents the best trade-off between climb-out (acceleration) and range capabilities for a particular volume-limited vehicle. The solid curves show air capture, and the dashed curves show shock-on-rim η_d versus M_0 for various α's. At small α's, the inlet may be operated stably with some subsonic air spillage when the normal shock is expelled. At large α's, high heat release could cause the previously described flow separation on the leeward side, but it can be avoided by reducing the fuel flow or opening cowl vents.

The specific flight condition for which a theoretical, inviscid compression surface should be corrected for boundary layer displacement thickness [26] is not generally obvious, except for a cruise vehicle that has only one important operating point. Any correction is associated with a specific altitude (Z) and M_0. If an inlet is to be operated over wide ranges of M_0, Z, and α, a compromise design is based upon its off-design performance characteristics. For $M_D \leq 4$, the considerable effort required to carry out the boundary-layer calculations probably is not justified, but for hypersonic inlets, viscous phenomena are of major importance [6e].

At high altitudes *e.g.,* $Z > 80$ k ft. for the inlet described in Fig. 4-10, the boundary layer may be laminar over the entire spike, and it may "bridge" part of the compressing surface (separate and reattach), reducing η_d and A_0/A_i and increasing D_A. In this situation, forced boundary layer transition (by trips or roughening) improves both η_d and A_0/A_i. Improved η_d also can be obtained by bleeding part of the boundary layer from the region where bridging tends to occur. If the diffuser throat is near the cowl lip, separation is apt to occur when the flow is turned too rapidly over the innerbody. Boundary layer bleed ($\sim 1\%$ of main flow) immediately downstream of the sharp turn can prevent this, provided that there is no internal compression [23, 25]. Another technique is to use a "dump" or a vortex trap just downstream of the throat; it reduces frictional losses at the expense of a q_2 loss [6d]. If a diffuser is to be located on the side of a fuselage or under a wing, it usually is placed partially or completely above the boundary layer, which may be diverted for use for auxiliary systems. As much as possible of the boundary layer's momentum must be recovered, and its drag must be taken into account in system analysis.

"Buzz" is an unstable, subcritical operation associated with fluctuating internal pressures and a shock pattern oscillating rapidly about the diffuser entrance. Referring to Fig. 4-4, the normal shock may move upstream toward a limiting position represented by sketch c, where it would allow much of the air to spill around the inlet, then move instantaneously to a limiting

position downstream, sketch d (or even into the combustor); this cycle is then repeated. This intermittent flow causes inefficient combustion, and in some cases, flameout, and the intermittent additive drag sharply reduces thrust capability. Continued buzz can cause catastrophic structural damage. A number of theories for buzz have been proposed (swallowed vortex sheet [27], unstable η_d versus $\dot{m}_0/\dot{m}_i$ characteristic [28], organpipe resonance [29]), but no single theory has been able to explain all characteristics.

For a ramjet with a long thru–duct and an aerodynamic grid (Fig. 4-1), the upstream feeding of perturbations from combustor to inlet is practically eliminated, so that inlet stability limits can be determined from small-scale tests. However, if inlet and combustor are close-coupled, combustion disturbances may significantly affect the inlet flow, and full-scale tests with burning will be needed. At high α, the cyclic leeward flow separation phenomenon previously described may occur; flow-separation and/or buzz limits may be determined with the same set of experiments and expressed in terms of minimun M_2's.

[4-2.3] Hypersonic Inlets

For hypersonic inlets, boundary-layer effects become more important, and temperatures, thermal stresses and distortions, and the pressure loads that might result at very high q_0's, can lead to severe structural problems. However, as M_D is increased, M_1 increases and M_2 decreases. When M_2 becomes very small, a "subsonic dump" can be used (Fig. 4-11a) [6d]; at $M_0 = 8$, a shorter diffuser and a 40% reduction in cooling requirement can be obtained with negligible loss in η_d. A variable-geometry, external-internal compression $(E–I)$ inlet that can perform well over a wide range of M_0 is shown in Fig. 4-11b [6e]. A centerbody with $\theta_s = 10°$ and an internally contoured cowl produce a series of weak oblique shocks in the annulus ahead of the "throat." Axial translation of the centerbody alters the throat area. To "start" the inlet, the centerbody is moved to its forwardmost position. The engine in sketch c [6d] could contribute to vehicle lift while obtaining some radiation-cooling relief of the heat load. Its small circular or elliptical combustor also would have a small heat load. Its inlet is in the all-external-compression class, because flow can spill around the edge of the "pen-point." The fact that much of the leading edge has a sweep angle also relieves heat transfer and drag problems. The various inlet types discussed throughout this chapter can be designed for hypersonic-to-supersonic operation for supersonic combustion ramjets (scramjets). The main difference in scramjet design lies in the combustor, which has no geometric exit throat.

(a) EXTERNAL COMPRESSION INLET WITH CYLINDRICAL COWL AND SUBSONIC DUMP (Ref. 6d)

M_D	6.2	8.0
L_1/D_0	2.00	2.17
L_2/D_0	0.72	0.78
θ_S, DEG	10	10

$D_0 = 2.40$ INCHES

CENTERBODY POSITION FOR STARTING

(c) AN EXTERNAL-COMPRESSION, EXTERNAL-EXPANSION, ("PEN-POINT") TYPE RAMJET (Ref 6d)
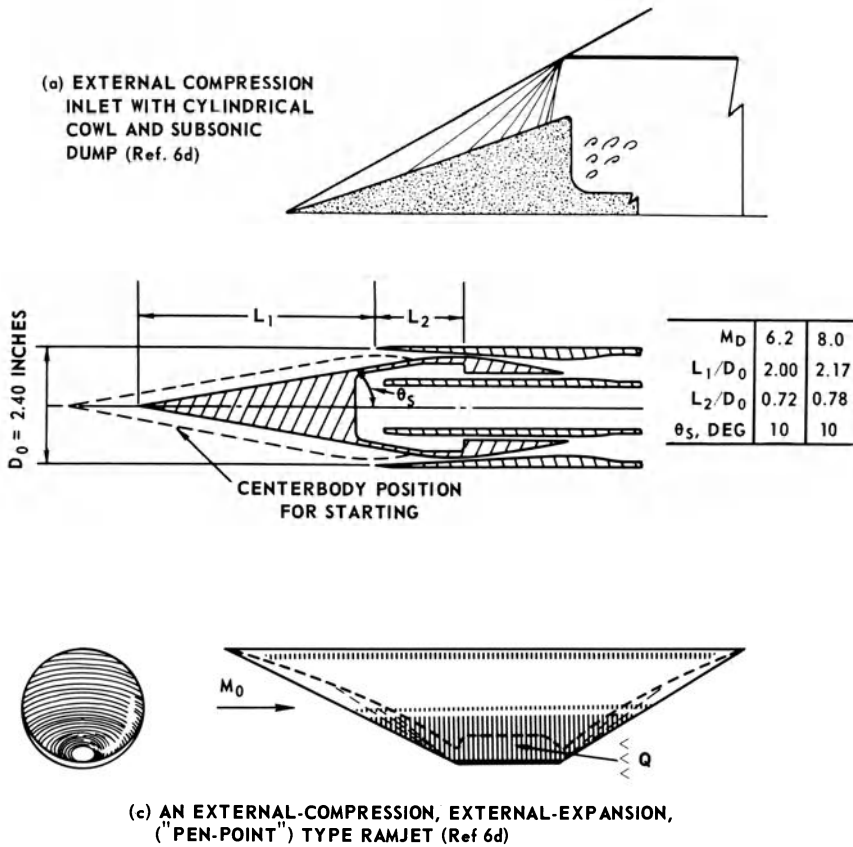
Fig. 4-11 Some alternative inlet configurations for high-speed ramjets.

McLafferty [6e] and Connors [6d] summarize the performance of all-external-compression $(A-E)$ inlets, and McLafferty also reports some work on the $E-I$ inlet of Fig. 11b. Figure 4-12 [6e] distributes the total pressure losses for these two inlet types. The $E-I$ type trades an increased oblique shock loss for a greatly reduced normal shock loss. The computed boundary layer loss (based on the von Karman boundary layer momentum equation and a method [26] of calculating the boundary layer shape parameter) increases more rapidly with M_0 for the $A-E$ inlets; however, their measured η_d's at the two design points tested agree well with the predicted curve (near $\eta_{KE} = 0.92$), whereas the data for the $E-I$ type fall below its predicted curve (which is near $\eta_{KE} = 0.95$), probably because the boundary layer losses exceeded predictions. An effect of off-design operation for the two inlets, each with $M_D = 8$, is shown in Fig. 4-13 [6e]. At Mach 3 the fixed $A-E$ type

CALCULATED PERFORMANCE ———
MEASURED PERFORMANCE ●, ■
LINES OF CONSTANT η_{KE} — — —

MEASURED PERFORMANCE ——— M_D = 6.2 ○
                                        M_D = 8.0 □
(FOR FIXED INLETS, ●, ■)

(a) FIXED GEOMETRY, EXTERNAL COMPRESSION TYPE
(10-DEG-HALF-ANGLE TIP, ISENTROPIC SPIKE)

(b) VARIABLE GEOMETRY, EXTERNAL-
INTERNAL COMPRESSION TYPE
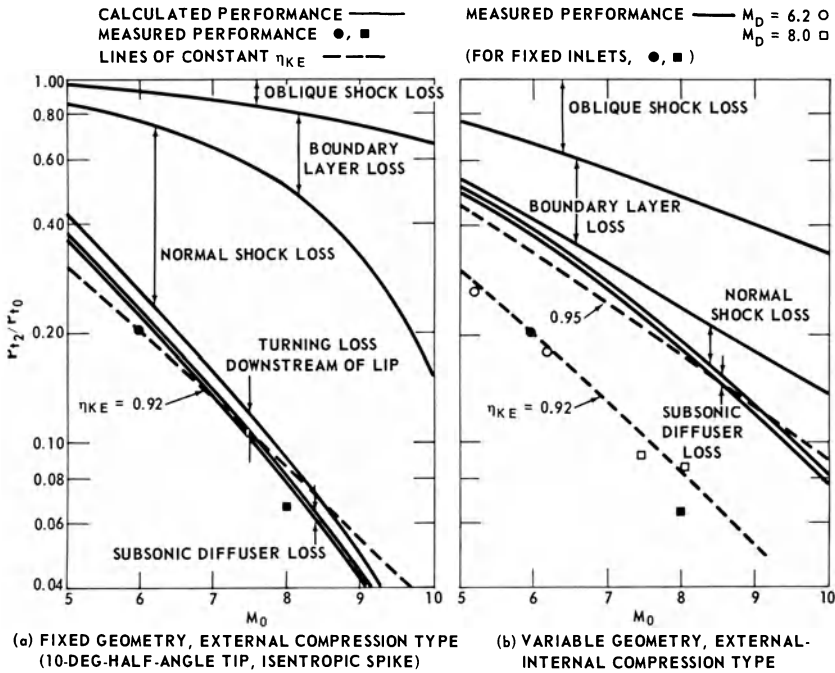
Fig. 4-12 Distributions of total pressure losses for hypersonic inlets [6e].

could produce no thrust for a ramjet burning hydrogen at $ER = 1$, because D_A due to air spillage would be equal to F_g with no spillage. In contrast, $D_A < 0.1 F_g$ for the variable inlet at $M_0 = 3$. Furthermore, the *A–E* inlet has a curved cowl lip (δ_e) with a wave drag equal to $0.1 F_g$, whereas the lip drag of the cylindrical cowl of the *E–I* type is only $0.01 F_g$ [6e]. For use on hypersonic aircraft, such improvements in performance would outweigh the penalties due to length, weight, and complexity of the variable inlet. However, for a rocket-boosted ramjet missile, one would simply boost the ramjet to a speed above which the inefficiency of the fixed inlet could be tolerated.

Connors [6d] makes interesting points about various trade-offs for *A–E* inlets. After showing that $\eta_{KE} = 0.90$ would allow an engine to achieve $\sim 90\%$ of the I_f obtained with $\eta_{KE} = 0.95$, he shows that the required modulation in A_0 for a "rubber" engine in going from Mach 5 to 9 would be reduced from 1:4.5 to 1:2 by accepting the lower η_{KE}. He also discusses the effect of boundary layer bleed: if 8% of the mass flow for a Mach 7 *A–E* inlet were removed and discharged through a sonic nozzle, the bleed drag would be 1/3 larger than the cowl wave drag, and 5% of engine thrust; η_{KE} would have to be improved by ~ 4 points, or η_d would have to be doubled,
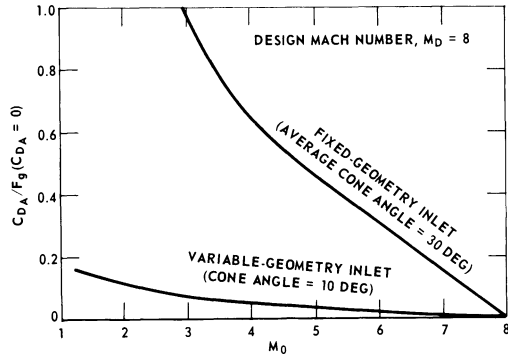
Fig. 4-13 Calculated ratio of additive drag to thrust with no additive drag for two inlet types; $M_0 \leq M_D = 8$ [6e].

to break even on performance, to say nothing of engine weight and cost penalties. However, detailed trade-off studies regarding bleed still may be warranted for any given vehicle.

[4-3] COMBUSTOR AND NOZZLE DESIGN

Fuel injection, atomization, evaporation, mixing, and combustion fundamentals for jet engines were studied at great length between 1945 and 1960 [2, 30]. Reference 30 surveys knowledge of these processes with respect to hydrocarbon fuels through 1954. Another good source is the books from the biannual International Symposia on Combustion [31].

Ram-air-driven turbine pumps usually are used to deliver the fuel to the injectors. For $M_0 \geq 5$, ducting of the hot ram air may become impractical, and "warm gas" generators (or electric power) may be used to drive the pump. The fuel delivery system must provide a sizable ΔP across the injector, say, 50 psia above the maximum P_2. Regarding fuel atomization, Weiss and Worsham [32] showed that a significant parameter is the *relative* velocity between fuel and air, $|V_a - V_f|$. For this reason, injectors often are pointed upstream. Spring-loaded pintle (or "poppet") nozzles that also provide a conical spray pattern and thus assist in fuel distribution are commonly used. With regard to evaporation of fuel drops, Agoston, *et al.* [31] show that data usually are correlated by semi-empirical equations of the type introduced by Frossling. In the absence of combustion or large temperature differences, diffusion controls the rate, and

$$\frac{dm}{dt} = C_1 \frac{dD^2}{dt} - C_2 \left(1 + 0.3 \, Re^{\frac{1}{2}} \, Sc^{\frac{1}{3}} \right) \qquad (4\text{-}14)$$

where C_1 and C_2 are empirically determined constants, D is drop diameter, and Re and Sc are the Reynolds and Schmidt numbers. Foster and Ingebo [33] found that for large temperature differences between the air and the drop, spray evaporation rate varied with $\Delta T^{0.28}$. For burning drops, heat transfer controls the rate, and Eq. (4-14) is altered simply by the replacement of $Sc^{1/3}$ by $Pr^{1/3}$, where Pr is the Prandtl number.

The "flameholders" are bluff objects behind which hot, nearly completely burned gases recirculate and serve as piloting regions for the main flames. In the perforated "can" or "basket" combustors used in turbojets and some ramjets, the recirculation zones occur behind the can areas between the holes. The gutter or baffle type of flameholder (sketched in Fig. 4-1) is simpler in principle, and many studies of the recirculation zones (wakes) and limits for stable operation have been described in the literature. The average wake temperature is about 90 percent of adiabatic flame temperature [34] and recirculation occurs in regular eddies parallel to the main flow at the wake boundary and opposite in direction in the wake core. Turbulent transfer of heat and mass occurs between fresh gas and wake at the boundary. Marble and Zukoski [34] proposed a simple concept for stabilization: if the fresh gas moving at velocity V_2' past the transfer region at the boundary has an ignition delay time τ greater than the time in which it reaches the end of the recirculation zone of length L_r, the main body of the flame will blow out:

$$\tau > \frac{L_r}{V_2'}, \text{ flame blows out;} \qquad \tau \le \frac{L_r}{V_2'} \text{ flame stable} \qquad (4\text{-}15)$$

where τ varies with fuel type, oxygen concentration and ER, has an Arrhenius-type temperature dependence (log $\tau \propto T^{-1}$), and varies inversely with P_2 [30]; L_r and V_2'/V_2 are characteristic of a given inlet-combustor system. The ignition delay concept can be used to predict lean screech limits (large amplitude, stable transverse oscillations); $\tau a/h$ is constant in a given system, where a is acoustic velocity and h is transverse duct dimension [34]. Weiss, *et al.* [31b] present evidence that reaction rate controls blow-out. Most of the results indicate overall reaction kinetics of approximately 1.8 order, so that for a given fuel and temperature, the loading factor ($\dot{w}_a$ divided by combustor volume and by $P_2^{1.8}$) is a function of ER.

When multiple gutters are used (*e.g.,* concentric arrangements), they are spaced so that the turbulent flames will merge within a foot or so. Flame spreading rates vary with T_{m_2} to some power between 1.4 and 2.0 [30]. Since turbulent flame speeds are of the order of 5 to 10 ft./sec. at room temperature and are affected little

by pressure, one usually sees flame spreading angles of the order of 5 to 15 degrees, increasing with T_{t_a} (M_0, Z). It is easier to design an efficient combustor for a Mach 4 ramjet than for a Mach 2 ramjet, because higher T_2's raise fuel evaporation and reaction rates, and, since M_2 decreases as M_0 increases, flameholder drag and burner pressure loss decrease. Combustion efficiency will depend on combustor length L_c to some degree, regardless of the efficiency of the preceding processes. Length is particularly important for operation near $ER = 1$, because when the overall system is stoichiometric, there must initially be over-rich zones as well as lean zones; a local excess of (cool) fuel will inhibit the burning, and greater mixing efficiency will be required to make air eventually available to this fuel. Thus, it is relatively easy to attain $\eta_c \geq 0.9$ at $ER \simeq 0.4$ with a moderate L_c, but the corresponding η_c at $ER = 1.0$ may be only 0.7, which might be increased to 0.85 or 0.9 by doubling L_c. Fortunately, the amount of fuel used for climb and acceleration of a rocket-boosted ramjet missile usually is small, so that efficient operation at high ER may not be critical.

With respect to structural integrity, for $M_0 \leq 4$, the "tailpipe," or main combustor wall, can be protected by providing an internal metal "liner." Part of the combustor inlet air is passed through the annular space between the tailpipe and the liner. The liner can be louvered so that part of the air passes inwardly through it to protect its inside surface from the flame impingement. This arrangement keeps the tailpipe, which must carry the flight loads, relatively cool. The tailpipe (and/or the liner) may be coated internally with a ceramic material to reduce the heat flux to it. Another possibility in some applications may be an ablative liner. Flameholders may be protected by ceramic coatings and/or regenerative cooling by the fuel. For hypersonic, long-range missiles or aircraft, forced cooling of the combustor will be required. Considerable progress has been made in the development of fuels with high cooling capacity due to endothermic reactions (*e.g.*, thermal cracking) as well as vaporization [35]. However, regenerative cooling of a ramjet may not be as straightforward as for a rocket chamber, because the fuel represents only 2 or 3% of the total flow through a ramjet during cruise. In some cases, supplemental water cooling may be a good solution [8]. One reason for the interest in liquid hydrogen as a fuel is its great cooling capacity [36].

The nozzle throat area A_* for a ramjet missile is selected as a compromise between requirements for a large A_* for thrust during climb and acceleration, and a smaller A_* (hence higher A_e/A_*) for higher I_f at cruise conditions. Maximum A_e usually is prescribed by a stowage envelope and seldom will exceed 1.5 A_i. For hypersonic cruise vehicles, an "external expansion" design integrated with a wing or fuselage could improve vehicle L/D while reducing cooling requirement [8] (see Section 4-4).

[4-4] CONSIDERATIONS FOR PRELIMINARY DESIGN OF RAMJET VEHICLES

The importance of dynamic pressure q_0 may be recognized by considering that for cruising flight $F = D = C_D A q_0$, and $W = L = C_L A q_0$. For a given M_0, q_0 increases by an order of magnitude for approximately each 50,000 feet in altitude. The wind area A_w required to sustain a fixed weight or to provide a given degree of maneuverability is inversely related to q_0. Typical curves for C_L, C_D and L/D versus α for a supersonic configuration [37] are given in Fig. 4-14; C_L is generally linear with α to 15 or 20 degrees, whereas C_D varies approximately quadratically with α. For cruise at optimum altitudes at $2 \leq M_0 \leq 4$, maximum L/D's usually are in the range $5.5 \geq L/D \geq 4.5$ for missiles and $7 \geq L/D \geq 6$ for aircraft configurations, as compared to ~ 30 for subsonic aircraft. Engines for supersonic vehicles should develop large thrust per unit frontal area (and volume) to minimize external drag, and, of course, high I_f is desired. Figure 4-15 shows typical curves for turbojets, ramjets, and sustainer rockets. The ramjet's superior position for $M_0 > 3$ is evident. Thrust per unit engine weight is important, too; typical values for Mach 1.8 at sea level are 12, 30, and 60 lbf/lbm for turbojets, ramjets, and liquid rockets, respectively; the relative ranking of turbojets and ramjets will not change appreciably with altitude for this speed, but the ramjet will improve, relatively, at higher speed, and the rocket's advantage will increase with increased altitude.
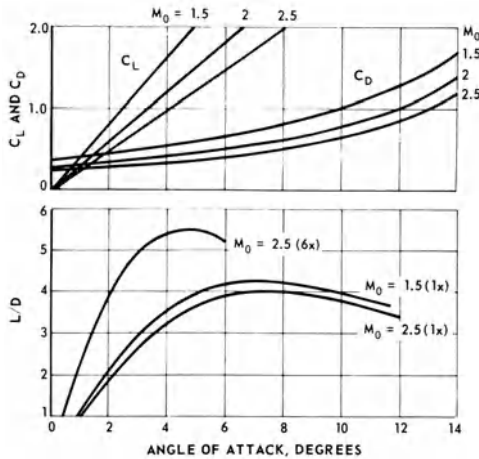
Fig. 4-14 Variation of lift and drag coefficients and L/D with angle of attack for typical supersonic vehicles. (1x) is basic wing area for missile; (6x) is six times wing area [37].
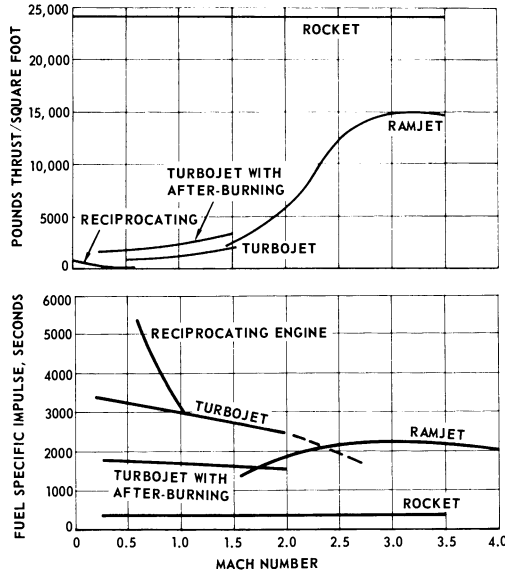
Fig. 4-15 Typical curves for thrust per unit frontal area (at sea level) and fuel specific impulse for various engine types [37].

The Breguet equation can be used for *cruise flight* in cases involving nearly constant L/D, V_0 ($=M_0 a_0$), and I_f; it is based on the relations $\Re = V_0$, $\dot{w}_f = F/I_f$, and $L/D = W/F$. Division of the first by the second, substitution of the third, and integration between limits gives

$$\Re = I_f V_0 \left(\frac{L}{D}\right) \ln\left(\frac{W_1}{W_2}\right) \tag{4-16}$$

where W_1 and W_2 are the weights at the beginning and the end of cruise, respectively. For a ramjet vehicle of total fueled weight W_0, the weight of fuel required for climb and acceleration from boost Mach number M_b to cruise Mach number M_c and altitude Z_c is a small fraction of W_0, that is relatively independent of scale or $\Re$. For a typical fixed-geometry missile, $M_b \simeq M_c - 1$, and

$$W_1 = 0.95 \, W_0, \text{ and } W_2 = W_p + W_s + W_{rf} \tag{4-17}$$

where W_{rf} is the fuel reserve for post-cruise operations, and W_p and W_s are payload and structure weights, respectively. Equations (4-16) and (4-17) give

$$\frac{W_0}{W_p} = \left[0.95 \exp\left(\frac{-\Re}{I_f M_0 a_0 \, L/D}\right) - \left(\frac{W_s + W_{rf}}{W_0}\right)\right]^{-1} \tag{4-18}$$
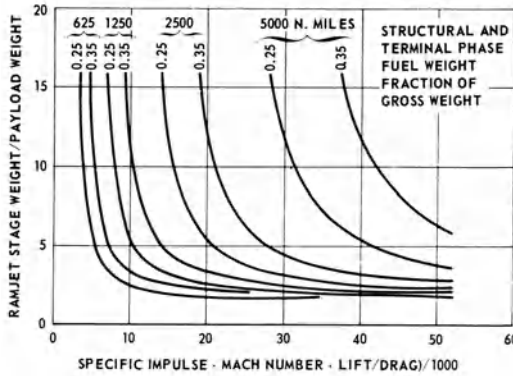
Fig. 4-16 Ratio of ramjet stage weight to payload weight versus Breguet range parameter for various ranges and terminal weight fractions [37].

Results are given in Fig. 4-16 [37] for four $\Re$'s and two values of $(W_s + W_{rf})/W_0$. Obtaining $I_f M_0 L/D = 30,000$, rather than $15,000-20,000$, greatly reduces weight for a vehicle with 2500- n.m. range, but improvement beyond this point is small. The $I_f M_0 L/D$ that must be achieved to get beyond the "knee" of the curve increases as $\Re$ is increased. Once past the "knee," reduction of W_s may be more important than further increase in $I_f M_0 L/D$. Since Figs. 4-14 and 4-15b indicate that $I_f M_0 L/D = 30,000$ can be achieved for high-altitude, kerosene-fueled ramjets, a 2500-n.mi. ramjet vehicle is easily obtainable; but for the 5000-n.mi. case, the need for superior characteristics in all departments of vehicle design (or use of H_2 fuel) is much more pressing.

For *low-altitude* flight, Eq. (4-16) is not a good choice for range computation, because L/D becomes small and very sensitive to α, whereas C_D is not sensitive to α when α is small (see Fig. 4-14). Thus, an assumption of constant $C_D = C_F$ for a given M_0 is reasonable, and

$$\frac{d\Re}{dW} = \frac{M_0 a_0 I_f}{C_D A_{ref} q_0} = \frac{K I_f}{C_D A_{ref} M_0} \qquad (4-19)$$

Integrating and substituting limits,

$$\Re = \frac{K I_f (W_1 - W_2)}{C_D A_{ref} M_0} \qquad (4-20)$$

where $K = 2a_0/\gamma_0 P_0$ = constant for a given altitude and "day." Thus, a slender vehicle with minimum frontal area, A_{ref} (which may be set by payload constraints), and small wings and tails to minimize

C_D, is desired, and its cruise speed should be chosen to maximize $I_f/C_D M_0$.

A *thrust margin* is needed, of course, to provide for factors such as inaccuracies in speed control mechanisms, variation of atmospheric conditions, and boost velocity tolerance. High-recovery diffusers improve fuel economy but may aggravate the available margin situation (*e.g.*, by "buzzing"); relief can be provided by variable geometry features (Section 4-3), but they are costly. For a typical fixed-geometry missile designed for cruise at high altitude, $C_{F_{max}}$ exceeds C_D for 1-g lift over a limited M_0 range (*e.g.*, $M_c \pm 0.2$). At lower altitude, the α needed for lift is smaller, so that C_D is smaller, and more thrust margin is available.

Engine-fuel-airframe interactions may be subtle. For example, experience has shown that high η_c is achievable in relatively short combustors as long as $P_2 > 1/3$ atm; and a normal-shock diffuser will provide $P_2 = 1/2$ atm at 62,000 feet and $M_0 = 2.5$, whereas an isentropic-spike diffuser will give the same P_2 at 78,000 feet. At the higher altitude, approximately twice the C_L, hence twice the α, would be used. Figure 4-14 shows that for a configuration with 6 x wing area at Mach 2.5, $L/D = 4$ at $\alpha = 2°$, but $L/D = 5.4$ could be obtained at $\alpha = 4°$, substantially increasing range capability. (However, the maximum $I_f L/D$ product may occur at a lower α than does L/D, because I_f increases as C_D and hence C_F for cruise is reduced; moreover, the inlet is more efficient at small α.) The optimum M_0 also increases with η_d, provided that drag and weight do not increase inordinately. Current state-of-the-art for inlets, combined with the nozzle kinetic effects (Fig. 4-2c), places the optimum M_0 near 5 with kerosene. While $\Re$ increases proportionally with I_f in Eq. (4-16), the effect of fuel density ρ_f is more subtle. For a given I_f, Eqs. (4-16) and (4-17) can be used (with assumptions of $I_f M_0 L/D = 30,000$ and $W_s/W_0 = 0.3$) to show that a 20% increase in ρ_f increases the range of a nominal 2500-n.mi. vehicle to 2760 n.mi., but the range of a 5000-n.mi. vehicle is only raised to 5080 n.mi. The required F_g for the missile with dense fuel is greater for the same L/D; consequently, $\dot{w}_f$ is greater. If ρ_f is increased at the expense of a proportionate decrease in I_f, the range actually goes down.

For *boost, climb and acceleration*, the equations of motion along and normal to the boost flight path, respectively, are

$$\frac{W\dot{V}}{g} = \sum F_x = F_g \cos \alpha - D - W \sin \gamma \qquad (4\text{-}21)$$

$$\frac{WV\dot{\gamma}}{g} = \sum F_z = L + F_g \sin \alpha - W \cos \gamma \qquad (4\text{-}22)$$

where γ is the flight path angle from horizontal. If the boost

acceleration is several g's, and $\dot{w}_f$, I_{sp}, and γ are nearly constant,

$$V_b \simeq g\, I_{sp} \ln \left(\frac{W_i}{W_{sb} + W_0} \right) - gt_b \left(\frac{\bar{D}}{\bar{W}} + \sin \gamma \right) \qquad (4\text{-}23)$$

where $W_i = W_b + W_0$ is the initial weight of the booster plus the ram-jet, W_{sb} is the structural weight of the booster, $\bar{D}/\bar{W}$ is an effective mean drag/weight ratio, and V_b and t_b are boost velocity and time. Obviously, W_b will increase rapidly as I_{sp} is decreased or W_{sb}/W_b, V_b, or t_b is increased. Figure 4-17 shows the effect of M_c on W_i and W_0 for typical configurations. Optimization based on minimizing W_i favors a lower M_c than would be inferred by optimizing W_0 alone. Therefore, the booster must be closely associated with the ramjet in design studies.
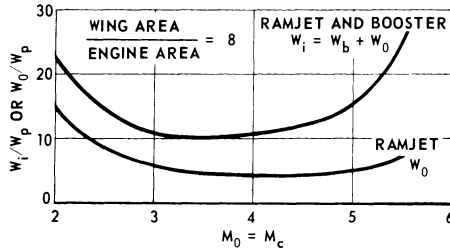
Fig. 4-17 Optimization of ramjet alone gives higher cruise speed than optimization of ramjet-booster combination for 2500-n.mi. range [37].

Figure 4-18 shows 3 classes of ramjet vehicle configurations. The nose-inlet configuration a (see also Fig. 4-1) provides pack-aging space between the air duct and external surface and in the inlet's centerbody. Its symmetry relieves diffuser and balancing difficulties, hence control requirements, in some missile applica-tions, *e.g.*, the Talos surface-to-air missile. The two-aft-engine configuration b resulted from extensive studies of missiles for 1250-n.mi. range [37]. The inlets below and just behind the wings, operate within the oblique-shock flow field of the wings and are substantially independent of α within the working range; moreover, the precompression by the wings permits either higher η_d for a given inlet size or reduced size for a given η_d. The lift pressure field of the wing also carries onto the afterbody and engine planform area, giving improved altitude and range performance, and the con-figuration's longitudinal stability changes little over a considerable M_0 range.

Configuration c is one concept of the even more intimate inte-gration of engines and airframe that will be typical of hypersonic aircraft [8]. Turbojets would be used for climb to Mach 3.5 at

(a) TALOS MISSILE WITH
    NOSE INLET

(b) ENGINE NACELLES IN
    WING FLOW FIELD

(c) HYPERSONIC TRANSPORT WITH
    EXTERNAL EXPANSION RAMJETS
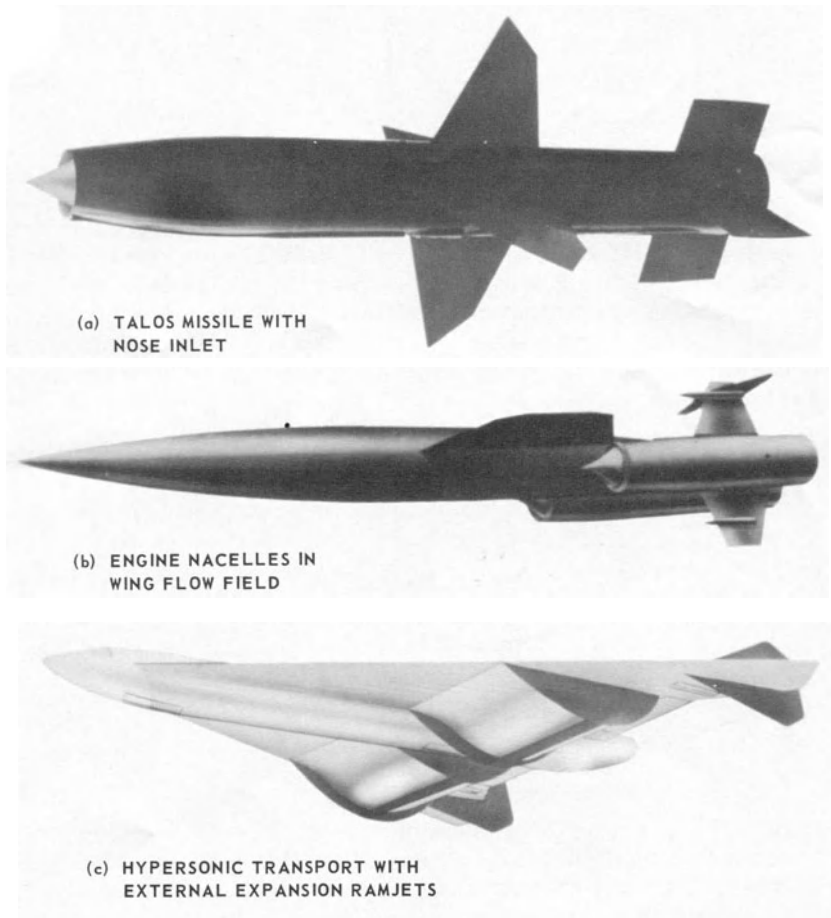
Fig. 4-18 Three classes of ramjet vehicle configurations [37].

70,000 feet. Two-dimensional, variable-ramp, "external expansion ramjets" would then be used for climb and acceleration to Mach 6 or 7 at 90,000–103,000 feet and for cruise at $I_f \simeq 1000$ seconds and $L/D \simeq 7$. The inlets operate in the favorable flow field of the wing. The largely exposed inlet and nozzle surfaces obtain radiative heat relief and contribute $\sim 12\%$ of vehicle L/D during cruise. Water cooling of the combustors is needed, however. Other examples of integration studies are References 6b, 36 and 38.

Figure 4-19 compares payload/volume versus range relation-ships for ramjet and solid rocket weapons for three mission classes [37]. The ramjet's use of air leads to fuel economy and inherent thrust variability; a thrust dynamic range of more than 1000 to 1 is
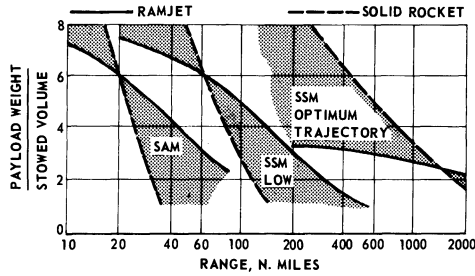
Fig. 4-19 Ramjet/solid-rocket comparisons based on payload-weight/stowed-weapon-volume for surface-air and surface-surface missiles [37].

readily possible. In contrast, the rocket can operate out of the atmosphere, and even for missions within the atmosphere, its lower weight fraction can make it superior if mission requirements are modest. The right-hand set of curves is for surface-to-surface missiles (SSM's) in which the rocket follows a ballistic trajectory but the ramjet follows an optimum cruise-type trajectory. The central set is for SSM's required only to cruise at low altitude. The left-hand set is for general-purpose surface-to-air missiles (SAM's) that must perform acceptably against both low- and high-altitude targets. The ramjet weapon is more efficient to the right of each crossover point. On a payload/total-weight basis, ramjets become superior at shorter ranges.
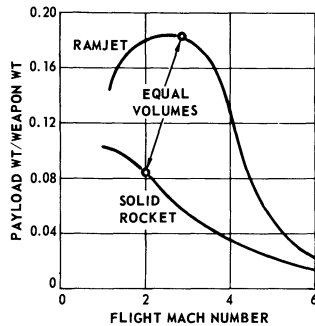
Fig. 4-20 Effect of M_0 on payload/weapon weight ratio for general-purpose SAM's with 20- n.mi range at low altitude [37].

Figure 4-20 shows how speed affects a comparison [37] for a low-altitude line-of-sight intercept of a target at 20 n.mi. (the cross-over range for the SAM's of Fig. 4-19). The equal-volume rockets and ramjets (circle points) operate at substantially different speeds, Mach 2.0 and Mach 2.8, respectively.

[4-5] AIR-AUGMENTED ROCKETS

The "ducted rocket" or "ram-rocket" is in principle very similar to the ramjet, but the fuel is supplied in fuel-rich gases from a "primary rocket" or "gas generator." The rocket could be within the centerbody of the inlet; a nozzle (or nozzles) would discharge the fuel-rich gas at sonic or supersonic speed into the combustion chamber [39]. A side-inlet configuration that has been flight-tested by Thiokol is shown in Fig. 4-21 [9]. It has an integral booster; *i.e.*, when the boost propellant is burned out, the boost chamber becomes the afterburner for the ducted rocket. Its performance analysis is nearly identical to that for a ramjet, but the momentum of the fuel entering the combustor is much higher because of its higher flow rate $\dot{w}_p$ for a given ER with respect to the air and its velocity ($M_p \geq 1$ and $T_{t_p} \geq 3000°R$). A ducted rocket missile that climbs and accelerates from $M_0 \sim 2$ may initially experience a relatively low $\dot{w}_a/\dot{w}_p$ (say, 3 or 4), and $\Im_{f_2}$ (or $\Im_{p_2}$) may even exceed $\Im_{a_2}$ in Eq. (4-9). It can give higher F_g/A_0 than a ramjet, but at lower I_f, since it does carry some oxidizer. If a solid propellant is used, the overall system is simpler than a ramjet (no fuel pumping and control system) and has a lower inert weight fraction; however, the extremely wide thrust variation capability of the ramjet is lost, because $\dot{w}_p$ is not varied as readily. With a very fuel-rich propellant and high $\dot{w}_a/\dot{w}_p$, effective I_{sp}'s for cruise may approach those for ramjets. Thus, a third, intermediate curve could be added to each comparison in Fig. 4-19, and the crossover between ducted rocket and rocket would occur at slightly smaller range than the ramjet-rocket crossover.
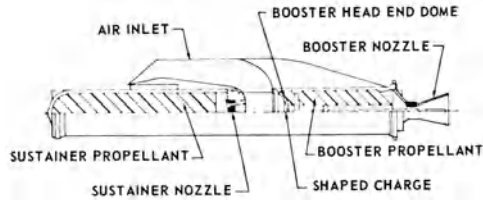
Fig. 4-21 Solid-propellant, ducted, air-augmented rocket with integral booster [9].

Another form of air-augmented rocket which is challenging to both the analyst and the experimentalist, is the "shrouded" type, which has no geometric throat between the combustor and the divergent nozzle (Fig. 4-22a) [40]. Air flow into the combustor may be either subsonic or supersonic, and even if it is subsonic, a supersonic, underexpanded rocket exhaust into the chamber can lead to a supersonic solution for the burned gas. At $M_0 \leq 5$, shrouded-rocket I_{sp} performance probably will be inferior to ducted rocket performance. However, at $M_0 > 5$, the shrouded
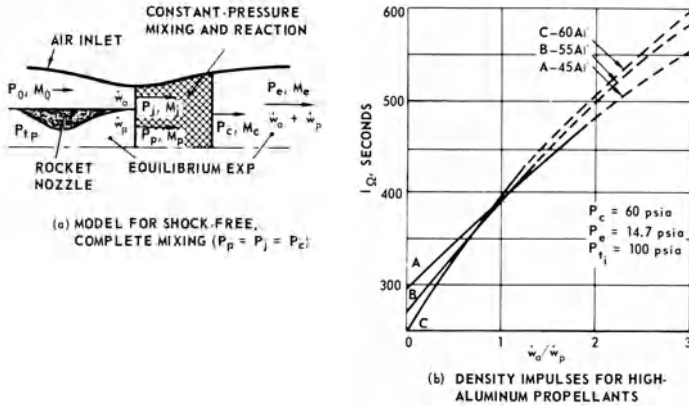
Fig. 4-22 Analytical model and typical density-specific-impulse estimates for a shrouded, air-augmented rocket [40].

rocket operated in the all-supersonic mode should become superior, just as the supersonic-combustion ramjet surpasses the subsonic-combustion ramjet at some hypersonic speed, for the same reasons: higher η_d (no·normal shock) and less dissociation (lower T_2) outweigh the loss from adding heat at higher M_2.

Perini, *et. al.* [40] computed theoretical I_{sp}'s and density specific impulses I_Ω of shrouded rockets for a number of fuel-rich solid propellants. Here, $I_\Omega \equiv I_{sp} (\rho/\rho_0)^{0.68}$, where ρ_0 is the density of a reference propellant, 0.063 lb./in.^{3}, and the 0.68 exponent approximates the worth of density for some volume-limited rocket stages. Figure 4-22a shows the basic one-dimensional flow model based on constant-pressure mixing and burning (the studies also covered effects of shocks, incomplete mixing, and η_d). Figure 4-22b shows that for high-aluminum propellants (with 10% binder, the balance being ammonium perchlorate), I_Ω is double the rocket value with only modest $\dot{w}_a/\dot{w}_p$ ratios.

An air-augmented, liquid bipropellant rocket could go to a pure ramjet mode at, say, $M_0 \simeq 2.5$ by shutting off the oxidizer. It also could provide static thrust, which a ramjet alone cannot. It has been suggested [39] that such "composite engines" might replace turbomachines for hypersonic aircraft, because higher fuel consumption during climb and acceleration would be compensated by lower inert weight, and the sonic boom problem could be alleviated by using the higher thrust capability to climb at a steeper angle.

[4-6] ENGINES WITH SUPERSONIC COMBUSTION

The simplest ramjet of all would compress air by an exterior vehicle surface and burn fuel behind a corner of that surface.

For a simple wedge-type "external ramjet" or ERJ (Fig. 4-23a) [31], in the absence of fuel injection, the air flow would expand around the corner (pressure profile A). When fuel is injected from a transverse row of holes just ahead of the corner, a second oblique shock occurs, and subsequent heat release produces profile B. If the longitudinal force on the rear wedge exceeds that on the front wedge, net thrust results. Even if the rear force is lower, drag is reduced and lift is increased so that L/D for a supersonic wing could be doubled or tripled by a small $\dot{w}_f$ [6f, 42]. In many experiments the rear profile was nearly flat, so that it was reasonable to assume constant-pressure burning (curve C) for a performance analysis. Figure 4-23b [41] shows $\Re$ versus M_0, where

$$\Re = \frac{I_f V_0 L/D}{6076} = \frac{L V_0 / \dot{w}_f}{6076} \quad \text{(n.mi.)} \qquad (4\text{--}25)$$

since $I_f = F_g / \dot{w}_f$ and $F_g = D$ for cruise. Relative to Eq. (4-16), this $\Re$ actually is range only when $\ln(W_1/W_2) = 1$, which means that cruise fuel weight is $0.63 \, W_1$ (probably impractically high). Prior calculations [41, 42] had indicated that $L/\dot{w}_f$ would be highest with small wedge angles (small perturbations); a 5° front wedge angle and the corresponding "optimum" rear wedge angle $\delta_{2_{opt}}$ were used here. Estimates for conventional ramjet (CRJ) vehicles are included for comparison. Because it operates with lower cycle temperatures and less chemical dissociation, the ERJ should surpass the CRJ at some high cruise speed with either kerosene or H_2. However, ERJ performance falls sharply as required thrust level is increased, so that ERJ's are not attractive as primary propulsion systems for accelerating vehicles. On the other hand, the ease of producing significant normal (side) forces suggests the use of external burning to produce maneuvering forces within the atmosphere.

By the early 1960's, interest in scramjets (ramjets using ducted supersonic combustion) was very high. A pioneering study by Weber and MacKay [43] was followed by various studies. Stable operation of an engine model with a 2-shock inlet, supersonic heat release, and net thrust was demonstrated by properly locating a flat plate beneath a wedge-type ERJ, and the heat release agreed remarkably well with an analytical model for constant-pressure heat release [44]. Theoretical performance studies [6a, 6b, 6g, 43, 45, 46] have shown that supersonic combustion will be superior to subsonic combustion at hypersonic speeds. Thus, it would be desirable to use subsonic combustion for, say, Mach 3 to Mach 6 or more (depending on engine design and fuel used), and then convert to supersonic combustion in the same engine for higher speeds. Variable fuel injection patterns and/or variable geometry might be involved.
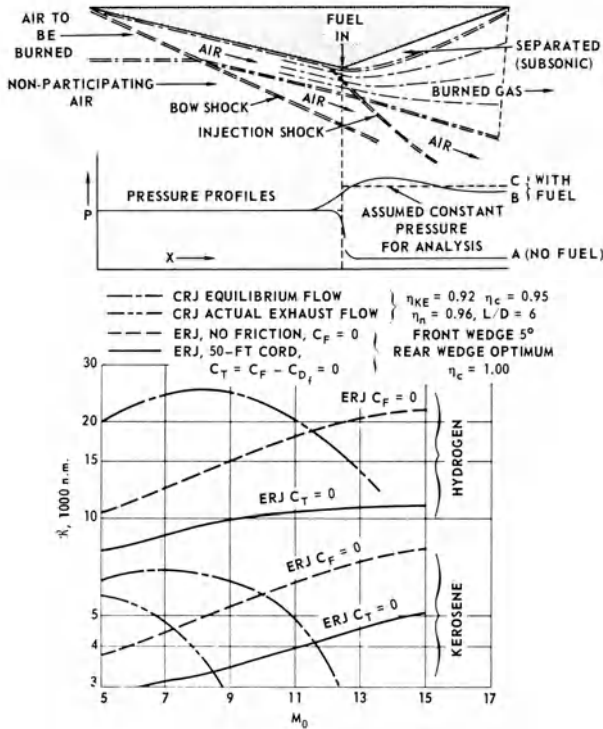
Fig. 4-23 Wedge-type external ramjet (ERJ) model and comparisons with conventional ramjet vehicles (CRJ) based on Breguet range parameter (q_0 = 1000 psf; optimum ER) [41].

An analysis that may help the designer to understand this trade-off problem was presented by Billig [46], who examined families of one-dimensional heat addition processes following $PA^{\epsilon/(\epsilon-1)} =$ constant (suggested by Crocco). He used it in the momentum equation, $\dot{m}_3 u_3 + \epsilon P_3 A_3 = \dot{m}_2 u_2 + \dot{m}_f u_f + \epsilon P_2 A_2$,* and with Eqs. (4-5) and (4-6) and an equation of state, he obtained subsonic and supersonic combustion solutions for various ϵ's. When $\epsilon = 0$, pressure is constant; when $\epsilon = 1$, area is constant. Billig suggested a fixed-geometry combustor/nozzle with staged fuel injection; it could be a cylinder followed by a divergent section [46]. At any given time, the point of first fuel injection might be at either end of the cylindrical section. Upon completion of burning, any remainder of the divergent section would be used for expansion. Figure 4-24 shows results for an inlet compressing to $M_2 = M_0/3$, with or without a subsequent normal shock, and H_2 combustion and expansion to $A_e = 1.5 A_0$. For equilibrium expansion, the optimum-ϵ processes (ϵ_{OPT}) for both subsonic and supersonic combustion are shown along

---

*In detailed analysis of supersonic combustors, a term for wall shearing stress would be added [36].
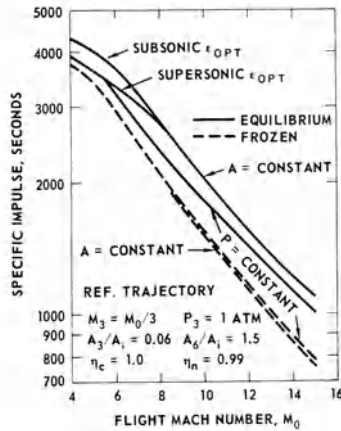
Fig. 4-24 Fuel specific impulse versus M_0 for various combustion processes with hydrogen [46].

with the $\epsilon = 0$ and $\epsilon = 1$ combustor solutions. In the subsonic case, the flow reaccelerates to $M \geq 1$ at the combustor exit. For $ER = 1$, the optimum subsonic and supersonic solutions coincide at $M_0 = 8.5$, where both are in fact constant-area ($\epsilon = 1$). The effect of optimization can be large; *e.g.*, at $M_0 = 8.5$ with equilibrium expansion, the difference in I_f between $\epsilon = 0$ and $\epsilon = 1$ is about 13%. Billig [46] also showed how the analysis could be used with combustor test results to predict changes in combustor shape that should either reduce required length for a given η_c or raise η_c.

[4-7] CONCLUDING REMARKS

Ramjet technology for speeds to Mach 5 or 6 is well developed, and work on air-augmented rockets and scramjets is proceeding well. The role of high-speed air-breathing engines in immediate future applications probably will be to extend powered-flight capabilities and/or payloads of guided missiles. As was emphasized in Section 4-4, propulsion system comparisons depend strongly on mission goals and constraints, *i.e.*, the ground rules. For hypersonic air transportation, some form of ramjet or composite engine including the ramjet mode surely will be used. The future appears to be brightening for the air-breathing enthusiasts.

[4-8] ACKNOWLEDGMENTS

Particular thanks are due to Mrs. I.D.V. Faro and Mr. J.L. Keirsey for much of the material [23] used in Section 4-3, to

Mr. J.H. Walker and his colleagues who prepared much of the material [37] used in Section 4-5, and to Dr. F.S. Billig who has worked with the writer for many years in the areas described in Section 4-6.

[4-9] NOMENCLATURE

A = area; A_{ref} is reference value for coefficients, ft^2

a = sound speed, ft/sec

C_D, C_L = drag coefficient = $L/q_0 A_{ref}$; and lift coefficient = $L/q_0 A_{ref}$

C_F = thrust coefficient = $F_g/q_0 A_{ref}$

D, D_A = drag and additive drag, respectively, lbf

ER = fuel-air equivalence ratio = $f/f_{stoichiometric}$

$F_g, \mathfrak{I}$ = gross thrust and stream thrust, Eqs. (4-1) and (4-2), respectively, lbf

f = fuel/air weight ratio = $\dot{w}_f/\dot{w}_a$

g = gravitational acceleration, 32.17 ft./sec.^{2}

H = net heating value of fuel, Eq. (4-10), ft-lbf/lbm

h = specific enthalpy, Btu/lb.

I_f = fuel specific impulse = $F_g/\dot{w}_f$, lbf-sec/lbm

I_{sp} = propellant specific impulse = $F_g/\dot{w}_p$; $I_{\Omega} = I_{sp}(\rho/\rho_0)^n$, lbf-sec/lbm

L = lift, lbf; or length (L_r = length of recirculation zone), ft

M = Mach number, V/a

$\dot{m}$ = mass flow rate = $\dot{w}/g$, slugs/sec.

P, q = pressure and dynamic pressure ($q = \rho V^2/2$), respectively, lbf/ft^2.

$\mathfrak{R}$ = range, ft ($\div 6076$ = n.mi.)

R = gas constant, ft.^{2}/sec.^{2} – °R

T = temperature, °R

t = time, sec

u, V = x component of velocity and velocity, respectively, ft/sec

$W, \dot{w}$ = weight, lbm, and weight flow rate, lbm/sec, respectively

Z = altitude, ft

α = angle of attack, deg

γ = ratio of specific heats; or flight path angle, rad

δ_i, δ_e = internal and external cowl lip angle, respectively, deg

ϵ = exponent for Crocco family, $PA^{\epsilon/(\epsilon-1)}$ = constant

η = efficiency; η_c = combustion efficiency = multiplier on $I_{f_{equil}}$; η_d = diffuser total pressure recovery = P_{t_2}/P_{t_0}; η_e = overall efficiency, Eq. (4-10); η_{KE} = diffuser kinetic energy efficiency, Eq. (4-7); η_n = nozzle efficiency = multiplier on $\mathfrak{I}_e$ in Eq. (4-1)

θ_s, θ_w = cone (surface) half-angle and conical shock angle, respectively, deg

ρ = density, slugs/ft^3; for I_Ω, ρ_0 is reference propellant density

$\emptyset$ = local flow angle, deg

τ = ignition delay time, sec

Subscripts

0   = free-stream (or flight) conditions

1   = behind bow shock, or nose cone; on weight, beginning of cruise

2   = diffuser exit = combustor inlet; on weight, end of cruise

3   = after combustion

a, f, m = air [note: $\dot{m}_a = \dot{m}_0$], fuel and mixture, respectively

b = burner, or end of boost ($t = t_b$)

c = combustor, or cruise

D = design value (M_D) or drag (C_D)

e = nozzle exit; or overall engine in Eq. (4-10)

i = geometric inlet area; on weight, missile + booster

P = value at end of external compression

p = payload; on weight flow, propellant

rf = reserve fuel at end of cruise

s = structure; also, value at surface (θ_s)

t = total or stagnation conditions; in Eq. (4-11), diffuser throat

w = wing

$*$ = sonic conditions (*e.g.,* at nozzle throat)

REFERENCES

1. Avery, W.H.: Twenty-five years of ramjet development, *Jet Propulsion* 25, p. 604 (1955).
2. Dugger, G.L.: Recent advances in ramjet combustion, ARS J., 29, 819-827 (1959).
3. ———: Ramjets, *Astronautics*, 7, 138-142 (1962).
4. Daum, N.: The Griffon aircraft and future of the turbo-ramjet combination in the propulsion of supersonic aeroplanes, *J. Royal Aeron. Soc.*, 63, 327 (1959).
5. Curran, E.T. and M.B. Bergsten: Discussion of inlet efficiency parameters, Air Force Aero. Propulsion Lab., Wright-Patterson AFB, Ohio, *ASRPR TM 62-68* (April 1963).
6. Jaumotte, A.L., *et al.*, Eds.: Combustion and Propulsion, Fourth AGARD Colloquium, Milan, April 4-8, High Mach number Air-Breathing Engines (Pergamon Press, New York, 1961): (a) Dugger, G.L., pp. 84-110; (b) Ferri, A., pp. 3-15; (c) Swithenbank, J., p. 119; (d) Connors, J.F., and Obery, L.J., pp. 123-134; (e) McLafferty, G.H., pp. 138-149; (f) Fletcher, E.A., p. 118; and (g) McLafferty, G.H., p. 154.

7. Franciscus, L.C. and E.A. Lezberg: Effects of exhaust nozzle recombination on hypersonic ramjet performance: II. Analytical investigation, *AIAA J.*, 1, 2077-2083 (1963).
8. Pietrangeli, G.J. and E.V. Nice: The feasibility of a Mach 7 transport employing airbreathing propulsion systems, Applied Physics Laboratory, The Johns Hopkins University, Silver Spring, Md., *CF-2900* (1960).
9. Goodrich, C.C.: Ducted rocket motors, *Aerospace Facts*, Thiokol Chemical Corp., III, No. 1, 8-10 (1967).
10. Applied Physics Laboratory, The Johns Hopkins University, Handbook of Supersonic Aerodynamics, *NavWeps Report 1488*: (a) Vol. 3, Sec. 8, (1961); (b) Vol. 2, Sec. 5, (1953).
11. Oswatitsch, K.: Gas Dynamics, New York, Academic Press, Inc., 1956.
12. Gunther, F.: Development of a two-dimensional adjustable supersonic inlet, *JPL/CIT Progress Report 20-247* (1954).
13. Mossman, E.A. and F.A. Pfyl: An experimental investigation at Mach numbers from 2.1 to 3.0 of circular-internal-contraction inlets with translating centerbodies, *NACA RM A56G06* (1956).
14. Scherrer, R. and W.E. Anderson: Investigation of the performance and internal flow of a variable-area, variable-internal-contraction inlet at Mach numbers 2.00, 2.50 and 2.92, *NACA RM A58C24* (1959).
15. Stitt, L.E. and L.J. Obery: Performance of an all-internal conical compression inlet with annular throat bleed at Mach number 5.0, *NACA RM E58E14* (1958).
16. Ferri, A. and L.M. Nucci: Theoretical and experimental analysis of low drag supersonic inlets having a circular cross section and a central body at Mach number 3.30, 2.75 and 2.45, *NACA RM L8H13* (1948).
17. Kennedy, E.C.: Tables of supersonic conical flow, Ordnance Aerophysics Lab., Daingerfield, Texas, *CM-973* (1960).
18. Connors, J.F. and R.R. Woollett: Performance characteristics of several types of axially symmetric nose inlets at Mach number 3.85, *NACA RM E 52I15* (1952).
19. Kennedy, E.C.: Calculation of the flow fields around a series of bi-conic bodies of revolution using the method of characteristics as applied to supersonic rotational flow, *OAL CM 873* (1956).
20. Connors, J.F. and R.C. Meyer: Design criteria for axisymmetric and two-dimensional supersonic inlets and exits, *NACA TN 3589* (1956).
21. Ames Research Staff: Equations, tables, and charts for compressible flow, *NACA Report 1135* (1953).
22. Dailey, C.L. and F.C. Wood: Computation Curves for Compressible Fluid Problems, New York, John Wiley & Sons, Inc., 1949.

23. Faro, I.D.V. and J.L. Keirsey: Supersonic inlets, *APL/JHU TG 610-3B* (1966).
24. Ferri, A.: Elements of Aerodynamics of Supersonic Flows, New York, The Macmillan Co., 1949.
25. Connors, J.F., J.C. Lovell and G.A. Wise: Effects of internal-area distribution, spike translation and throat boundary-layer control on performance of a double-cone axisymmetric inlet at Mach numbers from 3.0 to 2.0, *NACA RM E57F03* (1957).
26. McLafferty, G.H. and R.E. Barber: Turbulent boundary layer characteristics in supersonic streams having adverse pressure gradients, UAC Res. Labs., East Hartford, Conn., *Report R-1285-11* (1959).
27. Ferri, A. and L.M. Nucci: The origin of aerodynamic instability of supersonic inlets at subcritical conditions, *NACA RM L50K30* (1951).
28. Pearce, R.B.: *Aviation Week*, 52:3, 21-25 (1950).
29. Sterbentz, W.H. and J.C. Evvard: Criterions for prediction and control of ramjet flow pulsations, *NACA TN 3506* (1955).
30. Lewis Flight Propulsion Laboratory Staff: Basic considerations in the combustion of hydrocarbon fuels with air, *NACA Report 1300* (1959).
31. Sixth Symposium (Int.) on Combustion, New York, Reinhold Publishing Corp., 1957: (a) Agoston, G.A., Wise, H. and Rosser, W.A., p. 708; (b) Weiss, M.A., Rohrer, J.C. and Longwell, J.P., p. 439.
32. Weiss, M.A. and C.H. Worsham: Atomization in high velocity air streams, *ARS Jour.*, 29, 252-259 (1959).
33. Foster, H.H. and R.D. Ingebo: Evaporation of JP-5 fuel sprays in air streams, *NACA RM E55K02* (1956).
34. Marble, F.E. and E.E. Zukoski: Flame holding by bluff bodies, 12th Meeting AGARD Combustion and Propulsion Panel, Washington, D.C., Nov. 1957.
35. Nixon, A.C., *et al.*, Literature survey on vaporizing and endothermic fuels for advanced engine application, Shell Development Co., *Report S-13979* (1965).
36. Weber, R.J.: Propulsion for hypersonic transport aircraft, *Paper No. 64-558*, Int. Council of the Aeron. Sciences, Paris, France, 1964.
37. Walker, J.H.:   Preliminary design for supersonic flight, *APL/JHU TG 610-10* (1966).
38. Petersen, R.H., *et al.*, Some comparisons of turboramjet-powered hypersonic aircraft for boost and cruise missions, *J. Aircraft*, 3, 398-405 (1966).
39. Composite rocket/airbreathing engines, The Marquardt Corp., Van Nuys, Calif., *MP 5039* (October 1966).
40. Perini, L.L., *et al.*, Preliminary study of air-augmentation of rocket thrust, *J. Spacecraft Rockets*, 1, 626-634 (1964).

41. Dugger, G.L.: Comments on high performance combustion systems, XIIth International Aeronautical Congress, Washington, D.C., 1961, New York Academic Press, Inc., 1963, Vol. II, pp. 715-727.
42. Luidens, R.W. and R.J. Flaherty: Analysis and evaluation of supersonic underwing heat addition, *NASA Memo 3-17-59E* (1959).
43. Weber, R.J. and J.S. MacKay: An analysis of ramjet engines using supersonic combustion, *NACA TN 4386* (1959).
44. Billig, F.S.: A study of combustion in supersonic streams, *APL/JHU Bumblebee Report No. 321* (July 1964).
45. Swithenbank, J.: Theoretical performance of hypersonic ramjets with supersonic combustion, *Report No. SCS 25*, McGill University, Montreal (1960).
46. Billig, F.S.: Design of supersonic combustors based on pressure-area fields, Eleventh Symposium on Combustion, Berkeley, Calif., August 14-20, 1966.

Part Three

Rocket Propulsion

Rocket Classifications, Liquid Propellant Rockets,

Engine Selection, and Heat Transfer

George P. Sutton
Assistant to the President,
Rocketdyne Division,
North American Rockwell Corporation

[5-1] DEFINITIONS AND CLASSIFICATION OF ROCKET PROPULSION ENGINES

In a broad sense, *propulsion* is the act of changing the motion of a body. Propulsion mechanisms provide forces which move bodies that are initially at rest, change a constant velocity motion, or overcome retarding forces when a body is propelled through a medium. There are two essential elements in any propulsive mechanism: the energy source and an energy conversion device to transpose the energy into the form most suitable for propulsion. In an automobile, for example, a chemical combustion process of fuel with air furnishes the energy input, which is then transformed in an engine into thermal energy of a gas and subsequently by transformation into the mechanical energy through a rotating shaft and wheels to imparting momentum to the vehicle.

Jet propulsion is a special kind of propulsion; it is a means of locomotion whereby a reaction is imparted to a device by the momentum of ejected matter. There are two types of jet propulsion: *rocket propulsion*, where the matter which is to be ejected is stored internally within the moving device, and *duct propulsion*, where the surrounding fluid is ducted through the device and accelerated to a greater momentum by mechanical or thermal means prior to ejection. There are also combination schemes that eject both stored matter and some of the surrounding medium.

A *rocket engine* is the device or mechanism that converts the energy into suitable form and ejects stored matter to derive momentum. The working fluid or the ejected matter in rocket propulsion is called the *propellant* [1, 2, 3]. Among many possible energy sources, four are considered to be useful in rocket propulsion: (1) the chemical combustion reaction, (2) nuclear reaction, (3) captured radiation energy from an emitter such as the sun, and

(4) electric energy which is stored or created in the vehicle. Accordingly, the various propulsion devices can be categorized into chemical propulsion, nuclear energy propulsion, solar energy propulsion and electric energy propulsion (see Table 5-1).

Table 5-1   Energy Sources and Propellant Types for Several Different Rocket Propulsion Engines (Reproduced in part from Reference 1)

| Type of Propellant | Type of Energy Source | | |
	Chemical	Nuclear	Solar
Surrounding medium used as propellant working fluid	Aircraft with propeller	Nuclear turbojet Nuclear ramjet Nuclear submarine with propeller	
Surrounding medium plus stored propellant	Turbojet Ramjet Ducted rocket	Nuclear turbojet with chemical fuel afterburner	
Propellant stored inside vehicle	Liquid propellant rocket Solid propellant rocket Hybrid propellant rocket Chemical battery with electrical rocket propulsion	Nuclear fission rocket Nuclear reactor source with electrical rocket propulsion	Solar-heated hydrogen rocket
No propellant carried in vehicle		Photon rocket with nuclear reactor	Solar sail

Table 5-2 list several types of rocket engines together with ranges of typical key parameters. The first three use chemical energy, the next two use nuclear energy (the arc heating and the ion rocket are two forms of electrical propulsion), and the last one uses solar energy for heating of a thermodynamic working fluid. All these, with the exception of the ion rocket, use the nozzle expansion and acceleration of a heated gas as the mechanism for imparting momentum to a vehicle. The definition of some of the parameters in Table 5-2 are as follows:

The *specific impulse* is one of the important performance parameters used in rockets. It can be defined as the thrust that can be obtained from an equivalent rocket which has a propellant weight flow rate of unity. It is defined as

$$I_s = \frac{F}{\dot{w}}$$

$$= \frac{c}{g}$$

Table 5-2 Ranges of Typical Performance Parameters for Several Different Rocket Engine Types (Reproduced in part from Reference 1)

Engine Type	Specific Impulse (sec)	Maximum Temperature	Thrust-to-Weight Ratio	Duration	Specific Power (hp/lb)	Typical Working Fluid	Status
Chemical (liquid)	300 to 460	4,500 to 7,800	10^{-2} to 100	Seconds to a few hours	0.1 to 1,000	H_2 to O_2	in service use
Chemical (solid)	200 to 310	4,500 to 7,500	10^{-2} to 100	Seconds to minutes	0.1 to 1,000	fuel and oxidizer	in service use
Chemical (hybrid)	200 to 400	4,000 to 7,500	10^{-2} to 100	Seconds to minutes	0.1 to 1,000	fuel and oxidizer	experimental flight
Nuclear fission	600 to 1,100	5,000	10^{-2} to 30	Seconds to a few hours	0.1 to 1,000	H_2	in component development
Radioactive Isotope Decay	400 to 700	2,200 to 3,000	10^{-5} to 10^{-3}	Days	0.001 to 0.01	H_2	experimental static devices have been tested
Arc heating	400 to 2,000	10,000	10^{-4} to 10^{-2}	Days	0.001 to 1	H_2	experimental static devices have been tested
Ion	5,000 to 25,000	.....	10^{-5} to 10^{-3}	Months	0.001 to 1	Cesium	experimental engine has flown
Solar heating	400 to 700	2,500	10^{-3} to 10^{-2}	Days	0.001 to 1	H_2	research and analysis

where I_s is the specific impulse in pound of thrust per pound per second of propellant flow, F is the thrust in pounds, $\dot{w}$ is the weight flow rate in pounds per second, c is the effective exhaust velocity, and g is the gravitational constant. In a previous chapter, a discussion of specific impulse can be found. In general, I_s increases in engines using gas expansion as the gas temperature increases or the molecular weight of the reaction product gases decreases.

The *specific power* P_s is a parameter indicating the utilization of mass in the propulsion system in producing a maximum of kinetic gas power of the ejected matter. It is defined as

$$P_s = \frac{\frac{1}{2}\dot{m}v^2}{w_o} = \frac{F\,I_s\,g}{2\,w_o}$$

Here w_o includes the weight of the energy source (such as a nuclear reactor) as well as the propellants, the rocket engine system, and the structure weight. For chemical energy systems which operate only for short periods, the values of P_s can be several magnitudes higher than those for electrical propulsion devices which must carry a bulky, relatively inefficient source of electrical power as part of their loaded engine weight. The specific power is proportional to the thrust and the specific impulse.

The *thrust-to-weight* ratio expresses the acceleration (in multiples of the acceleration of gravity) that the engine is capable of giving to its own loaded propulsion system mass.

The chemical rockets, and to some extent also the nuclear fission rockets, have relatively low values of specific impulse, relatively light machinery (that is, low engine weights), a very high thrust capability, and therefore, high accelerations and high specific powers. At the other extreme, the ion propulsion devices have a very high specific impulse, but they must carry a heavy electrical energy source with them to deliver the power necessary for high ejection velocities. The radioactive isotope decay type, the arc heating rocket, and those using solar energy are intermediate in their values of specific impulse and thrust-to-weight ratio.

The specific impulse of the advanced electrical rocket engine types can be appreciably higher than those of chemical or some nuclear types. This means that they need to carry relatively little propellant because each unit or propellant is ejected at a very high velocity.

The very low acceleration potential for the electrical propulsion units and those using solar radiation energy usually requires a long period for accelerating, and thus is best used for those missions where the flight time is long. The low thrust values of electrical

systems imply that they are not useful in fields of strong gravitational gradients (such as for take-off or landing) but are best used in a true space flight mission far away from the strong gravitational field of the earth, moon or other heavenly bodies.

Table 5-3   Typical Classification Criteria

1. Propellant	a. Liquid Bi-propellant (fuel and oxidizer)
	b. Liquid Mono-propellant
	c. Solid propellant
	d. Gaseous propellant
	e. Hybrid propellant (*e.g.,* liquid oxidizer and solid fuel)
2. Type of mechanisms used for producing a high-velocity jet	a. Thermodynamic expansion of a hot gas in a nozzle (*e.g.,* liquid propellant rocket)
	b. Electrostatic acceleration of charged particles (*e.g.,* ion rocket)
	c. Sending a current through a conducting fluid (which is accelerated) in a magnetic field
3. Level of the thrust	a. Large (above 10,000 lbs.)
	b. Medium (500 to 10,000 lbs.)
	c. Small (less than a few hundred lbs.)
4. Manner of thrust application	a. Constant thrust single use
	b. Constant thrust repeated use
	c. Variable (pre-programmed) thrust single or repeated use
	d. Controlled variable thrust (not pre-programmed) either single or repeated use
5. Purpose of thrust application	a. To impart linear momentum (*e.g.,* boosters launch, sustainer or upper stage acceleration, space trajectory maneuvers)
	b. To impart rotational momentum (*e.g.,* attitude control and orientation of vehicles in flight)
	c. To separate adjacent stages in flight
	d. To eject stores during flight (eject pilot, fuel tank)
6. Application of rocket engine or rocket motor	a. Spacecraft propulsion
	b. Booster propulsion
	c. Air launched missile
	d. Ballistic missile (surface launched)
	e. Anti-aircraft missile
	f. JATO (jet assisted take-off)
	g. Catapult acceleration
	h. Aircraft power plant
	i. Attitude control
	j. Interplanetary vehicle propulsion
	k. Submarine launched missile
	l. Anti-ballistic missile devices
7. Status of development	a. Analysis and basic research
	b. Component research and development
	c. Experimental engine (static tests)
	d. Development for flight use
	e. In experimental flight use and/or pilot reduction
	f. In service use and production

TABLE 5-4

Table 5-4   Applications of Rocket Engines in Space Vehicles

Type	Application	Parameters	Remarks
Large liquid propellant rocket engine	Booster and sustainer stages of space launch vehicles	F = 100,000 to 1,500,000 lbs. t = 60 to 500 sec. I_s = 250 to 450 sec. Oxygen, jet fuel or $O_2 - H_2$	Constant thrust operation; sustainer may have one or two restarts
Medium-size, liquid propellant rocket engines	Maneuver of spacecraft; rendezvous and lunar landing maneuver	F = 1,000 to 15,000 lbs. t = 60 to 800 sec. I_s = 250 to 450 sec. Cryogenic or storable propellants	Throttling of thrust by factor of 10 to 1
Small-size liquid propellant rocket engines	Attitude control and trajectory correction of spacecraft	F = 1 to 150 lbs. t = 20 to 1000 sec. (cumulative) I_s = 250 to 300 sec. Storable propellants or mono-propellants	Many restarts required; pulsing operation
Large solid-propellant rocket	Take-off aid to launch vehicle; booster to a ramjet vehicle	F = 300,000 to 3,000,000 lbs. t = 30 to 120 sec. I_s = 220 to 250 sec.	Arranged in pairs
Medium-size solid propellant rockets	Emergency escape; ullage settling; stage separation; pilot ejection	F = 3,000 to 60,000 lbs. t = 1 to 20 sec. I_s = 220 to 300 sec.	Usually employed as a cluster
Small solid propellant rocket	Spin and despin of vehicle; separation of small stages; tilting of emergency tower	F = 50 to 5,000 lbs t = 0.5 to 10 sec.	

The last column of Table 5-2 indicates that the liquid and solid propellant rockets are the only ones with proven practical applications.

This chapter includes a brief discussion of liquid propellant rocket engines. Other types are covered in other chapters.

In addition to grouping by energy source as shown in Table 5-1, rocket propulsion devices can be classified according to many different criteria. The criteria listed in Table 5-3 indicate some of the many types and variations that have been investigated.

Of course there are other criteria which have been used to classify rocket propulsion devices other than those listed above. Each of the items listed could easily be expanded into a separate chapter, and many of these items will be covered in more detail later in this book. Table 5-4 lists several applications for chemical rocket engines as used in typical multi stage space vehicles. It gives an appreciation of the wide variety of engine types used on a single space vehicle.

[5-2] LIQUID PROPELLANT ROCKETS

Liquid propellant rocket engines use liquid propellant chemicals which are fed under pressure from *propellant tanks*, through pipes, and through an *injector* into a *combustion chamber*. The combustion takes place at relatively high pressures (100 to 1000 psi) resulting in very high temperature gases (4000 to 7500° F.) which are expanded in a supersonic nozzle to very high exhaust velocities (6000 to 14,000 feet per second). The assembly consisting of the injector, the combustion chamber, and the nozzle is known as the *thrust chamber*.

The two most common types of *feed system* for transporting the propellant from the vehicle tanks to the thrust chamber are the *pressure-feed system*, in which the liquid propellants are displaced and expelled by a high-pressure gas, and the *turbopump-feed system*, in which the propellants are pumped (Figs. 5-1 and 5-2). In the turbopump-feed system, a turbine drives the pump, and the turbine, in turn, derives its energy from a small combustion chamber known as a *gas generator*. The same two liquid propellants are usually burned in the gas generator but in a different proportion to produce gases cool enough (1200 to 1800° F.) to prevent melting of the turbine buckets. The pressure-fed system is simpler and usually lighter in weight for low-thrust or short-duration applications, and it can readily be used for variable-thrust operation. Its tanks operate at relatively high pressures and are usually quite heavy. The turbopump-fed system is usually lower in weight for high-thrust or long-duration applications; its tanks are thin and relatively light in weight. Because it has rotating machinery and gas generator and thus more controls, the turbopump-fed system is more complex.

The assembly consisting of a combustion chamber, injector and nozzle is known as a *thrust chamber*. In it the liquid propellants are metered, injected, atomized, vaporized, mixed, and burned to form hot gases, which in turn are accelerated and ejected at high velocity to impart a reaction force to the vehicle. Because of the high temperature, high density, and high velocity of these gases, the heat-transfer rate is very high and the thrust chambers must be cooled or constructed of special high-temperature materials.

In a *regeneratively cooled thrust chamber*, one of the liquid propellants (either usually the fuel, but sometimes also the oxidizer) is circulated through a cooling jacket or through tubes around the thrust chamber, and the coolant absorbs the heat transferred from the hot combustion gases to the walls. In a *radiation-cooled chamber*, the thrust chamber walls are constructed of special materials (usually refractory metals) which operate at sufficiently high wall temperatures (2000 to 3500° F.) to reject *heat* to their surroundings by radiation; the walls have a red-or-white-hot glow.
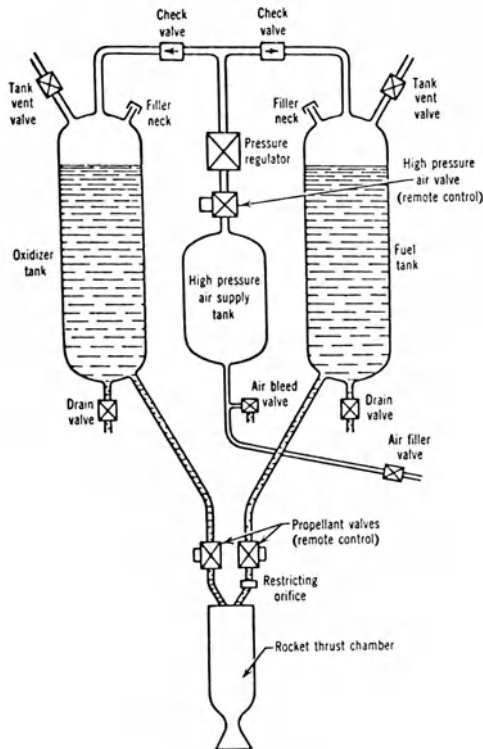
Fig. 5-1 Schematic diagram of a liquid propellant rocket with a gas pressure feed system.
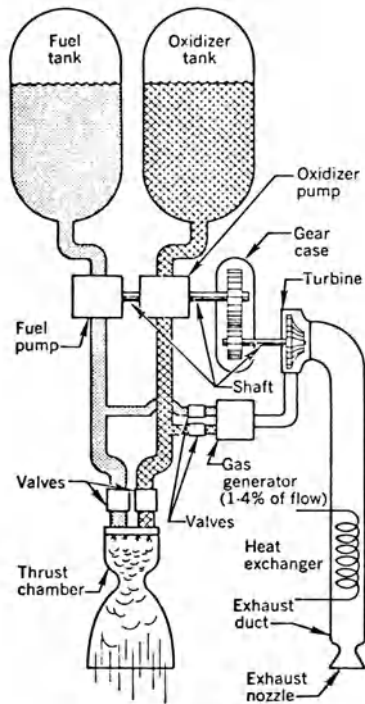
Fig. 5-2 Schematic diagram of a liquid propellant rocket engine with turbopump feed system.

In an *ablative thrust chamber*, the walls are made of special impregnated composite fabric-plastic materials (*e.g.,* glass filament cloths in an epoxy-type plastic matrix) which are consumed (burned, charred, melted, or vaporized) at a slow rate to form cool protective gas or liquid boundary layers near the chamber and nozzle wall. The internal dimensions of an ablative thrust chamber thus increase slightly with operating duration.

In the zero-gravity environment of space, emptying propellant tanks present special problems. When a liquid propellant rocket engine is to be started in a gravity-free environment, provisions must be made to ensure that the tank outlet is covered with liquid propellant. If gases or vapor are allowed to enter the thrust chamber, the rocket will perform erratically. One method of avoiding these conditions and ensuring delivery of liquids is to use a *positive expulsion system*, such as confining the liquid in a flexible (rubber like) bag inside the metal tank so as to be physically separated at all times from the pressurizing gas, which thus cannot enter into the tank discharge pipe.

All liquid propellant rocket engines have *controls* (usually various valves and their actuating mechanisms) to accomplish one or more of these tasks: (1) start the engine and ignite the propellant combination, (2) shut-off rocket engine operations, (3) restart,

Table 5-5   Liquid Propellant Performance Characteristics

Propellant type	Propellant Combination	Theoretical Specific Impulse (sec.)	Bulk Density (lb./cu.ft.)	Optimum Mixture Ratio	Combustion Temperature °F	Approx. Molecular Weight of Exhaust Gas (lb./mole)
Cryogenic	Oxygen-hdro-carbon (kerosene)	301	62.7	2.45	6,145	22.7
Cryogenic	Oxygen-hydrogen	391	18	4.0	4,915	9
Cryogenic	Fluorine-hydrogen	410	29	8.0	6,670	10
Storable	$N_2O_4 - N_2H_4$	292	76	1.31	5,320	21
Storable	$N_2O_4 - 50\%\ N_2H_4 + 50\%$ UDMH	289	74	1.88	5,520	22
Mono-propellant	90% H_2O_2	147	88	—	1,370	21
Solid	NH_4ClO_4, Al and organic polymer	265	100	—	5,400	25

*At a chamber pressure of 1,000 psia and a nozzle exit pressure of 14.7 psia (shifting chemical equilibrium)

(4) maintain a programmed operation (*e.g.*, predetermined variable thrust), (5) effect emergency shutdown when a safety device senses a malfunction or critical condition in the vehicle, (6) fill the system with propellants, (7) drain excess propellants after engine use, and (8) check out proper functioning of critical engine control components without actual engine operations.

Liquid propellants usually consist of an oxidizer (*e.g.*, liquid oxygen, nitrogen tetroxide [N_2O_4], or nitric acid) and a fuel (*e.g.*, hydrogen, hydrazine (N_2H_4), or kerosene). Table 5-5 list several liquid propellants and some of the performance characteristics.

Cyrogenic propellants are cold, liquefied gases, such as liquid hydrogen (-423°F.) or liquid oxygen (-297°F.). Because of their low temperature, they present some storage problems and thus require tank insulation. Rocket engines using cryogenic propellants have the best performance and are used in almost all large launch vehicles. *Storable propellants* are those that remain in liquid form over a range of ambient temperatures; typical is nitrogen tetroxide with dimethylhydrazine fuel. Storable liquid propellants are used extensively for air launched missiles, attitude control engines, lunar takeoff engines, rendezvous maneuvers, or midcourse correction engines. *Liquid monopropellants* contain an oxidizing agent and a combustible fuel, all in the same substance; hydrogen peroxide is a monopropellant when it is catalytically decomposed into oxygen and steam. Because there is only one propellant, the rocket engine and its feed system are simpler, but the performance is generally lower. The performance relations also apply to liquid propellant rocket engines. The performance can be determined quite accurately from a simplified one-dimensional theory, which assumes that the gas reaction products are homogeneous and invariant in composition throughout the thrust chamber, that these products obey the perfect gas laws, that there is only negligible friction in the flow through the chamber and nozzle, and that the flow is adiabatic (no heat transfer). The equations for thrust, specific impulse, nozzle area ratio thrust coefficient and exhaust velocity can be found on pages 74-75.

For liquid propellant rocket engines, the *propellant mixture ratio r* is defined as the ratio of the oxidizer flow rate $\dot{w}_o$ to the fuel flow rate $\dot{w}_f$:

$$r = \frac{\dot{w}_o}{\dot{w}_f}$$

$$w = \dot{w}_o + \dot{w}_f$$

The values of optimum mixture ratio listed in Table 5-5 refer to the ratio of which the specific impulse is a maximum. The equation

above can be solved for the respective propellant flow rates, $\dot{w}_o$ or $\dot{w}_f$ in terms of the total propellant flow rate $\dot{w}$ and the mixture ratio r:

$$\dot{w}_o = \frac{\dot{w}r}{r + 1}$$

$$\dot{w}_f = \frac{\dot{w}}{r + 1}$$

The *average density* ρ_{av} of the propellant combination is a value of a hypothetical mixture of liquid oxidizer and fuel; it gives an indication of the compactness of the propellant combination:

$$\rho_{av} = \frac{\rho_o \rho_f (1 + r)}{r\rho_f + \rho_o}$$

Here ρ_o = oxidizer density
      ρ_f = fuel density
Values of ρ_{av} range from 0.35 to 1.3 g/cc.

Liquid propellant rocket engines are used today for the large majority of manned and unmanned space programs (Saturn I, Saturn V, Atlas, Titan I, II, Centaur, etc.) and have proven to be reliable, serviceable, amenable to preflight checkout, and high in performance. In addition, they have proven to be a low-cost, reliable, missile-propulsion system in the form of a pre-packaged storable propellant rocket engine (Bullpup, Condor, Lance). To date, the majority of R&D and production funds have been spent on liquid propellant rocket engines.

    Liquid propellant rocket engines using H_2 fuel have given high performance and have been flown as upper stages on space launch vehicles. The 200,000 lb. thrust J-2 rocket engine (Figs. 5-3 and 5-4) is an example of a reliable, restartable engine used in this gimballed application. It uses two turbopumps (one for fuel and one for oxidizer) with a single separate gas generator; the exhaust gases are aspirated into the nozzle of the thrust chamber [4].

    Liquid bipropellant and monopropellant rocket engines with pressure-fed systems have been used extensively in the low thrust (1 to 150 lb. thrust) vehicle attitude control and maneuvering applications. Here, repeated reliable starts (sometimes several thousand restarts per flight), efficient pulse performance (*i.e.,* good specific impulse for very short durations of 0.020 seconds or less), zero leakage of propellant, operation in zero gravity and ability to withstand the space environment are important. Figure 5-5 shows a Gemini attitude control engine of 23.5 lb. thrust. In a

LEGEND

1. Gimbal
2. Oxidizer inlet duct
3. Oxidizer turbopump
4. Start tank
5. Auxiliary flight instrumentation package
6. Exhaust manifold
7. Thrust chamber
8. Oxidizer turbine bypass valve
9. Turbine bypass duct
10. Main fuel valve
11. High pressure fuel duct
12. Start tank discharge valve
13. Fuel turbopump
14. Fuel bleed valve
15. Fuel inlet duct
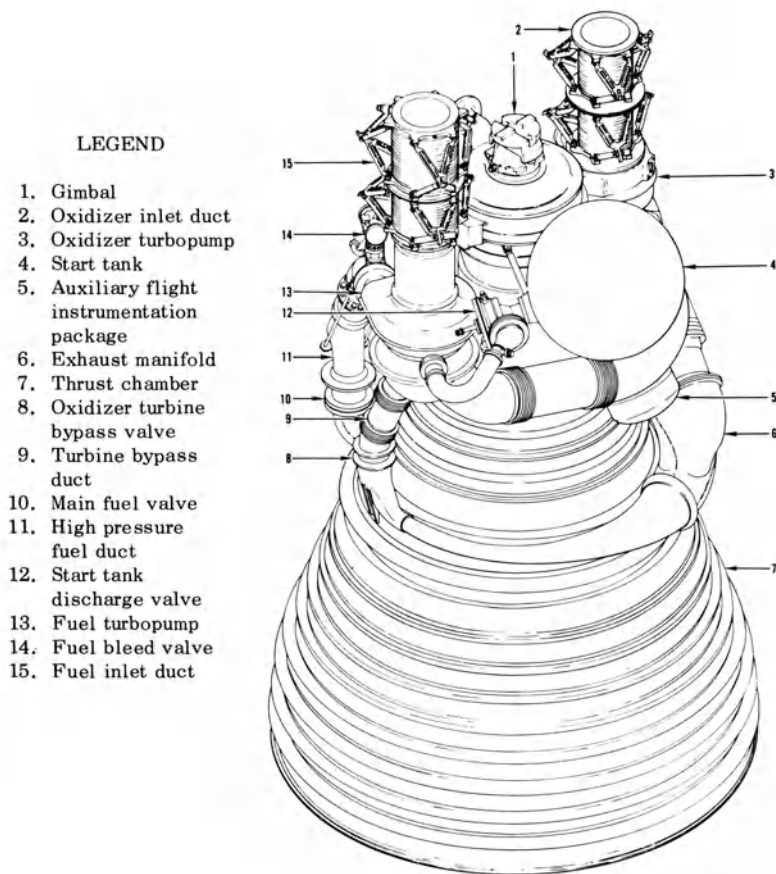
Fig. 5-3 J-2 Rocket Engine.

nominal mission, this ablative thrust chamber experiences approximately 3,000 restarts, a total accumulative duration of approximately 600 seconds, over a total mission time of 14 days.

Figure 5-6 shows the propulsion system for the Bullpup missile, which is typical of a reliable, low-cost liquid storeable propellant prepackaged system [5].

Performance of the aerodynamic spike nozzle is a function of various nozzle geometric parameters, the amount of secondary flow, the manner in which this secondary flow is introduced, and the relative energy between the primary and secondary streams (Fig. 5-7).

The primary flow (high pressure gases) which produces the major portion of the engine thrust is exhausted from an annular-type combustion chamber and expands against the metal surface of the center
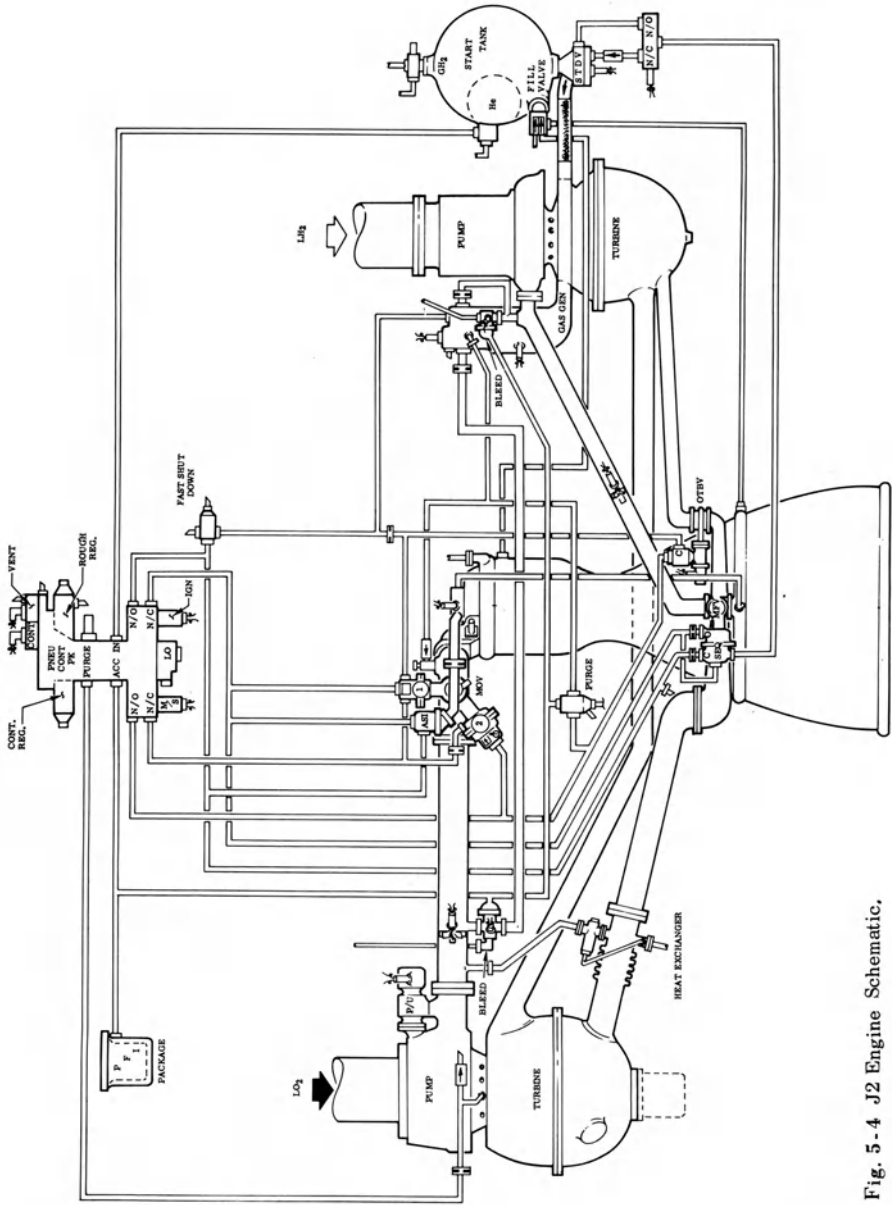
Fig. 5-4 J2 Engine Schematic.

PROPELLANT VALVES

INJECTOR

STAINLESS STEEL SHELL

6° ORIENTED ABLATIVE

PARALLEL WRAP ABLATIVE SLEEVE

GLASS WRAP (STRUCTURAL)

ASBESTOS WRAP

CERAMIC LINER

CERAMIC INSERT

PARALLEL WRAP ABLATIVE
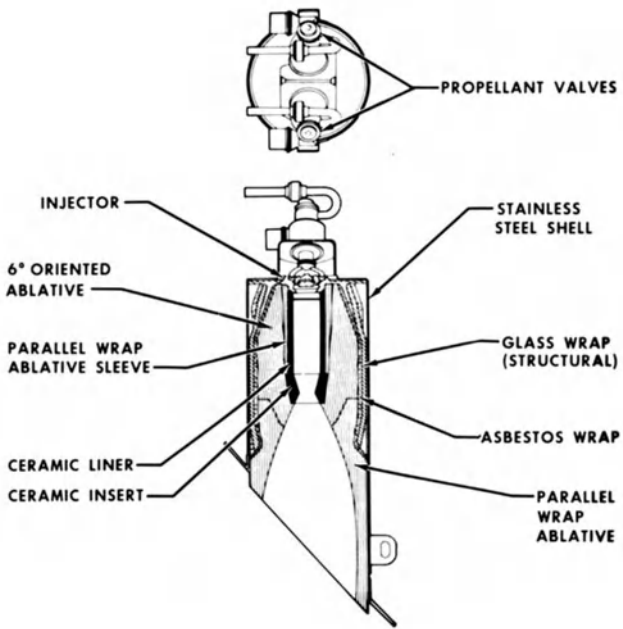
Fig. 5 - 5 Gemini 25-lb. thrust chamber for orbit attitude maneuver system.

truncated-spike nozzle. The characteristics of the primary flow
field upstream of the base (region 1) are determined by the annular
throat geometry, the nozzle wall contour, and the ambient pressure.
The annular primary flow continues to expand beyond the nozzle
surface and encloses a subsonic, recirculating flow field in the base
region (region 2). The pressure acting on the nozzle base contrib-
utes additional thrust to the nozzle.
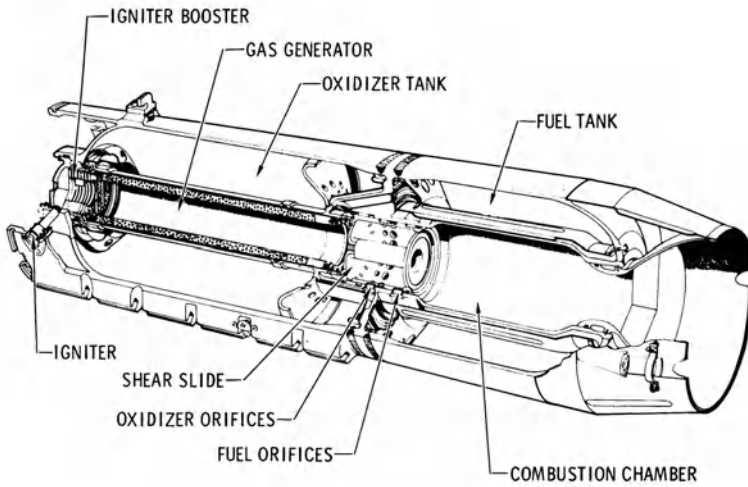
Fig. 5-6 Bullpup B prepackaged storable liquid propellant rocket propulsion system.
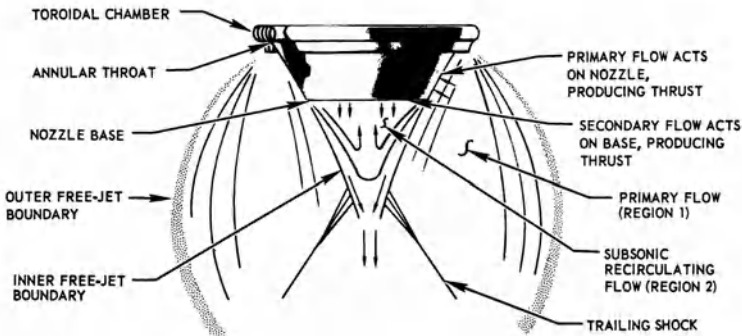
Fig. 5-7 Schematic diagram of an Aerospike engine.

When a small amount of secondary flow (1 to 3% of total flow) is introduced into the base (added to the recirculating flow), the base pressure is increased further. As the secondary flow is increased, the overall nozzle efficiency (considering the additional flow) increases because of this increase in base pressure. There is a limit to this gain in efficiency, and an optimum secondary flow exists for each configuration.

The outer surface of the annular primary flow is a free-jet boundary which is influenced by ambient pressure. This ambient pressure influence on the primary nozzle flow endows this type of nozzle with altitude compensation. In operation at high-pressure ratios (*i.e.*, altitude conditions), the outer free-jet boundaty of the primary flow expands outward, governed by the Prandtl-Meyer turning angle at the throat. At low pressure ratios (*i,e.*, sea level operation), the relatively higher ambient pressure compresses the outer free-jet boundary of the primary flow field. This compression increases the static pressure on the nozzle wall and partially offsets the negative effect of the higher ambient pressure on the back side of the nozzle. The base pressure also is increased with the higher ambient pressure, because the compressed primary flow field, which influences the base pressure, has higher static pressures. This combination of the flow field effects provides the altitude compensation inherent to the aerodynamic spike nozzle.

The ambient pressure influence causes the performance to be near an "ideal" variable-area-ratio nozzle at all p_c/p_a values; this effect is called altitude compensation [6].

[5-3] SELECTION CRITERIA

When selecting a specific rocket engine for a given application, a large number of factors have to be considered and evaluated. Very often more than one type of rocket engine will satisfy most of the requirements, and the selection then has to be based on minor differences, prior experience, and the background and prejudices of those who do the selecting. Table 5-6 is a list of typical selection criteria. Even though a list of this kind has to be tailored to a specific application and is not complete, it can be useful as a checklist. The table is divided into four major sets of criteria; namely, performance, logistic, economic and so-called judgment criteria. While this course deals primarily with the first category, namely, some of the engine performance criteria, the other three categories are usually equally or more important in selecting a rocket engine for a specific job.

Table 5-6   Selection Criteria

A. PERFORMANCE AND OTHER TECHNICAL CRITERIA

1. Engine Performance

    Magnitude and direction of thrust
    Specific impulse (guaranteed and nominal values)
    Total impulse (guaranteed and nominal values)
    Engine weight (with and without propellants)
    Propulsion system weight
    Starting transient and timing
    Shut-down impulse and timing
    Residual propellant
    Volume (length or maximum diameter) of engine/propulsion system
    Duration of operation (mission duty cycle)
    Number of operating cycles (restarts)
    Operating temperature limitations
    Sensitivity of performance to minor variations in propellant composition, density,
        or environmental conditions
    Sensitivity of start and stop transient to environmental factors
    Performance for short-duration pulses
    Wall temperature of critical engine parts
    Variation of specific impulse with altitude

2. Storability

    Storage life
    Storage temperature limitation
    Temperature cycling limitations
    Vibration during transport
    Vacuum environment
    Ability to perform engine checkouts during storage
    Deterioration of propellant/hardware

3. Reliability

    Margin of safety used in design analysis
    Complexity/simplicity of propulsion systems
    Degree of built-in redundancy
    Demonstrated reliability of engine
    Time between overhauls
    Ability to check out engine or critical components prior to use
    Instrument reliability
    Failure sensing and safe shutdown devices
    Reliability of related auxiliary system (*e.g.,* electrical heaters, telemetry)
    History of prior flight failures

4. Other Performance Criteria

    Flexibility for alternate missions
    Required vehicle supplied engine inputs (*e.g.,* electric power, voltage, hydrau-
        lics, pneumatic)
    Flame radiation to vehicle
    Flame RF emissions and absorptions
    Flame IR emissions
    Noise emission spectrum

Table 5-6   Selection Criteria (Cont.)

Vibration excitation to engine mount
Decontamination procedure after operation
Extent of smoke in exhaust
Required fuel and oxidizer supply conditions (pressure, tanks position)
Gimbal actuation (angle, moment of inertia, angular acceleration, power, etc.)
Thrust vector control (sensitivity, response, angle, etc.)
Growth potential of current design (higher thrust, more specific impulse, longer
   duration, etc.)

B. OPERATIONAL CRITERIA

1. Safety

Corrosiveness of propellant (chemical reaction with various materials)
Toxicity of propellant and/or exhaust products
Detonation hazard
Fire hazard
Devices and means for overcoming propellant hazards
Limitation on propellant storage quantity
Ignition safety devices
Arming system
Required safety procedures

2. Supply and Logistics

Ease or difficulty of storage, surveillance, engine replacement, maintenance, fuel-
   ing, defueling, repair, or servicing in the field and at the factory
Number and types of special tooling or spare parts
Complexity of checkout equipment
Mobility of checkout equipment and special tooling
Quality and type of records on each part, its history (design change, inspection,
   use, etc.)
Ease of checking and replacing or fixing critical components while engine is in-
   stalled in vehicle
Clarity, availability, and usability of handbooks

3. Operating Parameters

Time and effort required for checkout
Time and effort required for engine replacement
Number and type of engine controls
Number and type of measurements/indicators for engine operation
Number of interconnecting devices
Operating environmental limitation
Readiness for use

C. ECONOMIC CRITERIA

1. Cost of engine development
2. Cost of engine/vehicle integration
3. Cost of engine unit in production
4. Cost of engine operation (maintenance, repair, servicing and overhaul)
5. Availability of engine
6. Schedule of deliveries
7. Availability and condition of manufacturing tooling, static test facilities, vibra-
   tion test equipment, overhaul facilities, shipping containers, etc.)
8. Cost and schedule of training the operating and servicing crews

Table 5-6   Selection Criteria (Cont.)

9. Extent of need for critical materials, critical manufacturing processing, or critical facilities
10. Location of manufacturing and test facilities
11. Leadtime for key component manufacture

D. INTANGIBLES OR JUDGMENT CRITERIA

1. Relative advance in the state-of-the-art
2. Existence of experience background and its applicability to a specific application
3. Reputation of engine manufacturer and his prior performance, cost and schedule
4. Interference of the work on the selected engine with other urgent work in same factory
5. Credibility of attaining promised performance, cost and schedule
6. Applicability of same engine to other vehicles
7. Relative importance of engine program to other programs (priority)
8. Availability of funds

[5-4] HEAT TRANSFER (based largely on Reference 7)

In rocket propulsion devices a large quantity of heat is transferred from hot gases to the walls of the device. This high heat flux occurs in all types of propulsion devices including solid propellant combustion chambers and nozzles, liquid propellant gas generators and their piping, injectors, nozzles, chambers of liquid propellant thrust chambers, electric arc jets, or nuclear rocket thrust chambers.
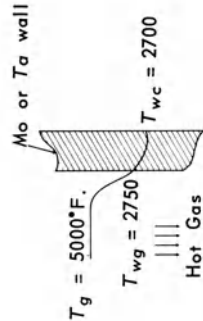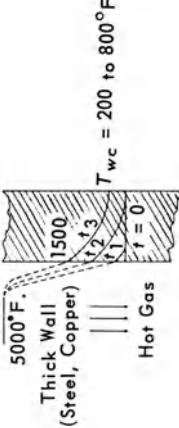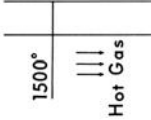
There are many different techniques for preventing this high heat flux from overheating the walls of the chambers or nozzles and several of these techniques will be discussed briefly approximately in the order of increasing heat flux. Table 5-7 shows a summary of several of these techniques.

[5-4.1] Radiation Cooling

In radiation-cooled chambers, there is a steady-state heat-transfer condition with radiation emission to the surrounding environment from the hot wall. These walls usually radiate at temperature of 2400-2900°F if refractory metal (Cb, W, Ta, and Mo) walls are used. The heat is transferred by convection from the hot gases to the chamber wall, conducted through the wall, and in turn is rejected to cooler surroundings by means of thermal radiation emission. This emission is strongly influenced by the surface condition of the wall.

Refractory metals are difficult to fabricate and some suffer from hydrogen embrittlement and lack of ductility. Some oxidize readily and need a protective coating.

Table 5 - 7   Cooling Methods Compared

Name	Description	Temperature Diagram	Application
Radiation Cooling Single Wall	High-temperature, lightweight, refractory-metal pressure vessel which glows white hot and rejects heat by thermal radiation. (Reaches thermal equilibrium)	Mo or Ta wall $T_g = 5000°F.$ $T_{wg} = 2750$ $T_{wc} = 2700$ Hot Gas	Low-thrust, low chamber-pressure unit for attitude control (*e.g.*, Apollo Service Module). Uncooled nozzle exit skirt extensions
Heat-Sink Cooling	Heavy-walled metal shell. (Does not reach thermal equilibrium)	$5000°F.$ Thick Wall (Steel, Copper) 1500 $t = 2, 3$ $t = 1$ $t = 0$ $T_{wc} = 200$ to $800°F$ Hot Gas	Short-duration, low-thrust, low-pressure units. (Typical experimental unit for evaluating propellants or feed-system, features, JATO's, or retrorockets)
Low Flame-Temperature Metal Chamber	Wall temperature achieves temperature of combustion; equilibrium condition	1500° Hot Gas	Low-performance propellants with low flame temperature. (Nitrate solid propellant or H_2O_2)

Table 5-7   Cooling Methods Compared (Cont.)
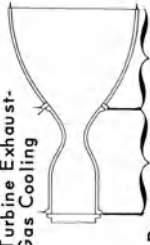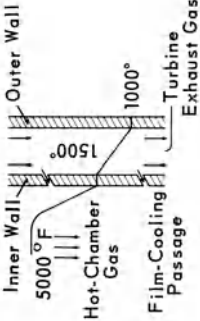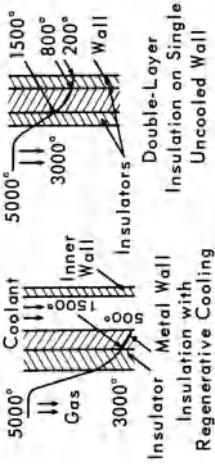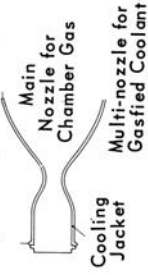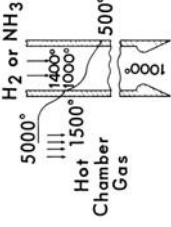
Name	Description	Temperature Diagram	Application
Turbine Exhaust-Gas Cooling	Turbine exhaust gas (900 to 1500°F.) is used as coolant in cooling jacket and/or as film-cooling fluid	Inner Wall, Outer Wall, 5000°F, 1500°, Hot-Chamber Gas, 1000°, Film-Cooling Passage, Turbine Exhaust Gas, Regenerative Cooling Jacket, Jacket Cooled By Exhaust Gas	Limited to nozzle exit skirt extensions because of small amount of available gas and heat capacity
Insulation Cooling	Low conductivity coating or layer on wall surface for heat flux reduction	5000° Gas, 5000° Coolant, Inner Wall, 3000°, 1500°, 500°, Insulator, Insulation with Regenerative Cooling, Insulators, Metal Wall, 1500°, 800°, 200°, Wall, Double-Layer Insulation on Single Uncooled Wall	High-pressure, high-performance solid or liquid propellants for high-heat-flux conditions
Dump Cooling	Fraction of propellant is used as coolant in cooling jacket and eventually dumped overboard for performance gain	H₂ or NH₃, 5000° Hot Chamber Gas, Hot 1500°, 1400°, 1000°, 500°, 1000°, Main Nozzle for Chamber Gas, Multi-nozzle for Gasfied Coolant, Cooling Jacket	Generally, H₂ or NH₃ fuels

Table 5-7 Cooling Methods Compared (Cont.)

Name	Description	Temperature Diagram	Application
Ablative Cooling	Progressive endothermic decomposition of wall surface, forming insulating char for passage of pyrolysis gases		Moderate- and low-pressure, limited-duration designs for combustion chamber and nozzle; skirt extensions; throttleable space engines; attitude-control space engines
Regenerative Cooling	One of propellants (fuel) circulation in wall cooling jacket and passed into injector for combustion; most commonly used method		Most liquid-propellant applications; low and high thrust to moderate chamber pressure; used on Atlas, Titan, Thor, Saturn, etc.
Film Cooling	Coolant film injected as heat-absorption boundary between combustion gas and wall surface		Very high-pressure and large-thrust applications

Table 5-7   Cooling Methods Compared (Cont.)

Name	Description	Temperature Diagram	Application
Transpiration Cooling	Diffusion of mass transfer coolant through thick porous or mesh wall wall with low velocity; absorption of heat through wall and blockage on surface		Nuclear, F_2–H_2 O_2–H_2 fueled designs for ultrahigh heat-flux application with low performance loss
Combined Methods	Use of two or more methods to reduce cooling pressure drop, increase performance, duration, reduce weight, etc.		High- and low-pressure-thrust, etc., special applications for heat-transfer optimization

The advantages of radiation cooling are that it provides a relatively simple and light construction, it can be throttled, and it can operate for long-firing durations. The principal applications for the radiation method are in small attitude-control liquid-propellant engines of space payloads or upper space-vehicle stages (usually less than 150 lb. thrust and 50 to 150 psia chamber pressure) where the rocket is mounted outside the spacecraft. It is also used as uncooled nozzle-skirt extensions of solid-or-liquid-propellant chambers of all sizes where the chambers themselves are cooled by other means. The radiation-cooled nozzle skirt becomes useful at locations where heat flux and local gas stream pressure are low and where the nozzle protrudes beyond the vehicle external envelope to permit adequate heat rejection.

[5- 4.2] Heat-Sink Cooling

The use of a single-wall metal combustion chamber and nozzle offers a simple, easy-to-make and inexpensive means of cooling. Because of the transient nature of this cooling method, it is limited by the heat capacity of the wall, which is determined by wall thickness, density, and specific heat; copper and steel have been used. At high heat-flux conditions, only relatively short-firing durations (of the order of a few seconds) may be possible. Failure occurs when inside wall temperature exceeds the point at which either melting or erosion takes place.

For solid-propellant motors, materials which exhibit good heat-sink properties, and also have high melting points, are high-density graphite, edge-grain pyrolytic graphite, and tungsten. Usually these materials have insulation layers in critical areas.

[5- 4.3] Low Flame Temperature Metal Chamber

When the maximum allowable wall temperature is higher than the flame temperature, there is really no cooling problem. This occurs, for example, when monopropellants such as H_2O_2 (1300° F.) or N_2H_4 (up to 2000° F.) are used with conventional metals such as the stainless steels (melting point 2600° F.). This type of rocket is useful in very special cases where cost, simplicity, and schedule considerations are of great importance.

[5- 4.4] Turbine Exhaust Gas Cooling

In the case of a turbopump-fed, liquid-propellant engine, which usually has relatively high thrust and long duration, the turbine which drives the propellant pumps provides a small flow of turbine exhaust gas (usually around 600 to 1000° F.) which can be used for some limited cooling applications.

The cooling capacity of this gas is limited not only by the low mass flow (1 to 4% of the total propellant flow) and the small available heat capacity, but also by the maximum temperature rise that can be absorbed without exceeding maximum tolerable metal wall temperatures.

The best application of this type of cooling is nozzle-skirt cooling in large liquid-propellant engines, where the chamber and converging section, throat region, and part of the supersonic diverging section are cooled by another cooling method, such as regenerative cooling. In such cases, turbines exhaust gases can be injected as a film coolant along the gas-side nozzle-wall surface (where pressures are low enough to permit it) and/or used as a coolant in a jacket along the nozzle surface and expelled at the chamber exit to augment thrust.

[5-4.5] Insulation Cooling

The application of insulation is not by itself a cooling method but is rather an auxiliary, but successful, means of enhancing other cooling methods. The use of various types of insulation introduces thermal resistance into the heat-flux path and thus reduces the amount of heat that must be absorbed or disposed of by the cooling mechanism. In addition, for a given cooling capacity, the added resistance permits an increase in the capability to handle hotter temperatures or high chamber pressures.

There are several types of insulation. For example, there are coatings which are painted on a metal surface and subsequently hardened or baked, such as certain silica, asbestos, or ablative formulations; thin ceramic coatings of refractories applied to metal surfaces, such as alumina, thoria or zirconia; and special sleeves or separate walls of ceramic, ablative material, asbestos-filled rubber bonded to the wall, graphite or other refractory materials. Numerous insulation methods and materials are found in each category.

All of these insulators have deviciencies. They are not always resistant to the oxidation or chemical corrosion action of the hot-reaction products, and they do not always readily resist the erosive action of the hot high speed gases. Many insulation layers cannot take the required high temperatures (they become soft and peel off), and most of these materials cannot readily take severe repeated thermal shock and stress.

[5-4.6] Dump Cooling

This Rocketdyne-developed concept employs low-molecular-weight fuels such as liquid hydrogen or liquid ammonia in a

cooling-jacket passage which surrounds the thrust chamber. It is similar to regenerative cooling, but instead of recirculating the heated coolant back to the injector and into the combustion chamber where it will enter into the combustion process, the fuel is evaporated in the cooling passages and then dumped overboard at the nozzle exit. Gasified coolant is ejected at supersonic velocity through a separate set of nozzles, thus adding to the total specific impulse of the vehicle.

Because the gases coming from the dump-cooling jacket are not as hot as those coming directly out of the combustion chamber, overall performance is somewhat reduced. Also, dump cooling is not suitable with propellants that form high-molecular-weight vapors.

[5-4.7] Ablative Cooling

Ablative cooling involves the use of wall materials which undergo endothermic thermal degradation (or chemical and physical changes) and consequent mass removal but leave enough material to preserve structural geometry and integrity.

Char-forming plastics reinforced with organic or inorganic fibers have proved to be satisfactory for thrust-chamber applications. Commonly-used materials include phenolic and epoxy resins reinforced with oriented high-silica glass, carbon or graphite fibers.

Initially, a resin-based ablative wall acts like an ordinary heat sink, but low thermal conductivity causes the surface temperature to rise very rapidly. At about 1000° F., the resin decomposes endothermically into a porous carbonaceous char and pyrolysis gases. As the char increases in depth and temperature, the pyrolysis gases may undergo additional endothermic thermal cracking as they percolate through the char and into the combustion gas boundary layer.

With silica reinforcement, as the surface temperature approaches 3000° F., a highly endothermic reaction with carbon in the char may take place, providing additional thermal protection. Above this temperature, the silica will melt to provide a very viscous film which may protect the char from chemical erosion.

In rocket-engine applications where regenerative cooling cannot be easily applied and where limited dimensional changes are tolerable, the use of ablative materials is quite satisfactory. Thus, in low-thrust space engines where insufficient fuel coolant is available for regenerative cooling, ablative materials are used in the combustion chamber and exit-cone regions. With relatively nonoxidizing or low combustion temperature propellants, suitable ablative materials can even be used in the throat region without affecting performance adversely. They are also used successfully

as liners for chambers, nozzles, blast tubes or exit cones of solid rocket motors.

The self-regulating thermal protection afforded by ablative cooling makes this method particularly suitable for engines that can be throttled. Ablative chambers have been particularly useful for pulsing or cycling operations where individual pulses may be of very short duration approaching a few milliseconds.

[5-4.8] Regenerative Cooling

In the past, regenerative cooling was the principle method of cooling all liquid-propellant engines, and it is still in satisfactory use in large liquid-propellant engines. With this method, the coolant is first circulated in a jacket with thin (0.010 to 0.080 inches thick) metal wall which separates the coolant from the combustion gases and is then passed through the injector into the combustion chamber. Fuel is generally used as the coolant principally because its total allowable heat capacity and heat transfer properties are generally the highest, and because it presents a nonoxidizing atmosphere to the heated inner-wall surface. Some oxidizers have been used experimentally as regenerative coolants.

Commonly used wall materials are stainless steel, nickel, and Inconel with temperature limitations around 1600° F. Thermal conductivity indicates the occasional use of copper or aluminum, but the minimal strength of these materials with increased temperature and weight implies low stress-level applications.

Thrust chamber walls are generally composed of a bundle of long coolant tubes which are shaped to the nozzle contour. At smaller thrust and pressure levels, a milled channel or double-wall approach appears more advantageous.

[5-4.9] Film Cooling

The film-cooling method is a unique approach which permits relatively simple thrust-chamber wall construction. Coolant is injected along the gas-side wall surface by means of a series of circumferentially located coolant holes, slots or louvers. If a combustion chamber of short length is employed, injection can be provided at the injector face, and the film-cooling effect will persist to the throat region. The wall temperature essentially assumes the film-coolant value, increasing from the inlet-coolant-injection temperature at the injection points to the final allowable wall-temperature value further downstream. In a fully film-cooled design, injection points are located at incremental distances along the wall length. Judicious spacing of injection locations can provide optimum wall-temperature distribution.

A principal disadvantage to the film-cooled design is the performance loss associated with unburned coolant adjacent to the wall surface (usually 1 to 10%). At high chamber pressures, the performance degradation caused by the coolant may result in an actual reduction of specific impulse when compared to other cooling methods.

The main film-cooling applications would be either in supplementation or in large-thrust designs where only localized portions of the chamber would be film cooled and only a small percentage of the total propellant flow would be required. Surface film stability under high turbulence, phase changes along the cooled length, and endothermic or exothermic decompositions are problems which require further study.

[5-4.10] Transpiration Cooling

Transpiration cooling is quite similar to film cooling, differing primarily in the injection technique. A transpiration-cooled surface is composed of either a porous sintered material or a fine-pored, compressed, multiple screen mesh. Coolant is diffused or percolated at low velocity through the surface into the hot combustion gas boundary layer with a blocking effect which reduces heat flux to the wall. The transpiration method is much more efficient (three to five times less flow) than film cooling because of the axial and circumferential uniformity of the wall temperature and the low propellant injection velocity, which results in small mixing losses with mainstream gases. Design and fabrication problems of porous walls with variable porosity, without degradation of the porosity and a loss in performance, continue to be problems with this method.

[5-4.11] Combined Methods

Two or more cooling methods can often be combined to advantage. One promising possibility appears to be a combined film-regenerative technique, in which the total heat-flux loading normally imposed on the wall surface can be divided up, with one part absorbed by a reduced film coolant flow and the remainder handled by a reduced-velocity regenerative coolant.

Combining film and radiative cooling techniques, particularly in low-pressure, low-thrust designs, has been satisfactory. Single-wall refractory metal chambers result, with the film-coolant boundary providing both a reducing atmosphere to prevent wall-surface oxidation and tolerable radiative wall temperatures.

Combined ablative and regenerative cooling is particularly attractive in small-thrust engines where a small coolant flow is

available to cool a large wall surface area and regenerative cooling cannot be fully employed but can be used for absorption of a fraction of the wall heat input. The ablator in this case would initially serve as a sacrificial coolant and, upon depletion, as an insulator.

Combining film cooling with ablation can result in a materially reduced char rate if some performance degradation can be tolerated. With the film-ablative combination, surface oxidation and erosion can be prevented, with a considerable improvement provided in the areas of firing duration and reliability.

Conclusion. No one single cooling method is applicable to all rocket devices. The relative merits of the various available methods for each particular heat transfer situation must be carefully evaluated to select the most satisfactory solution.

SYMBOLS

I_s = Specific impulse in pounds of thrust per pound per second of propellant flow

F = Thrust in pounds

$\dot{w}$ = Total propellant weight flow rate in pounds per second

c = Effective exhaust velocity, feet per second

g = Gravitational constant

P_s = Specific power, foot pound per pound of weight

w_o = Weight of the energy source

$\dot{w}_o$ = Oxidizer flow rate

$\dot{w}_f$ = Fuel weight flow rate

r = Mixture ratio ($r = \dot{w}_o / \dot{w}_f$)

ρ_{av} = Average density

ρ_o = Oxidizer density

ρ_f = Fuel density

p_a = Ambient pressure

p_c = Chamber pressure

REFERENCES

1. Sutton, G.P.: Rocket Propulsion Elements, 3rd ed., New York, John Wiley & Sons, Inc., 1963.
2. Barrere, M., *et al.*: Rocket Propulsion, Amsterdam, Elsevier Publishing Company, 1960.
3. Feodosiev, V.I. and G.B. Siniarev: Rocket Technology, London, Academic Press, 1959.
4. Hoffman, S.K.: Propulsion for Space Flight (Address before the Royal Aeronautical Society, London, April 14, 1966).
5. *Pocket Handbook SD 102B*, Packaged Liquid Propellant Rocket Engines, Reaction Motors Division, Thiokol Chemical Corporation, Denville, N.J., 1966.

6. Iacobellis, S.F.: Liquid Rocket Engines, Their Status and Their Future, *AIAA Paper 66-828*, Nov. 29, 1966.

7. Sutton, G.P., W. Wagner, and J. Seader: A Comparison of Advanced Cooling Techniques for Thrust Chambers, *Astro-nautics and Aeronautics*, Jan. 1966, pp. 60-71.

Solid Propellant Rockets

Stanley F. Sarner
Research Chemist
E. I. duPont de Nemours and Co.
Elastomer Chemicals Department

[6-1] COMPOSITION OF A SOLID PROPELLANT

Solid propellants are of two basic types: composites and double base propellants. The latter consist of a backbone of nitrocellulose (guncotton) onto which a quantity of nitroglycerine has been absorbed, resulting in a leathery propellant which can be cast or extruded into desired shapes.

More common today is the composite propellant consisting of three basic ingredients. The first is the polymeric binder system which serves to hold the propellant together, give it adequate mechanical properties, and act as a part of the fuel. The major portion of a composite propellant is the crystalline oxidizer, and most propellants contain a metallic fuel additive for increased specific impulse and density.

Double-base propellants have been upgraded in recent years by the development of "double base-composites" in which the nitro-gylcerine-nitrocellulose system is used as the binder system with an inorganic binder and metallic additive.

Conventional polymers forming cross-linked systems are shown in Table 6-1. The first of these to be used as a binder for propellants was the polysulfide Thiokol ST, of the ethyl formal type. Later the butyl formal and other polysulfides were developed. The prepolymers are difunctional mercaptans which may be cured by oxidation to $-R-S-S-R-$ linkages by metal oxides, organic peroxides, or p-quinone dioxime (GMF) with the reduction of the curing agent and subsequent elimination of oxygen with the oxime, or water with the oxides. Considerable care must be taken to prevent gas pockets from forming or to eliminate the water produced.

The use of polyurethanes which form condensation polymers without elimation of water or gases was a significant advantage. The curing reaction is between a diisocyanate and a glycol

$$R(NCO)_2 + R'(OH)_2 \longrightarrow HO(R'O\overset{O}{\overset{\|}{C}}NHR)NCO \tag{6-1}$$

308
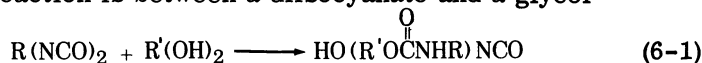
Table 6-1   Common Polymer Types

Polyethylene	$-CH_2-CH_2-$
Polyurethane	$-O-(CH_2)_n-O-\overset{\overset{O}{\|}}{C}-NH-(CH_2)_n-NH-\overset{\overset{O}{\|}}{C}-$
Polyester	$-(CH_2)_n-\overset{\overset{O}{\|}}{C}-O-$
Polybutadiene	$-CH_2-CH=CH-CH_2-$
Polyisobutylene	$-CH_2-\underset{\underset{CH_3}{\|}}{\overset{\overset{CH_3}{\|}}{C}}-$
Polyvinylchloride	$-CH_2-\overset{\overset{Cl}{\|}}{CH}-$
Polyacrylonitrile	$-CH_2-\underset{\underset{CN}{\|}}{CH}-$
Ethyl Formal Polysulfide	$-(CH_2)_2-O-CH_2-O-(CH_2)_2-S-S-$
Butyl Formal Polysulfide	$-(CH_2)_4-O-CH_2-O-(CH_2)_4-S-S-$
Polytetrafluoroethylene	$-CF_2-CF_2-$

which may then continue to polymerize. Water must be kept out of the system to prevent degradation, side reactions, and excessive cross-linking.

Carboxy-terminated polybutadienes or polybutadiene-acrylic acid systems illustrate the third basic type of curing system commonly used. With an epoxide, the cure reaction is

$$RCOOH + R'-CH\overset{\diagdown}{\underset{O}{\diagup}}CH-R'' \longrightarrow R\overset{\overset{O}{\|}}{C}-O-\overset{\overset{R'}{\|}}{C}H-\overset{\overset{R''}{\|}}{C}H-OH \qquad (6-2)$$
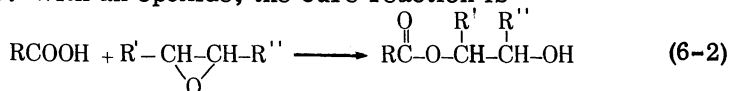
The polymer may also be cured using polyfunctional imines. This type of system results in the closest approach to a pure hydrocarbon and therefore high theoretical performance. The mechanical properties of these systems are excellent.

Hydroxyacids may be cured to form polyesters by the reaction

$$m\text{HO–R–COOH} \longrightarrow \text{HO–(RCOO)}_m\text{H} + m\text{H}_2\text{O} \qquad (6\text{–}3)$$

The elimination of water is again a problem. The presence of high oxygen content using C–O bonds is detrimental from the specific impulse viewpoint, but the polyesters find wide application in gas generator compositions. In these systems, low temperature is a requirement and high energy is not desirable. In addition, the high oxygen content serves to prevent the formation of solid carbon in the combustion products, which would cause difficulties when the gas stream produced is used to drive a turbine or similar device.

There is also the possibility of straight hydrocarbon polymerization by means of free radical initiated chain reactions, as in the case of the formation of polyethylene, but these have not been used to any large extent due to the poor mechanical properties resulting.

The oxidizers used are primarily inorganic perchlorates and nitrates, since these generate high energy output. The most common oxidizer today is ammonium perchlorate. Table 6-2 compares the performance of various binder types including the idealized hydrocarbon, CH_2, and several oxidizers in unmetallized propellants.

Table 6 - 2   Unmetallized Solid Propellants

Fuel	Wt. Pct. Fuel	Oxidizer	Specific Impulse (sec.)	Chamber Temp. ($^\circ$K)	Density (g/cm^3)
CH_2	9.5	NH_4ClO_4	252.8	3018	1.76
CH_2	15	NH_4ClO_4	246.5	2950	1.66
CH_2	15	$LiClO_4$	234.1	3060	1.94
CH_2	21	NO_2ClO_4	278.6	3603	1.70
Hydrocarbon	14	NH_4ClO_4	246.1	2942	1.68
Polyurethane	15	NH_4ClO_4	245.2	2912	1.70
Polysulfide	14	NH_4ClO_4	241.9	2926	1.81
Polyester	20	NH_4ClO_4	237.7	2834	1.73
Polyester	20	NH_4NO_3	202.8	1753	1.51
Polyester	32	NO_2ClO_4	258.0	3375	1.75
Double Base	40	NH_4ClO_4	250.7	3051	1.73

The most commonly considered additives are the metals aluminum and beryllium, and the hydrides of those metals. Of these, aluminum is the most commonly used; beryllium gives higher performance but lower density. The hydrides give higher performance and lower density than the respective metals, with

aluminum hydride being about the equivalent in both criteria to beryllium metal. Table 6-3 compares the performance of these additives with three oxidizers.

Table 6-3   Metallized Solid Propellants

Binder (Wt. %)	Additive (Wt. %)	Oxidizer	Specific Impulse (sec.)	Chamber Temp. ($^\circ$K)	Density (g/cm^3)
CH_2 (15)	Al (19)	NH_4ClO_4	264.1	3179	1.74
CH_2 (20)	Al (15)	NO_2ClO_4	281.5	3894	1.76
CH_2 (15)	Al (20)	$LiClO_4$	251.0	3726	1.97
CH_2 (14)	Al (16)	$KClO_4$	228.9	3492	2.04
Double Base (45)	Al (20)	NH_4ClO_4	263.5	3760	1.80
CH_2 (15)	AlH_3 (34)	NH_4ClO_4	274.2	2546	1.53
CH_2 (15)	AlH_3 (25)	NO_2ClO_4	298.3	3783	1.66
CH_2 (15)	AlH_3 (25)	$LiClO_4$	269.0	3119	1.72
Double Base (40)	AlH_3 (28)	NH_4ClO_4	285.2	3417	1.61
CH_2 (15)	Be (12)	NH_4ClO_4	285.6	3172	1.66
CH_2 (25)	Be (8)	NO_2ClO_4	291.2	3270	1.61
CH_2 (15)	Be (17.5)	$LiClO_4$	264.9	3453	1.86
Double Base (40)	Be (16.8)	NH_4ClO_4	279.3	4071	1.72
CH_2 (20)	BeH_2 (25)	NH_4ClO_4	304.0	2644	1.14
CH_2 (17.5)	BeH_2 (17.5)	NO_2ClO_4	313.8	3208	1.34
CH_2 (20)	BeH_2 (27)	$LiClO_4$	300.8	2732	1.21
Double Base (50)	BeH_2 (20)	NH_4ClO_4	313.8	3154	1.28

Catalysts do not in general affect the specific impulse or density of a propellant markedly, since they are used in small amounts. If the catalyst is an inorganic oxide, it will not contribute to the energy output since it is in the highest oxidation state and will therefore act as "dead weight," reducing the specific impulse slightly. Since most of these are more dense than the oxidizer, the propellant density will be increased slightly. Organic additives can be burned and thus will contribute to the energy somewhat. Solids will normally be added in place of oxidizer, rendering the propellant more fuel-rich and lowering both impulse and density slightly, but liquids can be used to replace portions of the binder system, causing essentially no change in either parameter.

[6-2] PROCESSABILITY CRITERIA

The propellant must contain a sufficient amount of binder to contain the crystalline oxidizer and metal additives. An insufficient amount of binder will result in the mix being too grainy or stiff; therefore, a minimum binder level is required for adequate processability.

Considering the binder system, including the polymer, the curing agent, and any placticizers or liquid catalysts which may be present, as liquids, and the oxidizer and metal additives as solids, an empirical correlation has been developed which relates the relative volumes of solids and liquids in the mix to the processability. The processability factor may be stated in terms of the solid-to-liquid volume ratio or the volume percent solid. The two are interconvertible by

$$\frac{S}{L} = \frac{VPS}{100-VPS} \qquad (6-4)$$

In general, the mix will become more difficult to handle as the solid-to-liquid volume ratio increases. For mixes with standard propellant ingredients, the guidelines shown in Table 6-4 can be followed. Factors which will decrease the values of solid-to-liquid volume ratio achievable include the use of an overly viscous binder, an extremely light or fluffy additive, or an oxidizer with an unusual crystal shape. The values of solid-to-liquid volume ratio shown in Table 6-4 are achievable only after considerable experience in handling the ingredients. It may at times be necessary to heat the mix, to use bimodal or trimodal distributions in the particle sizes of the solids, or to pelletize ingredients, in order to obtain maximum loading.

Table 6-4   Processability Criteria

S/L Volume Ratio	Characteristics
above 3.5	Virtually unprocessable
3.0 - 3.5	Processable with difficulty
2.5 - 3.0	Normal processability
2.0 - 2.5	Very easily processable
below 2.0	Settling difficulties may occur

[6-3] PERFORMANCE OF TYPICAL PROPELLANTS

The standard propellant system in use today is the hydrocarbon-aluminum-ammonium perchlorate system. Table 6-5 gives the theoretical performance of the system at the 14% binder level over the ranges of 0-25% aluminum, and 61-86% oxidizer, and the estimated efficiency and delivered specific impulse in each case. Included are the specific impulse, chamber temperature, density, density impulse, solid to liquid volume ratio, chamber molecular weight, chamber specific heat ratio, and characteristic velocity.

Table 6-5   Hydrocarbon–Al–NH_4ClO_4 Performance

Al, %	Isp, sec.	T_c, °K	Density Isp	Density g/cm³	S/L Ratio	Estimated Efficiency, %	Delivered Isp, sec.	$\bar{M}_c$	$\bar{\gamma}_c$	C^*, ft./sec.
14% binder										
0	246.5	2921	414.2	1.680	2.86	96.50	237.9	25.076	1.177	5004
1	248.0	2952	417.7	1.684	2.85	96.44	239.2	25.119	1.174	5021
2	249.4	2986	421.0	1.688	2.84	96.33	240.2	25.149	1.172	5038
3	250.7	3019	424.3	1.692	2.83	96.21	241.2	25.179	1.170	5055
4	252.0	3052	427.6	1.697	2.82	96.09	242.1	25.208	1.168	5071
5	253.3	3084	430.8	1.701	2.82	95.91	242.9	25.236	1.166	5086
6	254.5	3116	433.9	1.705	2.81	95.73	243.6	25.265	1.165	5101
7	255.7	3148	437.0	1.709	2.80	95.55	244.3	25.293	1.163	5116
8	256.8	3179	440.0	1.713	2.79	95.34	244.8	25.322	1.161	5129
9	257.9	3209	442.9	1.717	2.78	95.11	245.3	25.350	1.159	5143
10	258.9	3239	445.7	1.722	2.77	94.88	245.6	25.380	1.157	5155
11	259.9	3268	448.5	1.726	2.76	94.62	245.9	25.411	1.155	5167
12	260.8	3296	451.2	1.730	2.75	94.37	246.1	25.443	1.154	5178
13	261.6	3323	453.7	1.734	2.74	94.07	246.1	25.478	1.152	5188
14	262.4	3349	456.2	1.739	2.73	93.77	246.0	25.515	1.150	5197
15	263.1	3374	458.6	1.743	2.72	93.47	245.9	25.556	1.148	5205
16	263.7	3396	460.8	1.747	2.71	93.16	245.6	25.602	1.146	5211
17	264.3	3417	462.9	1.752	2.70	92.86	245.4	25.652	1.144	5215
18	264.7	3434	464.8	1.756	2.70	92.57	245.0	25.708	1.142	5218
19	265.0	3449	466.5	1.760	2.69	92.27	244.5	25.770	1.141	5217
20	265.1	3460	467.8	1.765	2.68	92.00	243.9	25.838	1.140	5213
21	264.9	3466	468.6	1.769	2.67	91.78	243.1	25.913	1.139	5206
22	264.3	3468	468.9	1.774	2.66	91.70	242.4	25.993	1.139	5194
25	260.6	3426	465.8	1.787	2.63	92.04	239.9	26.253	1.140	5128

All data are for the conditions of 1000 psia chamber pressure, isentropic optimum expansion to 14.7 psia exit conditions, and a 0° nozzle angle, except for the estimated delivered impulse which is based on a 15° nozzle divergence half-angle.

Similarly, computations can be made for other binder levels, building up a survey of potential performance available from the system. This is normally the first step in design, followed by narrowing the selection through the criteria of processability, availability of catalysts and specific particle sizes of ingredients, and modification of the cure system, finally arriving at a specific propellant which is optimum for the mission with respect to performance, burning rate and physical properties.

[6-4]   BURNING RATE — PRESSURE RELATIONSHIPS

The combustion of a solid propellant is entirely localized on the exposed surface of the grain. The burning surface regresses by burning parallel layers in a direction perpendicular to the surface itself [6] in accordance with Piobert's law. The rate at which the burning surface recedes along the normal to the surface is known as the linear burning rate. It is a characteristic of the propellant, and for a given composition is dependent only on the initial propellant temperature and the chamber pressure.

At any given initial temperature, the empirical relationship between pressure and burning rate may be written

$$r = a + bP^n \tag{6-5}$$

At very high pressures, in artillery, Muraour's law

$$r = a + bP \tag{6-6}$$

is preferred. For rocket motors, where combustion pressures do not normally exceed 2000 psia, the form known as Saint-Robert's or Veille's law

$$r = aP^n \tag{6-7}$$

is preferred. Equations (6-6) and (6-7) are merely simplifications of (6-5). In all three, a and b are constants dependent upon the propellant and the initial temperature. The exponent n is called the combustion index and is considered independent of temperature for simplicity in correlating data. It should be noted that the independence of the combustion index with respect to temperature has not been established by either theoretical or experimental methods. Equation (6-7) is normally used for convenience in the form

$$r = a (P/1000)^n \tag{6-8}$$

in which case the pressure is referred to the standard combustion pressure of 1000 psia, and the constant, a, becomes the linear burning rate at 1000 psia. The use of this simplifies comparison of data.

Summerfield [17] has developed an expression for the burning rate-pressure relationship from mathematical analysis. With some simplifying approximations, the result is

$$\frac{1}{r} = \frac{a}{P} + \frac{b}{P^{1/3}} \tag{6-9}$$

or, in another form,

$$\frac{P}{r} = a + bP^{2/3} \tag{6-10}$$

These expressions neglect radiative heat transfer but may be better than the simple exponentials used in Eqs. (6-5)-(6-8). The relationship has not, however, received wide acceptance.

Using Eq. (6-7) to represent the linear burning rate, the mass burning rate or mass flow rate (neglecting erosion) becomes

$$\dot{m} = A_s \rho r = A_s \rho a P_c^n \tag{6-11}$$

For stable operation, the mass flow rate must be the same at the propellant surface and at the nozzle exit. The mass burning rate must equal the mass discharge rate which is

$$\dot{m} = C_D P_c A_t \tag{6-12}$$

Therefore, equating the mass flow rate expressions, the requirement for stable operation is

$$A_s \rho a P_c^n = C_D P_c A_t \tag{6-13}$$

and the equilibrium chamber pressure will be

$$P_c = \left(\frac{A_s \rho a}{C_D A_t}\right)^{\frac{1}{1-n}} \tag{6-14}$$

from which it can be seen that the exponent, n, must be less than unity for stable operation. Should the exponent exceed unity, the pressure will continue to rise until the case bursts or the propellant is all burned.

[6-5] PROPELLANT AREA RATIO

From Eq. (6-13) the propellant area ratio, K_N, defined as

$$K_N = \frac{A_s}{A_t} \tag{6-15}$$

may be derived as

$$K_N = \frac{A_s}{A_t} = \frac{C_D}{a\rho} P_c^{(1-n)} \tag{6-16}$$

From the above, it is usually assumed that the sum of the exponents in an empirically derived equation for K_N

$$K_N = bP_c^{m} \tag{6-17}$$

and an empirically derived burning rate equation of the form of (6-7) for the same propellant should be unity. However, the mass flow rate or discharge coefficient, C_D, in Eq. (6-16) is not invariant with pressure. This can be seen to be true since the characteristic velocity is

$$C^* = \frac{1}{C_D} \tag{6-18}$$

and varies with pressure variation. Empirically, the relationship with pressure may be written as

$$C_D = \frac{h}{P_c^{q}} \tag{6-19}$$

or

$$C^* = \frac{1}{h} P_c^{q} \tag{6-20}$$

Substituting Eq. (6-19) into Eq. (6-16), the result is

$$K_N = \frac{h}{a\rho} P_c^{(1-n-q)} \tag{6-21}$$

from which it can be seen that the sum of the three empirical exponents should be unity.

$$m + n + q = 1 \tag{6-22}$$

In practice, however, it is found that the exponent, q, is less than 0.1 and normally of the order of 0.02. Therefore, the sum of $m + n$ is unity within experimental error. The comparison of these two exponents is a good measure of the consistency of the experimental data.

[6-6] TEMPERATURE SENSITIVITY OF BURNING EQUATIONS

The coefficient, a, in Eq. (6-7) varies with temperature according to the relationship

$$a = \frac{a_0}{T' - T_i} \tag{6-23}$$

When the initial temperature of the grain, T_i, is equal to the spontaneous ignition temperature of the propellant, T', the burning rate is essentially infinite.

The temperature sensitivity of the burning rate at constant pressure is then

$$(\pi_r)_p = \frac{1}{r} \left(\frac{\partial r}{\partial T_i} \right)_P = \left(\frac{\partial \ln r}{\partial T_i} \right)_P = \frac{1}{T' - T_i} \tag{6-24}$$

Similarly, the temperature sensitivity of the burning rate may be calculated at constant K_N

$$(\pi_r)_{K_N} = \frac{1}{r} \left(\frac{\partial r}{\partial T_i} \right)_{K_N} = \left(\frac{\partial \ln r}{\partial T_i} \right)_{K_N} \tag{6-25}$$

which is evaluated empirically.

A more common parameter is the temperature sensitivity of the K_N-pressure relationship, also evaluated empirically as

$$\pi_K = \frac{1}{P} \left(\frac{\partial P}{\partial T_i} \right)_{K_N} = \left(\frac{\partial \ln P}{\partial T_i} \right)_{K_N} = \frac{\ln \dfrac{P_2}{P_1}}{\Delta T} = \frac{1}{1-n} (\pi_r)_P \tag{6-26}$$

The coefficients (π's) may be evaluated empirically with respect to initial temperature, for any parameter, using the partial derivative of the natural logarithm with either K_N or pressure constant. The coefficients are normally expressed as the percent change per degree Fahrenheit.

[6-7] EROSIVE BURNING

The apparent burning rate of a propellant is increased above its normal value when the surface of the propellant is subjected to high gas velocities which erode the grain. Above a threshold velocity, the effect increases with gas velocity according to the equation

$$\frac{r_e}{r} = 1 + k_e (v - v_{th}) \qquad (6-27)$$

The erosion coefficient, k_e, and the threshold velocity, v_{th}, are probably dependent on pressure and motor geometry, but complete information is not yet available in this area. Green [9] found that the erosion coefficient is considerably higher at lower burning rates and is higher for double base propellants than for composite propellants.

[6-8] EFFECT OF SPIN ON BURNING RATE

In many instances a rocket motor must be spun on its axis in order to neutralize any effects of nonsymmetrical thrust. In such cases, an increase in the propellant burning rate has sometimes been noticed. A possible explanation has been postulated as the cause of this phenomenon, but additional work in this area will be necessary to completely elucidate the mechanisms involved.

It is likely that the centrifugal force caused by imparting spin to the motor compresses the flame zone, thereby increasing the propellant surface temperature and accelerating the propellant decomposition reactions. In addition, since most solid propellants produce condensed species as a portion of the combustion products, an increase in erosion may be caused by compression of the flame zone.

[6-9] MECHANISM OF HOMOGENEOUS PROPELLANT BURNING

The burning rate of homogeneous or double base propellants has been extensively investigated but is by no means thoroughly understood. The rate–determining step in the burning process has been proposed to be a solid phase unimolecular decomposition at the burning surface [21]. Although the decomposition reaction is unimolecular, the burning reaction is pseudo–zero order since the concentrations of reactants is constant, due to the dependence of the concentrations on the number of surface molecules. A steady-state surface temperature, T_s, is established by transfer of heat

from gas and solid phase reactions. The linear burning rate may then be expressed by the Arrhenius equation for the rate–controlling step

$$r = A_0 e^{(-E_a/RT_s)} \qquad (6-28)$$

A_0 is less temperature dependent than the exponential term and may be considered constant if the temperatures do not vary more than 100° K. The burning rate is then equivalent to the linear decomposition rate at the surface temperature.

Wilfong, Penner, and Daniels [21] estimated the surface temperature to be above 1300° K, but this is felt by Hugget [11] to be too high since the grain surface is not luminous. He calculates a maximum temperature of about 650° K. Recent investigations by Cotton and Austin [3], however, place the surface temperature at 965° K.

The burning process is normally described as a stepwise series of reactions occurring in several zones parallel to the burning surface. At some short distance below the surface the propellant is unaffected because of its poor thermal conductivity. As the burning surface approaches, the propellant layers immediately beneath the surface are heated by conduction. The resulting rise in temperature is sufficient to start the decomposition of nitrocellulose and nitroglycerine slightly below the surface, thus causing further heating since the decompositions are exothermic. Additional reactions between stabilizers and nitroglycerine and nitrocellulose also occur in this subsurface zone.

Above the burning surface is the "fizz zone" in which continued decomposition occurs in a narrow portion of the zone a few hundredths of a centimeter thick. In this region the temperature is only slightly higher than the surface temperature. In the remainder of the "fizz zone," the temperature increases to about 1700° K.

Following the "fizz zone" is an area of inactivity possibly due to delay in the accumulation of a critical intermediate, depletion of a reactant, or the building up of a critical temperature. This is followed by the flame reaction zone in which further decomposition occurs. The flame throughout all the zones to this point is non-luminous.

The final region is the flame zone in which most of the energy is liberated and the final combustion temperature is achieved. The zone is luminous, and the reaction products are in equilibrium at the flame temperature.

The thickness of the zones diminishes with an increase in pressure. At pressures of normal rocket operation (below 1500 psia), the zone of inactivity is much thicker than the other zones and heat transfer from the flame zone to the inner zones can therefore be neglected. The action of catalysts and the variance of burning rate with composition are therefore phenomena involving the inner zones only.

The low surface temperature of double base propellants is approximately equal to the spontaneous ignition temperature as a lower limit. Thus, the temperature sensitivity of these propellants must be high, as can be seen from Eq. (6-23).

Below 200 psia, the flame zone is nonexixtent causing intermittent burning. As the pressure increases, the flame zone appears and the thickness of the "fizz zone" decreases until it is very small at 1000 psia and disappears above that pressure, with the luminous flame nearly touching the burning surface. The increased heat transfer explains the dependence of burning rate on pressure.

[6-10] MECHANISM OF COMPOSITE PROPELLANT BURNING

The fundamental assumption for composite propellants is that the fuel (binder) and oxidizer regression rates are governed by the equations

$$r_f = A_f e^{-(E_f/RT_{sf})} \tag{6-29}$$

$$r_o = A_o e^{-(E_o/RT_{so})} \tag{6-30}$$

and that the rates of regression are approximately equal. Since the activation energies and the pre-exponential factors of the fuel and oxidizer regression are not equal, the surface temperatures must also be unequal. This is the basis for the "two temperatures postulate" of composite combustion theory.

The simplest method of procedure from this point is to assume the mechanism to be controlled by the thermal decomposition of binder and oxidizer. This has been treated in an analytical fashion and has given satisfactory results for ammonium nitrate propellants and to some extent for ammonium perchlorate propellants [10].

It is assumed that the regression of fuel and oxidizer is completely governed by the heat transfer between the surfaces of the two ingredients and the oxidizer decomposition products. If the surfaces are in the same plane, the temperatures are equal and the oxidizer regresses faster. The fuel then protrudes into a higher temperature zone and its regression rate increases, tending to bring the fuel surface back into the oxidizer plane. Thus, the overall effect is that the regression rate is equal to that of the oxidizer. For ammonium nitrate, the decomposition temperature is 1250° K, and for ammonium perchlorate it is 1430° K; thus the latter oxidizer yields higher burning rates. For ammonium nitrate oxidizer, at a burning rate of 0.1 in/sec, the surface temperatures would be 910° K for the oxidizer and 580° K for the fuel. The overall surface temperature is therefore considerably higher than predicted for double base propellants.

Summerfield [18] has postulated the "Granular Diffusion Flame Model" of composite propellant burning. This is a one-dimensional model assuming direct pyrolysis of both the fuel and oxidizer and all reactions occurring in a thin diffusion flame zone in the gas phase. Vapors of fuel and oxidizer are postulated to be released in the form of pockets and proceed to burn in the surrounding medium of the opposite reactant. The mass of each pocket is much smaller than that of an oxidizer crystal but related to it and independent of pressure. The pockets are consumed at a rate controlled by diffusional mixing and chemical reaction as they pass through the flame zone, and the heat of reaction is released at a corresponding rate. Burning occurs as a result of thermal conduction of energy back from the flame to the surface. The theory does not at the present stage predict absolute burning rates, but Eqs. (6-9) and (6-10) are derived in the process and serve well to correlate burning rate with pressure. This model may be applied to ammonium perchlorate propellants and may be the only reasonable approach to potassium perchlorate propellant combustion.

[6-11] CORRELATION OF BURNING RATES WITH OXIDIZER ACTIVATION ENERGY

The general order of the burning rate of a composite propellant can be predicted from the oxidizer activation energy for nonmetallic oxidizers when conventional binders are used. Figure (6-1) shows good correlation of burning rates with activation energies for a hydrocarbon binder. It can be seen that the metal perchlorates do not fit this pattern but give burning rates considerably in excess of the predicted value. It is also known that the pressure exponents of the burning rates are higher for these oxidizers than for the nonmetallic oxidizers. It can be assumed that the metal perchlorates would give agreement with the predicted results at low pressures, but at high pressures where the flame zone is closer to the surface, the higher energy release found with the metallic oxidizers results in more energy feedback to the surface and abnormally high burning rates. Additional study is required to obtain better understanding of these phenomena.

[6-12] EFFECT OF COMPOSITION ON BURNING RATE

The addition of metal powders or metal-containing compounds has been shown to have no significant effect on either the rate-determining mechanism of combustion or the burning rate [14]. The variation in particle size of metal powders also has little effect since, except with ultrafine powders, ignition and combustion of the metals take place in the gas stream [23]. This is not to say that the amount or particle size of the metal has no effect on the combustion efficiency. Since the combustion takes place from the
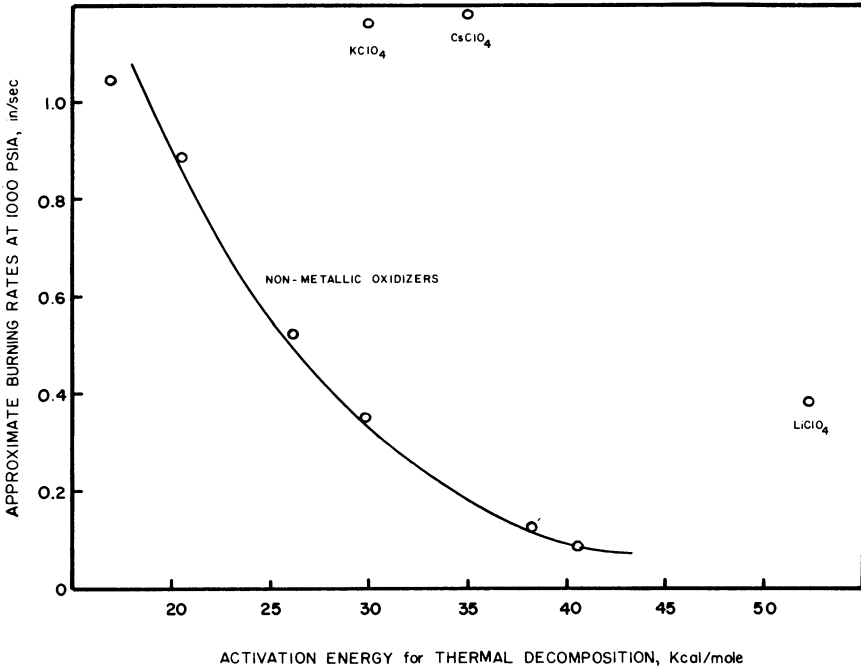
Fig. 6-1 Correlation of burning rates of solid propellants with activation energies for thermal decomposition of oxidizers.

solid or liquid metal particle[23, 7, 4, 8, 19], the particle size should have a substantial effect on efficiency but not on burning rate.

Ito [12, 13] has derived equations for the effect of quantity and particle size of oxidizer in asphalt-ammonium perchlorate mixtures on the burning rate. For oxidizer particle size, he obtained

$$r = 0.0059\ M + 0.50\ \text{mm/sec} \qquad (6\text{-}31)$$

where M is the Tyler mesh number for the screens used to retain the oxidizer particles. For oxidizer level, he found

$$r = 0.11\ W - 7.16\ \text{mm/sec} \qquad (6\text{-}32)$$

where W is the weight percent of ammonium perchlorate in the mixture. It would appear that the slope of the line for compositional changes is too steep, but that the oxidizer particle size correlation is approximately correct. In both respects, the variation of burning rate within the limits of practical changes in composition and particle size is small. Similar results have been obtained by Smith [16] and for potassium perchlorate-asphalt mixtures by Huggett [11].

Summerfield [18] also found variations in burning rate with composition and oxidizer particle size. Constants for Eq. (6-10) are given for ammonium perchlorate propellants with various binders. He found the burning rate to increase with decreasing particle size and with increasing chamber temperature.

[6-13] CATALYSTS

Several materials have been employed as burning rate catalysts in solid propellants. These are normally organic compounds or inorganic salts of the transition metals. Among the most common catalysts are iron oxide, copper chromite (a mixture of copper and chromium oxides), manganese dioxide, and ferrocene (Dicyclopentadienyl iron). In general, the effect of catalysts is of the same order of magnitude as that of oxidizer particle size variation. Summerfield [18], Friedman [5] and Penner [15] present data for several catalysts.

[6-14] MECHANICAL PROPERTIES

Some knowledge of the mechanical behavior of the filled polymers which make up solid propellant fuel systems is required for the prediction of the structural integrity of propellant grains during its life within an engine. Mechanical behavior involves the deformation of a material by applied forces. Three types of loading conditions are used to describe the mechanical response of a material: tension, shear and bulk.

[6-14.1]   Uniaxial Tensile Test

In the tensile test a force is applied longitudinally to a bar. The length, L_o, is subsequently increased by an amount, ΔL, to give a stretched length of L. The tensile force divided by the cross sectional area over which it is applied is called the tensile stress, σ, and the percent elongation, $\Delta L/L_o$, is called the strain, ϵ. Other definitions of strain are: $\Delta L/L$; $\ln(L/L_o)$; $1/3 \left[L/L_o - (L_o/L)^2 \right]$ The second of the definitions is sometimes called true strain and the third comes from the kinetic theory of rubber elasticity [20]. In the discussions to follow, strain will be defined as $\Delta L/L_o$. All the above definitions are essentially the same for infinitesimal deformations but are considerably different at large strain values.

For ideally elastic, homogeneous, isotropic materials, the relationship between stress and strain obeys Hooke's law:

$$\sigma = E \epsilon \qquad (6\text{-}33)$$

This expression states that a linear relationship exists between the tensile stress and strain, the slope of which is called Young's modulus, E.
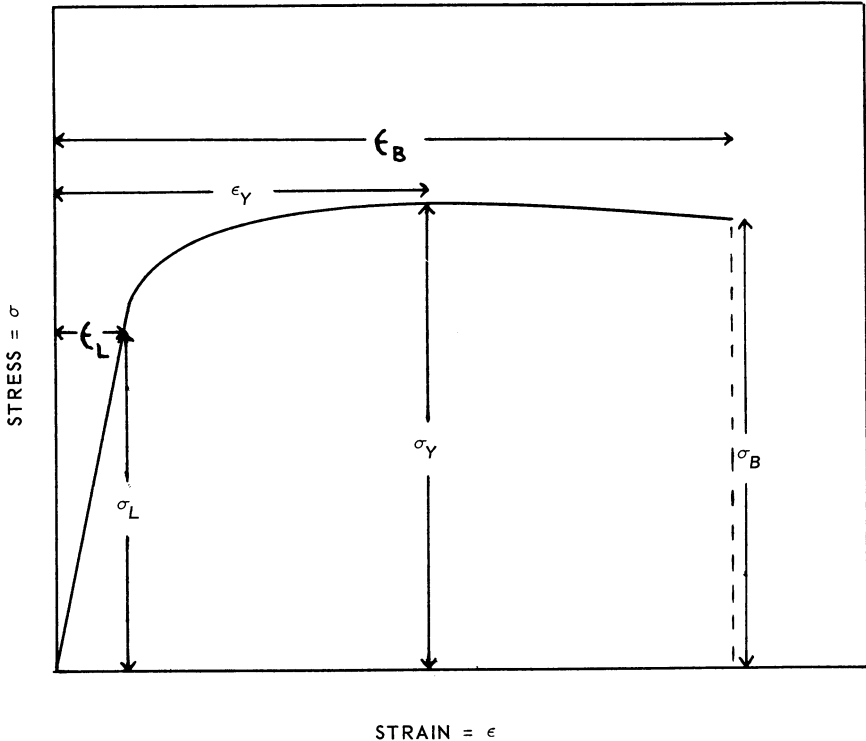
Fig. 6-2 Stress versus strain relationship in solid propellants.

One of the most common and useful means of analyzing the mechanical behavior of a polymer is to generate a stress versus strain diagram, Fig. (6-2). Initially the curve is linear indicating an elastic response; the slope of this portion of the curve is the Young's modulus, E. The curve continues until the material ceases to obey Hooke's law and is no longer linear. The stress and strain at this point are designated by σ_L and ϵ_L, respectively. In filled polymers, this corresponds to the point at which a breakdown of the interfacial bond between binder and solid occurs. With additional strain, the curve may go through a maximum stress point, σ_Y, and proceed to failure. Normally, reported values for mechanical properties of propellants are the maximum stress, strain at maximum stress, and initial modulus of elasticity. At the yield point, viscous flow takes place and the strain increases rapidly with little or no increase in stress. Finally, the material breaks. The stress at the

break point is called the ultimate tensile strength while the strain is called the rupture strain. The strain rate is quite important. Many materials appear soft under slow application of stress and brittle under rapid or shock application. This phenomenon is dependent upon the stress relaxation rate of the material.

Carswell and Mason [1, 2] grouped stress-strain curves into the five classifications shown in Fig. (6-3). Soft-weak materials have low moduli and tensile strength and only moderate elongations at the break point. Soft polymer gels and "cheesy" materials are examples. Hard-brittle materials have high moduli and tensile strength but small (less than two%) elongation at the break point with no yield point. Polystyrene and poly(methyl methacrylate) at and below ambient temperatures are examples. Hard-strong materials also have high moduli and tensile strengths with elongations of 5% at the break point. Rigid poly(vinyl chlorides) are examples. Soft-tough materials have low moduli, very high elongations (over 20%), and moderately high ultimate strengths. They show a definite yield point. Rubbers are examples. Hard-tough materials have high moduli and tensile strengths, large elongations, and show a yield point. Cellulose acetate and polyamides are examples.
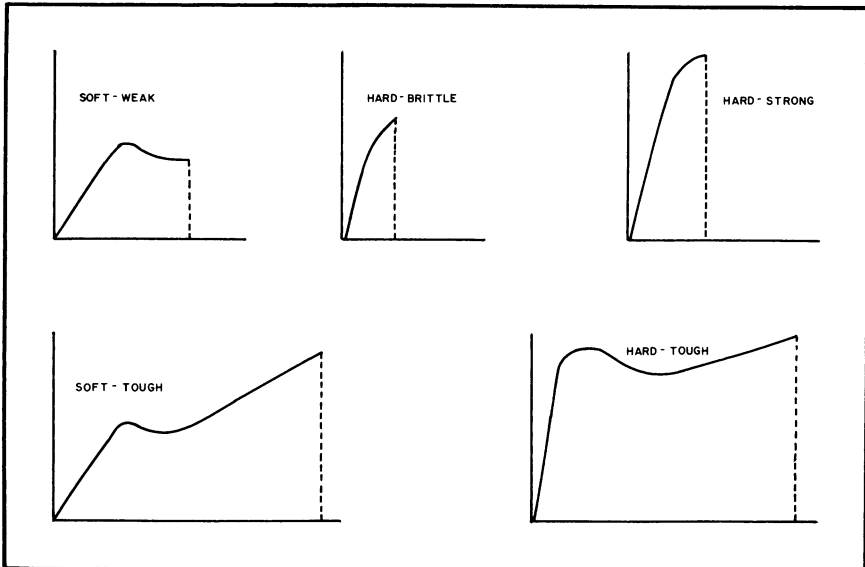
Fig. 6-3 Classifications of stress-strain curves.

The toughness of a material is best defined as the energy required to break a material. This may be determined by integrating the area under the stress-strain curve.

In general, propellants may be considered in the soft–tough classification, although a plateau through the viscous flow region is normal. The moduli range from 100 for fluorocarbon systems to over 1000 for polysulfides. Polyurethanes and polybutadienes give moduli in the range of 300–1000 psia. By varying the cure conditions a wide range of moduli may be obtained within these limitations. Typical values of yield stress for polyurethanes or polybutadienes range from 70–300 psia, with elongations in the range of 20–75%.

[6- 14.2] Uniaxial Shear Test

Another type of loading which describes the mechanical behavior of a material is shear. The shear stress, τ, as in the case of tension is the shearing force divided by the area over which it is acting. The shear strain, γ, is defined as the deformation per unit distance between shearing surfaces. A relationship similar to Hooke's law also exists for shear:

$$\tau = G\gamma \qquad (6-34)$$

where G is the shear modulus or modulus of rigidity. Stress–strain diagrams for a shear test can be generated in much the same manner as described for the tensile test.

[6-14.3] Bulk Dilution Test

The third loading, bulk, relates the percent change in volume, $\Delta V/V_0$, which occurs under a hydrostatic stress, p:

$$p = K\frac{\Delta V}{V_0} \qquad (6-35)$$

where the constant of proportionality in this case is called the bulk modulus.

All the other types of loadings (compression, torsion, flexture, gravitations, etc.) involve combinations of the above three basic loading conditions.

[6- 14.4] Poisson's Ratio

The loadings given above involve only uniaxial response. For the biaxial test, Hooke's law must be modified to account for lateral deformations by

$$\sigma = \frac{E\epsilon}{1 - \nu} \qquad (6-36)$$

where ν is Poisson's ratio, defined as the ratio between lateral strain, ϵ_2, and longitudinal strain, ϵ_1. For bodies under finite deformations in which a change in volume occurs, Poisson's ratio varies with longitudinal strain by

$$\nu = \frac{1}{\epsilon_1}\left[1 - \frac{V/V_0}{(1 + \epsilon_1)^{1/2}}\right] \tag{6-37}$$

For materials which remain incompressible during deformation, *i.e.*, $V/V_o = 1$, the above expression becomes

$$\nu = \frac{1}{\epsilon_1}\left[1 - \frac{1}{(1 + \epsilon_1)^{1/2}}\right] \tag{6-38}$$

For most materials, Poisson's ratio lies between 0.20 and the upper limit of 0.50. For rubbers and liquids the ratio follows Eq. (6-37). Generally speaking, the more rigid the material, the smaller ν becomes. The three moduli discussed above can be related through Poisson's ratio by means of the following equations:

$$E = 2G (1 + \nu) \tag{6-39}$$

$$E = 3K (1 - 2\nu) \tag{6-40}$$

[6-14.5] Glass Transition

Viscoelastic resins exhibit a glass temperature, T_g, where the material essentially loses its viscous characteristics and changes from soft to brittle. At this temperature, there is a marked change in physical properties such as specific volume, tensile strength, or refractive index. The glass temperature varies with molecular weight to a limiting value and then remains fairly constant. A type of phase diagram such as the one shown in Fig. (6-4) may be constructed. Below the glass temperature, the material is like a crystalline or partially crystalline solid (but may be an amorphous glass) and is hard and brittle. At the glass temperature, the material is leathery, as double base propellants whose glass temperature occurs at room temperature. Above the glass temperature, the material exhibits viscoelastic or even elastic behavior at sufficiently high molecular weights. As the temperature is increased or the molecular weight decreased, viscous flow is exhibited and there is little elastic recovery. Polymers of narrow molecular weight distribution are therefore most useful, since they show well defined properties.

The ease of rotation of the polymer chain has a marked effect on its properties. The inclusion of groups with limited rotational

or configurational possibilities increase the glass temperature and melting temperature and stiffen the polymer. The rigid aromatic rings are examples of such groups. The stiffening results in increased hardness and tensile strength and decreased elasticity. Groups which are extremely flexible due to ease of rotation result in low melting point and glass temperature and a high degree of softness and elasticity. Ether groups are prime examples of this type.
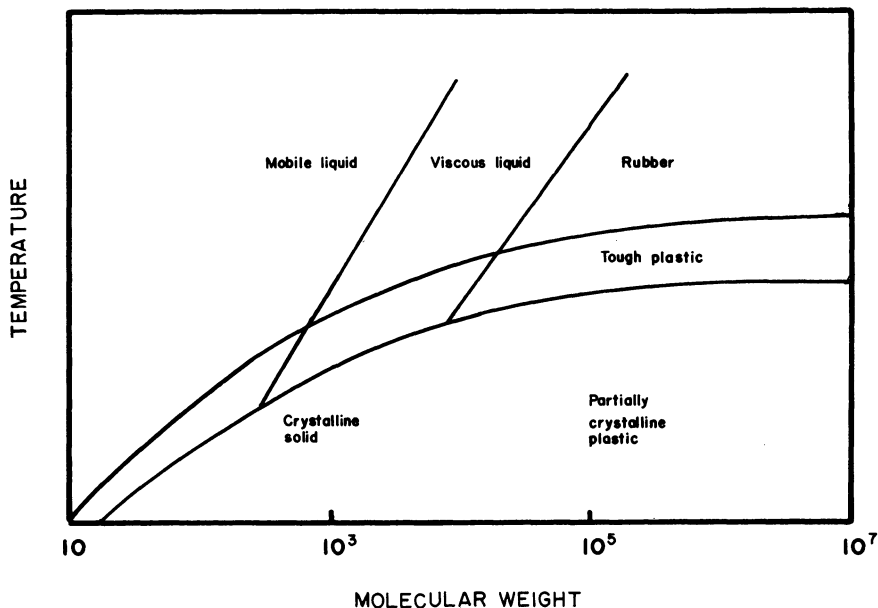
Fig. 6-4 Polymer phase diagram.

The addition of nonpolar side chains to a polar molecule reduces the Vander Waal's forces and thereby lowers the glass and melting temperatures. The tensile strength is lowered and the ultimate elongation increases. Some of the effect may be attributable to a decrease in crystallinity, particularly if the addition of side chains is random.

The principle of time-temperature superposition may be illustrated with relaxation modulus curves or creep curves. It is possible to define quantitatively the temperature dependence of the relaxation modulus (or creep compliance). If the material under consideration has a modulus, G, at a time, t_o, and a temperature, T_o, it will have the same modulus at another temperature, T, and another time, t, which satisfy the following relationship:

$$t_o = t\left(\frac{T\rho}{\eta}\right)\left(\frac{\eta_0}{T_0\rho_0}\right)$$

(6-41)

in which the change in viscosity, η, will be much greater than the change in density, ρ, or the change in temperature, so that Eq. (6-41) may be simplified to

$$t_0 = t \frac{\eta_0}{\eta} \tag{6-42}$$

It is possible, then, to replace log t_0 with log (t/η) to obtain a single relaxation modulus curve from tests conducted at various temperatures. It should be pointed out that materials exhibiting an equilibrium modulus will not obey this relationship in the section of the $G(t)$ curve representing the equilibrium modulus, because all viscous effects are absent from this region. The ratio of viscosities at the test temperature is the Williams-Landel-Ferry shift factor for time-temperature superposition

$$a_T = \frac{\eta}{\eta_0} \tag{6-43}$$

and the Williams-Landel-Ferry equation [22] is expressed as

$$\log a_T = \frac{-c_1(T - T_0)}{c_2 + T - T_0} \tag{6-44}$$

and when $c_1 = 17.44$ and $c_2 = 51.6$, $T_0 = T_g$. Equation (6-44) approximates a_T only when T is greater than the glass temperature by less than $100°$ C.

[6-15] NOMENCLATURE

A	area
a_T	Williams-Landel-Ferry shift factor
a, a_0, b, c	constants
A_o	preexponential term in Arrhenius equation
C_D	discharge coefficient
C^*	characteristic velocity
E	Young's (tensile) modulus
E_a	activation energy
G	shear modulus
h	constant in burning equations
K	bulk modulus
K_N	propellant area ratio
k_e	erosion coefficient
L	length
m	K_N exponent
$\dot{m}$	mass flow rate
n	combustion index or burning rate exponent

P	pressure
p	hydrostatic stress
q	C^* exponent
R	universal gas constant
r	linear burning rate
r_e	erosive burning rate
T	temperature
t	time
T'	spontaneous ignition temperature
V	volume
v	velocity
γ	shear strain
ϵ	tensile strain
η	viscosity
ν	Poisson's ratio
π	temperature sensitivity
ρ	density
σ	tensile strain
τ	shear stress

Subscripts

B	break point
c	chamber conditions
f	fuel (binder)
i	initial conditions
L	end of linear section
o	oxidizer
s	propellant surface
t	throat conditions
th	threshold
Y	yieldpoint
0	original value

REFERENCES

1. Carswell, T.S. and H.K. Mason: *Special Technical Publication 59*, Philadelphia, American Society for Testing Materials, 1944.
2. ———— and ————: *Modern Plastics*, 21, 121, (1944).
3. Cotton, D.J. and T.D. Austin: *Navweps Report 8573*, 1964.
4. Fossell, W.M., C.A. Papp, D.L. Hildebrand, and R.P. Sernva: Solid Propellant Rocket Research, Vol. I, New York, Academic Press, 1960.
5. Friedman, R., R.G. Nugent, K.E. Rumbel, and A.C. Scurlock: *Paper No. 79*. In Sixth Symposium on Combustion, New York, Reinhold, 1957.
6. Geckler, R.D.: Selected Combustion Problems—AGARD, New York, Pergammon Press, 1954.

7. Glassman, I.: In Solid Propellant Rocket Research, Vol. I, New York, Academic Press, 1960.

8. Gordon, D.A.: Ibid.

9. Green, L.: *Jet Propulsion*, 24 (1954).

10. ———, S.S. Penner, and R. Schultz: In Combustion and Propulsion, 3rd Colloquium, AGARD, London, Pergammon Press, 1958.

11. Huggett, C.: In Combustion Processes—High Speed Aerodynamics and Jet Propulsion, Vol. II, Princeton, Princeton University Press, 1956.

12. Ito, T.: Kogyo Kayan Kyokaishi, 20, 198 (1959).

13. ———: Kogyo Kagaku Zasshi, 63, 1894 (1960).

14. Nadoud, L.: Rech. Aeron., 85, 3 (1961).

15. Penner, S.S.: Chemical Rocket Propulsion and Combustion Research, New York, Gordon and Breach Science Publishers Inc., 1962.

16. Smith, J.M.: A.I.Ch.E.J., 6, 299 (1960).

17. Summerfield, M., G.S. Sutherland, M.J. Webb, H.J. Tarack, and K.P. Hall: Amer. Rocket, Soc. Preprint 737-58 (1958).

18. ———, ———, ———, ———, and ———: In Solid Propellant Rocket Research, Vol. I, New York, Academic Press, 1960.

19. Talley, C.P.: Ibid.

20. Treloar, L.R.G.: The Physics of Rubber Elasticity, Oxford, Clarendon Press, 1958.

21. Wilfong, R., S.S. Penner, and F. Daniels: J. Phys. Chem., 54, 863 (1950).

22. Williams, M.L., R.F. Landel, and J.P. Ferry: J. Am. Chem. Soc., 77, 3701 (1955).

23. Wood, W.A.: In Solid Propellant Rocket Research, Vol. I, New York, Academic Press, 1960.

Hybrid Rocket Theory and Design

H. S. Seifert
Professor of Aeronautics and Astronautics,
Stanford University;
Consultant, United Technology Center

[7-1] INTRODUCTION

A hybrid rocket is so named because one of the propellant components is liquid and the other solid. Normally the oxidizer is liquid and the fuel is solid. In a typical design (Fig. 7-1), the oxidizer is sprayed in at the head end of a solid cylindrical fuel grain. It is apparent that once the liquid oxidizer is injected, the combustion process proceeds according to natural law and the geometric constraints designed into the grain and is not subject to external control. It is very important, therefore, to understand the details of the combustion if it is to occur in the manner desired by the designer.

A schematic diagram of the process of hybrid combustion is shown in Fig. 7-2. In a relatively narrow region close to the solid surface, fuel vapor moving by convection away from the surface meets gaseous oxidizer diffusing from the central core, and combustion occurs. The temperature profile and velocity profile resulting are shown qualitatively in Fig. 7-3. The boundary layer grows until, in a typical case, if fills the cylindrical tube (merges) at about 5 calibers downstream. At about 25 calibers, the oxidizer is largely used up and further lengthening of the tube does not contribute to the available heat energy.

Hybrid rockets possess characteristics which set them apart from pure liquid or pure solid motors and which, in some instances, supply the motivation for their development. It is of interest to compare Hybrids with other chemical propulsors.

a) The range of possible specific impulse lies above that for solids and below the maximum for liquids.

b) The plumbing hardware is simpler than for a two-fluid liquid rocket but of course more complicated than for a solid rocket.

c) The hybrid affords on-off and throttled operation, which is impractical with solid rockets.
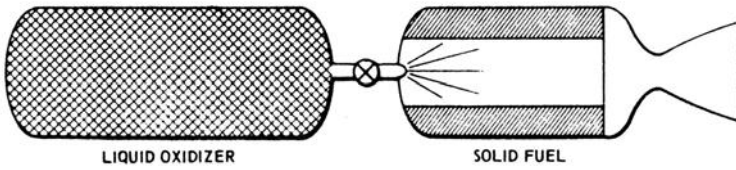
Fig. 7-1 "Direct" hybrid rocket system; left: liquid oxidizer; right: solid fuel.
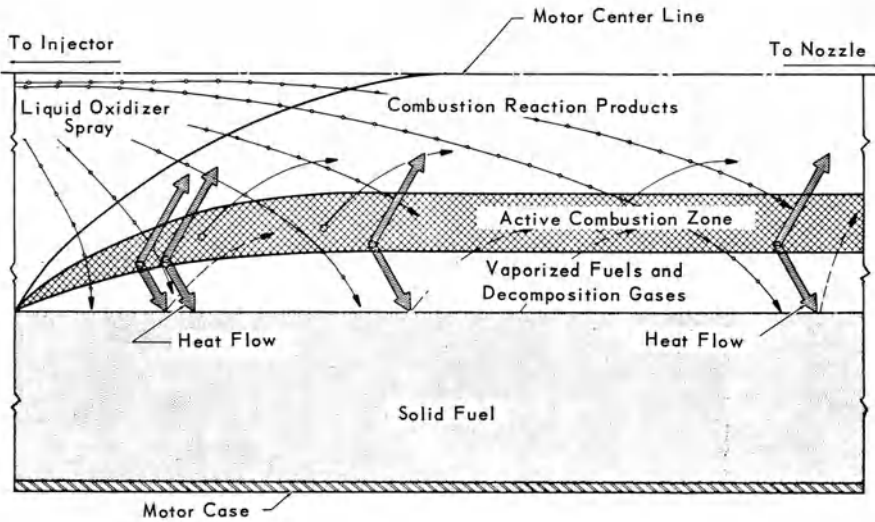
Fig. 7-2
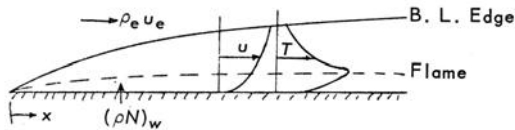
Fig. 7-3

d) Hybrids are safe in storage relative to solid rockets which must be handled as if they were explosives.

e) Combining a liquid and a solid phase makes available possible new propellant combinations which cannot be supplied as solid-solid mixtures or liquid-liquid combinations.

Hybrid combustion has of course been a matter of interest ever since the first forest fire. As long ago as twenty years (1946),

Bartel and Rannie [1] worked on solid-fuel ramjets. However, it has only been since 1962 that Gilbert, Marxman, Wooldridge and Muzzy, working at the United Technology Center, evolved a sufficiently complete analysis [2, 3, 4, 5] to make it possible to design a hybrid rocket with reliably predictable performance. The writer is indebted to these latter authors for the information in this exposition, which describes their work and endeavors to make a complex process physically understandable. The hybrid rocket is unique in that it is the first chemical rocket to be investigated in a fundamental way prior to its hardware development.

[7-2] HYBRID COMBUSTION WITH NEGLIGIBLE RADIATION

[7-2.1] The Physical Process

Hybrid combustion typically occurs in a thin sheet of flame within the turbulent boundary layer, shown schematically in Fig. 7-3. Fuel is partly decomposed and evaporated (gasified) at the solid surface by convective (or convective plus radiative) heat transfer and diffuses inward toward the center line of the combustion volume. Simultaneously, gaseous oxidizer diffuses outward from the center line through the turbulent boundary layer. At a point where the ratio of oxidizer to fuel concentration (*O/F* ratio) is somewhat on the fuel-rich side of a stochiometric, combustion occurs in a layer whose thickness is of the order of 10% of the boundary layer thickness. Figure 7-4 shows a schlieren photograph indicating the flame position which is substantially closer to the fuel surface than to the edge of the boundary layer.
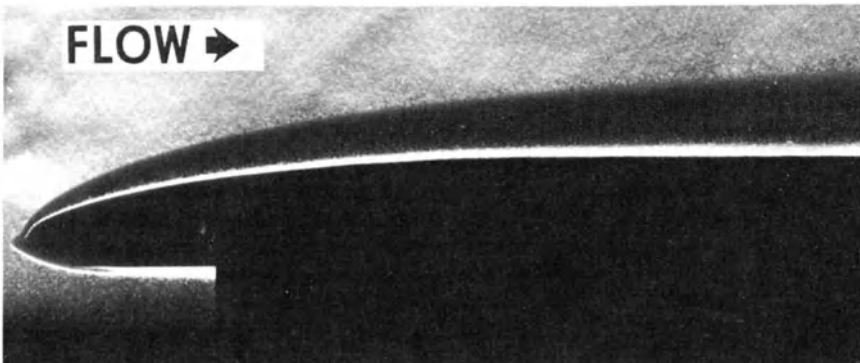
Fig. 7-4 Schlieren photograph of plexiglas-oxygen system ($K_{ox_e} = 1$). $Re = 2 \times 10^4$/in.

The rate of combustion is limited by the rate at which heat is transferred from the flame to the solid surface rather than by the

chemical kinetics of the flame, except at very low pressures. Thus, the rate of combustion is limited by fluid dynamic processes rather than chemical kinetics, as is the case for classical solid propellants. The fact that the rate of gasification or "regression rate" $\dot{r}$ of the solid surface depends upon heat transfer from the boundary layer means that the regression rate is closely coupled to G_0, the local oxidizer mass flow per unit area. G_0 varies both with time and with axial distance along the fuel grain. Thus no simple empirical expression can be written for $\dot{r}$ such as the expression $\dot{r} = a p_c^{\ n}$ often used for composite solid propellants. Derivation of relations for $\dot{r}$ in terms of known propellant properties will be the substance of this section.

In the steady state the heat transferred to the surface equals the heat transported away by the gasified fuel:*

$$\dot{Q}_w = \dot{m}_f h_v = \rho_f \dot{r} h_v \qquad (7\text{-}1)$$

h_v is the heat required to raise the temperature of the solid from ambient to the surface temperature T_s and includes five increments: heat to raise the fuel from ambient to melting temperature, heat of liquefaction, heat to raise the liquid to the boiling point, heat of vaporization, and the heat necessary to raise the vapor to the surface temperature, which is of the order of 600° K and may involve some "cracking" or degradation of the polymer. $\dot{Q}_w$ is the total heat transfer, including a convective part $\dot{Q}_c$ and a radiative part $\dot{Q}_r$. For the time being $\dot{Q}_r$ will be neglected, a reasonable approximation if one considers an unmetallized polymer such as Plexiglas.

[7 - 2.2] Convective Heat Transfer

The convective component of heat transfer $\dot{Q}_c$ may be considered as being driven by the enthalpy difference Δh_T between the flame zone and the surface. This assumption is often called the "thin flame" approximation. $\dot{Q}_c$ may be calculated from Δh using the Stanton number** C_H

$$\dot{Q}_c = C_H \rho_e u_e \Delta h_T \qquad (7\text{-}2)$$

In Eq. (7-2), $\rho_e u_e$ is the mass flux at the edge of the boundary-layer. C_H may be evaluated by using Reynolds analogy*** which

---

*Symbols are defined in a table at the end of the chapter.
**The use of Stanton coefficient C_H (or St) is discussed, for example, in Kuethe and Schetzer, Foundations of Aerodynamics, 2nd ed., 1959, p. 270 (Wiley).
***Reynolds analogy for simple flow without mass addition is discussed, for example, in Kuethe and Schetzer p. 325. Reynolds analogy with mass injection has been discussed by L. Lees, Combustion and Propulsion, 3rd AGARD Colloquim, p. 451, Pergamon, 1958, and by G. Marxman, 10th International Symposium on Combustion, pp. 1337-49, The Combustion Institute, Pittsburgh, 1965 (Pergamon).

relates the heat transfer coefficient C_H to the skin friction (shear stress) coefficient c_f defined by

$$c_f = \frac{\tau_w}{\frac{1}{2}\rho_e u_e{}^2} \tag{7-3}$$

Reynolds analogy states that if C_H is defined by Eq. (7-2), then

$$C_H = \frac{c_f}{2} \tag{7-4}$$

Equation (7-4) makes it possible to evaluate $\dot{r}$ in terms of known fluid properties and established boundary layer theory. Equations (7-1), (7-2) and (7-4) may be combined to yield

$$\rho_f \dot{r} = \rho_e u_e \left(\frac{c_f}{2}\right) \cdot \frac{\Delta h_T}{h_v}$$

$$= \rho_e u_e \left(\frac{c_f}{2}\right) \cdot B \tag{7-5}$$

The quantity B defined by Eq. (7-5) is called the "mass transfer number" and is an independent thermochemical parameter of fundamental importance. It may be expressed in two ways:

$$B \equiv \frac{\Delta h_T}{h_v} = \frac{\rho_f \dot{r}}{\rho_e u_e (c_f/2)} \tag{7-6}$$

Physically, B is the ratio between the enthalpy Δh_T which may be extracted from the flow and transferred to a unit area of the fuel surface, and the enthalpy h_v which is required to gasify unit mass flow of fuel per second through unit surface area. It is thus proportional to regression rate $\dot{r}$.

To make Eq. (7-5) useful, it is necessary to evaluate c_f, the skin friction, in the presence of surface mass addition or "blowing." In the absence of blowing, the well-known empirical relations for skin friction c_{f_0} in turbulent flow is

$$\frac{c_{f_0}}{2} \cong 0.03 \left(\frac{\rho_e u_e x}{\mu_e}\right)^{-0.2} = 0.03 \, Re_x{}^{-0.2} \tag{7-7}$$

where $Re_x = Gx/\mu$, $G = \rho_e u_e$ and x is measured from the leading edge of the propellant surface.
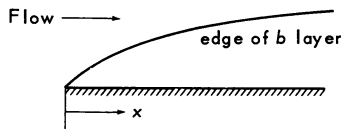
Fig. 7-A

"Blowing" or wall mass injection has the effect of blocking the convective heat transfer. This means that c_f in Eq. (7-5) is reduced from the value c_{f0} which can be calculated in the *nonblowing* case using Eq. (7-7). The problem of calculating the correction factor c_f/c_{f0} for use in evaluating $\dot{r}$ is an important one in hybrid analysis. Equation (7-5) may be rewritten as

$$\rho_f \dot{r} = \left[G \frac{c_{f0}}{2} \cdot \frac{c_f}{c_{f0}} \right] \cdot B \qquad (7-8)$$

The term in brackets is largely a fluid dynamics parameter, and B is a thermochemical parameter. The ratio c_f/c_{f0} is the reduction in heat transfer caused by mass transfer away from the wall. Such mass transfer changes the velocity profile of the boundary layer, causing the axial component u to grow more slowly than in the *nonblowing* case. Typical velocity profiles are shown in Fig. 7-5. The approach to calculating c_f is through its defining Eq. (7-3) repeated here.

$$\frac{c_f}{2} = \frac{\tau_w}{\rho_e u_e^2}$$

Where τ_w is the turbulent shear stress in the fluid defined by

$$\tau_w = (u + \rho\epsilon) \left(\frac{\partial u}{\partial y} \right)_w \qquad (7-9)$$

ϵ is the turbulent diffusivity and the subscript w refers to conditions at the wall. Analysis along these lines by Marxman [3], which is too lengthy to repeat here, shows that the friction correction factor c_f/c_{f0} is sufficiently accurately represented by a simple function of the mass transfer number B

$$\frac{c_f}{c_{f0}} \cong 1.2B^{-0.77} \qquad 5 \leq B \leq 100. \qquad (7-10)$$

In hybrid combustion work, B is of the order of 10, so Eq. (7-10) applies. Inserting Eq. (7-7) and (7-10) in Eq. (7-8), there results the useful equation

$$\rho_f \dot{r} = 0.036 \, GRe_x^{-0.2} \, B^{+0.23} \qquad (7-11)$$

We note from Eq. (7-7) that c_{f0} is really a function of $G = \rho_e u_e$ and that (7-11) may be written in the alternative form

$$\rho_f \dot{r} = 0.036 \left(\frac{x}{\mu_e}\right)^{-0.2} G^{0.8} B^{0.23} \tag{7-12}$$

where G is the combined mass flux per unit area of oxidizer plus fuel.

$$\phi = u/u_e \qquad \eta = y/\delta$$
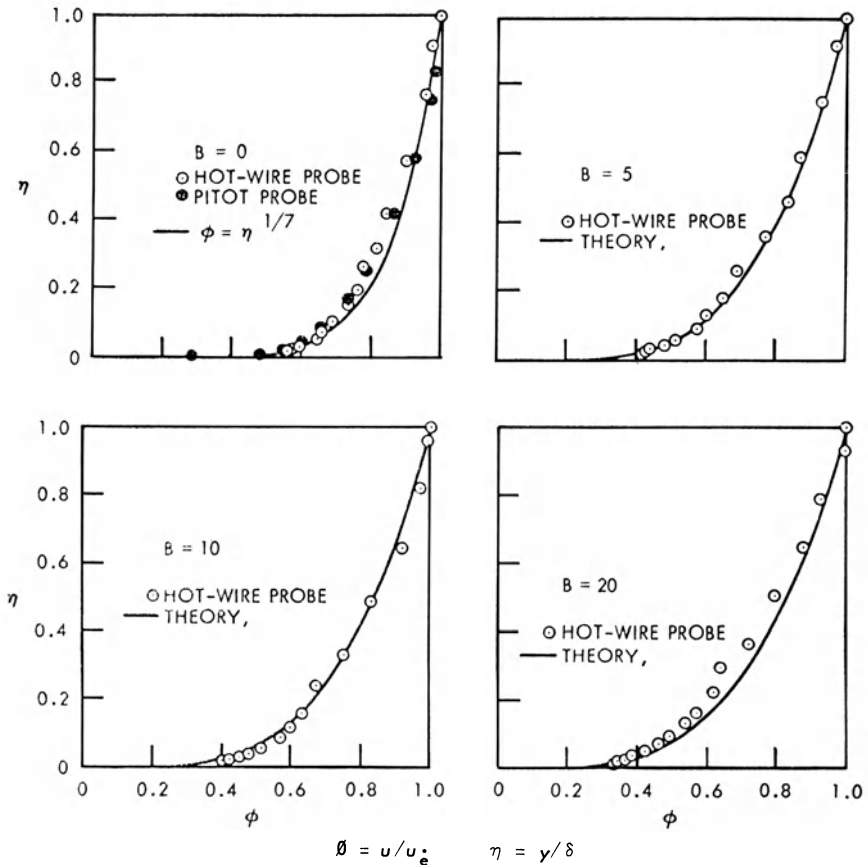
Fig. 7-5

[7-2.3] The Role of Nonvolatile Particles

Nonvolatile particles have several effects: (a) The presence of nonvolatile particles in the solid fuel increases the heat of gasification of the volatile component, since for each unit mass vaporized, some additional nonvolatile mass must be heated to the surface temperature. (b) The presence of nonvolatile particles in the combustion volume greatly increases the radiant energy flux falling

on the grain. (c) The particles in the flame normally are oxides and represent a "sink" consuming gaseous oxidizer and reducing total gas flux G. (d) During nozzle expansion, particles lower the I_{sp} performance because they lag behind the nozzle gases in velocity and temperature (*i.e.*, they are hotter and slower than the local gas temperature and velocity). It should be pointed out that the particles in the solid fuel are not the same particles which appear in the combustion process. Normally the aluminum fuel particles, which may be 30 microns in diameter, burn on their surfaces to produce Al_2O_3, meanwhile consuming the gaseous oxidizer. The Al_2O_3 then condenses into liquid or solid particles which are normally much smaller than the Al particles, with diameters lying between 0.1 micron and 10 microns.

Many solid fuel grains contain metal particles, *e.g.*, aluminum, to increase the heat of reaction. If these particles do not gasify at the surface, their volume relative to the volatile fuel vapor is very small (0.1% or less) and they do not participate in the convective heat transfer process on which Eq. (7-12) for regression $\dot{r}$ is based. The blocking effect on surface heat transfer depends only on the gas blowing rate, and the regression rate of Eq. (7-12) should be modified to be

$$\rho_v \dot{r} = \rho_f (1 - K) \dot{r} = 0.036 \left(\frac{x}{\mu_e}\right)^{-0.2} G^{0.8} B^{0.23} \qquad (7\text{-}13)$$

where K is the mass loading of metal particles, and therefore $\rho_f (1 - K)$ is the number of *gms/cc* of the *vaporizing* component (ρ_v) of the fuel.

The quantity h_v, heat of gasification, first defined in Eq. (7-1), should now be considered the sum of the heat necessary to gasify the volatile components of the fuel plus the heat necessary to heat the nonvolatile components to the surface temperature, T_s. This "effective" heat of gasification, $h_{v_{eff}}$, is equal to

$$h_{v_{eff}} = h_{v_b} + \frac{K}{1 - K} c_s (T_s - T_c) \qquad (7\text{-}14)$$

where h_{v_b} = binder heat of vaporization
   T_c = initial grain temperature
   c_s = heat capacity of nonvolatile particles
   K = mass loading of nonvolatile particle.

This value of $h_{v_{eff}}$ should be used to evaluate the mass transfer number B (Eq. [7-6]) for fuel containing nonvolatile particles. Most metal additives have relatively low heat capacity so that $h_{v_{eff}}$ does not differ much from h_{v_b}. Thus the regression rate is nearly inversely proportional to $(1 - K)$, since $\rho_v = \rho_f (1 - K)$.

[7-3] OPERATING CHARACTERISTICS OF HYBRID ROCKETS WITH NEGLIGIBLE RADIATION

[7-3.1] Regression Rate Insensitivity to Thermochemical Parameters

A large increase in the energy release Δh_T at the flame zone, or a large decrease in heat of gasification h_v of the solid, does not produce a large increase in regression rate $\dot{r}$ even though Eqs. (7-1) and (7-2) might suggest it. This is because increased $\dot{r}$, which in turn produces increased "blowing," tends to block heat transfer to the wall. This "negative feedback" or regulation property results in only a weak dependence of $\dot{r}$ on B, as is indicated by the 0.23 power of B in Eqs. (7-12) and (7-13). As a consequence, the attainable range of hybrid regression rates is considerably lower than composite solid propellants in the same pressure range.

[7-3.2] Regression Rate Dependence Upon Grain Configuration

Equation (7-12) states that $\dot{r}$ = constant$\times G^{0.8}$, where the mass flux density G_x = total mass flux through port area at station x divided by port area. Since gas is being added to the core flow continuously along the length of the grain and the port area is increasing continuously with time as regression proceeds, the quantity G increases with axial station and decreases with time. The decrease in $\dot{r}$ with time is in part compensated by the increase in burning perimeter with time, referred to as "progressivity" of the grain. The increase of G_x in axial station is in part compensated by the $x^{-0.2}$ term in Eq. (7-12), The net result is that $\dot{r}$ is reasonably insensitive to axial displacement for values of $L/D < 25$. This is fortunate, since wastage of fuel would occur if one axial station burned to the motor wall significantly before another.

[7-3.3] Throttling and Off-Design Point Operation

Although the regression rate $\dot{r}$ varies as $G^{0.8}$ where G is *total* mass flux, it varies more slowly with the mass flux G_{ox} of *oxidizer* alone. A typical dependence is

$$\dot{r} = \text{const.} \times G_{ox}{}^{0.5} \qquad (7\text{-}15)$$

The oxidizer mass flow, however, is the only parameter of a hybrid engine which is adjustable during operation. One consequence of Eq. (7-15) is that the changes in oxidizer mass flux G_{ox} strongly affect the overall *ratio* of oxidizer to fuel flow, and hence I_{sp}. This may be seen as follows. In a cylindrical motor of diameter D and length L, the total oxidizer flow O through the port is

$$O = G_{ox} \cdot \frac{\pi D^2}{4} \qquad (7\text{-}16)$$

The total fuel flow into the combustion volume from the gasifying cylindrical port is

$$F = \rho_v \dot{r} \pi DL$$

$$F \cong \text{const.} \times G_{ox}^{0.5} \, DL \qquad (7\text{-}17)$$

Therefore the ratio of oxidizer to fuel flow would be

$$O/F \cong \text{const.} \; G_{ox}^{0.5} \qquad (7\text{-}18)$$

The implication of Eq. (7-18) for the throttling process may best be seen with the aid of a simple numerical example. Suppose it were desired to throttle to 1/3 design point thrust, while maintaining constant O/F ratio for efficiency, then

$$O + F \rightarrow \frac{O}{3} + \frac{F}{3}$$

Since only the oxidizer flow is under control (*i.e.*, an independent variable), it would be necessary, in view of Eq. (7-17), to cut the oxidizer flow to 1/9 normal to reduce the fuel flow to 1/3 normal, *i.e.*,

$$F \rightarrow \frac{F}{3} \quad \text{only if} \quad O \rightarrow \frac{O}{9}$$

the combustion would then be running very fuel-rich; by Eq. (7-18), O/F would be 1/3 design value. The practical way to restore efficiency and establish the thrust at the desired level would be to restore the missing (2/9) O flow through an aft-end injector and mixer. A curve showing the relative values of fuel, head-end oxidizer, and aft-end makeup oxidizer is shown in Fig. 7-6.

[7-3.4] Combustion Efficiency

Since hybrid combustion occurs in a flame located well away from the surface, some of the vaporized fuel leaving the wall (typically 15%) is convected downstream under the flame and is not oxidized. Also, the flame zone tends to be fuel-rich [3], typically having local O/F ratios about 3/4 of the stoichiometric values. These characteristics of the combustion require that mixing occur downstream of the grain and ahead of the nozzle, and combined with possible need for added oxidizer at the aft end caused by throttling, make it necessary to provide suitable combustion volume prior to expansion.
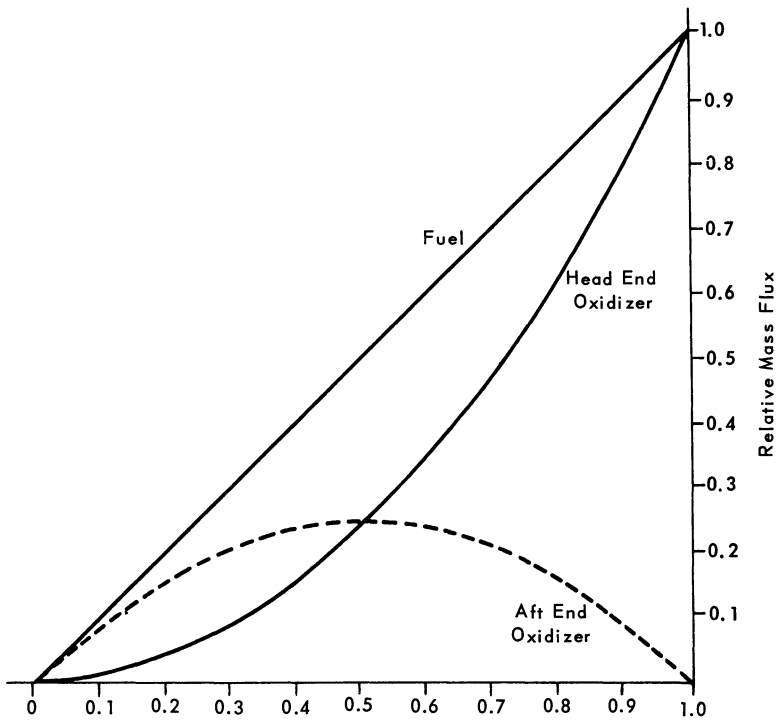
Fig. 7-6

[7-3.5] Regression Rate Dependence Upon Pressure

In practice, the regression rate is insensitive to pressure at higher pressure levels (say, above 150 psia) but not at low pressure where chemical kinetics of the reaction are slower (see Fig. 7-7). At low pressures the regression law has the form $\dot{r} \sim p^m G^n$, with $m < n < 1.0$.

[7-4] HYBRID COMBUSTION IN RADIATIVE MOTORS

[7-4.1] Regression Rate Dependence Upon Radiant Energy Flux

In large combustion chambers or in combustion gases containing large numbers of solid particles (circa 10^7/cc), an important part of the energy absorbed by the wall may be radiant heat. The addition of radiative heat transfer $\dot{Q}_r$ increases the regression
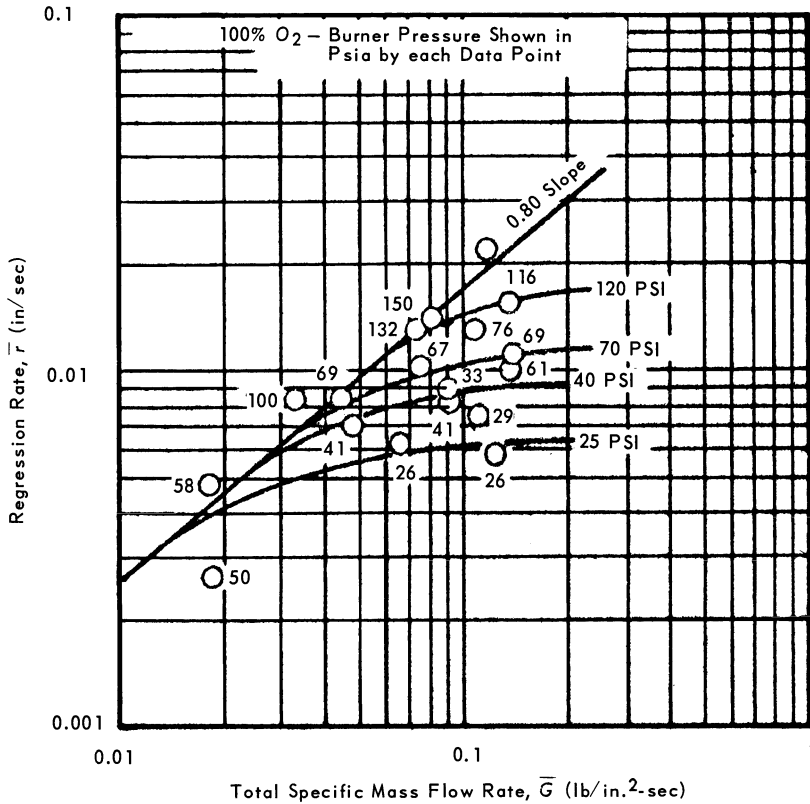
Fig. 7-7

rate $\dot{r}$ which in turn inhibits the convective heat transfer $\dot{Q}_c$. Marxman [2] has analyzed the coupling between $\dot{Q}_r$ and $\dot{Q}_c$. The dependence of $\dot{r}$ on $\dot{Q}_r$ is given by

$$\rho_v \dot{r} = \frac{\dot{Q}_c}{h_{v_{eff}}} \cdot \left(e^{-(\dot{Q}_r/\dot{Q}_c)} + \dot{Q}_r/\dot{Q}_c \right) \qquad (7\text{--}19)$$

Equation (7-19) shows that if, for example, an initial convective heat transfer $\dot{Q}_c$ existed without radiation ($\dot{Q}_r = 0$), the addition of an amount of radiant heat flux $\dot{Q}_r$ equal to the original convective value ($\dot{Q}_r = \dot{Q}_{co}$) would have the effect of depressing the resultant convective heat transfer $\dot{Q}_c$ to $1/e$ of its initial value, with the result that $\dot{r}$ would increase only 35% over its value at $\dot{Q}_r = 0$, but three-fourths of the final total heat transfer would be due to radiation. Figure 7-8 shows the fraction of the total heat transfer $\dot{Q}_w$ which is radiative (curve A) and also the factor by which total
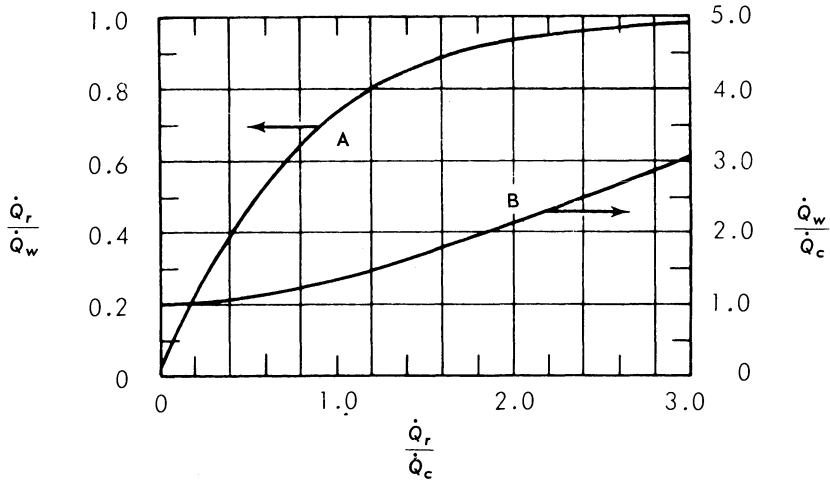
Fig. 7-8

heat transfer $\dot{Q}_w$ is increased by the addition of radiation (curve *B*). Both are plotted as a function of radiant heat flux measured in multiples of the initial undisturbed convective heat flux. Curve *B* is proportional to regression rate. Figure 7-8 is significant because it shows that the relative influence of $\dot{Q}_r$ increases rapidly, and in processes dominated by radiation, it will be shown later, $\dot{r}$ is pressure sensitive, whereas in nonradiative systems it is relatively independent of pressure.

[7-4.2] Evaluation of Convective Heat Transfer $\dot{Q}_c$

In order to use Eq. (7-19) to calculate regression rate $\dot{r}$ in the presence of radiation, the terms $\dot{Q}_c$, $\dot{Q}_r$ and h_v must be evaluated. h_v has already been discussed in connection with Eqs. (7-1) and (7-14). Q_c as used in Eq. (7-19) is the convective heat transfer without radiation, and its formal equation may be evolved from Eqs. (7-1) and (7-12), noting that $\dot{Q}_w = \dot{Q}_c$ in the absence of radiation. At pressures below 265 psia for Plexiglas (polymethlmethcrylate), there is a weak dependence of $\dot{r}$ on pressure, so an empirical dimensionless pressure factor $(p^*)^{0.23\beta}$ is inserted in Eq. (7-12) to give the result:

$$\frac{Q_c}{h_{v_{eff}}} = 0.036\,(p^*)^{0.23\beta}\,B^{0.23}\left(\frac{x}{\mu}\right)^{-0.2}\left(\frac{\dot{m}_g}{A_p}\right)^{0.8} \tag{7-20}$$

where $p^* = p/p_{\text{threshold}} = p/265$, and $\beta = 1.1$ for Plexiglas. Above $p = 265$ psia, β may be taken as zero as pressure effects vanish. The threshold pressure may vary with mass flux and propellant species however. β is determined by small-scale burning rate tests.

The mass transfer number, B, defined in Eq. (7-5), varies from 5 to 15 as the Reynolds number in the boundary layer varies from 10^4 to 10^6, but since it enters only as $B^{0.23}$, it may be considered to have the value 10 in preliminary design and still give adequate accuracy for $\dot{r}$. The geometrical port diameter should be adjusted downward by twice the displacement thickness of the boundary layer in calculating the equivalent port area A_p.

In calculating $G = \dot{m}_g/A_p$, the gas flow $\dot{m}_g$ at any station x must include the initial head-end oxidizer flow plus the gas evolved from the surface up to station x, corrected for the effect of possible evolution or absorption of gases by the metal particles in the fuel. In general, $\dot{m}_g$ will have the form

$$\dot{m}_g = \dot{m}_0 + \text{constant} \cdot \int_0^x \rho_v \, \dot{r} \, P dx \qquad (7\text{-}21)$$

where P is the grain perimeter and the constant accounts for particle activity [4].

[7-4.3] Evaluation of Radiative Heat Transfer $\dot{Q}_r$

The radiant heat transfer flux $\dot{Q}_r$ from the combustion products to the wall is given by the familiar law

$$\dot{Q}_r \cong \sigma \epsilon_w \, \epsilon_g \, T_r^4 \qquad (7\text{-}22)$$

Where T_r is the fluid temperature, ϵ_w is the wall absorptivity and ϵ_g is the fluid emissivity. Radiation returned from the wall to the gas is neglected, since wall temperature is typically 10% of fluid temperature. The fluid emissivity ϵ_g depends upon whether it is gaseous or particle-laden; if gaseous, then

$$\epsilon_g = 1 - e^{-\alpha p z} \qquad (7\text{-}23)$$

where α = empirical constant, p = pressure, z = optical path length. If many particles are present, their radiation is much greater than the gas radiation, which may be ignored. We then have

$$\epsilon_g = 1 - e^{-\alpha n} \qquad (7\text{-}24)$$

where n = number density of particles.

Equation (7-22) may now be written with a similar empirical pressure correction to that used in Eq. (7-20), except that now dimensionless pressure is raised to the β power (approximately 1.1) instead of the 0.23β power.

$$\dot{Q}_r \;\stackrel{\circ}{=}\; \sigma \epsilon_w p^* \beta T_r^4 \left(1 - e^{-\alpha \left[\frac{pz}{n}\right]}\right) \tag{7-25}$$

The temperature T_r appearing in Eq. (7-25) represents an "effective" flame temperature, which, because of the fourth power law, is nearly equal to the maximum temperature. However, because of the departure from stoichiometry in the combustion mentioned in Section 7-3.4, the actual maximum temperature is about 3/4 stoichiometric for aluminized Plexiglas and oxygen, and an appropriate value of T_r to use in equation (7-25) is 2/3 stoichiometric, which for this propellant is $T_r \stackrel{\circ}{=} 2200°$ K.

In Eq. (7-25), z may be taken as the interior diameter of the grain. The number density of the particles is obtained from previous burning tests of the propellants which yield particle radius and a knowledge of the vaporized fuel mass density G_f. Calculations for G_f are given by Wooldridge [4]. The quantity α is also determined by empirical small-scale burning tests. Typical results of calculations based on Eqs. (7-19), (7-20) and (7-25) are shown in Fig. 7-9.

It should be noted that while particle number density n increases with axial distance x, it plays a minor role in Eq. (7-25), and thus $\dot{Q}_r$ does not introduce significant axial variation in $\dot{r}$.

[7-5] TRANSIENT OPERATION OF HYBRID ROCKETS

[7-5.1] Penetration of Temperature Profile

The solid fuel of a hybrid rocket is not a good conductor of heat, and an appreciable time ranging from 1 to 30 seconds is required after ignition for the regression rate $\dot{r}$ to reach its equilibrium value $\dot{r}_\infty$ and for a steady-state thermal profile in the grain to be reached. The temperature in the grain may be calculated from the one-dimensional heat conduction equation applied to a semi-infinite slab whose surface is regressing at the instantaneous rate $\dot{r}(t)$. This equation is

$$\frac{\partial T}{\partial t} = \dot{r}(t)\,\frac{\partial T}{\partial x} + \kappa\,\frac{\partial^2 T}{\partial x^2} \tag{7-26}$$

where $\kappa = k/\rho_s C_s$ = thermal diffusivity of grain

T = temperature at any point x below the surface.

Figure 7-10 shows the temperature profile in the grain a short time after ignition. The surface reaches its vaporization temperature T_s almost immediately, and regression $\dot{r}$ begins at a low but increasing rate before any temperature increase has penetrated
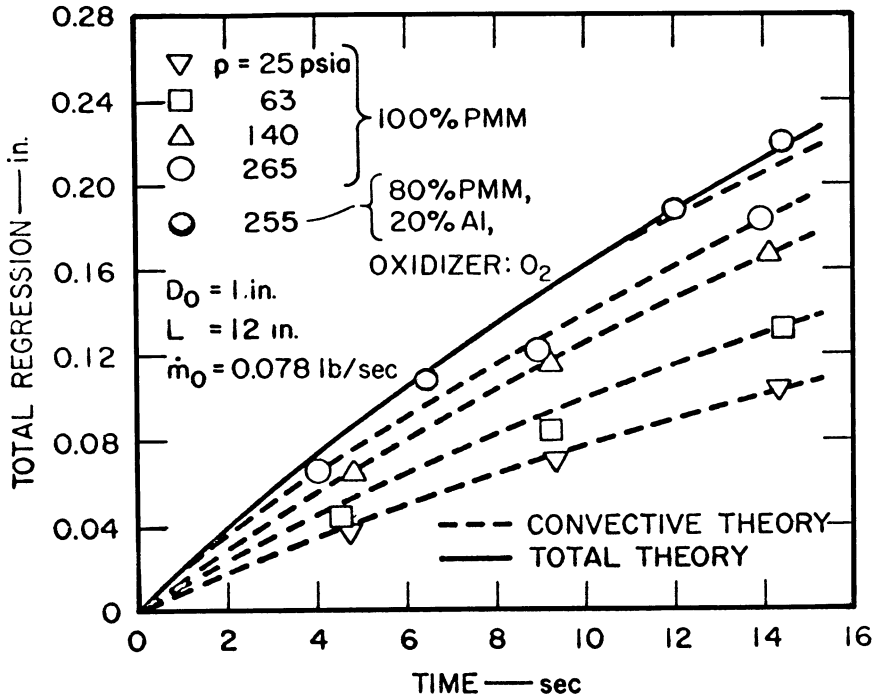
Fig. 7-9

significantly into the grain. At this time the heat flux $\dot{Q}_w$, assumed constant, is divided between gasifying the surface and heating the interior, according to the relation

$$\dot{Q}_w = \rho_s \dot{r} h_{v_{eff}} + \rho_s C_s \frac{\partial}{\partial t} \int_0^\delta (T - T_0)dx \qquad (7\text{-}27)$$
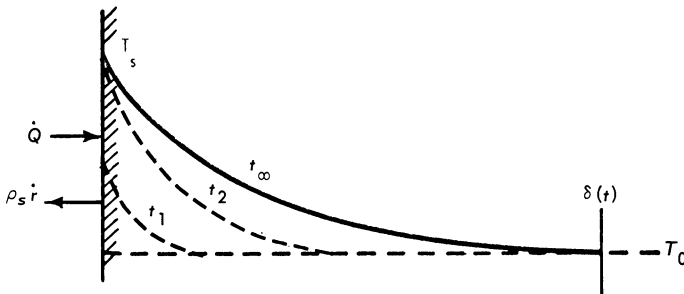
Fig. 7-10

After the steady-state conditions have been reached,

$$\dot{Q}_w = \rho_s \dot{r}_\infty h_{v_{eff}} \qquad (7\text{-}28)$$

and the depth of penetration δ of the point where T just begins to be greater than T_0, reaches an equilibrium value $\delta = \delta_\infty$. At equilibrium this penetration point travels inward at the same speed as the surface regression rate $\dot{r}$.

By appropriate operations [2] on Eqs. (7-26), (7-27) and (7-28), solutions may be found for $\delta(t)$ and $\dot{r}(t)$. The nondimensional value of $\dot{r}(t)$ as a function of t is in Fig. 7-11. The value of steady-state penetration depth of the temperature wave, δ_∞, is given by

$$\delta_\infty \cong \frac{3\kappa}{\dot{r}_\infty} \qquad (7\text{-}29)$$

In Plexiglas, for example, if $\dot{r}_\infty = 0.01$ in/sec., $\delta_\infty = 0.05$ in. (*i.e.*, the grain temperature .05 in below the surface will be nearly its pre-ignition value T_0). But if $\dot{r}_\infty = 0.001$ in/sec., $\delta_\infty = 0.5$ in. The transient time to reach $\dot{r}_\infty = 0.003$ in/sec. is about 20 seconds.
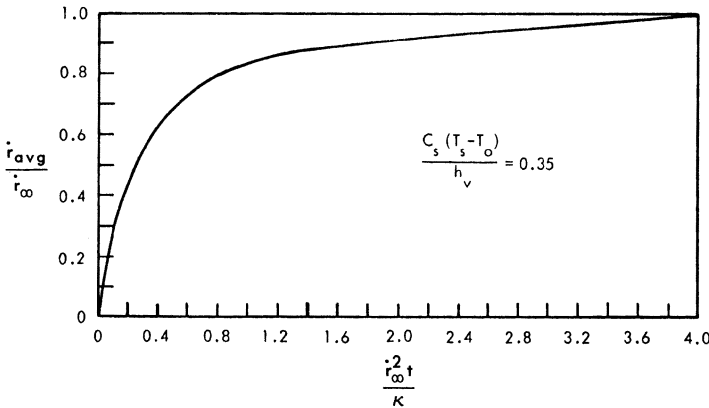
Fig. 7-11

[7-5.2] Critical Regression Rate

The possible presence of high temperatures in a thick layer of grain, apt to occur when $\dot{r}$ is low, may lead to practical problems. The sub-surface layers may "cook" for too long a time, leading to charring, softening or melting, attended by poor combustion. For any given fuel, it is usually possible to give a temperature T_{crit} which will cause undesirable side-effects if exceeded for longer than some specified time interval t_{crit}. Of course it is

expected that the fuel temperature must exceed T_{crit} for some short interval, and in general the surface temperature T_s is well above T_{crit}, but in normal operation these high temperatures are quite close to the surface and do not affect the integrity of the grain or the efficiency of combustion adversely.

According to the exact steady-state solutions of Eq. (7-26), the distance x_{crit} from the surface at which t_{crit} is reached is

$$x_{crit} = \frac{\kappa \ln\left(\dfrac{T_s - T_0}{T_{crit} - T_0}\right)}{\dot{r}} \tag{7-30}$$

If $x \leq x_{crit}$, $T \geq T_{crit}$. It is assumed that $T_s \geq T_{crit} \geq T_0$. As the surface regresses, the solid material remains at $T \geq T_{crit}$ for a period of time $t = x_{crit}/\dot{r}$, thus the critical regression rate is

$$\dot{r}_{crit} = \frac{x_{crit}}{t_{crit}} = \sqrt{\frac{\kappa \ln\left(\dfrac{T_s - T_0}{T_c - T_0}\right)}{t_{crit}}} \tag{7-31}$$

If the regression rate falls below $\dot{r}_{crit}$, the solid will be at a temperature T in excess of T_{crit} for a time greater than t_{crit}.

As an example of the use of Eq. (7-31), consider the softening of Plexiglas, which occurs at about 400° K. Softening one second prior to vaporization would be acceptable, but 100 seconds above 400° K would be unacceptable. If we postulate that $t_{crit} = 10$ seconds, from Eq. (7-31), with $T_s = 600°$ K, $T_0 = 300°$ K, $T_{crit} = 400°$ K, and $\kappa = 1.7 \times 10^{-4}$ in^2/sec.; we obtain $\dot{r}_{crit} = 0.004$ in/sec. A regression rate much below 0.004 in/sec. would probably cause the surface to melt and flow, with severe degradation of performance.

A practical consideration involving critical quantities is restart after shut-down. If combustion is stopped and the grain temperature levels off to something above its normal ambient of 300° K, this number must be used for T_0 in Eq. (7-31) when calculating $\dot{r}_{crit}$ for the second firing. Thus if the grain is ignited at $T_0 = 380°$ K, for example, we get $\dot{r}_{crit} = 0.006$ in/sec. This is an important consideration for certain missions.

[7-6] DESIGN OF HYBRID ROCKETS

[7-6.1] Specification of Mission

Preliminary design usually begins with specification of a propellant, including its specific impulse as a function of O/F ratio

and pressure, and a thrust-time program or total impulse require-
ment, together with an envelope into which it is desired to fit the
propulsion unit. When the propellant is specified, certain charac-
teristic quantities which determine its hybrid combustion behavior
are needed. These parameters are B, the mass transfer number,
α, the radiation constant (Eq. 7-23) and β, the pressure effect
exponent. These are ordinarily determined by laboratory burner
tests on the propellant in question, made over a range of G, p_c and
chamber dimensions of interest.

[7-6.2] Preliminary Design Procedure

The most significant single parameter of a hybrid r rocket is,
of course, its regression rate $\dot{r}$, which determines both the burning
surface required for a given fuel flow rate, and the web thickness
required for a given thrust duration. It is characteristic of hybrid
combustion that typical regression rates are about an order of
magnitude smaller than typical all-solid propellant burning rates.
The regression rate is of the form (see Eq. 7-12)

$$\dot{r} = a' G^{0.8}$$

The determination of G normally requires elaborate machine cal-
culations involving Eqs. (7-19), (7-20), (7-21) and (7-25). For
illustrative purposes, a different form of $\dot{r}$ relation, true only for
certain propellants and geometries, will be used, but which has
the effect of greatly simplifying calculations:

$$\dot{r} = a G_{ox}^{0.5} = a G_{ox}^{n} \tag{7-32}$$

If the $n = 1/2$ in the law (7-32), $\dot{r}$ has the property that in a burning
cylinder, the total flow of fuel $\dot{m}_f$ released is constant with time if
the total flow of ixidizer $\dot{m}_{ox}$ is constant. This can be seen as
follows:

$$\rho_f \dot{r} \pi D L = a \rho_f \left(\frac{4\dot{m}_{ox}}{\pi D^2}\right)^{\frac{1}{2}} \pi D L = \dot{m}_f \tag{7-33}$$

$$\dot{m}_f = a \pi^{1/2} \rho_f L (4\dot{m}_{ox})^{1/2}$$

Equation (7-33) is independent of D, so $\dot{m}_f$, and hence O/F ratio
remains constant, along with thrust, as D increases during
burning. Regression rate of course decreases as D grows.

The steps in carrying out the design of a cylindrical grain, using the assumptions implied by Eqs. (7-32) and (7-33) are:
1) Obtain I_{sp} or c^* from experimental curves
2) Specify thrust, O/F ratio, and burning time t_b
3) Calculate W_{ox} and $\dot{W}_{fuel}$ (adjust units of $\dot{m}$)
4) From regression rate experimental data (see Figs. 7-12 and 7-13) choose the constants a and n in Eq. (7-32).
5) Calculate the length of the cylinder from Eq. (7-33).
6) Calculate the initial radius, R_a, and the final radius, R_b, of the burning surface by the following procedure:

$$\dot{r} = \frac{dR}{dt} = a\left(\frac{\dot{W}_0}{\pi R^2}\right)^{\frac{1}{2}} = a\left(\frac{\dot{W}_0}{\pi}\right)^{\frac{1}{2}} \cdot \frac{1}{R}$$

$$\int_{R_a}^{R_b} R\,dR = \frac{R_b^2 - R_a^2}{2} = a\left(\frac{\dot{w}_0}{\pi}\right)^{\frac{1}{2}} t_b \tag{7-34}$$

[7-6.3] Example Configurations

In the example to follow, we shall take O_2 as the oxidizer and 80% polymethyl methacrylate (Plexiglas) with 20% Al as the fuel, with the following specifications assumed:

$$
\begin{aligned}
p_c &= 300 \text{ psia} \\
I_{sp} &= 250 \text{ sec.} \\
\rho_v &= 0.04 \text{ lb/in.}^2 \\
O/F &= 1.00 \\
\text{Thrust} &= 100 \text{ lbs.}
\end{aligned}
$$

Then
$$
\begin{aligned}
\dot{w}_{total} &= \text{Thrust}/I_{sp} = 0.4 \text{ lb/sec.} \\
\dot{W}_f &= 0.2 \text{ lb/sec.} \\
\dot{W}_0 &= 0.2 \text{ lb/sec.}
\end{aligned}
$$

From regression rate data as that shown in Figs. (7-12) and (7-13), we shall take $a = 0.09$. Note that G_{ox} is, within limits, an independent variable, since $G_{ox} = \rho_{ox} u_e$ and pressure is adjustable through the throat area of the nozzle. p_c will also have a weak influence on I_{sp} through C_F.

From Eq. (7-33), the length required to supply 0.2 lb/sec. of fuel is $h = 35.1$ in. If we choose (from experience) $G_{ox} = 0.0283$ lb/sec.^{2}, the initial diameter D_a to pass 0.2 lbs/sec. of O_2 will be

$$D_a^2 = \frac{\dot{W}_{ox}}{\pi/4 \cdot G_0} = 9 \text{ in}^2 \tag{7-35}$$

$$D_a = 3 \text{ in.}$$
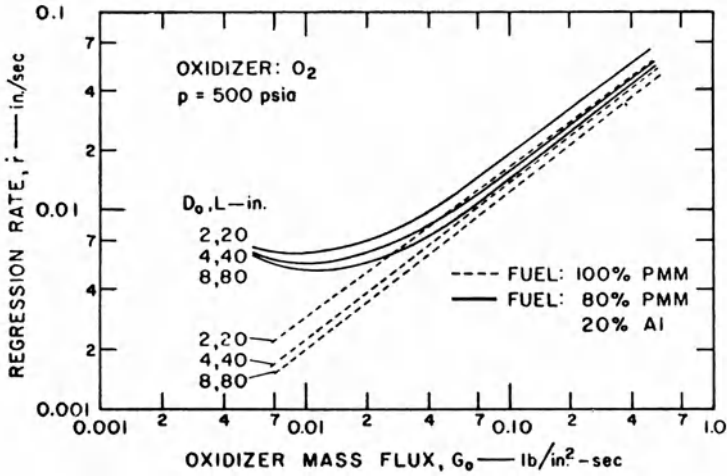
Fig. 7-12
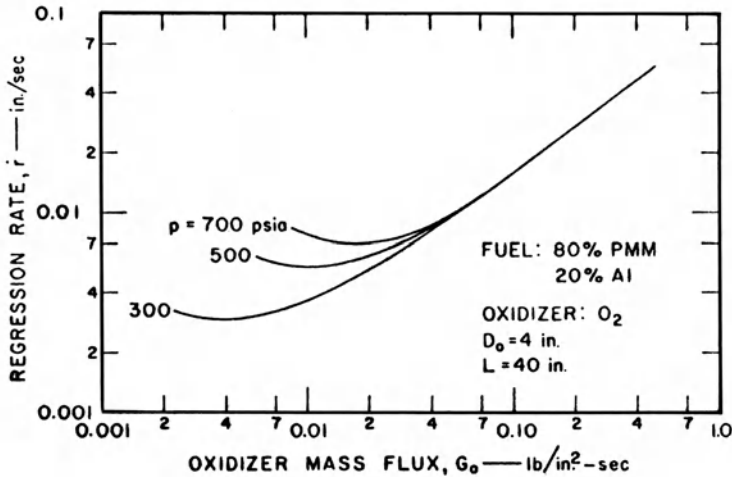
Fig. 7-13

The final diameter D_b is determined by the burning time t_b. If $t_b = 50$ seconds, then from Eq. (7-34),

$$D_b = 2R_b = 4.26 \text{ in.}$$

We can proceed in this manner to make a table (Table 7-1) of the various hollow cylindrical configurations which result if two G_0's (0.0283 and 0.0636 lb/in²-sec.), two t_b's (50 and 100 sec.) and two thrust levels, (50 lbs. and 100 lbs.) are specified. Two 50-lb. thrust cylinders can be clustered to give a 100-lb. thrust unit with a different and perhaps more convenient aspect ratio. The data of Table 7-1 are displayed diagrammatically in Fig. 7-14.

Table 7-1   Hybrid Grain Configurations

G_{ox} lb/in²-sec.	t_b sec.	R_a in.	R_b in.	Web W in.	L in.	L/D
			100# thrust single barrel			
.0283	50	1.5	2.13	0.63	35.1	11.7
.0283	100	1.5	2.61	1.11	35.1	11.7
.0636	50	1.0	1.81	0.81	35.1	17.5
.0636	100	1.0	2.36	1.36	35.1	17.5
			2 × 50# thrust double-barrel, each barrel			
.0283	50	1.06	1.66	0.60	24.8	11.7
.0283	100	1.06	1.85	0.79	24.8	11.7
.0636	50	0.707	1.46	0.75	24.8	17.5
.0636	100	0.707	1.93	1.22	24.8	17.5

L/D = 11.7 L/D = 17.5

t_b = 50
G_0 = .028

t_b = 50
G_0 = .064

t_b = 100
G_0 = .028

t_b = 100
G_0 = .064
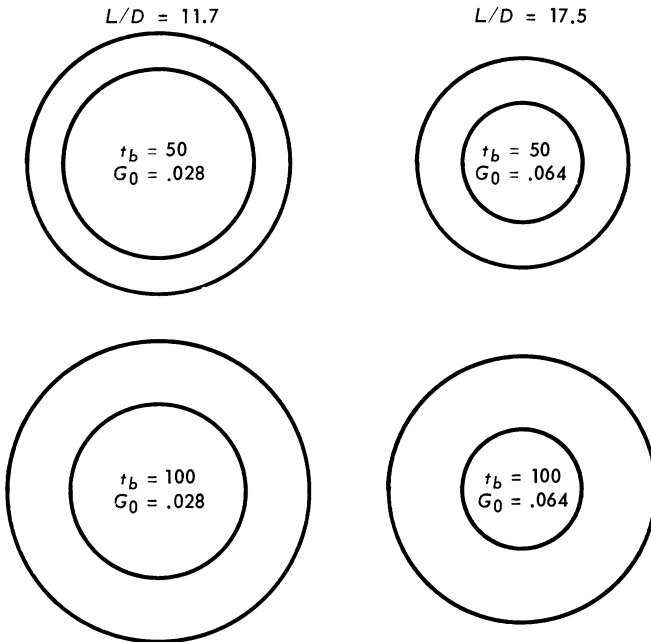
Fig. 7-14 Effect of variable t_b and G_{ox}; F = 100 lbs., L = 35 in.

TABLE OF SYMBOLS

a Empirical constant in regression rate law
A_p Flow port area
A_g Geometric port area

B	Thermochemical mass transfer number
c_m	Heat capacity of nonvaporizing fuel component
$\bar{c}_{p_s}$	Heat capacity at constant pressure of gases at the regressing surface
c_s	Heat capacity of solid fuel
D	Diameter
D_{eq}	Equivalent diameter of noncircular port
F	Thrust, or total fuel flow
G	Total mass flux $(= \rho_e u_e \cong \dot{m}_g / A_p)$ per unit area
G_0	Oxidizer mass flux per unit area
h_{v_b}	Heat of gasification of binder material
$h_{v_{eff}}$	Effective heat of gasification of solid phase
I_{sp}	Specific impulse
K	Mass fraction of nonvolatile surface material
L	Length of fuel grain
$\dot{w}_g$	Total gas flow rate
$\dot{w}_0$	Oxidizer flow rate
n	Pressure exponent in solid rocket burning rate law; exponent in empirical hybrid regression rate law; number density of particles
N	Radiation parameter in gas-phase emissivity; number of ports in a multiport grain
O	Oxidizer flow
P	Pressure
p^*	Dimensionless pressure
P	Internal perimeter of Fuel grain
$\dot{Q}_c$	Convective heat transfer in the absence of radiation per unit area
$\dot{Q}_r$	Radiative heat transfer
$\dot{Q}_w$	Total heat transfer
$\dot{r}$	Regression rate
R	Radius of fuel grain
Re_x	Reynolds number based on x
t	Time
T_e	Temperature at boundary layer edge, or on motor centerline
T_r	Effective radiation temperature
u	Longitudinal component of velocity
u_e	Longitudinal velocity at boundary layer edge, or on motor centerline
w	Web thickness of multiport grain
x	Longitudinal coordinate
z	Optical path length

GREEK SYMBOLS

α	Empirical radiation coefficient
β	Empirical pressure exponent
δ^*	Boundary layer displacement thickness

δ_∞ Thermal profile depth in the solid grain
Δh_T Enthalpy difference between the flame zone and the surface
ΔT Temperature difference between the surface and an ambient point deep in the grain
ϵ_w Emissivity of the surface
κ_s Thermal diffusivity of solid phase
μ Viscosity
ρ_e Density at edge of boundary layer, or on motor centerline
ρ_f Density of fuel
ρ_p Density of particulate combustion products
ρ_v Bulk density of volatile component of fuel
σ Stefan–Boltzmann constant

REFERENCES

1. Bartel, H.R. and W.D. Rannie: Solid Fuel Combustion Ramjets *Progress Report 3-12*, Jet Propulsion Laboratory, California Institute of Technology, September 1946.
2. Wolfhard, H., I. Glassman, and L. Green: Heterogeneous Combustion, Vol. 15, Progress in Astronautics, p. 485, New York, Academic Press, 1964.
3. Marxman, Gerald A.: Combustion in the Turbulent Boundary Layer on a Vaporizing Surface, 10th International Symposium on Combustion, pp. 1337-49, Pittsburgh, The Combustion Institute, 1965.
4. Wooldridge, C.E. and R.J. Muzzy: Internal Ballistic Considerations in Hybrid Rocket Design, *Journal of Spacecraft*, February 1967, pp. 255-261 (see also AIAA Reprint 66-628).
5. Investigation of Fundamental Phenomena in Hybrid Propulsion, *Final Report UTC 2097-FR*, Vol. I. (Unclassified), November 1965, United Technology Center, Sunnyvale, Calif.
6. Smoot, L.D. and C.F. Price: Regression Rates of Metalized Hybrid Fuel Systems, *AIAA Journal*, Vol. 4., pp. 910-915 (1966).
7. Barrere, M. and A. Moutet: La Propulsion par Fusees Hybrides, Proceedings of 14th Int. Astr. Congress, Paris, 1963, published by Int. Astr. Federation.
8. Barrero, M. and A. Moutot: Liquid–Solid Rockets, *International Science and Technology*, pp. 64-74, Aug. 1967.

Part Four

Nuclear Propulsion

Nuclear Rocket Propulsion

C. C. Ross
Senior Vice President
Nuclear Products and Services Group
Aerojet-General Corporation

and

H. S. McQueen
Senior Engineering Specialist
Nuclear Rocket Operations
Aerojet-General Corporation

[8-1] NUCLEAR ROCKET ENGINE DESIGN AND PERFORMANCE

[8-1.1] Types of Nuclear Rockets

Nuclear rocket engines may be divided into two general classes based on the type of reactor used, *i.e.*, solid-core systems and fluid-core systems. The latter may be further subdivided into liquid-, gas-, and plasma-core engines. Although fluid-core systems have been studied by a number of investigators during the past ten years, no major development activity has been initiated. Details of these systems are discussed in Chapter 9.

Solid-core reactor systems have been under active investigation since 1955. These engines utilize reactors with graphite, metal, or metal-carbide cores capable of operating at temperatures ranging from 2000 to 3000° K. These engines function by raising hydrogen to high pressure, heating it by passing it through the high-temperature reactor (after using it to cool the nozzle, reflector, and support structure) and then exhausting it through a convergent-divergent nozzle at extremely high speeds. The major effort has been associated with graphite-core systems.

[8-1.2] Overall Engine Design

Solid-core nuclear rocket engines are essentially an adaptation of the liquid propellant rocket engine with the chemical reaction (combustion) chamber replaced by the nuclear reactor and the

359

oxidizer-feed system eliminated as shown in Fig. 8-1. The pro-
pellant flowing from the pump first enters the nozzle then flows
upward through the neutron reflector surrounding the reactor
core, cooling both the reflector and the control drums contained
within it, and through a neutron and gamma ray shield placed at
the upper end of the reactor assembly to limit the radiation-heating
of propellant in the tank. Flowing downward, the propellant cools
the reactor support structure and is heated to the design tempera-
ture, exiting into the nozzle plenum chamber prior to being dis-
charged through the exhaust nozzle. Some propellant is bled off
from this chamber and is cooled to an acceptable inlet temperature
for the pump drive turbine. This cooling is accomplished primarily
by mixing the heated material with cold fluids. A small amount of
gas is also drawn from a convenient region of the engine, such as
the reactor core inlet plenum, for pressurization of the propellant
tank and operation of pneumatically actuated control system
components.
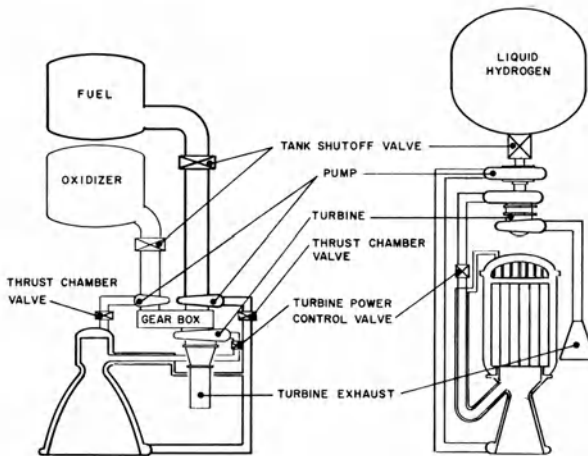
Fig. 8-1 Schematic comparison of nuclear and chemical rockets.

A control system must be provided for the engine to control
reactor power, gas temperature, and pump discharge pressure.
Several methods of control can be utilized, as will be discussed
later.

A thrust vector control (TVC) system is also provided to
maintain attitude control of the vehicle. The primary purpose of
this system is to maintain the thrust vector parallel to the velocity
vector and through the vehicle center of gravity. The TVC system
can be used to change the heading of the vehicle and the direction
of the velocity vector.

[8-1.3] Nuclear Rocket Performance

The performance of a rocket vehicle can be described in terms of its characteristic speeds. This is the speed increment that can be provided by a rocket propulsion system, excluding losses due to gravitational fields or other factors and is defined by the equation:

$$\Delta V = g_0 I_{sp} \ln \frac{W_0}{W_f} .$$
(8-1)

Gas temperature affects this performance through the specific impulse, I_{sp}, as follows:

$$I_{sp} = \frac{c^* C_F}{g_0}, \quad c^* = \left(\frac{2}{\gamma + 1}\right)^{\frac{\gamma + 1}{-2(\gamma - 1)}} \sqrt{\frac{g_0 R T_c}{\gamma M}}$$
(8-2)

$$C_F = \gamma \left(\frac{2}{\gamma - 1}\right)^{1/2} \left(\frac{2}{\gamma + 1}\right)^{\frac{\gamma + 1}{2(\gamma + 1)}} \left[1 - \left(\frac{P_e}{P_c}\right)^{\frac{\gamma - 1}{\gamma}}\right]^{1/2} + \left(\frac{P_e - P_0}{P_c}\right) \frac{A_e}{A_t} .$$
(8-3)

As indicated, the gas properties, γ and M, and the nozzle expansion ratio also affect the specific impulse. These equations are based on the frozen composition and constant specific heat ratio, but provide a fairly close approximation of the more correct values obtained through a point-to-point equilibrium expansion calculation. (Data from such calculations are shown in Fig. 8-2. The high values of specific impulse shown at low pressures is a result of dissociation and recombination of the hydrogen molecule). These equations depend primarily on the ratio T_c/M, so that the specific impulse will increase as the gas temperature is increased. Since the gas temperature in a solid-core nuclear rocket engine must be lower than that of the fuel-material at all times, the performance potential of the system is limited by the maximum temperature that engine structural materials are capable of withstanding.

Equation (8-2) indicates the desirability of using hydrogen ($M = 2.0$) as a propellant. Its low molecular weight is the source of the superiority of the nuclear engine over its chemical rival. There are three principal sources of gaseous exhaust from a nuclear rocket engine: The net specific impulse of the engine system is then defined by the equation

$$I_{sp_E} = \frac{\dot{w}_t I_{spt} + \dot{w}_a I_{spa} + \dot{w}_n I_{spn}}{\dot{w}_t + \dot{w}_a + \dot{w}_n}$$
(8-4)
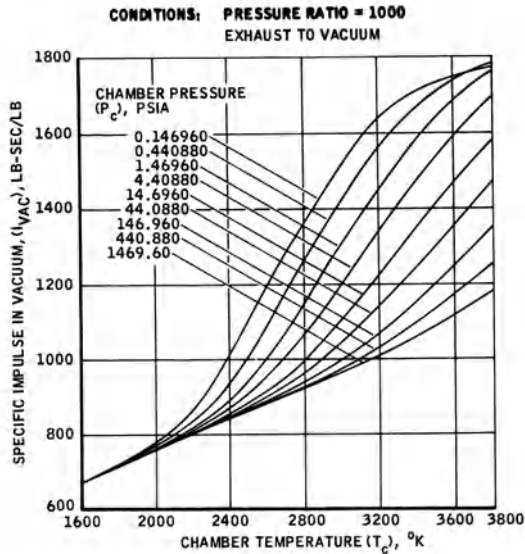
Fig. 8-2 Specific impulse of gaseous normal hydrogen.

These auxiliary flows can be eliminated and engine performance can be increased to its maximum possible value by the use of electromechanical acutators, which have not yet been developed for use in a radiation field of the intensity that occurs in these engines, and by the use of a topping-cycle turbopump.

[8-2] COMPONENT DESIGN

[8-2.1] Nuclear Rocket Reactors

[8-2.1.1] General Design Considerations

Nuclear reactors are assemblies containing sufficient fissionable material (uranium or plutonium) to produce a self-sustaining chain-fission reaction. The source of energy in such a system is the excess binding energy of the fissionable material compared with that of the fission products. The reaction is triggered by the absorption of a neutron by a fissionable atom. To be self-sustaining, an average of at least one of the neutrons released by a fissioning nucleus must be captured by another fissionable nucleus, producing a fission.

Figure 8-3 illustrates a generalized nuclear rocket reactor system. The central core contains a dispersal of fissionable uranium in a high-temperature matrix material. The assembly is
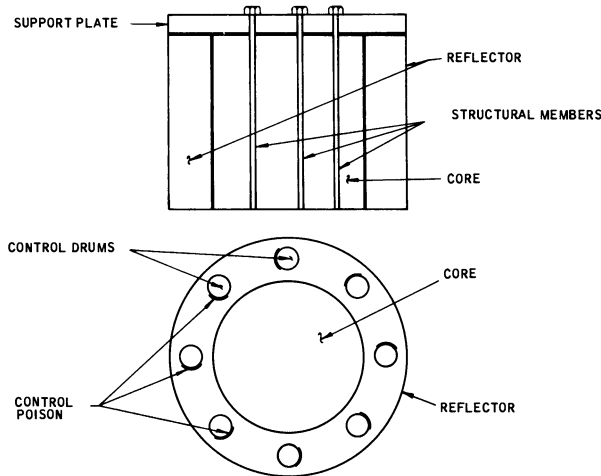
Fig. 8-3 Schematic of rocket reactor.

designed as a heat exchanger compatible with the desired power level. As the figure shows, the core-heat exchanger is supported by structural members attached to a support plate at the cold (coolant entry) end of the core. This assembly can also be supported by using high temperature or cooled compressive members at the hot end. The core is surrounded by a neutron reflector material that reduces neutron losses from the core region by "reflecting" neutrons back into the core. Neutron poison (absorbing) material is incorporated into rotating drum elements to control the number of neutrons returning to the core. As the poison material is withdrawn toward the outside of the reflector, the number of neutrons reflected back into the core increases, thereby increasing the reactor power. As the drums are turned in, the number of reflected neutrons diminishes, causing the power to decrease. Once the desired power level has been established, the drums are set to maintain a steady-state power operation.

Core materials must be capable of withstanding very high temperatures in the presence of hydrogen. Heat released by the fission reaction must be removed at the desired temperature while maintaining structural members within safe temperature limits. The mechanical design must be such that the unit will be structurally sound and the nuclear design must ensure that there is an adequate supply of fissionable material within the system to assure self-sustaining fission under the design operating conditions. Finally, control mechanisms must be provided to startup, regulate, and shut down the system on demand.

[8 - 2.1.2]   Reactor Core Materials

The first step is to select the core material. Since this material must perform at a temperature higher than that of the coolant (propellant), and since a very high temperature is desired, only a limited number of materials meet the design criteria. Prospective materials are graphite ($7050°$ R), tungsten ($6560°$ R), zirconium carbide ($6880°$ R), hafnium carbide ($7500°$ R), tantalum carbide ($7460°$ R), niobium carbide ($6790°$ R). References 1 through 4 provide data on these materials.

These melting points give a rough indication of the potential performance capability of the system. For example, typical reduction of $500°$ R must be allowed to provide the required strength. An approximate 10% margin must be allowed for variables during fabrication. The hot-spot factor of 10% may be reduced through the use of improved techniques and more stringent quality control.

There is a further modification of the maximum design temperature because of the thermal properties of uranium used in the assembly. Uranium dioxide is an attractive form of uranium, with a melting point of $5450°$ R, but it is incompatible with the carbides listed above. Tungsten–uranium oxide fuel, however, appears to be a promising material combination.

The carbide forms of uranium are promising due to their compatibility with the metal carbides indicated in the table. The melting points of UC and UC_2 are $5130°$ R and $4950°$ R, respectively. With a limitation on the carbon content of the carbide matrix, molten UC might be contained by the metal carbide at the carbide temperature limit. UC vapor pressure and the metal carbide porosity would establish the fuel element temperature limitation. These data, together with data pertaining to thermal conductivity and the mechanical properties of the carbides, are required to determine the maximum temperatures which might be realized in a nuclear rocket reactor.

At present, graphite is the preferred nuclear rocket core matrix material due to its current level of development. UC_2, which is limited to 2 to 3 volume percent in the graphite, can be fairly well contained for tens of minutes of operation, with an average exit temperature of $4500°$ R. Above $5400°$ R, material strength decreases rapidly and this temperature level establishes practical limitations to the use of graphite fuel structures.

The neutron poisoning effect must also be considered. The neutron-absorption cross sections of hafnium and tantalum are a serious disadvantage to these two carbides in rocket reactors. Niobium also has a fairly high cross section, which limits the utility of niobium carbide.

Chemical compatibility of the reactor core with the hydrogen coolant is another criterion of material selection. Hydrogen and graphite react rapidly to form methane and other hydrocarbon

gases at the temperatures of interest. Tungsten and hydrogen are compatible, but the UO_2 must be isolated from the hydrogen. The metal carbides also have good resistance to high-temperature hydrogen and provide a potential protective cladding for graphite.

[8-2.1.3] Thermal Design

The primary purpose of the nuclear rocket reactor is to generate thermal energy for heating the propellant. The preceding materials section indicated that the maximum allowable material temperatures range from 4800° R to 6300° R. The thermal design problem is one of maximizing the hydrogen exit temperature, while minimizing the core weight and volume, and providing adequate coolant for structural members. These structural members may be made of high-temperature metal alloys, so that cooling to less than 2100° R, and perhaps even below 1100° R, will be required. To provide a maximum gas temperature, distances from any point in the fuel matrix to the nearest coolant channel must be kept small, and local heat fluxes must be kept low. This requires a finely-divided core structure which may be achieved with closely spaced holes in a solid structure, a pebble bed, thin ribbed plates, or with similar techniques. A typical core segment is shown in Fig. 8-4. Minimum coolant-channel diameters and spacing will be determined principally by fabrication requirements and the structural integrity of the matrix. The thermal design can be accomplished by the use of conventional heat transfer theory. References 5, 6 and 7 present three of the basic theoretical sources; the essentials of the applicable theory have been compiled and are presented in Reference 8.

With a tentative thermal design established, nuclear and mechanical aspects of the design will be evaluated in accordance with the following sections. Resultant modifications will then be made in the thermal design model, and the process will be repeated until a satisfactorily balanced design is achieved.

[8-2.1.4] Mechanical Design

A major problem in the mechanical design of a high-temperature nuclear rocket reactor is that of supporting the reactor core so that it will withstand shock, vibration, acceleration, and fluid-flow loadings that occur during ground handling, the booster phase of flight, and in-flight reactor operation. To complicate this problem, the core most probably will be subdivided to prevent generation of excessive thermal stresses due to nonuniform temperatures. Flutter-type vibrations resulting from coolant flow phenomena must be prevented because of the brittle nature of the fuel element
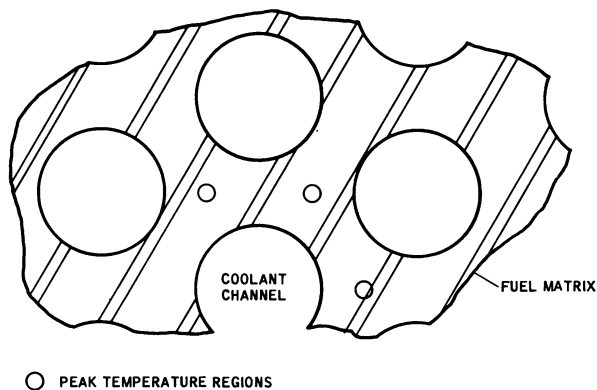
Fig. 8-4 Typical core segment.

material. The preceding condition existed in the early Kiwi-B reactors, resulting in the destruction of their cores. To prevent vibration, lateral support can be provided with a resilient refractory material packed between the core and the reflector, or with spring or coolant-pressure loading.

In addition, heating (due to the reactor radiation field) of all components in and around the core results in a requirement for coolant passages, which further complicates the design.

Material selection is restricted to metals, carbides, and ceramics that will not be damaged excessively by neutron and gamma radiation. In addition, some metals that have good thermal and strength properties cannot be used because of their neutron-capture characteristics.

Figure 8-5 shows a potential axial support concept. Metal support tubes are threaded into one or more of the coolant channels in each fuel element. These tubes can then be attached to a support plate spanning the cold end of the unit to assemble the core. The problem of providing a reliable joint between the metal tube and the refractory fuel material is of significant concern, since the fine structure of the fuel element limits the amount of material through which the loads must be transmitted. In utilizing tensile support concepts such as this, extreme care must be taken to reduce the probability of element breakage and the resultant ejection by pressure forces. Interlocking techniques should be used so that the material will not be ejected if breakage occurs.

The tie rods indicated in Fig. 8-3 are a possible solution to this problem. Cooled metal rods run from the support plate at the cold end to a refractory plate at the hot end, so that the fuel material is locked in place. Complete base support can be provided as indicated in Fig. 8-6 which shows two types of base support: a refractory dome and a cooled-metal grid structure. If required, as
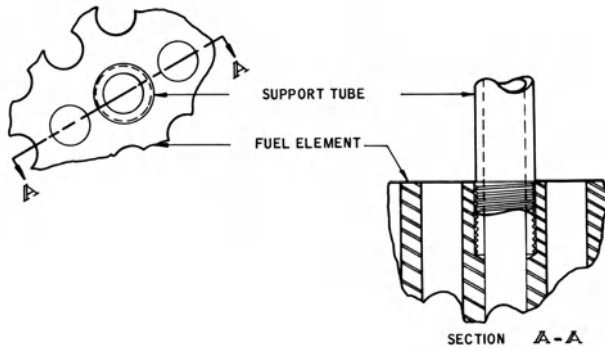
Fig. 8-5 Possible method for axial support of core.

in the case of the metal structure, coolant from the nozzle can be flowed through the base plate before entering the reflector. The complexity of the flow circuit, however, is a significant disadvantage.

[8-2.1.5] Nuclear Design

The nuclear design of a reactor involves the consideration of materials and their regional distribution in the reactor. Thermal and structural requirements impose constraints on the nuclear design that limit the weight and performance potential of nuclear powered rockets. Concomitantly, there are nuclear constraints that limit the thermal performance of the reactor system.

For analysis of a nuclear reactor system, the Boltzman transport equation serves as a rigorous representation of the neutron population in time, t, space, $\vec{r} = (x,y,z)$, and velocity, $\vec{v}(v, \vec{\Omega})$ where v is speed in the direction $\vec{\Omega}(\mu, \phi)$. Consider an incremental volume element of $d\vec{r} = dxdydz$ about the point $\vec{r} = (x,y,z)$ within which the density of neutrons, with speed v in the direction $\vec{\Omega}(\mu, \phi)$, at time, t, is given by $N(\vec{r}, v\vec{\Omega}, t)$. The time rate of change of these neutrons is the sum of

1. Those born in the region

$$S(\vec{r}, v\vec{\Omega}, t)$$

2. Those which are slowed down to the velocity interval $dvd\vec{\Omega}$ about $v\vec{\Omega}$ from higher velocity groups

$$\int_{v'} \int_{\vec{\Omega}'} N(r, v'\vec{\Omega}', t)\, v'f(v'\vec{\Omega} \to v\vec{\Omega})\, dv'd\Omega'$$
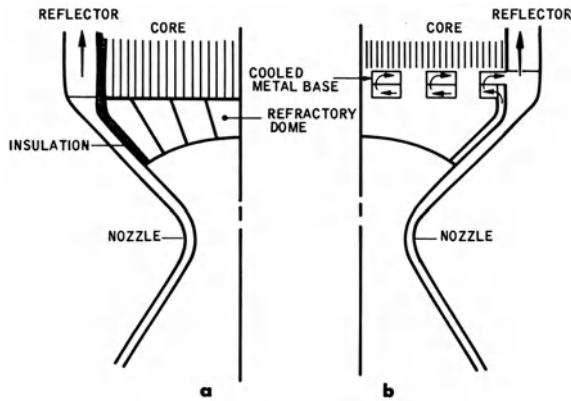
Fig. 8-6 Two base support concepts for reactor core.

3. Those within the velocity increment $d\,v\,d\,\vec{\Omega}$ about $v\vec{\Omega}$ which leave the volume element

$$- v\vec{\Omega}.\nabla N$$

and, finally,

4. Those within the volume and velocity increment which are lost by absorption or scattering out of $d\,r\,d\,v$

$$- Nv\,\Sigma_t\,(v\vec{\Omega})$$

Combining these terms with the appropriate sign for gain or loss, one has

$$\frac{\partial N}{\partial t} = S + \int_{v'}\int_{\vec{\Omega}} N(\vec{r},\,v'\vec{\Omega}',\,t)\,v'f(v'\vec{\Omega}\rightarrow v\vec{\Omega})\,dv'd\Omega'$$

$$= v\vec{\Omega}.\nabla N - Nv\,\Sigma_t\,(v\vec{\Omega}) \tag{8-5}$$

In general, each of the functions in this equation represents probabilities of occurrences, rather than firm identifiable quantities. As a consequence, the equation cannot be readily solved. For practical problems, the time dependence of the equation is eliminated, and any one of several techniques are used to obtain a solution. One method consists of tracing the paths of individual neutrons within the reactor, using random selection and weighted probability functions to determine direction of motion, energy level, and path length to first collision. The type of interaction

is then chosen randomly again, using a weighted probability function. If the interaction is a scattering one, the scattering angle and energy loss are again chosen by a weighted probability random technique. This continues until the neutron is absorbed or lost from the system. When enough neutrons have been examined, the degree of criticality of the system has been determined. This is known as the Monte Carlo technique and is the most precise method available. The calculation is quite lengthy even with high speed digital computers. For this reason, several approximations have been developed, the most important of which is the S_n approximation of Carlson [9].

One of the reactor components which has only been alluded to thus far is the control elements. These can be either nonfissioning neutron absorbers, referred to as poisons, or fuel materials arranged in suitable locations. An absorber that is moved toward a high-flux region or into a region between the core and reflector, will have an effect on reactor power generation which is similar to a fuel material being moved out of the same region. In current nuclear rockets, neutron poisons are being used. These poisons are located on a segment of the surface of a drum of moderator material located in the reflector. By rotating the drum, this segment can be moved from a position near the outer surface of the reflector into regions of higher flux, until it is between the reflector and the core. With the poison segment on the inside, the reactor is essentially shut down; that is, the number of neutrons produced is not sufficient to sustain a chain reaction. Conversely, with the poison segment at the outer surface, the number of neutrons produced in each successive generation is increased.

An excellent elementary discussion of nuclear theory is presented in Reference 10, with deeper fundamental discussion presented in Reference 11. Those interested only in the engineering aspects of nuclear reactors will find References 12 and 13 most fruitful and, for a detailed treatment of the nuclear analysis of reactors, References 14 and 15 should be studied. Numerous other excellent texts are also available.

[8-2.1.6] Shielding

Analyses of nuclear rocket vehicle systems indicate that the heating effects of the radiation field, although low, are significant. To prevent excessive heating, it appears that a radiation shield must be interposed between the reactor and the sensitive components. The effectiveness of such shielding is a function of the particular chemical elements of which it is composed and the number of atoms per unit area in the region through which the radiation must pass. Design studies indicate that a combination of lithium hydride and stainless steel have good shielding characteristics.

To minimize weight, the shield must be situated so that, for a given size, it will intercept the largest possible solid angle as seen from the reactor. This means that it should be placed inside the reactor pressure vessel, close to the upper face of the reactor. In this position, the main propellant stream can be used to extract the heat produced by attenuation of the radiation field, without significant complication of the flow path.

[8-2.2] Nuclear Rocket Nozzles

[8-2.2.1] General Design Considerations

Nozzles for nuclear rocket engines must be capable of withstanding essentially all of the environmental conditions to which chemical rocket nozzles are subjected. In addition, the nozzle operates in an intense radiation environment, which generates heat within the nozzle material and can also produce nuclear, chemical, and physical changes in the material. Ablative-type nozzles are not suitable for use due to the internal-heat generation caused by absorption of energy from the radiation field. With all-metal nozzles, only the heating effects are significant. Possible exceptions to this are in the use of alloys containing boron. Significant embrittlement occurs in these alloys at very high dose levels ($\sim 10^{19} \, nvt$).

A major difference between nuclear and chemical rocket nozzles is attributable to the physical size of the reactor core. The chamber-to-throat contraction area-ratio of liquid chemical rockets is usually in the range of 1.5 to 3.0. With nuclear rockets, this ratio may be in the range of 15 to 25. The wire-wrapped tube-bundle-type of construction used for liquid chemical rocket nozzles would fail in tension in a nuclear application; therefore, it is necessary to provide additional strength for this component.

The current design being used in the NERVA program is to attach U-shaped channels to the inner surface of the pressure shell, forming coolant tubes as shown in Fig. 8-7. This technique has proved to be very successful. The heat transfer design of these nozzles to ensure that the tube walls do not become excessively hot is critical.

Other nozzle configurations can also be used. For instance, heavy thermal barriers, capable of withstanding the local environment, can be installed on the inner surface of the pressure shell. By providing some coolant to the outer surface, the shell can be maintained at a suitable temperature with minimum heat extraction from the hot propellant stream.
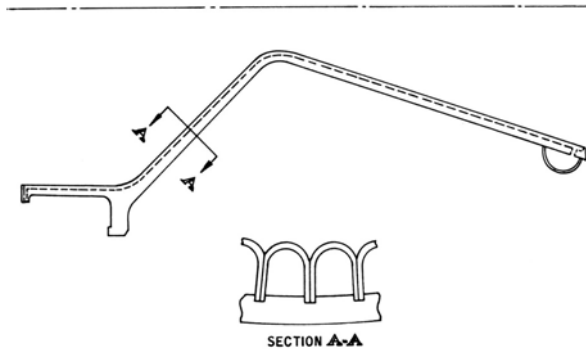
Fig. 8 - 7 *U*-Type nuclear rocket nozzle.

[8 - 2.2.2] Heat-Transfer Analysis

[8 - 2.2.2.1] Over-all Problem

The wall of a nuclear rocket nozzle is heated by thermal convection from the hot gas, thermal radiation from the reactor face, and by attenuation of the neutron and gamma ray fields generated by the reactor. The nozzle wall is cooled by the cold propellant prior to its entry into the reactor. There is also limited cooling due to thermal radiation or by convection to any local atmosphere.

Three sources of uncertainty exist in the heat transfer analyses of these nozzles. The first of these, significant only in thick metal sections, is the rate of heat generation caused by the nuclear radiation (analyses alone can give this value with an accuracy only within a factor or two, so that a suitable margin must be provided in the design); the remaining two uncertainties are related to the convective heat-transfer coefficients across the two fluid-to-metal boundaries.

[8 - 2.2.2.2] Hot-Gas Boundary

The general consensus of opinion is that for design purposes, the convective heat transfer coefficient of the hot gases can be adequately correlated by the Nusselt equation:

$$Nu = \frac{hD}{k} = K\,Re^x\,Pr^y. \qquad (8\text{--}6)$$

For turbulent flow, $x = 0.8$ and $y =$ either $1/3$ or 0.4.

Numerous correlations relating the hot-gas-side convective heat transfer coefficients have been formulated that explain and predict approximately the same total heat transfer for a given nozzle design. They differ in the values predicted for peak heat loads, and consequently, for peak metal-wall temperatures. These differences stem in part from the choice of the temperature at which the fluid transport properties are evaluated. Different correlations use the fluid bulk-stream temperature, the adiabatic-fluid temperature, the wall temperature, or some intermediate value of temperature. References 5 and 16 through 23 cover these correlations in greater detail. Of these correlations, the Bartz simplified equation [19], which is based on his boundary-layer solution [24], is perhaps the one most often employed in nozzle design.

The equation can be stated as:*

$$h = .026 \frac{C_{p_f} G^{0.8}}{Pr_f^{2/3}} \left(\frac{\mu_f}{D}\right)^{0.2} \left(\frac{T_\infty}{T_f}\right)^{0.8} \tag{8-7}$$

The transport properties were to be evaluated at a temperature defined as the average between the free-stream temperature and the wall temperature. Later work at the Jet Propulsion Laboratory [25] suggested, but did not clearly substantiate, that the use of Eckert's reference temperature would provide better data fit. Two areas were questionable, namely:

1. The data were obtained at low area ratios in the expansion section. It appears that only for higher Mach numbers of the free stream, and, therefore, for high area ratios in the expansion section does the numerical difference in the $(T_\infty/T_f)^{0.8}$ parameter become significant.

2. The data reported were for conical nozzles. Analysis and experimentation at NASA by H. Neuman and A. Fortini demonstrated that the mass flow term in any simplified equation should be related to the three-dimensional wall ρV value rather than to the isentropic one-dimensional ρV value. Again, this effect is more pronounced at the high Mach numbers.

In the NERVA engine program, a test program was conducted to obtain data on the hot-gas heat transfer rates to the NERVA nozzle contour. Reference 26 presents the results of this study in more detail. However, the conclusions are reviewed below.

If the entire body of test data is considered, the amended Colburn "*j*" equation for a flat plate

$$h = .0295 \frac{C_{p_f} G^{0.8}}{Pr_f^{2/3}} \left(\frac{\mu_f}{x}\right)^{0.2} \left(\frac{T_\infty}{T_f}\right)^{0.8} \tag{8-8}$$

*Current information indicates that the numerical coefficient in this equation is a function of the local area ratio of the nozzle.

provides a good correlation. The Bartz's simplified equation (amended to include the three-dimensional local mass-flow term instead of the one-dimensional local mass-flow term) is satisfactory for the exit section of the nozzle. For the convergent section, the "*j*" equation falls approximately in the middle of the data scatter, and the differences are apparently random, while Bartz's equation does not fit the data in this region. The high heat transfer coefficients in this region are believed to be the result of a leading edge effect that will probably be exaggerated by the core (which was not simulated during the majority of these tests). In the throat region, both equations yield results that are close enough to the test data to be adequate for computing maximum throat heat transfer conditions.

[8 - 2.2.2.3] Cold-Gas Boundary

Experimental measurements of heat transfer coefficients for liquid hydrogen have been reported, but these studies are limited in scope and usefulness. Data are particularly lacking for high heat fluxes at high pressures, high fluid velocities, and at the heating and flow conditions (curvature and partial heating) that occur in a nozzle tube bundle. Because of the need for more data, such studies have been significantly increased. Some of these programs are covered in References 27 through 41.

These investigations concern forced-convection heat transfer to liquid and gaseous hydrogen and to other fluids at pressures up to approximately 1350 lb/in.^{2} In most instances the studies have been made using straight, electrically heated tubes. Some curved tubes have also been used, as have heat-exchanger systems with gaseous helium as the heat source. Symmetrically and asymmetrically heated tubes have been used, with the latter providing better simulation of actual nozzle conditions.

To derive a mathematical expression for use in calculating nozzle heat transfer rates, most investigators have relied on Eq. (8-6) with various correction factors, to represent the data. Furthermore, 0.8 and 0.4, respectively, have been generally used for the values of x and y, based on the studies of Dittus and Boelter. One equation is

$$h_c = 0.028 \frac{k_b}{d} R_e^{0.8} Pr^{0.4} \left(\frac{T_w}{T_b}\right)^{-0.64} \tag{8-9}$$

The validity of this equation can be determined by examination of Fig. 8-8. In this figure the ratio of the experimentally determined heat transfer coefficient to the one calculated by Eq. (8-9) is plotted against coolant bulk temperature. The wide data scatter
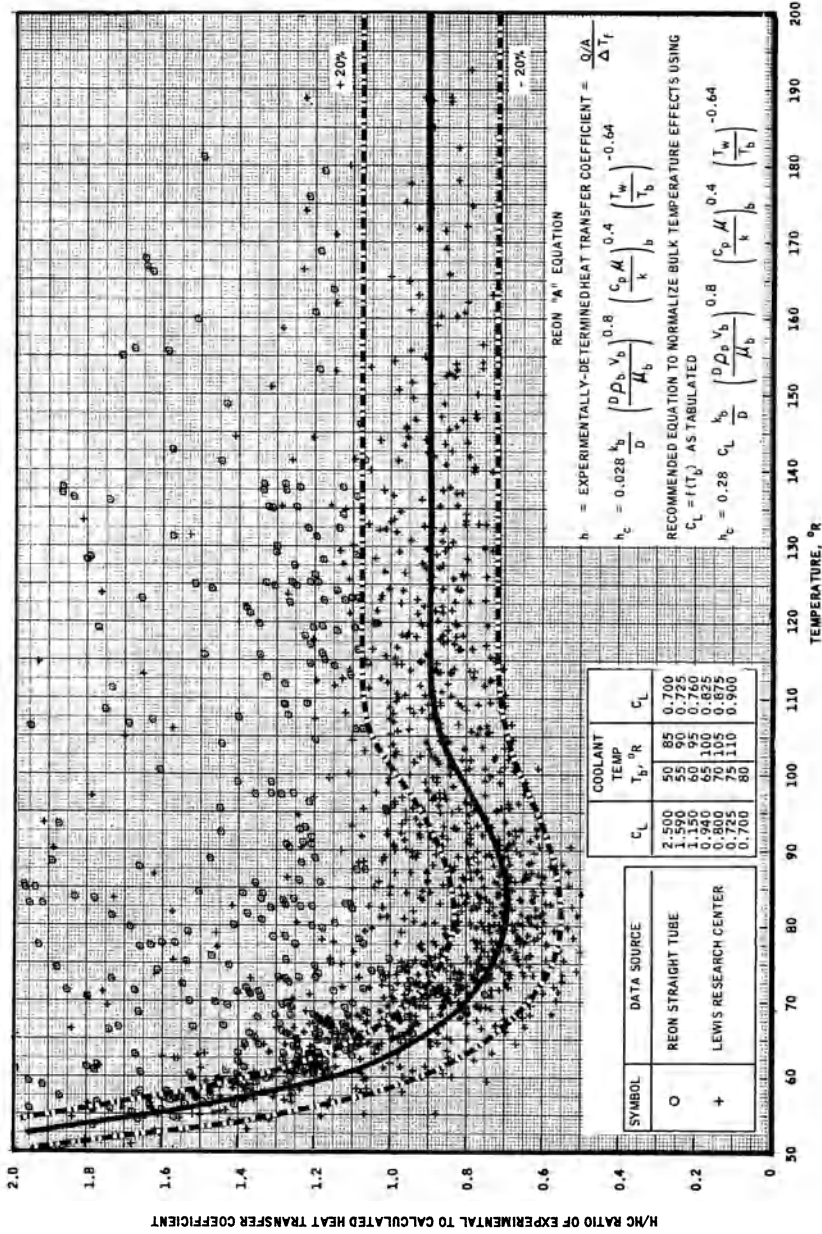
Fig. 8-8 Correlation of experimental heat transfer data.

and the deviation of the mean from unity indicated in this figure
are typical of hydrogen heat transfer data correlations and are
indicative of the difficulties encountered in attempting to predict
nozzle wall temperature.

[8-2.3] Propellant Feed Systems

[8-2.3.1] General Design Considerations

The propellant feed system consists of one or more turbopumps,
a propellant source, and a system of pipes and valves, including
control valves. These components differ from similar components
found in liquid chemical rockets only in the modifications required
to allow them to survive and function properly in the reactor radia-
tion environment. Of typical and primary concern in this respect
are valve seats, seals, bearing lubricants, and rolling contact
bearing retainers. In cryogenic chemical rockets, these are usually
made of organic materials that are subject to severe damage under
neutron and gamma bombardment. Also, valve actuators in most
chemical rocket systems are of the hydraulic type and the fluids
involved would change in a nuclear rocket either becoming highly
viscous or evolving gases under the action of high-energy radiation.
Consequently, pneumatically- or electrically-operated devices must
be used in the nuclear rocket engines. Radiation heating, though it
must be considered in the design, does not pose a significant prob-
lem in most of the components of this system due to the high flow
rates of cryogenic hydrogen in contact with the components.

The principal subassembly of the propellant feed system is the
turbopump and the primary factors influencing the design of this
unit are reliability, efficiency, and weight. Pump efficiency is
affected not only by the particular design selected, but also by
the net positive suction pressure (NPSP); *i.e.*, the difference
(available at the pump inlet) between the total absolute pressure
and the fluid vapor pressure. This effect is particularly apparent
if the NPSP is low.

The basic propellant feed system requires two valves: a pro-
pellant shut-off valve and a turbine power-control valve. Additional
valves may be required in the tank pressurization system and in
auxiliary coolant circuits in various parts of the engine.

[8-2.3.2] Turbopump Power Cycle

The turbopump system can utilize either a topping or bleed
cycle. These are shown schematically in Fig. 8-9.
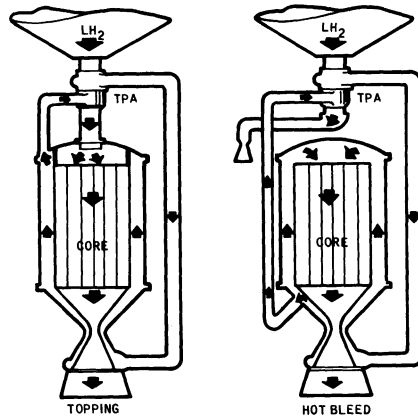
Fig. 8-9 Power cycles for nuclear rocket turbopumps.

In a topping cycle, the majority of the propellant flow is raised to some suitable temperature and then passed through the turbine, where it gives up a part of the added energy. The turbines involved here are low-temperature, one or two stage devices. A fraction of the flow can be bypassed to provide a control reserve. After leaving the turbine, the propellant continues through the system to the reactor core and out the nozzle. While this system offers minimum complexity and maximum reliability, the quantity of energy required to raise the hydrogen to a suitable temperature is quite large and the reactor system itself must be made more complex. This complication was the primary factor in rejecting this cycle for use in the NERVA engine program.

The bleed-cycle system, which was selected for NERVA, derives its name from the fact that a small flow of high-temperature gas is bled from the reactor exit plenum. After leaving the turbine (which, for performance reasons, is a multi-stage, high-temperature device) the bleed flow is discharged from the system through a thrust-producing nozzle. A performance penalty is incurred with this system because the fluid is discharged at a lower temperature than that of the main stream.

[8-2.3.3] Turbopump

[8-2.3.3.1] Pumps

The purpose of the pump is to increase the pressure of the liquid hydrogen propellant from its pressure level in the supply tank to the pressure required by the engine system. The required

energy can be imparted to the fluid in a single rotor blade row, as in a centrifugal pump, or by a series of rotor blade/stator blade rows, as in a multiple-stage, axial flow pump.

As indicated, two general classes of pumps are available for use in a nuclear rocket engine: (1) multiple-stage axial flow; and (2) single- or multiple-stage centrifugal flow. There is also an almost continuous variation between axial and centrifugal flow machines, referred to as mixed-flow pumps. In general, any of these types can be designed for use in a nuclear rocket system.

One of the most important factors in designing a rocket pump, particularly for a hydrogen system, is the magnitude of the net positive suction pressure, NPSP. In most pumping systems, the available NPSP limits the driving pressure that accelerates the fluid from its static condition in the tank to the pump inlet speed. With most pumping systems, operation at low values of NPSP results in cavitation—the formation of vapor bubbles adjacent to the vanes at the pump inlet—where the local static pressure reaches the fluid vapor pressure. This causes large local changes in fluid specific volume, which in turn reduces the mass flow rates that the pump can handle. With most fluids, cavitation can cause severe pitting of the impeller vanes. In hydrogen pumps, however, little or no cavitation damage has been detected, and continued operation under these conditions is feasible. Discussions of the design of pumps operating under cavitating conditions are presented in References 42, 43 and 44.

To minimize cavitation and its flow-limiting effects, special inducer sections can be added to the inlet section of the impeller. The function of this inducer is to increase the static pressure of the fluid before it enters the high-work sections of the pump. The angle of attack of the blades on the inlet fluid, the diameter of the section, and the configuration of the flow passages throughout the pump determine its suction characteristics. With liquid in the impeller passages, the vane system internally diffuses the relative flow and thereby causes a static pressure increase in the fluid. With proper design, it appears probable that zero NPSP can be handled satisfactorily.

Although the suction characteristics of centrifugal pumps are, in general, superior to those of axial flow pumps, the addition of an inducer section upstream of the forward bearing mount (overhung position), results in identical suction characteristics with both types. Subsequent stages of the axial pump will, of course, have to be modified if an inducer is added to an existing design.

The axial-flow pump is expected to be more efficient than the corresponding centrifugal pump. The margin should be greater for design applications requiring very high discharge pressure, and will be reduced under more difficult suction operating conditions. Efficiency has not been the paramount factor in rocket engine pump design to date. Suction performance, low weight, and

high reliability have been the most important design requirements. For instance, in a topping-cycle nuclear rocket engine, the pump efficiency has only a negligible effect on overall vehicle performance. However, for the bleed-cycle engine, the turbine bleed-flow increases with a decrease in pump efficiency and has an adverse effect on engine performance. To avoid high flow frictional losses in the flow system downstream of the pump, the stream should be diffused to a reasonable velocity, but most of the pump-flow losses occur in the diffusion process, so that the complete system should be considered when designing the pump. The effect of flow rate on the peak efficiency for several pump configurations is shown in Fig. 8-10, which also illustrates the effect of specific speed. The pump configurations most suitable for any given specific speed range per stage are also shown in this figure. Reduction in the number of stages of axial-flow pumps has been attempted by increasing the head rise per stage to reduce the flow losses caused by the ducting between stages. The result has been that specific speeds approaching those of the optimum mixed-flow pump have been achieved, but the efficiencies were not as high, undoubtedly because of the increased turning losses.

The energy input to the hydrogen by a single-stage impeller is limited by the structural capability of the rotor. This capability is improved by using high-strength-to-weight rotor materials and by special configurations, such as tapering the thickness of blades and supporting disks. Aluminum single-stage centrifugal-pump impellers have demonstrated hydrogen pressure rises of approximately 1400 psi, and titanium impellers have demonstrated rises in excess of 2100 psi per stage. Approximately four axial-flow stages are generally required to produce the pressure developed by a single centrifugal stage.
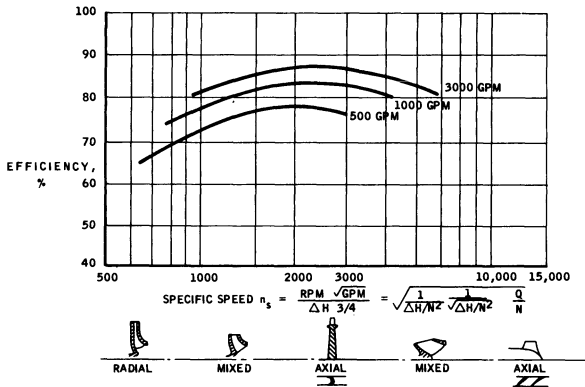
Fig. 8-10 Efficiency of several pump configurations.

The axial- and centrifugal-flow liquid-hydrogen pumps have significantly different head-capacity characteristics (Figs. 8-11 and 8-12).
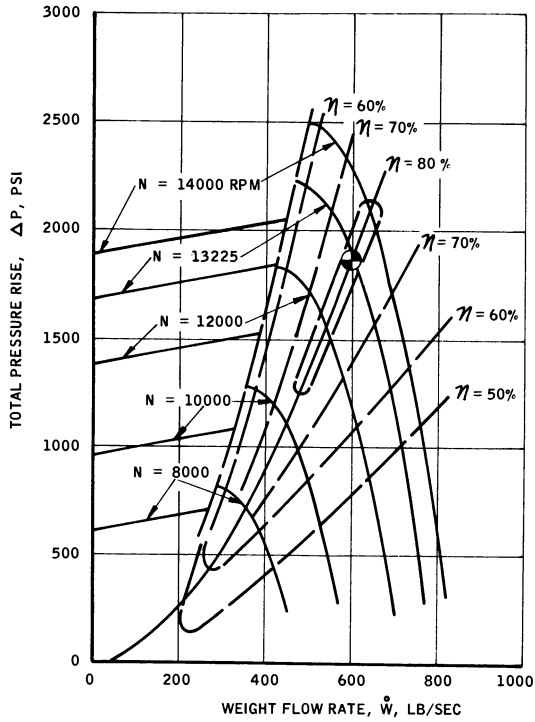
Fig. 8-11 Head-capacity characteristics of axial flow pump.
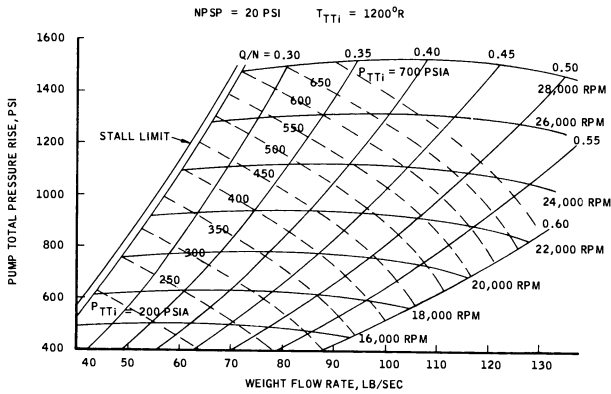
Fig. 8-12 Head-capacity characteristics of typical centrifugal pump.

To operate the axial-flow pump at near-maximum efficiency, the operating point must be close to the stall line; therefore, this pump must be carefully matched to the load characteristics. This is not the case with centrifugal-flow pumps which can have their operating point far removed from the stall region. When a nuclear rocket engine is performing at less than the design thrust level but at maximum core exit gas temperature, the pump operating point moves toward lower specific speed and toward the surge region. Since a wider margin is available, this potential operating condition could best be met with the centrifugal pump. As rocket engines increase in size, with corresponding increases in flow rates, more attention is being given to the possibility of parallel operation of turbopumps. Parallel operation of turbopumps will generally reduce overall engine weight and may reduce development cost. Conversely, increasing the number of turbopumps will reduce engine reliability, due to added valves, lines and control complexity, unless operation can be sustained with one or more of the turbopumps inoperative. The characteristic curve for the axial-flow pump is suitable for parallel pump operation. The relatively steep slope of the head-capacity characteristic tends to ensure stable operation and proper division of the flow between the pumps. However, in larger engines, where the use of multiple pumps may be considered, the operating specific speed of the centrifugal pump will be considerably greater than that of current units, and the centrifugal pump may be tailored for parallel operation.

Another important factor in pump selection involves the characteristics of the start transient. Unless the pump is prechilled, large thermal gradients will exist in the assembly when the propellant valve is first opened, and two-phase flow will occur in the system. This condition will result in some oscillation or pulsation in the flow and may cause engine-start problems. Prechilling, on the other hand, is undesirable in terms of engine design because of the requirement for valves and seals downstream of the pump, and the possibility of propellant loss during the chilldown procedure. Centrifugal flow pumps have demonstrated the ability to pump hydrogen without initial prechilling, which may not be possible with axial flow units. It should be noted that some flow fluctuation results from this type of operation, which appears to be acceptable in a nuclear rocket, but would not be in a chemical rocket system due to combustion problems.

The envelope for a turbopump assembly having an axial-flow pump is markedly different from that of an assembly with a single-stage centrifugal-flow pump. The axial-flow pump is a comparatively long and slender assembly and requires a bearing at each end of the pump rotor. Because the pump rotor assembly requires two bearings, a similar two-bearing arrangement has been used in the past for the turbine driver. These two shaft assemblies are generally connected by a flexible coupling. In comparison, the

single-stage centrifugal-flow pump is of short length and has a large diameter. Because the pump is short, the pump impeller may be overhung. Also the turbine may be overhung at the opposite end of the pump shaft, thereby eliminating two bearings, their mountings, and the flexible coupling. In some recent axial-flow turbopumps, the turbine has been overhung to significantly shorten the assembly, but the unit is still relatively long and heavy. Considering the above factors and the current state of hydrogen-pump technology, the centrifugal pump is more adaptable to nuclear rocket engine configurations.

With a gimbaled nuclear engine, the turbopump assembly should be mounted on the engine to avoid crossing the gimbal joint with lines containing high-pressure pump discharge and hot turbine working fluid. The extra length of an axial-flow machine would be undesirable in this configuration.

[8- 2.3.3.2] Turbines

The turbine design and the materials of construction depend primarily on the engine power cycle. If a topping cycle is used, the turbine will generally be a one- or two-stage unit designed to handle all or nearly all of the pumped fluid. The turbine inlet temperature generally ranges between 300 and 610°R, so light alloys can be used. For bleed-cycle engines, consideration of engine performance factors suggest the use of the highest practical temperature and the minimum flow rate, so the turbine will necessarily be a multistage machine made of dense, high-temperature alloys.

The turbine must be matched to the pump requirements in speed and power output. Minimum weights are usually obtained if direct-coupled, equal-speed systems are used.

[8- 2.3.3.3] Power Transmission

Whether a turbine operates at a speed equal to or different from that of the driven pump, a device must be provided to transfer power from the turbine to the pump. As indicated, this transfer can be most readily accomplished in a nuclear rocket system by using a short shaft to rigidly couple the rotors of the turbine and the pump. This shaft must be supported on a bearing system with a housing that can also unite the pump and turbine housings.

To prevent the rotating members from rubbing against their housings, the supporting bearings must provide both axial and radial positioning of the rotating member. In high-speed machinery, axial positioning is most readily achieved with ball bearings, whereas radial positioning is best achieved with roller bearings,

particularly when radial loads are substantial. This combination results in a minimum of sliding contact, while providing adequate bearing contact area and stiffness. To further reduce frictional losses in the assembly, symmetrical designs and thrust-balancing devices are used.

Heat developed by residual friction in the bearings and by the radiation field in the massive shaft and bearings must be removed to avoid overheating and subsequent failure of the bearings. In a nuclear engine, this heat is most readily removed by ducting a small amount of fluid from the pump discharge into the bearing housing and allowing it to flow through the bearings. To avoid shaft seals of a leak-tight variety the bearing coolant flow is discharged into the turbine cavity. This flow then exits through the turbine exhaust, which increases the engine total mass-flow but contributes little to the engine thrust. The flow must therefore be held to the lowest possible value to minimize performance degradation.

[8-2.3.3.4] Critical Speeds

In this discussion, a critical speed is defined as any rotational speed of the complete rotor assembly which coincides with one of the natural frequencies of the complete turbopump assembly, installed for operation. In determining these frequencies, bending modes of the turbine disc and their effect on shaft frequencies, as well as the effect of the bearings, housing and supporting structure must be considered and the assembly analyzed as a single spring-mass system. The significance of critical speed to the machine designer is similar to that of the natural vibratory frequency in any system. Despite modern developments in balancing machinery, some residual unbalance mass is always present in a rotor, impeller, or shaft of a turbopump. A slight unbalance of a rotating part will cause vibration to occur, which can increase in magnitude if a critical speed is involved. If displacement continues to increase until some component of the machine yields, the corresponding critical speed is said to be unstable.

The critical speed of a turbopump is a function of the masses of the rotating parts and the stiffness of the shaft, discs, bearings, housing, and supporting structure. The shaft cross section and length and the positions of the discs, impellers, and bearings all influence critical speed.

[8-2.3.4] Valves

Valves used in nuclear rocket engines and in chemical rockets have two significant differences, both involving the reactor radiation field. The more significant of the two differences is that seals

and lubricants, which in other applications are generally organic materials, must be designed for maximum insensitivity to radiation effects. The simplest approach to the redesign of these items for use in a radiation field is to use metal seals and dry-film lubricants. Otherwise, the design of these valves can generally follow the practice established for valves in high-temperature service.

Several dry-film lubricants are suitable in both vacuum and radiation environments. Noteworthy among these is molybdenum disulfide, which has excellent lubricity, good wear resistance, and is not significantly affected by radiation.

The other significant aspect of nuclear engine valve design involves radiation heating, which requires that thick sections be avoided. In chemical rocket systems, the weight of a component has always been a major criterion, so the need to avoid thick sections in nuclear components is not unique. Heat removal is not expected to be a serious problem unless the valve must be closed when the reactor is operating, in which case a separate coolant circuit may be required.

[8-2.4] Nuclear Rocket Engine Control

[8-2.4.1] General Design Considerations

The control system of a nuclear rocket engine is significantly more complex than that of a chemical rocket, primarily because the reactor power level is completely independent of engine thrust. Furthermore, because of minor differences in fuel distribution and reactor configuration resulting from the allowable manufacturing tolerances, the steady-state position of the reactor control drums will be slightly different for each reactor. For this reason, some method is required to detect the steady-state position and adjust the power level to the desired value.

A nuclear rocket engine control system consists of two separate control loops; one for the propellant feed system and one for reactor power. Since power is related to flow rate and temperature, these loops are coupled through the relationship between sonic nozzle flow rate and inlet pressure:

$$\dot{w} = \frac{P_c A_t g_0}{c^*} \qquad (8\text{-}10)$$

in which the characteristic velocity, c^*, is defined by Eq. (8-2). Further coupling between the loops is provided by the moderating effect of hydrogen in the reactor. Because of the epithermal nature of the reactor, changes in hydrogen density in the core have a significant effect on the reactivity of the system. In a typical situation,

the hydrogen flow rate might be increased by some change in the propellant feed system. The chamber pressure would then increase in accordance with Eq. (8-10). The increased hydrogen density will drive the reactor super-critical, and the power level will increase at a rate defined approximately by the equation

$$P(t) = P(0) e^{\frac{t\,\delta k}{1^*}} \qquad (8\text{-}11)$$

The result will be an increase in temperature and, therefore, thermal expansion. The consequent reduction in the density of hydrogen in the reactor will reduce the value of δk. The system will therefore seek a new steady-state condition at some higher power level unless the action is compensated for by use of the reactor control drums.

Equation (8-10) shows that the required control can be obtained by using any two of three variables: chamber temperature, chamber pressure, and flow rate. Further consideration suggests that the two most logical variables to select are chamber temperature and chamber pressure. There are several reasons for this. First, both can be measured directly with response rates and accuracies that are compatible with the control requirements. Second, excessive values of either parameter will lead directly to system failure. Third, these two parameters define engine thrust level and specific impulse, the two parameters of primary importance in evaluating engine performance.

A functional block diagram of a control system based on these reference parameters is shown in Fig. 8-13. This system is suitable for current engine design, but may require modification for more advanced engines. The system consists of the two interlocked control loops and an engine programmer. The engine programmer defines the desired values of the measured parameters at any point in time so the two loops can maintain these values. Also shown in Fig. 8-13 are several manual controls that might be used in ground testing or in a man-rated system if difficulties should develop in the automatic control system.

[8-2.4.2] Power Level Control

The power level of a nuclear reactor is proportional to the neutron flux within the core and thus, to the neutron flux in the vicinity of the reactor. The proportionality factor, however, is not completely independent of time (though very nearly so), nor is it exactly the same for two reactors of the same design. The difference is caused by slight variations in fuel loading and other manufacturing variables. For these reasons, neutron flux measure-
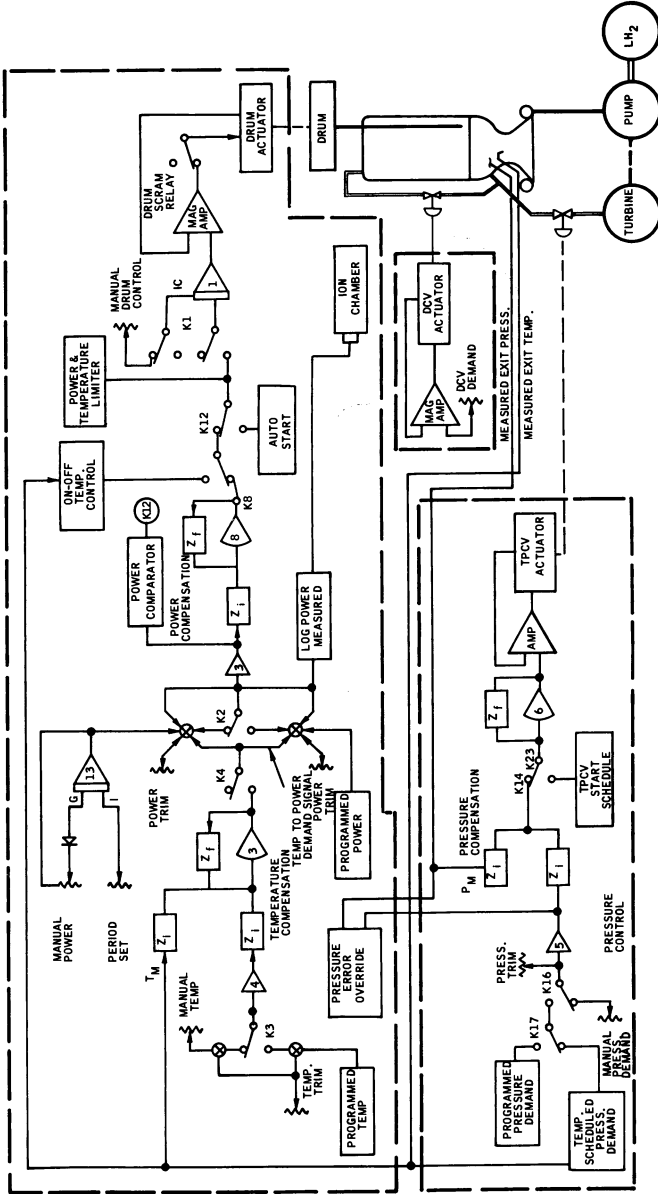
Fig. 8-13 Functional block diagram of engine control system.

ments can be used to determine whether or not power generation is constant or to determine the rate of change under transient conditions, but they are not too useful in determining absolute power for a nuclear rocket. Because ion chambers and other flux-measuring devices respond very rapidly to flux variations, either the steady-state condition or any desired rate of change of the reactor power can be maintained very precisely.

In the system presented here, the reactor is controlled by use of a preselected e-folding period while rising in power from source strength to some specified value of neutron flux, at which time power control is shifted to a closed-loop system utilizing chamber temperature as the reference. Propellant flow is initiated when the flux level indicates the reactor is in the range of 0.1 to 10% of full power, which is the level required to produce smooth temperature transients in the system without propellant waste.

A primary difficulty in the measurement of nuclear engine gas temperatures is the severe environment of the sensing device. Operational nuclear rockets will have exhaust temperatures of 4500 to 6300° R, and very few materials can operate in this temperature range. Tungsten and its alloys are suitable for use at the lower portion of this range but are probably too weak for use at temperatures near the upper limit. The carbide-carbon systems will fail at the higher temperatures, because of the carbon leg. The carbon would also have to be protected from the propellant at all temperatures of interest.

An alternative method of determining gas temperature would be to compute it on the basis of a measured value at some intermediate temperature point within the reactor, but the accuracy of this approach is questionable. A second method of computing temperature involves Eq. (8-9). By measuring pressure and weight flow, the c^* value and, in turn, the gas temperature can be determined. Although present hydrogen mass flow meters are less accurate than might be desired, the significant inaccuracies inherent in core measurements, combined with future improvements in flow meters, may well make measurement of pressure and weight flow rate the preferred method.

[8-2.4.3] Chamber-Pressure Control

The portion of the control system used to control chamber pressure consists of a pressure sensor, suitable signal-conditioning equipment, a reference signal, and the turbine power-control valve and actuator.

Several types of pressure sensors are available that are basically suitable for this application and appear to be readily adaptable for the task. If these sensors are mounted in a position to measure chamber pressure directly, some cooling may be required. In systems where the environment near the chamber becomes too severe,

pressure may be measured at some point upstream. Although this technique would reduce the precision with which chamber pressure and thrust are determined, it would assure that chamber pressure is no greater than the measured value. The system could be designed with safety margins adequate to prevent failure because of the uncertainties involved. Any measurement other than direct chamber pressure, however, would increase the uncertainty in determining temperature by the use of Eq. 8-9, if this were required.

[8- 2.5] Thrust-Vector-Control Systems

[8- 2.5. 1] General Design Considerations

A rocket system must have thrust vector control to maintain stable flight and to make any necessary changes in the direction of its velocity vector. For systems operating in the atmosphere, external distrubances can be quite large, and must be corrected rapidly; otherwise the vehicle will enter an erratic flight path or tumble. This atmospheric environment is the major reason for requiring fast response in thrust-vector control of the first and second stages of launch vehicles. For a third stage, which is normally started above the sensible atmosphere, the only significant external force is due to residual rotation imparted by the preceding stage or by other problems during the separation. The rotation will normally be extremely small, and, because of the large moment of inertia of the stage, the results of a bad separation will also be minor. For systems that operate only in space, the only other external forces will be extremely small gravity gradients. Thus, nuclear rockets, which in the near future will be operated only as third-stage or space-start systems, will require only very low response rates to maintain stable flight.

[8- 2.5.2] Types of Systems

Several methods of thrust vector control can be provided. These methods can be grouped into three classes: (1) auxiliary thrusters, (2) jet-deflection systems, and (3) gimbals or other engine-nozzle-deflection systems. In selecting a particular system, its effect on engine specific impulse and total vehicle weight must be considered as well as the degree of complexity that is introduced. For instance, heavy structural members should be avoided to reduce weight and minimize requirements for auxiliary coolant circuits to remove radiation-induced heat. Careful attention must also be given to the effects of convective heating and to performance degradation caused by systems that interfere with the supersonic exhaust stream.

[8- 2.5.2. 1] Auxiliary Thrusters

Small thrust units can be provided at strategic locations on the vehicle to supply the thrust needed for vector corrections. The type of unit can vary from a simple plenum and nozzle, supplied with gaseous hydrogen from the propellant tank or bleed fluid from the main engine, to a completely independent chemical rocket engine. These thrusters are ideally located a maximum distance from the vehicle center of mass, as shown in Fig. 8-14, so that fairly large corrections can be made with a minimum mass expenditure.

Such a system is complex, particularly where chemical rocket engines are involved. Hydrogen from the main tank can be used as the fuel, but a separate supply of oxidizer must be provided, together with a complete engine control system for each thruster (a minimum of three would be required).

These devices would also reduce system performance, because the attainable specific impulse would be in the range of 300 to 450 seconds, depending on the propellant combination and nozzle area ratios involved. The disadvantage of the low specific impulse is compounded by the fact that this thrust is not applied in the same direction as the main thrust vector. The magnitude of thrust required is defined by the equation:

$$F_{tv} = \frac{F_E \, \bar{x} \, \sin \delta}{r_{tv}} \tag{8-12}$$

These quantities are defined in Fig. 8-14. Assuming that $\bar{x}$ and r_{tv} are equal, the specific impulse of the complete vehicle may be determined in terms of the specific impulse of the main engine and the auxiliary thruster is

$$I_{spv} = I_{spe} \left[1 + \frac{I_{spe} \, \sin \delta}{I_{sp_{tv}}} \right] \tag{8-13}$$

Assuming that I_{sp_e} = 800 sec., I_{spTV} = 400 sec., δ = 1.0 deg., the net specific impulse of the vehicle is reduced to less than 773 seconds. In terms of complete vehicle performance, this reduction is a significant penalty.
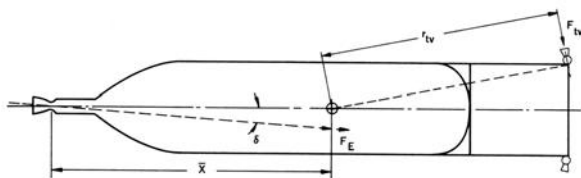
Fig. 8-14 Thrust vector control by auxiliary thruster.

[8 - 2.5.2.2] Jet-Deflection Systems

[8 - 2.5.2.2.1] Fluid-Injection Systems

Fluid-injection systems have been investigated extensively over the past five to ten years, principally for use with solid-propellant rocket motors. These systems consist of three or more jets passing through the nozzle wall and aimed radially inward or perhaps slightly upstream (see Fig. 8-15). Flow in these jets is varied by control valves to provide the desired deflection of the thrust vector. The interaction of these streams with the main jet provides a
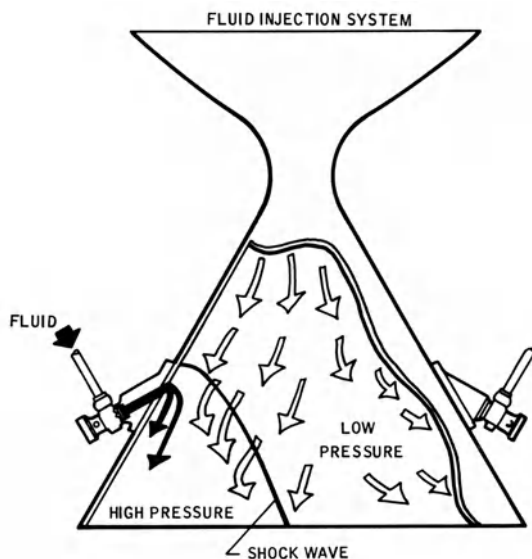
Fig. 8-15 Thrust vector control.

higher normal force than would be obtainable from the injectant flow alone if directed normal to the engine at this point and increases the axial thrust of the engine, but produces a reduction in engine specific impulse [45-49]. The current best estimates indicate that this loss can be determined approximately by the expression:

$$\sin \theta = 1.9 \frac{\Delta Isp}{Isp} \qquad (8-14)$$

This expression, where θ is the angular change in the thrust vector direction, applies for angles of less than 2.5 degrees. For larger

angles, the performance loss is apparently greater than indicated by this equation. This loss is less than that imposed by the auxiliary thrusters, but a continuous loss of even this magnitude would be significant for an interplanetary vehicle. This system can still be considered for short-duration attitude corrections, however.

[8- 2.5.2.2.2] Jetevators and Jet Vanes

Information in References 46 and 47 indicates that the performance losses of jetevators and jet vanes, shown schematically in Fig. 8-16, can be described by Eq. (8-14). Consequently, jetevators and jet vanes also should not be used for steady-state correction of thrust-vector misalignment.
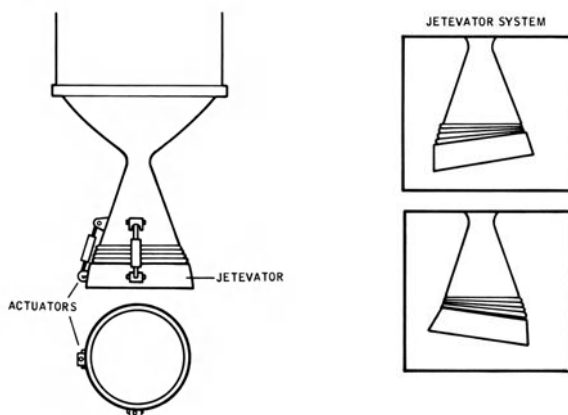
Fig. 8-16 Thrust vector control.

[8- 2.5.2.3] Gimbal Systems

The term "gimbal" is used herein to denote any thrust-vector-control device that does not perturb the supersonic flow in the main nozzle or require the use of auxiliary systems to stabilize the vehicle (see Fig. 8-17). The first two systems have a high power requirement if fast response is required, but this may not be necessary. The third system may have some difficulty because of the requirement for a moving seal against high-temperature, high-pressure hydrogen in an intense nuclear-radiation environment.

Performance of these systems is not adversely affected by compensation for steady-state errors in thrust vector alignment and have a significant advantage over competing systems, despite the expected higher installed weights. Even the weight penalty may be negligible, since Reference 50 indicates no weight difference
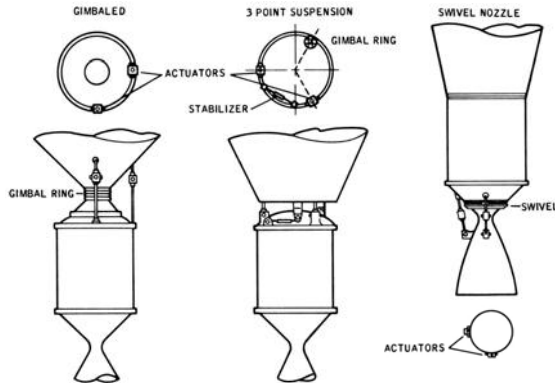
Fig. 8-17 Thrust vector control gimbal systems.

between fluid injection systems and gimbaled systems, with the former being more complex.

Some fairly detailed investigations have been made of single- and three-point suspension systems [51, 52], with a comparison made between the two. These investigations indicate that there is no compelling reason to eliminate one in favor of the other.

Limited studies have been made of swivel-nozzle techniques, but more detailed data are required before this approach can be realistically evaluated. The major problems associated with these systems involve an adequate hot gas seal, satisfactory component cooling, pressure balancing to hold actuator loads to acceptable values, and the design of actuators that will perform satisfactorily in the operational environment.

REFERENCES

1. C.R. Tipton, Jr.: Reactor Handbook, 2nd ed., Chap. 43, Vol. 1: Materials, New York, Interscience Publishers, Inc., 1960.
2. R.T. Dolloff and J.T. Meers: Status and Future of Graphite and Refractory Compounds, Research Laboratory, National Carbon Company, High Temperature Materials II, AIME Metallurgical Society Conference, Vol. 18, Interscience Publishers, Inc.
3. Batelle Memorial Institute, Refractory Ceramics for Aerospace, Columbus, Ohio, American Ceramic Society, Inc., 1964.
4. NERVA Materials Manual, Aerojet-General Corporation, 30 September 1966.
5. McAdam, W.H.: Heat Transmission, New York, McGraw-Hill Book Company, Inc.

6. Eckert, E.R.G.: Introduction of the Transfer of Heat and Mass, McGraw-Hill Book Company, Inc.

7. Jakob, M.: Heat Transfer, New York, John Wiley & Sons, Inc., Vol. 1.

8. Bussard, R.W. and R.D. Delauer: Nuclear Rocket Propulsion, Chap. 4, McGraw-Hill Publishing Company, 1958.

9. Carlson, B.G.: Solution of the Transport Equation by S_n Approximations, Los Alamos Scientific Laboratory, *Report LA-1891*, 1955.

10. Glasstone, S. and M.C. Edlund: The Elements of Nuclear Reactor Theory, Princeton, D. Van Nostrand Company, 1952.

11. Weinberg, A.M. and E.P. Wigner: The Physical Theory of Neutron Chain Reactors, Chicago, The University of Chicago Press, 1958.

12. Glasstone, S.: Principles of Nuclear Reactor Engineering, D. VanNostrand Company, Inc., 1955.

13. ———and A. Sesonske: Nuclear Reactor Engineering, D. Van Nostrand Company, Inc., 1963.

14. Meghreblian, R.V. and D.K. Holmes: Reactor Analysis, McGraw-Hill Book Company, Inc., 1960.

15. Davison, B.: Neutron Transport Theory, Oxford University Press, 1957.

16. Greenfield, S.: Determination of Rocket Motor Heat Transfer Coefficient by Transient Method, *J. Aero. Sciences*, August 1951.

17. Rose, R.K.: Experimental Determination of the Heat Flux Distribution in a Rocket Nozzle, Purdue University Rocket Laboratory, *Report No. F58-1*, January 1958.

18. Long, W.L.: The Determination of Coefficients of Heat Transfer to a Rocket Motor Nozzle by a Transient Method, Royal Aircraft Establishment, *Technical Note No. RPD 114*, 1954.

19. Bartz, D.R.: A Simple Equation for Rapid Estimation of Rocket Nozzle Convective Heat Transfer Coefficients, *Jet Propulsion*, January 1957.

20. Humble, L.V., W.H. Lowdermilk, and L.G. Desmon: Measurements of Average Heat Transfer and Friction Coefficients for Subsonic Flow of Air in Smooth Tubes at High Surface and Fluid Temperatures, *NACA Report 1020*, 1951.

21. Aialkos, J.A. and O.A. Saunders: Heat Transfer in Pipe Flow at High Speeds, Institution of Mechanical Engineers (London) Preprint, 1956.

22. Saunders, O.A. and P.H. Calder: Some Experiments on the Heat Transfer from a Gas Flowing Through a Convergent-Divergent Nozzle, Heat Transfer and Fluid Mechanics Institute Preprints, Stanford, June 1951.

23. Grover, S.S.: Analysis of Rocket Nozzle Heat Transfer Coefficients Correlations, Second Symposium on Materials and

Design for Rocket Insulation and Nozzles, Aerojet-General Corporation, March 16-17, 1960.

24. Bartz, D.R.: An Approximate Solution of Compressible Turbulent Boundary Layer Development and Convective Heat Transfer in Convergent-Divergent Nozzles, *Trans. ASME*, November 1955.

25. Welsh, W.E., Jr. and A.B. Witte: A Comparison of Analytical and Experimental Local Heat Fluxes in Liquid-Propellant Rocket Thrust Chambers ASME Aviation Conference (Los Angeles), Preprint, March 1961.

26. Kasahara, M., B. Mandell, and B.L. McFarland: Experimental heat Transfer Coefficients in a Contoured Nozzle, ARS/ANS/IAS Nuclear Propulsion Conference (Monterey), August 15-17, 1962.

27. Powell, W.B.: Heat Transfer to Fluids in the Region of the Critical Temperature, *JPL Progress Report No. 20-285*, 1 April 1956.

28. Mulford, R.N. and J.P. Nigon: Heat Exchange Between a Copper Surface and Liquid Hydrogen and Nitrogen, U.S. Atomic Energy Commission, Los Alamos Scientific Laboratory, *L.A. 146*, 21 May 1952.

29. Wright, C.C. and H.H. Walters: Single Tube Heat Transfer Tests Gaseous and Liquid Hydrogen, *WADC TR 59-423* (August 1959).

30. McCarthy, J.R. and H. Wolf: Forced Convection Heat Transfer to Gaseous Hydrogen at High Heat Flux and High Pressure in a Smooth Round, Electrically Heated Tube, *ARS Journal*, Vol. 30, April 1960.

31. Wolf, H. and J.R. McCarthy: Heat Transfer to Hydrogen and Helium with Wall to Fluid Temperature Ratios to 11.09, *Abs. 100*, presented at AIChE Meeting, (Washington), December 4-7, 1960.

32. Thompson, W.R. and E.L. Geery: Heat Transfer to Cryogenic Hydrogen at Supercritical Pressures, Vol. 7 of Advances in Cryogenic Engineering, 1962.

33. King, C.R.: Compilation of Thermodynamic Properties, Transport Properties and Theoretical Rocket Performance of Gaseous Hydrogen, *NASA TN D-275*, April 1960.

34. Properties and Performance of Hydrogen as a Rocket Fuel, Aerojet-General Corporation *Report No. CR 127-360*, March 1960.

35. Benser, W.A. and R.W. Graham: Hydrogen Convection Cooling of Rocket Nozzles, *Preprint 62-AV-22*, ASME, 1962.

36. Hendricks, R.C., R.W. Graham, Y.Y. Hsu, and R. Friedman: Experimental Heat Transfer and Pressure Drop of Liquid Hydrogen Flowing through a Heated Tube, *NASA TN D-765*, 1961.

37. ————,————,————, and A.A. Medeiros: Correlation of Hydrogen Heat Transfer in Boiling and Supercritical Pressure States, *ARS Journal*, 32:2, February 1962.
38. Zuber, Novak, Fried, and Erwin: Two-Phase Flow and Boiling Heat Transfer to Cryogenic Liquids, *ARS Journal*, 32:9, September 1962.
39. Martinelli, R.C., *et al.*: Isothermal Pressure Drop for Two-Phase Two-Component Flow in a Horizontal Pipe, *Trans. ASME*, 66:2, February 1944.
40. Timmerhaus, D.E. Drayer, and J.W. Dean: An Experimental Investigation of Overall Heat Transfer Coefficients for Condensing and Boiling Hydrogen Films, Paper presented at Int. Heat Transfer Conference (Boulder), August 28, 1961.
41. Core, T.C., J.F. Harkee, B. Misra, and K. Sato: Heat Transfer Studies, Aerojet-General Corporation, September 1959.
42. Ross, C.C. and G. Banerian: Some Aspects of High Suction Specific Speed Pump Inducers, *Transactions of the ASME*, November 1956.
43. Stahl, H.A. and A.J. Stepanoff: Thermodynamic Aspects of Cavitation in Centrifugal Pumps, *Ibid*.
44. Wislicenus, G.F.: Critical Considerations on Cavitation Limits of Centrifugal and Axial Flow Pumps, *Ibid*.
45. A Survey of Thrust Deflection Methods, Part I, *Technical Report 6602-5a*, Cleveland Pneumatic Industries, Inc., 4936 Fairmount Ave., Bethesda, Md., July 1960.
46. A Survey of Thrust Deflection Methods, Part II, Technical Report 6602-5b, Cleveland Pneumatic Industries, Inc., December 1960.
47. Hozaki, S., E. Mayer, and G.V.T. Rao: Thrust Vector Control by Secondary Injection into Rocket Exhaust, National Engineering Science Co., Pasadena, Calif., 1962.
48. Mockenhaupt, J.D.: Performance Characteristics and Analysis of Liquid-Injection Thrust-Vector Control, *TM-16-SRO*, 15 March 1965.
49. McCullough, F., Jr.: Thrust-Vector Control by Secondary Injection, Propulsion Development Dept., USNOTS, China Lake, Calif., January 1962.
50. Comparison of Gimbal and Gas Injection Systems for Thrust Vector Control of the NERVA Engine, Aerojet-General Corporation, *Report 2305*, July 1962.
51. Evaluation and Comparison of Attitude Control Systems for Spacecraft with NERVA Engines, Aerojet-General Corporation, *REON Report No. 2585*, June 1963.
52. RIFT/NERVA Installation-TVC/TVT Description and Weight Comparison, Aerojet-General Corporation—REON, and Lockheed Missiles and Space Company, *NSP, LMSC-A304195*, 16 August 1963.

Radioisotope Propulsion

John S. Martinez,
Manager, Propulsion Laboratory
TRW Systems

[9-1] ALTERNATIVE APPROACHES

The concept of employing radioisotope energy for space propulsion is not a new one. Several approaches for doing so have been considered during the past decades, but all except one have thus far been considered impractical. This paper briefly reviews some of these various approaches, indicates their advantages and disadvantages, and summarizes the mission capabilities and the current state of the technology of those approaches which currently appear most promising.

[9-1.1] Direct Recoil Method

Perhaps the most straightforward manner in which isotopes might be employed to impart momentum to a space vehicle is the *direct recoil* approach [1] (see Fig. 9-1) in which the radioisotope is positioned on an external surface of a spacecraft in such a manner that some of the radioactive decay particles are emitted directly to space and the remainder are absorbed in the spacecraft structure. Direct recoil propulsion produces extremely high specific impulses. For example, the I_{sp} of a 5 Mev α particle (typical of that produced by Po-210 or Pu-238) is about 1.6×10^6 seconds.

Unfortunately, the direct recoil method also generates very low thrust levels for a given quantity of source. For example, 1KWth of directed Po-210 α particles will generate about 3×10^{-5} lbs. thrust. Assuming that 10% of all of the momentum of the α particles emitted within the source is actually emitted in the desired direction (and the remainder absorbed in surrounding structure), we immediately see that a 1KW source will only be capable of generating a few micropounds of thrust. Furthermore, even at this very low thrust level, the energy absorbed in the surrounding structure is sufficient to cause considerable spacecraft thermal control problems. Most space propulsion applications other than, perhaps,
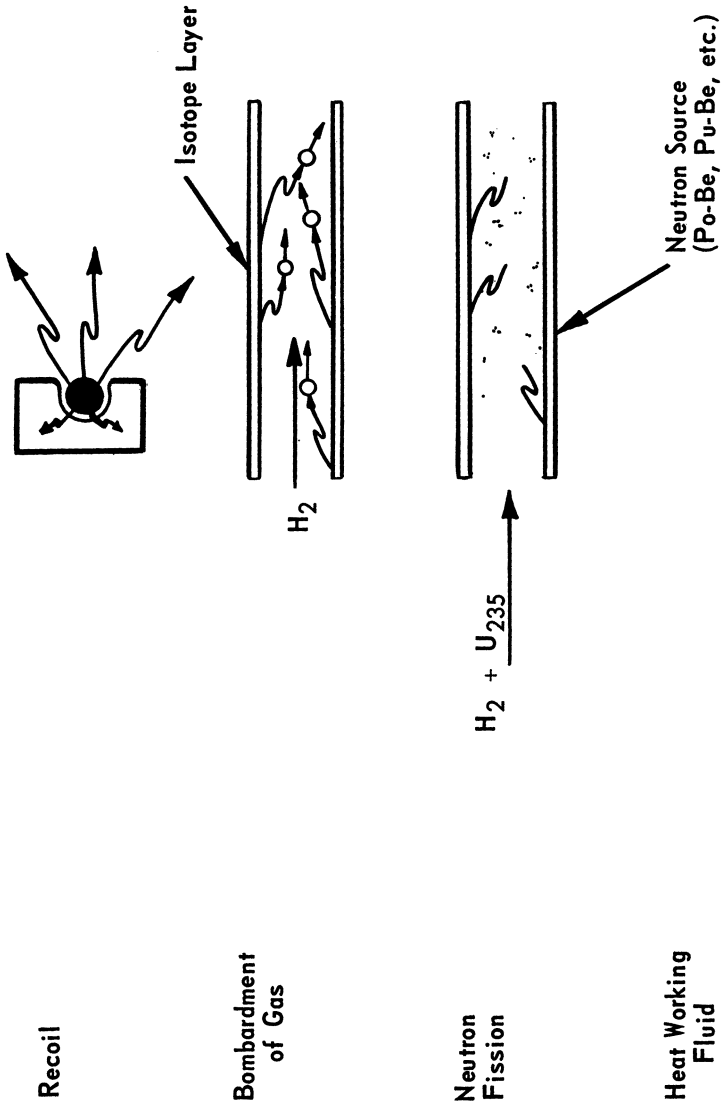
Fig. 9-1. Various isotope propulsion schemes.

gravity gradient satellite stabilization systems, involve thrust levels considerably in excess of that attainable from practical quantities of polonium. The few micropound applications envisioned can readily be performed by less sophisticated, less expensive means. Therefore, it can be concluded that practical limitations on source quantity (hence, thrust level) established by current and projected isotope cost and availability, as well as practical considerations associated with mechanization, eliminate direct recoil propulsion from further consideration for propulsion applications envisioned at this time.

[9-1.2] Thermal Heating Method

Several techniques have been proposed for using isotope energy to heat a propulsive working fluid, such as H_2 or NH_3, which is then expanded through a nozzle to produce directed momentum. Because of thermal limitations, the I_{sp}'s (which depend on the attainable stagnation temperature of the fluid) obtainable from the thermal heating methods are considerably lower than those of the direct recoil method. On the other hand, useful thrusts can be generated from practical quantities of isotope.

Three alternative thermal heating methods are depicted in Fig. 9-1. Two of these involve deposition of energy directly within the working fluid. In one case this is achieved by direct bombardment of the working fluid with particles (*i.e.*, α particle collision with H_2 atoms) emitted from isotope sources lining the passage through which the working fluid flows. In the next case, fissionable material is dissolved in the working fluid and bombarded by neutrons from sources (such as polonium-beryllium or plutonium-beryllium) lining the passage through which the working fluid flows. Fissioning occurs and the released particles collide with the molecules of the working fluid, thereby generating heat. The appeal of these two energy deposition techniques lies in the fact that heating takes place directly in the working fluid, thereby greatly increasing the potentially attainable working fluid temperatures (thus I_{sp}) relative to those attainable from conductively heated systems in which the heat is transferred from source to fluid by conduction through solid materials.

Thus far, unfortunately, no techniques have been found within the bounds of practical source or fissionable materials quantities, to generate sufficient heat within the working fluid to produce useful I_{sp}'s.

Insofar as the current state of the art is concerned, the only practical approach to isotope propulsion [2, 3] involves thermal heating of the working fluid by passing it over the surface of an isotope-containing capsule; hence, the remainder of the technical discussion will be devoted to this approach.

Before going farther, it should be noted that several other propulsion techniques involving isotopes have been proposed [4, 5, 6] in which isotopic energy can be used to improve the performance of other types of propulsion systems. In the NIMPHE [4] system, isotopic heat is used to improve the performance of hydrazine monopropellant engines; in RIP [5] isotopic heat is used to improve the efficiency of cesium contact ion engines, whereas, in Reference 6, a technique is described for employing isotopic energy in conjunction with electric propulsion technology to yield a radically new type of propulsion system. However, in accordance with current terminology, these latter approaches are not considered to fall within the realm of isotope propulsion; hence, they and other similar techniques will not be considered further.

[9-2] BASIC THRUSTER CONFIGURATIONS

During the past five years, isotope propulsion work has been seriously pursued in this country. More recently, two studies have been initiated in Europe [7]. One of these is a six-nation cooperative effort being conducted under the auspices of ELDO, and the other is part of a separate French national effort. Two basic thruster configurations have emerged from the work which has been performed to date. The first of these is typified by the Poodle thruster which was evolved by TRW Systems under USAEC sponsorship. This thruster generates approximately 1/4 lb. of thrust, and an I_{sp} in the 700- to 800-second range when hydrogen is used as the working fluid. Designed for steady-state operation, Poodle offers considerable promise as a high performance primary propulsion system for powering small upper stages on highly energetic, difficult space missions.

The first basic consideration in thruster design involves selection of the isotope. Some typical isotopes one has to choose from are shown in Table 9-1. Spacecraft integration and launch handling considerations tend to eliminate those isotopes having significant surrounding radiation fields; hence Co-60 and Sr-90 (as well as all other γ sources and most β-emitting sources) do not appear practical for most applications. The remaining three, Pm-147, Pu-238 and Po-210, do appear to have merit. Of these three, Po-210 is least expensive and the most readily producible in large quantities, but its short half-life eliminates it from consideration for long duration missions. In continuous thrusting applications involving H_2 working fluid, the thruster operating duration generally will not exceed 60 days. Therefore, Po-210 which is an α-emitter was selected for the Poodle thruster because of its satisfactory half-life, its relatively low cost, its potential availability in sufficient quantity to support near-term applications, and its low radiation field. The very high power density (140

Table 9-1   Characteristics of Radioisotope Heat Sources

Isotope	Half-life	Power Density Watt/GM	Gamma Dose r/hr. per Watt @ 1 Meter	Availability	Future Cost $/Watt
Pm 147	2.6 years	0.361	0.374×10^{-7}	Limited Production	91
Po 210	138 days	141.3	1.103×10^{-4}	Good	10
Sr 90	29.3 years	0.932	0.1826	Good	20
Pu 238	89 years	0.56	0.55×10^{-5}	Limited Production	890
Co 60	5.3 years	5.69	189.5	Good	30

watts/gm) as well as the existence of refractory Po compounds also contributed materially to the selection of Po-210 for use in Poodle. (However, we should not lose sight of the fact that changes in the future cost and availability of other isotopes could subsequently change this choice.)

A simplified, artist's conceptual view of the Poodle thruster is shown in Fig. 9-2. It is 17 inches long and 4 inches in diameter. With re-entry fins (not shown) it weighs 40 pounds. A total of 5 thermal kilowatts is generated by Po-210 distributed in three sealed capsules placed end-to-end within a cylindrical module. This power is transferred at high efficiency to about 1 lb/hr. of hydrogen flowing spirally through an annular passage surrounding the heat source module. The entire thruster is externally insulated to obtain high thermal efficiency.
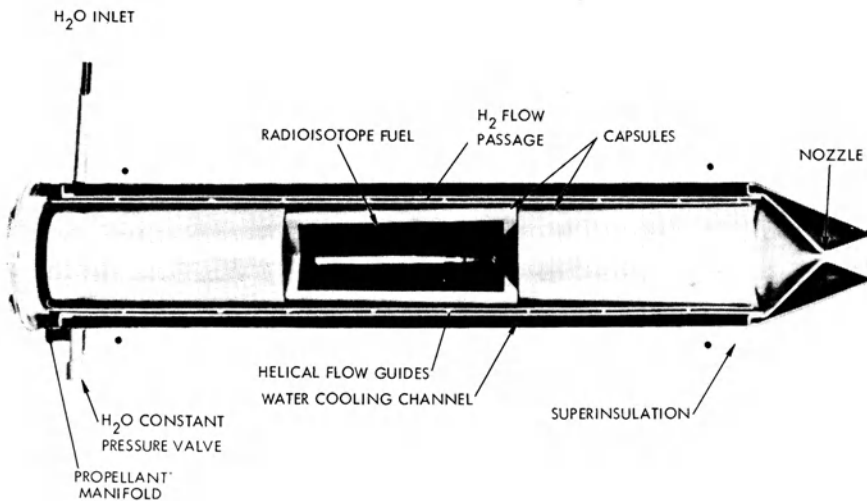
Fig. 9-2 Poodle thruster model.

The second basic type of thruster configuration which has emerged from the work performed to date is typified by the DART thruster being developed by TRW Systems under USAF Contract. This thruster, a prototype version of which has recently successfully completed testing, is designed for use in spacecraft auxiliary propulsion systems which operate intermittently over extended time durations (*e.g.*,1–5 years). Because of the operative duration, a long-lived isotope and a storable working fluid are required for this type of thruster. Therefore, NH_3 was selected as the propellant for DART and Pu-238 was selected as the isotope because of its long half-life, its reasonable availability in sufficient quantity to support near term applications, and the advanced state of its fuel form technology. A view of the DART thruster complete with insulation and re-entry aids is shown in Fig. 9-3. The DART thruster shown here is designed to insure complete containment of radioisotope material in the event of accidental launch abort or re-entry from orbit.

[9-3] PROPULSION SYSTEM AND UPPER STAGE

The design and operation of an isotope upper stage* is heavily influenced by the characteristics of the thruster. For example, the presence of both low-temperature liquid hydrogen propellant and high-temperature isotope capsules in close proximity to each other requires that ample consideration be given to thermal control; the low thrust, hence, long thrusting times may impose longer than normal operating lifetimes on certain system components; the peculiar nature of the low thrust trajectory affects the design of guidance, control and telemetry systems; the external radiation field of the thruster may require special launch pad ground equipment and influence interstage design and the location of experiment packages within the payload.

A view of a model of a 7300-lb. (including payload), 10-ft. diameter, liquid H_2-fueled isotope propelled stage which has been designed at TRW for use on a Titan II A-class booster is shown in Fig. 9-4. That stage contains four 5KW Poodle thrusters located immediately below and near the outer radius of the propellant tank. (By using four swiveled thrusters instead of one 20 KW thruster, it is possible to provide all pitch, yaw and roll control as well as primary thrust with the same thrusters.) This stage is capable of placing more than 2300 pounds of useful payload into 24-hour equatorial orbit, a considerable increase in the capability of the Titan II booster over that obtainable using state-of-the-art upper

---

*The term "isotope upper stage" is used here to mean an upper stage which contains an integral isotope propulsion system as its primary source of thrust (as opposed to a spacecraft which employs isotope thrusters for auxiliary propulsion purposes).
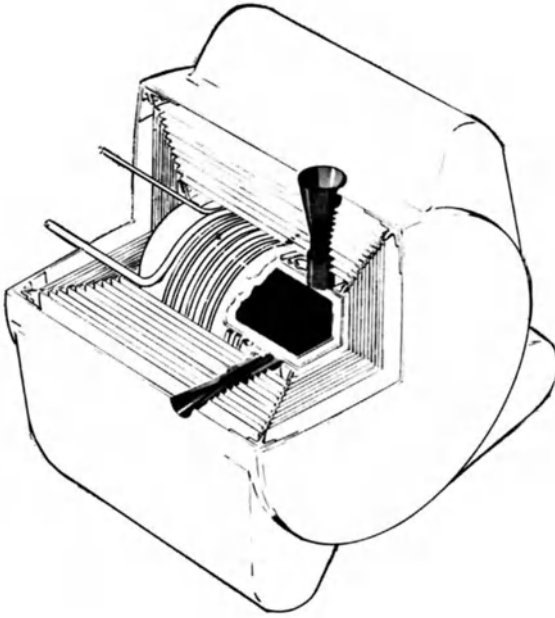
Fig. 9-3 DART thruster.
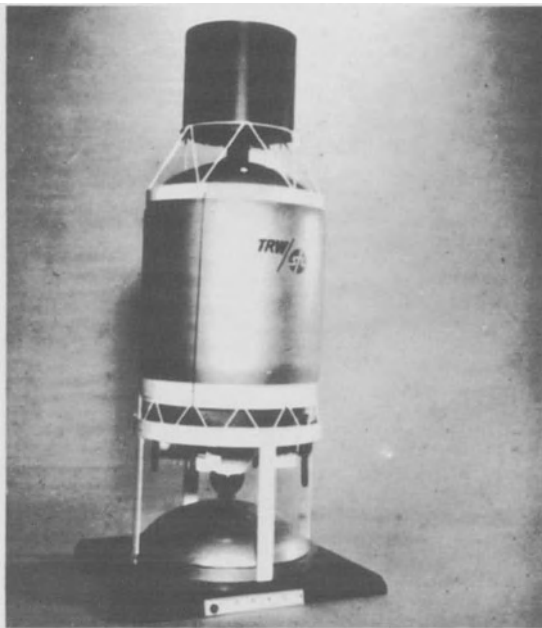
Fig. 9-4 Poodle thruster model.

stages. The Titan II booster would place the Poodle stage in a 300-mile apogee elliptical orbit which would then be circularized by a lightweight high thrust chemical rocket injection motor contained on board the stage. Once the 300-mile orbit is established, H_2 flow through the Poodle thrusters would commence and the stage would slowly spiral out to 24-hour orbit, gradually making the plane change as it goes. The orbit transfer would take a little more than 30 days to perform. To avoid large H_2 tank insulation weights and/or H_2 boiloff penalties, the Poodle stage is designed to feed gaseous H_2 into the thrusters at a rate approximately equal to the boiloff rate in the tank. Insulation weights are therefore minimized and tank weights can be reduced to those necessary to provide adequate structural and micrometeorite integrity.

This stage, which has a ratio of dry weight (not including payload) to fueled weight of 0.216, will carry to 24-hour orbit about 45% more payload than Centaur and about 15% more than an optimized F_2/H_2 stage using the same booster. F_2/H_2 propulsion systems have not yet been developed to the point where they can be incorporated into a flight stage, but their performance is characteristic of the best which could be obtained from a chemical system within the foreseeable future. In general, because of the large fixed weights associated with the engine or the power supply, nuclear rocket and nuclear-electric propulsion systems (capable of performing primary propulsive missions within a reasonable thrusting time) are too heavy for launch with intermediate class boosters such as Titan II.

This same Poodle stage when employed as a third stage on the Saturn I launch vehicle or as a fourth stage on Saturn V is capable of significantly out-performing other systems for many highly energetic deep space missions in which the isotope stage is injected after being boosted to velocities in excess of earth escape velocity.

[9-4] RELATIVE MISSION CAPABILITIES

[9-4.1] Primary Propulsion

Systematic mission studies have been conducted [8, 9] to identify where, if at all, isotope propulsion should fit into the propulsion system/space mission spectrum. These studies, the results of which are summarized in Fig. 9-5, have compared the performance of the following launch vehicle combinations:

Saturn IB/Centaur
Saturn IB/Centaur/HEKS (High Energy F_2/H_2 Kick Stage)
Saturn IB/Centaur/Poodle
Saturn IB/Small Nuclear Rocket
Saturn IB/Small Nuclear Rocket/HEKS
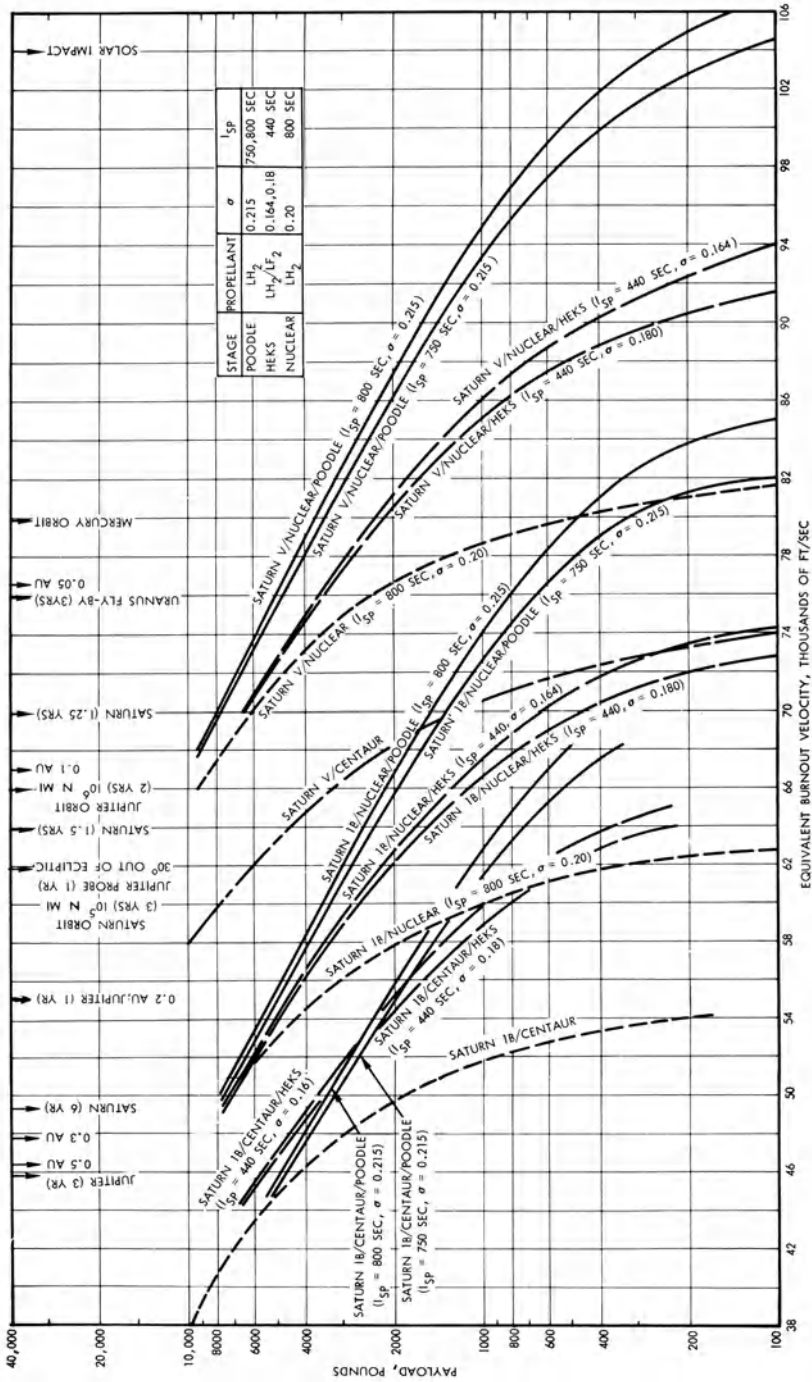
Fig. 9·5 Payload as a function of equivalent burnout velocity.

Saturn IB/Small Nuclear Rocket/Poodle
Saturn V/Centaur
Saturn V/Small Nuclear Rocket
Saturn V/Small Nuclear Rocket/HEKS
Saturn V/Small Nuclear Rocket/Poodle

In conducting the mission studies, the structure factor of the Poodle stage was set at 0.215 (a value obtained from stage design studies) and results were generated for I_{sp}'s of 750 seconds and 800 seconds. An I_{sp} of 800 seconds and a structure factor of 0.20 was used for the small nuclear rocket. The I_{sp} of the F_2/H_2 stage (HEKS) was assumed to be 440 seconds and payloads were calculated for structure factors of both 0.16 and 0.18.

In computing the data shown in Fig. 9-5, the net payload capability of each launch vehicle was determined using precise orbital mechanics calculations. Due to the greater gravity losses associated with the low thrust propulsive mode, the actual momentum imparted to the isotope stage to perform a given mission is greater than that of the impulsively thrusted stages. However, to provide simple, valid comparison between the low-thrust isotope system and the impulsive thrust systems, the payload capabilities of the isotope system for given missions are plotted opposite the impulsive ("equivalent") burnout velocity required to perform that mission.

It can be seen from Fig. 9-5 that, when used as a fourth stage on S1B/Centaur, the isotope stage outperforms the HEKS for all missions requiring impulsive burnout velocities in excess of 58,000 ft/sec. When used as a fourth stage on the S1B/nuclear rocket vehicle, the isotope stage outperforms the HEKS for all missions considered and even extends the capability of the S1B/ nuclear rocket launch vehicle to beyond that of the SV/nuclear rocket launch vehicle. The SV/nuclear/isotope launch vehicle combination is capable of performing virtually every mission within the solar system including possibly the highly energetic solar impact mission.

[9-4.2] Auxiliary Propulsion

As spacecraft become more sophisticated and missions more complex, we find the total auxiliary propulsion impulse required in the low thrust mode to perform the more complicated orientation, stabilization, vernier velocity and related requirements rapidly increasing. Cold gas systems which were acceptable for earlier spacecraft having modest total impulse requirements are found to be excessively heavy for many spacecraft now in development or in planning.

System design studies indicate that on-off radioisotope propulsion systems of the DART type offer the lightest weight low-thrust propulsion system for a variety of auxiliary propulsion applications. The weights of a number of different types of low-thrust propulsion systems are compared as a function of total impulse in Fig. 9-6. The closest competitors to the DART system are monopropellant N_2H_4 and the chemical bipropellant CTF/monomethylhydrazine systems. Because of limitations in the current state of the art of liquid propellant systems, a lower thrust limit exists below which they cannot be operated effectively. This lower limit lies somewhere in the 0.1 to 0.5 lb. thrust range. Hence, for high total impulse auxiliary propulsion needs requiring thrust levels below 0.1 lb., the radioisotope systems outperform their competitors by a factor of two or more.
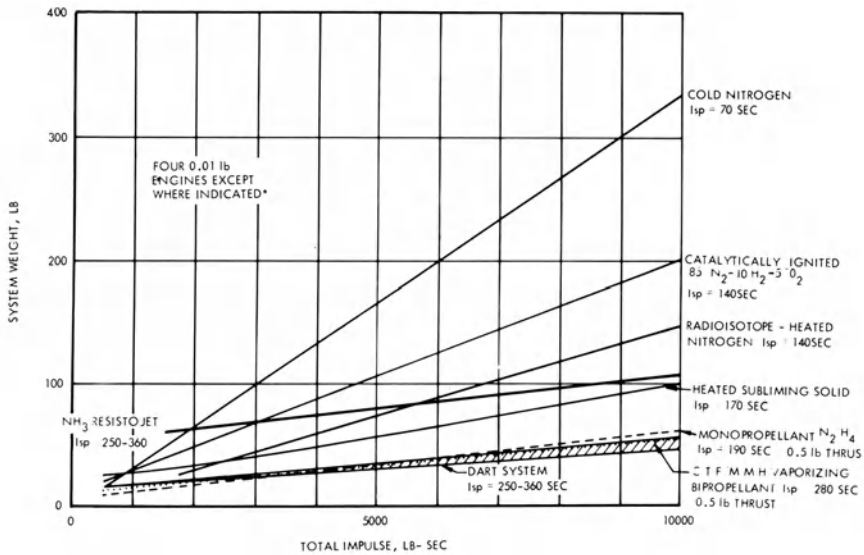
Fig. 9-6 Weight versus total impulse for low-thrust systems.

[9-5] THRUSTER TECHNOLOGY

[9-5.1] Design Criteria

[9-5.1.1] Performance

Radioisotope thruster design is governed both by performance and by aerospace safety criteria. Since I_{sp} depends upon the efficiency of the nozzle as well as upon the gas temperature attained,

thruster performance is a function of nozzle design as well as all system parameters which affect maximum operating temperatures. The dependence of I_{sp} on working fluid temperature (for idealized nozzle flow) is shown in Fig. 9-7 for both H_2 and NH_3. For a prime thrust system of the Poodle type to be competitive, I_{sp}'s in the 700–800–second range are required; hence, H_2 fluid temperatures in the 1800° C range must be achieved. For a storable auxiliary thruster of the DART type to be competitive, I_{sp}'s in the 250–300– second range are required; hence, NH_3 fluid temperatures in the 1000° C range must be obtained. Because of nozzle inefficiencies associated with viscous losses, the working fluid temperatures actually required to obtain given I_{sp} levels can be as much as 20% higher than those shown in Fig. 9-7. Therefore, the required I_{sp} level establishes heat source temperature and nozzle performance requirements.
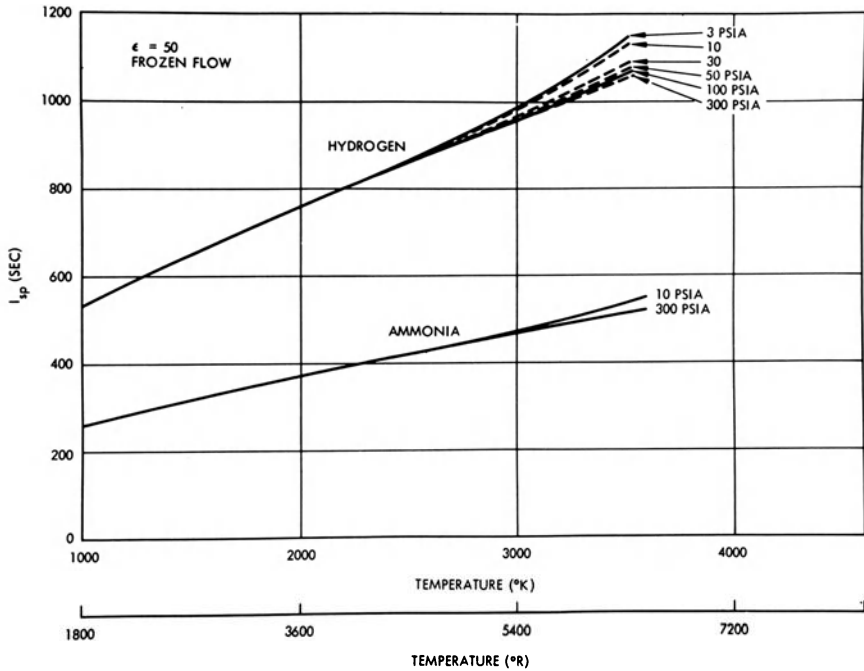
Fig. 9-7 I_{sp} versus temperature. Calculated effective strain map. W-Re capsule after 30 days at 2000°C.

[9-5.1.2] Safety

The present aerospace safety philosophy for Poodle and other large polonium heat source systems requires complete radio-isotope containment under all circumstances, including re-entry. The thermal environment characteristic of a launch pad booster

explosion is shown in Fig. 9-8, while the temperatures to which a Poodle isotope capsule would be heated upon re-entry from earth orbit are shown in Fig. 9-9. From these thermal and other considerations, it can be shown that the re-entry environment is more severe than those considerations arising from possible mishaps during transportation, handling, and launch operations including launch pad fires.
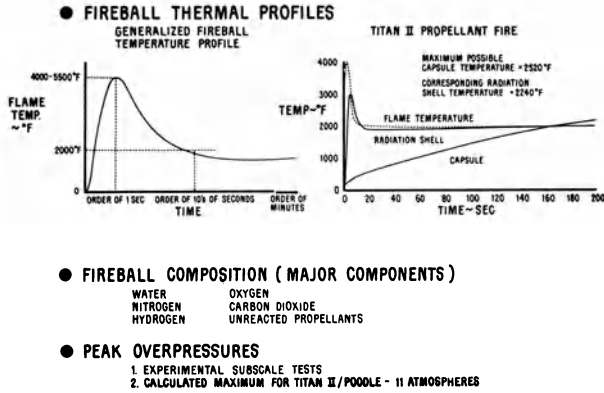
Fig. 9-8 Launch abort environment.
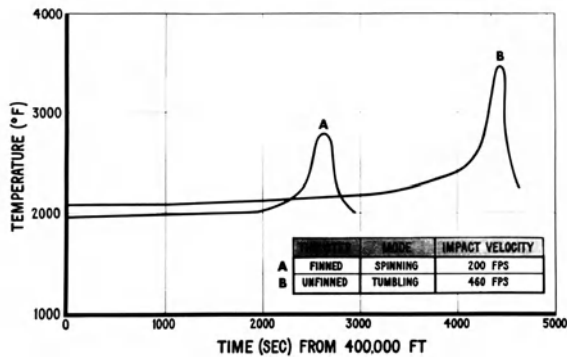
Fig. 9-9 Capsule temperature during re-entry.

The probability of a propellant explosion due to booster malfunction during powered flight decreases with increasing altitude. Above 200,000 feet, explosive aborts are virtually impossible. The propellants mix and burn rapidly, but the strong shock front normally associated with explosions is absent because of the extremely low atmospheric pressure. The explosive forces are probably not sufficient to damage the thruster or to remove the

capsule from it. Hence, after a suborbital abort, the thruster starts its re-entry phase intact.

For systems re-entering from orbit, if the orbital decay time is long enough in relation to the half-life of the isotope, subsequent re-entry presents no hazards because the isotope decays sufficiently. If, on the other hand, the final orbital lifetime is short in relation to the isotope half-life, or if the secondary propulsion system fails to inject the payload into the proper final orbit, radioisotope capsule integrity must be assured in an orbital decay re-entry environment.

Aerodynamic calculations indicate that peak re-entry temperatures experienced by unaided Poodle thrusters approach allowable limits (about 1900° C) for state-of-the-art oxidation resistant coatings on refractory metals. Predicted impact velocities are in the vicinity of 430 ft/sec. These exceed velocities at which capsules can be expected to survive. Ablative and heat-sink shields to protect the engine from re-entry environments and to cushion subsequent impact have been considered and rejected on a weight basis.

An alternative re-entry aid, which weighs much less and which is simpler to attach, has been designed for Poodle. In this design approach, longitudinal wings or fins are added to the cylindrical body of the thruster. The fins decrease the ballistic coefficient $W/C_d A$ and induce a spinning motion about the thruster longitudinal axis, distributing the aerodynamic heating more evenly. In combination, these effects greatly reduce the effective aerodynamic heat flux, peak re-entry temperature and impact velocity. The extent to which impact velocity is influenced by fin size and thruster orientation is shown in Fig. 9–10.
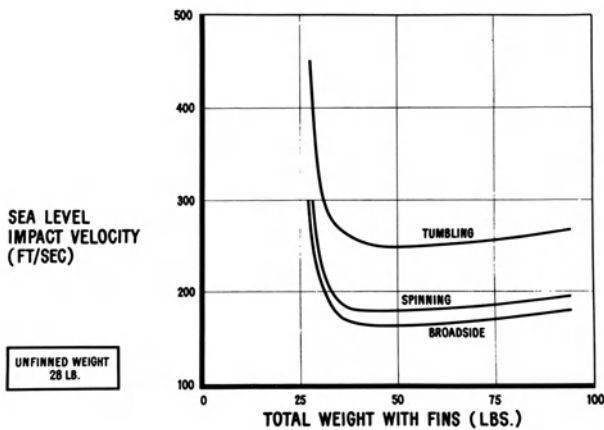
Fig. 9-10 Thruster impact velocity versus weight.

The minimum impact velocity achievable and the additional fin weight required are quite sensitive to the basic thruster configurations which are primarily governed by capsule dimensions. Hence, every effort must be made to minimize capsule size. Experimental data obtained from thruster drop tests from 15,000 ft. altitude demonstrate that impact velocities are accurately predictable and can be reduced to less than 200 ft/sec. with reasonable size fins, while analyses indicate that the heat flux to the thrusters can be reduced by nearly a factor of three. The peak temperature of capsules housed within the thruster body can be reduced to about 1530° C, nearly 400° C lower than in a tumbling thruster without re-entry aids.

After impact, the capsule must continue to provide complete containment for a significant time either to permit retrieval of the capsules or to allow the isotope to decay to negligible levels. Typical post-impact environments which the capsules must withstand include exposure to air and soil at temperatures which slowly decrease from a maximum of about 1200° C down to ambient and immersion in water.

[9-5.1.3] Design Criteria Summary

In summary, the principle criteria governing the design and development of a Poodle type thruster are: material compatibility for periods of months with H at temperatures in the 2000° C range, minimum nozzle viscous losses, minimum capsule size, compatibility with air for durations of a few hours at temperature in the 1500–1600° C range, compatibility with air for a period of years at temperatures in the vicinity of 1200° C, and ability to survive impact at velocities in the 200 ft/sec. range. Basically, the same criteria govern the design and development of a DART-type thruster except for the operating temperature (2000° F instead of 2000° C) and for compatibility under operating conditions (several years with NH_3 instead of several months with H_2). The remainder of this section is devoted to a discussion of the progress which has been made toward achieving these design goals.

[9-5.2] Heat Source Development

[9-5.2.1] Radioisotope Fuel

The basic Poodle heat source unit consists of a Po–210 fuel-form distributed within a matrix, sealed within a protective liner and placed within a containment vessel (capsule). With Po–210, as with other alpha emitters, a problem arises due to the production of helium as a decay product. The helium does not diffuse appreciably through capsule materials. At the temperatures concerned, no means have yet been found to vent it without permitting

the escape of fuel or the entry of oxygen.* Accordingly, the capsule must provide adequate void space for helium and must function as a pressure vessel.

The internal pressure causes creep strain to occur in the capsule at a rate which is extremely temperature-dependent. Therefore, it is essential that the fuel form itself have a low vapor pressure. Otherwise, instead of building up gradually, pressure will be high at the outset and will remain high during the operating period—a period when maximum temperature is experienced and pressure is least tolerable. For this reason, polonium in metallic form (b.p. 962° C) is not suitable.

A classified AEC program to develop polonium compounds which are usable at high temperature is being pursued at Mound Laboratory. A 1500° C capability was demonstrated in radioisotope thruster tests conducted in early 1965 and research is underway to develop forms capable of operating at temperatures exceeding 2000° C. If, in addition, the fuel form development program should lead to an inert, insoluble chemical compound which forms irrespirable particle sizes, the containment requirement could be waived, greatly simplifying capsule design. In that event, internal gasses could be vented without concern about the escape of minor quantities of fuel.

In the absence of such an ideal fuel form, major considerations in heat source development include means to reduce the high temperature creep of encapsulating materials under the influences of internal pressure; means to survive re-entry heating and impact shock without release of fuel; and means to resist post-impact oxidative and corrosive environments until the fuel has decayed to acceptably safe levels. (For Po-210, this occurs in about five years after encapsulation.) Capsules containing Pu-238, which has a half-life in excess of 90 years, cannot be expected to satisfy this latter requirement; however, inert, insoluble, irrespirable fuel forms are expected to be available shortly, hence permanent post-impact containment may not need to be a firm requirement for systems employing this fuel.

[9-5.2.2] Capsule Technology

[9-5.2.2.1] General Considerations

The heart of a radioisotope propulsion system is the isotope heat source. It must be capable of satisfying the power level, heat flux, temperature, lifetime and duty cycle requirements of the mission, be light in weight and have a configuration which is

---

*Several promising efforts aimed at development of a "vented" capsule are currently underway but as of the time of this writing no satisfactory vented capsule has yet been developed.

compatible both with thruster thermal and hydrodynamic characteristics as well as with aerodynamic constraints imposed by aerospace safety requirements. Additionally, it must have sufficient structural and corrosive integrity to enable it to satisfy rigorous safety qualification testing.

The primary components of a heat source, as indicated in Table 9-2, are: fuel, liner, strength member (substrate), claddings, coatings, and structural heat transfer elements. When selecting the appropriate materials and design for these components, ample consideration must be given to their nuclear, thermal, chemical, metallurgical and mechanical properties as well as to such matters as fabrication, joining and quality assurance techniques and to the degree to which the system can be proven out through testing with non-nuclear, simulated heat sources. This latter consideration can have a significant bearing on the cost, the pace with which progress can be made, and the degree of reliability which can be demonstrated in a heat source development program.

Table 9-2   Heat Source Design Process Elements

Subsystem Requirements	Design Considerations	Heat Source Components
Power level	Nuclear	Fuels
Heat flux and temperature	Thermal	Liners
Weight and shape	Chemical	Strength members
Lifetime and duty cycle	Metallurgical	Claddings
Safety	Mechanical (pressure impact, vibration, shock)	Coatings
	Fabrication	Structural and heat Transfer elements
	Joining	
	Quality Assurance	
	Non-nuclear simulation	

While no single capsule material will satisfy all of the physical and chemical requirements generated by performance and containment objectives, a composite capsule combining the features of several materials may do so. At the present time, promise is shown by a capsule system consisting of a refractory metal alloy substrate protected from internal and external chemical attack by a system of liners, coatings, diffusion barriers and claddings. In this combination, the refractory metal alloy substrate provides the required high temperature mechanical strength and creep resistance, the external cladding provides long-term oxidation and corrosion resistance to operating and abort environments, and the internal liner provides compatibility with the fuel form.

Although a final choice of substrate material has not been made, W-25Re is currently preferred for Poodle because of its compatibility with H_2 at all temperatures, with the noble metal external claddings now under development and with the tantalum alloys currently being employed for internal capsule liners. In arc-cast form it has relatively good creep resistance and ductility and its ability to withstand impact, though not as good as some of the candidate materials, has been experimentally demonstrated to be adequate to satisfy the impact criteria discussed earlier. Because of its extreme hardness, W-25Re is difficult to machine. Thus, high fabrication costs are added to high material costs. As a practical consequence, testing with suitably configured specimens has been limited.

Several alternate substrate materials have also been considered, including Ta-W and Ta-W-Hf alloys, both of which are relatively inexpensive, easily fabricated and have exhibited superior impact resistance. However, substrate/cladding compatibility tests with these alloys have been unfavorable at operating temperature and their creep resistance at 2000° C is poorer than W-25Re. Furthermore, in certain ranges below 1000° C, compatibility tests have shown that severe hydrogen embrittlement occurs. As indicated previously, the capsule must be able to withstand the build-up of internal helium pressure resulting from the α decay process. In designing the capsule, considerable attention must be given to minimizing the stress levels whenever possible since the creep resistance of the substrate materials is quite low at 2000° C. In principle, stress can be reduced any desired amount by scaling capsule size upward while holding fuel inventory constant. However, since the size and effectiveness of proposed re-entry aids are quire sensitive to the heat source configuration, every effort must also be made to minimize capsule dimensions. This can be achieved most effectively by unequal distribution of the fuel between the capsules such that the coldest capsule (the one nearest to the propellant inlet end) contains the most fuel and the hottest capsule (the one nearest to the nozzle end), the least. Thus, internal pressure is increased where it is most tolerable and decreased where it is least tolerable.

[9- 5.2.3] Thermal Design

An optimum thermal design for a capsule thruster subsystem is one in which:

a. The maximum temperature of the fuel is minimized for a given maximum working fluid temperature, or conversely, the maximum possible working fluid temperature can be attained for a given maximum fuel temperature.

b. The maximum thermal efficiency which is consistent with requirement (a) is achieved. Thermal efficiency is defined as the

net fraction of the total heat source output which is transferred to the working fluid.

To minimize the temperature difference between the fuel and the working fluid, considerable effort must be expended both in minimizing the contact resistance at all of the interfaces between the fuel and the fluid as well as to maximize the effective thermal conductivity of the fuel. Effective fuel conductivity can be significantly improved through insertion of high conductivity fins within the fuel. Two of the schemes under consideration are shown in Fig. 9-11. Contact resistance between metallic surfaces can be materially reduced through injection of helium into the interface region.
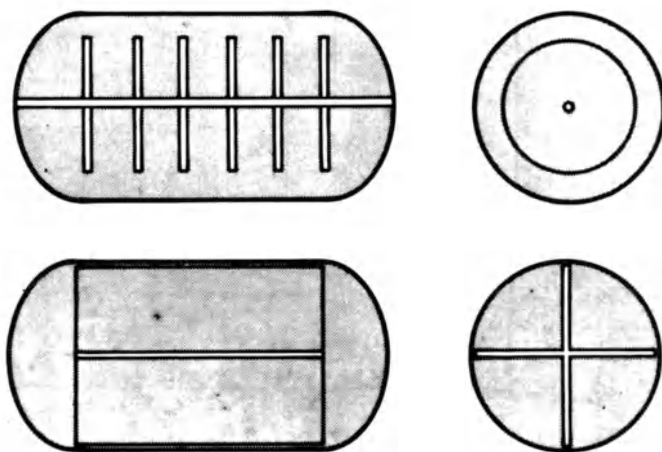
Fig. 9-11 Fuel temperature flattening techniques. Top: circular fin design; bottom: rectangular fin design.

To achieve maximum thermal efficiency, careful consideration must be given to each heat path leading from the capsule to the surrounding structure. Perhaps the greatest potential source of heat loss is through radiation from the outer shell of the thruster module to space (or to surrounding structure). To minimize the heat leakage, considerable attention has been given to the development of high temperature concentric, multiple radiation shielding of the type shown in Fig. 9-12. Experimental efficiencies in excess of 65% have been obtained in DART-type thrusters using the "free standing" configuration, whereas efficiencies in excess of 90% have been achieved with Poodle–type thrusters which use ample multiple foil insulation.

[9- 5.2.4] Fabrication and Non-Destructive Testing Techniques

Although the materials technology and design constraints involved in the fabrication of high temperature radioisotope capsules are new and unique, it has been found that conventional joining, machining, and nondestructive testing techniques are adequate. At TRW complete capsules have been fabricated from a wide variety of material including: more than 30 from W–25Re, 32 from TZM, 9 from Ta–10W, 10 from Haynes 25, 16 multiwall–TZM/Haynes 25, and numerous multiwall TZM/Pt–Rh.

DIMPLED – CORRUGATED
FOILS

FIBER SEPARATED
FOILS

FREE STANDING

WIRE SEPARATED FOILS
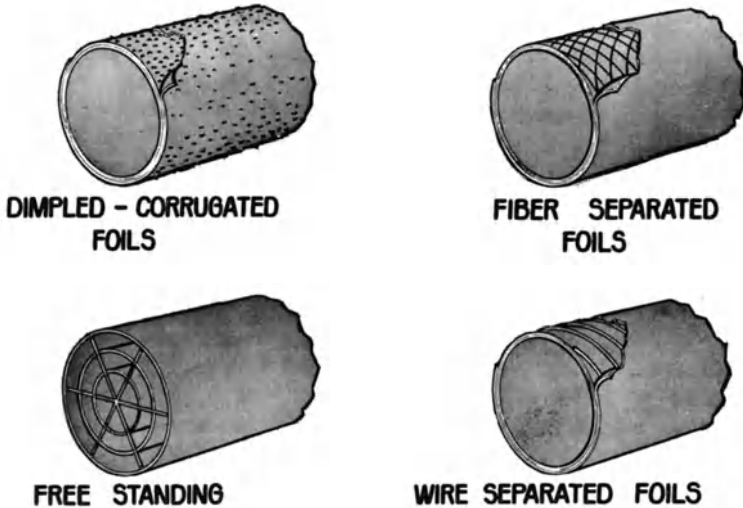
Fig. 9-12 Radiation shields assembly techniques.

[9- 5.2.5] Pressure Containment

As previously mentioned, the internal pressure created by the production of helium from the α decay process causes creep strain to occur in the capsule. Since the creep resistance of the candidate substrate materials decreases rapidly with increasing temperature, it is essential that every effort be made to minimize the internal pressure at high temperatures. This can be achieved by selecting a fuel form which has a low vapor pressure, by increasing the void volume within the capsule, or by development of an inert, insoluble fuel form thereby enabling He to be vented from the capsule.

Significant increases in capsule void volume can significantly add to the weight of the entire thruster and adversely influence

the effectiveness of the re-entry aids. Therefore, every effort must be made to minimize capsule size.

Computerized analytical techniques have been developed at TRW for predicting capsule creep capabilities. An example of the output of this program showing a detailed strain map of a specific capsule configuration is given in Fig. 9-13 and a comparison of predicted strain versus experimentally measured strain is shown in Table 9-3. A view of the capsule pressurizing test fixture used for generating this experimental data is given in Fig. 9-14.
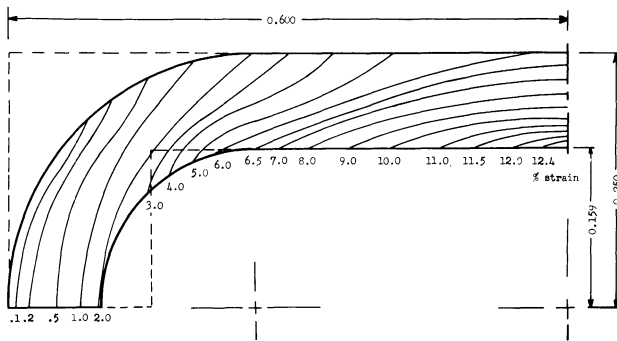
Fig. 9-13

Table 9-3   Experimental and Analytical Results

Capsule Material	Operating Temperature (°C)	Duration (Days)	Pressure	Experimental Circumferential Strain at Midplane (Percent)	Predicted Circumferential Strain at Midplane from Crash Program (Percent)
Haynes 25	930	60	Variable	0.79	1.17
Haynes 25	930	60	Variable	1.55	1.23
W-25Re	2000	30	Variable	1.74	1.23
W-25Re	2000	30	Constant	1.35	1.15
W-25Re	2000	30	Constant	1.56	1.50
W-25Re	2000	30	Variable	4.42	5.54
W-25Re	2000	30	Constant	7.30	7.83

[9-5.2.6] Impact

To qualify for space use, radioisotope capsules must demonstrate their ability to survive impact resulting from a variety of abort
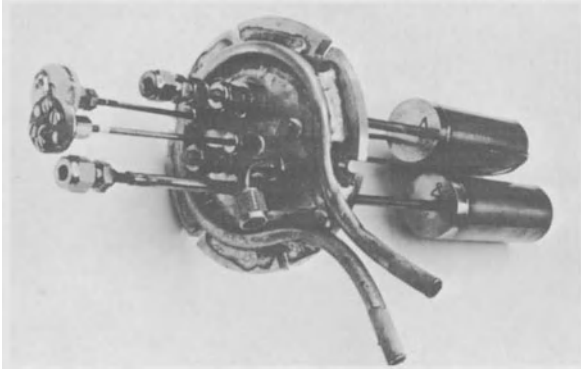
Fig. 9-14 Test fixture for creep testing.

conditions including re-entry from earth orbit. The impact resistance of refractory metal capsules is affected by the processing, fabrication and joining techniques, the operating stress and temperature history, the capsule temperature and orientation at impact, the surrounding structure and the nature of the impact surface.

We are not yet able to predict accurately, from analysis, the impact resistance of hot refractory metal capsules. Therefore, the capability to survive impact at the velocities of interest must be demonstrated experimentally. A view of an apparatus for conducting such tests is shown in Fig. 9-15. The results of a large number of tests at the temperatures and velocities of interest using capsules fabricated from a wide variety of materials indicate that capsules fabricated from most of the refractory materials of interest can be designed to satisfy the necessary impact criteria. Sectional views
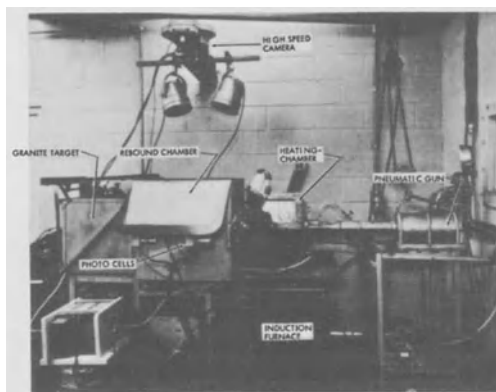
Fig. 9-15 Impact test apparatus.

Fig. 9-16 Sectioned views of impacted TZM capsules.
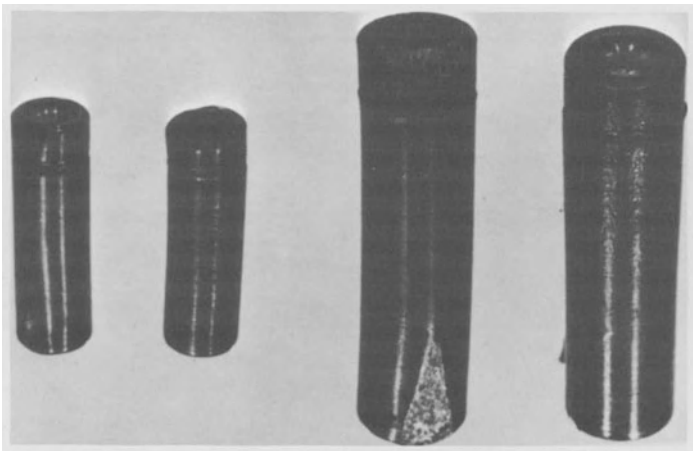
Fig. 9-17 Impacted refractory capsules.

of impacted TZM DART capsules are shown in Fig. 9–16 and outer views of impacted W–Re Poodle capsules are shown in Fig. 9–17. Though deformed, each of these capsules was found to be leak-proof after impact.

[9-5.2.7] Heat Source Simulation

Because of the large number of tests required to demonstrate system feasibility and reliability and because of the high expense associated with performing tests with fueled capsules, a significant portion of radioisotope development programs involves testing with simulated heat sources. In particular, extensive use is made of resistively heated sources configured as closely as possible to heat source dimensions. Therefore, early in a program, it is necessary to develop long-lived resistive heaters capable of operating in the same environment as will the isotope heat source. A view of a tungsten heating element developed for use in simulating the Poodle thruster is shown in Figs. 9-18 and 9-19. That heater operated continuously under H_2 flow conditions at 2100° C for 30 days with no difficulty or signs of failure.
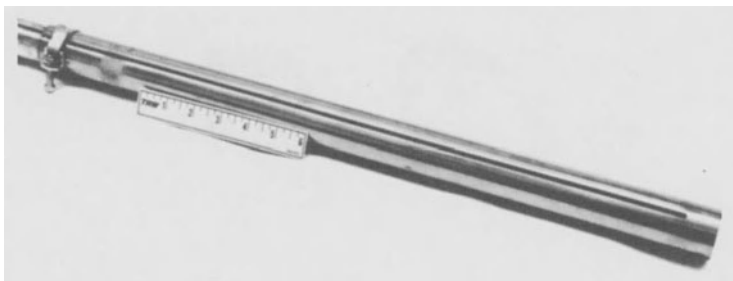
Fig. 9-18 Tungsten heating element for Poodle heat source simulation.
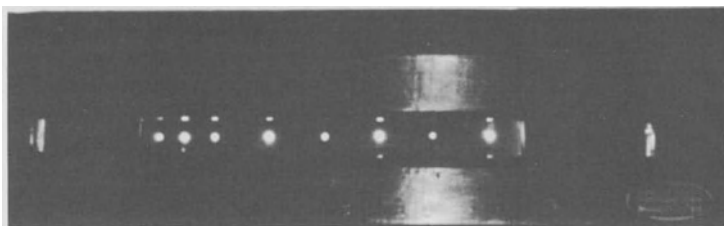
Fig. 9-19 2100° electric heater under test.

[9-5.2.8] Oxidation and Corrosion of Encapsulating Materials

As previously indicated, the capsules must be capable of surviving post-impact exposure to air, water or soil for extended time periods as well as of surviving peak re-entry heating temperatures and launch pad explosion temperatures in oxidizing environments.

It has been established that the refractory metal strength members (substrate) require high temperature oxidation resistant claddings. Work performed at TRW over the past several years has further established that, for the TZM DART capsules, Pt-Rh alloys are satisfactory. Not only have these capsules operated for 30-day periods, at temperature within a thruster, but they have also survived impact testing under realistic re-entry conditions. Furthermore, oxidation rate data indicate that these claddings will maintain their integrity for many years.

The TRW work [11] has also indicated that satisfactory noble metal claddings involving iridium-rhodium alloys can be developed to satisfy the Poodle thruster requirements. These alloys have been found to have sufficiently high melting points to withstand the thruster operating environment and, at the same time, low enough air oxidation rates to maintain their integrity for the life of the Poodle fuel (approximately 5 years). Furthermore, it has been found that W-25Re is chemically compatible at 2000° C with all Rh-Ir alloys containing greater than 25 atomic present iridium. On the other hand, T-222 alloy (Ta-10W-2.5Hf) is chemically incompatible at 2000° C with all Rh-Ir alloys, including pure Ir. Moreover, at temperatures below which liquid phases form, the rate of solid state interdiffusion between W-25Re and Rh-Ir alloys is much slower than the interdiffusion rate between T-222 and the Rh-Ir alloys. Therefore, it is concluded that of the two candidate Poodle capsule substrate materials (W-25%Re and T-222), the W-25%Re is by far the more desirable from the point of view of chemical interactions with the candidate noble metal cladding materials.

Multiple coupon-stacking compatibility experiments of the type indicated in Fig. 9-20 have also demonstrated that pure iridium has promise as a diffusion barrier material for use between a W-25%Re substrate and another noble metal cladding at 2000° C whereas Al_2O_3 and ZrO_2 were found to satisfactorily inhibit diffusion between TZM and Pt-Rh and T-222 and Pt-Rh in the DART temperature range.

[9-5.3] Nozzle Performance

When the flow at the throat of a converging-diverging nozzle is in the laminar regime, a rapid growth of the boundary layer takes place in the diverging section. Poodle nozzles are subject to this phenomenon, since they have characteristic throat Reynolds numbers under 2000. Without careful design and optimization, a significant loss in nozzle efficiency can result. During the past several years, TRW Systems has been conducting analytical and experimental studies of laminar nozzle behavior. Results thus

far indicate that nozzle efficiencies in excess of 88% at an area ratio of 100 are achievable with Poodle thrusters.
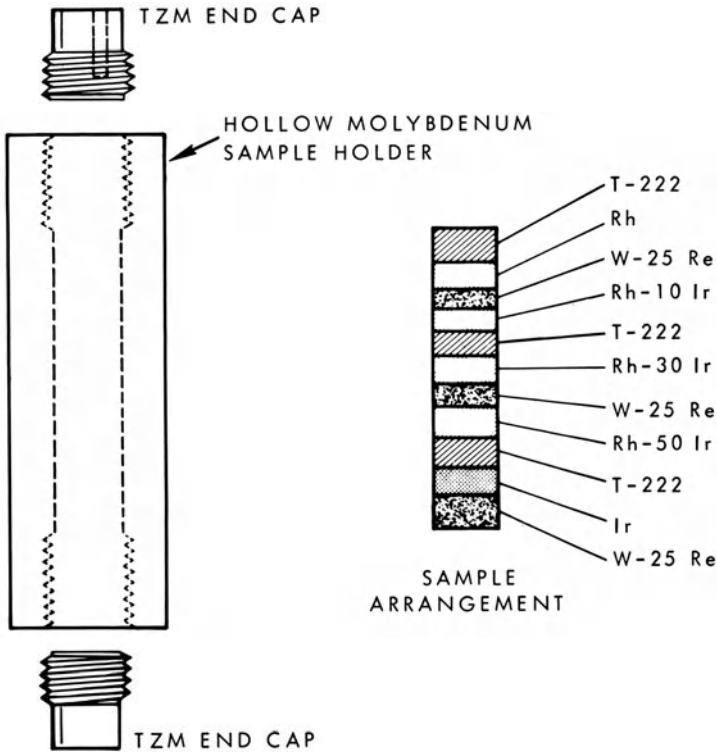
Fig. 9-20 Compatability test apparatus.

Nozzle efficiency is defined here as the ratio of delivered specific impulse to theoretical specific impulse. Since specific impulse varies approximately as the square root of the absolute temperature, the increase in operating temperature required to offset nozzle losses in maintaining a given performance can be substantial. For example, a 10% loss in nozzle efficiency must be compensated by almost a 20% increase in absolute temperature in order to hold specific impulse constant.

The effect of the boundary layer as a function of Reynolds number can be seen in Fig. 9-21 where the radius of a conical nozzle having a central inviscid core with a given gas density and velocity at the nozzle exit plane is compared to the radius of an ideal, frictionless nozzle which expands the same mass flow to the identical exit plane conditions. The results, based on boundary-layer analysis developed by Cohen and Reshotko, are
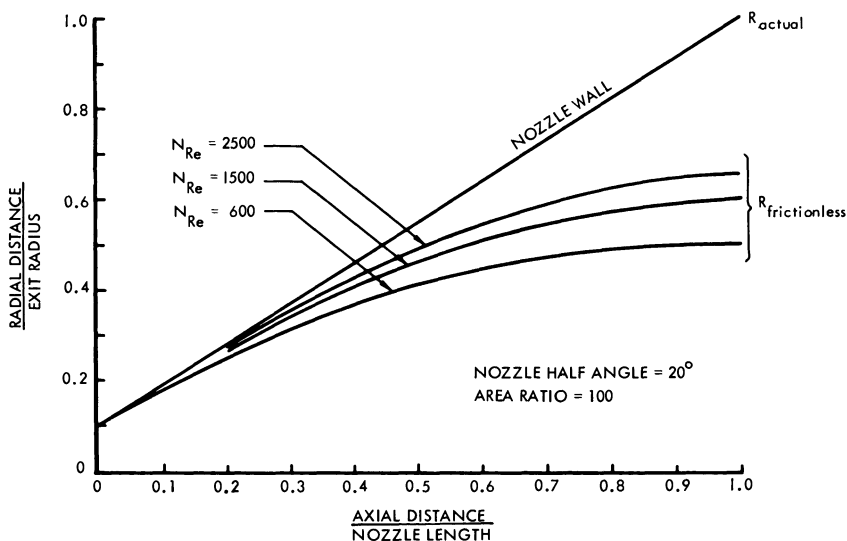
Fig. 9-21 Comparison of actual and frictionless nozzle radii.

for a conical nozzle with an area ratio of 100 and a nozzle half-angle of 20°. It is seen that the frictionless nozzle radius is substantially smaller than the actual nozzle radius, even at a Reynolds number of 2500. Fortunately, the average momentum at the exit plane is not decreased proportionately. Since the boundary layer near the insulated wall is at a higher temperature and lower density, most of the flow remains in the inviscid core. The predicted efficiency for the above nozzle is compared with experimentally determined efficiency data in Fig. 9-22 for area ratios of 20, 40 and 100. The experimental curves were obtained by simulating the Poodle nozzle throat Reynolds number with N_2 at 760° C instead of H_2 at 2000°. This procedure eliminates the need for refractory components and permits a more accurate determination of the propellant temperature. Subsequent test data with H_2 at higher temperatures confirmed these results.

Thrust was measured with a dynamometer which was accurate to less than a millipound over the range from 0 to 0.1 lb. Performance data were obtained for supersonic nozzle configurations having divergence half angles of 10°, 20° and 35° and area ratios of 20, 40 and 100 over a wide range of throat Reynolds numbers.

The experimental results for the 10° and 35° half-angle nozzles were similar to those for the 20° nozzle, except that the nozzle efficiencies were several percent lower. Although the nozzle efficiency decreased with increasing area ratio in all cases, the value of specific impulse which is the parameter to be maximized, continued to increase. Since the frictional losses in the divergent
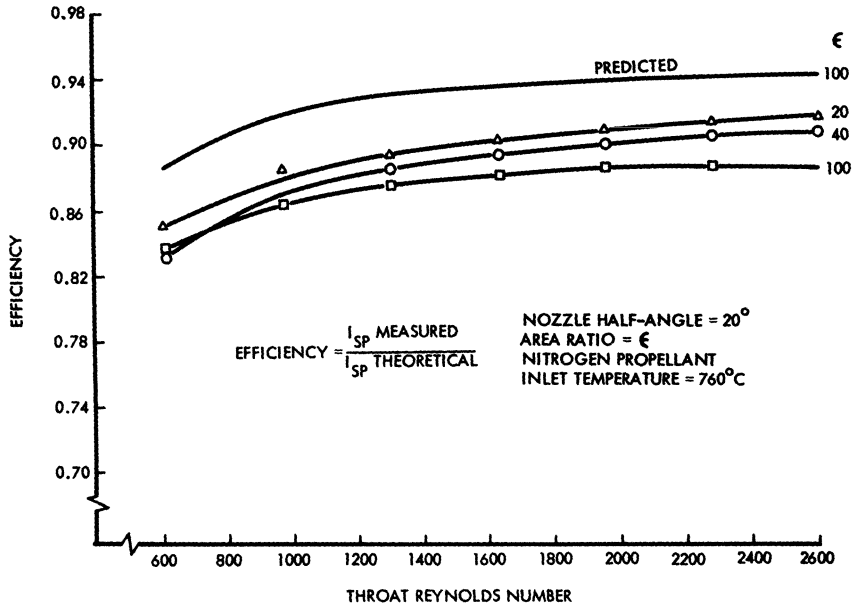
Fig. 9-22 Nozzle efficiency.

section increase with length while the incremental performance gains from further expansion decrease, an optimum area ratio exists. Experimental results with various nozzle contours and half-angles indicate that the optimum is about 100 for flows having Reynolds numbers of 2000. Of the divergent half-angles tested, the 20° nozzles produced the highest specific impulse followed by the 10° and 35° nozzles, respectively. The efficiency of the sonic nozzle was in excess of 99%, confirming that the losses occur in the divergent section of the nozzle.

A comparison of computed and experimentally determined nozzle efficiences shows that the dependence of efficiency on Reynolds number and area ratio is correctly given, but the absolute values of the theoretical efficiencies are about 5% higher. Experimental measurements of the radial distribution of impact pressure at the nozzle exit plane indicate that this discrepancy is associated with the fact that the boundary layer at the nozzle exit occupies a larger portion of the flow area than predicted by analysis.

[9-6] SUMMARY

Competitive auxiliary propulsion applications exist today for radioisotope thrusters operating in the 2000° F range using NH_3

working fluid and having an unlimited on-off capability. Further-more, the state of the art of today's thruster, capsule and fuel form technology is sufficient to enable immediate development of these thrusters.

No immediate application exists for the higher performing (I_{sp} 700-800 secs.), higher temperature (> 2000° C), higher thrust (~ 1/4 lb.) primary propulsion systems of the Poodle type. How-ever, mission studies clearly indicate that a Poodle upper stage is capable of greatly extending our ability to perform difficult space missions, particularly when used in conjunction with a nuclear rocket lower stage.

Strong progress in the Poodle thruster and heat source tech-nology areas during the past several years indicates that an acceptable thruster could be developed within 2 to 3 years pro-viding sufficient efforts are expended to simultaneously extend polonium fuel form technology into the 2100-2200° C regime.

REFERENCES

1. Seifert, H.S., M.M. Mills, and M. Summerfeld: The Physics of Rockets, *American Journal of Physics*, 15:1, 1-21, Jan.-Feb., 1947.
2. Martinez, J.S.: Isotope Propulsion, *Space/Aeronautics*, Nov. 1964.
3. ————: Isotope/Thermal Thrusters and Applications, paper presented at Second AGARD/NATO Lecture Series on Nuclear Propulsion (Brussels), Oct. 1964.
4. ————, L.J. Van Nice, A.F. Grant: Nimphe, A New Rapid, Restartable Monopropellant N_2H_4 Engine, paper presented at AIAA Summer Meeting, June 17-20, 1963.
5. Forbes, S.G., B.I. Friedman, and J.S. Martinez: Ionic Pro-pulsion Systems, Patent No. 3210926 dated 12 October 1965.
6. Mickelsen, W.R. and C.A. Low, Jr.: Potentialities of the Radioisotope Electrostatic Propulsion System, paper pre-sented at AIAA Electric Propulsion Conference, (Colorado Springs), March 11-13, 1963, *AIAA Paper No. 63048-63*, 11 pp.
7. Private Communication, Jean-Pierre Contzen, Member of Staff, European Launcher Development Organization (ELDO), June 1966.
8. Jortner, D. and J.S. Martinez: System and Mission Con-siderations for a Radioisotope Propulsion System (Poodle), paper presented at AIAA First Propulsion Joint Specialist Conference, (Colorado Springs), June 14-18, 1965.
9. Simms, R.: Comparative Capabilities of Advanced Propulsion Systems for Upper Stage Propulsion, paper presented at AIAA Third Propulsion Specialist Conference, (Washington) July 1967.

10. Jones, I.R. and G.E. Austin: Poodle Radioisotope Propulsion Technology, *Radioisotopes for Aerospace*, Part 2: Systems and Applications, Plenum Press, 1966.
11. Ogren, J.R., J.L. Blumenthal, and R.C. Ham: Radioisotope Propulsion Technology Program (Poodle), Final Report, Vol. III, *STL-517-0049*, Oct. 1966.

Part Five

Electric and Ion Propulsion

Electric and Ion Propulsion

S. G. Forbes, *Assistant Manager*
Atomic Energy Division
Phillips Petroleum Company

[10-1] BASIC CONCEPTS

[10-1.1] Energy Sources

Early workers [1] in rocketry recognized the desirability of producing higher exhaust velocities than can be obtained chemically. This recognition comes directly from the basic rocket equation

$$\Delta V = C \ln \frac{m_i}{m_f} \tag{10-1}$$

where ΔV = the change in velocity achieved in free space acceleration
$\quad C$ = exhaust velocity of the rocket
$\quad m_i$ = initial mass of the rocket
$\quad m_f$ = final mass of the rocket

In a chemical rocket the exhaust velocity C is limited by the energy available per unit mass of exhaust products. Higher velocity increments may be obtained by increasing the mass ratio m_i/m_f by staging, etc., but the logarithmic nature of the velocity gain combined with practical aspects of fixed masses such as structure, nozzles and pumps, impose limitations on this approach. The alternative is to find some way to raise the exhaust velocity to values higher than can be obtained from the energy of chemical reactions. Energy density requirements can be estimated by computing the velocity that the energy source would achieve if all of its available energy were converted to kinetic energy. Thus,

$$E = \frac{1}{2} m v^2 \tag{10-2}$$

where $\quad E$ = total energy available
$\quad m$ = mass of the energy source
$\quad v$ = hypothetical velocity of the energy source.

427

Solving for v,

$$v = \sqrt{\frac{2E}{m}} \equiv V_c \qquad (10\text{--}3)$$

which is called the "characteristic velocity"* of the energy source.

As an example of a high-energy chemical system, the total enthalpy available from room-temperature oxygen and hydrogen is about 6.8×10^3 Btu/lb. which, if it were all converted into translational** kinetic energy, would produce a velocity of about 5620 meters per second. By contrast, a solar array with a specific weight of 50#/KW operating for one year would produce 6×10^5 Btu/lb. giving $V_c = 52{,}800$ meters/second. Another possible source having high energy density is a nuclear reactor. For example, if a complete nuclear-electric generator could be built with a specific weight of 20#/KW and operated in space for two years, the energy output would be 3×10^6 Btu/lb. giving $V_c = 118{,}000$ meters/second.

Energy sources such as these offer from 100 to 1000 times the energy density available from chemical sources. Both examples have several characteristics in common: the weight of the actual energy source is negligible in comparison to the weight of the system required to extract the energy, the weight (mass) of the system is proportional to the power output, and the energy available is proportional to the operating time.

To illustrate the first point, a solar array actually has no energy source aboard the spacecraft but extracts energy from the sun, while the weight of nuclear fuel for a reactor system always represents a negligible fraction of the system weight.

The second statement can be written mathematically in the form:

$$m_w = \alpha P \qquad (10\text{--}4)$$

where m_w = mass of the power plant
α = specific weight of the power plant (*e.g.,* lb/KW)
P = power output (KW)

The third statement can be written

$$E = P\tau \qquad (10\text{--}5)$$

where τ = the operating time of the power plant (*e.g.,* mission duration).

---

* The term "characteristic velocity" in this context has a different meaning from that used in chemical rockets.
** This cannot be done even in a perfect rocket. Energy taken up in molecular rotation reduces the theoretical value to about 80% of that calculated above.

Then the characteristic velocity can be found to be

$$V_c = \sqrt{\frac{2E}{m_w}} = \sqrt{\frac{2\tau}{\alpha}} \qquad (10\text{-}6)$$

The characteristic velocity of power plants is shown parametrically in Fig. 10-1.
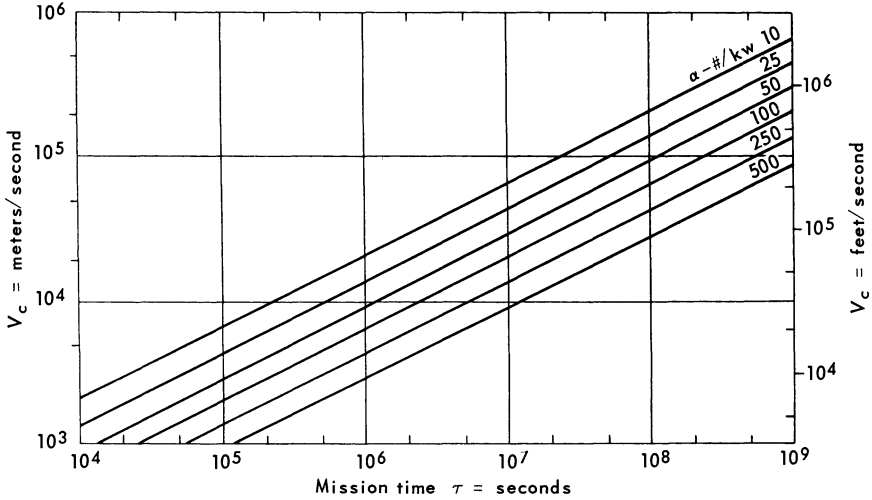
Fig. 10-1

The important things to notice in Eq. (10-6) and Fig. 10-1 are that the characteristic velocity increases with operating time (mission duration) and with decreasing specific weight of the energy source. Most important, the characteristic velocity of state-of-the-art solar-electric systems is of the order of 5×10^4 meters/second or 1.5×10^5 ft/second. As we shall see, this leads to attractive payloads and velocity increments, although not as high as might be expected by analogy with chemical systems.

[10-1.2] The Separately Powered Rocket

The high energy density sources (solar and nuclear) provide no reaction mass that can be used for propulsion in a space environment. In fact, that characteristic is inherent in the statement of negligible "fuel" weight. Therefore, reaction mass must be added to the system to make it useful as a space rocket. The generalized form of the separately powered rocket is shown schematically in Fig. 10-2. It consists of four essential elements: (1) the power
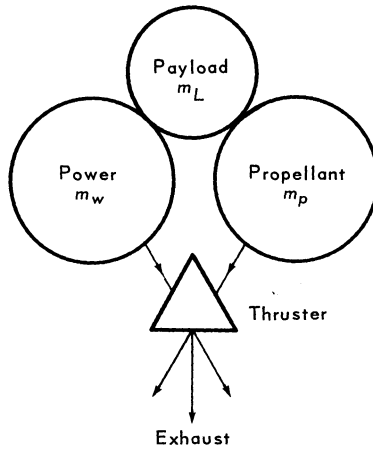
Fig. 10-2

source, (2) the reaction mass or "propellant," (3) the thruster which combines energy and mass to produce momentum of the exhaust beam and, hence, thrust, and (4) the "payload" which is defined as all other system elements not directly related to (1), (2) or (3).

The impact of adding the propellant mass to the system relates primarily to the choice of exhaust velocity v which can be made as high as desired, short of relativistic complications. However, we do not want the highest attainable velocity as can be shown by considering the influence of v on the masses of the propellant and power supply. In an ideal rocket (no losses)

$$\text{thrust, } F = \dot{m}_p v \text{ (conservation of momentum)}^* \tag{10-7}$$

and

$$\text{power, } P = \frac{1}{2} \dot{m}_p v^2 \text{ (conservation of energy).} \tag{10-8}$$

Then

$$P = F \frac{v}{2} \tag{10-9}$$

and the power plant mass will be

$$m_w = \alpha P = \alpha \frac{Fv}{2} \tag{10-10}$$

---

* Dots indicate time derivatives, hence $\dot{m}_p$ is the propellant mass flow rate.

The total impulse delivered during a time τ is

$$I = F\tau \tag{10-11}$$

giving

$$m_w = \frac{\alpha}{2\tau} I v = I \frac{v}{V_c^2} \tag{10-12}$$

We see that the power plant mass is proportional to the total impulse, I, multiplied by the exhaust velocity and hence will be very large if v is increased to high values.

The propellant mass is

$$m_p = \dot{m}_p \tau = \frac{F\tau}{v} = \frac{I}{v} \tag{10-13}$$

and therefore varies inversely with the exhaust velocity for a fixed total impulse produced. The individual masses and their combined mass are shown in Fig. 10-3.
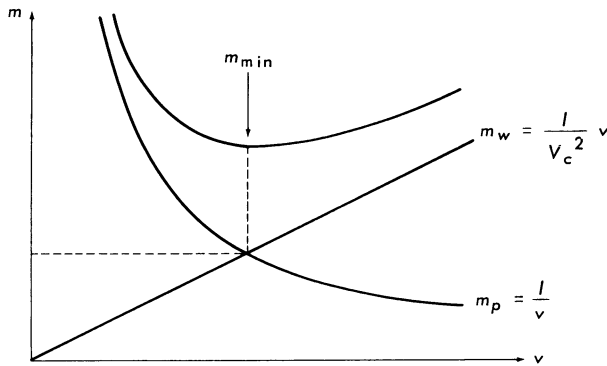
Fig. 10-3

It is evident that the total mass becomes infinite for very high or very low exhaust velocities. The minimum mass for the combined propellant-power plant system occurs when the two masses are equal, giving

$$m_w = \frac{I v_{opt}}{V_c^2} = \frac{I}{v_{opt}} = m_p \tag{10-14}$$

and the minimum total mass occurs when

$$v_{opt} = V_c \tag{10-15}$$

Since the characteristic velocity is dependent only on power plant specific weight and mission duration, we draw the important conclusion that these elements alone determine the *desired* exhaust velocity v_{opt}.

We have from Eqs. (10-11) and (10-14) all the necessary quantities to determine the initial acceleration, a_i, of the system.

$$a_i = \frac{F}{m_i} \qquad (10\text{-}16)$$

since

$$F = \frac{I}{\tau} \qquad (10\text{-}17)$$

$$m_i = 2\,m_w = \frac{2Iv}{V_c^{\,2}} = \frac{2I}{V_c} \qquad (10\text{-}18)$$

$$a_i = \frac{V_c}{2\tau} = \frac{1}{\sqrt{2\alpha\tau}} \qquad (10\text{-}19)$$

We see that high accelerations go with short mission times (and light power plants) and, conversely, that long mission times lead to low initial accelerations. For example, taking the solar electric rocket with $\alpha = 50\#/KW$ for which we found $V_c = 5.3 \times 10^4$ m/sec. ($\sim$174,000 ft/sec.) and dividing by twice the mission time (1 year $\times$ 2 = 6.3 $\times$ 10^7 sec.) gives

$$a_i = \frac{1.74 \times 10^5 \text{ ft./sec.}}{6.3 \times 10^7 \text{ sec.}} = 2.77 \times 10^{-3} \text{ ft./sec.}^2$$

or dividing by g,

$$a_i = \frac{2.77 \times 10^{-3} \text{ ft./sec.}^2}{32.2 \text{ ft./sec.}^2} = 8.6 \times 10^{-5} \text{ g's}$$

It is emphasized that this low value is characteristic of the power plant and mission time, not the thrust device about which nothing has been said thus far.

[10-1.3] Effects of Variable Mass

The simple model presented is incomplete since only initial mass has been minimized. For more detailed derivations, the reader is referred to works of D.B. Langmuir [1] and E. Stuhlinger

[2]. Some of these results are summarized briefly.
Starting with the basic rocket equation (10-1)

$$\Delta V = v \ln \frac{m_i}{m_f}$$

and the definitions (for ideal rockets)

$$m_i = m_w + m_p + m_L \quad \text{(payload)} \tag{10-20}$$

$$m_f = m_w + m_L \tag{10-21}$$

$$\beta \equiv \frac{v}{V_c} \equiv \sqrt{\frac{m_w}{m_p}} \tag{10-22}$$

$$K \equiv \frac{m_L}{m_i} \tag{10-23}$$

then it can be shown that

$$\frac{\Delta V}{V_c} = \beta \ln \frac{1 + \beta^2}{K + \beta^2} \tag{10-24}$$

As we would expect from previous results, this function has a
maximum in the vicinity of $v = V_c$ or $\beta = 1$. Since the payload
fraction K enters the equation, it is clear that some modification
will be expected. The exact results are plotted in Fig. 10-4 which
shows $\Delta V / V_c$ versus v/V_c for several values of K. We see that the
locus of maximum velocity increments begins at $v = 0.505 \, V_c$ for
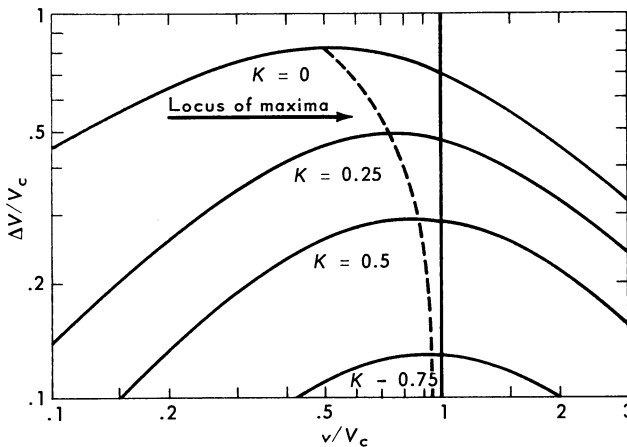
Fig. 10-4

zero payload and approaches $v = V_c$ (our previous result) as the payload fraction approaches unity. This limit is not a trivial case since it is typical of a satellite auxiliary propulsion system in which the electric propulsion system represents a small portion of the system weight. Likely values for K are 0.2 to 0.3 for primary propulsion systems and 0.9 or higher for auxiliary propulsion systems. For primary propulsion, convenient rules of thumb are

$$\Delta V_{opt} \cong 0.5\, V_c \qquad (10\text{-}25)$$

$$v_{opt} \cong 0.7\, V_c \qquad (10\text{-}26)$$

For auxiliary propulsion systems, convenient figure of merit is the system specific impulse or "system effectiveness" which is defined as the total impulse produced per pound of initial propulsion system weight. From the previous derivations Eq. (10-18) we find

$$\frac{I}{g m_i} = \frac{I\, V_c}{2 I g} = \frac{V_c}{2\, g} \qquad (10\text{-}27)$$

To summarize for auxiliary propulsion,

$$\text{Effectiveness} = \frac{V_c}{2g} \qquad (10\text{-}28)$$

$$v_{opt} = V_c \qquad (10\text{-}29)$$

[10-1.4] Power Requirements and Rocket Efficiency

An important aspect of electric rockets is the power required to produce a given amount of thrust at the high specific impulses of interest. By definition,

$$F = \dot{m}_p g\, I_{sp}$$

We found before Eq. (10-10) that

$$P = F\frac{v}{2} = \frac{\dot{m}_p g\, I_{sp}\, v}{2} \qquad (10\text{-}30)$$

and since (10-7)

$$F = \dot{m}_p\, v$$

then for an ideal rocket

$$P = \frac{F\, I_{sp}\, g}{2} \qquad (10\text{-}31)$$

In a real rocket the power will be higher than that for an ideal rocket so we define the Rocket Efficiency η_R as

$$\eta_R = \frac{P_{\text{ideal}}}{P_{\text{real}}} \tag{10-32}$$

thus the power requirement for a real rocket is

$$P = \frac{F \, I_{sp} \, g}{2 \, \eta_R} \tag{10-33}$$

or

$$\eta_R = \frac{F \, I_{sp} \, g}{2 \, p} = \frac{F^2}{2 \, P \, \dot{m}_p} \tag{10-34}$$

This is sometimes called the power efficiency, but since this may easily be confused with the electrical efficiency, the term rocket efficiency is preferred by the author. Note that in its second form Eq. (10-34) it clearly shows that waste of power (electrical efficiency), waste of propellant (propellant utilization), or loss of thrust (exhaust velocity dispersion in magnitude or direction), all reduce η_R in appropriate magnitude so that inefficiencies of all kinds are properly accounted for. Note also that as long as the proper definition of I_{sp} is adhered to, a plot of η_R versus I_{sp} for an electric rocket is a complete description of its effectiveness as a system component.

Some idea of the quantitative aspects of power requirements can be obtained by finding the power-to-thrust ratio in familiar units which turn out to be

$$\frac{P}{F} = \frac{22 \text{ watts}}{\eta_R \text{ lb(thrust)}} \, I_{sp} \text{ (seconds)} \tag{10-35}$$

Thus at 5000 seconds an ideal rocket would require 110 KW/lb. thrust and a real rocket might take 1.5 times this. Note that the power-to-thrust ratio, P/F, given in KW/lb., is similar to the specific power $(1/\alpha)$ in KW/lb. Since these are easily confused, the author prefers to use α as the specific weight lb./KW instead of its reciprocal KW/lb. used by some authors [1].

The numerical example shows that even low thrust at high I_{sp} demands considerable power. On the other hand, a pound of thrust is sufficient to give a vehicle weighing initially five tons a very high free-space velocity in the course of a year ($\sim$100,000 ft/sec.).

[10-1.5] Effects of Gravitational Fields

The gravitational fields present near massive bodies such as the earth can produce, accelerations that are much greater than

the acceleration produced by electrical propulsion systems. It is obvious that escape from the earth's surface is not possible with such a system. Less obvious is the effect of continuous exposure to the gravitational acceleration after orbit is achieved by other means. If the thrust vector has any appreciable component parallel to the gravity vector, the latter will greatly influence the net thrust and accordingly modify the velocity increment. This effect is called the "*gt*" loss in chemical rocketry and represents impulse lost while thrusting along the gravity vector.

For low thrust propulsion, trajectories near earth remain nearly circular during thrusting, and the velocity vector is perpendicular to the gravity vector. In this case, the ΔV required is very nearly equal to the change in equilibrium orbital velocity at the two orbits. For example, to raise a satellite from 200 nautical miles where the orbital velocity is 25,213 ft/sec. to a synchronous orbit of 19,351 nautical miles where the orbital velocity is 10,078 ft/sec. requires a free space ΔV of

$$\Delta V = 25,213 - 10,078$$

$$= 15,135 \text{ ft./sec.}$$

At greater distances from earth, the trajectories acquire greater radial components, and it is not possible to keep the thrust vector simultaneously at right angles to the gravity vector and parallel to the vehicle velocity vector. As a result, the calculation of velocity increments and trajectories become more complex. Even after earth escape, the gravitational acceleration of the sun ($\sim 6 \times 10^{-4} g$'s at 1 AU) is large compared to that of the vehicle, and velocities achieved may be less than half that calculated for free space if the trajectory has a large radial component.

[10-2] THRUST DEVICES

The function of the thruster is to combine the energy from the power source with mass from the propellant supply to produce collimated exhaust stream of the desired velocity. There are a number of thrust devices that can be used to achieve our purpose. For convenience, these are grouped in accordance with the basic principles used in the acceleration process which, broadly speaking, falls into three categories:

(1) *Thermal thrusters*. Thermal thrusters as separately powered rockets include all gas and nozzle systems in which the energy source is not inherent in the propellant. The propulsive force is derived from aerodynamic pressures against the rocket nozzle.

(2) *Electrostatic thrusters*. In electrostatic thrusters, some form of electrically charged propellant is expelled from the thruster by virtue of potentials applied to electrodes. The forces arise from the interaction of charged particles with electric fields.

(3) *Electromagnetic of plasma thrusters*. In plasma thrusters, highly ionized gases or plasmas are accelerated by interaction with electromagnetic fields. Both positive and negative particles are accelerated simultaneously, and the propulsive force arises from interaction between electric currents within the plasma and magnetic fields either self-induced or externally imposed.

[10-2.1] Thermal Thrusters

A cold gas jet falls into this category because the enthalpy of the gas (nitrogen, for example) is derived primarily from the sun which brings the gas to the neighborhood of 300° Kelvin, at which temperature it is released to a nozzle whose function is to convert the random molecular motion into directed kinetic energy in the exhaust with as little residual random motion (temperature) as possible. If extra heat is added to the gas in an electrically powered heat exchanger, the specific impulse of the exhaust stream can be raised to higher values and the thruster is called electrothermal.

[10-2.1.1] The Resistojet

In the resistojet, an electric heater of the resistive type is used to add heat to the gas stream. Two methods have been used. One is to wind a jacketed heater similar to that used in an electric range around a mandrel with a similar length of gas feed line interwound with it. This makes an efficient heat exchanger which can accommodate several gas lines for multiple nozzle operation needed for attitude control systems. Attainable temperatures are limited somewhat by the temperature gradients needed to transfer heat from the resistance element through the insulation, double walls and into the gas. This can be reduced and higher gas temperatures achieved by using the gas conduit walls as the resistive element at the expense of mechanical complications.

The caption of Fig. 10-5 gives the operating characteristics of an electrothermal thruster flown on the Vela satellite, the first electric thruster to be put to practical use.

Temperature limitation of materials limit the specific impulse of resistojets to less than 10^3 seconds for hydrogen. Practical considerations usually make the storage of hydrogen impractical in a small system. An attractive alternate is ammonia which can be decomposed at relatively low temperatures ($\sim$1400° F) into nitrogen and hydrogen. In this manner, I_{sp} as high as 350 seconds can be reached at temperatures of about 3000° F. The efficiency of this type of thruster begins to drop rapidly as I_{sp} is raised, because of the energy required to decompose the propellant. This energy is not recovered as thrust energy and is thus lost.
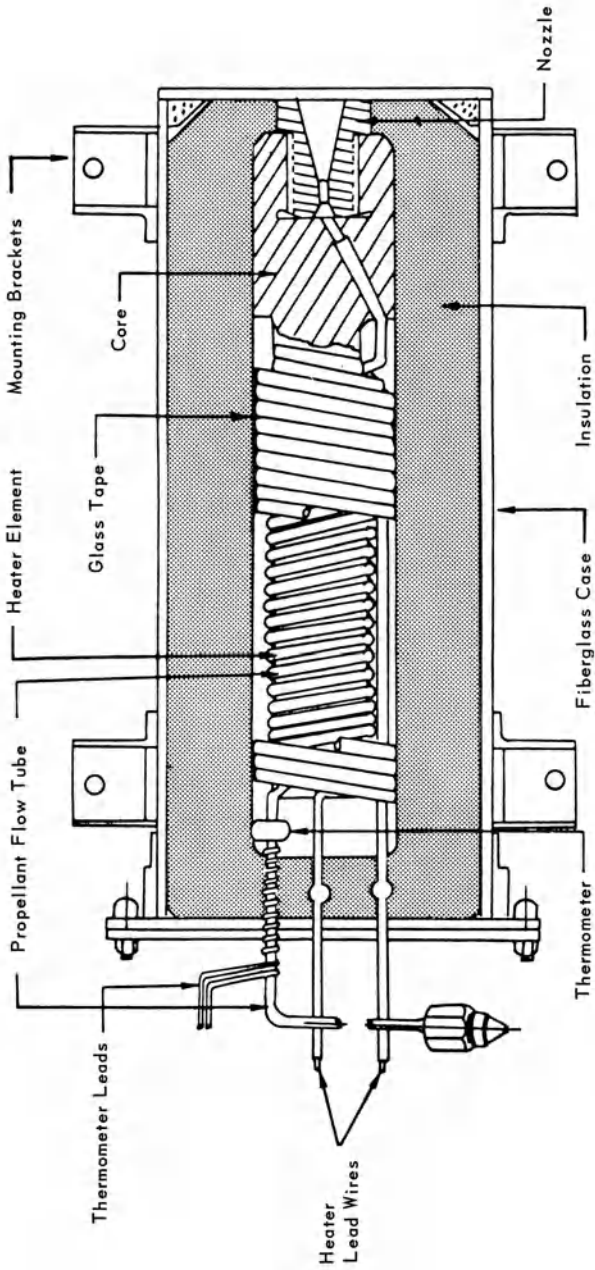
Fig. 10-5 Vela thruster. Characteristics: propellant, nitrogen; thrust, 0.042 lbs.; I_{sp}, 123 secs.; temperature, 1000°F; electrical power input, 96 watts; thruster weight, 0.65 lbs.

A typical efficiency curve for a decomposed ammonia thruster is shown as Curve 1 in Fig. 10-17. Although the efficiency tends to be low at higher I_{sp}, the simplicity and reliability of this system makes it attractive in many cases.

[10-2.1.2] Arc Jets

Specific impulse limitations imposed by materials can be overcome in principle by adding energy directly to the gas in a high intensity arc. A schematic of an arc jet configuration is shown in Fig. 10-6.
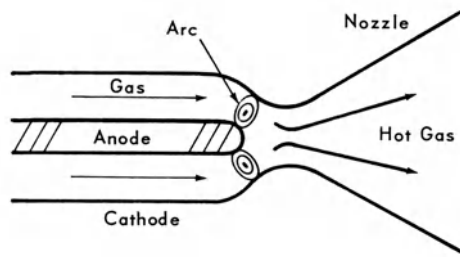
Fig. 10-6

In this manner, the gas temperature can be raised above the melting point of the electrodes to perhaps $10^{4\circ}$ K. At these temperatures, appreciable dissociation and ionization of the gas occurs, absorbing energy which cannot be recovered in the nozzle. Additional losses occur at the electrodes. Radiation losses also reduce the overall efficiency. The predominant losses, however, are those of dissociation and ionization. These cause the efficiency curve to have the general characteristics shown in Curve 2 of Fig. 10-17 which is for ammonia propellants.

[10-2.1.3] Ablative Thrusters

A variant of the arc jet is the ablative thruster in which a high intensity arc, usually a capacitor discharge, is used to produce gaseous propellant by ablation of a solid or liquid. The arc is used to heat the resulting gas which in a confined volume may reach 10 to 20,000° C. Propellants used are usually hydrocarbons or other compounds containing light elements. Energy losses of three kinds occur: heating of the walls (some of which provides the propellant generation), ionization losses (fairly high at these temperatures), and black body radiation from the hot gas. Efficiencies run from 10 to 20% in the I_{sp} range of 500 to 1000 seconds. Performance

is similar to arc jets with some advantage in the ability to provide small impulse increments (bits) in the pulsed mode operation which also permits low average power. Minimum power–to–thrust ratios run in the 100 to 150 KW/# range. These systems are compact and simple to implement.

[10-2.2] Electrostatic Thrusters

Electrostatic thrusters have three basic elements: a source of ions or other charged particles, an accelerator electrode which provides the electric field for accelerating the particles, and a neutralizer which is usually an electron emitter for providing a neutral exhaust beam. These elements along with the requisite power supplies are shown schematically in Fig. 10-7.
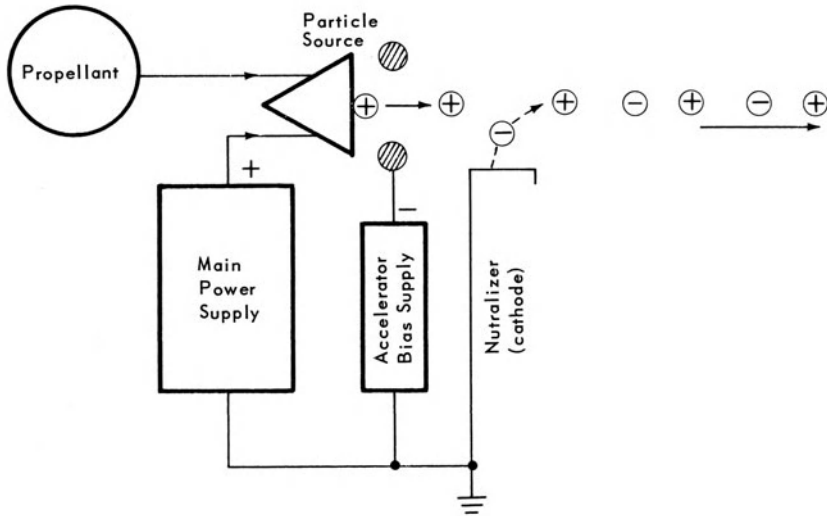
Fig. 10-7

Electrostatic thrusters are customarily classified according to the type of charged particle used and further by the method used to produce these particles. Thrusters using charged atoms such as Hg^+ or Cs^+ are called ion engines while those using charged aglomerates of many atoms or molecules are called colloid thrusters to indicate their microscopic but multiparticle nature. Three types of ion sources have had intensive development, high pressure arcs (plasmatrons), low pressure arcs (bombardment engines) and surface ionization (contact engines). Colloids have been generated by droplet condensation on ions in supersonic

nozzles, contact charging of micro-spheres and by electrostatic spraying. A basic consideration is of course how the desired velocities are to be achieved. The velocity of a charged particle of charge q and mass m accelerated through a potential V_0 is given by

$$v = \sqrt{\frac{2\,q}{m}}\; V_0 \qquad\qquad (10\text{--}36)$$

We see that the important characteristic of the particle is its charge-to-mass ratio q/m rather than the values of q or m. The relationship in Eq. (10-36) is plotted in Fig. 10-8 with q/m as the abscissa and particle velocity as ordinate with the accelerating potential V_0 as a parameter. Charge-to-mass ratio for singly ionized mercury and cesium atoms is indicated along with values that have been achieved in practice with colloids. It is seen that desirable velocities are reached in the 1 to 10 KV range for ions and in the 10 to 100 KV range for colloids.
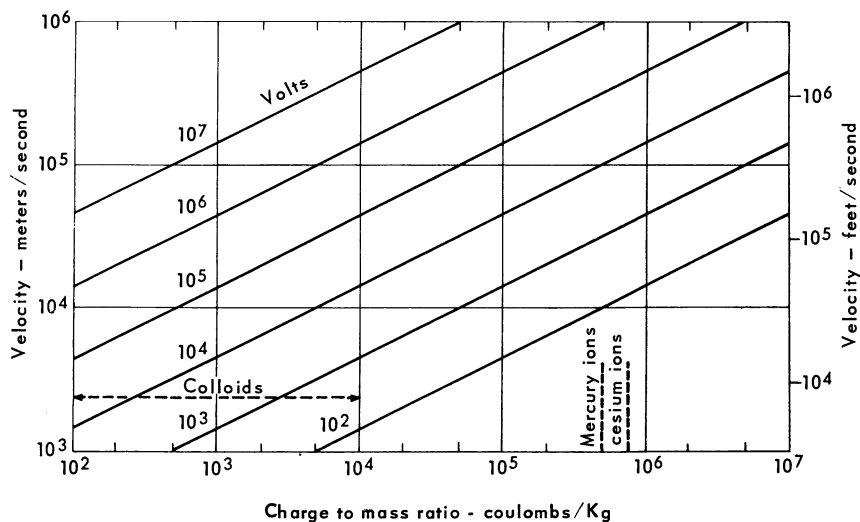
Fig. 10-8

[10-2.2.1] Ion Engines

[10-2.2.1.1] High Pressure Arcs (Duoplasmatron)

The principle ingredient of the duoplasmatron is a magnetically confined arc running at high pressure. Production of ions is quite efficient and very high current densities can be collimated through small apertures to provide an ion source for the accelerator.

The crucial difficulty in this approach is caused by a process called resonant charge exchange which turns out to be a dominant consideration in all ion engines conceived thus far. The problem arises because of the high probability that an ion in flight encountering a neutral atom will take away an electron and proceed on as a neutral atom leaving the stationary particle behind in the ionized state. The original ion is now neutral and proceeds in a straight line with whatever velocity it possessed at the time of the encounter. This velocity is not the desired one, and the particle may strike the accelerator which, in a proper design, the original ion would have missed. Similarly, the new ion will not acquire the full potential of the accelerator because it was created at a point in space having some intermediate potential. Its trajectory may also intersect the accelerator electrode. The loss of ions is not serious, but their impact with the accelerator can be disastrous. An ion having a velocity of the order of 50 KM/sec. striking a solid object may remove from 5 to 10 atoms of the target material by an erosion process called "sputtering." The seriousness of this effect can be appreciated by hypothesizing that 1% of the exhaust ions undergo charge exchange and that subsequent impacts on the accelerator remove (on the average) 5 atoms per impact. If these atoms are of comparable weights, every kilogram of propellant expelled will produce 10 grams of charge exchange ions which will remove 50 grams of electrode material. Under these conditions, a thruster operating at 0.1 lb. force for one year at an I_{sp} of 3000 seconds would eject 1000 pounds of propellant and would erode away 50 pounds of electrodes. This is many orders of magnitude more than can be tolerated in an ion engine.

The rate of production of charge exchange ions is proportional to the neutral gas density, the path length, and the ion current. The high pressure arc suffers particularly from charge exchange because of its high neutral gas density and small electrode size needed to produce high current densities. As a result, this approach has been largely abandoned as being efficient but having inadequate durability for the long missions characteristic of electric rocket applications.

[10-2.2.1.2] Contact Thrusters

The process of surface ionization was discovered by I. Langmuir [3] who found that alkali metals (Li, Na, K, Rb, Cs and Fr) absorbed on the hot surface of a high work function substrate such as tungsten were desorbed as ions under proper conditions. This phenomenon can be understood qualitatively by recognizing that the energy of the adsorbed atom's valence electron will be lower when it is in the Fermi band of the substrate than when it is

attached to its atom. This energy difference is the difference
between the work function of the substrate and the ionization
potential of the atom. Under these conditions, statistical equili-
brium greatly favors desorption of the atom in the ionized state
leaving the electron behind in the substrate. To obtain a high
percentage of ionization, it is desirable to have a large energy
difference. It is also desirable to hold the substrate at a high
temperature to provide the rapid desorption necessary for reason-
able ion fluxes from the surface. Cesium is a desirable propellant
because of its low ionization potential (3.8 volts) and its high mass,
and tungsten with its high work function (4.6 volts) and good
mechanical and refractory properties is a good substrate.

The ionizer then consists of a heated tungsten surface supplied
with cesium atoms which are thermally desorbed as ions and sub-
sequently accelerated by the electric field as shown in Fig. 10-9.
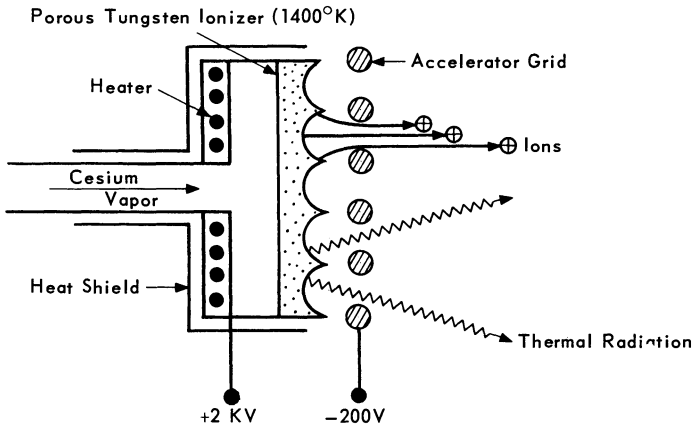
Fig. 10-9

Delivery of cesium atoms on the ionizer surface can be by several
means, but diffusion (as a gas) through a porous tungsten structure
is most common in practice. In this manner, ionization efficiencies
greater than 99% can be achieved at ion current densities of 15 to
20 ma/cm^2; thus propellant losses are insignificant in this type of
ion source. Similarly the loss of thrust through velocity dispersion
in the exhaust beam can be held to a few percent. The major
efficiency loss is through thermal radiation from the heated ionizer.
The temperature required to desorb ions at the rate of 20 ma/cm^2 is
about 1400° K, at which temperature the heat loss (for a 15 cm^2
ionizer, for instance) is about 10 watts/cm^2. This represents an
energy loss per ion formed of

$$E_{ion} = \frac{10 \text{ watts}/\text{cm}^2}{0.02 \text{ amps}/\text{cm}^2}$$

$$= 500 \text{ volts}$$

this despite the fact that the actual ionization energy for cesium is only 3.8 eV. Thus the energy efficiency of ion production is less than 1%.

Similar values are encountered in other ion sources. How serious is this energy loss? The electrical efficiency of an ion thruster can be written

$$\eta_\epsilon = \frac{V_0}{V_0 + E_{ion}} \tag{10-37}$$

where V_0 = the net acceleration potential.

E_{ion} = ionization energy in volts.

In other words, the loss of 500 eV per ion formed is the same as though the ion had fallen through 500 volts potential without acquiring any kinetic energy. A representative value of V_0 for a cesium ion is 2000 volts (I_s = 5500 seconds); then the electrical efficiency is 80% which is quite acceptable. However, if the mission is short (say, 1/2 year) and the power source (including power converters and controls) weighs 100#/KW, the desired I_{sp} is about half this or 2750 seconds, which requires a net accelerating potential of 500 volts, and the electrical efficiency drops to 50%. This is characteristic of all thrusters which display a fixed energy loss per particle which is typical of ion engines. A representative efficiency curve for a contact ion thruster with one- or two-year electrode life is shown in Curve 3 of Fig. 10-17. Since other losses are small, the rocket efficiency is essentially identical with the electrical efficiency in the contact thruster.

It is apparent that 500 ev/ion is a significant energy loss and that lower values would be preferred. One way this might be achieved is to raise the current density j in order to get more ions per unit heat loss. Raising the current density requires higher ionizer temperatures to desorb the ions, but a net gain results as seen in Fig. 10-10 which shows a typical relationship between current density and ionization energy loss for a porous tungsten emitter. The drawback to this approach is once more the problem of electrode erosion by ions formed by charge exchange. As stated before, the charge exchange rate is proportional to the product of the current density and the neutral particle density divided by the path length. Since the neutral density is proportional to the neutral fraction multiplied by the current, charge exchange increases as the square of the current density from this fact alone. Furthermore, it is found, for a number of reasons, that the neutral
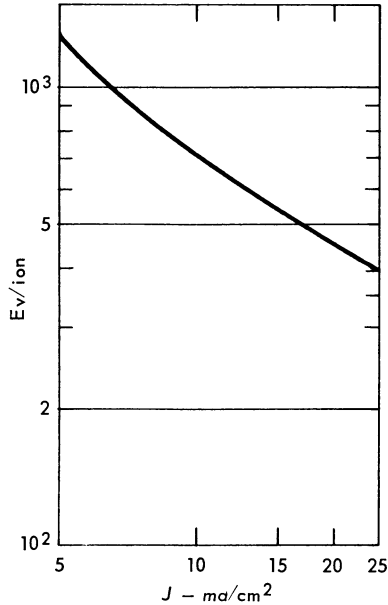
Fig. 10-10

fraction (percentage of neutrals) increases rapidly with current density. As a result, the charge exchange rate increases as the third to fourth power of the current density. These combined effects lead to an electrode life versus current density curve similar to that shown in Fig. 10-11. It is this tradeoff between life and ionization energy that limits the efficiency of contact ion engines.

The question then arises whether the electrodes can be made more massive in order to achieve greater durability. Here the problem of space charge limited flow enters in dictating the fundamental dimensions of the accelerating region. The relationship between current density, voltage and electrode spacing is given by Child's Law for space charge limited flow in a planer diode

$$J = \frac{\epsilon_0}{9\pi} \sqrt{\frac{2q}{m}} \frac{V^{2/3}}{X_0^2} \tag{10-38}$$

where J = current density

     q/m = charge-to-mass ratio of the particles

       V = accelerating potential

      X_0 = accelerating gap length.

Putting in typical values for a cesium ion engine, $J = 0.02$ A/cm^2, $V = 2000$ volts and $q/m = 7.5 \times 10^5$ coulombs/kg gives the required
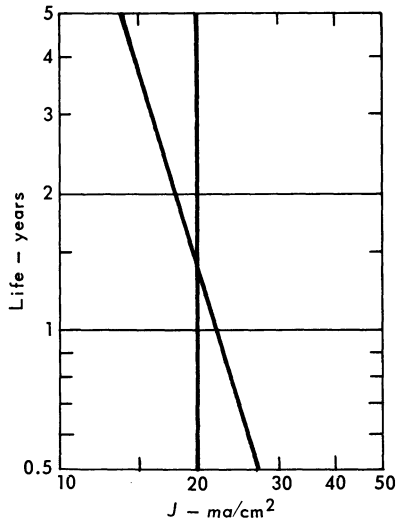
Fig. 10-11

accelerating gap as 0.15 cm or about 0.06". This is the maximum value of X_0 that can be used to obtain 20 ma/cm^2 of cesium ions at 2 KV potential.

In designing an ion accelerator, the dimensions of the electrode tend to be comparable to the accelerating distance X_0. Since X_0 is small, the mass of the electrode is small and only a small mass loss by erosion can be tolerated.

Attempts to increase electrode life by increasing the electrode dimensions run into fundamental difficulties. To make room for larger electrodes, the accelerating distance X_0 must be increased, which, in turn, requires higher potentials, V_0, to maintain the current density. The resulting excessive ion velocities are later offset by adding a second electrode with a retarding potential applied. This second electrode is referred to as a decelerating grid and the arrangement is called an "accel–decel" system. It has the advantage of permitting larger dimensions which simplify construction problems, but unfortunately the added electrode mass is more than offset by increased charge exchange erosion. This comes about in a number of ways. First the ion path length in the accelerating section is increased in proportion to the increase in electrode size. Since the charge exchange rate is proportional to the path length, the erosion rate tends to increase in proportion to the electrode size (mass). Furthermore, the higher potentials used increase the sputtering yield per ion impact causing additional material loss. Finally, additional charge exchange ions are formed in the decel–region and these also are drawn to the accelerating electrode where they produce even greater erosion. The net result

is a severe life penalty in accel-decel systems, and it is found in theory and practice that a simple accel system has the greatest possible durability. This leaves reduced neutral atom emission through improvement of ionizer materials and/or selection of sputtering resistant materials for electrodes as the primary avenues open for improvement of thruster life at a given current density. The alternatives are reduced heat losses by good thermal design, ionizer materials of low thermal emissivity, or lower operating temperatures as means for reducing the ionization energy at a given current density. Curve 3 of Fig. 10-17 is felt to be about the best that can be expected from the surface ionization approach without new innovations.

[10-2.2.1.3] The Bombardment Thruster

Bombardment thrusters are similar to contact thrusters except for the method used in the production of ions. In this engine type, ionization is produced in a magnetically constrained arc operating at low gas pressure ($\sim$10 torr). The bombardment thruster is shown schematically in Fig. 10-12. The arc consists of a cathode at the center of a cylindrical anode with an axial magnetic field imposed by a solenoid around the outside of the anode. Electrons leaving the central cathode are drawn radially toward the anode, but, because of the magnetic field, are caused to execute curved paths leading back to the cathode. Collisions with gas molecules interrupt these paths and permit the electrons to diffuse to the anode. In the process, many of the gas molecules are dissociated and ionized. The magnetic field may be thought of as a means of extending the electron trajectories in the gas without increasing
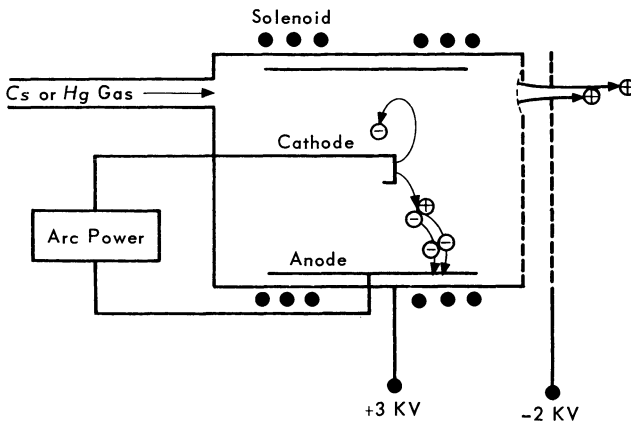
Fig. 10-12

the physical dimensions of the arc chamber. The ends of the arc chamber are at the same potential as the cathode, and the ions created by "electron bombardment" of the propellant gas are drawn to the cathode and the chamber ends. One of these ends called the screen is provided with a large number of holes from which ions may be drawn by applying an accelerating potential to a grid having a matching set of holes. The arc plasma behind the holes in the screen is perturbed by penetration of the accelerating field into the arc region. A concave sheath is formed which separates positive and negative particles and provides appropriate focussing action for launching the ions in the proper direction to prevent collisions with the accelerating electrode. Like the contact ion engine, the accelerator potential may be larger than is desired for the final ion velocity, and accel-decel systems may be employed.

By adjustment of the gas pressure and arc current, the percentage of gas ionized may be adjusted from low values to over 90%. The higher ionization levels are achieved at the expense of greater arc power which results in a greater expenditure of energy per ion created. Therefore, there is a trade off between high propellant utilization and high electrical efficiency. The main advantage of the bombardment engine is that the ionization energy, E_{ion}, is essentially independent of the ion current density. As a consequence, even though the neutral particle efflux may be from 5 to 20% of the ion beam, the charge exchange rate can be kept within acceptable limits (by reducing j) without a serious efficiency penalty. Fabrication of this type of thruster is relatively uncritical compared to the considerable care needed to make a contact ion thruster.

Disadvantages are lower thrust per unit area and greater thruster weight per unit thrust. Power conditioning and control is somewhat more complicated but not prohibitive.

Two types of propellant have been tested extensively: cesium and mercury. Cesium, because of its lower ionization potential, has a somewhat higher ionization efficiency and lower E_{ion}. However, some of this advantage is lost due to the lower net potentials, V_0, needed with the lighter (atomic weight 133) cesium ions to obtain desired I_{sp} values. Mercury is a more convenient propellant from the handling standpoint, but ionization is less efficient because of its higher ionization potential. Some benefit accrues from the higher potentials needed for the heavy (atomic weight 200) mercury ions. The greatest problem in the mercury bombardment thruster is the arc cathode which is slowly destroyed from "sputtering" by the Hg^+ ions in the arc. The cesium thruster avoids this problem by utilizing the low work function property of cesium to make a continuously replenished cathode fed by the propellant which subsequently is ionized and expelled in the usual way.

Bombardment thrusters tend to have constant ionization energy losses, and therefore their efficiency curves look much like those of the contact ion engine. A representative curve (Curve 4) for the cesium bombardment engine is shown in Fig. 10-17. Mercury bombardment engines are somewhat lower than the cesium bombardment engines. Both types of bombardment thrusters have undergone extensive operational testing and are ready for development as propulsion system elements.

[10-2.2.2] Colloid Thrusters

The discussion of electrical efficiency in ion engines pointed out the importance of keeping the energy per ion formed as low as possible. It was also noted that heavy ions could tolerate greater ionization energy losses than lighter ions because of the higher potentials needed to reach the desired velocities. Pursuing this idea farther, we can show that the real criterion in determining efficiency is not electron volts/ion but electron volts per unit mass of charged particles formed. This can be seen by rearranging Eq. (10-36) to find the potential needed to reach a velocity v, then

$$V_0 = \frac{m}{q} \frac{v^2}{2} \qquad (10\text{-}39)$$

Since the desired v is determined by other factors, only V_0 and the charge-to-mass ratio may be varied. The electrical efficiency equation may be written

$$\eta_\epsilon = \frac{1}{1 + \dfrac{E_{\text{ion}}}{V_0} \text{ (volts)}} \qquad (10\text{-}40)$$

$$= \frac{1}{1 + \dfrac{2 \, q \, E_{\text{ion}} \text{(volts)}}{m \, v^2}}$$

The term E_{ion} has been used loosely to mean both volts (potential) and electron volts (energy), with the tacit understanding that each ion had only one electronic charge. Here the charge on the mass m is q and the energy consumed in the charging process is $q \times E$ ion (volts). It is apparent that the real efficiency-determining factor for a desired factor for a desired value of v^2 is the term $q \, E_{\text{ion}}/m$ or electron-volts/mass as stated at the outset. This

observation makes it clear that heavier charged particles with lower charge-to-mass ratios would be desirable if the charging losses could be kept comparable to those of ions.

One method of forming small charged particles is by a process called electrostatic spraying. Historically this phenomenon was observed early in the experimentation with high voltage electricity from electrostatic generators. Lord Rayleigh computed the relationship between droplet size and charge-to-mass ratio which has been confirmed experimentally over a wide range of sizes. In the low q/m regime, the process is presently used commercially in the electrostatic spraying of paint.

Electrostatic spraying occurs when the surface of a conducting liquid is exposed to a strong electric field produced by an accelerator electrode, for example. The presence of this field causes charges to accumulate at the surface, and the liquid surface is attracted toward the accelerator. The situation is unstable, since any unevenness in the surface will cause the charges to concentrate at the point nearest the accelerator, and additional force is applied to this region. The result is a tendency for the surface to break up into a number of jets of charged fluid which fly off under the influence of the field. These jets, in turn, are unstable and eventually break up into small charged droplets.

A more precise (and elegant) description of the process results if it is recognized that the surface charge represents a negative surface energy which opposes the surface tension of the fluid. In sufficiently high fields, this energy becomes greater than the surface tension energy, and the fluid proceeds to generate the maximum surface possible by breaking up into a large number of small droplets. As the jets are accelerated away from the fluid, no additional charges can flow into it, and the amount of available charge reaches a fixed value per unit mass. The breakup process stops when the total surface generated is large enough to accommodate these charges with a net excess of surface tension over electrostatic pressure. It is this limiting size that Rayleigh calculated as a function of the charge-per-unit mass. In practice, these droplets turn out to be of the order of 100 molecules in diameter; hence, the name colloid.

Figure 10-13a shows a typical electric spray needle for use in a colloid thruster. It consists of a capillary needle held at high potential and supplied with a propellant composed of glycerol which has been made conducting by the addition of sodium iodide. An annular extractor electrode surrounds the needle tip to provide the field for the spraying process. In situations where a low I_{sp} is acceptable, no further acceleration is needed, and a needle becomes a thruster with a thrust of 2 to 3 micropounds. Arrays of many needles can be used to develop thrusts of a few hundred micropounds. This thrust range is suitable for satellite stationkeeping or orbit adjustment. Higher thrusts and higher I_{sp} can
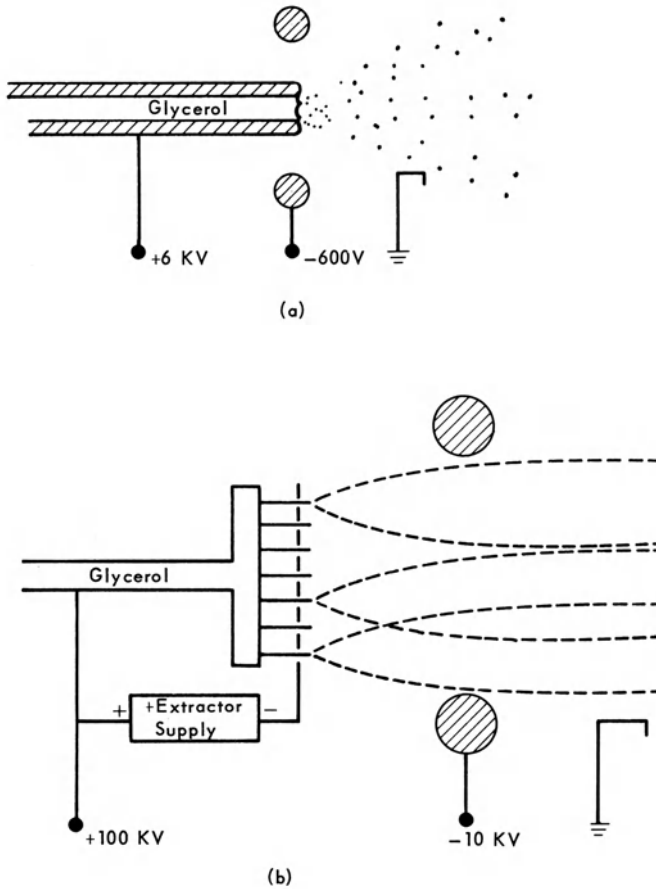
Fig. 10-13 (a) Basic needle geometry; (b) post-acceleration configuration.

be obtained by adding additional acceleration voltages to other electrodes downstream from the extractor. In this case, the needle array serves primarily as a particle generator rather than a thruster.

The efficiency of these thrusters is quite high. There are no hot ionizers to radiate heat or arcs to consume power, and virtually no propellant is wasted. There is, however, a loss due to velocity dispersion which has been mentioned before but not explained. This loss comes about because not all particles have the same velocity due to variations in charge–to–mass ratio of the droplets. This can be recognized as an efficiency loss by the following example.

Imagine a thruster expelling mass at a rate $\dot{m}$ and a velocity v_0 which is the same for all of the propellant ejected. If we hold the

thrust constant and $\dot{m}$ constant (constant I_{sp}) but allow part of $\dot{m}$ to be expelled at a higher velocity than v_0, part must be expelled at a lower velocity than v_0.

The power required will be proportional to the square of the new velocities, and although the lower velocity portion uses less power, the high velocity portion will take even more power, and a net increase in power will result with no increase in thrust or I_{sp}.

Equations can be derived which show that the velocity dispersion efficiency can be written as

$$\eta_d = \frac{\overline{(v \cos \theta)^2}}{\overline{v^2}} \tag{10-41}$$

which, if the velocity dispersion is independent of angle, can be separated into two components:

$$\eta_d = \frac{\overline{v}^2}{\overline{v^2}} \ \overline{\cos \theta^2}. \tag{10-42}$$

Note that the velocity term is the square of the ratio of average velocity to rms velocity.

In the electrostatic spraying process, the distribution of particle sizes (and, hence, charge-to-mass ratio) leads to efficiencies in the range of 60 to 90%, with 75% being a representative figure. This is the major efficiency loss in the colloid thruster. Other losses are beam spreading and neutralizer power which are similar to those for ion engines. A representative efficiency curve for a small colloid thruster is shown in Curve 5 of Fig. (10-17).

[10-2.3] Plasma Thrusters

Plasma thrusters depend on interaction between magnetic fields and currents in highly ionized gases or plasmas. Negative (electron) and positive ions are accelerated together, and the problems are similar to those of motors using conducting solids or liquids which are, in fact, plasmas.

Interest in plasma thrusters arises from several considerations. First, there is no neutralization problem since both positive and negative charges are accelerated in equal amounts to produce a completely neutral exhaust stream. Second, the thrust densities available are higher than in electrostatic devices. This is apparent from evaluation of electrostatic and magnetic pressures. Both types of fields can be properly treated as having pressures given by

$$p = \frac{\epsilon E^2}{2} = \frac{B^2}{2\mu} \tag{10-43}$$

A pressure of one atmosphere ($14.7\#/in^2$ or $1\,kgf/cm^2$) requires $E = 1.5 \times 10^6\ V/cm$ and $B = 5 \times 10^3$ gauss. Production of kilogauss magnetic fields is feasible, but electric fields of megavolts/cm are very difficult because of field emission from points, photo-electron currents and vacuum breakdown which may involve both of these. Electrostatic thrusters typically operate at thrust pressures of 10^{-4} atmospheres or less.

The power represented by a pressure of one atmosphere resulting from an exhaust jet having a velocity of 5×10^4 meters per seconds is

$$P = \frac{1\ kgf}{cm^2}\ \frac{5 \times 10^4\ meters/sec}{2}$$

(10-44)

$$\cong 250\ kw/cm^2\ .$$

Obviously a thruster would need to be small in size or extremely high-powered. More practically, the magnetic pressure would be reduced to more manageable values to permit larger dimensions and lower power. There is a limit to this approach set by operating characteristics of plasma devices which tend to be more efficient at higher fields. Another way to reduce average power levels is to operate the thrusters in a pulsed mode so that peak power can be efficiently high but average power can be kept low. Pulsing is usually done by discharging capacitors in a very short time (microseconds) to obtain the needed power peaks.

[10-2.3.1] $j \times B$ Machines

In a magnetic field, the force on a current-carrying element is given by the vector cross-product of the field strength and the current. This principle is used in electric motors and in magnetic coils for "blowing out" arcs in circuit breakers. A simple device called the "rail gun" using this principle is shown in Fig. 10-14.
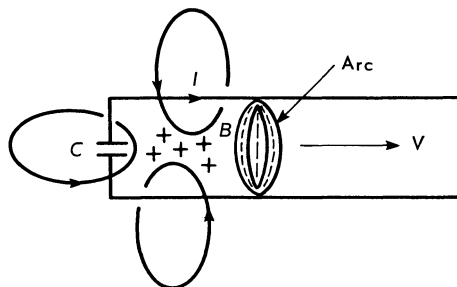
Fig. 10-14

A capacitor C is discharged through an arc in a gas between two conductors or rails. The discharge current flowing through the closed loop produces a magnetic field B which generates a magnetic pressure $B^2/2\mu$ inside the loop.

This pressure is exerted against the conductors and against the plasma column present in the arc. As a result, the arc is accelerated to the right, and velocity is imparted to the plasma. Some heat losses occur at the electrodes, and of course energy of ionization is not recovered as kinetic energy. More serious is the fact that not much of the gas in which the arc moves is converted to high velocity plasma. This propellant loss can be diminished by using a coaxial configuration where the outer rail completely surrounds the central rail and by introducing propellant in puffs so that the propellant is localized around the current sheet in the co-ax. All of these measures are helpful, and reasonable efficiency can be obtained but not high enough to be attractive as a thrust device.

[10-2.3.2] MPD Arcs

The magneto-plasma-dynamic arc grew out of work on arc jets. In the course of trying to improve arc jet performance, it was found that higher efficiencies and higher I_{sp} values were obtained at low values of propellant flow, *i.e.*, with the arc starved for propellant. It was deduced that the plasma was being driven by magnetic fields generated by the currents in the arc, and the geometry was changed to maximize this effect as shown in Fig. 10-15.
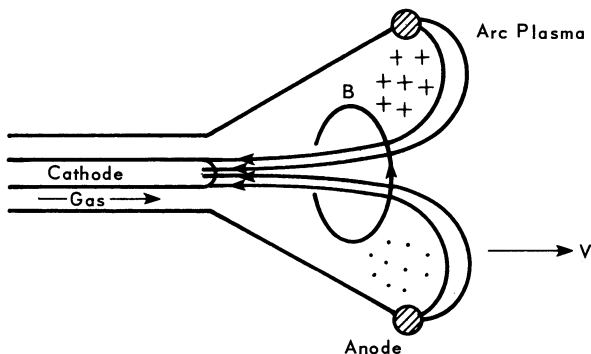
Fig. 10-15

The current from the ring anode to the control cathode produces an azimuthal (ring) field B which exerts a magnetic pressure

against the arc plasma. This action is similar to the rail gun except that the arc is stationary. Propellant from the nozzle flows through the arc where it is ionized and blown away by the magnetic field. Some controversy over the efficiency of these devices exists because of the difficulty of making the necessary measurements (a problem common to all plasma thrust devices), but the most believable, in the author's view, give a curve similar to that shown in Curve 6 of Fig. 10-17. Some workers believe the efficiency is twice that shown.

[10-2.3.3] Pulsed Inductive Accelerators

The conductivity of a fully ionized gas is high enough to resist the intrusion of a rapidly changing magnetic field by setting up induced currents which oppose the field in much the same way that good conductors, such as copper, oppose penetration of rapidly changing fields. This principle can be used to accelerate an ionized gas or plasma in an arrangement illustrated in Fig. 10-16.
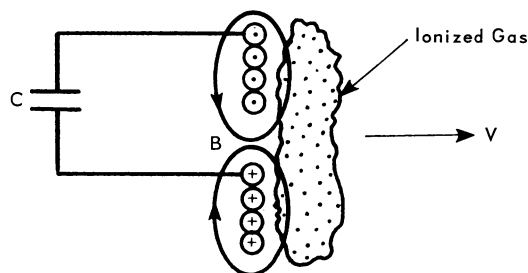
Fig. 10-16

A capacitor is discharged through a flat spiral coil to produce a rapidly rising magnetic field B. Currents (ions and electrons) in the ionized gas in front of the coil confine the field to a thin layer between the coil and the gas and a magnetic pressure develops which accelerates the plasma. Problems with this concept are related to obtaining good coupling between the field and the plasma so that efficient energy transfer can be obtained. Ionization losses cannot be recovered, and residual magnetic fields after the pushing stroke represent lost energy. Advantages are lack of electrodes with their attendant life problems and low losses in the driving coil so that heating is not a serious problem. Efficiencies of over 50% are calculated but remain to be demonstrated.
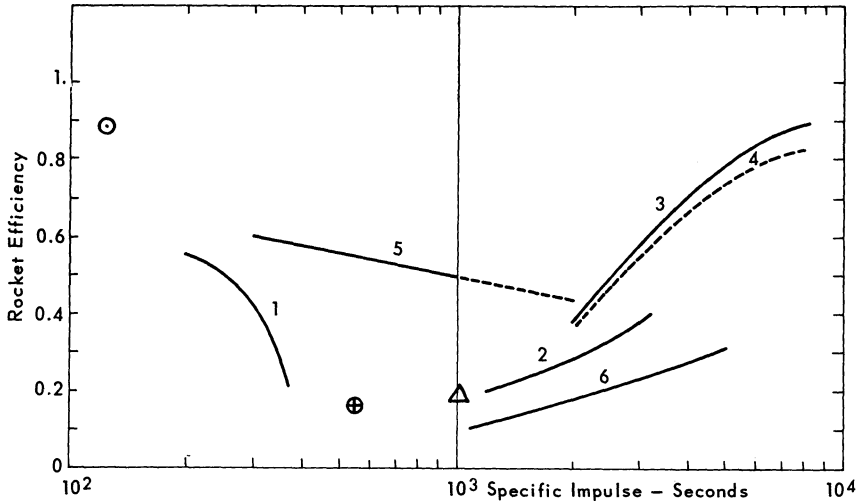
Fig. 10-17 Thruster efficiency curves. (1) NH_3 resistojet (TRW); (2) NH_3 arc jet (Avco); (3) Cs contact (TRW); (4) Cs bombardment (EOS); (5) Colloid (TRW); (6) MPD arc (G.D.); ⊙ : N_2 resistojet (Vela) (TRW); ⊕ : Solid ablative (TRW); △ : Liquid ablative (GE).

[10-3] STATE OF THE ART AND FUTURE TRENDS

Development of efficient electric thrusters has progressed rapidly during the last few years. Performance projections which were considered over-optimistic a few years ago have been met and exceeded almost without exception. At the same time, the weight of solar arrays has been decreasing while the maximum feasible size has increased to the power range needed for electrically propelled spacecraft. Solar arrays of 50 #/kw are under development at the present time. Power converters and controls for operating thrusters from these sources can be built for not more than 25 #/kw and perhaps half this figure. Analysis of missions that can be performed under these conditions shows a number of attractive possibilities such as solar probes, out-of-the-ecliptic missions, asteroid belt explorations, Jupiter probes, and perhaps the "grand tour" to the outer planets using a Jupiter swingby. Ion engines suitable for these primary thrust applications have undergone flight demonstration tests of short duration (by both NASA and USAF) and extended ground testing approaching one year of continuous operation. An orbital test program leading to six months or more of thruster operation at the 1 kw level is presently in progress under NASA sponsorship. At the present time, it is clear that although improvements are to be expected and newer concepts may replace those presently favored, good electric thrusters are available for space missions. The problems remaining are principally those of spacecraft engineering and system integration.

In auxiliary propulsion (attitude control, station keeping, orbit adjustment), there is a growing demand for more total impulse capability to permit longer mission life. Cold gas systems which have been used widely are often the limiting element on long-lived satellites. On existing satellites, electric power may be available in some cases by virtue of solar array overdesign or by using off-peak power that might otherwise be wasted. In new designs, additional solar array area may be added to accommodate higher performance thrusters. Because power is often limited, systems are not always optimized, and thrusters in the low I_{sp} range may be favored even at lower efficiency because of their power economy.

The electrothermal thrusters have established their value and reliability in actual missions. Since these represent the least departure from cold gas systems, many applications are indicated in the near future. Ion engines in the low-thrust range have most of the characteristics of the larger versions (except for somewhat lower efficiency), and programs leading to flight-proven hardware are currently underway. A small colloid thruster is scheduled to be tested in a flight experiment to demonstrate the utility of this concept.

It appears that applications of auxiliary electric propulsion to working satellites will become state of the art about 1970 and that a space demonstration of a complete electric-propelled vehicle could occur as early as 1972. The future of electric propulsion depends not only on technical achievements but also on long range plans for the exploration of space which are still in their formative stages.

[10-3.1] Sample Problem 1

A solar-electric vehicle is planned for a Venus probe. The power plant output averaged between earth and Venus is 30 watts per pound.

(a) Estimate the optimum I_{sp} for the mission. Since mission time τ is not specified, we will estimate that the orbital transfer will require about half the mean period of the two planets, or about 0.4 earth years (1.2×10^7 sec.). The power plant specific weight is

$$\alpha = \frac{1000 \text{ watts/KW}}{30 \text{ watts/lb. } 2.2 \text{ lb./Kg}} \cong 15 \text{ Kg/KW (MKS units)}$$

then

$$V_c = \sqrt{\frac{2\tau}{\alpha}} = \sqrt{\frac{2 \times 1.2 \times 10^7 \text{ sec } 1000 \text{ w/Kw}}{15 \text{ Kg/Kw}}}$$

Note that watt sec. = joules = Kg m^2/sec.^{2}

$$V_c = \sqrt{\frac{2.4 \times 10^{10}}{15} \frac{m^2}{sec^2}} = 4 \times 10^4 \text{ meters/second}$$

then the estimated optimum exhaust velocity is

$$V_{opt} \cong 0.7 \, V_c = 2.8 \times 10^4 \text{ meters/second}$$

and since

$$I_{sp} = V/g \text{ the optimum } I_{sp} \text{ is}$$

$$I_{sp_{(opt)}} = \frac{2.8 \times 10^4 \text{ meters/second}}{9.8 \text{ meters/sec}^2} \cong \underline{2850} \text{ seconds.}$$

Repeating in engineering units

$$\alpha = \frac{1000 \text{ watts/Kw}}{30 \text{ watts/lb. } 32.2 \text{ lb./slug}} = 1.03 \text{ slugs/Kw}$$

$$\tau = 1.2 \times 10^7 \text{ sec (as before)}$$

$$V_c = \sqrt{\frac{2.4 \times 10^7 \text{ sec}}{1.03 \text{ slugs/Kw}}}$$

Note that 1 Kw sec. = 737 ft lbf

$$1 \text{ lbf} = \text{slug ft/sec}^2$$

$$V_c = \sqrt{\frac{2.4 \times 10^7 \times 737}{1.03} \frac{ft^2}{sec^2}} = 1.31 \times 10^5 \text{ ft/sec}$$

then

$$V_{opt} \cong 0.7 \, V_c = 9.2 \times 10^4 \text{ ft/sec}$$

and

$$I_{sp_{(opt)}} = \frac{V_{opt}}{g} = 2850 \text{ seconds}$$

(b) Assuming the rocket efficiency of 50% at 2850 seconds, what is the maximum thrust that can be obtained from a 25 KW solar array? From the empirical equation for the power-to-thrust ratio,

$$F = \frac{\eta_R P}{22 \text{ watts}/\text{lbf } I_{sp}}$$

$$= \frac{0.5 \times 2.5 \times 10^4 \text{ watts}}{22 \text{ watts}/\text{lbf } 2850}$$

$$= 0.206 \text{ lbf}$$

(c) What is the total impulse delivered in 0.4 year?

$$I = Ft.$$

$$= 0.2066 \times 1.2 \times 10^7 \text{ sec.}$$

$$\cong 2.5 \times 10^6 \text{ lb-sec}$$

(d) What is the initial propellant weight?

$$W_p = \frac{I}{I_{sp}} = \frac{2.5 \times 10^6 \text{ lbf sec}}{2850 \text{ sec}}$$

$$= 876 \text{ lb}$$

(e) What is the power plant weight?

$$W_p = \alpha P$$

$$= 33 \text{ lb}/\text{KW} \times 25 \text{ KW}$$

$$= 830 \text{ lb}$$

(f) Estimating that the vehicle weight including payload and structure is initially 2000 pounds, what is the initial acceleration?

$$a_i = \frac{F}{W_i} = \frac{0.2 \text{ lb}}{2 \times 10^3 \text{ lb}} = 10^{-4} g\text{'s}$$

(g) Compare the result of f with the approximate formula given in the text.

$$a_i = \frac{1}{\sqrt{2 \alpha \tau}}$$

$$= \frac{1}{\sqrt{2 \times 1.03 \text{ slugs}/\text{KW } 1.2 \times 10^7 \text{ sec}}}$$

$$= \sqrt{\frac{2.4 \times 10^7 \text{ sec } 1.03 \text{ slugs}}{737 \text{ ft lb/sec}}}$$

$$= \frac{1}{\sqrt{3.38 \times 10^4 \text{ sec}^4/\text{ft}^2}}$$

$$a_i = 5.44 \times 10^{-3} \text{ ft/sec}^2$$

or

$$a_i = \frac{5.44 \times 10^{-3} \text{ ft/sec}^2}{32.2 \text{ ft/sec}^2} = 1.7 \times 10^{-4} \text{ g's}$$

(h) **Explain the difference between** f **and** g. The difference between f and g arises from the inclusion of 294 lb. of structure and payload and the rocket efficiency η_R of 0.5. Note that the thrust is proportional to $\sqrt{\eta_R}$. Then correcting result g for these factors gives

$$a_i = 1.7 \times 10^{-4} \text{ g's } \frac{1706 \text{ lb}}{2000 \text{ lb}} \sqrt{0.5}$$

$$= 1.02 \times 10^{-4} \text{ g's Q.E.D.}$$

[10-3.2] Sample Problem 2

A satellite auxiliary propulsion system has an operating life of 3 years at 10^{-4} pounds thrust. Available power from a solar array is limited to 5 watts. Assume that 1 watt is needed for the neutralizer and controls. Estimate the performance of a colloid thruster in this application.

(a) **What** I_{sp} **should be used?** The thruster efficiency will be about 0.7 and power conversion efficiency (high voltage supplies) will also be about 0.7 in the small sizes (possibly lower). The overall efficiency is therefore ~0.5. Then

$$I_{sp} = \frac{P}{F} \frac{\eta_R}{22}$$

$$I_{sp} = \frac{4\text{w} \times 0.5}{10^{-4} \text{ lbf } 22 \text{ w/lbf sec}} = 910 \text{ seconds.}$$

(b) What is the total impulse delivered (allowing ~5% margin)?

$$I = 10^{-4} \text{ lbf} \times 10^8 \text{ seconds}$$

$$\cong 10^4 \text{ lbf-seconds}$$

(c) What is the propellant weight?

$$W_p = \frac{I}{I_{sp}} = \frac{10^4 \text{ lbf sec}}{910 \text{ sec}} = 11 \text{ lbs}$$

(d) If the dry system weight is six pounds and power is not chargeable to the system, what is the system effectiveness?

$$\text{Eff} = \frac{I}{W_0} = \frac{10^4 \text{ lbf sec}}{(11 + 6) \text{ lbf}} = 590 \text{ lb sec/lb}$$

(e) If the solar array weighs 3 pounds and was added specifically for this purpose (chargeable weight), what is the effectiveness?

$$\text{Eff} = \frac{10^4 \text{ lb sec}}{(11 + 6 + 3) \text{ lb}} = 500 \text{ lb sec/lb}$$

(f) Find the effectiveness for a six-month mission including power weight. The total impulse will be $\dfrac{10^4 \times 1/2 \text{ Yr}}{3 \text{ Yr}} = 1.67 \times 10^3 \text{ lbf sec.}$

The propellant weight is $\dfrac{1.67 \times 10^3 \text{ lbf-sec}}{910 \text{ sec}} = 1.83 \text{ lb.}$

$$\text{Effectiveness} = \frac{1.67 \times 10^3 \text{ lb sec}}{(1.83 \times 6 \times 3) \text{ lb}} = 154 \text{ lb sec/lb.}$$

(g) Find the effectiveness for a 5-year mission.

$$I = 10^{-4} \text{ lb} \times 5 \times 3.15 \times 10^7 \text{ sec} = 1.58 \times 10^4 \text{ sec}$$

$$W_p = \frac{1.58 \times 10^4}{910} = 17.4 \text{ lb}$$

$$\text{Eff} = \frac{1.58 \times 10^4 \text{ lbf sec}}{(17.4 + 6 + 3) \text{ lbf}} = 600 \text{ lb sec/lb}$$

[10-3.3] Sample Problem 3

A thrust device produces 0.1 lbf for one hour at a power of 2 Kw. Propellant consumption was 1 lb.

(a) What is the specific impulse?

$$I_{sp} = \frac{F}{\overline{W}} = \frac{0.1 \text{ lbf} \times 3600 \text{ sec}}{1 \text{ lbf}} = 360 \text{ seconds}$$

(b) What is the rocket efficiency?

$$\eta_R = \frac{F I_s g}{2P}$$

$$= \frac{0.1 \text{ lbf} \times 360 \text{ sec} \times 32.2 \text{ ft/sec}^2}{2 \times \text{Kw } 737 \text{ ft lb/sec Kw}} = 0.392$$

or

$$\eta_R = 39.2\%$$

REFERENCES

1. Seifert, H.S.(ed.): Space Technology, New York, John Wiley & Sons, Inc., Chaps. 9 and 10 (D.B. Langmuir).
2. Stuhlinger, E.: Ion Propulsion for Space Flight, New York, McGraw-Hill Book Co., 1964.
3. Suits, Guy (ed.): The Collected Works of Irving Langmuir, Pergamon Press, 1961.
4. Stuhlinger, E.: Electric Propulsion Development, AIAA Vol. 9, 1962.
5. Stuhlinger, E., D.B. Langmuir, and J.M. Sellen, Jr.: Electrostatic Propulsion, ARS Series, Vol. 5, 1960.
6. Snyder, N.W.: Space Power Systems, ARS Vol. 4, 1960.

Ion Propulsion

R. H. Boden
Senior Staff Scientist, Rocketdyne Division
North American Rockwell Corp.

[11-1] INTRODUCTION

Concepts of electrical power plant systems are varied, both from the system standpoint and in the use of components. Basically, the electrical rocket engine has three important subsystems: the energy source, the power convertor, and the electrical thrust devices, Fig. 11-1.
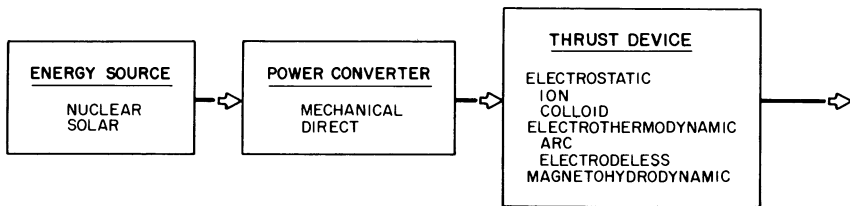
Fig. 11-1 Basic subsystems of electrical rocket engine.

Electrical thrust chambers have a variety of forms. The electrothermodynamic thrust chamber, variously described as the arc or plasma jet, uses electrical energy for heating the propellant gas, which in turn is expanded through a de Laval nozzle to generate thrust in the same manner as a chemical rocket. Other devices generate a plasma which may be accelerated by external, or induced, electromagnetic fields. Ions can be extracted from the plasma or formed directly by surface contact phenomena and then accelerated electrostatically. This is the ion rocket engine. Substitution of charged colloid particles for ions offers the potential advantages of low specific impulse to the electrostatic ion rocket. The concepts embodied in the electrical thrust chambers are as varied as those in the power conversion systems.

The purposes of this discussion are, first, to evaluate the technical and scientific status of present ion propulsion work;

second, to evaluate and predict the technical possibilities and growth potential of ion propulsion; and third, to summarize the advantages and needs on the basis of mission requirements and expected general advancement of space technology.

[11-2] FUNDAMENTALS

A number of fundamental relationships govern the behavior of electrical propulsion systems and the vehicles in which they are installed. Before considering the current status of electrical propulsion systems, a brief review of these basic relationships will serve to clarify the development objectives now being explored in this field. The power plants to be considered are reaction-type engines that generate thrust by the ordered expulsion of energetic, charged particles from the engine.

The propellant of an electrical rocket from which the energetic particles are obtained is first raised to an intermediate energy level by direct heating or applications of electrical power. With one exception, this intermediate-level working fluid is a plasma, a homogeneous gaseous mixture of electrons, ions, and neutral particles. If no neutrals are present, the plasma is defined as being ideal. The gas as a whole is electrically neutral. The plasma is similar to a metal in its properties, since the ions and the detached electrons remain uncombined for relatively long periods and can move about at random within the boundaries of the gas volume.

The exception is the working fluid of the surface-contact ion engine. In this case, the propellant is evaporated from a metallic plate as an ion gas, leaving the electrons behind in the metal. The ions have little excess energy on leaving the surface of the plate.

In either case, plasma or evaporated ions, electromagnetic fields can react on the charged particles to energize them to very high levels and direct the flow to product thrust.

Electrical power is required to carry out this energizing process. The thrust, F, and the gross power, P_g, that must be generated in the vehicle, are the significant variables of primary interest to the engineer and scientist engaged in space power plant projects. The basic analyses presented here emphasize these two primary factors. The analyses of the system are obtained from consideration of Newton's laws of motion.

The thrust for the case of many kinds of particles being ejected from the electrical rocket engine is

$$F = Mg\, G = \sum \dot{N}_i M_i C_i \tag{11-1}$$

in which the subscript i refers to the particular species of particle: ion, electron, or charged colloid.

The power that is converted into directed energy flow to produce thrust is expressed by the relation,

$$P = 1/2 \sum \dot{N}_i M_i C_i^2 = \eta P_g \qquad (11\text{-}2)$$

The gross vehicle powers, P_g and P, are related by the engine efficiency, η. The design parameters for low-thrust electrical rocket engines derived from these relations are summarized in Table 11-1.

Table 11-1   Summary of Performance Parameters, Electrical Rocket Engines

Parameter	English System	CGS System
Specific Power	$\dfrac{P_g}{M_g} = \dfrac{21.8\, GI_s}{\eta}$ watts/lb	$\dfrac{P_g}{M} = \dfrac{4.91 \times 10^{-5}\, A\, I_s}{\eta}$ watts/gm
	$\dfrac{P_g}{M_g} = \dfrac{0.0293 GI_s}{\eta}$ hp/lb	
Power per Unit Thrust	$\dfrac{P_g}{F} = \dfrac{21.8\, I_s}{\eta}$ watts/lb	$\dfrac{P_g}{F} = \dfrac{4.91 \times 10^{-5}\, I_s}{\eta}$ watts/dyne
	$\dfrac{P_g}{F} = \dfrac{0.0293\, I_s}{\eta}$ hp/lb	
Exhaust Velocity	C ft/sec	C cm/sec
Propellant Flow Rate per Unit Thrust	$\dfrac{M}{F} = 1/I_s$ sec^{-1}	$\dfrac{M}{F} = \dfrac{1}{980\, I_s}$ sec^{-1}
Specific Impulse	$I_s = \dfrac{C}{32.2}$ sec	$I_s = \dfrac{C}{980}$ sec
	$t = \dfrac{1-\exp\!\left(\dfrac{-\triangle v}{32.2 I_s}\right)}{G} I_s$ sec	$t = \dfrac{1-\exp\!\left(\dfrac{-\triangle v}{980 I_s}\right)}{G} I_s$ sec

[11-2.1] Performance Analysis

[11-2.1.1] Characteristic Velocity

Application of an electrical rocket engine requires a knowledge of the mission. Mission analyses for rocket-powered vehicles have been topics of investigation for many scientists and engineers

in recent months. References 3 through 9 cover a variety of methods for investigating low-thrust space travel.

The critical variable to be determined from mission analyses, and which affects the application of the propulsion system, is the characteristic velocity, Δv. This variable is the change in velocity of the vehicle in free space from the engine thrust program. After the characteristic velocity has been determined from a mission analysis, the specific impulse, or net exhaust velocity, and operating time of the rocket engine can be estimated.

Equation (11-3) is integrated to determine the characteristic velocity:

$$\Delta v = \int_{t0}^{t} a\,dt = \int_{t0}^{t} \frac{\dot{N}_i m_i C_i}{M_g - N_i m_i t}\,dt \tag{11-3}$$

When this operation is performed, the characteristic velocity is given in the form familiar to the engineer working in the rocket field:

$$\Delta v = C \ln \frac{M_g}{M} \tag{11-4}$$

M_g is the gross weight of the vehicle, and M is the weight at termination of the engine thrust program.

If a controlled flight is visualized as a series of changes under constant thrust from one orbit to another, the total characteristic velocity required is the sum of the characteristic velocities for each maneuver.

$$\Delta v \text{ total} = C \ln \frac{M_g}{M_1} + C \ln \frac{M_1}{M_2} + C \ln \frac{M_2}{M_3} + \cdots C \ln \frac{M_{n-1}}{M_n}$$

$$= C \ln \frac{M_g}{M_n} \tag{11-5}$$

In this equation, M_1 and $M_2 \ldots M_n$ are the vehicle weights at the end of the first, second. . .and n'th maneuvers. M_n is the empty weight of the vehicle, all the propellant being expended.

The exhaust velocity, C, is defined by the ratio

$$C = \frac{\sum \dot{N}_i m_i C_i}{\sum N_i m_i} \tag{11-6}$$

When C is divided by the gravitational constant, g, the specific impulse is obtained. The specific impulse is a convenient parameter

for discussion of electrical powerplants because it has the same numerical value in both English and metric units. For this reason, much of the discussion of this paper will relate the engine and vehicle parameters to the specific impulse.

[11-2.1.2] Payload

Once the characteristic velocity for a mission has been specified, the power plant specialist can predict the maximum payload which the vehicle can carry on the mission. The gross weight of the vehicle includes the payload weight, M_x, the propellant weight, M_p, and the power plant section weight, M_e. The power plant section weight includes the weight of the power plant, vehicle structure, and the tanks for the propellant. In practice, this weight is found to be proportional within close limits to the total power of the vehicle, P_g.

$$M_e = \alpha P_g \text{ lb.} \qquad (11\text{-}7)$$

The proportionality factor, α, is expressed in pounds/weight of vehicle per horsepower, the reciprocal of the specific power.

The power plant generates power for guidance, controls, communications and other demands of the vehicle, including power losses attendant to the generation of thrust in addition to that poured into the exhaust jet. In terms of the characteristic velocity of the mission, Δv, and the specific impulse of the engine, the gross power requirements are:

$$P_g = \frac{\dot{M} C^2}{1100 \, \eta} = \frac{\Delta v \, F}{1100\eta \, \ln\left(1 - \dfrac{Gt}{I_s}\right)} \text{HP.} \qquad (11\text{-}8)$$

in which η is the function of the total electrical power transmitted to the jet.

From these relations and the characteristic velocity, the ratio of the payload weight to the gross weight of the vehicle,

$$\frac{M_x}{M_g} = 1 - \frac{M_e + M_p}{M_g} \qquad (11\text{-}9)$$

becomes

$$\frac{M_x}{M_g} = 1 + \frac{9.10 \times 10^{-4} \, \Delta v \, G\alpha}{\eta \, \ln\left(1 + \dfrac{Gt}{I_s}\right)} - \frac{Gt}{I_s} \qquad (11\text{-}10)$$

in which G is the thrust-to-weight ratio of the vehicle. The payload ratio increases rapidly with specific impulse, exhibits a relatively flat maximum, then decreases more slowly with specific impulse greater than the value for maximum payload, Fig. 11-2. The data of Fig. 11-2 are for traveling from a 100-mile satellite orbit to the moon's orbit. In selecting a specific impulse for a particular design, a slightly high value is desirable to prevent a possible drop in efficiency of the power plant over a long operating period.

[11-2.1.3] Specific Power

The vehicle performance depends upon the specific weight, α/η, of the power plant section of the vehicle and the thrust-to-weight ratio of the vehicle. As shown in Fig. 11-2, increasing the specific weight decreases the payload weight, shifts the optimum specific impulse, and makes the payload become increasingly sensitive to engine operation at specific impulses above the optimum values.
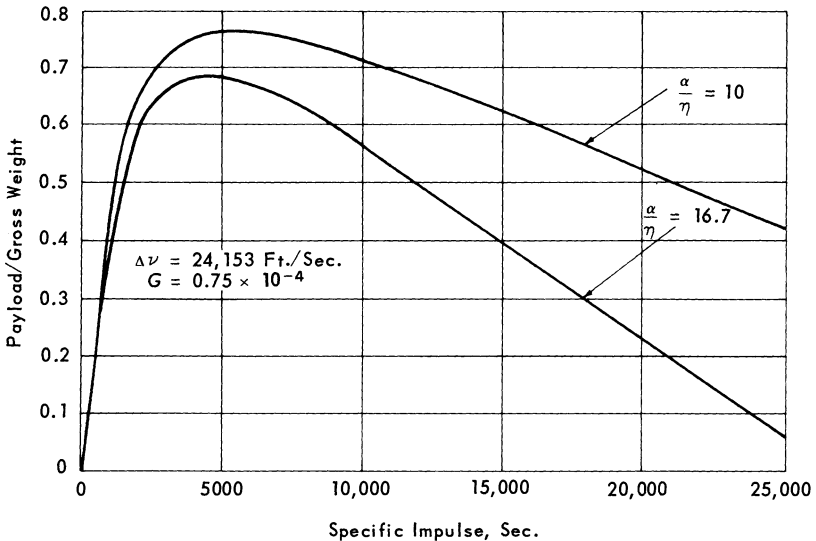
Fig. 11-2 Typical variation of payload versus specific impulse ion rocket.

To establish the power demand of the engine, the relation for the specific power is developed from the basic power relation, Eq. (11-8):

$$P_g = \frac{1}{1100} \frac{\dot{M} \; C^2}{\eta \; g} \text{ hp} \qquad (11\text{-}8)$$

and from the specific impulse

$$I_s = \frac{F}{\dot{M}g} = \frac{C}{g} \text{ sec} \qquad (11\text{-}11)$$

and thrust

$$F = M_g\, G \text{ lb} \qquad (11\text{-}12)$$

The specific power of the vehicle is then

$$\frac{P_g}{M_g} = \frac{1}{\alpha} \frac{(M_e)}{(M_g)} = \frac{0.0292\ GI_s}{\eta} \text{ hp/lb.} \qquad (11\text{-}13)$$

The specific power of the vehicle thrust-to-weight ratio and specific impulse of modern aircraft and various chemical rockets have been computed from performance data. The same performance parameters for the plasma rocket and the ion rocket have been estimated or obtained from the work of other investigators. These data are summarized in Fig. 11-3. If the power plant manufacturer is capable of building a nuclear-powered electrical propulsion system of a specific power comparable to that of modern aircraft, an electrical rocket engine that will develop a thrust-to-weight ratio between 10^{-4} and 10^{-3} appears assured.
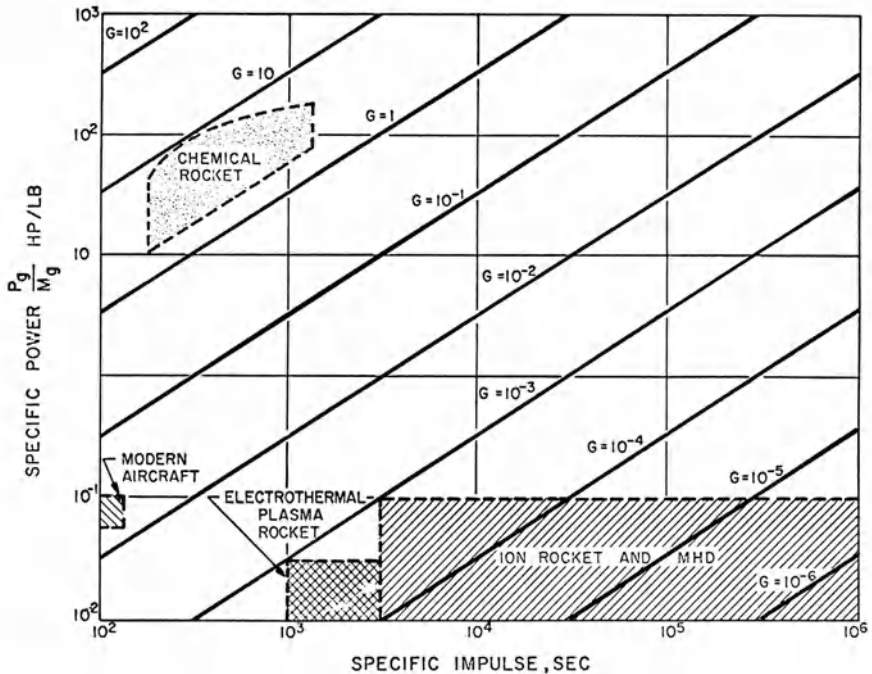
Fig. 11-3 Specific power requirements of vehicles.

[11-2.2] Electrical Thrust Devices

The electrical thrust devices discussed here are basically dependent upon the formation of a plasma which is an electrically neutral gaseous mixture of electrons, ions, and neutral particles. If no neutral particles are present, the plasma is classified as ideal. The single exception to this general statement is the surface-contact ion rocket engine which depends upon the evaporation of alkali metal ions from a heated metal plate having a work function greater in magnitude than the ionization potential of the propellant.

[11-2.2.1] Ion and Colloid

The exhaust velocity, C_i, of a particular particle species in the ion and colloid rocket engines is expressed in terms of the potential drop, V, of the accelerating fields; the degree of ionization, h_i; the particle mass, m_i; and the charge on the electron. The degree of ionization, h_i, is the number of electron charges carried on the particle. In the case of an ion rocket, it is the number of electrons stripped from the atom in the ionization process and is an integer.

$$C_i = \left(\frac{h_i \; eV}{150 \; m_i} \right)^{1/2}$$
(11-14)

The total current in the exhaust jet is the sum of the currents of each species of charged particle. The total current must vanish if a stable thrust is generated by an electrical rocket. In the case of an ion rocket engine, the current of the ion jet must be balanced by the current of an electron emitter.

Use of the current equation reduces the thrust relationship to terms which can be measured by straightforward physical techniques.

$$F = \sum I_i \left(\frac{m_i}{h_i} \right)^{1/2} \left(\frac{V}{150e} \right)^{1/2}$$
(11-15)

When this equation is modified by expressing the current in terms of the ratio of the current of each particle species to the total current, the thrust can be expressed in terms of the equivalent mass of a particle carrying a single electron charge. The thrust on the vehicle becomes

$$F = I \; m^{1/2} \left(\frac{eV}{150} \right)^{1/2}$$
(11-16)

in which the definition of the weighted, equivalent particle mass is:

$$m^{1/2} = \sum \frac{I_i}{I} \left(\frac{m_i}{h_i}\right)^{1/2}.$$ (11-17)

The equivalent singly ionized particle weight is then defined by

$$A^{1/2} = \frac{I_i}{I_i} \left(\frac{A_i}{h_i}\right)^{1/2}.$$ (11-18)

A_i is the atomic, or molecular weight if ions are used to generate thrust. If charged particles are used, A_i is the weight of 6.02×10^{23} particles in grams. The parametric design equation for the thrust results after taking into account the mechanical and electrical units which the investigator wishes to use. In the cgs system of units, the thrust becomes

$$F = 14.39 \; \eta \; IV \left(\frac{V}{A}\right)^{1/2} \text{ dynes,}$$ (11-19)

and in the foot–pound–second system,

$$F = 3.235 \times 10^{-5} \; \eta \; IV \left(\frac{V}{A}\right)^{1/2} \text{ lb.}$$ (11-20)

The parameter, V/A, expressed in volts per gram, occurs in all of the engineering design parameters which are summarized in Table 11-2 for the English and metric unit systems [1].

[11-3] ION ROCKET ENGINE

The concept of the ion rocket engine evolved from these analyses is a system including three major subsystems: the energy source, the power convertor, and the ion thrust chamber (Fig. 11-1). A complete engine system which is based upon known engineering and scientific techniques is shown in Fig. 11-4. The heart of the thrust-producing system is the thrust chamber. For the purpose of the schematic illustration, the thrust chamber lies within the rectangle enclosed by the dashed lines. This thrust chamber includes an ion source, an array of electrodes to focus and accelerate them, and an electron emitter.

Vaporized propellants are fed to the ion source where they are ionized either by contact with heated metals of high work function

Table 11-2   Summary of Performance Parameters, Electrical Rocket Engines

	Definition	
	English System	Metric System
Specific Power	$\dfrac{P}{M} = 3.089 \times 10^4 G \left(\dfrac{V}{A}\right)^{1/2}$ watts/lb $\dfrac{P}{M_g} = 41.42\, G \left(\dfrac{V}{A}\right)^{1/2}$ hp/lb	$\dfrac{P}{M} = 0.0695\, a \left(\dfrac{V}{A}\right)^{1/2}$ watts/gm
Power per Unit Thrust	$\dfrac{P}{F} = 3.089 \times 10^4 \left(\dfrac{V}{A}\right)^{1/2}$ watts/lb $\dfrac{P}{F} = 41.42 \left(\dfrac{V}{A}\right)^{1/2}$ hp/lb	$\dfrac{P}{F} = 0.0695 \left(\dfrac{V}{A}\right)^{1/2}$ watts/dyne
Average Exhaust Velocity	$C = 4.557 \times 10^4 \left(\dfrac{V}{A}\right)^{1/2}$ ft/sec	$C = 13890 \left(\dfrac{V}{A}\right)^{1/2}$ meters/sec
Exhaust Current per Unit Thrust	$\dfrac{I}{F} = \dfrac{3.089 \times 10^4}{A\left(\dfrac{V}{A}\right)^{1/2}}$ amps	$\dfrac{I}{F} = \dfrac{0.0695}{A\left(\dfrac{V}{A}\right)^{1/2}}$ amp

Propellant Flowrate per Unit Thrust

$$\frac{\dot{M}}{F} = 7.060 \times 10^{-4} \left(\frac{V}{A}\right)^{-1/2} \text{ sec}^{-1}$$

$$\frac{\dot{M}}{F} = 7.199 \times 10^{-7} \left(\frac{V}{A}\right)^{-1/2} \text{ sec}^{-1}$$

Specific Impulse

$$I_s = 1417 \left(\frac{V}{A}\right)^{1/2} \text{ sec}$$

$$I_s = 1417 \left(\frac{V}{A}\right)^{1/2} \text{ sec}$$

Minimum Throat Area per Unit Thrust (Ion Rocket Only)

$$\frac{A_t}{F} = 5.651 \times 10^{11} \left(\frac{V}{A}\right)^{-2} \text{ sq ft}$$

$$\frac{A_t}{F} = 127.1 \left(\frac{V}{d}\right)^{-2} \text{ (meters)}^2/\text{DYNE}$$

Engine Operating Time

$$t = \left[\frac{1 - e^{\dfrac{-\Delta V}{4.557 \times 10^4 \left(\frac{V}{A}\right)}}}{7.060 \times 10^{-4}\, G}\right]^{1/2} \cdot \left(\frac{V}{A}\right)^{1/2} \text{ sec}$$

$$t = \left[\frac{1 - e^{\dfrac{-\Delta V}{1.386 \times 10^6 \left(\frac{V}{A}\right)^{1/2}}}}{7.199 \times 10^{-7}\, a}\right]^{1/2} \cdot \left(\frac{V}{A}\right)^{1/2} \text{ sec}$$

Equivalent Particle Weight

$$A = \left[\sum \frac{I_i}{I} \left(\frac{A_i}{h_i}\right)^{1/2}\right]^2 \text{ gm}$$

$$A = \left[\sum \frac{I_i}{I} \left(\frac{A_i}{h_i}\right)^{1/2}\right]^2 \text{ gm}$$
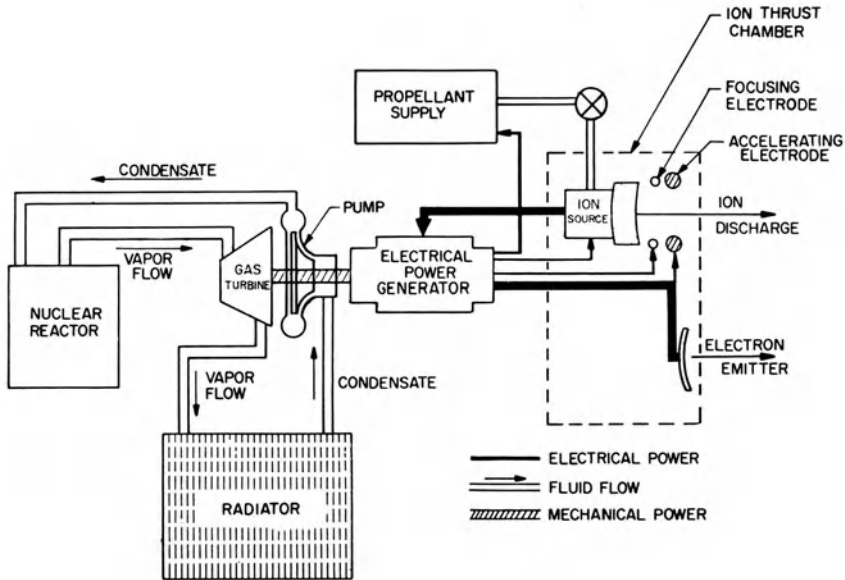
Fig. 11-4 Typical ion propulsion system.

or by being subjected to electron bombardment within electromagnetic fields. The latter method of ionization is commonly described as the arc source.

The ionized propellant is directed from the ion source of this particular engine through focussing electrodes. The focussing electrodes direct the ion current through the accelerating electrode, which imparts kinetic energy to the ions. This results in the required changes of momentum of the particles to develop the major portion of the thrust for the vehicle. The accelerating electrode has been set at the potential of the vehicle skin for safety and to minimize the electrical field outside of the vehicle.

The ion discharge is balanced by an equal flow of oppositely charged particles; otherwise the surface of the vehicle develops a high induced charge, causing the ion flow to slow down and stop. An electron emitter is shown in Fig. 11-4. The electron discharge can be achieved by thermionic emission from a heated tungsten plate or by field emission of electrons from discharge points incorporated in the accelerating electrodes. An alternative method of obtaining a neutral beam is by charge-exchange techniques. Power to drive the ion thrust chamber is obtained from high-speed electrical power generators. Three types may be applied to the ion rocket engine: a permanent magnet generator, an a-c generator, or an electrostatic generator. The distribution of power to the various components of the system is shown by the solid lines in

Fig. 11-4. Most of the power is absorbed in pumping the electrons, which are collected at the ion source, up to the potential of the accelerating electrode. Power required to generate ions in the ion source is a significant factor in determining the power efficiency of the thrust device. Therefore, it is timely to discuss ion sources.

[11-3.1] Ion Sources

Several types of ion sources, including radio frequency, thermionic-arc type [8], and surface contact [12], have been investigated for application in ion rocket engines.

What little information is available on radio frequency ion sources indicates that the efficiency is low and the associated operating equipment is heavy. These factors eliminate these sources for applications in the ion engine. Thermionic sources are based on the emission of ions from heated mixtures of chemical compounds. These also have proved heavy and inefficient.

The adoption of an arc-type ion source or a surface contact source depends upon the power demands of the source. A brief preliminary analysis of the efficiency is carried out for both sources.

The power required for a surface-contact source includes that radiated from the heated ionizer surface, the heat required to vaporize the propellant from ambient conditions, and radiation from structural parts. The last is difficult to predict except by test.

The power radiated from the ionizer surface is

$$P_R = 5.67 \times 10^{-12} \ \epsilon T^4 S \text{ watts.} \tag{11-21}$$

The area S is measured in cm^2, ϵ is the total emissivity of the surface, and T is the absolute temperature in degrees Kelvin.

The minimum area, A_t, of the ionizer surface is dependent upon the accelerating field strength of the engine (Table 11-2).

$$A_t = 0.1271 \times 10^7 \ F \left(\frac{V}{d}\right)^{-2}$$
$$= 0.1271 \times 10^7 \ FX^{-2} \text{ cm} \tag{11-22}$$

The field strength, X, is measured in volts per cm, and F, the thrust, in dynes. The power into the exhaust jet (Table 11-2) is:

$$P = 0.06949 \left(\frac{V}{A}\right)^{1/2} F \text{ watts.} \tag{11-23}$$

The efficiency of the surface-contact engine is

$$\eta = \frac{P}{P + P_R + P_R{}'}$$

$$= \frac{1}{1 + \dfrac{1.04 \times 10^{-4} \ \epsilon \ T^4}{X^2 \left(\dfrac{V}{A}\right)^{1/2}} + \dfrac{P_R{}'}{P}} \ . \qquad (11\text{-}24)$$

$P_R{}'$ represents the power required to vaporize the propellant, beam loss from interception, and other external losses. Preliminary computations indicate that these power losses are small in comparison to the radiation loss if the ion engine is well designed.

An ion engine equipped with an arc type source, Fig. 11-5, draws a heavy current but low voltage in the arc. The ratio, Z, of the ionizing electron current to the ion engine current is

$$Z = \frac{I \text{ electron}}{I \text{ ion}} = \left(\frac{A}{m_e}\right)^{1/2} = \sqrt{1836A} \qquad (11\text{-}25)$$

in which A is the weight of the ion in grams [20]. The ion current in the arc is the ion current of the rocket engine:

$$I_{\text{ion}} = \frac{0.06949 \ F}{A\left(\dfrac{V}{A}\right)^{1/2}} \ \text{amp.} \qquad (11\text{-}26)$$

The electron current in the arc is

$$I_e = \frac{0.06949 \ F}{A\left(\dfrac{V}{A}\right)^{1/2}} = \sqrt{1836A} \ . \qquad (11\text{-}27)$$

Since the power $P = IV$, the efficiency of the arc system becomes

$$\eta = \frac{P}{P + P_{\text{arc}} + P_R{}'}$$

$$= \frac{1}{1 + \dfrac{Va}{V} \sqrt{1836A} + \dfrac{P_R{}'}{P}} \qquad (11\text{-}28)$$
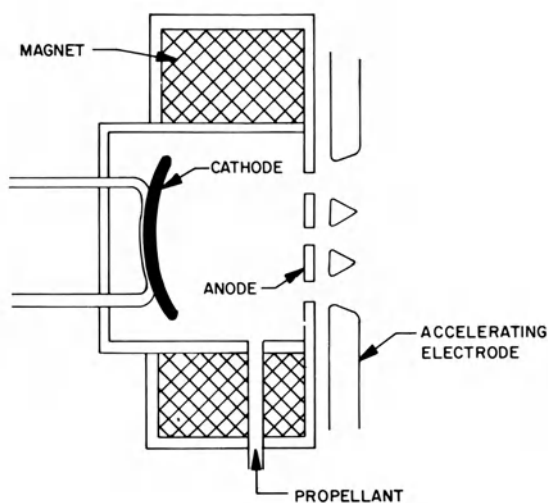
Fig. 11-5 Arc-type ion source.

in which V_a is the operating voltage of the arc. Again $P_R{}'$ represents the power for vaporization of propellant, loss from beam interception, and other external losses.

The data of Fig. 11-6 summarize and compare the variation of the power efficiency, η, of an arc-type ion engine and a surface contact engine. These preliminary data indicate how this parameter can be expected to vary, furnish additional information for selection of a propellant, and present areas of application for the two types of engines. Curve 1 is the efficiency variation with accelerating voltage of an arc-type engine with the arc operating at 20 volts and using cesium propellant. Curve 2 is similar data for an engine incorporating a 10-volt arc, again with cesium metal as the propellant. Many possible propellant materials are most efficiently ionized for arc voltages between 100 and 150 volts. Curve 5 indicates the efficiency of a 100-volt arc, using a propellant of the same ion weight as cesium.

Curve 3 is the efficiency variation of a survace-contact engine using cesium which is ionized by a 2200° K tungsten plate. The strength of the accelerating field, X, is maintained at 10,000 volts/cm. As the field strength exceeds 100,000 volts/cm, the efficiency approaches 100%, as shown in Curve 4. In all computations, the total emissivity of the tungsten ionizer was assumed to be 0.28.

The power output per unit thrust that the vehicle must develop for the arc-type ion engine has been estimated from Curve 1, Fig. 11-7, and the surface-contact ion engine from Curve 3, Fig. 11-6. In both cases summarized in Fig. 11-7, cesium metal is the
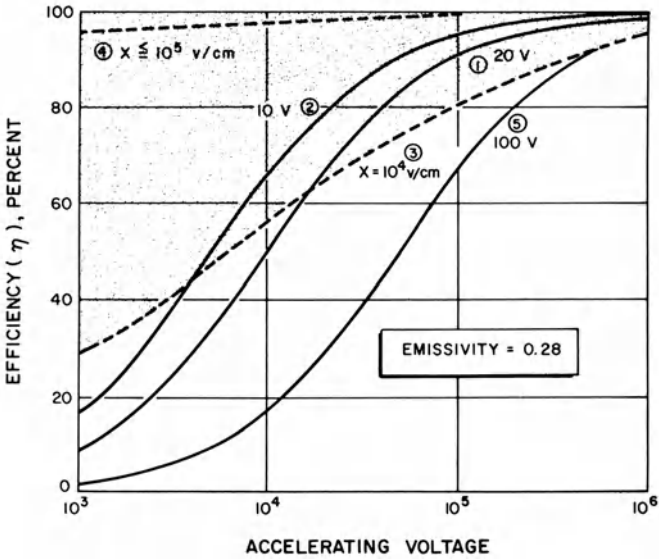
Fig. 11-6 Comparative efficiencies of ion rocket engine.
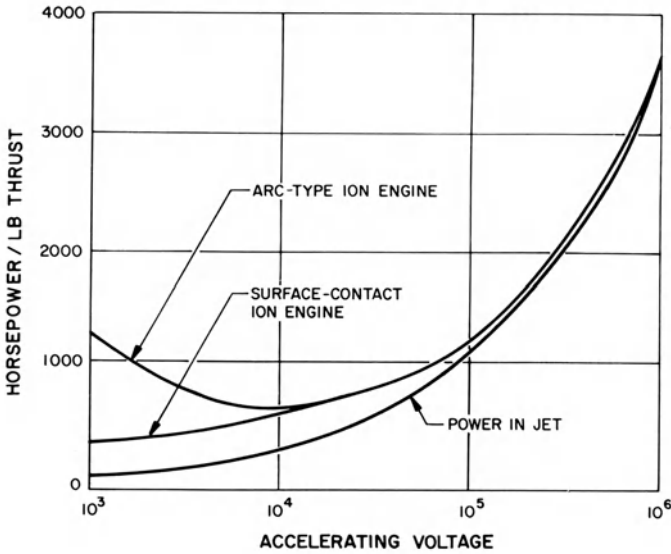
Fig. 11-7 Power requirements of ion engine.

propellant. The arc engine assumes an arc operating voltage of
20 volts, which is close to the value for maximum operating effi-
ciency [13]. The surface-contact source assumes an operating

temperature of 2200° K, an emissivity of 0.28, and accelerating field strength of 10,000 volts per centimeter.

These curves are not generally applicable, being computed for specific operating conditions which were selected to establish the minimum efficiences and maximum power per unit thrust of the two types of engines. The significant factors are that in the specific impulse range covered by this summation, 3900 to 124,000 seconds, the total power demand of the arc-type engine can be expected to have a minimum for a specific impulse between 11,000 and 13,000 seconds.

These qualitative data indicate that, within the limits of the analysis, cesium ionized on tungsten is superior for low accelerating voltages and low specific impulse. In the intermediate range of specific impulse, a cesium arc is competitive with a cesium surface-contact engine and is superior to an arc engine using a propellant requiring a high operating voltage. For high accelerating voltages and specific impulse, the two types of sources are competitive. The difference between the power requirements at lower specific impulse indicates a significant superiority for the surface-contact engine if the accelerating field strength is high. An accurate evaluation can be made only from the experimental results from tests of the two different engine types.

The Von Ardenne, or duo-plasmatron source, Fig. 11-8, is capable of a high current density of ions [14]. The high current density is achieved by the combination of a number of techniques including ionization by electron bombardment, magnetic field collimation, a magnetic mirror at the exit point, and the use of an extracting electrode at high potential (40-60 kv). In operation, a small bubble of plasma is formed in the aperture of the source. At the design operating potential, ion extraction occurs at a rate to cause the bubble to form a plane, or concave, surface in the aperture and emit a parallel beam of ions. In this source, the
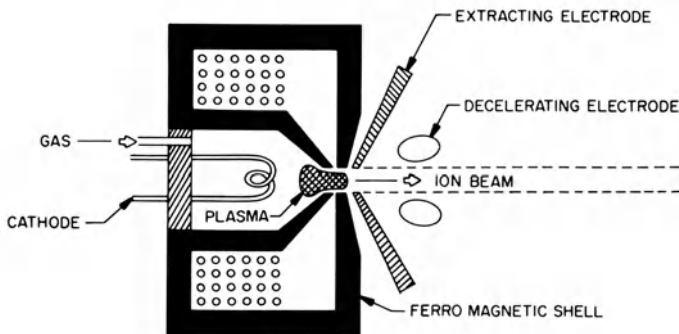
Fig. 11-8 Von Ardenne ion source.

velocity of the extracted ions is far too high for most applications. To incorporate the source in an ion engine, a decelerating electrode is required to retard the ions and obtain the desired specific impulse. Because of its high current density and potential high total current, it must be seriously considered for application in ion thrust devices.

[11-3.2] Electromagnetic Fields

Electric and magnetic fields always exist together. If charged particles are accelerated under a high intensity electrostatic field, magnetic fields are induced around the charged particle current in accordance with Lenz's law. By superimposing a magnetic field on an electrostatic field, the motion of the charged particles can be controlled to achieve focussing effects or increase the path length of the charged particles within the gas volume and thereby increase the number of collisions which produce additional charged particles.

Two forces act on a charged particle of mass, M, and charge, e, when it moves through a region in which an electric field, E, and a magnetic field, H, exist. If e is the charge of the particle, the produce $e\,E$ is the electrostatic force parallel to the field. The magnetic force is at right angles to the particle velocity, v, and to the magnetic field, H, and is the vectorial cross product of v and H.

$$M\,\frac{dv}{dt} = e(E + v \times H) \tag{11-29}$$

When H vanishes, the charged particles move with constant acceleration, $e/m\,E$, as in the electrostatic ion engine. When there is no electric field, the acceleration, $e/m\,(v \times H)$, is perpendicular to the particle velocity curving its trajectory but not changing scalar velocity, v.

The motion in an electromagnetic field that is changing slowly both in space and time can be described as a gyration around a moving point plus the motion of the point—the drift velocity. It can be shown [13] that the drift velocity is

$$v_d = \frac{E \times H}{H^2} \tag{11-30}$$

and the velocity of rotation, v_g, is defined by the equation

$$m\,\frac{dv_g}{dt} = e(v_g \times H) \tag{11-31}$$

The velocity, v_g, is independent of the electric field, and the motion is a rotation around the lines of force at the Larmor frequency, $c = (e\,H)/m$.

Focussing of the ion beam is achieved by directing the beam through a magnetic coil. The coil establishes a magnetic field parallel to the charged particle current. If the charged particle motion is parallel to the field, there is no force on the particle; however, if a charged particle develops a velocity component at an angle to the magnetic field lines, it is constrained to move in a spiral path and a focussing effect is achieved which is governed by the equations of motion above [5]. This phenomenon contributes to the formation of a plasma bubble at the exit port of the Von Ardenne ion source.

Another application of magnetic fields is in the electron bombardment ion engine [8]. The ion source of this engine has a cathode mounted at the center of the source. Ionizing electrons are emitted and travel at high velocity toward the outer surface of the source because of a radial electrostatic field. By superimposing a weak magnetic field normal to the electrostatic field, a spiral motion of the electron is induced, thereby increasing the path length through the gas to be ionized and increasing the probability of collisions with subsequent production of ions and electrons. The ions are extracted from the resulting plasma through a grid which is held at a negative potential. This technique is frequently incorporated in high density ion forces [4].

[11- 3.3] Charged Colloid Sources

The generation of charged colloid particles is a two-stage process. First, the propellant must be dispersed as colloidal-sized particles in a near vacuum. Then the colloidal particles are charged to give the desired charge-to-mass ratio. For the dispersal of the propellant into colloidal particles, there is an extensive background of experience on gas-dispersed systems which involve condensation or atomization. Condensation techniques include vaporization followed by cooling, the expansion of a vapor through a nozzle, chemical reactions, and mechanical methods. Atomization of solids can be achieved by grinding, which requires substantial amounts of power. Liquids are conveniently atomized in high-intensity electrostatic fields [15].

Charging of colloid particles includes most of the methods for producing ions, including ion or electron bombardment, electron emission, and surface contact. The charged particle can also be formed by condensation of material on an ion or other charged particle.

Colloid propulsion is in early stages of research. It is still early to predict what combinations of techniques and equipment can be devised to produce a useful thrust device [16].

SYMBOLS

a = Acceleration
A = Equivalent weight of particle with charge of single electron
A_i = Atomic or molecular weight of particular species of particle
A_t = Cross sectional area of particle beam or thrust chamber
C = Average exhaust velocity
C_i = Velocity of particle, i'th species
d = Separation of acceleration electrodes
e = Charge of electron
F = Thrust of rocket engine
G = Thrust-to-weight ratio
h = Number of electrons stripped from particle
H = Magnetic field strength
I = Current
I_s = Specific impulse
J = Current density
m_i = Mass of particle, i'th species
M_g = Gross weight of vehicle
M_0 = Gross mass of vehicle
M = Propellant flowrate
M_e = Weight of power plant section
M_s = Weight of structure
M_x = Weight of payload
M_p = Weight of propellant
N = Particle flow rate in exhaust jet
P = Power in exhaust jet
P_R = Radiated Power
P_g = Gross power of vehicle
t = Engine operating time
v = Particle velocity
V = Accelerating potential
X = Electric field strength
Δv = Characteristic velocity
α = Weight/unit power
η = Ratio of exhaust jet power to gross vehicle power

SUBSCRIPTS

i refers to particular particle species

REFERENCES

1. Boden, R.H.: The Ion Rocket Engine, *AFOSR RN 57-573, R-645*, Rocketdyne, Division of North American Aviation, Inc., Canoga Park, Calif., July 3, 1958.

2. Massachusetts Institute of Technology (Staff of Electrical Engineering Department), Applied Electronics, New York, John Wiley & Sons, Inc., 1943.

3. Pierce, J.R.: Rectilinear Electron Flow in Beams, *Journal of Applied Physics*, August 1940, Vol. 11, pp. 548-554.

4. Guthrie, A. and R.K. Wakerling: Sources and Collectors for Use in Calutrons, *TID-5218*, University of California Radiation Laboratory, Berkeley, Calif., June 1949.

5. Lamb, W.A.S. and E.J. Lofgren: High-current Ion Injector, *Review of Scientific Instruments*, 27:11, November 1956, pp. 907-909.

6. Alperin, M. and G.P. Sutton: Advanced Propulsion Systems, Pergamon Press, 1959.

7. Final Report—Solar Powered Electric Propulsion Spacecraft Study, *JPL Contract No. 95144/December 1965/SSD 50094K*, Hughes Aircraft Company, Space Systems Division, Culver City, Calif.

8. Kaufman, H.R.: The Electron Bombardment Ion Rocket—Advanced Propulsion Concepts, Vol. I, Proceedings of the Third Symposium on Advanced Propulsion Concepts (Cincinnati), pp. 3-18, October 2-4, 1962.

9. Seiffert, H.S.: Survey of Electrically Powered Rockets, *Tech. Memo. TM-33-63-08*, United Technology Corp., Sunnyvale, Calif., December 1963.

10. Katz, E.L.: Electric Propulsion—Short Lecture Series, American Institute of Aeronautics and Astranautics, New York, N.Y., March 30, 1965.

11. Hayes, Judith: Astronautics Information—Electric Propulsion, *Literature Search # 587*, Jet Propulsion Laboratory, California Institute of Technology, Pasadena, Calif., June 1964.

12. Cybulski, R.J., J.J. Kotnik, and D.L. Lockwood: Experimental Performance of an Ion Rocket Engine Using a Rectangular Slot, Porous Tungsten Emitter, *NASA TN D1321*, National Aeronautics and Space Administration, Washington, D.C., 1962.

13. Spitzer, W.: Physics of Fully Ionized Gases, New York Interscience Publishers, 1956.

14. Von Ardenne, M.: New Developments in Applied Ion and Nuclear Physics, (Atomkern-Energis, 1956), Vol. 4, pp. 121-126.

15. Schultz, R.D.: Ion and Plasma Propulsion, Second AFOSR Contractors' Meeting, Rocketdyne, Canoga Park, Calif., July 8-9, 1959.

16. Hendricks, C.D.: Colloid Propulsion State of Art In Review of Current Research, 4th Sym. on Adv. Prop. Concept, AFOSR (Washington), April 1965.

Part Six

*Theory on Combustion, Detonation and
Fluid Injection*

Interaction Flows Due to Supersonic

Secondary Jets

Andrew F. Charwat
Department of Engineering
University of California, Los Angeles

[12-1] INTRODUCTION

The technology of propulsive systems draws on a substantial body of formal fluid mechanical theory. The design of exhaust nozzles, turbine and compressor blade cascades, the analysis of the design-point operation of subsonic and supersonic inlets, etc., involve mathematically sophisticated solutions of the fluid motion and aero-thermochemical coupling between it and the medium. As difficult as some of these problems are, their basic formulation is usually reasonable clear. With enough effort, a theoretical framework can be developed and extended by controlled experimental work.

In recent years, there has also been an increasing amount of research in the local use of very "unclean" aerodynamic flow fields associated with secondary subsonic and supersonic jets discharging into the stream in the propulsive duct and with regions of separated flow at steps or notches in its boundaries. It is extremely difficult and often useless to attempt a purely theoretical description of these flows. Instead, a growing body of basic experimental work and semi-empirical models of the flow which are being accumulated can be used to provide a framework for the "understanding" of the phenomena. One cannot overemphasize the need for caution in extrapolating such results to untested situations. Nonetheless, with care, experience, ingenuity and some developmental testing, it is possible to apply with success these "building block" experiments and idealized theoretical solutions to the complex flow occurring in specific applications.

In this paper, we propose to review some of the experiments and conceptual models which illustrate the structure of flow-fields involving secondary jet interactions and separated regions.

The use of secondary jets injected at an angle into the supersonic flow in a rocket nozzle to generate asymmetrical forces for thrust vector control is a highly successful application. Such

secondary jets produce net transverse forces several times larger than the reaction force of a sidejet alone. The thrust vector control system is usually more reliable and simpler than mechanical vanes or gimballed nozzles.

The study of jets discharging parallel to the wall, at an angle to it, or issuing from nozzles in a direction normal to that of the main supersonic stream, is applicable not only to force vector control problems but also to the recent research on supersonic combustors [1] (the "Scramjet"). The key problem is to mix the injected fuel with the free stream and complete the combustion stably and predictably over a wide range of pressure, temperature and velocity of both streams (which relates back to the flight regime of the engine). The optimum injection configuration is still a question for study; for instance, inclined injection causes cooling problems on the neighboring walls (heat fluxes as high as 20 times the heat flux without combustion have been observed immediately upstream of inclined jet injectors) but improves the efficiency of the chemical reaction due to precompression of the free stream through the interaction shock structure. This couples with the thermodynamic cycle efficiency through the associated losses in stagnation pressure.

[12-2] JETS DIRECTED UPSTREAM

We shall limit the following discussion to a very few examples of the complex interaction generated by jets issuing into an established flow, which often involves separated regions as an element of the flow field. We begin with a problem illustrating the role played by the separated region (Charwat & Faulmann, 1964) in establishing the structure of the flow. This problem has to do with a supersonic jet opposing a supersonic stream. In terms of practical applications the situation may be thought of as a model for a retro-rocket operating in atmosphere during re-entry or as a possible injector of gaseous fuel in a supersonic combustor.

There are regimes in which a very stable bow-shock interaction is observed. Figure 12-1 is an example of this. The standoff distance of the double normal shock structure on the axis is governed by the condition that the total pressure of both supersonic streams must be equal. Thus, there is a free overexpansion at the edge of the jet nozzle which increases the centerline Mach number until that condition is met (see the explanatory sketch included in Fig. 12-1. All this can be calculated exactly (using, for instance, the method of characteristics) and correlates extremely well with experimental work (see Fig. 12-2). Under other conditions, however, the stable structure described in the preceding breaks down completely leading to a highly unstable oscillating, spike-type penetration of the jet into the free stream.
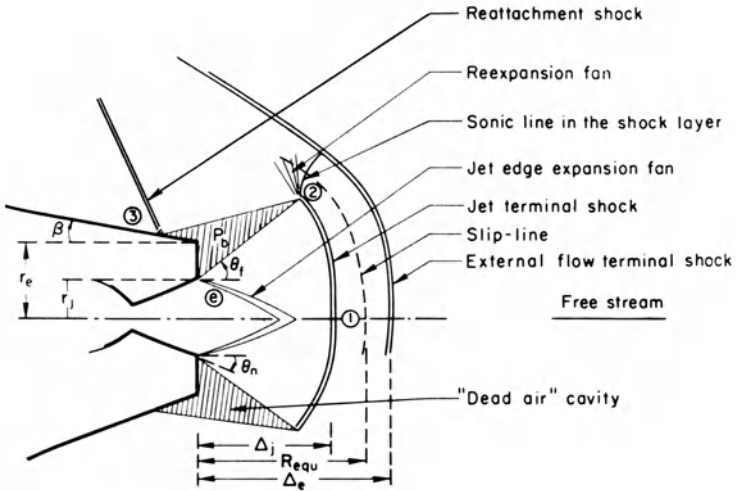
Fig. 12-1 Supersonic jet opposing supersonic flow: stable interaction regime; (a) $M_j = 1$, $r_e/r_d = 6$, $M_\infty = 7$; (b) sketch of blunt interaction flow field (Charwat & Faulmann, 1964).

The following model seems to explain this phenomenon. Figure 12-3 is typical Schlieren picture of this.

The equilibrium of total pressures on the line of symmetry is a necessary but not sufficient condition for there to exist a unique stable flow. The jet-flow and the free stream flow must be compatible across their entire common boundary, *i.e.,* across the subsonic shock layer and the vortical "dead-air" base cavity, the shape of which is itself determined by the solution. One is led
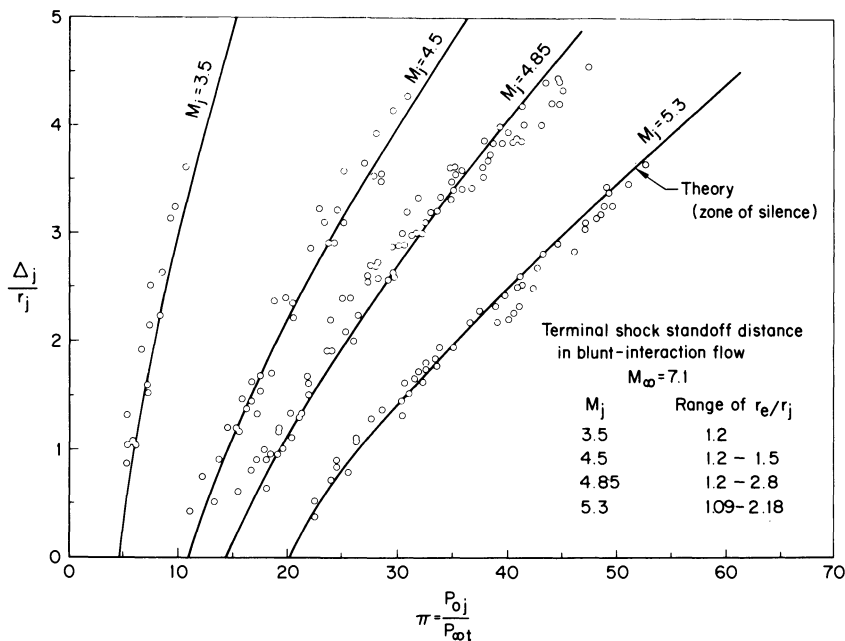
Fig. 12-2 Jet terminal shock standoff distance in blunt flow.

to seek a simplified model of this extremely difficult theoretical problem by isolating, if possible, a single dominant matching condition. The most inflexible characteristics of the flow field would seem to be this: the base-cavity cannot support any appreciable internal pressure gradients. consequently, the flow around its closed boundaries (3)-(2)-(3) must maintain an approximately constant static pressure (P_b).

Suppose that the ratio of the base pressure to jet stagnation P_b/P_{j0} and the jet exit Mach number are given, then the total jet expansion angle θ_f and the Mach number along the edge of the free jet* are known as a function P_b/P_{j0}. At point 2, the jet edge streamtube crosses a normal shock, turns and re-expands isotropically (transonically) back to the static pressure P_b. One can calculate the stagnation pressure ratio across the normal shock at point 2 (P_{jt2}/P_{j0}) and the Mach number along the external boundary (M_{23}) as a function of P_b/P_{j0}. However, the direction of this returning streamtube cannot be determined because the direction of the sonic line in the shock layer is not known.

---

*The jet edge Mach number is constant for a free-jet in two-dimensional flow, and it can be shown that it also a good approximation for the initial development of axi-symmetric free-jets.
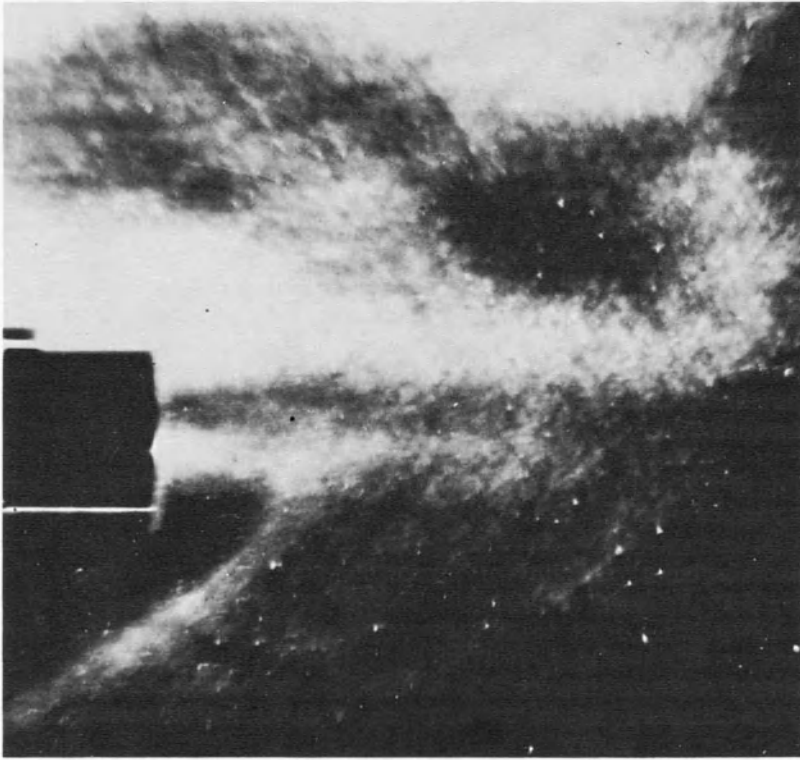
◄──────── Oscillations of shock layer ────────►

Fig. 12-3 Example of shock oscillations occurring beyond limit of blunt flow region $M_\infty = 2.75$, $M_j = 3.1$, $r_e/r_j = 3.3$.

We now consider the reattachment at point 3. In analogy with the well-established model of base flows, we assume that the pressure in the free streamtube (2)-(3) must return at point 3 to the undisturbed static pressure on the afterbody, which can be related to the local angle of the wall (Newtonian flow). Data supporting this assumption were obtained. In the case of cylindrical afterbodies, the reattachment pressure simply equals the free-stream static pressure. The ratio $P_b/P_{\infty s}$ and the Mach number M_{23} determine the flow turning angle θ_3 as a function of P_b/P_{j0}, the external Mach number, the impact pressure ratio and the afterbody angle at reattachment, β.

In summary, the isobaric characteristic of the dear-air cavity leads to a coupling of the flow angles θ_f and θ_3 for each set of six principal parameters. It is convenient to consider the ratio

$$\phi = P_{jt2}/P_{\infty t}$$

instead of P_b/P_{j0} as one of them. It can easily be seen that the angles θ_f and θ_3 are expressible parametrically as

$$\theta_f = f(M_{je}, \pi, \phi, \theta_n)$$

$$\theta_3 = f(M_\infty, \pi, \phi, \beta)$$

The analytic expressions of these functional relations are algebraically very complex and will be omitted. Compressible flow tables would normally be used to perform calculations.

The external shoulder of the afterbody may be included in the isobaric cavity without consequence, since there is no appreciable fluid motion in the cavity. This is the situation shown on the sketch on Fig. 12-1. Imagine, however, that the ratio of the afterbody to the jet exit radius is increased to the point where point 3 just falls on the corner. Any further increase in r_e/r_j would cause reattachment to occur on the face of the body which does not satisfy the model.

The jet-terminal shock can be approximately described as straight between the axis and r_j, and circular with radius Δ_j beyond this point. The shock standoff distance (Δ_j/r_j) is fixed by the parameters $M_j(P_{t0}/P_{t\infty})$ and θ_n. It follows that the *maximum radius ratio for stable blund interaction* is approximately given by

$$\left(\frac{r_e}{r_j}\right)_t = 1 + \frac{\Delta_j}{r_j}(\tan \theta_f + \tan \theta_e)\cos \theta_f = f(\pi, \phi, M_{je}, M_\infty, \beta, \theta_n)$$

stable blunt		
interaction	$\longleftarrow \quad \dfrac{r_e}{r_j} < \left(\dfrac{r_e}{r_j}\right)_t < \dfrac{r_e}{r_j} \quad \longrightarrow$	unstable spike interaction

The above is the basic relation for transition to the stable blunt-body interaction derived from the postulated model.

Further consideration of the model indicates that the analysis above sometimes predicts stable blunt interaction flow under conditions under which the recompression pressure ratio $P_{\infty s}/P_b$ exceeds reasonable limits which can be estimated from experiments and theory describing the recompression of a separated shear layer. This means that one can expect two stable–unstable flow transitions: one when each of the stability conditions is crossed (if parameters are chosen so that some region of stable flow is at all possible). Experiments indeed confirm this (see Fig. 12-4). Figure 12-5 shows the closed domain of stable blunt-interaction for two Mach numbers as determined by experiment. The model described in the preceding, while admittedly oversimplified, does seem to portray the mechanism establishing this complex interaction, and, in particular, the role of the isobaric character of the separated cavity.
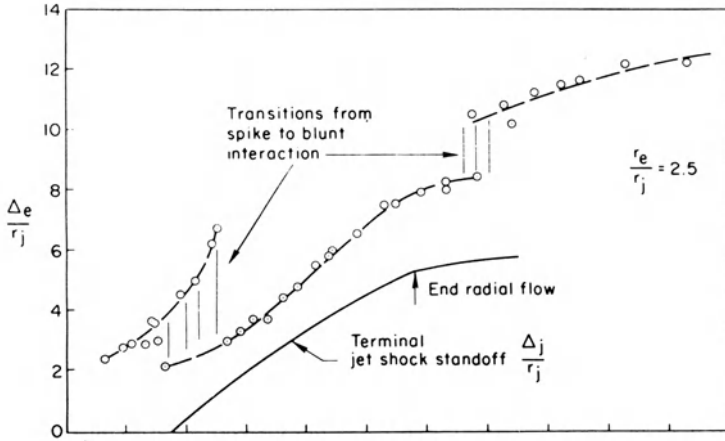
Fig. 12-4 Transition from stable to unstable interaction regime; jet at $M_j = 3.1$ discharging upstream into a flow at $M_\infty = 2.71$ (Charwat & Faulmann, 1964).
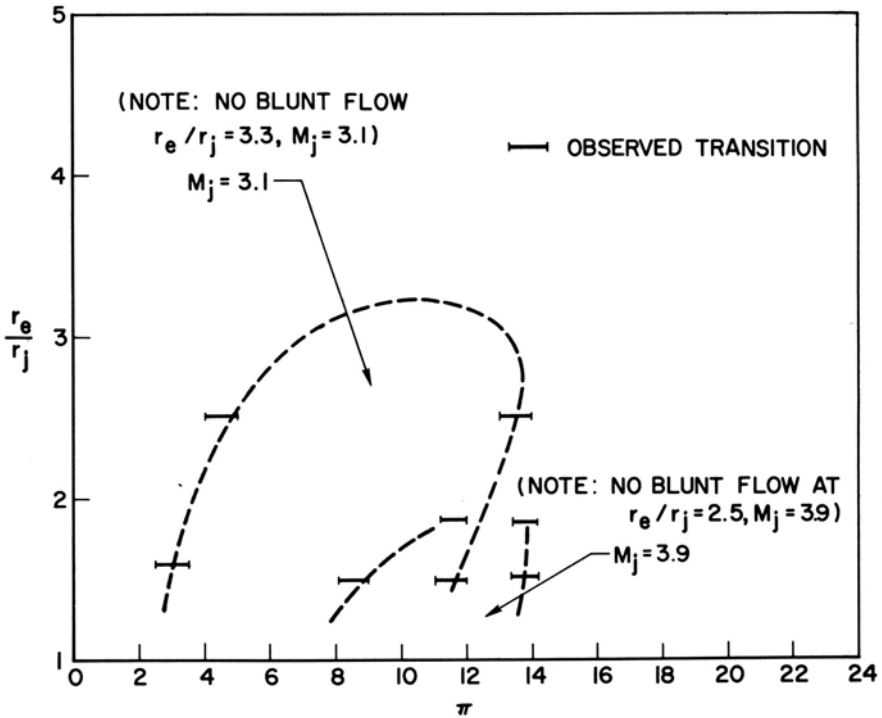
Fig. 12-5 Observed region of stable blunt flow at $M_\infty = 2.75$ compared to calculations.

The action of such a "retro-jet" can be the opposite of what one expects: the upstream facing jet can decrease the total aerodynamic drag on the body. This occurs because in certain regimes of operation, the modification of the flow field around the nose dominates over the reverse thrust of the jet.

The jet-thrust increases monotonically with jet stagnation pressure. It is a complex function of pressure and nozzle geometry up to values of P_{j0} (or π) at which the jet begins to flow "full." Beyond this value (π_s) the thrust is a linear function of jet stagnation pressure

$$F_v = m_j V_j + P_{jse} A_{je} = \left(1 + \gamma M_j{}^2\right)\left(1 + \frac{\gamma - 1}{2}\right)^{-\frac{\gamma}{\gamma - 1}} A_j P_{j0}.$$

It is convenient to present force data in terms of dimensionless coefficients defined as follows:

$$C_D = \frac{D}{q_\infty A_\infty}$$

$$C_f = \frac{F_v}{q_\infty A_\infty} = \left(1 + \gamma M_j{}^2\right)\left(1 + \frac{\gamma - 1}{2} M_j{}^2\right)^{-\frac{\gamma}{\gamma - 1}}\left(\frac{r_j}{r_\rho}\right)^2 \frac{P_{\infty t}}{q_\infty} \pi$$

This presentation normalizes the end points of the region of aerodynamic interaction. At $C_f = 0$, C_d must coincide with the drag coefficient of the body without jet. At large C_f, the data must approach asymptotically a straight line defined by $C_d = C_f$. Measurements of drag were obtained at $M_\infty = 2.75$ by mounting the model on a torsion balance.

The typical cases shown in Fig. 12-6 all exhibit a minimum which results from the interplay of the increasing jet thrust and the decreasing aerodynamic force. They all approach the jet-thrust-dominated asymptote at high values of the thrust coefficient. Except for local fluctuation which reflect the changes in the structure of the flow, the gross features of the variation in streamwise force do not depend on the type of interaction. The drop of drag coefficient to its minimum value appears to be related to the point at which supersonic nozzle flow is first established at the jet exit $(\pi = \pi_s)$ which is also where the base pressure decreases suddenly. This point is marked on the curves. The difference between tests in which transition to blunt flow occurs and tests where it does not occur is that in the first case the drop in drag is abrupt, while in the second it is more gradual.
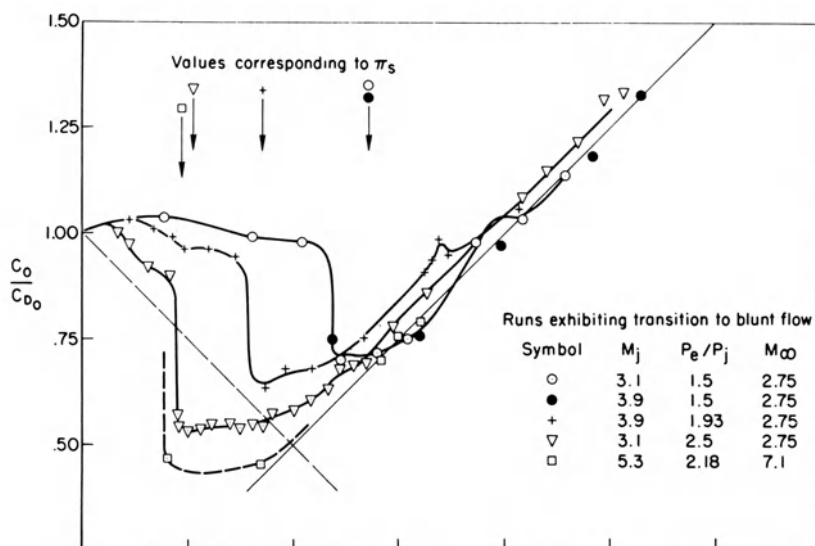
Fig. 12-6 Measurements of drag as a function of jet thrust.

The movement of the minimum-drag point can be analyzed by substituting an expression for π_s for π in the preceding equation. The equation becomes

$$(C_F)_m = \left(1 + \gamma_j M_j^2\right)\left[\left(\frac{2}{(\gamma_j + 1)M_j^2}\right)^{\frac{\gamma_i}{\gamma_j - 1}}\left(\frac{2\gamma_j M_j^2 - (\gamma_j - 1)}{\gamma_j + 1}\right)^{\frac{1}{\gamma - 1}}\left(\frac{P_{\infty t}}{q_\infty}\right)\frac{A_j}{A_e}\right]$$

where the term in square brackets is simply the Rayleigh pitot pressure ratio at the exit Mach number. The dominant factor is the area ratio A_j/A_e since both the functions of M_j and M_∞ rapidly approach constant limits as the Mach numbers increase.

The normalized presentation of the drag data as a function of C_F leads to one interesting observation. Suppose that the objective is to reduce the net streamwise force on the body, *i.e.*, to decrease its deceleration by applying thrust. The decrease in overall drag which would result from an application of a conventional thrust-jet discharging in a direction opposite to that of the motion is approximately portrayed by the dotted line in Fig. 12-6, having a negative slope of unity. It is seen that the drag decrease due to the aerodynamic interference caused by a retrojet discharging against the direction of motion, when the parameters are chosen appropriately,

can be twice as large for the same jet thrust coefficient which is proportional to the expenditure of propellant.

The appended bibliography lists a wider scope of studies dealing with subsonic as well as supersonic blowing upstream (at low or high velocity) from the stagnation point of blunt bodies.

[12-3] TRANSVERSE JETS

Transverse jets have been investigated for internal (thrust-nozzle) and external (jet-flap) control of the aerodynamic force-vector, as well as a possible fuel injection mechanism in subsonic and supersonic combustors. Because of the lack of symmetry, the interpretation of these flow-fields is even more difficult than in the case of opposing jets. A picture of a two-dimensional jet issuing out of a slot is shown in Fig. 12-7. The oncoming flow separates ahead of the injection orifice (or slot), creating an upstream facing cavity; a second cavity exists downstream of the jet. Each of these regions is characterized by a specific cavity-pressure which is governed by either the "free-interaction" mechanism separating the oncoming boundary layer (the upstream cavity) or a reattachment mechanism (the downstream cavity). It follows that the free jet expands at the exit of the secondary nozzle into a nonuniform pressure field; moreover, if the jet is circular as it most often is in practice, the jet exit conditions in a plane containing the jet axis and normal to the mean flow differ from those in the plane of the free stream. Combining flow-visualization with measurements of static and impact pressure (Fig. 12-8) throughout the interaction region, we have attempted to reconstruct the gross features of the outflow from a transverse circular jet as shown in Fig. 12-9.

Attempts at a theoretical analysis of this flow field have been made, but their practical value is limited. For example, Ting, Libby and Roger (1964), Ackberg and Pal (1965), and Vizel and Mostinskii (1965) treated the problem of an inviscid, incompressible two-dimensional interaction by elegant mathematical methods. The analyses involve assumptions which are very idealized and probably disregard essential "interaction" between the elements of the flow, especially when the jet is strong. Experiments show evidence of how complex these interactions are; for example, the distribution of static pressure on the wall of a nozzle fitted with transverse secondary jet changes significantly as the molecular weight of the secondary injectant is changed (even more so when gaseous and liquid injection are compared, although that is less surprising). This is particularly evident in the region of reattachment of the flow on the axis.

If there is combustion of the injected gas, it appears to start at the top of the interaction region and move upstream into the separated cavity (where very high heat-transfer rates to the wall
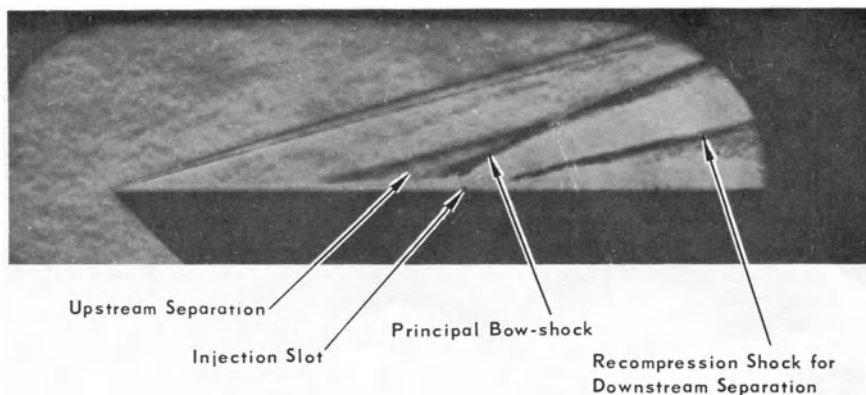
(a)
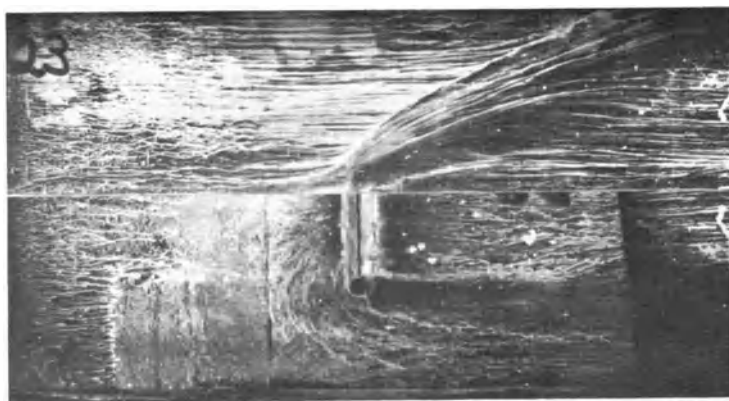
(b)

Fig. 12-7 Shock pattern produced by secondary injection through two-dimensional slot. Free stream M = 4.0; jet to free-stream pressure P_j/P_∞ = 30; (a) schlieren picture; (b) streaklines on side wall.

are experienced); combustion tends to move the upstream separation farther upstream. Combustion can also occur in the downstream cavity. This depends on whether the pressure level in that cavity, which is in general the lowest in the entire field, is high enough. If combustion takes place there, the cavity pressure increases and this modifies the trajectory of the jet, affecting, in turn, the situation upstream. In general, the structure of the flow field set up by a reacting jet is very sensitive to variations in the absolute pressure level and the main-stream parameters (flight parameters).
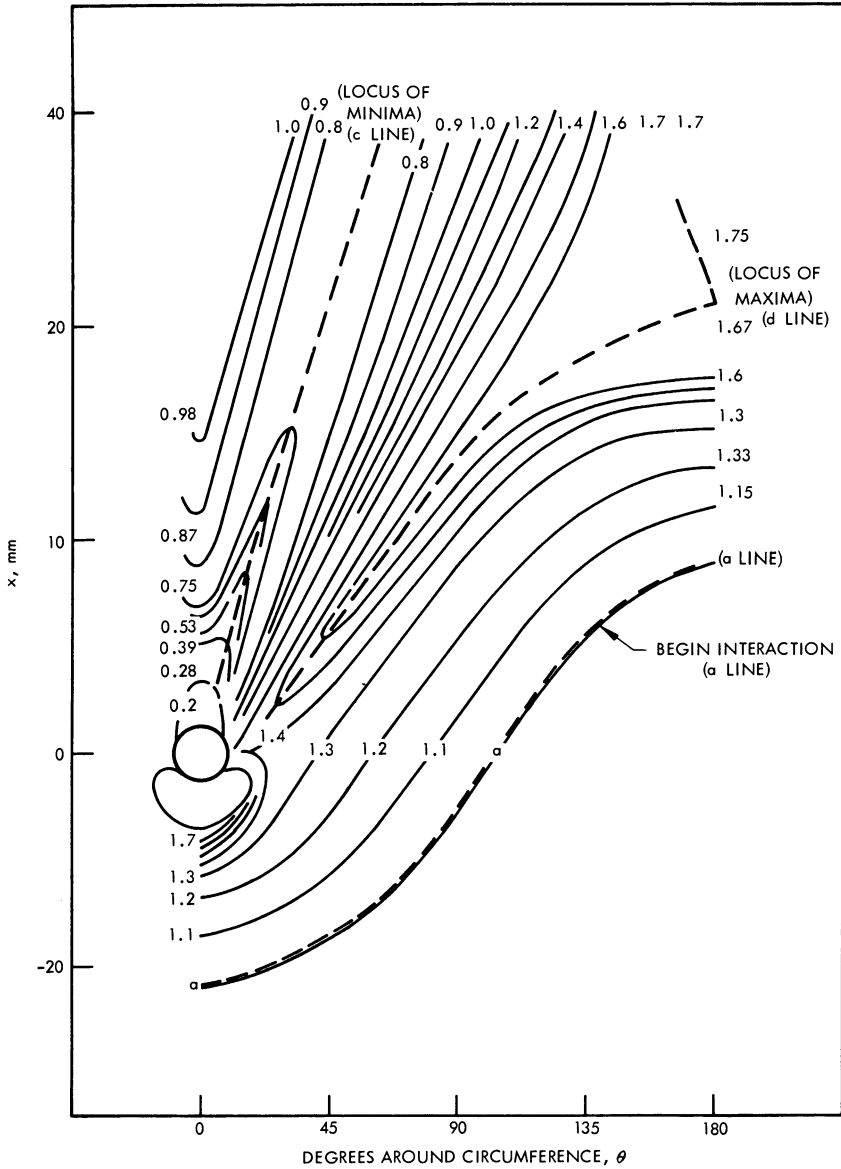
Fig. 12-8 Isobars of wall pressure (as ratios to the local ideal undisturbed static pressure) on surface of nozzle with a transverse jet; sonic jet exit (Charwat & Allegre, 1965).

The class of problems dealing strictly with the average asymmetric force field set up by the transverse jet as in application to aerodynamics force vector control can be dealt with semi-analytically with some cuccess. Two classes of models have been used to correlate the data. The first class focuses on estimating
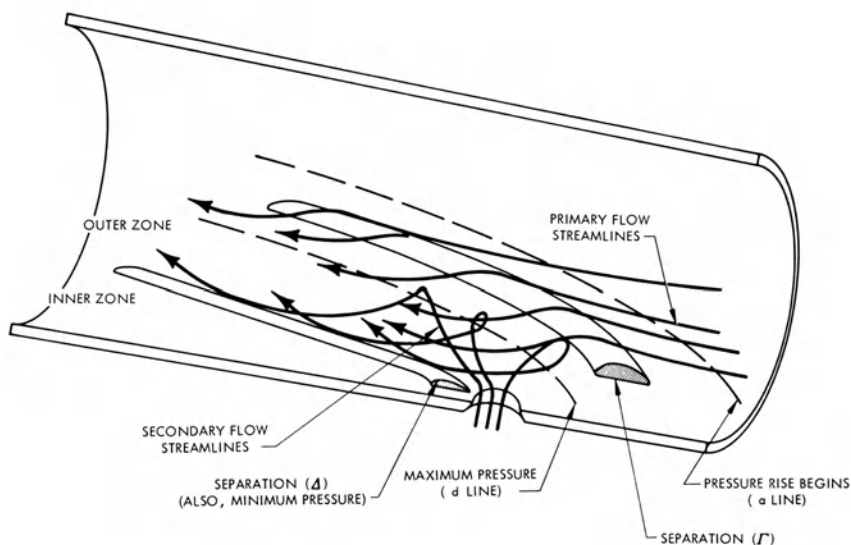
Fig. 12-9 Schematic of three-dimensional interaction of a circular transverse sonic jet discharging into a supersonic stream (Charwat & Allegre, 1964).

the "equivalent height" of a protrusion representing the jet. Typically, it is assumed that it expands to free stream pressure, turns, and flows downstream through a streamtube of diameter h. Next the axial pressure force on a blunt body of cross-sectional diameter h is estimated, using for example, the Newtonian pressure coefficient formula and prescribing a shape for the "nose" of the equivalent body. Equating these, an estimate for h is obtained.

It is not reasonable to consider realistic this type of model, of which several versions have been proposed: *e.g.*, Zukoski and Spaid (1964), Chapkis, Mager, and Wu (1961). They should be thought of merely as a framework in what is essentially an argument to isolate the dimensionless grouping of governing parameters which are believed to dominate the gross characteristics of the interaction. The true picture of the expansion and turning of the jet, especially when it is sonic or supersonic at the exit, would have to be derived from consideration of the local three-dimensional solution for the plume; Charwat and Allegre (1965) used, for example, qualitative features of the pressure distribution on the axis of the secondary jet to suggest that there are situations where the "penetration height" of the jet is determined by a mechanism governing the normal-shock standoff distance similar to what was described in the preceding discussion of opposing jets.

Perhaps the simplest and most effective analytical correlation of transverse-jet force data is that due to the Broadwell (1963) and elaborated by Hsia (1966) to second order. In order to estimate

the shape and strength of the main shock in the main stream which envelops the interaction region, Broadwell proposes the use of the "blast-wave analogy" well known in the treatment of blunt-nosed slender bodies in hypersonic flow. Once again, the "analogy" as such is tenuous but is a simple way to isolate the dominant dimensionless parameters.

According to this model, the crossflow due to the jet (an axisymmetric disturbance in a steady flow) is analogous to the effect of a two-dimensional explosion (one-dimensional unsteady problem) of a line-charge. The energy of the explosion is set proportional to the transverse momentum of the jet

$$E \sim \dot{m}_j V_j$$

and using the known solution of the time-unsteady problem which gives for the radius of the shock (c is the velocity of sound)

$$R = \left(\frac{2ctR_0}{J^{1/2}}\right)^{1/2} \left(1 - \frac{J^{1/2} \lambda ct}{2R_0}\right)$$

$$R_0 = \left[\frac{1}{2\pi} \frac{E}{P_\infty}\right]^{1/2}$$

$$\left.\begin{array}{l} J = .88 \\ \lambda = -1.989 \end{array}\right\} \text{ for } \gamma = 1.4$$

one obtains the shape of the interaction shock generated by the secondary jet, replacing t (time) by X/U_∞ (with origin at the shock which is practically identical with the upstream edge of the orifice). The theory supplies a characteristic dimension which is

$$R_c = \left(\frac{\dot{m}_i}{\dot{m}_0} A_\infty \frac{V_j}{V_\infty}\right)^{1/2}$$

and which normalizes both the shape of the shock and its strength. An example (Hsia, Seifert, Karamchetti, 1964) is shown in Fig. 12-10. This permits one to correlate uniquely the net transverse force due to the secondary jet. Various refinements have been treated: the "blast wave analogy" can be carried out to second order, evaporation of a liquid or chemical reactions can be introduced, and so on.

The Brodwell model can be applied only to round secondary jets. It neglects entirely the overpressure due to upstream separation.
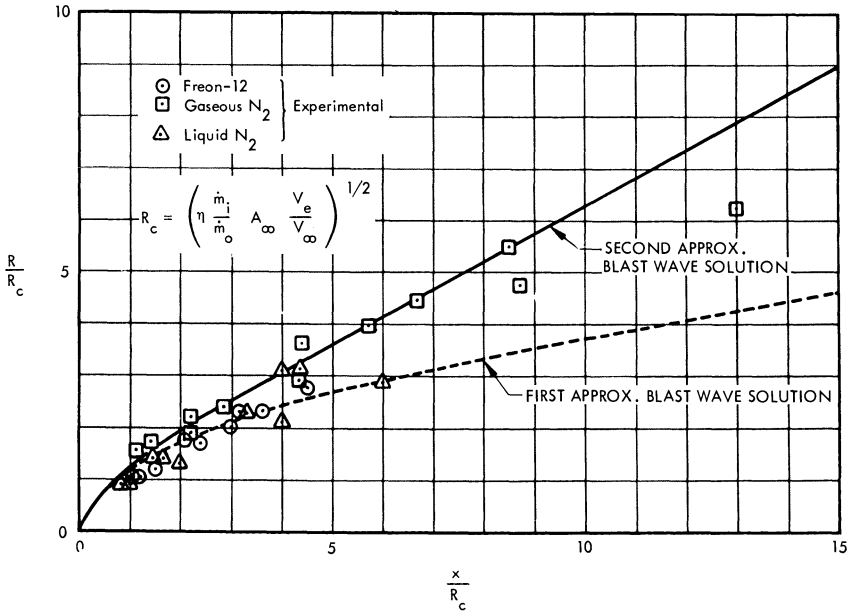
Fig. 12-10 Correlation of shock shape for M_∞ = 3.20 with blast-wave analogy model (Hsia, Seifert & Karamchetti, 1964).

This contribution is, indeed, small for round jets, supersonic free streams and thin turbulent boundary layers. This is typical of thrust-vector control injection into nozzles. Conversely, in hypersonic, laminar flow with two-dimensional jets from long-span slots, the upstream separation zone contributes most of the side force. Downstream overpressures have also been observed in hypersonic flow; *e.g.*, Kaufmann, 1967. In these situations, which are typical of jet-flap application to external aerodynamic surfaces, ratios of the total transverse interaction force to the thrust of the side jet alone as high as 20 have been observed (Kaufmann, 1967).

The existing force correlations are all extremely imperfect and wide variations among different test conditions and different models are common. This is because none of the models on which the correlation is based takes into account the spectrum of phenomena which contribute. It seems questionable that a reasonably complete model of the interaction could be constructed and, if it were defined, that it would not be much harder to deal with than developmental testing.

A bibliography of side-jet literature is appended.

[12-4] SUMMARY

The present review outlined the structure and the properties of
a class of flows involving regions of flow separation induced by
secondary jets. In general, no theoretical analysis of these complex,
interacting, composite flows is possible. However, many of their
basic properties and the nature of the mechanism which governs
their structure can be identified and correlated in terms of simple
semi-empirical models. With experience and caution, it becomes
possible to control them and use them as a design element, and,
as such, they can have interesting applications.

SELECTED BIBLIOGRAPHY ON JETS DIRECTED UPSTREAM

1. Baron, J.R. and E. Alzner: An Experimental Investigation of
   Two-layer Inviscid Shock Cap due to Blunt Body Nose Injection,
   J. Fluid Mech., 15, Pt. 3, pp. 442-448, 1963.
2. Charczenko, N. and K.W. Hennessey: Investigation of a Retro-
   Rocket Exhausting from the Nose of a Blunt Body into a
   Supersonic Free Stream, *NASA TN D-751*, 1961.
3. Charwat, A.F. and D. Faulmann: Investigation of the Flow and
   Drag due to Control Jets Discharging Upstream into a Super-
   sonic Flow, Proc. XV, Intern. Astronautical Congress, Warsaw,
   1964, Vol. III, pp. 85-108.
4. Eminton, E.: Orifice Shapes for Ejecting Gas at the Nose of a
   Body in Two-dimensional Flow, *RAE (Brit.) Rep. Aero. 2711*,
   August 1960.
5. Ferri, A. and M.H. Bloom: Cooling by Jets Directed Upstream
   in Hypersonic Flow, *WADC TN 56-382*, September 1956.
6. Gollnick, Jr.: Experiments on Blunt-Body Flows with Central
   Injection, *AFOSR 65-1149*, May 1965.
7. Hayman, L.O. and R.W. McDearmon: Jet Effects on Cylindrical
   Afterbodies Housing Sonic and Supersonic Nozzles which
   Exhaust Against a Supersonic Stream at Angles of Attack
   from 90° to 180°, *NASA TN D-1016*, March 1962.
8. Lam, S.H.: Interaction of a Two-dimensional Inviscid In-
   compressible Jet Facing a Hypersonic Stream, *AFOSR, TN
   53-274, Rep. 447*, March 1959.
9. Lopatroff, M.: Wing-flow Study of Pressure-Drag Reduction
   at Transonic Speeds by Projecting a Jet of Air from the Nose
   of a Prolate Spheroid of Finess Rato 6, *NACA RM L51E09*,
   1951.
10. Love, E.S.: The Effects of a Small Jet of Air Exhausting from
    the Nose of a Body of Revolution in Supersonic Flow, *NACA
    RM-L52I19a*, 1952.
11. McMahon, H.W.: An Experimental Study of the Effect of Mass
    Injection at the Stagnation Point of a Blunt Body, *GALCIT
    Memo No. 42*, May 1958.

12. Peterson, V.L. and R.L. McKenzie: Effects of Simulated Retro-rockets on the Aerodynamic Characteristics of a Body of Revolution at Mach Numbers from 0.25 to 1.90, *NASA TN D-1300*, May 1962.

13. Prosnak, W.J.: On the Viscous Flow Near the Stagnation Point on an Interface, Archivum Mechaniki Stosowaney (Warsaw) Vol. 14, pp. 506-541, 1962 (see also *Princeton University Report 563, AFOSR Contract AF 49 (368)-465*, 1962).

14. Romeo, D.J. and J.R. Sterrett: Exploratory Investigation of the Effect of a Forward-Facing Jet on the Bow Shock of a Blunt Body in a Mach Number 6 Free Stream, *NASA TN D-1605*, February 1963.

15. Sutton, E.P. and P.J. Finley: The Flow of a Jet From the Nose of an Axisymmetric Body in a Supersonic Airstream, Archivum Mechaniki Stosowaney (Warsaw) Vol. 16, pp. 782-804, 1964.

16. Tucker, L.M.: An Experimental Investigation of Contoured Nose Orifices with Ejection at Free-Stream Mach Numbers of 1.86 and 4.3, *RAE (Brit.) Tech. Note Aero 2923*, November 1963.

17. Wang, Chang-Yi: Contours for Stagnation Point Mass Injection in Hypersonic Flow, *AIAA J.*, p. 179, January 1964.

18. Warren, C.H.E.: An Experimental Investigation of the Effect of Ejecting a Coolant Gas at the Nose of a Blunt Body, *J. Fluid Mech.*, 8, Part 3, 400-417, 1966.

19. Watts, G.A.: An Experimental Investigation of a Sonic Jet Directed Upstream Against a Uniform Flow, University of Toronto, *Inst. Aerophys. TN No. 7*, January 1956.

SELECTED BIBLIOGRAPHY ON TRANSVERSED JETS

1. Ackerberg, R.C. and A. Pal: On the Interaction of Two-dimensional Jet with a Parallel Flow, *PIBAL Report 889*, September 1965 (AD 631-873).

2. Amick, J.L.: Circular Ark Jet Flaps at Supersonic Speeds— Two-dimensional Theory, *University of Michigan APL/JHU CR-24*, July 1966.

3. ——— and G.F. Carvalho: Interaction Effects of a Jet Flap on a 60° Delta Wing at Mach Number 4, and Comparison with Two-dimensional Theory, University of Michigan, Dept. of Aerospace Engr., *Rep. APL/JHU CM 1031*, February 1963.

4. ——— and P.B.Hays: Interaction Effects of Side Jets Issuing from Flat Plates and Cylinders Alined with a Supersonic Stream, *WADD Technical Report 60-329*, June 1960.

5. Bankston, L.T. and G.G.Barnes: Gas Injection Thrust Vectoring, *NOTS Report IDP 662*, China Lake, July 23, 1959.

6. ——— and H.M. Larsen: Thrust Vectoring Experiments with Gas Injection, *NOVORD Report 6548*, China Lake, May 1959.

7. Baxter, A.I.V.: The Application of Jet Pumping to Liquid Injection Thrust Vector Control, *AIAA Paper 64-231*, 1st Annual Meeting, Washington, D.C., June 1964.

8. Broadwell, J.E.: An Analysis of the Fluid Mechanics of Secondary Injection for Thrust Vector Control, *AIAA J.*, 1, 1067-1075, 1963 (see also *STL Rep. 6120-7744 MU 000*, March 1962).

9. ————: Correlation of Rocket Nozzle Gas Injection Data, *AIAA Journal*, 1, 8, August 1963, pp. 1911-1913.

10. Chamay, A.J. and R.A. Sederquist: An Experimental Investigation of Shock Vector Control with Gaseous Secondary Injection, *ARS Preprint 2216-61*, August 1961.

11. Charwat, A.R. and J. Allegre: Interaction of a Supersonic Stream and a Transverse Supersonic Jet, *AIAA J.*, 2, 1965-1972, 1964.

12. Cubbison, R.W., B.H. Anderson and J.J. Ward: Surface Pressure Distributions with a Sonic Jet Normal to Adjacent Flat Surfaces at Mach 2.92 to 6.4, *NASA TN D-580*, February 1961.

13. Dowdy, M.W. and J.F. Newton, Jr.: Wind Tunnel Experiments on Freon-12 Secondary Injection, *Space Program Summary No. 37-17*, Vol. IV, Jet Propulsion Laboratory, Pasadena, October 1962.

14. ————and————: Investigation of Liquid and Gaseous Secondary Injection Phenomena an a Flat Plate with M = 2.07 to M=454, Jet Propulsion Laboratory, *Tech. Rept. 32-542*, December 1963.

15. Dupuichs, G.: Les Performences du Pilotage par Injection Fluids Secondaire en Atmosphere Rarefree, III European Space Flight Symposium, Stuttgart, May 1963, *Paper No. 1547*.

16. ————: Mecanisme de la deviation d'un ecoulment supersonique par un jet transversal, *Tech Sci. Aeronaut. Spaciale* 2, 130-142, 1962.

17. ————and C. Pavlin: Deviation de Jets des Fusees, *Technique det Sciences Aeronautiques et Spaciales*, Vol. 2, 1962.

18. Erickson, L.H. and H.S. Bell, Jr.: Optimum Design Investigation of Secondary Injection Thrust Vector Control, Thiokol Chemical Corp., *Report AFSC-TR-61-1, TW-965-12-61*, 1962.

19. Ferrari, C.: Interference Between a Jet Issuing Laterally from a Body and the Enveloping Supersonic Stream, Johns Hopkins University, Applied Physics Laboratory, *Bumblebee Report 286*, April 1959.

20. Green, C.J. and F. McCullough, Jr.: Liquid Injection Thrust Vector Control, *AIAA Journal*, 1, 573-578, 1963.

21. Gregory, E.A.: Rocket Nozzle Vectoring Force Study, *Test 191T*, The Boeing Airplane Company, Aerospace Division, November 1960.

22. Hausmann, G.F.: Thrust Axis Control of Supersonic Nozzles by Airjet Shock Interference, *United Aircraft Corporation Department Report R-63143-24*, May 2, 1952.
23. Hawk, N.E. and J.L. Amick: An Experimental and Theoretical Investigation of Two-dimensional Jet Flap Aerodynamic Interaction at Supersonic Speeds, University of Michigan, *Dept. of Aerospace Engr. Rep. APL/JHU, CR 23*, October 1965.
24. Heyser, A. and F. Maurer: Experimental Investigation on Solid Spoilers and Jet Spoilers at Mach Numbers of 0.6 and 2.8, *Zeitschrift fur Flugwissenschoften*, 10:4, 5, 1962.
25. Hsia, H.T.: Equivalence of Secondary Injection to a Blunt Body in Supersonic Flow, *AIAA J.*, 4:10, 1832-1835, 1966.
26. ————, H. Seifert and K. Karamchetti: Induced Shocks by Secondary Fluid Injection in Supersonic Nozzle Flow, *J. of Spacecraft and Rockets*, 2, 67-72, 1965.
27. Hanos, J.J.: Loads Induced on a Flat-Plate Wing by an Air Jet Exhausting Perpendicularly Through the Plate and Normal to a Free-stream Flow of Mach Number 2.0, *NASA TN D-649*, March 1961.
28. Kallis, J.M. and Marvin Adelberg: Recent Advances in the Fluid Dynamics of Gas Injection for Thrust Vector and Trajectory Control, *Report No. ATN-63 (3305)-3*, Aerospace Corporation, July 1963.
29. Karamchetti, K. and H. Hsia: An Integral Approach to the Analysis of Thrust Vector Control by Secondary Injection, *AIAA J.*, November 1963.
30. Kaufman, L.G.: Hypersonic Flows Past Transverse Jets, *AIAA Paper 65-190*, 5th Aerospace Science Meeting, New York, January 1967.
31. Kehlet, A.B.: Free Flight Investigation of Comparative Zero Lift Rolling Effectiveness of Leading Edge and a Trailing Edge Air-jet Spoiler on an Unswept Wing, *NACA RM L57510*, August 1957.
32. Lefko, W.: Loads Induced on a Flat Plate at a Mach Number of 4.5 with a Sonic of Supersonic Jet Exhausting Normal to the Surface, *NASA TN D-1935*, July 1963.
33. Lingen, A.: Jet-Induced Thrust-Vector Control Applied to Nozzles Having Large Expansion Ratios, *United Aircraft Corp. Research Dept. Report R-0937-33*, March 1, 1957.
34. Mauer, F.: Interference Effects Produced by Gaseous Side-Jets Issuing into a Supersonic Stream (Translated from DVL Bericht 382, Deutsche Luft und Raumfahit Forschungstericht 65-04) *APL Library Bulletin Translation Series TG 230-T460*.
35. ————, Three-Dimensional Effects in Shock Separated Flow Regions Ahead of Lateral Control-Jets Issuing From Slot Nozzles of Finite Length, *AGARD CP 4*, Pt. 2, p. 597, May 1966.

36. Moak, H.: Thrust Vector Control Schemes for Solid Propellant Rockets, *Astronautics*, 7, 28, 1962.

37. Newton, J.F., Jr. and F.W. Spaid: Interaction of Secondary Injectants and Rocket Exhaust for Thrust Vector Control, *ARS Journal 32*, 1204-1211, 1961.

38. ————, and————: Experiments on the Interaction of Secondary Injectants and Rocket Exhaust for Thrust Vector Control, *Jet Propulsion Laboratory Technical Report 32-203*, February 12, 1962. Also *ARS Journal*, 32, August 9, 1962, pp. 1203-1211.

39. Poisson-Quinton, P. and L. Lepage: French Research on Control of Boundary Layer and Circulation, in: Boundary Layer and Flow Control, Vol. 1 (C.V. Lachman, ed.), Pergamon Press, 1961.

40. Rodriguez, D.J.: An Experimental Investigation of Jet-Induced Thrust Vector Control Methods, presented at the 17th Annual JANAF-ARPA-NASA Solid Propellant Meeting, Denver, May 23-25, 1961.

41. Spaid, F.W., E.E. Zukoski, and R. Rosen: A Study of Secondary Injection of Gases into a Supersonic Flow, Jet Propulsion Laboratory *Tech. Rep. 32-834*, August 1966.

42. Sterrett, J.R. and J.B. Barber: A Theoretical and Experimental Investigation of Secondary Jets in a Mach 6 Free Stream with Emphasis on the Structure of the Jet and Separation Ahead of the Jet, *AGARD CP 4*, Pt. 2, pp. 667, May 1966.

43. Strable, W.C.: Theoretical Studies on the Effects of Blowing and Suction in Laminar Separated Regions, *AIAA Paper 67-192*, 5th Aerospace Sciences Meeting, New York, 1967.

44. Strike, W.T., Jr.: A Study at Mach 10 of the Aerodynamic Disturbances Generated Over a Flat Plate Containing Lateral Jet Nozzles, *AEDC TR 66-48*, April 1966 (title unclassified, report confidential).

45. ————, C.J. Schueler, and J.S. Deitering: Interactions Produced by Sonic Lateral Jets Located on Surfaces in a supersonic Stream, *AFDC TRD 63-22*, April 1963.

46. Taylor, G.I., The Use of a Vertical Air Jet as a Windscreen, Jubile Scientifique de M.D.P. Ribouchinsky, pp. 313-17, 1954.

47. Ting, L., P.A. Libby, and C. Ruger: The Potential Flow due to a Jet and a Stream With Different Total Pressures, *PIBAL Report No. 855*, 1964.

48. Vinson, P.W., J.L. Amick, and H.P. Liepmann: Interaction Effects Produced by Jet Exhausting Laterally Near Base of Ogive-Cylinder Model in Supersonic Main Stream, *NASA Memo 12-5-58W*, February 1959.

49. Vizel, I.M. and L.L. Mostinskii: Bending of a Jet in a Drift Flow, *Inzhernerno-Fizicheskii Zhurnal*, 8, pp. 238-242 (in Russian), 1965.

50. Walker, R.E. and M. Shandor: Influence of Injectant Properties for Fluid Injection Thrust Vector Conteol, *AIAA Preprint 64-112*, January 1964.

51. ————,————and A.R. Stone: Secondary Gas Injection in a Conical Rocket Nozzle, *AIAA Journal*, 1, 334-338, 1963.

52. ————and————: Theoretical Performance of Selected Fluid Injectants for Thrust Vector Control, *Applied Physics Laboratory/Johns Hopkins University CM 1027*, November 1962.

53. ————, A.R. Stond and M. Shandor: Basic Experiments on Gas Injection and Probe TVC, paper presented at 6th BOWACA Symposium on Aeroballistics sponsored by Bureau of Naval Weapons (Oct. 31—Nov., 1963); see also Interaction Between Sonic Side Jets and Supersonic Duct Flow, *Applied Physics Laboratory/Johns Hopkins University BB 316*, December 1963.

54. Wu, J.M., R.L. Chapkis and A. Mager: An Approximate Analysis of Thrust Vector Control by Fluid Injection, *ARS J.*, 31, 1677-1685, 1961.

55. Zukoski, E. E. and F.W. Spaid: Secondary Injection of Gases into a Supersonic Flow, *AIAA J.*, 2, 1689-1696, 1964.

Gasdynamics of Explosions

A. K. Oppenheim
Professor of Aeronautical Sciences
University of California, Berkeley

ABSTRACT

Gasdynamics of explosions concerns the interrelationship between rate processes resulting in the deposition of a significant amount of power in the working substance, and its concomitant nonsteady motion. Fundamentals of this subject are based on nonsteady gasdynamics and the detonation theory; applications bear upon the extension of performance range of rocket propulsion systems. Presented here are basic elements of the theory.

[13-1] THEORETICAL ASPECTS

[13-1.1] Fundamentals of Non-steady Gasdynamics

In order to consider the fundamentals of nonsteady gasdynamics in the most practical manner, the treatment is restricted here to one-dimensional flow field. However, within this scope we do not limit ourselves to plane motion but include also cylindrical and spherical flow. Furthermore, we limit our attention to inertial effects only, so that the influence of transport phenomena is essentially neglected.

As in any aerothermochemical problem, the flow is constrained by restrictions imposed by the principles of the conservation of mass, momentum and energy. In view of our emphasis, however, it is more convenient to use the entropy equation as it is expressed by the second law of thermodynamics, rather than the energy equation as it is usually considered in aerothermochemistry. This does not introduce any fundamental differences, of course, but it provides considerable help in the transition from the typically Lagrangean concepts of energy transfer to the Eulerian description of the time-dependent flow field.

The fundamental equations are introduced here in the same general manner as in most standard texts [1-4] with the important

difference, however, that the restrictions introduced by the equation of state are relegated to the very last step, as it is indeed done in some cases of hypersonic flow theory [8]. As a consequence, the equations are first presented in a form not only unrestricted by the perfect gas assumption, as is usually the case, but applicable in effect to any chemically reactive substance. For the sake of simplicity, it is assumed that the state is fully determined by two independent thermodynamic parameters. Although, in principle, the analysis is restricted thereby to equilibrium states, in practice it can also be applied to nonequilibrium mixtures, provided that the composition in the course of the process in question is a function of the state which is fully defined by the two parameters.

[13-1.1.1] Continuity Equation

The mass balance for a differential segment of a stream tube is

$$\frac{\partial}{\partial t}(\rho \mathcal{A}) + \frac{\partial}{\partial x}(\rho U \mathcal{A}) = \phi$$

where ϕ is the mass flux added to the stream per unit length. Carrying out the differentiation and dividing by $\partial \mathcal{A}$, this yields

$$\frac{1}{\rho}\frac{\partial \rho}{\partial t} + \frac{u}{\rho}\frac{\partial \rho}{\partial x} + \frac{\partial u}{\partial x} = -\frac{1}{\mathcal{A}}\frac{\partial \mathcal{A}}{\partial t} - \frac{u}{\mathcal{A}}\frac{\partial \mathcal{A}}{\partial x} + \frac{\phi}{\rho \mathcal{A}}$$

or

$$\frac{1}{\rho}\frac{D\rho}{Dt} + \frac{\partial u}{\partial x} = -\frac{1}{\mathcal{A}}\frac{D\mathcal{A}}{Dt} + \frac{\phi}{\rho \mathcal{A}} \tag{13-1}$$

where $D/Dt \equiv (\partial/\partial t) + u(\partial/\partial x)$ is the so-called substantial derivative. For general one-dimensional flow,

$$\frac{1}{\mathcal{A}}\frac{\partial \mathcal{A}}{\partial x} = \frac{\sigma}{x}$$

where

$$\sigma \begin{cases} = 0 & \text{for plane flow} \\ = 1 & \text{for cylindrical flow} \\ = 2 & \text{for spherical flow} \end{cases}$$

[13-1.1.2] Equation of Motion

The equation of motion restricted to inertial effects only, is expressed in terms of the Euler equation:

$$\frac{Du}{Dt} + \frac{1}{\rho}\frac{\partial p}{\partial x} = \psi \tag{13-2}$$

where ψ represents all the body forces in the x-direction per unit mass.

[13-1.1.3] Entropy Equation

If the state is fully determined by two independent parameters,

$$ds = \frac{dh}{T} - \frac{dp}{\rho T} \tag{13-3}$$

It follows immediately from the above that

$$\left(\frac{\partial p}{\partial a}\right)_s = \rho\left(\frac{\partial h}{\partial a}\right)_s \tag{13-4}$$

where a may represent any other parameter of state, the velocity of sound, in particular.

Considering $\rho = \rho(a,s)$ where $a^2 \equiv (\partial p/\partial\rho)_s$ is the local speed of sound, or, what is more appropriate here, the relative velocity of a characteristic,

$$\frac{d\rho}{\rho} = \left(\frac{\partial\rho}{\partial a}\right)_s \frac{da}{\rho} + \left(\frac{\partial\rho}{\partial s}\right)_a \frac{ds}{\rho}$$

and, since from the definition of a and Eq. (13-4),

$$\left(\frac{\partial\rho}{\partial a}\right)_s = \left(\frac{\partial\rho}{\partial p}\right)_s \left(\frac{\partial p}{\partial a}\right)_s = \frac{\rho}{a^2}\left(\frac{\partial h}{\partial a}\right)_s$$

it follows that

$$\frac{d\rho}{\rho} = 2\left(\frac{\partial h}{\partial a^2}\right)_s \frac{da}{a} + \left(\frac{\partial\rho}{\partial s}\right)_a \frac{ds}{\rho} \tag{13-5}$$

Considering, similarly, $p = p\,(a, s)$

$$\frac{dp}{\rho} = \left(\frac{\partial p}{\partial a}\right)_s \frac{da}{\rho} + \left(\frac{\partial p}{\partial s}\right)_a \frac{ds}{\rho}$$

whence, with Eq. (13-4),

$$\frac{dp}{\rho} = 2\left(\frac{\partial h}{\partial a^2}\right)_s a\, da + \left(\frac{\partial p}{\partial s}\right)_a \frac{ds}{\rho} \qquad (13\text{-}6)$$

By the introduction of

$$\left.\begin{aligned}
\alpha &\equiv 2\left(\frac{\partial h}{\partial a^2}\right)_s \\[2ex]
\chi &\equiv -\frac{1}{\rho}\left(\frac{\partial \rho}{\partial s}\right)_a \\[2ex]
c^2 &\equiv \left(\frac{\partial p}{\partial \rho}\right)_a
\end{aligned}\right\} \qquad (13\text{-}7)$$

whence

$$\frac{1}{\rho}\left(\frac{\partial p}{\partial s}\right)_a = \left(\frac{\partial p}{\partial \rho}\right)_a \frac{1}{\rho}\left(\frac{\partial \rho}{\partial s}\right)_a = -c^2\chi$$

Equations (13-5) and (13-6) become, respectively,

$$\frac{d\rho}{\rho} = \alpha \frac{da}{a} - \chi\, ds \qquad (13\text{-}8)$$

and

$$\frac{dp}{\rho} = \alpha\, a\, da - c^2\chi ds \qquad (13\text{-}9)$$

The physical meaning of the definitions of Eqs. (13-7) can be brought out by the example of a perfect gas with γ = constant. In this case, $a^2 = \gamma RT;\ h = (\gamma/\gamma - 1)R'T;\ (\partial\rho/\partial s)_T = -(\rho^2 T/p) = -(\rho/R)$ and $(\partial p/\partial\rho)_T = RT$ so that

$$\alpha = 2\frac{dh}{da^2} = \frac{2}{\gamma - 1}$$

$$\chi = -\frac{1}{\rho}\left(\frac{\partial \rho}{\partial s}\right)_T = \frac{1}{R}$$

$$c^2 = \left(\frac{\partial p}{\partial \rho}\right)_T = RT = \frac{a^2}{\gamma}$$

and

$$c^2 \chi = T = \frac{a^2}{\gamma R}$$

[13-1.1.4] Characteristic Relations

Substituting Eq. (13-8) into (13-1) and multiplying by a, one obtains:

$$\alpha \frac{\partial a}{\partial t} + \alpha u \frac{\partial a}{\partial x} + a \frac{\partial u}{\partial x} = -a \frac{D \ln \mathbb{Q}}{Dt} + a \chi \frac{Ds}{Dt} + \frac{a^3 \phi}{\Gamma p \mathbb{Q}} \qquad (13\text{-}10)$$

where

$$\Gamma \equiv \frac{\rho}{p} a^2 = \frac{\rho}{p} \left(\frac{\partial p}{\partial \rho}\right)_s = \left(\frac{\partial \ln p}{\partial \ln \rho}\right)_s = \left(\frac{\partial h}{\partial e}\right)_s \qquad (13\text{-}11)$$

Substitution of Eq. (13-9) into (13-2) yields

$$\frac{\partial u}{\partial t} + u \frac{\partial u}{\partial x} + \alpha a \frac{\partial a}{\partial x} = c^2 \chi \frac{\partial s}{\partial x} + \psi \qquad (13\text{-}12)$$

Adding and subtracting Eqs. (13-10) and (13-12) under the assumption that α is constant (a fundamental restriction which limits the scope of the analysis to a regime where $(\partial h / \partial a^2)_s$ is virtually invariant), one finally obtains:

$$\frac{\partial}{\partial t}(\alpha a \pm u) + (u \pm a)\frac{\partial}{\partial x}(\alpha a \pm u)$$

$$= -a \frac{D \ln \mathbb{Q}}{Dt} + a \chi \left(\frac{Ds}{Dt} \pm \frac{c^2}{a}\frac{\partial s}{\partial x}\right) + \frac{a^3 \phi}{\Gamma p \mathbb{Q}} \pm \psi \qquad (13\text{-}13)$$

The above can be simplified by the introduction of the so-called referential derivatives, namely:

$$\frac{\delta_+}{\delta t} \equiv \frac{\partial}{\partial t} + (u + a)\frac{\partial}{\partial x}$$

$$\frac{\delta_-}{\delta t} \equiv \frac{\partial}{\partial t} + (u - a)\frac{\partial}{\partial x} \qquad (13\text{-}14)$$

which are related to the substantial derivative as follows:

$$\frac{\delta_+}{\delta t} = \frac{D}{Dt} + a\frac{\partial}{\partial x} \quad \text{and} \quad \frac{\delta_-}{\delta t} = \frac{D}{Dt} - a\frac{\partial}{\partial x}$$

so that

$$a\frac{\partial}{\partial x} = \frac{S_+}{\delta t} - \frac{D}{Dt} = -\frac{S_-}{S t} + \frac{D}{Dt}$$

Consequently, Eq. (13-13) becomes

$$\frac{\delta_\pm}{\delta t}(\alpha a \pm u) = -a\frac{D\ln\mathfrak{a}}{Dt} + \frac{c^2\chi}{a}\frac{S_\pm s}{St} + a\chi\left(1 - \frac{c^2}{a^2}\right)\frac{Ds}{Dt} + \frac{a^3\phi}{\Gamma p\mathfrak{a}} \pm \psi$$

$$(13\text{-}15)$$

It may be noted that for a perfect gas with $\gamma = $ constant, $c^2\chi/a = a/\gamma R$ and $a\chi[1 - (c^2/a^2)] = (a/R)[(\gamma - 1)/\gamma]$

Equations (13-15) can be expressed in nondimensional form by introducing the following parameters:

$$A \equiv \frac{a}{a_0}; \quad U \equiv \frac{u}{Q_0}; \quad (A_0 = 1)$$

$$\mathfrak{P} \equiv \alpha A + U \quad \left.\begin{array}{c} \text{Riemann} \\ \text{} \end{array}\right.$$

$$\mathfrak{Q} \equiv \alpha A - U \quad \left.\begin{array}{c} \text{} \\ \text{parameters} \end{array}\right\}$$

$$\mathfrak{s} \equiv \frac{c^2\chi}{a^2} s \quad (\mathfrak{s}_0 = 0)$$

$$\xi \equiv \frac{x}{L_0} = \frac{x}{a_0 t_0}; \quad \tau \equiv \frac{a_0 t}{L_0} = \frac{t}{t_0}$$

$$\Phi \equiv \frac{L_0 a_0 \phi}{\Gamma p_0 \mathfrak{a}}; \quad \Psi \equiv \frac{L_0 \psi}{a_0^2}$$

$$(13\text{-}16)$$

One should note, in this connection, that for variable entropy flow, the scope of the analysis will have to be restricted to regimes where $c^2\chi/a^2$ is virtually invariant. Furthermore, from Eqs. (13-9) and (13-11) it follows, that

$$\frac{dp}{p} = \Gamma\left(\alpha\frac{da}{a} - \frac{c^2\chi}{a^2} ds\right)$$

so, if Γ remains also invariant,

$$\frac{p}{p_0} = \left(\frac{A}{A_0}\right)^{\Gamma\alpha} e^{-\Gamma(\delta-\delta_0)} = A^{\Gamma\alpha} e^{-\Gamma\delta}$$

since $A_0 = 1$ and $\delta_0 = 0$.

Equation (13-15), multiplied by L_0/a_0^2, yields, consequently,

$$
\left.
\begin{aligned}
\frac{\delta_+ \mathcal{P}}{\delta\tau} &= -A\frac{D\ln\alpha}{D\tau} + A\frac{\delta_+\delta}{\delta\tau} + A\left(\frac{a^2}{c^2} - 1\right)\frac{D\delta}{D\tau} + \Phi A^{3-\Gamma\alpha} e^{\Gamma\delta} + \Psi \\[2em]
\frac{\delta_- \mathcal{Q}}{\delta\tau} &= -A\frac{D\ln\alpha}{D\tau} + A\frac{\delta_-\delta}{\delta\tau} + A\left(\frac{a^2}{c^2} - 1\right)\frac{D\delta}{D\tau} + \Phi A^{3-\Gamma\alpha} e^{\Gamma\delta} - \Psi
\end{aligned}
\right\}
$$

$$(13\text{-}17)$$

For complete solution, this has to be supplemented by information on entropy variation:

$$\frac{D\delta}{D\tau} = F(A, U, \delta, \xi, \tau)$$

The above describes the variation of the Riemann parameters $\mathcal{P}$ and $\mathcal{Q}$ in the ξ-τ plane along the characteristic directions given by

$$
\left.
\begin{aligned}
\frac{d\xi}{d\tau} &= U + A \qquad \text{for} \quad \mathcal{P} \\[1.5em]
\frac{d\xi}{d\tau} &= U - A \qquad \text{for} \quad \mathcal{Q} \\[1.5em]
\frac{d\xi}{d\tau} &= U \qquad\qquad \text{for} \quad \delta
\end{aligned}
\right\}
\qquad (13\text{-}18)
$$

and

as shown in Fig. 13-1a.

This is then the essence of the formulation of nonsteady compressible flow in terms of the method of characteristics. In general, as it is seen from the above treatment, the problem is resolved in terms of three characteristic directions. The solution involves an initial value problem with all conditions prescribed along a given characteristic curve; in principle, therefore, it can be obtained from Eqs. (13-17) by finite differences taken along triangular meshes

of the three characteristic directions. The reader interested in be-coming acquainted with the computational details of such solutions is referred for this purpose to the excellent text of Rudinger [1].
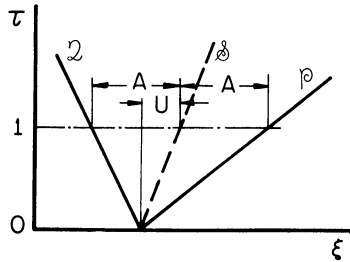
(a)
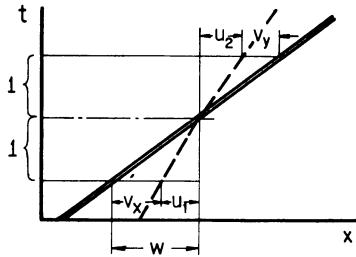
(b)

Fig. 13-1 Characteristics and discontinuity in the time-space domain.

[13-1.2] Gasdynamic Discontinuity

A distinguishing feature of gasdynamic flow fields is the exis-tence of discontinuities, *i.e.*, planes across which a finite change of state takes place without the variation in the mass flow rate per unit area, $\dot{m}$, and the stream force per unit area, f.

[13-1.2.1] Mechanical Conditions

The above definition leads immediately to the formulation of the so-called mechanical conditions between the density, ρ, normal relative flow velocity, v, and pressure, p, across the discontinuity, as depicted in Fig. 1b, namely,

$$\dot{m} = \rho_y v_y = \rho_x v_x$$

and

$$f = p_y + \rho_y v_y^2 = p_x + \rho_x v_x^2$$

(13-19)

where subscript x refers to the state ahead and y to that behind the discontinuity. By introducing $u \equiv v_x - v_y$, Eqs. (13-19) can be written in a more convenient form as:

$$
\left.
\begin{aligned}
u &= v_x \left(1 - \frac{\rho_x}{\rho_y}\right) \\[2ex]
\frac{p_y}{p_x} - 1 &= \frac{\rho_x}{p_x} v_x u = \frac{\dot{m} v_x}{p_x}\left(1 - \frac{\rho_x}{\rho_y}\right)
\end{aligned}
\right\}
\qquad (13\text{-}20)
$$

In order to represent the relations for a gasdynamic discontinuity in a nondimensional form, the most convenient and unambiguous reference parameter is $z_x^2 \equiv p_x/\rho_x$, rather than the velocity of sound in the undisturbed medium. Introducing then $\mathfrak{U} \equiv u/z_x$, $\mathfrak{O} \equiv v_x/z_x$, $\mathfrak{V} \equiv v_y/z_x$, $P \equiv p_y/p_x$ and $\nu \equiv v_y/v_x = \rho_x/\rho_y$, Eqs. (13-20) become

$$
\left.
\begin{aligned}
\mathfrak{U} &= \mathfrak{O}(1 - \nu) = \mathfrak{V}\,\frac{1}{\nu} - 1 \\[2ex]
P - 1 &= \mathfrak{U}\mathfrak{O} = (\mathfrak{O} - \mathfrak{V})\mathfrak{O}
\end{aligned}
\right\}
\qquad (13\text{-}21)
$$

or

$$
\left.
\begin{aligned}
\mathfrak{U}^2 &= (\mathfrak{O} - \mathfrak{V})^2 = (P - 1)(1 - \nu) \\[2ex]
\mathfrak{O}^2 &= \Gamma_x M_x^2 = \frac{\mathfrak{V}^2}{\nu^2} = \Gamma_y \frac{P}{\nu} M_y^2 = \frac{P - 1}{1 - \nu}
\end{aligned}
\right\}
\qquad (13\text{-}22)
$$

the relationships involving Mach numbers having been obtained by virtue of the definition of Eq. (13-11).

To determine the change of state across the discontinuity, the mechanical conditions are supplemented by the Hugoniot Relationship, $F(P,\nu) = 0$, which is derived from the energy balance.

[13-1.2.2] The Hugoniot Relationship

The energy equation for a discontinuity can be expressed in general as

$$
h_y - h_x - q = \frac{1}{2}\left(v_x^2 - v_y^2\right)
\qquad (13\text{-}23)
$$

where $h_y - h_x$ represents, in effect, that component of the enthalpy change that can be considered proportional to the thermodynamic state parameter, z, while q is the remaining component of enthalpy change which, for a given Hugoniot curve, is regarded as a constant. In order for this to be valid, it must be possible to express the enthalpy of state y so that

$$\left(\frac{\partial h}{\partial z^2}\right)_{@y} = \text{constant} \qquad \text{while} \qquad h = 0 \qquad \text{at} \qquad z = 0,$$

(13-24)

partial differentiation being taken along the process path.

It is convenient then to introduce a parameter

$$\beta_y \equiv \frac{1}{2\left(\dfrac{\partial h}{\partial 2^2}\right)_{@y} - 1}$$

(13-25)

in terms of which the enthalpy at y can be expressed simply as

$$h_y = \frac{1 + \beta_y}{2\beta_y} z_y^2 = \frac{1 + \beta_y}{2\beta_y} \frac{p_y}{\rho_y}$$

Similarly, of course

$$h_x = \frac{1 + \beta_x}{2\beta_x} z_x^2 = \frac{1 + \beta_x}{2\beta_x} \frac{p_x}{\rho_x}$$

(13-26)

and Eq. (13-23) can be written as

$$\frac{1 + \beta_y}{2\beta_y} \frac{p_y}{\rho_y} - \left(\frac{1 + \beta_x}{2\beta_x} \frac{p_x}{\rho_x} + q\right) = \frac{v_x^2}{2}\left[1 - \left(\frac{v_y}{v_x}\right)^2\right]$$

(13-27)

With the nondimensional parameters introduced for Eqs. (13-21) and (13-22), and taking advantage of the last of these equations, the above becomes

$$\frac{1 + \beta}{2\beta} P\nu - \left(\frac{1 + \beta_x}{2\beta_x} + Q\right) = \frac{P - 1}{2}(\nu + 1)$$

(13-28)

where

$$Q \equiv \frac{q}{z^2} = \frac{p_x q}{p_x}$$

while subscript y has been omitted as one referring to the variable end state $y = y(P,\nu)$.

The above can be reduced to

with

$$(P + \beta)(\nu - \beta) = C$$

$$C = (1 + \beta)(\nu_F - \beta)$$

or

$$C = (P_G + \beta)(1 - \beta)$$

$$(13\text{-}29)$$

where

$$\nu_F = \frac{2\beta}{1 + \beta}\left(\frac{1 + \beta_x}{2\beta_x} + Q\right) \qquad (13\text{-}30)$$

is the specific volume or velocity ratio attainable by a constant pressure combustion and

$$P_G = \frac{2\beta}{1 - \beta}\left(\frac{1 - \beta_x}{2\beta_x} + Q\right) \qquad (13\text{-}31)$$

is the pressure ratio attainable by constant volume combustion.

For constant β, Eq. (13-29) represents a rectangular hyperbola. Salient properties of such a Hugoniot curve for $Q > 0$ are demonstrated by curve H in Fig. 13-2. Points J and K, denoting the upper and lower Chapman–Jouguet states respectively, have the well-known property of local Mach number of unity.

On the basis of the above equations, this can be demonstrated as follows. According to Eq. (13-29), the slope of the Hugoniot curve is

$$-\left(\frac{\partial P}{\partial \nu}\right)_Q = \frac{P + \beta}{\nu + \beta} \qquad (13\text{-}32)$$

The slope of the Rayleigh Line passing through state $x(1,1)$ is given by the last of Eqs. (13-22). At the point of tangency, the two are equal. Hence,

$$\frac{P_J + \beta_J}{\nu_J - \beta_J} = \frac{P_J - 1}{1 - \nu_J} \qquad (13\text{-}33)$$

Fig. 13-2 The Hugoniot curve.

and a similar relation is valid for K. By cross-multiplying and rearranging, Eq. (13-33) becomes

$$(2P_J - 1 + \beta_J)(2\nu_J - 1 - \beta_J) = 1 - \beta_J^{\,2} \qquad (13\text{-}34)$$

which, in terms of

$$P_N = 1 + 2(P_J - 1)$$

and $\qquad\qquad\qquad\qquad\qquad\qquad\qquad\qquad\qquad\qquad (13\text{-}35)$

$$\nu_N = 1 - 2(1 - \nu_J)$$

acquires the form of the Rankine–Hugoniot Relationship, that is, Eq. (13-29) with $P_G = \nu_F = 1^*$. The upper branch of the corresponding curve is shown in Fig. 13-2 under symbol *RH*.

---

*This has been noted especially by Langweiler, Z.f Techn. Physik, 19:9, p. 276, 1938.

Invoking the relationship of Eq. (13-22) that involves M_J and rearranging further Eq. (13-34), one obtains, respectively, the following two equations:

$$\Gamma_J \frac{P_J}{\nu_J} M_J{}^2 = \frac{P_J - 1}{1 - \nu_J} = \frac{1 + \beta_J}{1 - \beta_J} \frac{P_J}{\nu_J} \qquad (13\text{-}36)$$

The equality between the outside terms in the above implies that $M_J = 1$, provided that

$$\Gamma_J = \frac{1 + \beta_J}{1 - \beta_J} \qquad (13\text{-}37)$$

Substituting then Eqs. (13-11) and (13-25) into Eq. (13-37), one obtains:

$$\left(\frac{\partial h}{\partial e}\right)_s = \frac{\left(\dfrac{\partial h}{\partial z^2}\right)_{@J}}{\left(\dfrac{\partial h}{\partial z^2}\right)_{@J} - 1} = \left[\frac{\partial h}{\partial (h - z^2)}\right]_{@J}$$

which, by definition of enthalpy, remembering that $z^2 = p/\rho$, yields

$$\left.\begin{array}{c}\left(\dfrac{\partial h}{\partial e}\right)_s = \left(\dfrac{\partial h}{\partial e}\right)_{@J} \quad \text{or} \quad \left(\dfrac{\partial h}{\partial z^2}\right)_{@J} = \left(\dfrac{\partial h}{\partial z^2}\right)_s \\[3ex] \text{that is,} \\[1ex] \beta_J = \beta_s\end{array}\right\} \qquad (13\text{-}38)$$

Equation (13-37) implies, therefore, that at state J (or K) the Hugoniot curve is tangent to the isentrope, which is indeed the fundamental property of the Chapman–Jouguet condition.* Equation (13-35) is recognized consequently as the locus of states of $M = 1$, and provides, similarly, as either Eqs. (13-33) or (13-34), a rational manner of evaluating β_J to match a given Chapman-Jouguet state, namely, with Eq. (13-22):

$$\beta_J = \frac{2 P_J \nu_J - P_J - \nu_J}{P_J - \nu_J} = \frac{\emptyset^2 + 1 - 2 P_J}{\emptyset^2 + 1} \qquad (13\text{-}39)$$

---

*For proof of salient properties of the Hugoniot Curve, see Section 13-3 of this chapter.

or, by virtue of Eqs. (13-35):

$$\beta_J = \frac{P_N \nu_N - 1}{P_N - \nu_N} = \frac{\mathbb{O}^2 - P_N}{\mathbb{O}^2 + 1} \tag{13-40}$$

There are many computer codes available today for the evaluation of the Chapman–Jouguet state [6]. Equations (13-29) and (13-39) permit description of the Hugoniot curve in the vicinity of this state in terms of a simple expression for a rectangular hyperbola. This curve is fully defined by two parameters: β which can be evaluated from Eq. (13-39) and C which can be subsequently determined by the use of Eq. (13-29).

[13-1.2.3] Oblique Discontinuity

In order to treat oblique discontinuities, one has to consider only the additional features associated solely with the geometry of flow, *i.e.*, with kinematic relations. Consider for this purpose an oblique wave front, as shown in Fig. 13-3a. Its angle of incidence with respect to the streamline is θ, while the incident flow velocity, w_x, consists of normal and tangential components, v_x and v_t, with respect to the wave front. Since plane front can affect only normal component of flow, change in the velocity vector can be represented by the hodograph shown in Fig. 13-3b where velocity vectors $\overline{w}_x$ and $\overline{w}_y$ have a common tangential component, v_t. The flow is deflected by an angle, δ, and the downstream velocity, w_y, acquires a different normal component, v_y.

In order to express the oblique wave relations in the simplest form, it is convenient to introduce a new parameter:

$$\omega \equiv \frac{\mathbb{W}_x^{\ 2}}{P - 1} \tag{13-41}$$

where $\mathbb{W}_x \equiv w_x / z_x$.

Since, as evident from Fig. 13-3, $v_x = w_x \sin \theta$, the mechanical condition expressed by the first of Eqs. (13-21) gives

$$\mathbb{W}_x (1 - \nu) \sin \theta = \mathbb{U} \tag{13-42}$$

while the last of Eqs. (13-21) and (13-41) yields

$$\omega (1 - \nu) \sin^2 \theta = 1 \tag{13-43}$$

Equation (13-42) reduces, therefore, to

$$\mathbb{W}_x = \omega \, \mathbb{U} \sin \theta \tag{13-44}$$
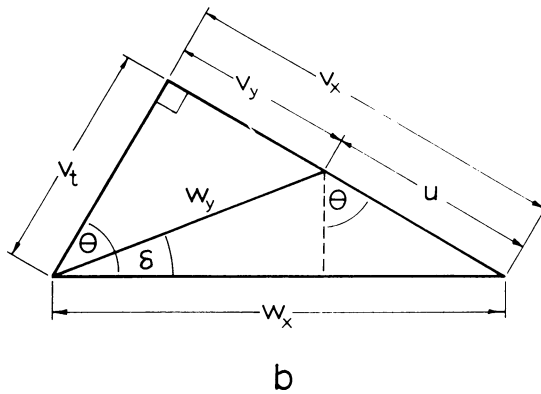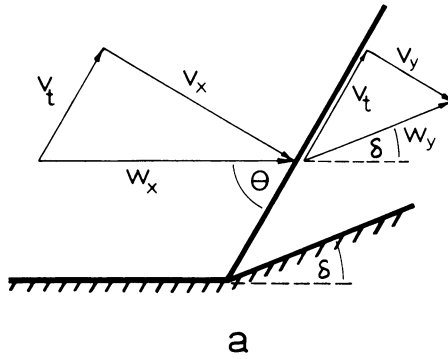
Fig. 13-3 Oblique discontinuity.

and, as a consequence of the identity $\tan \theta = (\sin^{-2}\theta - 1)^{-1/2}$, Eq. (13-43) becomes

$$\tan \theta = \frac{1}{\sqrt{\omega(1 - \nu) - 1}} \tag{13-45}$$

From the velocity hodograph of Fig. 13-3b,

$$\tan \delta = \frac{u \cos \theta}{w_x - u \sin \theta}$$

or

$$\tan \delta = \frac{1}{\left(\dfrac{w_x}{u \cos \theta} - 1\right) \tan \theta} \tag{13-46}$$

so that, as a consequence of Eqs. (13-44) and (13-45),

$$\tan \delta = \frac{\sqrt{\omega(1 - \nu) - 1}}{\omega - 1} \tag{13-47}$$

In order to evaluate the downstream velocity, one notes from the velocity hodograph of Fig. 13-3b that

$$w_y = \frac{w_x - u \sin \theta}{\cos \delta}$$

which, with the use of Eqs. (13-44) and (13-47), becomes

$$\mathbb{W}_y = \mathbb{W}_x \sqrt{1 - \frac{1 + \nu}{\omega}} \tag{13-48}$$

where $\mathbb{W}_y \equiv w_y / z_x$.

[13-1.3] Simple Wave

In a gasdynamic flow field, a simple wave is distinguished by the fact that its characteristics are straight lines. As apparent from the characteristic relations, Eqs. (13-17) and (13-18) this can occur only if one of the Riemann parameters is invariant and the referential velocity is constant. Under such circumstances, the characteristic is also a locus of a constant state. Consequently, a simple wave is bounded, as is a discontinuity, by regimes of constant states. It renders itself therefore to direct integration, yielding a functional relationship between the parameters of these states.

[13-1.3.1] Simple Wave in Non-Steady Flow

The invariance of the Riemann parameter implies immediately, by virtue of Eq. (13-13), the relationship

$$du = \alpha da \tag{13-49}$$

where, according to definition, Eq. (13-7), $\alpha \equiv 2(\partial h / \partial a^2)_s$.

It is of interest to note that the same relation is also obtained directly from the continuity equation for a discontinuity, as given by the first of Eqs. (13-20), which, in a differential form, yields:

$$du = \frac{v_x}{\rho} d\rho$$

Equation (13-49), then, is a direct consequence of the above; for a characteristic of a simple wave, $v_x = a$, while for an isentropic process the differential of density is related to velocity of sound by Eq. (13-8), with, of course, $ds = 0$. The characteristic of a simple wave is indeed an infinitesimal discontinuity, and, in accordance with the fundamental property of the Hugoniot curve, in the vicinity of the initial state, the change of state brought about by this wave is isentropic, as indeed demanded by Eq. (13-13) in consequence of Eq. (13-49).

The integral of Eq. (13-49) is, in terms of our nondimensional parameters,

$$U = \alpha(A - 1) \tag{13-50}$$

where $U \equiv (u/a_x) = \mathrm{U}/\sqrt{\Gamma_x}$, while, according to definitions of Eqs. (13-25) and (13-29), the relationship of Eq. (13-37) and the property expressed by Eq. (13-38),

$$\alpha = 2\left(\frac{\partial h}{\partial z^2}\right)_s \left(\frac{\partial h}{\partial a^2}\right)_s = \frac{\beta_s + 1}{\beta_s \Gamma} = \frac{2}{\Gamma - 1} \tag{13-51}$$

while, it should be remembered, for a perfect gas with constant specific heats, $\Gamma = \gamma$.

[13-1.3.2] Simple Wave in Steady Flow

Simple wave in steady flow has particular significance as a centered rarefaction fan, known as the Prandtl-Meyer expansion. In accordance with the foregoing treatment, its theory is introduced here, in contrast to the usual manner, without any restrictions introduced by the equation of state [5].

A ray of a rarefaction fan and the corresponding velocity hodograph are shown in Fig. 13-4, in the same manner as it was done in Fig. 13-3 for the discontinuity. From Fig. 13-4b it appears that

$$b = \cot(\theta + d\delta)\left(dw + 2w\sin^2\frac{d\delta}{2}\right)$$

or in the limit, when second order terms vanish identically,

$$b = \cos\theta\,dw$$

so that

$$d\delta = \frac{b}{w} = \cot\theta\,\frac{dw}{w} \tag{13-52}$$
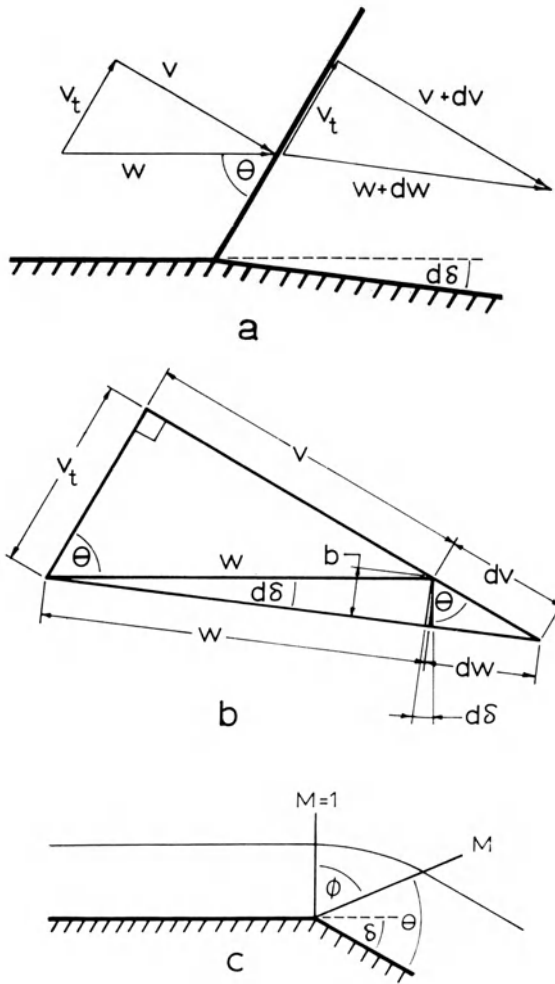
Fig. 13-4 Simple rarefaction wave in steady flow or the Prandtl-Meyer expansion.

and since

$$d\delta = \sqrt{M^2 - 1}\, \frac{dw}{w} \tag{13-53}$$

while, as $d\theta = [d(\sin\theta)]/\sqrt{1 - \sin^2\theta}$,

$$d\theta = -\frac{dM}{M\sqrt{M^2 - 1}} \tag{13-54}$$

The energy equation, as a consequence of the fact that the flow is isentropic, can be expressed as

$$\left(\frac{\partial h}{\partial w}\right)_s + w = 0 \tag{13-55}$$

whence

$$\frac{dw}{w} = -\left(\frac{\partial h}{\partial a^2}\right)_s \frac{2a\,da}{w^2} = -\frac{2}{M^2}\left(\frac{\partial h}{\partial a^2}\right)_s \frac{da}{a}$$

or, in terms of $\alpha \equiv 2(\partial h/\partial a^2)_s$, as per Eq. (13-7), and noting that $da/a = dw/w - dM/M$,

$$\frac{dw}{w} = -\frac{\alpha}{M^2}\frac{dw}{w} + \frac{\alpha}{M^2}\frac{dM}{M}$$

whence

$$\frac{dw}{w} = \frac{\alpha}{M^2 + \alpha}\frac{dM}{M} \tag{13-56}$$

The rarefaction fan is fully described in terms of the relationship between the angle ϕ, defined in Fig. 13-4c, and the Mach number. According to the diagram,

$$\phi = \frac{\pi}{2} + \delta - \theta \tag{13-57}$$

while Eqs. (13-53) and (13-56) yield

$$d\delta = \frac{\alpha\sqrt{M^2 - 1}}{M^2 + \alpha}\frac{dM}{M} \tag{13-58}$$

Consequently, with the use of Eq. (13-54),

$$d\phi = d\delta - d\theta = \frac{\alpha + 1}{(M^2 - 1) + (\alpha + 1)}\frac{M\,dM}{\sqrt{M^2 - 1}} \tag{13-59}$$

whence

$$\phi = \int \frac{\alpha + 1}{(M^2 - 1) + (\alpha + 1)}\frac{M\,dM}{\sqrt{M^2 - 1}} = \int \frac{\alpha + 1}{\mu^2 + (\alpha + 1)}\,d\mu \tag{13-60}$$

where $\mu \equiv \sqrt{M^2 - 1}$.

If α = const., the above can be integrated, yielding

$$\phi = \sqrt{\alpha + 1} \ \tan^{-1} \frac{\mu}{\sqrt{\alpha + 1}} = \sqrt{\alpha + 1} \ \tan^{-1} \sqrt{\frac{M^2 - 1}{\alpha + 1}}$$

(13-61)

where the constant of integration has been adjusted so that $\phi = 0$ at $M = 1$, as indicated on Fig. 13-4c.

Finally, since $\pi/2 - \theta = \cos^{-1}(1/M)$, it follows from Eq. (13-57) that

$$\delta = \sqrt{\alpha + 1} \ \tan^{-1} \sqrt{\frac{M^2 - 1}{\alpha + 1}} - \cos^{-1}\left(\frac{1}{M}\right)$$ (13-62)

while, as before, for a perfect gas with constant specific heats, $\alpha = 2/(\gamma - 1)$, so that $\alpha + 1 = (\gamma + 1)/(\gamma - 1)$.

[13-2] ANALYTICAL ASPECTS

[13-2.1] Vector Polar Method

One of the most useful ways of treating problems in nonsteady gasdynamics is to consider the flow field in the time-space domain as consisting of regimes of uniform states bounded by wave fronts. One needs only to recognize the existence of two types of waves: steady waves, or gasdynamic discontinuities, and simple waves, since these are the only fronts that can be bounded by constant state regimes. The whole flow field is determined then by the solutions of all the wave interaction processes. This can be accomplished by the use of the Polar Method which can be considered a "method of characteristics in the large," in that the flow field is thought to be made up solely of fronts associated with finite changes of state, rather than characteristics associated with infinitesimal changes.

In practice this is fruitful only if attention is focussed on a sufficiently large flow field so that the wave interaction events are short in comparison to the overall wave propagation process. Since a noninteracting wave front propagates through a uniform regime at a constant velocity, the cases where the Polar Method can be applied are recognized in experimental records such as those of Fig. 13-5 as regimes where the world-lines, *i.e.*, traces of wave fronts in the time-space domain, can be approximated by straight line segments. Each point of intersection between these segments represents a wave interaction process which, in principle, is amenable to solution by this method.
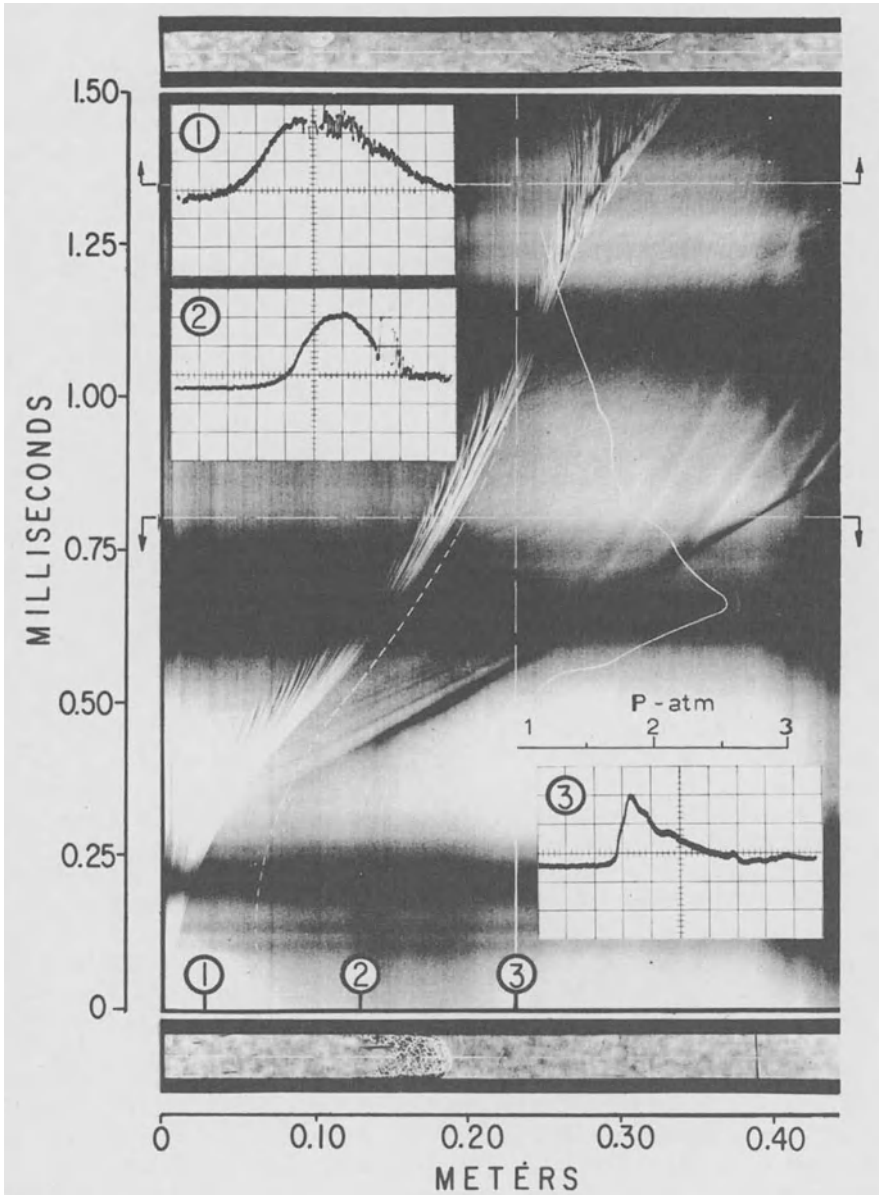
Fig. 13-5 Streak schlieren photograph of accelerating flame and the concomitant flow field (9) in a stoichiometric hydrogen–oxygen mixture maintained initially in a 1" × 1-1/2" cross-section tube at NTP. Displayed as inserts are pressure records at positions 1, 2 and 3. Vertical scale: 5.2 psia/cm for record (1), 10.4 psi/cm for records (2) and (3); horizontal sweep from left to right: 100 μsec/cm for records (1) and (2) 200 μsec/cm for record (3).

Polar Method is based upon the principle that a wave interaction process creates a regime of uniform pressure and flow velocity. The solution is obtained by finding the intersection between Polars, *i.e.*, loci of pressures and flow velocities attainable by the wave fronts in question. The most convenient manner of determining such intersections is, of course, by a graphical technique. This is then accomplished by the Vector Polar Method, where the polar diagrams are rendered a vectorial character by the use of proper scales for the coordinates. The solution obtained by the use of Vector Polars represents, in effect, a vector determined by the summation of component vectors, each representing the change of state brought about by a wave front participating in the interaction process.

[13- 2. 1. 1] Wave Interactions

a. Steady Wave Polars

Equation for the wave polar of a discontinuity is obtained by the use of the Hugoniot Relationship, Eq. (13-29) to eliminate ν from the first of Eqs. (13-22), yielding

$$u^2 = \frac{(P - 1)(P - P_G)(1 - \beta)}{P + \beta} \tag{13-63}$$

where P_G is given by Eq. (13-31). The corresponding expression for the wave propagation velocity is derived similarly from the second of Eqs. (13-22), leading to

$$\mathbb{D}^2 = \frac{(P - 1)(P + \beta)}{(P - P_G)(1 - \beta)} \tag{13-64}$$

The velocity of sound ratio across the discontinuity

$$A \equiv \frac{a}{a_x} = \sqrt{\frac{\Gamma z}{\Gamma_x z_x}} = \sqrt{\frac{\Gamma}{\Gamma_x} P\nu} \tag{13-65}$$

can be expressed similarly by the use of Eq. (13-29) as:

$$A^2 = \frac{\Gamma}{\Gamma_x} P \left[\frac{P_G + \beta}{P + \beta} (1 - \beta) + \beta \right]. \tag{13-66}$$

For a perfect gas with constant specific heats $\Gamma = \Gamma_x = \gamma$ and $\beta = (\gamma - 1)/(\gamma + 1)$, so that Eq. (13-31) reduces to

$$P_G = 1 + \frac{2\beta}{\beta - 1} \, Q = 1 + (\gamma - 1) Q = 1 + \frac{q}{c_v T_x} \qquad (13\text{-}67)$$

as it indeed should, since for a constant volume combustion under such circumstances, $P_G = T/T_x$.

For a shock $q = 0$ and $P_G = 1$. Eq. (13-63) yields then for $U \equiv u/a_x = \mathsf{U}/\sqrt{\gamma}$

$$U^2 = \frac{2}{\gamma(\gamma + 1)} \frac{(P - 1)^2}{(P - 1) + \dfrac{2\gamma}{\gamma + 1}} \qquad (13\text{-}68)$$

and, noting that if $\Gamma = \gamma$, $\mathfrak{D}_x{}^2 = \gamma M_x{}^2$, Eq. (13-64) reduces to the well-known relation

$$P - 1 = \frac{2\gamma}{\gamma - 1} \left(M_x{}^2 - 1 \right) \qquad (13\text{-}69)$$

while Eq. (13-66) becomes

$$A^2 = P \, \frac{\beta P + 1}{P + \beta} = P \, \frac{P + \dfrac{\gamma + 1}{\gamma - 1}}{\dfrac{\gamma + 1}{\gamma - 1} P + 1} \qquad (13\text{-}70)$$

Shock Polars expressing Eqs. (13-68) and (13-70) for $\beta = 1/6(\gamma = 1.4)$ and $\beta = 1/11(\gamma = 1.2)$ are presented by Fig. 13-6 with the auxiliary Mach number plot based on Eq. (13-69). It should be noted that the polar plots are rendered vectorial character by the use of logarithmic scales for P and A, while a linear scale is retained for U.

For any given wave interaction problem, U has to refer to the same value of the reference velocity, a_0. It has to be expressed therefore in terms of

$$U_0 \equiv \frac{u}{a_0} = \frac{a_x}{a_0} \frac{u}{a_x} = A_x U \qquad (13\text{-}71)$$

where, it is understood, $A_x = a_x/a_0$. Consequently, the scale for U has to be appropriately adjusted, or stretched, by a horizontal shift implied by Eq. (13-71). It is for this reason then that Fig. 13-6 gives a family of polars for $A_x = 1, 2$ and 3 with the help of which any intermediate polar can be obtained by linear interpolation.

Figure 13-7 represents deflagration polars for $\beta = 1/11$, $\gamma_1 = 1.4$ and $C = 5.55$ ($\gamma_1 = 1.4$) corresponding to deflagration in equimolar hydrogen-oxygen mixture initially at 1 atm and 70° F. ($q = 931$ cal/gm).
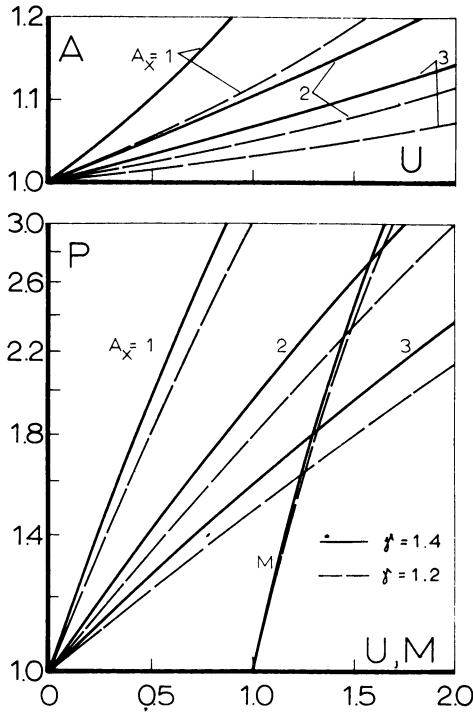
Fig. 13-6 Shock polars in the $P-U$ and $A-U$ planes for $\beta = 1/6$ ($\gamma = 1.4$) and $\beta = 1/11$ ($\gamma = 1.2$).

b. Simple Wave Polars

The equation for a simple wave polar is obtained from Eq.(13-50) with the use of proper relationship $A = A(P)$ for an isentropic process. For a perfect gas with constant specific heats, in terms of $U \equiv u/a_x = \mathcal{U}/\sqrt{\gamma}$ and, noting that under such circumstances $\alpha = 2/(\gamma - 1)$, this yields

$$U = \frac{2}{\gamma - 1} \left(P^{\frac{\gamma - 1}{2\gamma}} - 1 \right) \tag{13-72}$$

while the corresponding U-A relation follows directly from Eq. (13-50) as

$$U = \frac{2}{\gamma - 1} (A - 1) \tag{13-73}$$

and, of course,
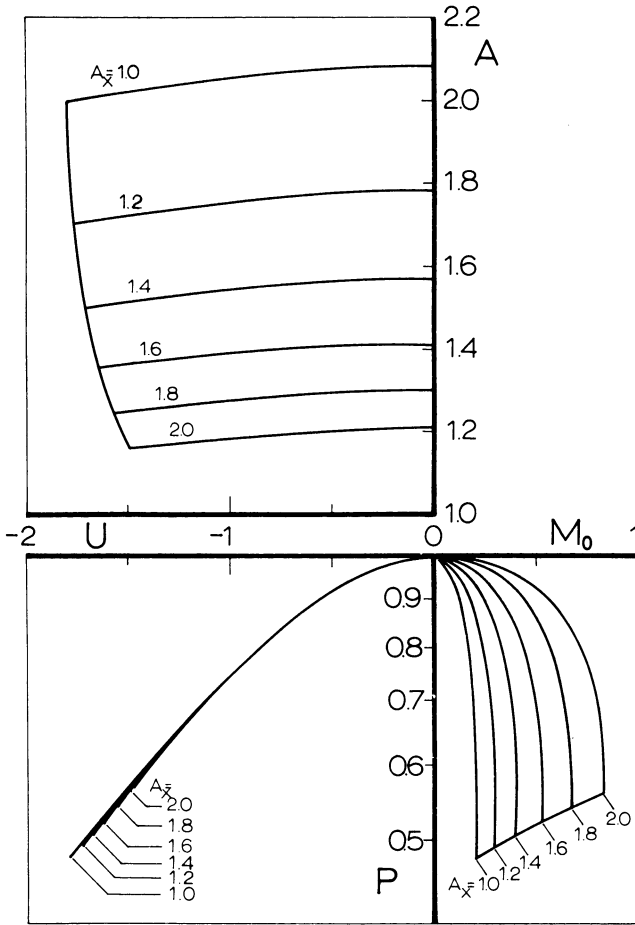
Fig. 13-7 Deflagration polars in the $P-U$ and $A-U$ planes for $\beta = 1/11$ and $C = 5.55$ ($\gamma_1 = 1.4$) corresponding to deflagration in equimolar hydrogen-oxygen mixture initially at 1 atm and 70° F. ($q = 931$ cal/gm).

$$A = P^{\frac{\gamma-1}{2\gamma}} \qquad\qquad (13\text{-}74)$$

Plots of Eq. (13-72) with $A_x = 1$, 2, and 3, are given by Fig. 13-8 for a rarefaction wave in a perfect gas with $\gamma = 1.4$ ($\alpha = 5$). Unlike the shock, the simple wave is bounded by a "head" and a "tail" of different propagation velocities, each equal to the velocity of sound in the appropriate regime. For this purpose, Fig. 13-8 is supplemented by the plot of Eq. (13-74).
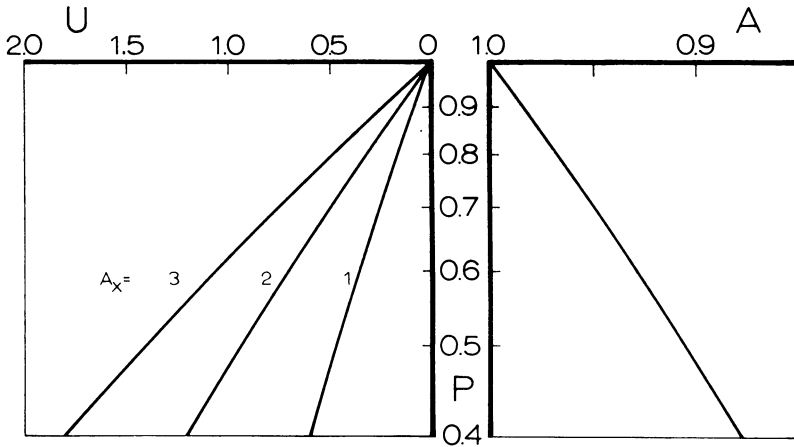
Fig. 13-8 Rarefaction polars in the $P-U$ plane and the auxiliary $P-A$ plot for $\alpha = 5$ ($\gamma = 1.4$).

c. Examples

1) Shock Tube Phenomena. The simplest illustration of wave interactions is provided by the processes occurring at the start of a shock tube. Initially there are two regimes, each at a different pressure but both at rest, separated by a diaphragm. The diaphragm is suddenly destroyed, producing a shock wave that moves into the low-pressure regime, and a rarefaction fan that propagates into the high-pressure regime.

Let the initial diaphragm pressure ratio be 2.62. The substance on both sides of the disphragm is kept initially at the same temperature, and it is assumed that it behaves essentially as a perfect gas with $\gamma = 1.4$. The solution is depicted in Fig. 13-9 and given in Table 13-1. The fact that there is a shock propagating into the regime 0 is represented on the $P-U$ and $A-U$ planes by shock polars for $A_x = 1$ of Fig. 13-6, starting from points ($U = 0, P = 1$) and ($U = 0, A = 1$), respectively. At the same time, the rarefaction moving into state 4 is represented on these planes by simple wave polars for $A_x = 1$ of Fig. 13-8, starting from points ($U = 0, P = 2.62$) ($U = 0, A = 1$). The intersection of the two polars on the $P-U$ plane determines the pressure and velocity of state 1, while the corresponding points in the $A-U$ plane specify the conditions 1 and 1a on the two sides of the contact discontinuity, a front across the same P and U but different A which, as demonstrated by Fig. 13-5, must be generated by such a process due to different history of particles that are adjacent to its sides. Included in Fig. 13-5 is the reflection of the shock wave from the closed end establishing state 2, and the reflection of the rarefaction fan from the other side producing state 3. These two states are determined directly by the intersection with the axis of a shock polar starting from state 1 for $A_x = 1.067$, and of a rarefaction polar starting from state 1a for $A = 0.933$.
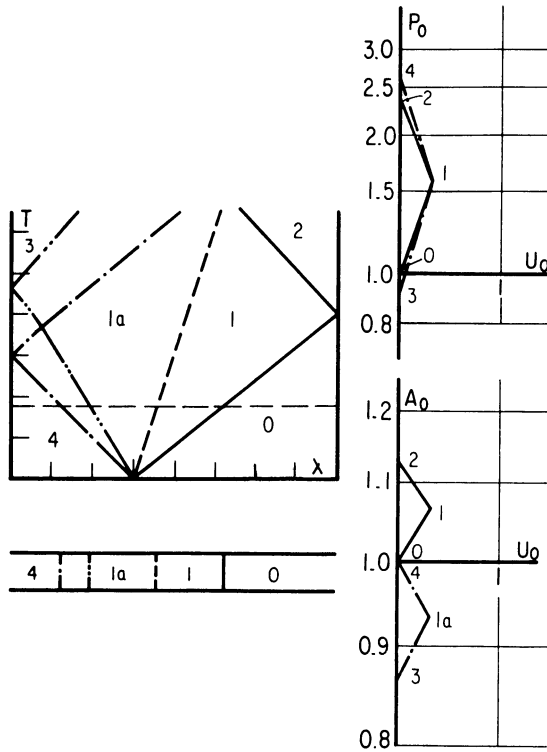
Fig. 13-9 Wave interaction processes in a shock tube. Solution for P_4 = 2.62, A_4 = 1,
β = 1/6 (γ = 1.4).

The determination of state 1 is indeed so simple that for a perfect gas with constant specific heats it can be accomplished algebraically. Noting that the relationships between U_1 and P_1 must be satisfied simultaneously by Eqs. (13-68) and (13-72), the latter taken in the

Table 13-1   Solution of Wave Interaction Processes in a Shock Tube Represented by Fig. 13-9; P_4 = 2.62, A_4 = 1, β = 1/6 (γ = 1.4).

State	P	A	U	Wave	M	V	W
4	2.62	1	0	—	0	0	0
1a	1.584	.933	.33	4–1a	−1	−1	−1
					− .933	− .933	− .60
1	1.584	1.067	.33	0–1	1.25	1.25	1.25
2	2.41	1.133	0	1–2	1.2	1.28	− .95
3	.887	.86	0	1a–3	1	.933	1.263
					1	.86	.86

proper orientation with respect to state 4, it follows immediately that

$$\frac{4}{(\gamma - 1)^2} \left[1 - \left(\frac{P_1}{P_4}\right)^{\frac{\gamma - 1}{2\gamma}} \right] = \frac{2}{\gamma(\gamma + 1)} \frac{(P_1 - 1)^2}{(P_1 - 1) + \dfrac{2\gamma}{\gamma + 1}}$$

whence

$$P_4 = P_1 \left\{ 1 - \frac{(\gamma - 1)^2 (P_1 - 1)^2}{2\gamma(\gamma + 1) \left[(P_1 - 1) + \dfrac{2\gamma}{\gamma + 1} \right]} \right\}^{-\frac{2\gamma}{\gamma - 1}}$$

(13-75)

The above equation gives the required diaphragm pressure ratio, P_4, to produce a given shock pressure ratio, P_1, which, in turn, is related to the shock Mach number, M_x, by Eq. (13-69).

Similarly it can be shown that, as a consequence of the requirement that particle velocity must be zero behind the reflected shock wave,

$$P_2 = P_1 \frac{(2\beta + 1) P_1 - \beta}{\beta P_1 + 1} = P_1 \frac{\dfrac{3\gamma - 1}{\gamma - 1} P_1 - 1}{P_1 + \dfrac{\gamma + 1}{\gamma - 1}} \qquad (13\text{-}76)$$

It is of interest to note that the pressure ratio across the reflected shock wave has a limiting value

$$P_{2_{max}} = 2 + \frac{1}{\beta} = \frac{3\gamma - 1}{\gamma - 1} \qquad (13\text{-}77)$$

which, for $\gamma = 1.4$, is 8.1. This leads to a maximum attainable temperature or speed of sound ratio whose corresponding value is, by Eq. (13-66),

$$A_{2_{max}}^2 = \frac{2(2\beta + 1)}{\beta + 1} = 3 - \frac{1}{\gamma} \qquad (13\text{-}78)$$

which, for $\gamma = 1.4$, is 2.285.

2) Flame-Shock Interactions.   In contrast to the previous example, the flame-shock interaction problem presented here cannot be treated satisfactorily by any technique other than the graphical Vector Polar Method. The reason for this is that the analysis this time involves the matching of a number of experimental records. The solution is obtained at each step by trial and error. Any attempt to accomplish this by a numerical technique would have been unduly cumbersome.

Figure 13-10 presents a streak-Schlieren record of flame-shock interactions in an equimolar hydrogen-oxygen mixture contained in a 1" × 1 1/2" rectangular cross-section tube [8]. Two shock waves moving to the left collide with the right-moving flame, the first sweeping the flame back toward the left end of the tube and the second producing a noticeable alteration in its structure. Following the reflection from the end of the tube, the transmitted shocks again interact with the flame, accelerating it to the right.

Displayed in the insert in Fig. 13-10 are pressure records obtained at two stations, $PG1$ and 2. They were measured by means of shock-mounted Kistler 601 transducers with Kistler 568 charge amplifiers. The first signal on both transducer records represents the pressure pulse produced by the initial motion of the flame. This is followed by the attainment of a relatively uniform pressure field ahead of the flame just prior to the interaction.

The salient feature of the Schlieren record of Fig. 13-10 is the appearance of relatively straight line traces of wave fronts, providing the justification for the finite wave interaction analysis in which the flow is treated essentially as one-dimensional and the only changes of state admitted are those brought about by wave action. The waves are considered plain discontinuities with the exception of the rarefaction fan, which is treated as a zone of a continuous isentropic expansion. Thus all considerations associated with the structure of the wave processes are neglected in favor of their dynamic effects.

The solution of the wave-interaction analysis is shown in the time-space diagram of Fig. 13-11 and the pressure-particle velocity hodograph of Fig. 13-12. The flame is denoted in Fig. 13-12 by the double solid line and the shock fronts by single solid lines; the bounds of the rarefaction fan are indicated by chain-dotted lines. For comparison, the observations of Fig. 13-10 have been reproduced in Fig. 13-11, the flame trace represented by a double-dash line and the shock waves by a single-dash line. Each regime in the time-space domain is denoted by a number which indicates its thermodynamic state on the pressure-velocity diagram. In performing the analysis, the contact surfaces generated by each interaction were ignored, since their effects were of second order and had negligible influence on the results.

From experimental observations of the initiation process, it has been established [8] that the pressure of state 1 is 2.01
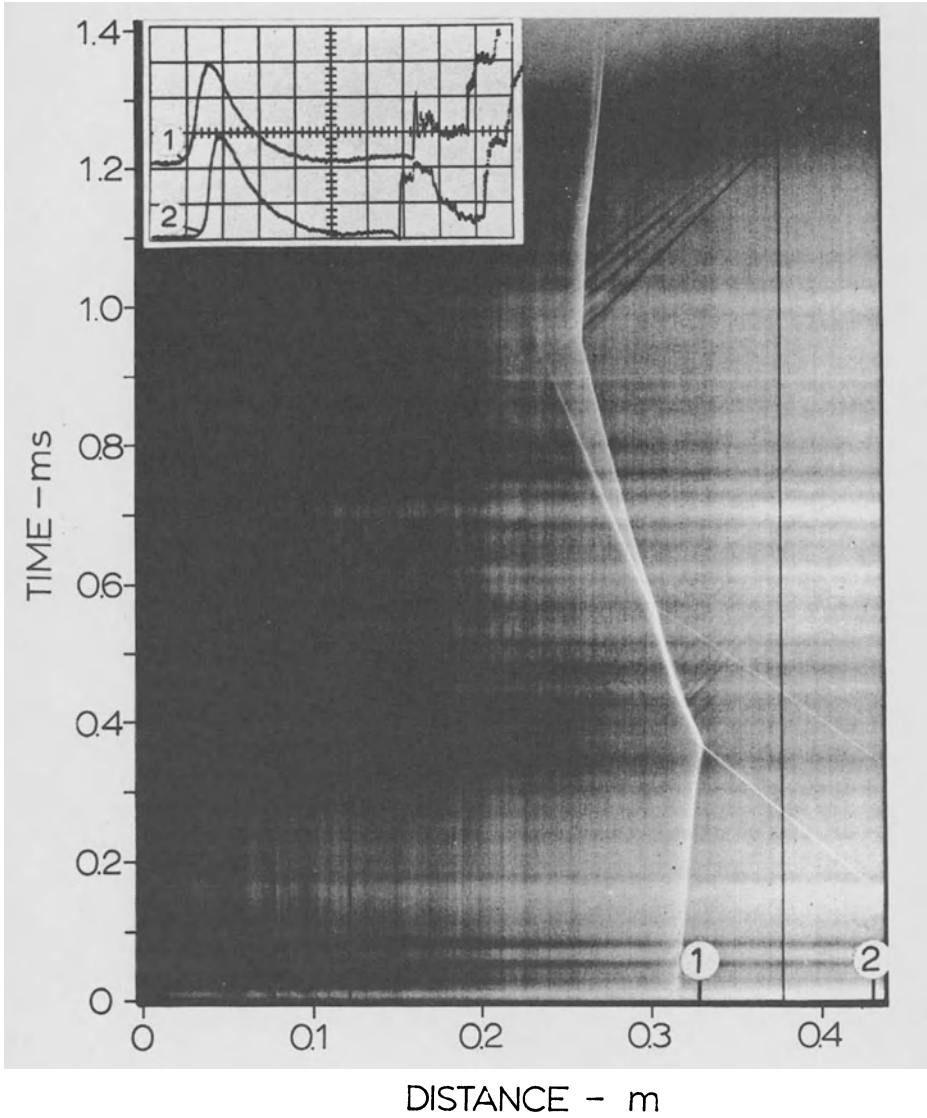
Fig. 13-10 Streak-schlieren and pressure transducer records of flame-shock interactions in a stoichiometric hydrogen-oxygen mixture initially at 1 atm and 60° F. For the oscilloscope record displayed in insert, vertical scale: 0.5 psi/cm; horizontal scale: 0.5 msec/cm. Oscilloscope sweep leads the streak record by 3.38 msec.
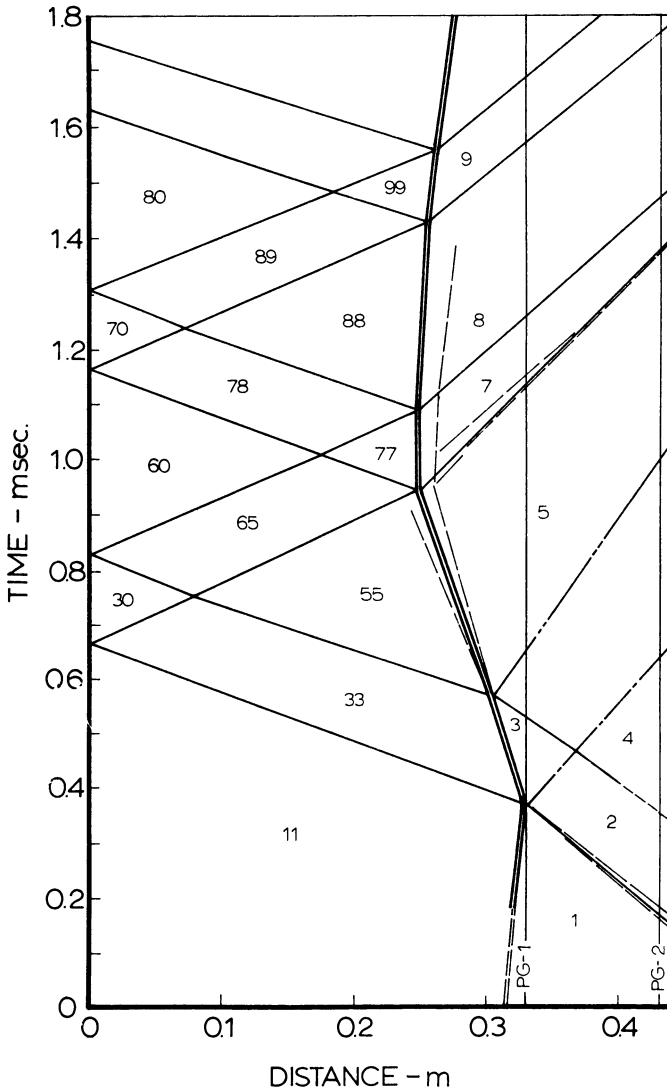
Fig. 13-11 Solution of the flame-shock interaction processes recorded in Fig. 13-10 in the time-space domain. Distance — *m*.

psi, and the corresponding particle velocity is 13 m/sec. State 1 and waves 1-2, 2-4, and 1-11 provide the initial conditions for the analysis. For convenience, the reference conditions are taken as those of the undisturbed mixture, so that state 1 is slightly displaced from the origin in the *P–U* diagram of Fig. 13-12.
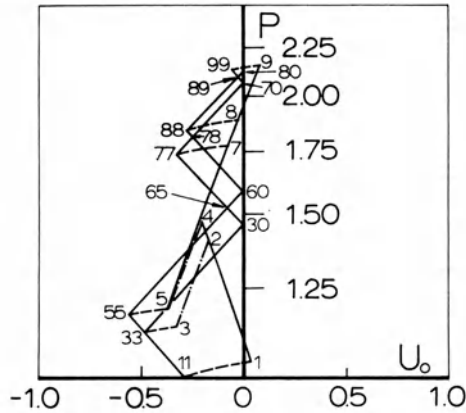
Fig. 13-12 Solution of the flame-shock interaction processes recorded in Fig. 13-11 in the $P - U$ plane.

Curve 1-2 in Fig. 13-12 represents the locus of states attained behind the shock wave propagating to the left into medium 1, with the terminal point, state 2, determined from the observed pressure and wave velocity. Curve 1-11 represents the locus of states created behind the deflagration moving to the right into medium 1. State 11 is specified by the deflagration polar of Fig. 13-7 to fit the observed flame velocity.

The rarefaction that arises from the collision between flame 3-33 and shock 2-4 is quite weak. It is considered, therefore, to be centered at the point of collision, and its effects are combined with those of the first expansion. As a consequence, there appears an extended regime of uniform state 5, in agreement with experimental observations. Although flame 3-33 propagates into the nonuniform regime within the reflected rarefaction wave, the medium ahead of it is assumed to have a constant state 3, whose properties correspond to those behind the rarefaction produced by the first flame-shock collision. This should be considered a fair approximation, especially in view of experimental evidence. The rarefaction waves attributed to changes in flame shape propagate in both directions, so that shock 11-33 is actually followed by an expansion that tends to "smear out" the subsequent interactions. For purposes of analysis, however, state 33 is considered uniform, with properites corresponding to those behind the transmitted shock wave after it was overtaken by the weaker rarefaction.

States 3 and 33 are determined on the P–U plane of Fig. 13-12 by closing the pentagon whose remaining vertices are state points 11, 1, and 2. A unique solution is obtained by requiring that the velocity of the transmitted deflagration 3-33 match the flame trace (world-line) on the schlieren record, while point 33 is that behind

the transmitted shock 11-33. The results of such a solution are quite approximate, since the pressure and velocity changes across the deflagration are sensitive to small deviation in flame velocity. However, an upper bound to state 3, and hence state 33, is provided by state 5 (which, together with state 55, is found in a similar fashion as states 3 and 33, whose pressure was recorded by both pressure transducers. The results of the analysis are summarized in Table 13-2. On the basis of the time-space diagram of Fig. 13-11, pressure variations at the locations of the two pressure transducers are determined. The resulting profiles are shown in Fig. 13-13 in comparison to the experimental pressure records.

The satisfactory agreement between the results of the analysis and the experimental records permits the deduction of specific

Table 13-2   Solution of Flame-Shock Interactions of Fig. 13-10 Represented by Figs. 13-11 and 13-12

State	P	$\triangle P$ (psi)	A	U	Wave	M	V	U + V	w (m/sec)
1	1.04	.075	1.0056	+ .028	0–1	—	0	.028	13
2	1.393	.76	1.05	− .17	1–2	−1.14	−1.145	−1.117	− 502
11	1.003	.005	2.085	− .29	1–11	—	.078	.106	48
3	1.133	.26	1.02	− .33	2–3	1	1.05	.88	392
						1	1.02	.69	310
33	1.119	.23	2.19	− .485	11–33	−1.05	−2.19	−2.48	−1120
					3–33	—	.035	− .295	− 133
4	1.47	.91	1.06	− .21	2–4	−1.024	−1.075	−1.25	− 563
5	1.185	.36	1.03	− .375	4–5	1	1.06	.85	
						1	1.03	.655	+ 294
55	1.168	.325	2.19	− .56	5–55	—	.040	− .335	− 150
					33–55	−1.02	−2.235	−2.720	−1225
30	1.447	.865	2.24	0	33–30	1.13	2.53	2.045	920
65	1.514	.995	2.25	− .08	30–65	−1.02	−2.29	−2.29	−1030
					55–65	1.135	2.55	1.99	896
60	1.576	1.115	2.25	0	65–60	1.02	2.29	2.21	995
7	1.77	1.495	1.09	− .07	5–7	1.190	1.30	.925	915
77	1.725	1.405	2.27	− .33	7–77	—	.07	0	0
					65–77	−1.065	−2.42	2.50	−1125
8	1.88	1.70	1.10	− .025	7–8	1.03	1.12	1.05	472
88	1.84	1.62	2.28	− .28	8–88	—	.07	.0450	22
					78–88	−1.01	−2.30	−2.555	1150
78	1.803	1.55	2.28	− .255	77–78	1.02	2.32	1.99	896
					60–78	−1.06	−2.46	−2.46	1100
70	2.065	2.06	2.30	0	78–70	1.06	2.42	2.165	972
89	2.095	2.12	2.30	− .03	88–89	1.06	2.42	2.14	962
					70–89	1.008	−2.32	−2.32	−1045
80	2.125	2.17	2.31	0	89–80	1.008	2.32	2.29	1030
9	2.15	2.22	1.12	.08	8–9	1.06	1.165	1.14	512
99	2.125	2.17	2.32	− .06	9–99	—	.03	.11	50
					89–99	−1.007	−2.32	−2.35	−1060
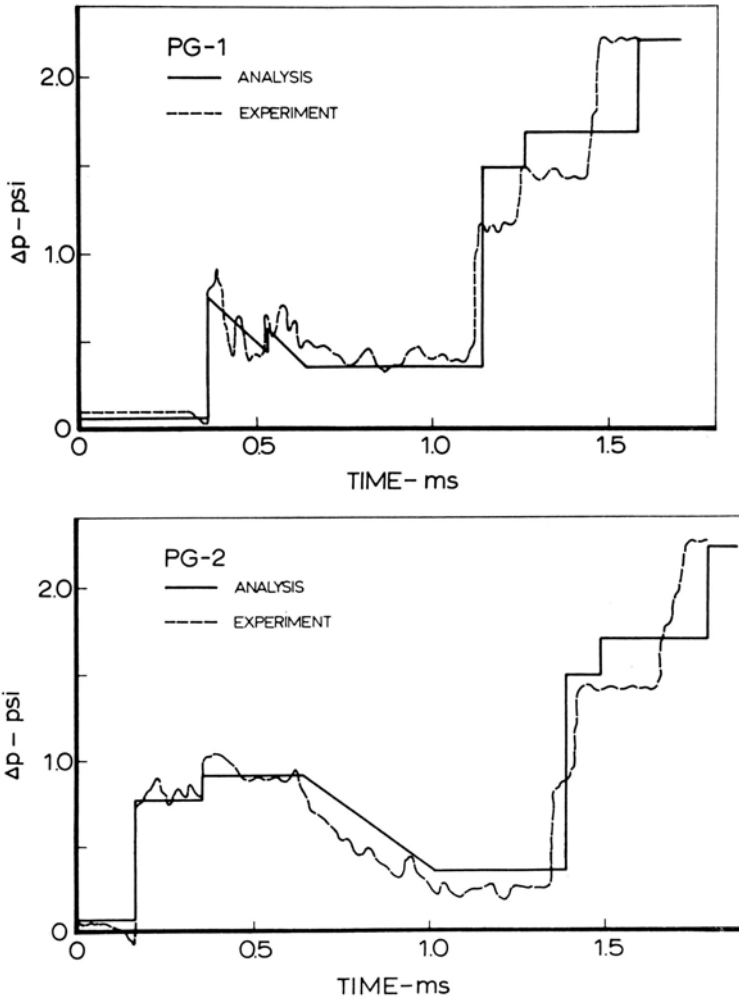
Fig. 13-13 Comparison between experimental pressure profiles of Fig. 13-10 and the corresponding analytical results deduced from the solutions of Figs. 13-11 and 13-12.

conclusions concerning the effect of wave interactions on the relative flame propagation speed. The various changes of this speed are represented in Table 13-2 by the different values of V corresponding to waves 1-11, 3-33, 5-55, 7-77, 8-88, and 9-99. They indicate especially the significance of the head-on collision with a shock, as illustrated by the case of wave 3-33 whose relative speed of $V = 0.035$ (or 15.8 m/sec.) is significantly lower than the $V = 0.078$ (or 35.1 m/sec.) of wave 1-11 that represented the same flame front just before the collision with shock 1-2.

[13-2.1.2] Wave Intersections

It is convenient to use the term "intersections" for wave interactions in steady flow. Although both are concerned with interactions between steady and simple waves, a wave intersection creates a regime of the same pressure and velocity direction so that instead of a contact discontinuity, it gives rise to a slip-line. The solution is therefore based on the $P-\delta$ rather than $P-U$ polars.

a. Steady Wave Polars

As before, equations for these polars are obtained by the use of the Hugoniot Relationship, Eq. (13-29), to eliminate ν from the expression for δ given by Eq. (13-47). Eliminating ω according to its definition Eq. (13-41), one obtains:

$$\tan^2\delta = \frac{(P - P_G)(1 - \beta)\mathbb{W}_x^2 - (P + \beta)(P - 1)}{\left[\mathbb{W}_x^2 - (P - 1)\right]^2} \quad \frac{P - 1}{P + \beta}$$

$$\text{(13-79)}$$

The corresponding expression for the angle of inclination is then, by virtue of Eq. (13-45), as follows:

$$\tan^2\theta = \frac{(P + \beta)(P - 1)}{(P - P_G)(1 - \beta)\mathbb{W}_x^2 - (P + \beta)(P - 1)} \quad \text{(13-80)}$$

and the expression for flow velocity behind the discontinuity Eq. (13-48) becomes

$$\mathbb{W}_x^2 = \mathbb{W}_x^2 - [2(P + \beta) - (P - P_G)(1 - \beta)]\frac{P - 1}{P + \beta} \quad \text{(13-81)}$$

while, A is given by Eqs. (13-65) or (13-66).

For a shock in a perfect gas with constant specific heats $P_G = 1$, $\beta = (\gamma - 1)/(\gamma + 1)$ and $\Gamma = \Gamma_x = \gamma$.

Shock polars for $\beta = 1/6$ or $\gamma = 1.4$, based on Eq. (13-79) are given by Fig. 13-14, with Figs. 13-15 and 13-16 furnishing the auxiliary plots based on Eqs. (13-80) and (13-81). They are represented there with $M_x = \mathbb{W}_x/\sqrt{\gamma}$ used as a parameter, while $M_y = \mathbb{W}_y/A\sqrt{\gamma}$.

The supplementary curve on the plane of the polars in Fig. 13-14 furnishes the relationship between pressure and Mach number for a normal wave, or the Mach number for the points on the P axis. With the help of this curve, one can locate such points for any given value of M_x and, with the $\delta_{\max}$ coordinate which can be obtained from the supplementary curve of Fig. 13-15, one can reconstruct,

Fig. 13-15 Wave angle-flow deflection plots for polars of Fig. 13-14.

Fig. 13-14 Shock polars in the $P - \delta$ plane for $\beta = 1/6$ ($\gamma = 1.4$).
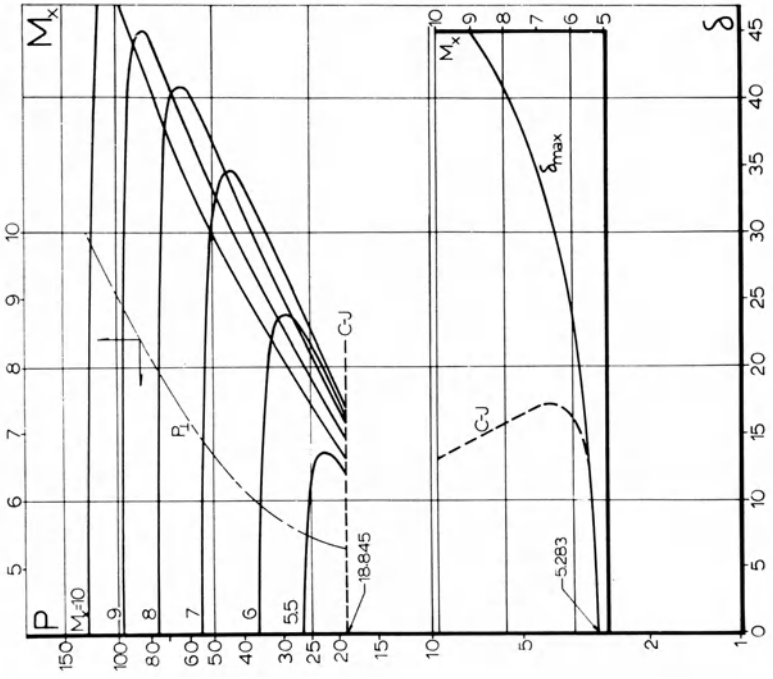
Fig. 13-17 Detonation polars in the $P-\delta$ plane for $\beta = 0.06$ and $C = 9(\gamma_1 = 1.4)$ corresponding to stoichoimetric hydrogen-oxygen mixture initially at NTP.
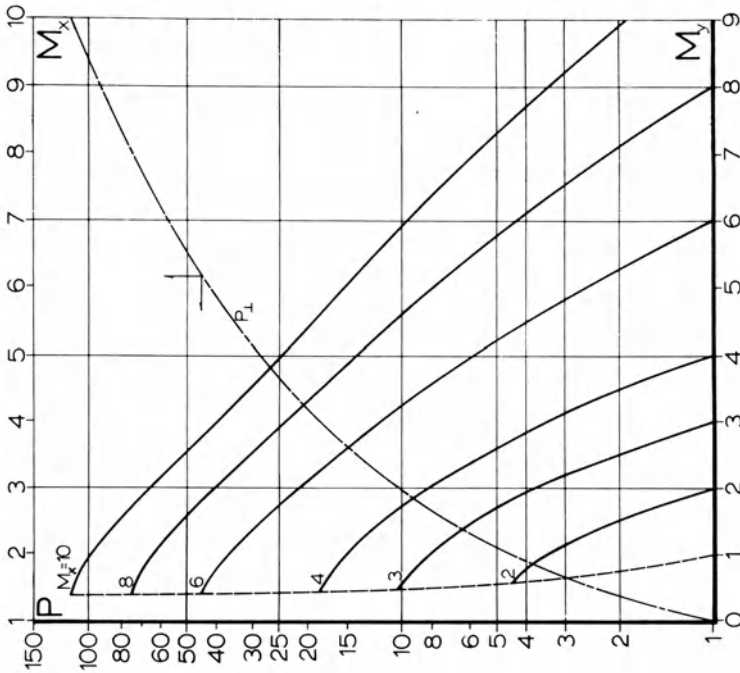
Fig. 13-16 Pressure ratio-downstream Mach number plots for polars of Fig. 13-14.
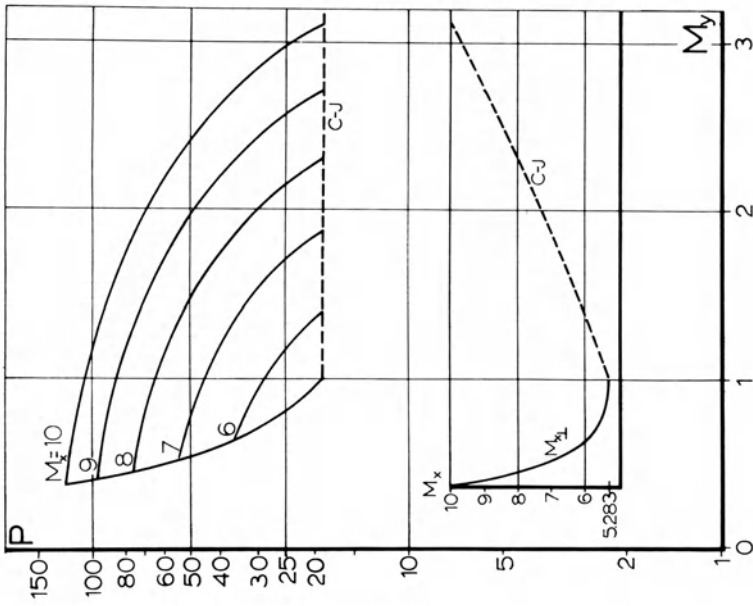
Fig. 13-19 Pressure ratio-downstream Mach number plots for polars in Fig. 13-17.
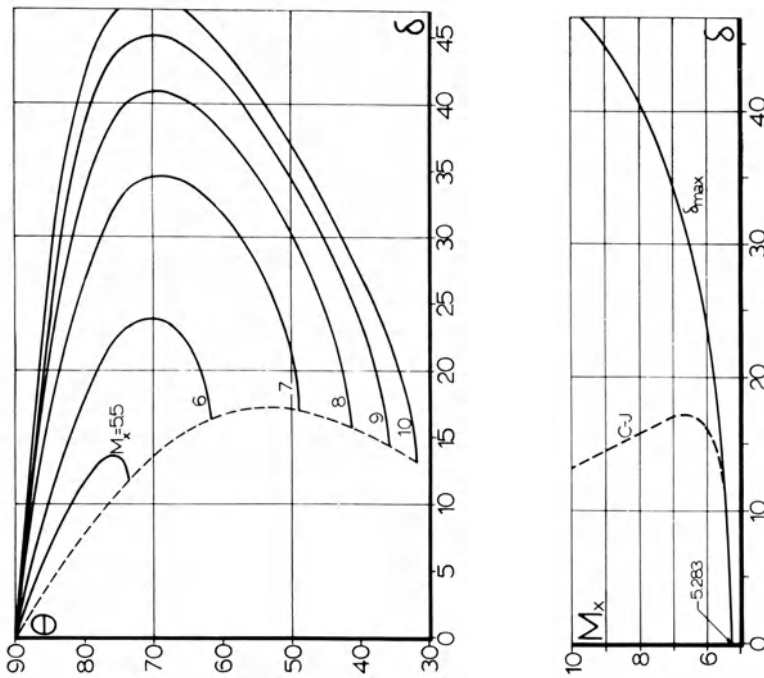
Fig. 13-18 Wave angle-flow deflection plots for polars of Fig. 13-17.
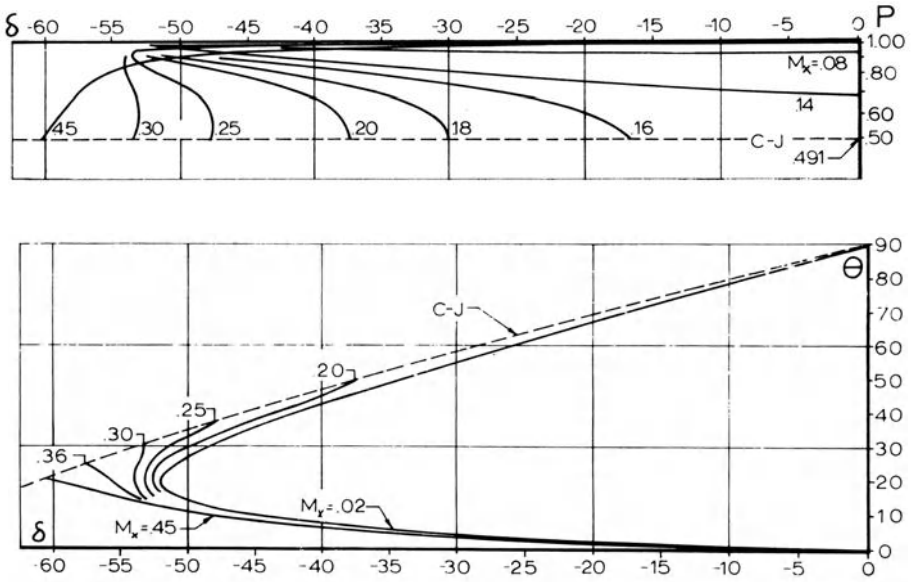
Fig. 13-20 Deflagration polars in the $P-\delta$ plane and the wave angle-flow deflection plots for $\beta = 0.06$ and $C = 9$ ($\gamma = 1.4$).
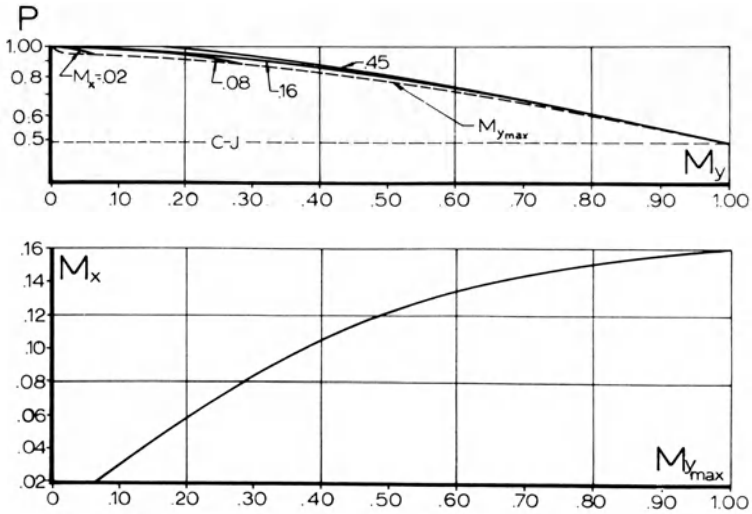
Fig. 13-21 Pressure ratio-downstream Mach number plots for polars of Fig. 13-20.

with acceptable accuracy, the required polar by graphical inter-
polation between polars given in Fig. 13-14. The supplementary
curves in Fig. 13-15 provide means for interpolation between the
incident Mach numbers. They help to locate points on the θ-axis
associated with the intermediate values of M_x and the corresponding
δ_{max}, between which the required curve can be reconstructed with
good accuracy.

Figure 13-17 gives the detonation polars for $\beta = .06$ and $C = 9$
corresponding to the case of stoichiometric hydrogen-oxygen
mixture initially at NTP. The polars are restricted to the physically
significant regime of strong detonation, from normal front at a given
Mach number of incident flow, down to the Chapman-Jouguet wave
which, in this case, corresponds to the pressure ratio $P_J = 18.845$
and the normal component of incident Mach number $M_x = 5.283$.
The supplementary curves are similar to those of Fig. 13-14,
and their use is self-explanatory.

Figure 13-18 represents the corresponding θ-δ plots, while
Fig. 13-19 shows the diagram for the evaluation of M_y. Figures
13-20 and 13-21 represent the set of graphs for a deflagration
wave, namely the P-δ polars, the θ-δ plots, and the diagram for
the evaluation of M_y, respectively, with the appropriate supple-
mentary curves for interpolation. They correspond to the same
Hugoniot curve as the detonation graphs of Figs. 13-17 to 13-19,
i.e., to $\beta = .06$ and $C = 9$. The most striking property of these
polars is the relatively small variation in P, especially on the
upper branch, so that by postulating the existence of a deflagration
wave in the flow field, one can rationalize quite a wide variation
in deflection angles, δ, without requiring any change in pressure.
The auxiliary diagrams of the θ-δ and the M_y - P plots are rela-
tively insensitive to the value of the incident Mach number except
for the end points corresponding to the Chapman-Jouguet condition.

b. Rarefaction Polars

For a rarefaction polar in the case of a perfect gas with
constant specific heats, $\alpha = 2/(\Gamma - 1) = 2/(\gamma - 1)$, and the expression
for the deflection angle, Eq. (13-62) acquires the well-known form

$$\delta = \sqrt{\frac{\gamma + 1}{\gamma - 1}} \ \tan^{-1}\sqrt{\frac{\gamma - 1}{\gamma + 1} (M^2 - 1)} \ - \cos^{-1}\left(\frac{1}{M}\right) \quad (13\text{-}82)$$

The information about the change of state is then completed by
the isentropic flow relations.

$$P = \left[\frac{2}{\gamma + 1} \left(1 + \frac{\gamma - 1}{2} M^2\right)\right]^{\frac{\gamma - 1}{\gamma}} \quad (13\text{-}83)$$

where the reference value for P, as for δ, corresponds to $M = 1$, while the angle of inclination is the Mach angle, $\theta = \sin^{-1}(1/M)$. Plots of these relations are given in Fig. 13-22. Since the locus of attainable states is at the same time the process path, unlike the steady wave polars of Figs. 13-14, 13-17, and 13-20, a single curve rather than a family is sufficient for all cases. For a given initial Mach number, the plot can be entered at any point; the change of state is then evaluated with reference to the coordinates of this point.
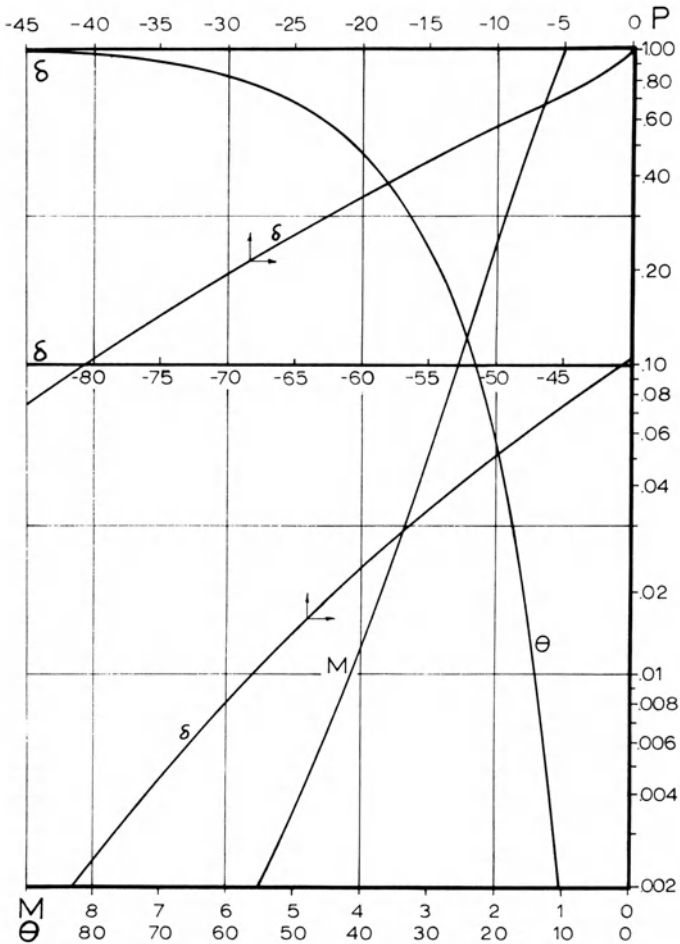
Fig. 13-22 Rarefaction polar in the $P-\delta$ plane and auxiliary plots for $\alpha = 5$ ($\gamma = 1.4$).

c. Examples

The use of the Vector Polar Method is illustrated by the following elementary problems: shock merging or the so-called "arrowhead" intersection, Mach Intersection of shock fronts, and Mach intersection involving a detonation front. The method is applied to the analysis of the reflection of a Mach intersection from a rigid wall which represents, in effect, an interaction of intersections. It should be pointed out that in all these examples only the so-called simple solutions are obtained, *i.e.*, ones associated solely with the generation of slip–lines. According to the prevalent opinion [9], the validity of such solutions is restricted in scope only to strong incident wave fronts.

1) Shock Merging or the "Arrowhead" Intersection. The intersection of this kind is created by two given incident fronts. They can be specified in terms of the Mach number of incident flow, M_1, and two deflection angles, δ_{12} and δ_{23}, as shown in Fig. 13–23. The given Mach number, M_1, specifies the polar in the P–δ plane, and the angle δ_{12} fixes state 2 so that, with the help of the auxiliary M–P plot, the Mach number M_2 is fixed and, hence, the polar for the second shock. State 3 is then located on this polar by the given second deflection angle, δ_{23}, as demonstrated on Fig. 13–23b. Since the transmitted shock must propagate into state 1, the state brought about by its action must lie on the same polar as state 2. A compatible solution is obtained either by an emerging rarefaction fan, as shown in Fig. 13–23a, producing states 4, or by an emerging shock wave of the opposite family, producing states 4" shown also in Fig. 13–23b. This is, in essence, a Mach intersection produced by two incident waves. Except for the trivial difference of one incident wave rather than two, this case is discussed as the next example. The two solutions reduce to a single one, if the second incident shock is of such strength that the state brought about by its action lies on the initial polar, as illustrated by point 3' of Fig. 13–23b. In this case, except for the transmitted shock, no emerging waves are produced, and the intersection involves only three shocks. Numerical solutions for $M_1 = 8$, $\delta_{12} = 10°$ and $\delta_{23} = 15°$ in the case of a perfect gas with $\gamma = 1.4$ are given in Table 13–3.

2) The Mach Intersection. This case is illustrated by Fig. 13–24. The problem is fully defined in terms of two parameters, *e.g.*, the Mach number of incident shock 1, M_{1s}, and the angle between its front and the incident flow, θ_{1s}. The auxiliary θ–δ plot shown in Fig. 13–24d fixes then the deflection angle δ_{12}, and hence state 2 on the appropriate polar, as demonstrated on Fig. 13–24b. The
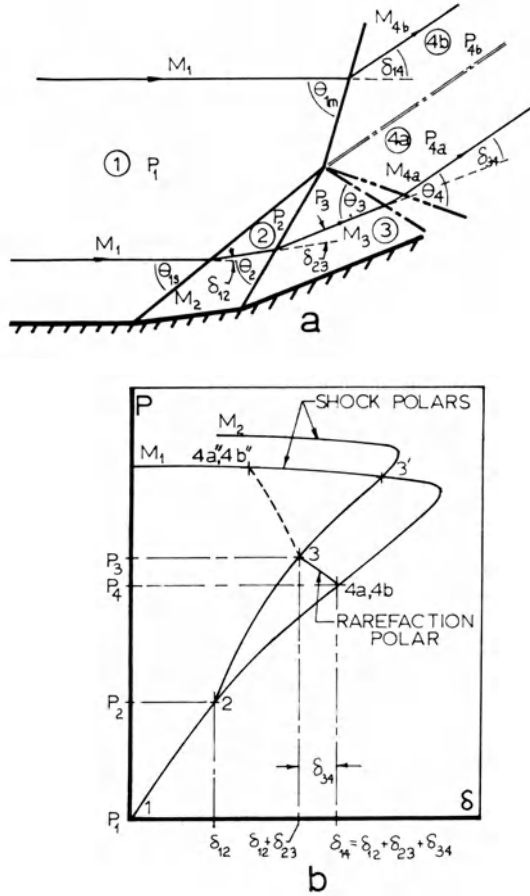
Fig. 13-23 Shock merging or the "Arrowhead" intersection; $M = 8$, $\delta_{12} = 10°$, $\delta_{25} = 15°$, $\beta = 1/6$ ($\gamma = 1.4$).

Table 13-3   Shock Merging or the "Arrowhead" Intersection, $M_1 = 8$; $\delta_{12} = 10°$; $\delta_{23} = 15°$; $\beta = 1/6$ ($\gamma = 1.4$).

State	1	2	3	4a	4b
Mach Number	8.0	5.77	3.75	3.9	2.93
Pressure Ratio	1.0	5.25	29.3	24.5	24.5
Wave Angle	θ_{1m}	θ_{1s}	θ_2	θ_3	θ_4
Degrees	35.9	16.3	23.4	15.2	14.6
Deflection Angle	δ_{12}	δ_{23}		δ_{34}	δ_{14}
Degrees	10.0	15.0		2.2	27.2
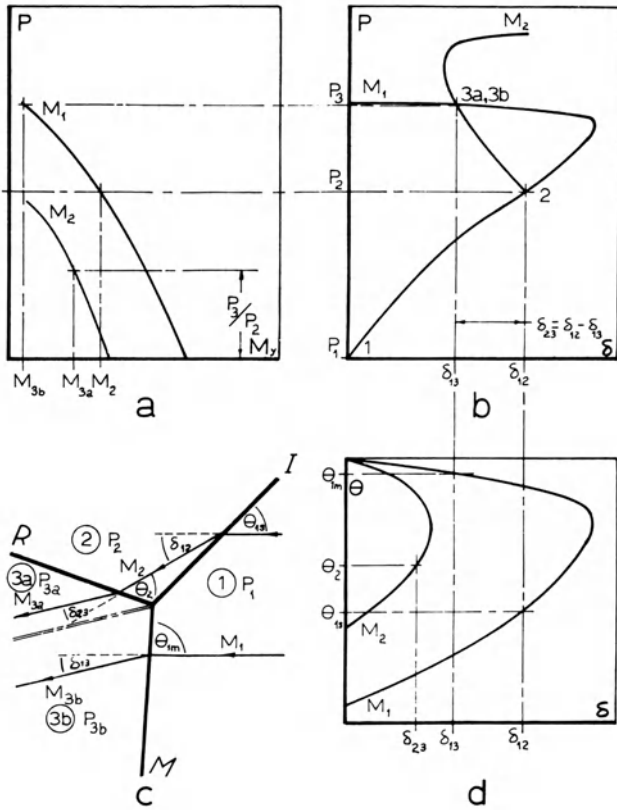
Fig. 13-24 Mach intersection of shock fronts; $M_1 = 6$, $\theta_{1s} = 45°$, $\beta = 1/6$ ($\gamma = 1.4$).

Table 13-4   Mach Intersection of Shock Fronts; $M_1 = 6$; $\theta_{1s} = 45°$; $\beta = 1/6$ ($\gamma = 1.4$).

State	1	2	3a	3b
Mach Number	6.0	2.08	1.50	.40
Pressure Ratio	1.0	21.5	42.0	42.0
Wave Angle	θ_{1m}	θ_{1s}		θ_2
Degrees	85.2	45.0		42.0
Deflection Angle	δ_{12}	δ_{23}		δ_{13}
Degrees	32.9	−13.6		19.3

Mach number, M_2, is then obtained from the $P-M_y$ plot illustrated in Fig. 13-24a. This specifies the polar for the reflected wave, R, producing state 3a, while the corresponding state 3b, represented by the same point on the $P-\delta$ plane, is brought about by the action of the so-called Mach stem, M, as shown on Fig. 13-24c. Numerical solution for $M_{1s} = 6$ and $\theta_{1s} = 45°$, in the case of a perfect gas with $\gamma = 1.4$, is given in Table 13-4.

An analogous situation may, in principle, be obtained with detonation front as one of the participating waves in the intersection. The usual situation obtained with a shock acting as the incident wave, is represented by Fig. 13-25. The solution is, in principle, the same as that of Fig. 13-24, with the exception that the appropriate detonation polar for the incident flow Mach number, M_1, is used instead of the shock polar. The case illustrated in Fig. 13-25 is that of the strongest incident shock that can still produce a Mach intersection involving a detonation wave. A stronger shock can produce only a triple shock intersection, since, as evident from the $P-\delta$ plane, the polar of the reflected shock cannot intersect that of the detonation wave. Numerical solution for $M_1 = 6$ and $\theta_{1s} = 43°$ in the case of $\beta = .06$ and $C = 9$ corresponding to a stoichiometric hydrogen-oxygen mixture initially at NTP, is given in Table 13-5.

3) Reflection of Mach Intersection from a Rigid Plane. The case considered here is characteristic of detonation phenomena where Mach intersections play a predominant role. One of the intersecting waves is assumed to be perpendicular to the plane of reflection. Before reflection, it is the incident shock, and after reflection it is the Mach stem, as shown in Fig. 13-26c. The basic premise of the solution is the fact that any point of the wave front, acting as the Mach stem before the reflection and the incident shock after the reflection, does not know about the reflection until it is reached by the reflected intersection point. Consequently, the pressure ratio across the incident shock of the reflected intersection is equal to that across the Mach stem of the incident intersection; the angle between the incident shock and the Mach stem remains invariant. These conditions are sufficient for the determination of the reflected wave system.

Given, as before, is the Mach number of flow relative to the incident intersection point, M_1, and the relative direction of flow, or the direction of motion of the intersection point with respect to the plane of the incident shock, θ_{1s}. Since the incident shock is perpendicular to the plane of reflection, it follows that

$$\alpha = \frac{\pi}{2} - \theta_{1s}.$$

All the properties of the incident intersection are determined as before, the solution for unprimed states in Fig. 13-26 being, in essence, the same as that of Fig. 13-24.
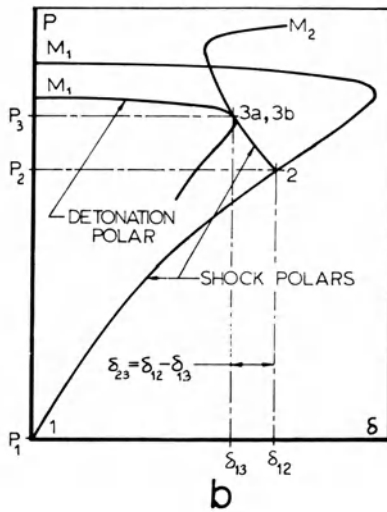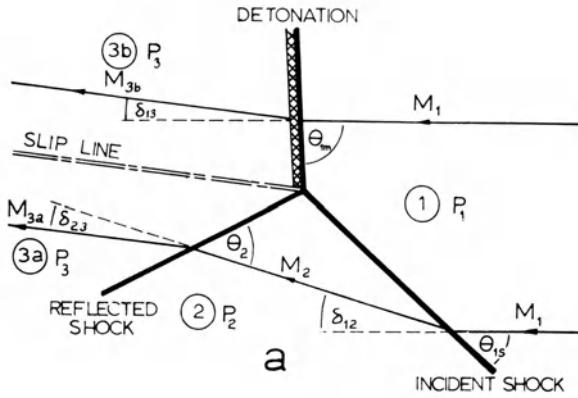
Fig. 13-25 Mach intersection involving a detonation front; $M_1 = 6$, $\theta_{1s} = 45°$, $\beta = 1/6$ ($\gamma = 1.4$).

Table 13-5 Mach Intersection Involving a Detonation Front; $M_1 = 6$; $\theta_{1s} = 43°$; $\beta = 1/6$; $C = 9$ ($\gamma = 1.4$).

State	1	2	3a	3b
Mach Number	6.0	2.15	1.81	.91
Pressure Ratio	1.0	19.5	31.0	31.0
Wave Angle	θ_{1m}	θ_{1s}		θ_2
Degrees	73.75	43.0		35.25
Deflection Angle	δ_{12}	δ_{12}		δ_{13}
Degrees	31.5	− 8.3		23.2
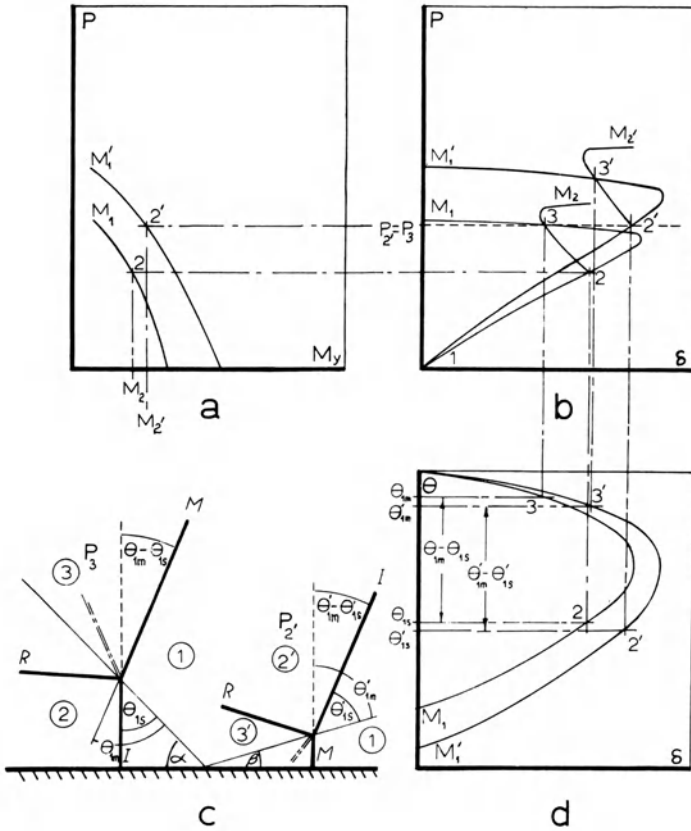
Fig. 13-26 Reflection of Mach intersection from a rigid plane; $M_1 = 6, \theta_{1s} = 45°, \beta = 1/6$
$(\gamma = 1.4)$.

The condition of pressure invariance $P_{2'} = P_3$ fixes one coordinate of state 2', as shown by the horizontal broken line on Fig. 13-26. The condition of invariance of the relative angle $\theta_{1m} - \theta_{1s}$ imposes a further restriction on state 2', in that, with reference to Fig. 13-26d, $\theta_{3'} - \theta_{2'} = \theta_3 - \theta_2$. This can be satisfied only by one particular value of the Mach number, M_1, which is determined by a graphical trial and error solution. Thus, all the states of the reflected intersection, 1', 2' and 3' are fixed. In particular, as is evident from Fig. 13-26c, the angle of reflection,

$$\beta = \frac{\pi}{2} - \theta'_{1m}.$$

Moreover, it should be noted that for a gas with $\gamma = 1.4$ this angle cannot exceed a value of approximately 25° since, as shown in Fig. 13-15, the inclination angle of a Mach stem, corresponding as a rule to the subsonic branch of the θ-δ curve above the point of

Table 13-6   Reflection of Mach Intersection from a Rigid Plane;
$M_1 = 6$; $\theta_{1s} = 45°$; $\beta = 1/6$ ($\gamma = 1.4$); Parameters of Incident
Mach Intersection are in Table 13-4.

State	1	2'	3'a	3'b
Mach Number	8.60	2.20	1.65	0.40
Pressure Ratio	1.0	42.0	85.5	85.5
Wave Angle	θ'_{1m}		θ'_{1s}	θ'_2
Degrees	85.6		45.4	38.5
Deflection Angle	δ'_{12}		δ'_{23}	δ'_{13}
Degrees	33.5		−12.5	21.0

δ_{max}, must be larger than 65°. Numerical solution for $M_1 = 6$ and $\theta_{1s} = 45°$, in the case of a perfect gas with $\gamma = 1.4$, is given in Table 13-6.

It should be noted that, as in the previously presented flame-shock interaction problem, the solution of the reflection of the Mach intersection is based on a trial and error procedure. It lends itself therefore to treatment by the Vector Polar Method as the most convenient technique for such purpose.

[13-3] APPENDIX: SALIENT PROPERTIES OF THE HUGONIOT CURVE

The Hugoniot curve is distinguished by the two following properties:* (1) the Chapman–Jouguet condition which implies that, when the curve is tangent to the Rayleigh Line passing through point x, representing the initial state, it is also tangent to the isentrope, since, as demonstrated by Eq. (13-36), this is tantamount to the conditions of local Mach number of one at state J or K; and (2) the states corresponding to the intersection points between the Hugoniot curve and the Rayleigh line passing through point x of the initial state are adiabatically related, *i.e.*, they satisfy the adiabatic Rankine–Hugoniot Relationship. The validity of these properties is demonstrated here in order to illustrate the physical meaning of the relations presented in Section 13-1.2.

Without the introduction of the parameter β, Eq. (13-28) expresses essentially the Hugoniot Relationship in the general form

$$H - (H_x = Q) = \frac{1}{2}(P - 1)(\nu + 1) \tag{13-84}$$

where $H \equiv (\rho_x h)/p_x = H(P,\nu)$ represents the enthalpy of state $y(P,\nu)$, while H_x and Q are, for a given Hugoniot curve, constant. The differentials along this curve are related, therefore, as follows:

*As demonstrated especially by E. Jouguet in Mecanique des Explosifs, O. Doin et Fils, Paris, 1917, Section 193, p. 278, and by R. Becker, Z. Phys., 8, p. 352, 1922.

$$\left(\frac{\partial H}{\partial P}\right)_\nu dP + \left(\frac{\partial H}{\partial \nu}\right)_P d\nu = \frac{\nu + 1}{2} dP + \frac{P - 1}{2} d\nu$$

Hence, its slope on the $P - \nu$ plane is

$$\phi_H \equiv -\left(\frac{\partial P}{\partial \nu}\right)_Q = \frac{\left(\frac{\partial H}{\partial \nu}\right)_P - \dfrac{P - 1}{2}}{\left(\frac{\partial H}{\partial P}\right)_\nu - \dfrac{\nu + 1}{2}} \tag{13-85}$$

The slope of the Rayleigh line passing through point $x(1, 1)$ is given by the last of Eqs. (13-22) as

$$\phi_R \equiv -\left(\frac{\partial P}{\partial \nu}\right)_R = \frac{P - 1}{1 - \nu}. \tag{13-86}$$

The second law, on the other hand, demands that for an isentropic process,

$$\left(\frac{\partial H}{\partial P}\right)_\nu dP + \left(\frac{\partial H}{\partial \nu}\right)_P d\nu - \nu dP = 0$$

so that the slope of the isentrope is

$$\phi_s \equiv -\left(\frac{\partial P}{\partial \nu}\right)_s = \frac{\left(\frac{\partial H}{\partial \nu}\right)_P}{\left(\frac{\partial H}{\partial P}\right)_\nu - \nu}. \tag{13-87}$$

At the point of tangency between the Hugoniot curve and the Rayleigh line,

$$\phi_H = \phi_R \tag{13-88}$$

or, by virtue of Eqs. (13-85) and (13-86),

$$\left[\left(\frac{\partial H}{\partial P}\right)_\nu - \frac{\nu + 1}{2}\right](P - 1) = \left(\frac{\partial H}{\partial \nu}\right)_P (1 - \nu) - \frac{1 - \nu}{2}(P - 1)$$

whence

$$\frac{P - 1}{1 - \nu} = \frac{\left(\frac{\partial H}{\partial \nu}\right)_P}{\left(\frac{\partial H}{\partial P}\right)_\nu - \nu}. \tag{13-89}$$

The above, according to Eqs. (13-86) and (13-87), means that

$$\phi_R = \phi_S \tag{13-90}$$

which, with Eq. (13-88) completes the proof of the Chapman-Jouguet condition.

The adiabatic property of the intersection points between the Hugoniot curve and the Rayleigh line is a direct consequence of the energy equation on which Eq. (13-84) is based, namely,

$$H - (H_x + Q) = \frac{1}{2}(\mathbb{D}^2 - \mathbb{U}^2). \tag{13-91}$$

Applying this to any two points of the Hugoniot curve, say, A and B, and subtracting the two equations, one obtains:

$$H_A - H_B = \frac{1}{2}(\mathbb{U}_B^2 - \mathbb{U}_A^2 + \mathbb{D}_A^2 - \mathbb{D}_B^2).$$

which reduces itself to the adiabatic Rankine-Hugoniot Relationship that is a relation of the form of Eq. (13-91) with $Q = 0$ provided that

$$\mathbb{D}_A = \mathbb{D}_B \tag{13-92}$$

which means, in effect, that the two points, A and B, must lie on the same Rayleigh line, and thus completes the proof of the adiabatic property. Becker* demonstrated this property by a geometric proof. The above simple arguments can be interpreted as giving the physical reason why the Becker proof works.

NOMENCLATURE

α = velocity of sound

A = sound velocity ratio, a/a_0

$\mathbb{a}$ = cross-section area

b = segment in velocity hodograph of a simple rarefaction wave in steady flow

c = $\sqrt{(\partial p/\partial \rho)_a}$, or $\sqrt{RT} = a/\sqrt{\gamma}$ for a perfect gas with constant specific heats

c_p = specific heat at constant pressure

C = constant of the Hugoniot hyperbola, $(1 + \beta)(\nu_F - \beta)$ or $(P_G + \beta)$ $(1 - \beta)$ in Section 13-1.2

$\mathbb{D}$ = nondimensional velocity of wave front or discontinuity, v_x/z_x

e = internal energy per unit mass

f = stream force per unit area, $p + mV$

h = enthalpy per unit mass

H = nondimensional enthalpy per unit mass, h/z_x^2

L = reference length

$\dot{m}$ = mass flow rate per unit area, ρv

*See R. Becker, Z. Phys., 8, p. 353, 1922.

M = the Mach number

p = pressure

P = nondimensional pressure, p/p_0 in Sections 13-1.1 pressure ratio across a discontinuity, p_y/p_x, in Sections 13-1.2 and 13-2.1

$\wp$ = the Riemann parameter: $\alpha A + U$

q = the Hugoniot constant in Section 13-1.2

Q = nondimensional Hugoniot constant, q/z_x^2, in Section 13-1.2

$\mathfrak{Q}$ = the Riemann parameter: $\alpha A - U$

r = particle radius

s = entropy per unit mass in Section 13-1.1

$\mathscr{s}$ = nondimensional entropy, $C^2 \chi s/a^2$, or $s/\gamma R$ for a perfect gas with constant specific heats

t = time coordinate

u = mass velocity in nonsteady flow field or mass velocity induced by a discontinuity, $v_x - v_y$

U = nondimensional mass velocity, u/a_0

$\mathfrak{u}$ = nondimensional mass velocity induced by a discontinuity, u/z_x

v = normal relative velocity of wave or of flow with respect to wave front

v_t = tangential relative flow velocity

V = nondimensional normal relative velocity of wave or of flow with respect to wave front in Sections 13-1.2 and 13-2.1, v/a_0

$\mathfrak{V}$ = nondimensional normal relative flow velocity behind wave front or discontinuity, v_y/z_x

w = relative mass velocity in steady flow field in Sections 13-1.2 and 13-2.1

W = nondimensional absolute velocity of wave front, $V_x + U_x$ in Sections 13-1.2 and 13-2.1

$\mathfrak{W}$ = nondimensional relative mass velocity in steady flow field,

x = space coordinate
state in front of discontinuity in Section 13-1.2

y = state behind a discontinuity in Section 13-1.2

z = reference parameter for nondimensionalizing relations of a gasdynamic discontinuity, $\sqrt{p/\rho}$

α = $2(\partial h/\partial a^2)_s$ or $2/(\gamma - 1)$ for a perfect gas with constant specific heats
angle of incidence of the trace of a triple point, $(\pi/2) - \theta_{1s}$

β = $1/[2(\partial h/\partial z^2) - 1]$, or $(\gamma - 1)/(\gamma + 1)$ for a perfect gas with constant specific heats
angle of reflection of the trace of a triple point, $\pi/2 - \theta'_{1m}$

γ = specific heat ratio

Γ = $(\rho/p) a^2 = (\partial h/\partial e)_s$ or γ for a perfect gas with constant specific heats

δ = flow deflection angle

ζ = $\gamma/(\gamma - 1)$

θ = relative angle of incidence of oblique discontinuity or of characteristic in a simple wave in Sections 13-1.2 and 13-2.1

μ = $\sqrt{M^2 - 1}$ in Section 13-1.3

ν = velocity or density ratio across a discontinuity in Sections 13-1.2 and 13-2.1

ξ = nondimensional space coordinate, $x/L_0 = x/a_0 t_0$

ρ = density

σ = integer coefficient for one-dimensional flow (0 for plane, 1 for cylindrical, and 2 for spherical)

τ = nondimensional time coordinate, $a_0 t/L_0 = t/t_0$

ϕ = mass flux added to stream per unit length in Section 13-1.1 the Prandtl-Meyer expansion angle in Section 13-1.3 negative slope of a curve in the $P - \nu$ plane in the Appendix

Φ = nondimensional mass flux added to stream per unit length, $L_0 a_0 \phi / \Gamma p_0 \mathcal{C}$, in Section 13-1.1

χ = $-(1/\rho)(\partial\rho/\partial s)_a$, or $1/R$ for a perfect gas with constant specific heats

ψ = body force in the x-direction per unit mass

Ψ = nondimensional body force in the x-direction per unit mass, $L_0 \psi / a_0^2$

ω = parameter in relations for oblique discontinuity in Section 13-1.2, $\mathbb{W}_x^2/(P - 1)$

SUBSCRIPTS

F = denotes end state attained by constant pressure combustion

G = denotes end state attained by constant volume combustion

J = denotes the Chapman-Jouguet state of detonation

K = denotes the Chapman-Jouguet state of deflagration

0 = denotes the reference or initial state

x = denotes the state in front of a discontinuity in Section 13-1.2

y = denotes the state behind a discontinuity

$1,2$ = denote states of regimes in the time-space domain between wave fronts

$1m$ = denotes the angle of incidence of the Mach stem

$1s$ = denotes the angle of incidence of the shock front

REFERENCES

1. Rudinger, George: Wave Diagrams for Nonsteady Flow in Ducts, New York, D. Van Nostrand Company, Inc., 1955.
2. Glass, I.I. and J. Gordon Hall: Handbook of Supersonic Aerodynamics - Section 18 - Shock Tubes, Bureau of Ordnance, Department of the Navy, *Navord Report 1488*, 6, December 1959.

3. Courant, R. and K.O. Friedrichs: Supersonic Flow and Shock Waves, New York, Interscience Publishers, Inc., 1948.
4. Owczarek, Jerzy A.: Fundamentals of Gas Dynamics, Scranton, International Textbook Company, 1964.
5. Hayes, Wallace D. and Ronald F. Probstein: Hypersonic Flow Theory, New York, Academic Press, 1959.
6. Zeleznik, Frank J. and Sanford Gordon: A General IBM 704 or 7090 Computer Program for Computation of Chemical Equilibrium Compositions, Rocket Performance, and Chapman-Jouguet Detonations, National Aeronautics and Space Administration, Washington, *TN D-1454*, Lewis Research Center, Cleveland, October 1962.
7. Oppenheim, A.K., P.A. Urtiew, and A.J. Laderman:Vector Polar Method for the Evaluation of Wave Interaction Processes, *Archiwum Budowy Maszyn*, Tom XI, Zeszyt 3, pp. 441-495, 1964.
8. Laderman, A.J., P.A. Urtiew, and A.K. Oppenheim: Gasdynamic Effects of Shock-Flame Interactions in an Explosive Gas, *AIAA Journal*, 3, 5, pp. 876-883, May 1965.
9. Polachek, H. and R.J. Seeger, Shock Wave Interactions, Section E in: Fundamentals of Gas Dynamics, Howard W. Emmons, ed. Princeton, Princeton University Press, Vol. III, Sec. E., pp. 482-524, 1958.

Supersonic Combustion Technology

Antonio Ferri
Director, Guggenheim Aerospace Laboratories,
New York University

[14-1] INTRODUCTION *

The introduction of ballistic missiles as a major element of a modern military strategic offense has abruptly arrested the systematic development of advanced air transportation systems which have been traditionally supported in the initial stages on the basis of military requirements. However, recently the decision to develop supersonic commercial transports has revived the interest of the technical world in the possibility of future hypersonic airplanes and, therefore, of hypersonic engines. At the same time, the plans for a large-scale space exploration, which rely strongly on the capability of developing economically feasible launching systems, have recently generated much interest in the concept of recoverable boosters. It is evident that any recoverable booster will, of necessity, have somewhat larger structural weight than disposable boosters; therefore, the development of such boosters is closely related to the development of supersonic propulsion systems more efficient than those in use today.

In light of these new requirements, the investigation of air-breathing propulsion systems has received renewed attention for possible applications to hypersonic flight. The most evident differences between rocket engines and air-breathing engines are:

1. The air-breathing propulsion system theoretically has a much larger specific impulse than any chemical type rocket engine known today. The reason is evident: the ramjet carries only the fuel and does not carry the oxidizer.

2. The structural weight of a ramjet is probably larger for the same thrust than the structural weight of a rocket engine because it must handle the nitrogen together with the oxygen and must have an air intake which probably is heavier than the oxidizer tank and pressurization system.

---

*A large part of this material, including the figures presented herein, have been taken from two previous papers written by the author on this subject [27, 38].

3. The thrust of the ramjet engine is a function of flight Mach number and altitude of flight. Large thrust–per–unit frontal area can be obtained only if flight occurs in the dense atmosphere while rocket engines can operate in vacuum.

4. The necessity of flight in the atmosphere introduces severe structural problems related to aerodynamic heating. In addition, the performance of the engines is somewhat reduced by the aerodynamic drag of the vehicle. However, the vehicle has a better flying and maneuvering potential than any vehicle travelling in vacuum, because of the possibility of using aerodynamic lift. Hypersonic airplanes and recoverable boosters must have the possibility of flying in the dense atmosphere, independent of the propulsion system requirements; therefore, air–breathing engines appear particularly suited for these types of applications.

[14-2] PERFORMANCE OF SUPERSONIC COMBUSTION RAMJET

[14-2.1] Possible Air-breathing Engine Schemes

Several types of air–breathing engines can be considered for hypersonic flight. Classical types are the turbojet and the ramjet. The main limitation of the turbojet engine for hypersonic flight is related to the structural integrity of the rotating machine. Pre–cooling of the air is required at high Mach numbers for such types of engines. Such a requirement increases the weight and complications of the system and reduces the amount of cooling available for the vehicle. At high speed, the heat capacity of the fuel available is not sufficient for cooling the engine air and the structure at the same time; therefore, the use of rotating machinery at high supersonic speeds does not appear to be too promising.

Several types of hypersonic ramjets have been investigated for hypersonic flight. The different types are distinguished here on the basis of the combustion process used. The classical approach used in ramjets is to decelerate the air through an air intake or inlet to low subsonic speed in the burner. Here fuel is added at low velocity, combustion takes place, and then the flow is accelerated through a nozzle. The second type of combustion suggested is based on combustion through a shock wave. The air and a gaseous combustible are pre–mixed at supersonic speeds, and the temperature and pressure of the mixture are then raised through a shock wave; a detonation type of combustion is produced [1]. Such a scheme requires that the fuel be pre–mixed with air at low temperature and pressure so that the ignition delay is large enough to prevent combustion in front of the shock. The pressure and temperature jump taking place across the shock reduces by an order of magnitude the ignition delay behind the shock, and combustion then occurs rapidly. Because of opposite requirements

in front of and behind the shock, strong shocks are necessary. In such a scheme, the detonation shock is controlled by the combustion process and is very sensitive to any variation of fluid dynamic and thermodynamic parameters; therefore, the design is critical.

The combustion process proposed in Reference 2 and investigated for some time by my group is combustion controlled by mixing, which takes place in a burner in a supersonic stream. In this scheme, the flow (Fig. 14-1) is decelerated gradually to a lower Mach number in an inlet in order to increase the static temperature and pressure of the air. Subsequently, the fuel is injected at high velocity and mixes gradually with the flow. If the temperature and pressure of the mixture are sufficiently high, reaction occurs and the time for combustion is very short. In this case, the heat release is controlled by the mixing process which is gradual and stable because the flow is supersonic. The combustion chamber must be designed to match the mixing and combustion processes; by using a suitable design, formation of shocks in the burner can be avoided.

The differences between the different schemes are very large from a practical point of view. The supersonic combustion controlled by mixing can be utilized throughout a large range of Mach numbers without the necessity for variable engine geometry, because the mixing process depends on the difference of velocity of the air and of the injected gas [2]. In contrast, the subsonic combustion ramjet requires complex variable inlets and nozzles, and the structural weight and complexity of such components increase sharply with Mach number.
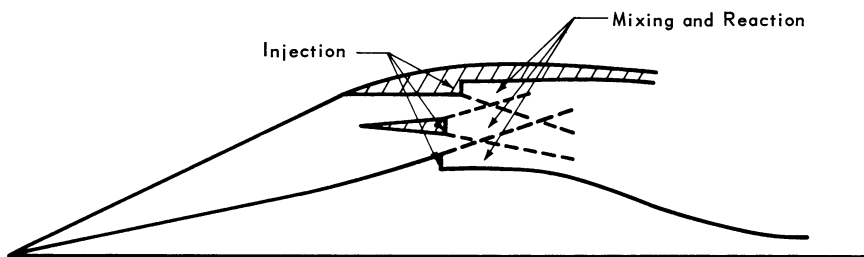
Fig. 14-1 Supersonic burning with detonation shock.

The main requirement of a supersonic combustion ramjet of this type is that the reaction rates which control the chemical reactions be very fast so that the mixing of fuel and oxidizer can be a much slower process and, therefore, the controlling factor of the combustion. This is possible if the static pressure and temperature of the air and fuel are sufficiently high, at least at some initial point of the mixing region, so that combustion can start. The rapidity of mixing depends on the design of the injector

system and on the mixing process; large differences exist between laminar and turbulent mixing. Recent results show that for turbulent mixing, the mixing process is sufficiently fast to permit combustors of practical length even at very high stream velocities. At present, the fuels considered for such applications are gaseous at the injection station. The gas is injected at supersonic speed and the mixing then takes place between two supersonic streams. The fuel considered most suitable for such application, especially for high Mach numbers, is hydrogen [2] because of its attractive thermodynamic and cooling characteristics.

[14-3] SUPERSONIC COMBUSTION

[14-3.1] Qualitative Description of Supersonic Combustion Controlled by Mixing

The aerodynamic design of a combustor in scramjet speed is related to two basic problems: mixing and combustion. Two different effects produced by the mixing of two jets can be used to control the supersonic combustion, depending on the static conditions of the jets before combustion. When the static pressure and temperature of the two mixing streams are sufficiently high so that chemical reaction rates are fast, the diffusion of one species in the other produced by the mixing is used, *e.g.,* for a controlling mechanism for combustion. This type of control is used in the higher range of flight Mach numbers and is the type considered in References 2, 7 and 8. When the static temperature and pressure of the two mixing streams are low, supersonic combustion can still take place, but it must be controlled by the heat convection produced by mixing and needs some kind of pilot flame. This second process is important because it extends the possibility of using supersonic combustion for ramjets into the lower range of Mach numbers.

[14-3.1.1] Supersonic Combustion Controlled by Diffusion

To illustrate the basic characteristics of supersonic combustion processes controlled by diffusion, consider two axially symmetric jets of different composition, velocity, and temperature injected in a chamber at high velocity. The mixing can be either laminar or turbulent, depending on the conditions of the two flows. Depending on the initial conditions at the boundaries of the mixing and on the flow parameters of the jets involved, the mixing can occur with or without large pressure variations. For simplicity, here the two streams are assumed to be parallel and to have the same static pressure at injection. The gas of the central jet is

hydrogen and the external jet is air. The mixing is assumed to be turbulent. The mixing of the two jets tends to reduce the difference of temperature, velocity, and concentration of the two streams. In the cases illustrated in Figs. 14-2 and 14-3, the air stream moves at a velocity, u_e, of 3070 ft/sec., and has a static temperature, T_e, of 2500° R, and a static pressure, p_e, of 0.38 atm; the hydrogen stream moves at a velocity, u_j, of 1030 ft/sec., and has a static temperature, T_j, of 500° R, and static pressure, p_j, of 0.38 atm.

Consider first the limiting case of infinite reaction rates: the oxygen of the air and the hydrogen react in zero time as soon as their molecules collide and form water. Then a flame is produced and heat is released in the mixing region. In the outer part of the mixing region, the flow is oxygen-rich; therefore, the gas contains water vapor, nitrogen, and oxygen. In the inner part of the mixing, the gas is hydrogen-rich, and the gas contains water vapor, hydrogen and nitrogen. The two regions are divided by a surface corresponding to the stoichiometric mixture ratio [8]. The distribution along the axis is shown in Fig. 14-2.
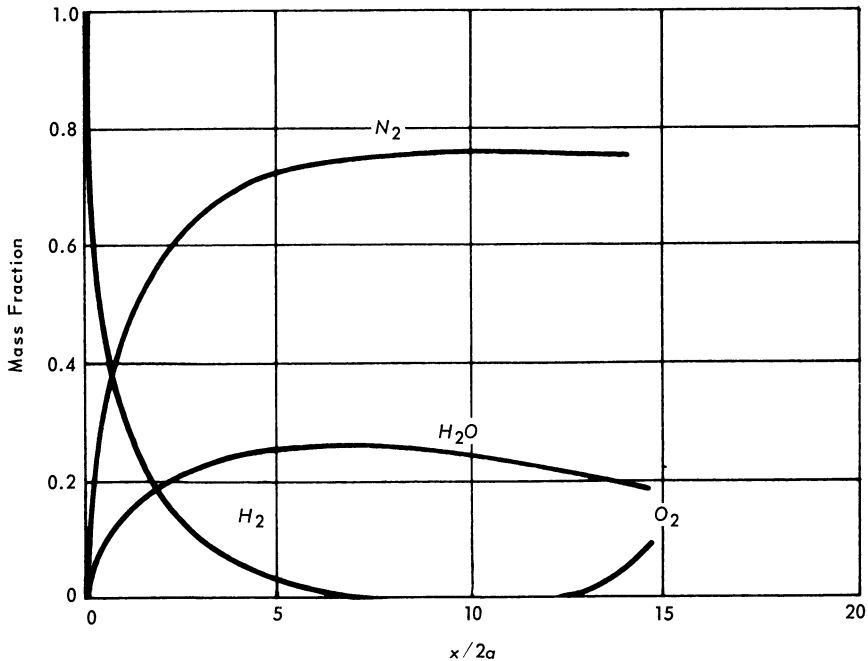
Fig. 14-2 Mixing with equilibrium chemistry; centerline concentrations. $T_e = 2500\,\text{R}$; $T_j = 500\,\text{R}$; $P_e = P_j = 0.038$ Atm; $U_e = 3070$ ft/sec.; $U_j = 1030$ ft/sec.

In reality, the chemical reaction of H_2 and O_2 is complex; radicals and atoms are produced in the process of reaction and the reaction rates have finite values. Depending on the values of static pressure and temperature of the two jets, the actual phenomenon
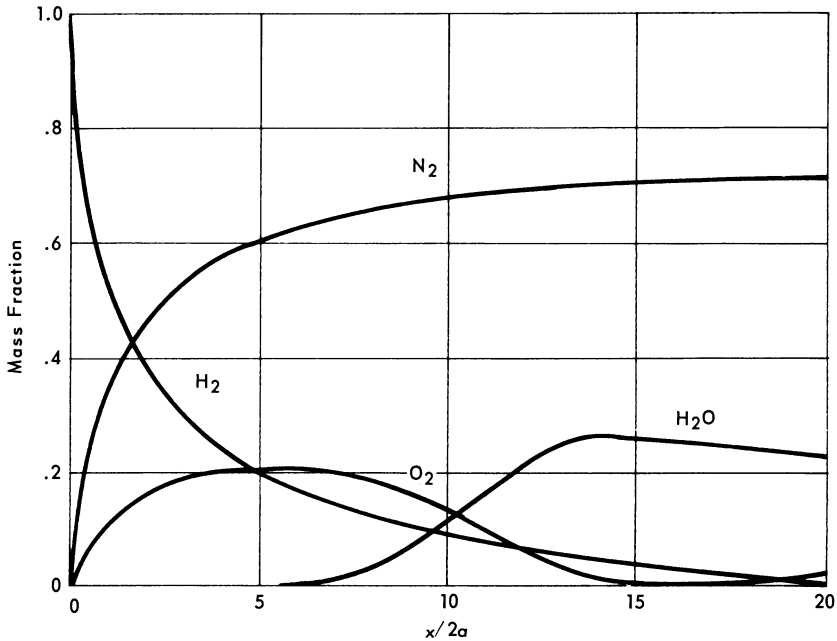
Fig. 14-3 Centerline concentrations with finite rate chemistry. $T_e = 2500$ R; $T_j = 500$ R; $P_e = P_j = 0.038$ Atm.; $U_e = 3070$ ft/sec.; $U_j = 1030$ ft/sec.

is close either to the first or to the second case described above. For very low pressure and temperature of the gases, the reaction rates are very small, the mixing occurs before reaction and the flow is frozen chemically during mixing. For large values of static pressure and temperature in the jets, the reactions occur extremely fast, so that the mixing process is close to the second case (equilibrium flow). In this case, the reaction times are much smaller than the flow times and therefore can be neglected in the analysis; thus the chemical composition at any given point can be determined from the concentration of atomic species, local pressure and temperature at the point considered. The problem again becomes one of fluid dynamic nature, and the combustion is controlled exclusively by the diffusion process produced by mixing.

If the reaction times are of the same order as the flow times, the fluid dynamic and chemical processes are strongly coupled and interdependent. The mechanism of the heat release depends on both processes; mixing occurs first and later reaction is initiated slowly. When the static temperature starts to increase, the reaction process accelerates because the reaction rates depend strongly on temperature. At this point, mixing has already occurred and the heat release progresses rapidly in a localized region.

Results of an analysis that takes into account finite reaction rates for the case defined above are shown in Figs. 14-3 and 14-4.
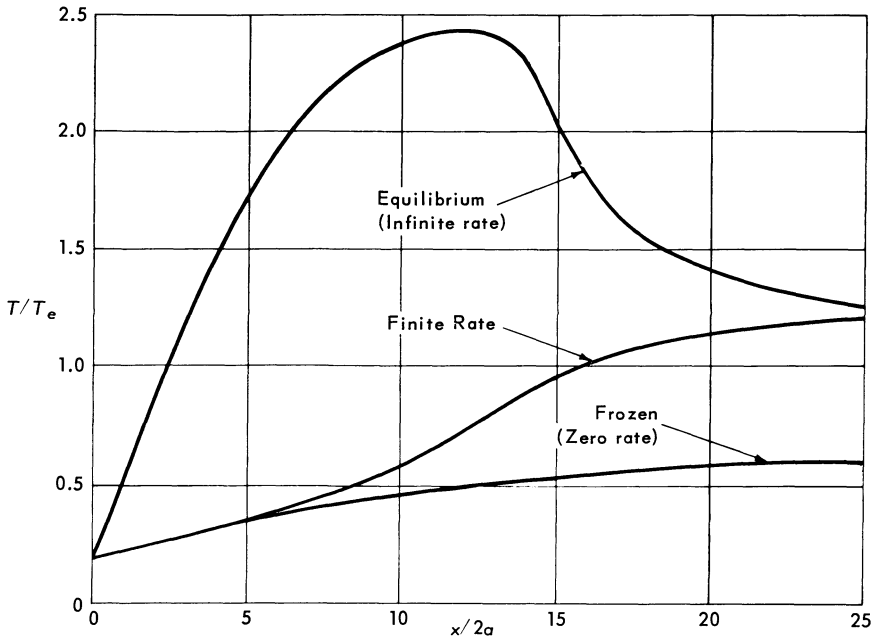
Fig. 14-4 Centerline temperatures. T_e = 2500 R; T_j = 500 R; $P_e = P_j$ = 0.038 Atm.; U_e = 3070 ft/sec.; U_j = 1030 ft/sec.

The analysis used computing programs described in References 9, 10 and 11. Figure 14-3 gives the concentration of species at the axis. For the pressure and temperature assumed, reaction times and flow times are of the same order; substantial mixing takes place before the heat is released by the combustion process. The oxygen diffuses to the axis before burning. The concentration of the oxygen at the axis at first increases and then decreases until combustion is completed and the hydrogen is completely burned. The heat release occurs later and in different regions of the flow than for the equilibrium case. In Fig. 14-4 the static temperature along the axis is shown for the three cases. Figures 14-5 and 14-6 give the temperature distribution in the flow for the equilibrium and the finite reaction rate cases.

The process of heat release controlled by the diffusion of one species into the other, when the two streams are supersonic, is graudal and continuous. The chemical reaction releases heat and produces a locally large variation of temperature, density and pressure. The pressure variation produced by the combustion propagates in the flow by means of a wave mechanism. If the flow is supersonic, the pressure disturbances propagate downstream only, while if it is subsonic, they propagate upstream also. The chemical reaction rates are strongly dependent on pressure and temperature, and mixing is affected by pressure variations;
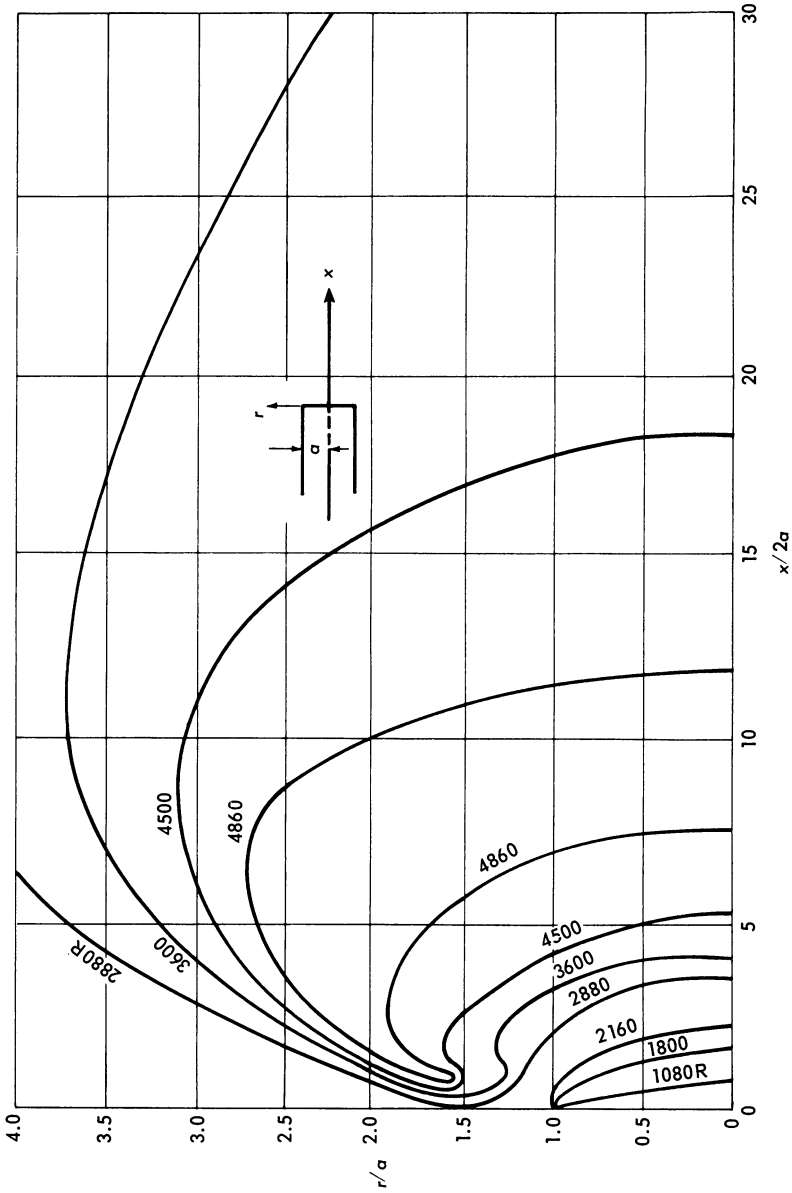
Fig. 14-5 Isotherms with equilibrium chemistry. $T_e = 2500$ R; $T_j = 500$ R.
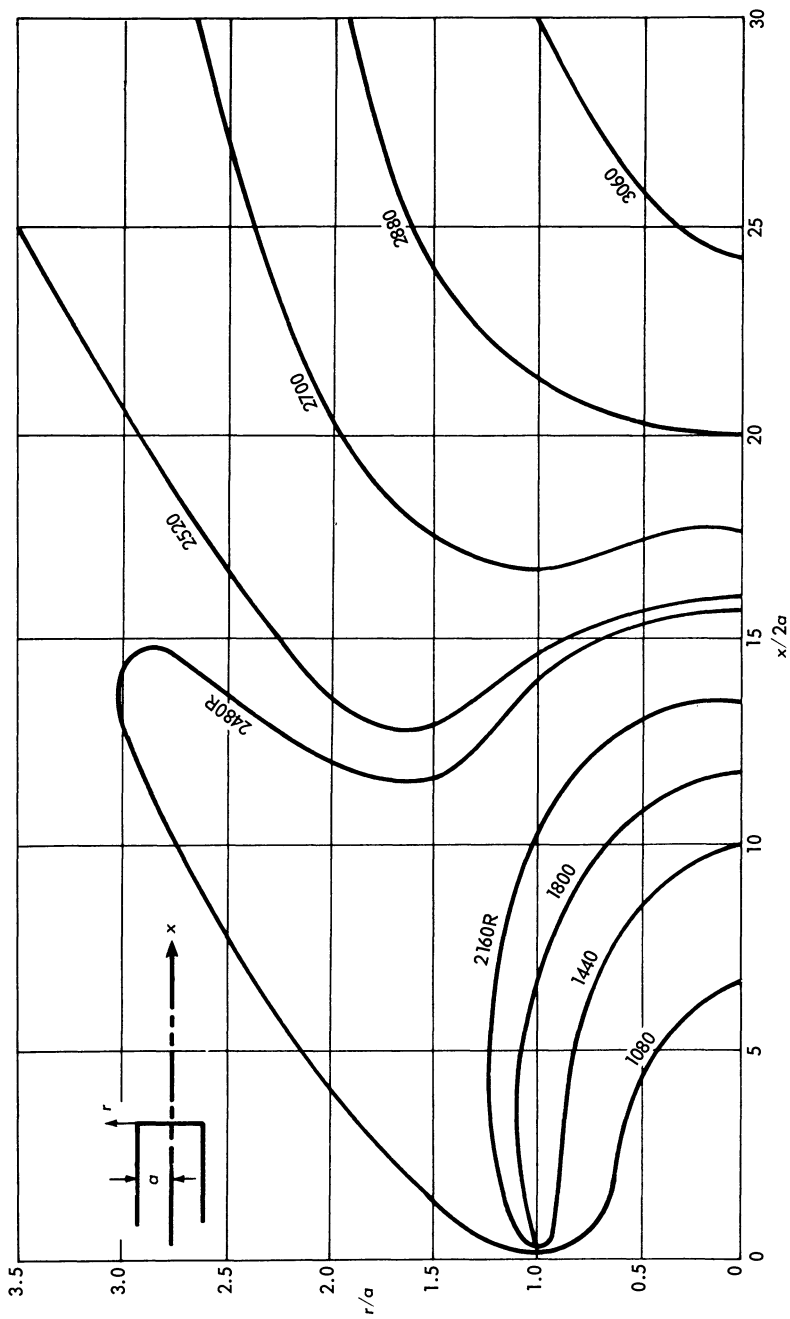
Fig. 14-6 Isotherms with finite rate chemistry. $T_e = 2500R$; $T_j = 500R$.

therefore, for subsonic flow, any pressure disturbance created in the flow by the combustion affects the upstream flow and changes the concentration, pressure and temperature at the point where the disturbance is generated. This coupling can create instability. For supersonic flows, the pressure disturbance produced by combustion propagates only downstream and does not affect the physical chemical properties of the flow at the point where the disturbances are generated; no coupling exists that can produce instability in the flow.

[14- 3.1.2] Supersonic Combustion Controlled by Heat Convection

The heat convection process produced by mixing can be used in place of the diffusion process as a controlling mechanism for a supersonic flame. To illustrate this concept, consider a small jet of gas having very high static temperature and discharging in a flow having high velocity and low static temperature (Fig. 14-7). For simplicity, assume that the two gases are at the same pressure. Because of the mixing process, the concentration of the two gases changes gradually and the static temperature changes. The gas from the external jet mixes with the hot gas and is heated while the gas from the central jet is cooled. If the mixing takes place without chemical reaction, the temperature at the axis of the jet gradually decreases. However, if the gas of the external jet is a premixed reacting mixture and the temperature of the central jet is sufficiently high, then because of the heating process due to mixing, the external gas reacts and combustion takes place. The heat released by the reacting gases tends to keep up the temperature of the central core of the flow and, if the balance of heat is favorable, the combustion continues while mixing takes place and propagates towards the external flow. The propagation is controlled by the heat convection related to the mixing process. The example presented in Fig. 14-7 considers a jet of combustion products and hydrogen discharging in a jet of a stoichiometric mixture of propane and air at low static temperature. The temperature distribution of the flame is given in Fig. 14-8. In this case, the central jet performs as an igniter for the supersonic external stream. The temperature of the main stream is too low to produce chemical reaction in the mixture, but combustion is maintained because the central jet has sufficiently high temperature to produce rapid combustion which avoids the cooling produced by mixing.

The mechanism of combustion described here is of practical importance because it permits us to produce combustion in flows having static temperatures below the temperature required for rapid ignition and, therefore, extends the possibility of using supersonic combustion controlled by mixing in the range of flight Mach numbers below 6 or 7. This scheme also allows the possibility
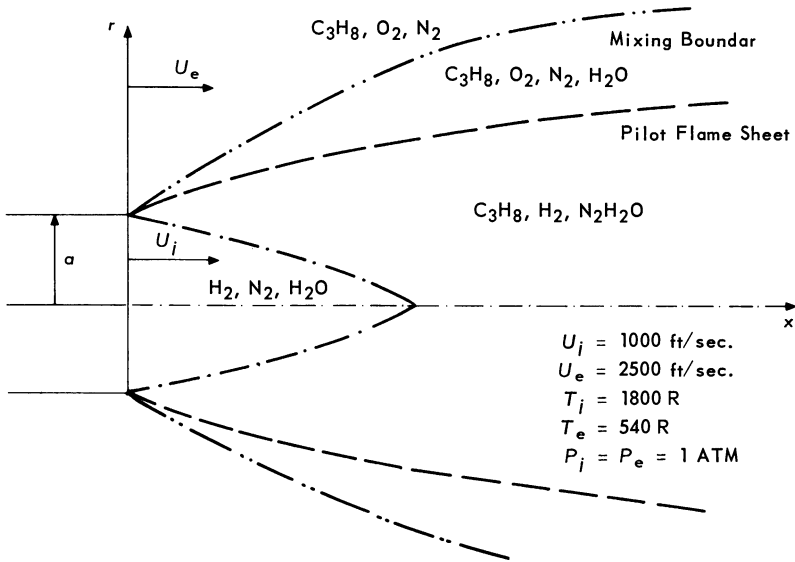
Fig. 14-7 Schematic of ignition of propane-air mixture with hydrogen-air pilot.
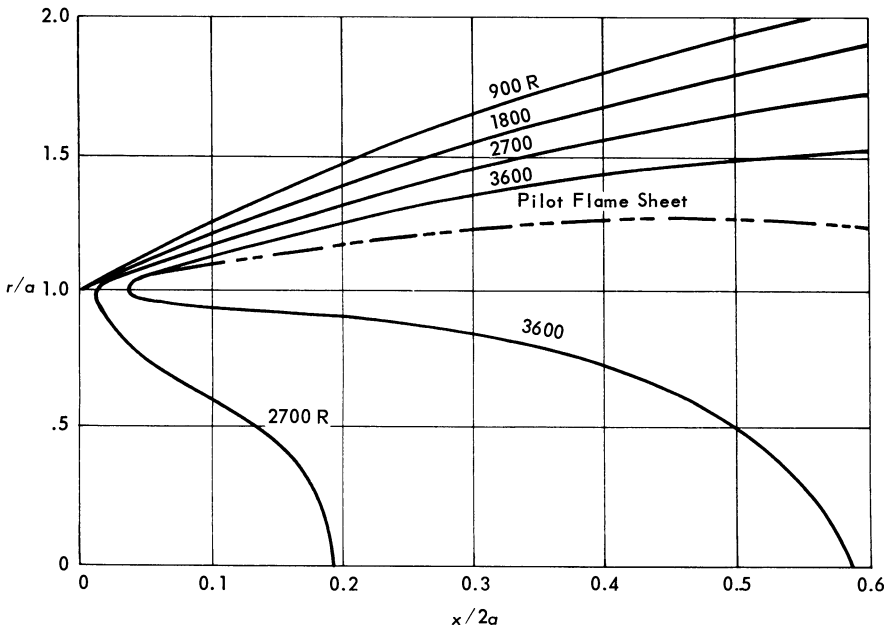
Fig. 14-8 Isotherms and pilot flame sheet.

of supersonic combustion with fuels having very long reaction times at the static temperature and pressure existing in the burner of the

engine for the flight conditions considered. The propane-air reaction for the conditions assumed in Fig. 14-7 is too slow and combustion controlled by diffusion would not be possible. However, the reaction time is sensitive to temperature; reaction immediately occurs locally if the temperature is sufficiently increased by mixing with the gas of the pilot flame. Flammability limits exist which are determined by the balance between heat released by the reaction and heat absorbed by the low temperature mixture [12].

In the preceding discussion, it has been assumed that the fuel is gaseous and is injected parallel to the air stream. Substantial progress has been made on the analysis of turbulent mixing of gases in the case of tangential injection. However, tangential injection requires injectors to be placed in the stream. The use of inclined injection where the fuel is injected at an angle with respect to the direction of the air stream would eliminate such a requirement.

The problem of inclined injection is more difficult to analyze. Presently it is difficult to predict with satisfactory approximation the distribution of fuel in an airstream when the fuel is injected in the flow by means of an inclined jet. Some comments must be made on the relative advantages of the two approaches. The interest in inclined injection is due to the fact that when the fuel is injected with a velocity component normal to the air flow, the fuel reaches a region at some distance from the point where the fuel enters the channel because of the kinetic energy of the fuel; the fuel penetrates the air without the necessity of having a physical tube that brings the fuel totally into the stream. In addition, because of its inclination, the fuel entering the stream produces a local compression and increases the pressure of the air in front of the jet and facilitates combustion. However, where the angle of injection is large, such advantages are in part fictitious and are coupled with several disadvantages that make this approach unattractive for a practical engine.

A schematic description of the flow field is shown in Fig. 14-9. The fuel is injected from a wall where boundary layer exists. In the case of injection of an inert gas, the shock produced by the injection locally separates the boundary layer flow, and the compression starts somewhat upstream of the injection. The jet is deflected and the gas mixes with the air. The pressure in the base region, region 2 of Fig. 14-9, is below free stream pressure while in region 1 it is above free stream pressure. The pressure difference tends to bend the jet, which at some distance from the wall becomes parallel to the free stream. Two sets of shocks are produced; one in front of the jet and the other where the flow behind the jet re-attaches to the wall. Such shocks produce losses in the flow outside the continuum which must be considered in the cycle analysis and are difficult to analyze.
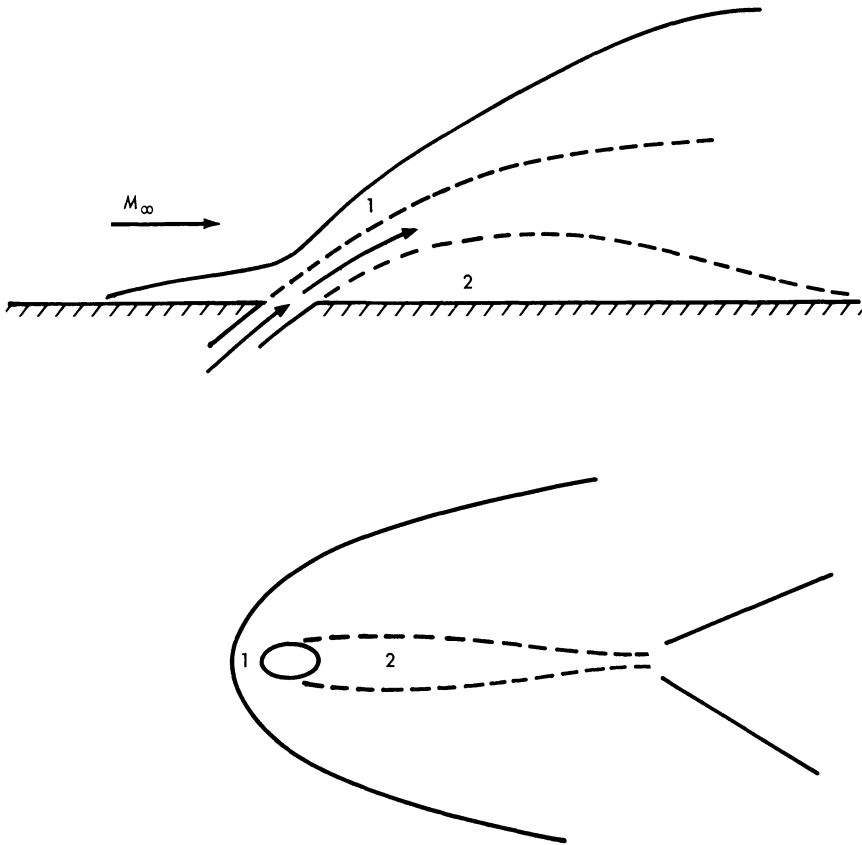
Fig. 14-9 Combustion with inclined fuel injection.

In the case of combustion, the combustion starts in region 1 and propagates upstream into the separated region. In this region, the local heat transfer is extremely high because the combustion takes place very close to the wall. Heat transfer as high as 10 to 20 times the local heat transfer before injection has been measured in this region. The combustion and the pressure rise tend to move the separation upstream and can separate the flow in the inlet. The flow in region 2 behind the jet is at low velocity and the temperature is high; for some conditions, combustion can take place here. This would tend to increase the local pressure and therefore change the trajectory of the jet. The amount of combustion that takes place in region 2 is affected strongly by static pressure variation and by the amount of combustion taking place at 1; it is very sensitive to variations of Mach number, altitude of flight and tupe of separation produced. The penetration is strongly affected by all such parameters.

When the engine must be designed for a large range of flight Mach numbers, the problem exists of matching the fuel penetration with the values of stagnation pressure of the fuel which is determined by the amount of fuel that must be injected at a given flight condition. Such matching requirements impose additional constraints on the selection of cycle design. At low Mach numbers, the injectors located near the minimum areas of the burner must inject very small mass flow in order to avoid choking the stream, and the largest part of the fuel must be injected downstream. At high Mach numbers, the opposite requirement exists. Note that in this case much of the fuel must burn near the wall and will thus increase the local heat transfer.

In addition, for any given flight condition and local flow conditions, the penetration of the jet depends on the stagnation pressure of the fuel. A change in fuel mass flow (variation of Φ) requires a change in the dynamic pressure of the jet; therefore the penetration and the region reached by the fuel will change. A small value of Φ corresponds to a large amount of burning near the wall and a small amount of burning in the main stream, which is the opposite of what is required for good cooling characteristics. It must be noted that the cooling requirements are most severe at low values of Φ.

[14-3.2] Analysis of the Reaction Process

Combustion controlled by mixing tends to generate pressure gradients in the flow. To achieve good engine performance, formation of strong shocks must be avoided; this can be obtained only if the compression waves produced by the combustion process are neutralized by expansion waves produced at the boundary of the jet. As a consequence, the problem of burner design requires some quantitative knowledge of reaction processes, mixing processes and wave propagation in a reacting diffusive process. The analysis of such a flow is very complex and in many cases is not yet possible. Several steps are required for such an analysis. First, the chemical reactions which are significant in describing the overall system must be determined. Second, an evaluation of the reaction rates for each reaction considered in the analysis must be performed. Such a determination is based at present on experimental results. In a nonequilibrium process, each single reaction can proceed forward and backward. A relation between the two rate constants must be established. Usually such rate constants are related to each other on the basis of the equilibrium constant. Third, the combined chemical kinetic and fluid dynamic processes must be analyzed simultaneously to determine the values of concentration of species and elements, static pressure and temperature, which in turn determine the values of the reaction

rates. Such a final step can be performed only for simple chemical processes and for simplified boundary conditions. The description of the actual fluid dynamic process is based on conservation of momentum, total enthalpy, elements and species that enter into the chemical process. In stating these conservation laws, viscous diffusive and convective processes must be taken into account which affect the concentration of elements along the streamline, the total enthalpy, and the momentum. The transport properties of turbulent mixing of reacting flows are not known and must be determined experimentally. In addition, three-dimensional pressure variations must be considered. Then the problem becomes extremely complex analytically unless simplifications are introduced.

As a first step, the chemical kinetic process will be considered and the effects of transport properties will be neglected. Such a simplified analysis will furnish information on reaction times which can be compared with flow times related to the fluid dynamic process and will give an indication of the practical dimensions required for a combustor. In addition, if the reaction times turn out to be much smaller than flow times, the variation of fluid dynamic properties can be neglected in the analysis of the chemistry; it can be assumed that the chemical reaction process occurs at constant total enthalpy, constant pressure, and constant concentration of elements and is a function only of local conditions. Under these conditions, chemical kinetic effects can be neglected and chemical equilibrium can be assumed in the flow analysis.

[14-3.2.1] Determination of Reaction Times

To determine the value of reaction times in the absence of transport properties, the following conservation equations must be solved for the analysis of a chemical reacting mixture [13, 14]: conservation of species

$$\rho V \frac{dY_i}{ds} = \dot{w_i}' \quad i = 1, 2, \ldots N-L \tag{14-1}$$

conservation of elements

$$\frac{d\tilde{Y}_j}{ds} = 0, \quad j = N-L+1, \ldots N \tag{14-2}$$

where

$$\tilde{Y}_j \equiv \sum_{i=1}^{N} \frac{\mu_{ij} W_j Y_i}{W_i} \tag{14-3}$$

where μ_{ij} is the number of atoms of element j in species i. Conservation of energy

$$\frac{dH}{ds} = 0, \quad H \equiv \frac{V^2}{2} + \sum_{i=1}^{N} Y_i h_i. \tag{14-4}$$

Conservation of momentum

$$\rho V \frac{dV}{ds} = -\frac{dp}{ds}. \tag{14-5}$$

The mass rate of production per unit volume is given by

$$\dot{w}_i = w_i \sum_{j=1}^{K} (\nu_{ij}'' - \nu_{ij}') k_j \rho^{n_j} \prod_{i=1}^{N} \left(\frac{Y_i}{W_i}\right)^{\nu_{ij}'} G_j \tag{14-6}$$

where

$$G_j \equiv 1 - \rho^{m_j} K_{c,j}^{-1} \prod_{i=1}^{N} \left(\frac{Y_i}{W_i}\right)^{\nu_{ij}'' - \nu_{ij}'} \tag{14-7}$$

$$n_j = \sum_{i=1}^{N} \nu_{ij}'$$

and

$$m_j = \sum_{i=1}^{N} (\nu_{ij}'' - \nu_{ij}')$$

and the summation is extended to the reactions containing species i. k_j is the forward rate constant (reaction proceeding to the right) and $K_{c,j}$ is the equilibrium constant based on the molar concentrations for the jth reaction expressed in the form

$$\sum_{i=1}^{N} \nu_{ij}' M_i \overset{k_j}{\rightarrow} \sum_{i=1}^{N} \nu_{ij}'' M_i; \quad j = 1, \ldots K \tag{14-8}$$

where ν_{ij}' and ν_{ij}'' are the stoichiometric coefficients of the reaction. In addition, the following relation is needed:

$$p = \rho R_0 T \sum_{i=1}^{N} \frac{Y_i}{W_i} = \frac{\rho R_0 T}{W} \tag{14-9}$$

The assumption introduced here is that the forward and backward rate constant can be related to the equilibrium constant.

The initial boundary conditions for such a type of analysis are usually given in the form of static pressure, temperature, and velocity and the complete chemical composition of the mixture at the beginning of the reaction. In addition, another boundary condition that defines the variation of pressure along the streamline must be stated. Here, as a first step, the static pressure will be assumed to be constant.

Some numerical difficulties are associated with starting the calculations from equilibrium [15]. Such difficulties can be by-passed by recently-developed numerical procedures [11]. The chemical reactions pertinent to hydrogen air reaction are as follows:

$$H + O_2 \rightarrow OH + O \qquad\qquad (14\text{-}10)$$

$$O + H_2 \rightarrow OH + H \qquad\qquad (14\text{-}11)$$

$$OH + H_2 \rightarrow H_2O + H \qquad\qquad (14\text{-}12)$$

$$2OH \rightarrow H_2O + O \qquad\qquad (14\text{-}13)$$

$$H_2 + M \rightarrow 2H + M \qquad\qquad (14\text{-}14)$$

$$H_2O + M \rightarrow H + OH + M \qquad\qquad (14\text{-}15)$$

$$OH + M \rightarrow H + O + M \qquad\qquad (14\text{-}16)$$

$$O_2 + M \rightarrow 2O + M \qquad\qquad (14\text{-}17)$$

k_j used $(\text{mole/cc})^{-1}\,\text{sec}^{-1}$		k_j [19]
$3(10^{14})\,e^{-8810/T(^\circ K)}$	[Eq. (14-10)]	$4(10^{14})\,e^{-9080/T}$
$3(10^{14})\,e^{-4030/T}$	[Eq. (14-11)]	$3(10^{14})\,e^{-3030/T}$
$3(10^{14})\,e^{-3020/T}$	[Eq. (14-12)]	$3(10^{14})\,e^{-1260/T}$
$3(10^{14})\,e^{-3020/T}$	[Eq. (14-13)]	$3(10^{14})\,e^{-1260/T}$
$C(10^{19})\,T^{-1}\,e^{-54,000/T}$	[Eq. (14-14)]	$(10^{21})\,T^{-1.5}\,e^{-52,000/T}$
$D(10^{21})\,T^{-1}\,e^{-62,200/T}$	[Eq. (14-15)]	$(10^{23})\,T^{-1.5}\,e^{-58,000/T}$
$E(10^{19})\,T^{-1}e^{-52,000/T}$	[Eq. (14-16)]	$(10^{21})\,T^{-1.5}\,e^{-51,000/T}$
$2.9(10^{19})\,T^{-1}\,e^{-60,600/T}$	[Eq. (14-17)]	$1.4(10^{25})\,T^{-2.5}\,e^{-59,600/T}$

	C	D	E
RR1	1.85	0.966	0.8
RR2	9.25	9.66	8.0
RR3	20.8	30.6	25.3

Reactions (14-10) to (14-13) are the bimolecular reactions which form H_2O, O, H and OH radicals. Reactions (14-14) to (14-17) are the recombination reactions which produce the major portion of the energy release.

The symbol M in the equations represents a third body; because of lack of sufficient information, all third bodies are assumed equally effective in the analysis. The forward rate constants for reactions (14-10) to (14-13) and backward rate constants for reactions (14-14) to (14-17) denoted by RR1 and RR2, are the constants considered possible in References 16, 17 and 18. Recent tests tend to indicate that the larger values of the constants are probably more realistic for reactions (14-14) to (14-16). Such values are denoted by RR3. The difference between the different sets of constants are important at low static pressures [20]. For comparison, some different values suggested in Reference 19 are also shown.

[14-3.2.2] Numerical Results

Numerical results of the analysis with constant pressure, constant mass of elements, and total enthalpy indicate the following trends [14]. The bimolecular reactions are faster than the recombination reactions and dominate the first part of the process. Later the other reactions start to take place and become important. The first part of the reaction occurs without appreciable temperature rise. The concentration of the free H radicals increases until it reaches a peak value. During this first period, the formation of water is energetically balanced by the dissociation of oxygen and hydrogen molecules. Because of its large heat of formation, the creation of atomic hydrogen plays an important role in this phase. The disappearance of hydrogen radical in the latter part of the process tends to produce a rapid increase in the temperature of the gas. Therefore, two characteristic times can be devined [14, 20]: the ignition delay time, defined as the time from the beginning of reaction to peak concentration of atomic hydrogen, and the heat release time defined as the time between the end of ignition delay time and equilibrium state. Figures 14-10 to 14-12 show typical temperature histories as a function of time for particular cases
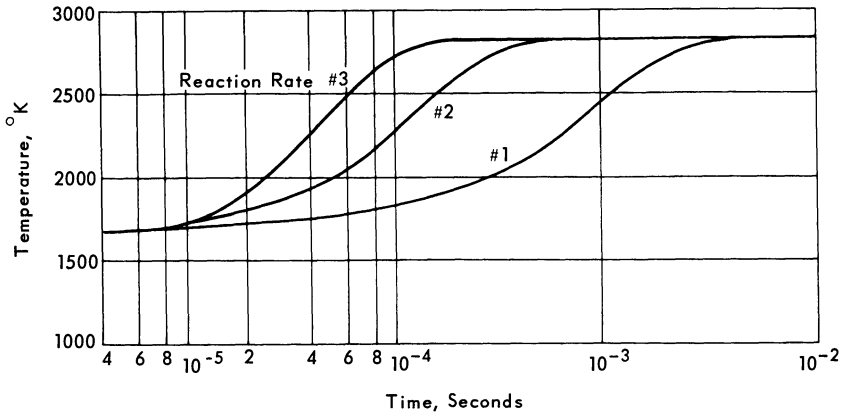
Fig. 14-10 Temperature-time history of stoichiometric hydrogen-air reaction; P = .2 atmosphere.
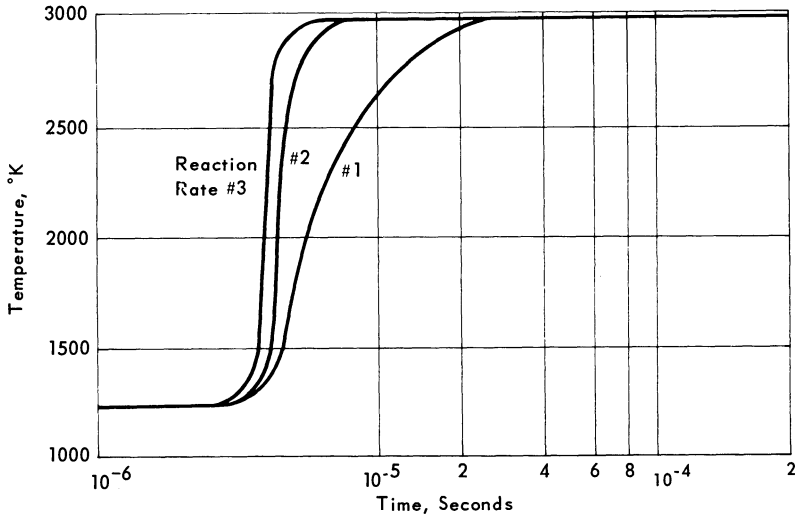
Fig. 14-11 Temperature-time history of stoichiometric hydrogen-air reactions; P = 4.7 atmosphere.

[14, 20, 21]. Figures 14-10 and 14-11 indicate the effect of the variation of the reaction constants in Eqs. (14-14) to (14-16) for two different values of static pressure. Figure 14-12 indicates the effect of the initial static temperature and the fact that the ignition delay is strongly affected by the initial temperature and pressure, it is not affected by a variation of equivalence ratio or by the values of the constants of the recombination reactions. The heat release time is also strongly affected by pressure and temperature; in addition, at low static pressure it is strongly affected by the values of the constants assumed for the recombination reaction. The heat release time is insensitive to the equivalence ratio of the mixture.
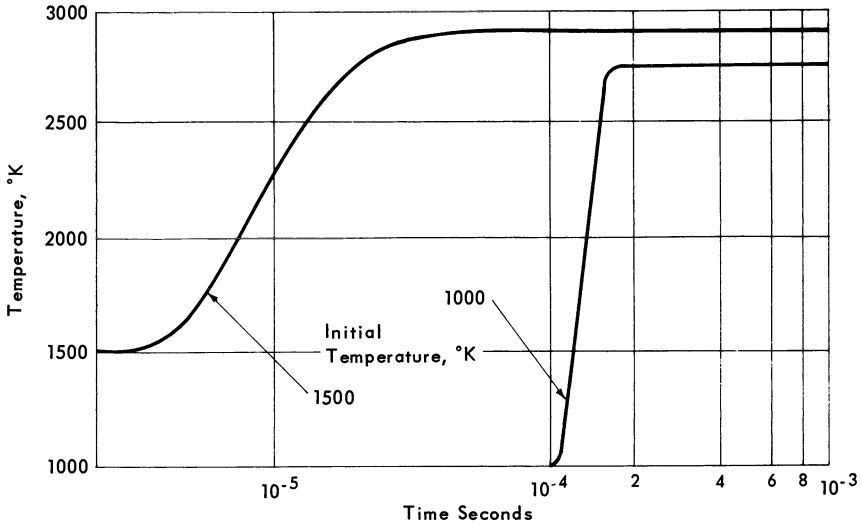
Fig. 14-12 Temperature-time history of stoichiometric hydrogen air with reaction rate no. 2; P = 1.0 atmosphere.

From the analyses performed, analytical expressions that give the variation of ignition delay time and heat release time as a function of initial pressure and temperature have been obtained [23, 24]. The ignition delay time is controlled principally by the bimolecular reactions and must be inversely proportional to pressure for a given temperature. In addition, the temperature dependence must be exponential because of the form of the reaction rate constants. The following form of equation, which correlates all the data obtained from the analysis for equivalence ratio between 0.4 and 2, was suggested in References 23 and 24 for the ignition delay time (τ in microseconds, p in atmospheres, T in °K):

$$p \, \tau_{ID} = 8 \times 10^{-3} \, e^{9600/T}.$$

However, the values of the constant used in this equation are those suggested in Reference 20; new experimental data on ignition delay have recently been obtained [14, 22, 26]. The experimental data correlates well with the equation obtained, as shown in Fig. 14-13. The curves corresponding to the constants suggested originally in References 23 and 24 are also indicated. During the heat release time, the three-body recombination reactions are important; therefore, the effect of the pressure on the heat release time is larged than on the ignition delay time. The following expression that fits the results of the numerical analysis in the range between 0.2 and 5 atm. and 1000 to 2000° K for a stoichiometric mixture with constants RR2 has been given in Reference 20:

$$p^{1.7} \, \tau_R = e^{-1.12T/1000}.$$
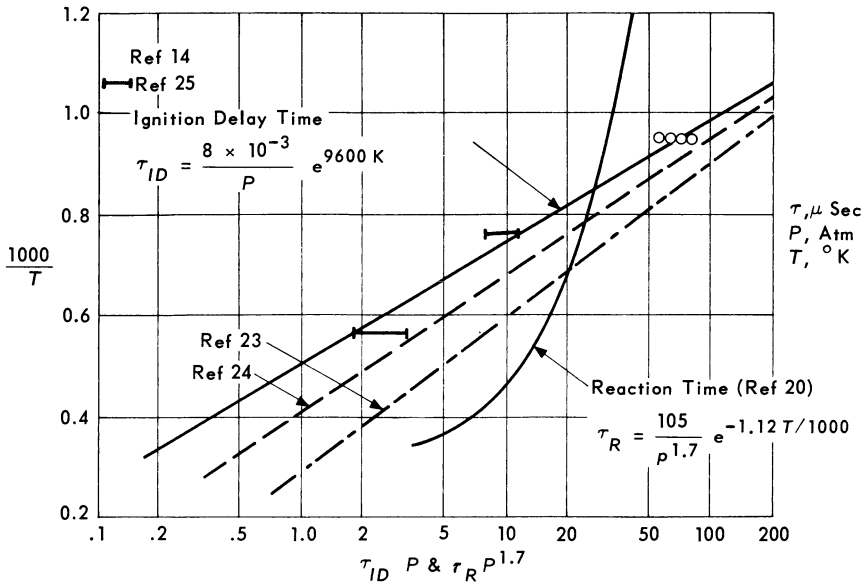
Fig. 14-13 Correlation of ignition delay time and reaction time.

The expression is also plotted in Fig. 14-13 as a function of $1000/T$.

[14-3.2.3] Discussion of Results

The results of the numerical calculations are of direct interest for the supersonic combustion problem. The performance analyses presented for an accelerating engine indicate that the values of the static pressure considered to be practical are of the order of several atmospheres. For these conditions, the total reaction time is of the order of 10^{-6} seconds for initial static temperatures of the order of 2000° R. Then, even if the flow moves at velocities of the order of 20,000 ft/sec., the combustion is completed in a distance of the order of 1/4 in. The temperature of the mixture increases rapidly as soon as the combustion is initiated locally at a point; this is the largest delay to be expected in all combustion processes. Then, for practical purposes, at high pressure and temperature the chemistry can be considered to be in equilibrium. At low static pressure, the reaction time becomes important, and practical combustion times can be obtained only if the static temperature of the mixture is very high.

The type of analysis presented here can be applied directly to the analysis of nonequilibrium flow in a nozzle. In this case, the flow is already mixed and transport phenomena are not important; one-dimensional analysis along the streamline applies. The analyses of nonequilibrium phenomena show that such effects are not

important and do not reduce the nozzle performance substantially for practical values of expansion ratio and static pressure in the burner.

[14- 3.2.4] Tangential Injection with Chemical Reaction

The turbulent mixing of a heterogeneous coaxial stream has been investigated in detail analytically and experimentally in the last few years, and many of the available results have been presented in References 27, 14, 21, 8, 28, 29. On the basis of present knowledge, the mixing in the absence of large pressure gradient can be represented, with sufficient accuracy for engineering purposes, by the analytical expressions suggested in these references. Good agreement between experiments and analytical results is found when diffusion and heat conduction processes are investigated. (These are the physical properties of interest in a mixing process with combustion.) However, discrepancies are found in many instances when the same types of analyses are applied to determine velocity decays and Mach number decays produced by mixing processes. Such discrepancies are not too important for the problems under investigation; however, they are important here because they have often been attributed to major shortcomings of the representation used. It is the writer's opinion that a careful analysis of the experiments where the velocity or enthalpy distributions have been measured in a mixing process proves that the discrepancy found is due not to large discrepancy in the transport properties assumed but to incorrect interpretation of the experiments. Velocity variations in the mixing process can be generated by two different effects: a small pressure gradient normal to the flow at the initial conditions, or viscosity. An initial pressure gradient usually exists in the free flight experiments, while in controlled experiments, any small longitudinal pressure gradient existing in the flow outside the mixing regions has equivalent effects.

These small pressure gradients in the flow outside the mixing region which are present in any experiment are usually neglected and often not even measured. However, in axially symmetric mixing which is the mixing usually investigated for such small pressure gradients, the gradients can produce large effects on the flow because of the focussing effect of the compression waves at the axis of the jet. The focussing produces large Mach number variations near the axis due only to inviscid effects and changes the mixing profile. It can produce local shocks which in turn affect the decay at the axis. Experiments have been performed at New York University in order to investigate this point [30]. A small disturbance was placed at the wall of the tunnel. This disturbance, which produced very small variations far from the axis induced large variations at the center of the tunnel and strongly affected the Mach number decay at the axis of the mixing.

In addition, the initial conditions must be carefully considered. When coaxial jets are investigated experimentally, the initial conditions with respect to velocity and stagnation temperature cannot be defined by simple parameters because of the existence of the boundary layers on the internal and external surfaces of the jet. The only parameter that can be defined with accuracy is the species concentration. The presence of boundary layers and of pressure gradients are especially important in the initial region of the mixing. Furthermore, for subsonic flow, large pressure gradients are produced upstream of the mixing by the mixing process when large differences of physical properties exist between the two streams. For these reasons, a very careful and detailed analysis is required in order to obtain correct conclusions.

[14-3.3] Analysis of Mixing Processes

The next step in the analysis of the combustion process is to analyze the mixing process in the presence of reaction. The analytical problem is largely simplified if the pressure variation in the direction normal to the streamline can be assumed to be negligible so that a boundary layer type of analysis applies. With this simplification, the analysis requires solution of the following group of equations:

conservation of momentum

$$\rho u \frac{\partial u}{\partial x} + \rho v \frac{\partial u}{\partial r} = r^{-1} \frac{\partial}{\partial r} \left(\epsilon \rho r \frac{\partial u}{\partial r} \right) \tag{14-18}$$

conservation of energy

$$\rho u \frac{\partial H}{\partial x} + \rho v \frac{\partial H}{\partial r} = r^{-1} \frac{\partial}{\partial r} \left[\left(\rho \epsilon P_{rt}^{-1} r \frac{\partial H}{\partial r} \right) + \right.$$

$$\left. + (P_r - 1) \rho \epsilon P_{rt}^{-1} r u \frac{\partial u}{\partial r} + (L_{et} - 1) \rho \epsilon P_{rt}^{-1} r \sum_{i=1}^{N} h_i \frac{\partial Y_i}{\partial r} \right] \tag{14-19}$$

global conservation of mass

$$\frac{\partial}{\partial x} (\rho u) + r^{-1} \frac{\partial}{\partial r} (\rho v r) = 0 \tag{14-20}$$

species conservation

$$\rho u \frac{\partial Y_i}{\partial x} + \rho v \frac{\partial Y_i}{\partial r} = r^{-1} \frac{\partial}{\partial r} \left(\rho \epsilon S_c^{-1} r \frac{\partial Y_i}{\partial r} \right) + \overset{\circ}{w} \tag{14-21}$$

$$i = 1, 2, \ldots N - L$$

$$\rho u \frac{\partial \widetilde{Y}_j}{\partial x} + \rho v \frac{\partial \widetilde{Y}_j}{\partial r} = r^{-1} \frac{\partial}{\partial r} \left(\rho \epsilon S_c^{-1} r \frac{\partial \widetilde{Y}_j}{\partial r} \right). \tag{14-22}$$

$$j = 1, 2, \ldots L$$

Numerical analyses for the solutions of such equations have been obtained which use available information on chemical rates discussed before. Such analyses require that the transport properties which enter in the definition of the Prandtl, Lewis and Schmidt numbers are known, as functions of the local flow properties [9, 10, 11]. Such quantities can be calculated for laminar mixing as functions of local pressure, temperature and concentration of species; however, they are not well known for turbulent mixing which is of more interest for supersonic combustion. In turbulent mixing, such quantities must be determined experimentally. Recently much work has been done on this subject [14, 21, 25, 26, 31–35], and some of the pertinent results relating to mixing of air and hydrogen are presented here.

[14- 3.3. 1] Mixing of Non-Reacting Flows

The analysis of hydrogen–air mixing requires a careful evaluation of all simplifications usually accepted in the analyses of viscous flow problems because of the large difference in properties between air and hydrogen.

The analysis of turbulent mixing presents a difficult problem because of the lack of a basic formulation of the transport properties of such flow. Initially, because of the lack of experimental confirmation, analyses have been performed based on a reasonable extrapolation of the transport properties which have been determined experimentally for gases having small density gradients. Such types of analyses, used extensively for other applications, indicate that the mixing process would be very slow, especially when the velocities of the two jets are of the same order; supersonic combustion as suggested here would not be too practical. However, recent experimental results with gases moving at high velocity and having large density differences show that the mixing is very fast and indicate that different types of relations must be used for the representation of the turbulent transport properties.

To emphasize the large differences corresponding to the different types of relations used for the transport properties in the turbulent mixing, it is of interest to present the results of an analysis of a combustion process occurring at constant pressure. The analysis considers an axially symmetric jet of hydrogen discharging in a stream of air and assumes that chemical equilibrium exists everywhere. Two different representations of transport properties have been used in the analysis. Some results are presented in Figs. 14-14 and 14-15 in which the lines represent the shape of the flame sheet which is the surface that divides the region of the oxygen-rich flow from the central hydrogen-rich region. Figure 14-14 gives the radius of the flame sheet as a function of the distance from the jet, when values of the eddy viscosity obtained from recent experimental data (proportional to the quantity
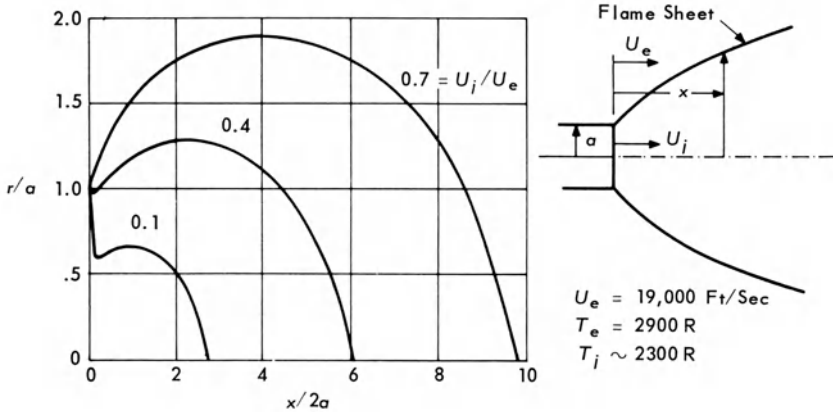
Fig. 14-14 Flame sheet location with eddy viscosity based on mass flow rate.
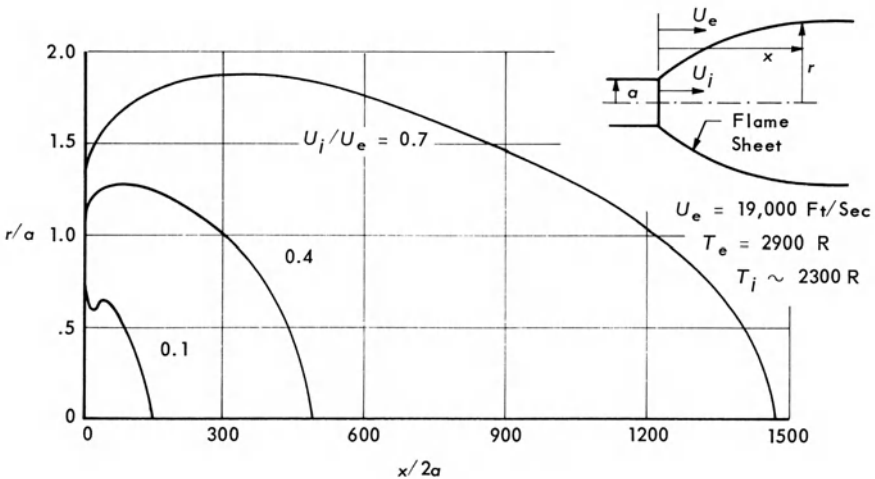
Fig. 14-15 Flame sheet location with eddy viscosity based on velocity difference.

$\rho_j u_j / \rho_e u_e$) are used, while Fig. 14-15 gives the same radius when the values of the eddy viscosity are extrapolated from low speed values and are based on the velocity differences [8]. The difference in the lengths of the flame is very large.

[14-3.3.2] Discussion of Experimental Results of Non-Reacting Gases

To obtain information on the mixing properties of heterogeneous nonreacting gases, several experiments have recently been made by my group by discharging a circular jet of a given gas in a moving air stream. Several types of gases have been used for the central stream to determine the effect of the gas density; in addition, several values of velocities, velocity differences and temperatures have been investigated during the tests. The tests have been for both supersonic and subsonic velocities. Velocity and concentration profiles and properties along the center line have been determined. The experiments and analyses of results have been presented in detail in References 14, 21, 25, 26 and 35. The most important conclusions are summarized here. For turbulent mixing in the region investigated, which is a few diameters (between 5 and 50) downstream of the jets, the measured radial distribution of velocity and concentration is in good agreement with the distrubition determined analytically by assuming average and constant values for the Prandtl, Lewis and Schmidt numbers. The decay of concentration along the axis is very rapid and has a constant trend for all the cases investigated.
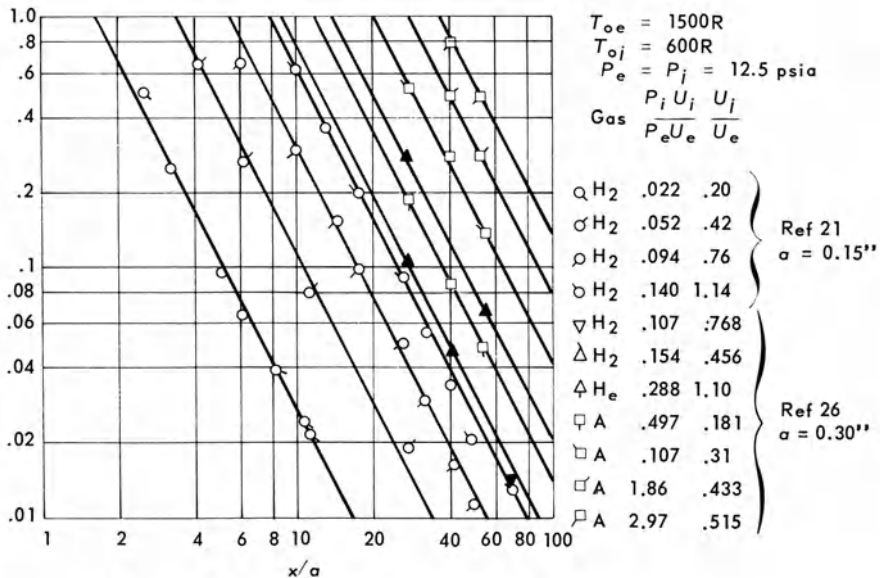
Fig. 14-16 Variation of centerline concentration with distance, air velocity = 2460 ft/sec.

Figure 14-16 presents typical results of several investigations [21, 25, 26, 25] giving the concentration decay along the axis as a function of the physical distance from the exhaust of the jet, non-dimensionalized for the radius of the jet. Such results have been obtained experimentally in several different investigations, using different experimental apparatus. In all the tests the two streams have had the same static pressure at the exit of the jet.

These experimental results indicate that the decay of concentration along the axis in the region near the exit of the jet is approximately proportional to $(x/x_0)^{-2}$, where x is the distance from the jet along the axis and x_0 the distance of the point where the concentration starts to change. If the concentration along the axis is plotted as a function of the quantity x/x_0 (Fig. 14-17), a unique curve is obtained for all of the experiments, indicating that the parameter x/x_0 is a similarity parameter for the mixing in this region [26]. The experiments give Y_c proportional to $(x_0/x)^2$, and it is interesting to determine the relation between x_0 and λ from the experimental results. This has been done in Fig. 14-18. The experiments indicate that the quantity x_0 is approximately proportional to $\sqrt{\lambda}$, and the coefficient of proportionality is of the order of 26.

[14-3.3.3] Mixing with Pressure Gradients

In the analysis of combustion, the assumption that the static pressure is constant at any given section notably simplifies the problem, but it is not sufficiently accurate for detailed design of combustion chambers because of the large variation of temperature and density produced locally by the reaction. Such a variation produces pressure variations which are generated in the streams, propagate in the flow, and affect the combustion process. For the type of process analyzed, the reaction produces much larger pressure variation than the diffusive process and is the main cause of large pressure gradients. In this case, it can be assumed in the analysis that the variation of pressure due to mixing is small with respect to the variation of pressure produced by the reaction and can be calculated as a perturbation to the other variation. When this assumption is introduced, an approximate analytical method can be developed that takes into account the pressure variations due to reactions [37].

Consider an axially symmetric flow of reacting gases. If the transport phenomena are neglected along the streamline and considered only in the direction normal to the streamlines, the two momentum equations can be expressed as

$$\rho q q_s + p_s = B \tag{14-23}$$

$$\rho q^2 \theta_s + p_n = 0 \tag{14-24}$$

Fig. 14-17 Variation of centerline concentration with distance parameter.
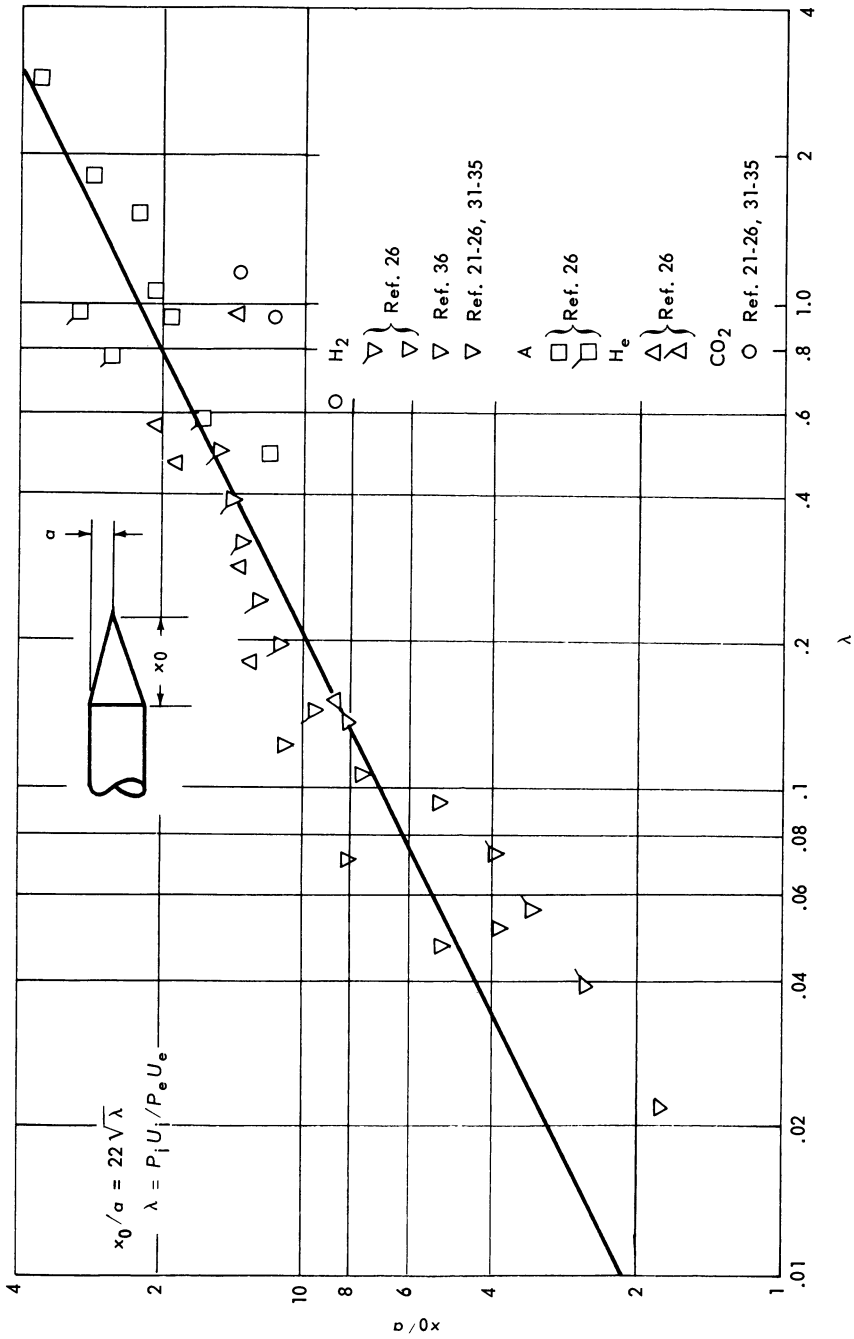
Fig. 14-18. Distance defining distance parameter.

where ρ is the density, q and θ are the modulus and the argument of the velocity, s and n are the coordinates tangent and normal to the streamline, and the subscript indicates derivative along the coordinate represented by the subscript. The quantity B represents the effect of transport properties and is given by

$$B = \frac{\left\{ \sigma[1 + j(r - 1)] \, q_n \right\}_n}{[1 + j(r - 1)]} \qquad (14\text{-}25)$$

where j is either 0 for two-dimensional flow or 1 for axially symmetric flow, σ is an appropriate viscosity, and r the radial coordinate. The equations of conservation of energy, mass species, and elements are the same as for the case of zero pressure gradients. This group of equations is of higher order than its counterpart in an inviscid gas. However, if the combustion process is localized, the effect of the right side of Eq. (14-23) on the pressure and velocity variations can be considered to be small and accounted for only as a perturbation of a basic inviscid flow motion represented by Eqs. (14-23) and (14-24) where B is a constant.

Similarly, the equation of conservation of energy can be written by collecting all terms related to convection and diffusion on the right-hand side, leaving only the terms representing the inviscid gas on the left-hand side of the equations. Then if the right-hand side terms are considered to vary slowly and to be known, the flow can be analyzed by means of the method of characteristics. The Mach angle ϵ is defined by

$$\tan \epsilon = \pm \left(\frac{\rho q^2}{p} - \frac{q^2}{F - 1} \right)^{-1}$$

where F is defined by

$$F = T \sum_1^N \alpha_i \frac{dh_i}{dT}$$

where h_i is the enthalpy per unit mass and α_i is the mass fraction of specie i.

The compatibility equations along the characteristic lines are

$$r_{1,2} - b p_{1,2} = \pm G$$

where $r = \tan \theta$, $b = 1/(\rho q^2 \cos^2 \theta \tan \epsilon)$ and the quantity G depends on the transport properties that are considered to be known in each step:

$$G = \frac{1 + r^2}{F} \left[E - \left(\frac{1 + F}{q^2} \right) \frac{B}{\rho} \right] \tan \epsilon$$

In this formula, E (for Prandtl number equal to one) is

$$E = \frac{\{\mu[1 + j(r-1)H_n]\}_n}{\rho q[1 + j(r-1)]} - j\frac{F\cos\theta}{r} - \sum_1^N h_i\left(D_i + \frac{\omega_i}{q}\right) +$$

$$+ \frac{(R\rho FT/p)\sum_1^N (D_i + w_i/q)}{W_i}$$

The quantity D_i represents the diffusion term and ω_i the chemical rate of change of α_i; W_i is the molecular weight of specie i.

With this approximation, the flow can be analyzed numerically, following a calculation net as shown in Fig. 14-19. The quantity G is determined by a finite difference procedure applied along line (a) and is known at the initial points 1 and 2 of a given step. The value of G is assumed to be constant in any given step 2-3, 1-3. Then characteristic lines can be defined (lines 1-3, 2-3), which permit the evaluation of the variation of pressure and velocity defined by the left side of the equations: determine these quantities at points of the line (b). Here the effects of transport phenomena are evaluated along line (b) normal to the streamlines, as in a mixing problem, and a second iteration is performed (if required) where values of the quantity G averaged between initial and final point are considered. A numerical program has been developed for such analysis [37]. This type of analysis can be applied, for example, to the determination of the shape of a combustor that
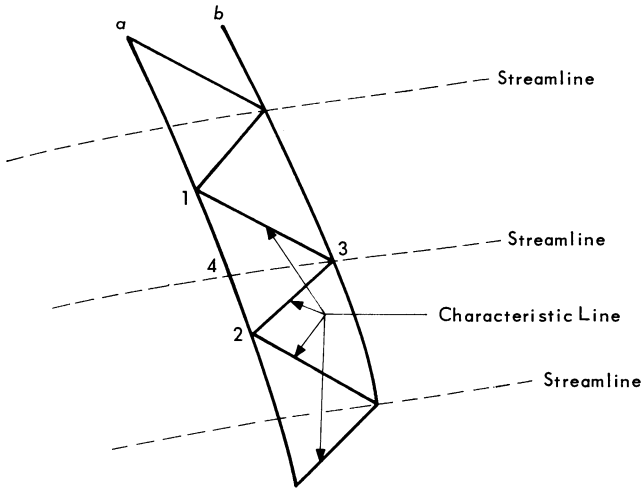
Fig. 14-19 Calculation net for analysis of viscous flow with pressure gradients.
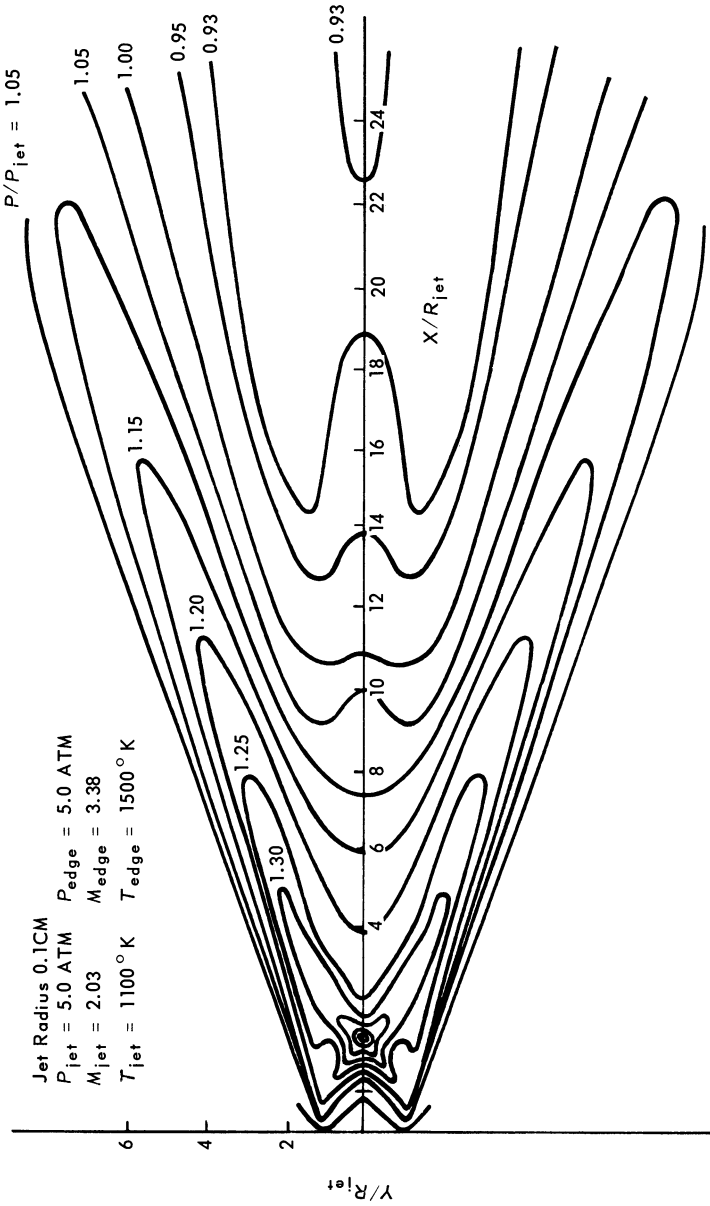
Fig. 14-20 Pressure field for a free jet of hydrogen in air computed by a method of characteristics with viscosity and finite rate chemistry.

Jet Radius 0.1CM

P_{jet} = 5.0 ATM. P_{edge} = 5.0 ATM.
M_{jet} = 2.03 M_{edge} = 3.38
T_{jet} = 1100°K T_{edge} = 1500°K

ϕ = 1 Streamline

Mach Line

Wedge Surface

5°

2000°K
2200°K
2600°K
2800°K

2600°K

2200°K

2000°K

1500°K

1300°K

X/R_{jet}

Y/R_{jet}
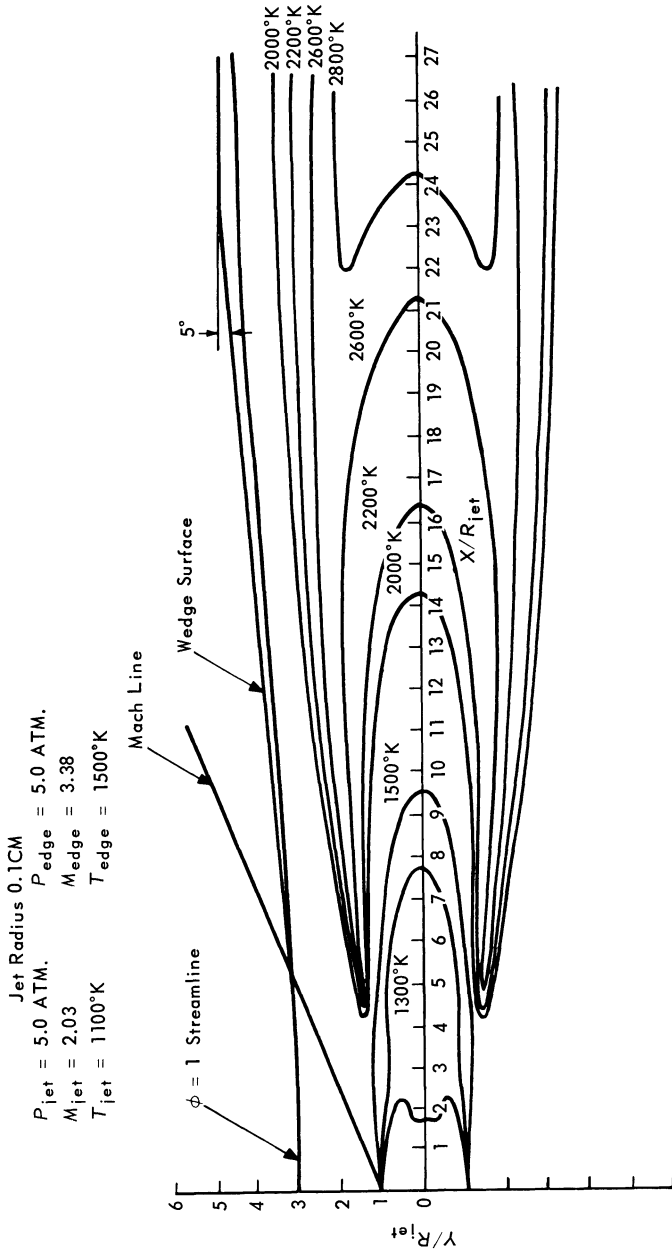
Fig. 14-21 Temperature field for a free jet of hydrogen in air computed by a method of characteristics with viscosity and finite rate chemistry.

gives a given pressure distribution along a streamline. Such a type of analysis is necessary for the design of short combustors which avoid formation of strong shock due to the combustion process.

An example of such a type of calculation is shown in Figs. 14-20 and 14-21. In this analysis, the chemistry has been assumed to be in equilibrium. The figures show that large variations of pressure occur inside the mixing region in spite of the fact that the flow outside is uniform. However, outside of the reacting region, the deviation of the streamline is fairly constant. The same process has been analyzed by means of a mixing type of analysis. The results are shown in Fig. 14-22. The deviation of the streamline is the same; however the initial point of deviation is displaced and is on a vertical line and not along the Mach line. This agreement between the two types of analyses permits us to analyze in simplified form the combustion process.

The combustion process produces changes in the streamline shape that affects the pressure. Such deviation of direction propagates as waves in the outside flow. It is well known that the effect of heat sources in a flow is equivalent aerodynamically to the introduction of equivalent volume sources. In order to obtain the wave pattern produced by combustion in the flow, a detailed study of this equivalence has been performed for a mixing process with combustion. In the analysis, the pressure distribution has been assumed to be known along the mixing, and the deviation of the streamline outside of the combustion region has been determined analytically [29].
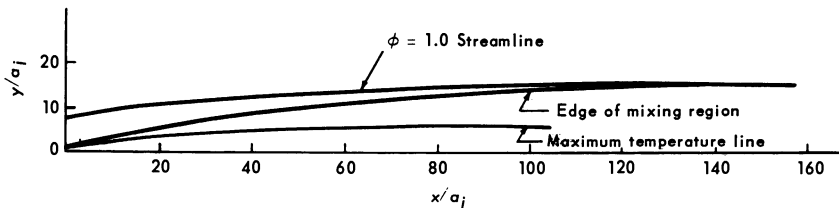
Fig. 14-22 Two-dimensional, constant pressure mixing and combustion region.

The streamline shape obtained and the pressure distribution assumed must be consistent with the outside flow. For constant pressure mixing, an average deviation of streamline produced by combustion can be calculated. Then an equivalent body can be assumed to exist in the combustor that represents the combustion phenomena. In this way, the flow field can be determined.

LIST OF SYMBOLS

a = Radius of jet
A_0 = Capture area of the inlet

A_0' = Frontal area of the inlet
B = Quantity defined by Eq. (14-25)
C_T = Thrust coefficient
G_j = Quantity defined by Eq. (14-7)
H = Total enthalpy
I_a = Air specific impulse, thrust per lb. of air flow
I_f = Fuel specific impulse, thrust per lb. of fuel flow
k_j = Rate constant for the jth reaction
K_{cj} = Equilibrium constant based on molar concentration for the jth reaction
L_e = Lewis number
L_{e_T} = Turbulent Lewis number = $P_{rt}S_{ct}^{-1}$
M_∞ = Flight Mach number
M_∞ = Free stream Mach number
M_i = Chemical species i
m_i = Quantity defined by Eq. (14-7)
n = Normal to the streamline
n_i = Quantity defined by Eq. (14-7)
P_r = Prandtl number
P_{rt} = Turbulent Prandtl number
p = Pressure
p_∞ = Free stream pressure
p_0 = Stagnation pressure
p_{03}, p_3,
T_3, V_3, M_3 = Conditions at the entrance of the burner
RR = Reaction rate constants, Eqs. (14-14) to (14-16)
R_0 = Universal gas constant
r = Radial coordinate
S = streamline
S_c = Schmidt number
S_{ct} = Turbulent Schmidt number
T = Thrust of temperature
T_0 = Stagnation temperatures

U = $(u - u_e)/(u_j - u_e)$
U_c = U at the axis
u = Velocity component along the x-axis
u_c = Velocity at the axis of the jet
u_e = Air velocity
u_j = Jet velocity
V = Velocity
v = Velocity component normal to the x-axis
$\dot{w}_i$ = Rate of creation of species i due to k reactions
W_i = Molecular weight og species i
x = Axial coordinate
Y_i = Mass fraction of species i
$\tilde{Y}_j$ = Mass fraction of element j
Y_c = Mass fraction at the axis of the jet

ϵ = Turbulent eddy viscosity
λ = $\rho_j u_j / \rho_e u_e$
μ_{ij} = Number of atoms of elements j in species i
ν'_{ij} = Stoichiometric coefficients of reaction j on left-side terms
ν''_{ij} = Stoichiometric coefficients of reaction j of right-side terms
ρ = Density
ρ_e = Density of the outer stream
ρ_j = Initial density of the jet
σ = Viscosity (turbulent = $\rho\epsilon$ or laminar)
τ_{ID} = Ignition delay time
τ_R = Reaction time

REFERENCES

1. Gross, R.A. and W. Chinitz: A study of supersonic combustion, *J. Aero. Sci.*, 27:7, 517–524, July 1960.
2. Ferri, A.: Possible Directions of Future Research in Air-breathing Engines, in: AGARD Combustion and Propulsion Colloquium, Pergamon Press Ltd., 1960, pp. 3–15.
3. Kuehn, M.: Experimental investigation of the pressure rise required for the incipient separation of turbulent boundary layers in two-dimensional supersonic flow, *NASA Memo 1-21-59A*, February 1959.
4. Sterrett, R. and C. Emery: Experimental separation on studies for two-dimensional wedges and curved surfaces at Mach numbers of 4.8 to 6.2, *NASA TN D-1014*, February 1962.
5. Stroud, J.F. and L.D. Miller: An experimental and analytical investigation of hypersonic inlet boundary layers, *AFFDL-TR65-123*, Vol. I, August 1965.
6. Zakkay, V., A. Bos, and P.F. Jensen, Jr.: Laminar, transitional and turbulent flow with adverse pressure gradient on a cone-flare at Mach 10, *NYU-AA-65-6*, June 1965.
7. Mordell, D.L. and J. Swithenbank: Hypersonic Ramjets, in: Advances in Aeronautical Sciences, Proc. of 2nd International Congress in Aeronautical Sciences (Zurich), New York, Pergamon Press, 1960, Vol. 4, pp. 12–16.
8. Libby, P.A.: Theoretical analysis of turbulent mixing of reactive gases with application to supersonic combustion of hydrogen, *ARS J.*, 32, 388–396, March 1962.
9. Zeiberg, S. and G.D. Bleich: Finite difference calculation of hypersonic wakes, Paper presented at AIAA Conference on Physics of Entry into Planetary Atmospheres, Massachusetts Institute of Technology, August 26–28, 1963, *Preprint 63-449*; also General Applied Science Laboratories, *TR-338*, February 1963.
10. Slutsky, S.: Stable computation techniques of coupled diffusion and chemical reaction in shear flows, General Applied Science Laboratories, *TM-101*, December 1963.

11. Moretti, G.: A new technique for the chemical analysis of nonequilibrium flows, General Applied Science Laboratories, *TR-412*, January 1964.

12. Shetz, J.A. and J. Jannone: The ignition of flowing hydrocarbon-air mixtures by a hydrogen pilot flame, General Applied Science Laboratories, *TR-432*, April 1964.

13. Penner, S.S.: Chemistry Problems in Jet Propulsion, Oxford, Pergamon Press Ltd., 1957, pp. 267-276.

14. Ferri, A., P.A. Libby, and V. Zakkay: Theoretical and experimental investigation of supersonic combustion, Aeronautical Research Laboratories, *ARL 62-467*, September 1962; also Paper presented at Third ICAS Congress, Stockholm, August 27-31, 1962; also Polytechnic Institute of Brooklyn, *PIBAL Report No. 713 (ARL 62-467)*, AD 291 712, September 1962.

15. Libby, P.A.: Treatment of partial equilibrium in chemical reacting flows, *ARS J.*, 32:7, 1090-1091, July 1962.

16. Duff, R.W.: Calculation of reaction profiles behind steady state shock waves, I—Application to detonation waves, *J. Chem. Physics*, 28:6, 1193-1197, June 1958.

17. Schott, G.L.: Kinetic studies of hydroxyl radicals in shock waves, III—The OH concentration maximum in the hydrogen-oxygen reaction, *J. Chem. Physics*, 32:2, 710-716, March 1960.

18. ————and J.L. Kinsey: Kinetic studies of hydroxyl radicals in shock waves, II—Induction times in the hydrogen-oxygen reaction, *J. Chem. Physics*, 29:5, 1177-1182, November 1958.

19. Ellis, G.E.: Literature survey of the kinetics of the H-O-M system, The Marquardt Corp., *Report No. 20-202*, November 1962.

20. Pergament, H.S.: A theoretical analysis of nonequilibrium hydrogen-air reactions in flow systems, *Paper No. 63-113*, AIAA-ASME Hypersonic Ramjet Conference, April 23-25, 1963.

21. Zakkay, V. and E. Krause: Mixing Problems with Chemical Reactions, in: Supersonic Flow, Chemical Processes and Radiative Transfer, New York, Pergamon Press, 1964; also Polytechnic Institute of Brooklyn, *PIBAL Report No. 776*, March 1963.

22. Tamagno, J. and O. Lindemann: Experimental results on supersonic combustion, General Applied Science Laboratories, *TR-322*, December 1962.

23. Momtchiloff, I.N., E.D. Taback, and R.F. Buswell: An analytical method of computing reaction rates for hydrogen-air mixtures, Paper presented at Ninth International Meeting of the Combustion Institute, Cornell University, August 1962.

24. Nicholls, J.A.: Stabilization of gaseous detonation waves with emphasis on the ignition delay zone, *Thesis for Ph.D.*, University of Michigan, 1960; available from University Microfilms, Inc., Ann Arbor, Mich.

25. Ferri, A.: Axially symmeteic heterogeneous mixing, Paper presented at IUTAM International Symposium on Applications

of the Theory of Functions in Continuum Mechanics, Tblisi, Russia, September 18-24, 1963; also Polytechnic Institute of Brooklyn, *PIBAL Report No. 787, AFOSR 5326*, September 1963.

26. Zakkay, V., E. Krause, and S.D. L. Woo: Turbulent transport properties for axisymmetric heterogeneous mixing, Paper presented at AIAA Conference Meeting, January 20-22, 1964; also Polytechnic Institute of Brooklyn, *PIBAL Report No. 813*, March 1964.

27. Ferri, A.: Review of problems in application of supersonic combustion, Seventh Lanchester Memorial Lecture, *J. Royal Aero. Soc.*, 68:645, September 1964.

28. Slutsky, S., J. Tamagno, and N. Trentacoste: Supersonic combustion in premixed hydrogen-air flows, *AIAA J.*, 3:9, September 1965.

29. Edelman, R.: Diffusion controlled combustion for scramjet application, Part I—Analysis and results of calculations, General Applied Science Laboratories, *TR-569*, December 1965.

30. Fox, H., V. Zakkay, and R. Sinha: The review of some problems in turbulent mixing, Paper presented at IAA International Symposium on Fluid Dynamics of Heterogeneous Multi-Phase Continuous Media, Naples, Italy, October 3-6, 1966; also New York University, *Report No. NYU AA-66-63*, September 1966.

31. Kleinstein, G.: An approximate solution for the axisymmetric jet of a laminar compressible fluid, *Quart. Appl. Math.* 20:1, 49-54, April 1962.

32. ————: On the mixing of laminar and turbulent axially-symmetric compressible flows, Polytechnic Institute of Brooklyn, *PIBAL Report No. 756*, February 1963.

33. Schetz, J.A.: Supersonic Diffusion Flames, New York, Pergamon Press, 1963; Paper presented at 21st Meeting of the AGARD Combustion and Propulsion Panel, London.

34. Libby, P.A. and J.A. Schetz: Approximate analysis of slot injection of a reactive gas in laminar flow, General Applied Science Laboratories, TR-299, June 1962.

35. Alpinieri, L.J.: An experimental investigation of the turbulent mixing of nonhomogeneous coaxial jets, Polytechnic Institute of Brooklyn, *PIBAL Report No. 789*, August 1963.

36. Keagy, W.R. and A.E. Weller: A Study of Freely Expanding Inhomogeneous Jets, in: Proc. Heat Transfer and Fluid Mechanics Inst., New York, American Society of Mechanical Engineers, 1949, p-. 89-98.

37. Moretti, G.: Analysis of two-dimensional problems of supersonic combustion controlled by mixing, AIAA Aerospace Science Meeting, New York, January 1964.

38. Ferri, A.: Review of scramjet propulsion technology, Paper presented at AIAA Third Annual Meeting, Boston, November 29-December 2, 1966, *AIAA Paper No. 66-826*.

Combustion Instability Theory

Sin-I Cheng, Professor
Department of Aerospace and Mechanical Sciences
Princeton University

[15-1] INTRODUCTION

[15-1.1] Unstable Combustion

Temporal variations in a combustion system are always present and take varieties of forms and intensity under different environments. A system is stable if a disturbance introduced into the system decreases in amplitude with time and eventually becomes lost in the random fluctuations prevailing in the system. A system is unstable if the amplitude increases with time. If an unstable combustion system is weakly coupled with the environment, a new equilibrium state of combustion will be reached without modifying the surroundings appreciably. A good example of this is the transition of a flame in open atmosphere from the laminar to the turbulent state. The instability of small disturbances (often referred to as Tollmien–Schlichting waves) is an inherent property of the flow of the combustible mixture. The unstable oscillations are present in a broad band rather than a few selected frequencies. The instability of such weakly coupled systems is of considerable scientific interest but does not possess direct relation with the instability of combustion in a rocket motor where the combustion is strongly coupled to its environment.

The pressure in the combustion chamber of a rocket, either with liquid or solid propellant, is determined by the balance of the rate of generation and the rate of exhaust of the gaseous combustion products. The chamber pressure determines the burning rate and the exhaust rate. Any change in the chamber pressure (or others) leads to a corresponding change in both the burning rate and the exhaust rate, and vice versa. Whether a disturbance in the system is stable or not must be determined by the consideration of the dynamics of the entire coupled system.

The stability characteristics of each component of a coupled system are of course important in determining the system behavior, but to infer the stability characteristics from the behavior of the

599

components without synthesis is hardly justifiable. The following example will fully illustrate this point.

An increase in burning rate following a rise in chamber pressure is known as a destabilizing influence. One might well infer that a decrease in burning rate following a pressure rise would be a stabilizing influence. However, Fig. 15-1 shows clearly that a decrease in burning rate with a time lag equal to half the period of the pressure oscillation will also reinforce the pressure oscillation.
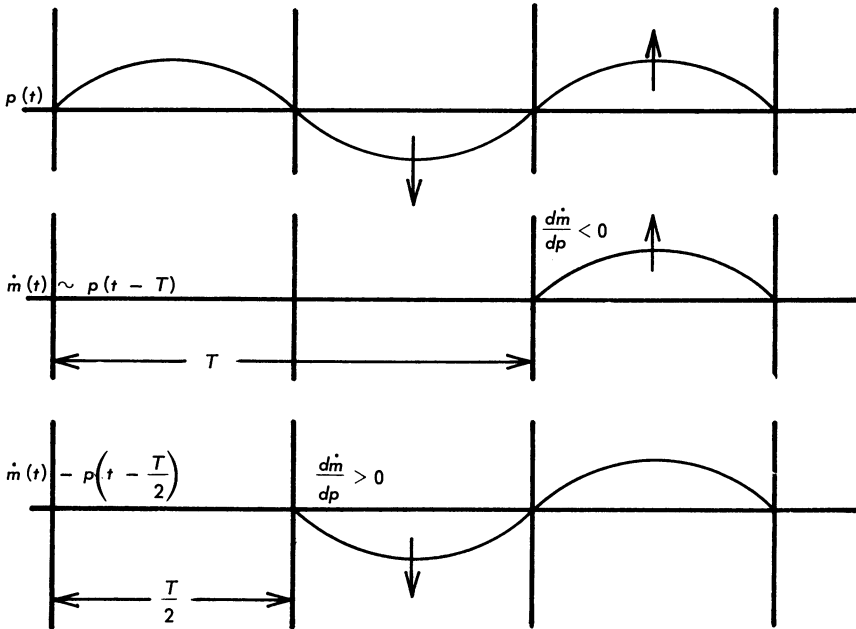
Fig. 15-1.

We shall be concerned only with the strongly coupled pressure oscillations in the combustion chamber of rocket motors with a choked exhaust nozzle. The dynamic situation of gases in the combustion chamber is very complex and highly turbulent. The flow Mach number in the chamber is usually low. We are not interested in the "random" turbulent fluctuations of appreciable magnitude. We shall neglect this "noise" and assume that the gas flow in the chamber is "steady" and "laminar" in the mean without viscous and heat transfer effects. We are concerned only with chamber oscillations of a well defined frequency and of a magnitude substantially above those of the prevailing turbulent fluctuations. We shall, however, consider at times the fractional variation of chamber pressure as small to permit a linearized treatment, but this is not "acoustics" in the conventional sense of the word.

[15-2] REVIEW OF THEORETICAL DEVELOPMENTS

[15-2.1] Early Developments and the Time Lag Concept

Interest in combustion instability in rocket motors was motivated by the desire to understand the origin of the often disasterous, sudden rise of chamber pressure in the combustion chambers of rocket motors with either liquid or solid propellants. Through such understanding, we hope to control, eliminate or avoid the undesirable consequences.

In 1942, von Karman [1] recognized that an oscillatory chamber pressure could be reinforced by the delayed response of the supply of propellants into the combustion chamber. It can be expected that the frequency of the unstable oscillation is characterized by that of the feeding system, typically less than 100 cps. In 1951, Crocco [2] recognized that the induction period of the combustion process of both physical and chemical origin can respond to the chamber oscillations, and that this time lag is small enough to couple with the wave motion in the combustion chamber to generate unstable oscillations of the order of 1000 cps. or more. The conceptual and mathematical development of this time lag concept was treated in some detail in Reference 3 for liquid propellant rockets. The constant time lag concept was applied to solid propellant rockets by Grad [4], and the variable time lag concept was adapted to the physical situation in solid propellant rockets by Cheng [5]. In the meantime, the development of pressure transducers with high frequency response enabled the experimentalists to identify that the sudden rise in pressure in the rocket chambers is indeed rapidly diverging or amplifying unstable oscillations at high frequencies. Moreover, the measured frequencies agree well with the acoustic frequencies in the combustion chamber filled with hot gases. The time lags and the interaction index required to promote such unstable oscillations, as revealed by the theoretical developments, are of the correct order compatible with the burning processes so far as we understand them. Thus, the time lag theories are essentially confirmed on a qualitative basis.

The understanding that the disasterous pressure rise is an unstable coupled dynamic oscillation of chamber gas with combustion did suggest some passive measures for suppressing incipient instability, *i.e.,* disrupting the coupling either temporally or spatially to uncouple the resonance, and increasing the dissipation of the gas oscillation in the chamber. The "acoustic" modes and the period of oscillation of the gas in the chamber can be effectively modified by changing the geometry of the combustion chamber, the introduction of baffle walls or interconnecting passages, etc. To suppress unstable oscillations in a given rocket motor based on such qualitative understanding, it is often necessary to follow some costly

trial and error procedures without any assurance that stable conditions will be achieved in a new configuration.

For design purposes, we would like to know beforehand whether a given propellant will run smoothly in a given rocket design. To achieve this end, we would have to know the corresponding time lags and interaction indices in addition to the wave propagation characteristics of the chamber. The time lag theories as described in Reference 3 and extended in Reference 5 are deliberately vague at this point in full recognition of the complicated sequence of physico-chemical processes leading to the ultimate combustion of the heterogeneous propellant mixture. Any attempt to formulate an analysis for the complete process in an effort to determine the time lags (τ's) and the interaction indices (n's) will necessarily involve great empiricism in the model and numerous physical and chemical constants whose magnitudes can at best be estimated to the order of magnitude. We question the relative merit of expressing the time lags (τ's) and the interaction indices (n's) in terms of a large number of phenomenological constants of uncertain magnitudes and through simplified models far removed from physical realities. The mathematical difficulty is also tremendous. There is little hope to calculate these n's and τ's to the accuracy that might be meaningful for design purposes. A sensible approach to the problem is to visualize these quantities as phenomenological constants like viscosity and heat conductivity coefficients in friction and heat transfer problems or the overall activation energy of a complicated sequence of chemical reactions. We hope that these time lags and indices, as determined experimentally, may be identified as physical entities. They should, in general, be expected to depend on propellant constituents, mixture ratio, grain size or injector design, frequency of oscillation, etc., but we don't know of any such dependence explicitly.

[15-2.2] Current Status in Liquid Propellant Rockets

For the liquid propellant rockets, Crocco *et. al.,* [6] have pursued the experimental approach, determined n and τ from one set of data, predicted a new stability boundary and verified it by additional sets of experiments in their experimental rockets. How well the results from such experimental motors relate to what is to be expected from practical motors needs to be demonstrated. Furthermore, proven results for small disturbances can at best be indicative of the behavior of large disturbances in practical motors. As such, the development of the large-scale liquid propellant rocket motors (like Saturn H-1 engine) still rely on the disruption of the unstable acoustic modes and on increasing dissipation [7].

Based upon observations of unstable oscillations of different rocket motors, different mechanisms, representing different fragmentary stages of the combustion processes which dominated the different experimental situation, were singled out and proposed as the key mechanisms of causing instability. Many of these ideas have been discovered and rediscovered but remain as plausible suggestions without any further development in their precise formulation to permit further evaluation.

Crocco and his associates tried [6] to unravel analytically some crucial aspects of the time-dependent combustion processes of liquid fuels. Unfortunately, such attempts did little more than confirm the anticipated analytical difficulties. Our understanding of the steady state combustion processes is very incomplete. Accordingly, it will not permit a reasonable time-dependent analysis.

The lack of unanimity and the profuseness of plausible suggestions are understandable in view of the complicated situation of combustion in liquid propellant rocket motors. The reluctance to pursue the simple phenomenological course is also understandable, since a great number of apparently simple and direct mechanisms kept up the appeal to many for achieving some direct solution. However, some phenomenological constants have to be introduced eventually to formulate such simple concepts in definitive terms.

[15-2.3] Current Status in Solid Propellant Rockets

The fluid mechanical situation in a solid propellant rocket motor is somewhat simpler than that in liquid propellant rocket motors. This is due largely to the fact that the burning zone is limited to the propellant surface except when metallic powders like aluminum are added to the propellant.

The stability of the solid propellant rocket is, however, more complicated in other respects. The combustion chamber volume and its geometry change as propellants are burned away. Thus, the dynamics of the gas in the combustion chamber changes with time [5]. The visco-elastic nature of the solid propellant and the bindings of the solid propellant to the motor casing will also significantly modify the wave propagation characteristics in the combustion chamber [8]. All these factors render any realistic evaluation of the dynamic coupling between combustion and chamber gas dynamics difficult. The fundamental difficulty, however, still revolves around the explicit formulation of the burning rate response function. The solid propellants are present in a great many varieties as to their constituents and additives. Each of these should, in principle, be considered as a distinct propellant. It would indeed be fortunate if the response function of such a varied group of propellants should possess many major characteristics in common.

Time and again, it was proposed that a certain kind of solid propellant was "spontaneously unstable" at its preferred frequency(ies) in any rocket motor. One of the proposals was very well developed [9] and was later fully discussed in Reference 10. Such inherent instability is irrelevant to the coupled oscillation in a rocket chamber (see also Section 15-1.1). Likewise, the recent suggestion of Denison and Baum [11] that a propellant will become spontaneously unstable at its own frequency in the low frequency range is irrelevant. As will be explained in Section 15-3.1, the propellant does possess a characteristic time (or frequency) based upon the mean time lag of its combustion process. It is the capacitive type coupling that favors unstable oscillations at such frequencies.

In view of the apparently simpler fluid mechanical situation in solid propellant burning, Hart and McClure [12] attempted a linearized analysis of the burning rate response function under oscillatory pressure. The thermal model of combustion is simplified in the gaseous phase by introducing an ignition temperature and, in the solid phase reaction, by employing a mean Arrhenius factor. Little information can be drawn analytically. Even with the extensive use of high speed machine computation, few qualitative inferences can be obtained with respect to the effects of half a dozen crucial parameters which are not known with any degree of certainty for a given propellant. With little quantitative knowledge of steady state combustion processes of these propellants, any of these uncertain parameters are just different forms of phenomenological parameters for the particular simplified model of combustion analyzed. Whether ignition temperature or overall activation energy and the like are less phenomenological than time lags appear to be a matter of semantics.

A general feature of the results of Hart and McClure's calculation is that the frequency dependence of the burning rate response function is much weaker than that implied by the two parameter-phenomenological representation through variable time lags [10]. This suggests that the mean time lag must decrease with higher frequency. The experimental results of the burning rate response function of a family of composite propellants based on the growth-decay method [13] do show such weak frequency dependence, but the peak of the response function appears to lie in the frequency range ($\lesssim$ 1000 cps.) compared with $\sim$10,000 cps. indicated by Hart and McClure's typical calculations. The experimental situation need not be comparable to the cases calculated. Whether a different combustion model will modify the calculated results to permit better correlation is yet to be shown. The quantitative determination of the burning rate response function remains the most crucial problem.

The success of the aluminized solid propellant in suppressing high frequency combustion instability has shifted current interest to instabilities in the very low frequency range. The burning rate

response function of the aluminized solid propellant in such a low frequency range will undoubtedly be a key problem for solid propellant research.

[15-3] FORMULATION AND ANALYSIS

[15-3.1] Low Frequency, Capacitive Type Stability

The combustion chamber is filled with hot, burned gas at a pressure substantially higher than the ambient pressure. The hot gas is forced out of a choked nozzle under the high chamber pressure and is replenished by the generation of the gaseous combustion products. In stable equilibrium operation, these two rates balance each other. The chamber pressure is not changing with time and is substantially uniform over the entire chamber volume if the nozzle throat area is small compared with the sectional (or port) area of the combustion chamber. Any pressure disturbance created at a given point in the chamber will generate a pressure wave, propagating in all directions with a speed comparable to or larger than the typical speed of sound. The time required for such pressure waves to travel across a characteristic dimension of the chamber is the wave propagation time τ_w, typically of the order of 10^{-3} seconds per foot of chamber dimension. If the gas inside the chamber is forced by "external" agents to oscillate at a frequency much slower than π/τ_w, *i.e.*, the typical frequency of acoustic oscillations in the chamber, the pressure inside the chamber will be almost uniform spatially in a quasi-steady fashion. The passage of many waves reflected from the bounding surfaces would have evened out all the pressure differences prior to any appreciable change of the forcing function. Accordingly, the combustion chamber volume acts merely as a capacitor, storing proportionately more gas at higher pressure, regardless of where the gases are generated in the volume. The exhaust of the burned gas through the nozzle is also essentially quasi-steady, *i.e.*, proportional to the instantaneous value of the chamber pressure. The inertia of the gas in the converging section of the nozzle for such low frequency oscillations will produce a phase difference between the oscillations of the mass outflux and the chamber pressure. This phase difference can be simply accounted for by a small increase of the chamber volume by approximately $0.95/\gamma$ times the volume of the converging section of the nozzle. (For a more accurate estimate of this effective nozzle volume, see Appendix B, Eq. B-61, 2, Reference [3]...For a detailed analysis, see Reference [14].)

The equation governing the low frequency oscillations in a combustion chamber is the mass conservation relation,

$$\frac{d\phi}{dz} + \phi(z) = \mu_b(z) \tag{15-1}$$

where z is the reduced time expressed in terms of the effective residence time θ_r of the gas in the combustion chamber modified by the additional contribution from the nozzle when necessary. ϕ is the fractional increase of the chamber pressure. μ_b is the fractional increase of the rate of generation of the burned gas in the chamber volume. Equation (15-1) is valid even for large amplitude oscillations (except for the minor approximation concerning the effective volume of the nozzle). The ratio μ_b/ϕ is the burning rate response function. This formulation is valid for both liquid and solid propellant rockets, the difference between the two being implied in the response function μ_b/ϕ. The first term $d\phi/dz$ expresses the increase of chamber pressure due to the accumulation of gas in the limited volume. The second term ϕ expresses the increase of outflow through the nozzle. The detailed linearized solution for the small amplitude oscillations in a liquid propellant rocket motor including the feeding system dynamics is given in Chapter 2 of Reference 3, based upon the time lag theories. There the most important practical result is that a pressure drop through the injector larger than one half the mean chamber pressure insures stability [1] regardless of the time lag. Without feeding systems and injectors, there is, in a solid propellant rocket, no counterpart of this important conclusion, and the implication of a quick remedy at the sacrifice of performance is not available to solid rocket motor designers.

The possibility of capacitive type instability in solid rockets was first suggested by Cheng [10] in a theoretical discussion of the stability problem with aluminized propellant in large motors where the mechanism of interaction between the burning of the aluminized propellants appears to favor such low frequency capacitive type instability. It is also suggested that such capacitive instability, in the absence of metal additives, is much the same for solid propellant and liquid propellant rockets. In the same Symposium, Angelus [15] reported some observations of low frequency instability: it is apparently independent of chamber geometry, and its frequency is generally less than 50 cps. and decreases with lowering chamber pressure. That such unstable oscillation is independent of geometry suggests strongly that such oscillations are of the capacitive type. Following the brief suggestions made in Reference [10] and adopting the time lag formulation of the burning rate response function, μ_b, in terms of the overall interaction index, S, the steady state burning rate pressure exponent, n, and the time lag, $\bar{\tau}$, we can solve Eq. (15-1) as

$$f(\bar{\tau}; S, n) = \left(S - \frac{n}{2}\right)\bar{\tau}\exp\left[\left(1 - S - \frac{n}{2}\right)\bar{\tau}\right]$$

$$= \frac{\Omega\bar{\tau}}{\sin\Omega\bar{\tau}}\exp\left[-\frac{\Omega\bar{\tau}}{\tan\Omega\bar{\tau}}\right] = h(\Omega\bar{\tau})$$

(15-2)

and

$$\exp[\Lambda\bar{\tau}] = \left(S - \frac{n}{2}\right)\bar{\tau} \cdot \frac{\sin\Omega\bar{\tau}}{\Omega\bar{\tau}}$$

$$= \frac{\left(S - \frac{n}{2}\right)\bar{\tau}}{K(\Omega\bar{\tau})} \tag{15-3}$$

for the determination of the amplification factor, Λ, and frequency, Ω, for the exponentially amplifying $(\Lambda > 0)$ or decaying $(\Lambda < 0)$ oscillations of the form

$$\phi \sim \exp[\Lambda z + i\Omega z] \tag{15-4}$$

The functions $h(\Omega\bar{\tau})$ and $K(\Omega\bar{\tau})$ are identically the same as those given in Fig. 5, Section 2.03 of Reference [3]. The only difference lies in replacing the interaction indices. The stability boundary with $\Lambda = 0$ is again similar to Fig. 6 of the same reference. Hence, qualitatively, the lowest or the fundamental mode of such capacitive oscillations is likely to be the most pronounced, possibly with superposed sub-acoustic overtones if the interaction indices happen to be sufficiently large. The period of oscillation of the fundamental mode should be roughly five to ten times the mean time lag for the particular propellant. Thus, different propellants (or the same basic propellant with different additives) should "select" unstable frequencies corresponding to the mean time lags of their combustion processes even if such unstable oscillations occur in the same combustion chamber. Since the mean time lag of a given propellant is expected to decrease with increasing mean chamber pressure, the frequency of unstable oscillation is expected to increase with mean chamber pressure. Without some idea as to how the interaction indices may be and would behave, it is not possible to make further inferences regarding the amplification rate and the relative magnitudes of the mean time lag of the propellant versus gas residence time (modified for nozzle volume if necessary). It is apparent that data of the kind reported by Angelus [15] can yield much more information concerning the overall characteristics of the burning rate response; for example, the phenomenological constants in the time lag theory if one is interested in expressing their results in terms of such a phenomenological approach.

In Reference 16, Price discussed the low frequency instability within the framework of energy balance now widely adopted for the high frequency acoustic oscillations and related the observed sub-acoustic oscillations with such mechanisms like "thermal waves," etc. The coupling mechanism for the low frequency oscillations is described in the beginning of this subsection as capacitive and is governed by *overall* mass conservation only. The coupling for the high frequency, acoustic oscillations is a wave process and is

governed by the *local* conservation of mass, momentum and energy
of the oscillating gas. If one agrees that the observed low frequency
oscillations are indeed capacitive, independent of the chamber
geometry or even the arbitrary introduction of baffle walls, etc.,
the acoustic energy balance of the oscillations in the chamber is
irrelevant. The primary effect of the outflow through the nozzle
is shown [14] to be capacitive in modifying the chamber volume
rather than the energy drain. The energy approach should not be
followed especially in view of the somewhat subtle aspects to be
discussed in Subsection 15-3.3. Since the low frequency instability
is likely to be the important type of instability in large solid pro-
pellant rocket motors, a clear and definitive recognition of the
basic mechanism of such instability is deemed essential.

[15-3.2] High Frequency, Wave Type Instability

If the gas in the combustion chamber is forced to oscillate with
a period comparable to the wave propagation time, τ_w, the state
and dynamic variables of the gas in the chamber varies spatially
as well as temporally. Every single step of the complicated
physico-chemical processes leading to the combustion of the
propellant is affected by these variations. The evolution of the
burned gas adds mass (and possibly heat) to the system and inter-
feres with the wave propagation process. The mutual interaction
is most intensive in bi-propellant liquid rockets or aluminized
solid propellant rockets where combustion may be distributed over
the chamber volume. The liquid sheets, droplets, or particles may
disperse the waves and further distort the wave form.

With the burning rate response represented through the time
lag concept, the analysis of the gas phase oscillation with com-
bustion distributed over the chamber is extremely complicated
(Reference 3, Chapter 3). It becomes clear, however, that the
distortion is primarily in the details of the wave form, not the
overall qualitative results of system stability. Accordingly, the
wave form in the combustion chamber may be approximated by
the corresponding ones in inert gas. The wave form distortion
due to combustion may be neglected as a higher order small per-
turbation along with the random variations like turbulent fluctua-
tions in the characteristic equation that governs the system
stability.

The burning rate, $\dot{m}(t)$, depends not only on the instantaneous
values but the past values of the thermodynamic state variables
(p, ρ, t), the flow variables (relative velocity V), and variables of
spatial distribution and others. Under the assumption that we are
looking at the interaction with a particular periodic disturbance
(or wave), we can drop the explicit time dependence of $\dot{m}(t)$. Accord-
ingly, following References 3 and 10, we can write the burning rate

response function in terms of pressure (or any other convenient variable):

$$\frac{d\dot{m}/\dot{m}}{dp/p} = \left[F_p + F_T \frac{\partial \ln T}{\partial \ln p} + F_\rho \frac{\partial \ln \rho}{\partial \ln p} \right.$$

$$\left. + F_{v_t} \frac{\partial \ln v_t}{\partial \ln p} + F_{v_n} \frac{\partial \ln v_n}{\partial \ln p} + \cdots \right]$$

(15-5)

where F is the functional dependence of $\dot{m}(t)$ on these variables, and subscripts represent partial differentiation with respect to the designated variable. v_t and v_n stand for the tangential and normal components of the velocity relative to the propellant surface.

Let us assume, in addition, that, for a given propellant, the functions F_p, F_T, F_{v_t}, etc., are all unique functions of frequency. The response function will, in general, be different for different modes of oscillation under consideration because the relative weighting functions in Eq. 15-5, notably $\partial \ln v_t / \partial \ln p$ and the logarithmic derivatives of the distribution parameters, will be different both in magnitude and phase. Thus, in Reference 10, it is pointed out that to associate a unique burning rate response function to a propellant (or combination) irrespective of the modes of oscillation is erroneous. For example, the response to a travelling mode may be quite different from that to a standing mode of the same frequency.

When the distribution pattern of a heterogeneous propellant mixture is not sufficiently random, as is in most bi-propellant liquid rocket motors, the situation can be very much aggravated. Crocco, in a somewhat different manner, introduced additional phenomenological constants in the time lag formulation (see Eq. 4.10, 4.11, Reference 6) to account for these effects. The additional phenomenological constants are necessary because the relation between the relative velocity and displacement of the liquid propellants and the pressure oscillation cannot be simply correlated.

In the case of solid propellants, the interaction through the distribution pattern of a heterogeneous, gaseous combustible mixture may not be as serious as is in a liquid motor, but it is certainly present to some extent, especially for propellants with coarse grain oxidizers. Even for the propellants with fine grains or homogeneous propellants, the convective heat transfer effects will render the response function depending on the gas dynamic situation in the chamber especially for fully developed travelling waves or for charge configurations favoring the formation of trapped vortices. The response function of a given propellant is not likely to be a unique function of frequency. However, in view of the simplifying assumptions introduced for other reasons and of the scarcity of the

detailed knowledge, we shall take the burning rate response function $d \ln \dot{m}/d \ln p$ as a "known" function of frequency. The time lag theory probably yields the simplest phenomenological expression of this response function with the proper qualitative behavior, while values of the phenomological constants may be chosen to fit the characteristics of each propellant under consideration.

A wave of a given form (or mode) in the combustion chamber must satisfy the condition on the burning surface given as the specific response function and the condition of a choked nozzle through which the burned gas escapes. These boundary conditions are homogeneous for the linearized small disturbances so that a characteristic determinant must vanish to permit nontrivial solutions. Thus, the particular wave must amplify or decay or remain neutral as circumstances require. This is the differential approach with which the stability of a given wave should be investigated within the linearized framework [2—6]. This is a well-known mathematical procedure, tedious but straightforward. The details of such analyses are well documented in the references and will not be elaborated here.

[15- 3.3] The Energy Approach

To provide a simple, qualitative physical discussion of the high frequency combustion instability problems in solid rocket motors, Cheng [10] adopted the point of view of disturbance energy. With full cognizance of its implication and limitation, the discussion was meant to be only qualitative. The energy approach is never attempted in discussing combustion instability in liquid propellant rocket motors. This energy approach, being attractive intuitively and simple mathematically, has, for one reason or another, gained wide acceptance since then and apparently not only for qualitative discussions. One must be careful, however, in drawing inferences as to the stability or instability of a given system from such energy consideration alone. The energy approach has been widely used and has led to many controversial arguments in the stability theory. There should be good reasons why the earlier investigators [1-6] did not approach the problem directly from the simple energy point of view.

When we consider a disturbance (or wave) either travelling in a flow field or confined in a given spatial volume, the kinetic energy associated with the disturbance motion must increase with the growing amplitude of the unstable disturbance. This energy criterion that the disturbance energy gain must exceed the loss is a necessary integral condition only for the selected wave form with which the gain and loss are evaluated. Whether the selected wave form is appropriate for describing the disturbance of interest,

whether it is compatible with the kinematic and dynamic conditions of the system, and whether it is compatible with the gain and loss mechanisms under consideration are left open. In order to determine the overall stability characteristics or the stability boundary of a given system, one has to consider every wave form compatible with the system kinematics and dynamics and no others. From the energy consideration alone, we would obtain many unstable oscillations that would not exist in the system. On the other hand, by considering a few typical disturbances without regard to the dynamic aspects of the chamber oscillations, one cannot expect to achieve any quantitative results of the stability behavior of the system.

The equation governing the variation of the disturbance energy can be obtained by integrating the equation of momentum balance after it is multiplied scalarly by the disturbance velocity vector. The evaluation of the integrals over the boundary surface and over the volume is a rather delicate matter with their direct physical interpretation often obscure. This is due to the fact that we are only concerned with the energy exchange with that particular disturbance among a number of other energy exchange processes taking place at the same time. It is not so obvious as one is led to believe intuitively. The disturbance energy is a small quantity of higher order than the amplitude of the disturbance and is, hence, affected by many interaction processes that might appear negligible dynamically.

The loss and gain mechanism considered in the energy balance must clearly be compatible with the physical factors taken into consideration in selecting the wave form. Thus, in considering the energy balance of an inviscid wave in a combustion chamber with rigid walls, the only disturbance energy influx and outflux are due to the burning surface and the nozzle outflow. Other dissiative losses are irrelevant. If one believes that viscous effect is important in the particular case under consideration, the wave form should not be the inviscid acoustic mode but properly corrected for viscous effects. Likewise, in the presence of nonrigid wall such as visco-elastic propellant as a bounding surface, the energy drain through the visco-elastic boundary should be considered only when the wave form in the chamber has been accordingly modified.

Hart and McClure [17] adopted the energy approach and formulated the results in acoustic terms. A number of formulas are given for evaluating different "acoustic losses and gains" under varying specific conditions. Their efforts are highly commendable and many of these formulas are useful in indicating the qualitative dependence of each loss term and its relative importance under varying operating conditions. (There are variances in opinion, and these formulas should not be used indiscriminately.) One must be cautioned against attempts to evaluate such loss and gain terms with some approximately correct and apparently reasonable wave

form for drawing conclusions concerning the stability boundary of a solid rocket motor in view of the discussions given above.

It might be argued that in conventional acoustics, energy consideration alone often gives useful results, even quantitatively. Why should we be extra cautious here? First, in conventional acoustics, we deal with small oscillations of a broad frequency band in an otherwise stationary system. Second, the kinematic and dynamic conditions are never critical at the acoustics level due to weak coupling and a slight change in the details of the wave form never matters to the acousticians. We are dealing with a problem of sharply selective coupled oscillation, where the kinematic and dynamic compatibility conditions are important. Moreover, we neglected turbulent fluctuations in the chamber of a rocket motor, which are very loud acoustic noises indeed. Although we employed linearized analysis (or the acoustic approximation), the physical situation is much different from conventional acoustics. The small oscillations we deal with here are much larger than the turbulent fluctuations. If one prefers to force the linearized analysis for combustion instability in rocket motors to fit the acoustic radiations and analyze them consistently and correctly, one may very likely get lost in the turbulence.

[15- 3.4] Non-linear Effects

The linearized treatment of oscillations is tedious but straightforward mathematically. The result is, however, applicable only so long as the disturbance amplitude remains "small." For unstable disturbances, the amplitude grows with time exponentially and will reach large magnitudes in a few cycles of oscillations in a small fraction of a second. When the disturbance amplitude becomes large, dissipative mechanisms often become more significant (or new effective mechanisms will participate) to limit the growth of the unstable disturbances to some finite amplitudes. If the combustion chamber is still intact, the system may reach an equilibrium state (limit cycle) with large amplitude oscillations present in the system. Both the dissipative and the excitation mechanisms in balance will not be the same as those when the disturbances are small. In this sense, the nonlinear problem not only calls for distinct mathematical technique for analysis but also for possibly distinct physical formulation.

The Arrhenius factor for many stages of physico-chemical processes involved in the combustion process of either liquid or solid propellant is highly nonlinear. The dominant process (if any) in determining the burning rate response function may be entirely different under large amplitude oscillations. The cracking of the solid propellant and the shattering of the liquid sheets or droplets under large amplitude gas oscillations can greatly alter the burning

rate response. These are just typical examples among many other plausible mechanisms. From a gas dynamic point of view, large amplitude pressure oscillations often take the form of travelling shock waves (or successively reflected at chamber boundaries) which will call for a gas dynamic treatment basically different from the linearized stability analysis.

The higher order small perturbation analysis based upon the time lag formulation was carried out by Sirignano in his Ph.D. dissertation at Princeton for a simple configuration of liquid propellant rocket motors. When the limit cycle on nonlinear oscillations exist in the linearly stable region, the limit cycle is unstable. It is thus inferred that for the simple configuration, shock-free, cyclic solutions are not possible. While this conclusion need not be generally valid, attempts to carry the small perturbation analysis to higher orders are not very meaningful.

Both Culick [18] and Sirignano and Crocco [19] analyzed the simple model of cyclic shock reflection from a burning surface with instantaneous Arrhenius type response. Self-consistent re-results were obtained which appear to be qualitatively in agreement with experimental observations. Much remains to be done whereever nonlinear aspects are involved.

[15-3.5] Nozzle Outflow

In steady state, the choked throat limits the outflux of the burned gas through the nozzle. The pressure in the combustion chamber is thus maintained for a fixed burning rate. The pressure variation in the chamber will clearly be very much affected by the variation of this outflux rate through the nozzle. Within the framework of inviscid analysis of gas oscillations in a rigid combustion chamber volume, the response of this outflux rate is the only one, besides burning rate response, that is of concern. The physical limitation of a choked nozzle flow is that the mass outflux rate responds only to the upstream flow conditions. The quantitative determination of this nozzle outflow response is complicated due to the variable geometry of the nozzle section even if the quasi-one-dimensional steady state flow is assumed. Published quantitative results are available (Appendix B, Reference 3) only for a particular nozzle with linearly increasing velocity and for isentropic longitudinal oscillations. For transversal oscillations, unpublished results of Crocco are available. While qualitative behavior of the nozzle response function (*i.e.*, fractional velocity perturbation divided by fractional pressure oscillation at the "entrance" to the nozzle) of a practical rocket motor can be inferred, its quantitative determination will involve a substantial amount of high speed machine computation and analytical work.

The behavior of the nozzle in response to longitudinal oscillations in the chamber is such that the perturbation velocity (axial) and the pertubation pressure at the nozzle entrance always possess an in-phase component. Thus, the longitudinal oscillations in the nozzle always work on the fluid in the nozzle to entertain the gas oscillation in the nozzle. From the energy point of view, the nozzle drains energy from chamber oscillations and hence tends to stabilize them.

For transversal oscillations superposed on a "one-dimensional axial nozzle flow," the perturbation velocity components (both axial and radial) and the perturbation pressure at the nozzle entrance are generally out of phase in such a way as to produce a destabilizing contribution to the transversal oscillation in the chamber. It is not clear whether this destabilizing contribution may be attributed to pressure work. This destabilizing contribution from the nozzle is never large enough to compensate for the convective loss of the disturbance energy carried by the fluid into the nozzle. The energy aspect of the nozzle loss for transverse oscillations is not clear (see Subsection 15-3.3 on the energy approach). The matching condition that the oscillations in the nozzle and in the chamber must join smoothly at the nozzle entrance shows quite conclusively the following observation. The outflow through the choked nozzle does not provide as much damping to the transversal oscillations in the chamber as it does to the longitudinal oscillations.

The reflection of shock waves of moderate strength from the converging section of the nozzle involves extremely complicated shock patterns (the Mach reflection). If the incident shock is planar and propagates along the axis, the reflected wave pattern from the inclined nozzle wall may become approximately planar a few diameters upstream of the nozzle entrance. Thus, for slender combustion chambers of uniform section, an incident planar shock may be reflected as a planar shock. The strength of the reflected shock compared with that of the incident shock cannot be determined, however, without detailed analysis of the reflection process. This nozzle reflection problem is no less formidable than the shock reflection from the burning surface. If the chamber volume is not slender, the reflected shock pattern reaching the burning surface will not be planar. The gas dynamics problem multiplies in difficulty accordingly. Investigations of combustion instability involving shock waves in the chamber cannot make substantial progress before such shock reflection processes can be treated in some satisfactory manner.

[15-4] CONCLUDING REMARKS

We have critically reviewed the theoretical approaches to the combustion instability problems in rocket motors. The purely gas

dynamics problems of nozzle outflow, wave propagation and reflection are complicated but do not appear insurmountable. The theoretical determination of the burning rate response function in terms of known physical and chemical properties, however, appears quite remote.

The burning of liquid propellants in the wake of oscillatory droplets in a turbulent stream is not likely to be tractable in the near future even if one adopts the equivalent laminar diffusivities. Without any complications of a fluid mechanical nature in the combustion chamber, the burning rate response function of a homogeneous solid propellant in an otherwise stagnant gas under oscillatory pressure should be the least difficult. Yet Hart and McClure and his group did not have much success in bringing out the significant parameters of this "simple" problem either analytically or through extensive computation involving half a dozen crucial parameters. They did not attempt to modify their combustion model in pursuit of simpler results or fewer parameters although they were fully aware of the need to do so, apparently for good reasons. Are ignition temperature and overall activation energy not phenomenological constants for complicated reactions? Do we know these constants for a given propellant any better than we know the time required for a propellant element to reach the ignition temperature, *i.e.,* the time lag?

The value of a physical theory does not necessarily lie in its completeness but in its simplicity and ability to keep the major qualitative features and to facilitate the solution. There is nothing wrong with phenomenological representation. Indeed it is a virtue if it brings out the significant parameters that can be demonstrated as physical entities in some range of practical interest. It helps to break down an almost intractable problem into manageable parts. Thus, in evaluating friction and heat transfer effects in gases, we do not start from the molecular levels and attempt to express results in terms of inter-molecular potentials. We adopted transport coefficients to facilitate the solution of the macroscopic part of the problem, leaving the theoretical determination of such transport coefficients in terms of molecular properties as a separate problem. That the transport coefficients as experimentally determined vary considerably for different gases at different temperatures, at different mixture ratio, etc., does not hinder the usefulness of the phenomenological concept of transport properties. Proponents of phenomenological theories may possibly be pessimists who anticipated the difficulties of a comprehensive approach and admitted impotence in attacking the overall problem from the very fundamentals. They may also be optimists who believe the important features of the problem to be independent of those detailed properties but dependent only on a few parameters and made a guess as to what these significant parameters may be.

The time lag theory is not necessarily the best phenomenological approach to the problem of combustion instability in rocket motors. The early workers in the field did show, nevertheless, its qualitative value. If the dependence of the burning rate response function on frequency should indeed be generally as broad as calculations indicate [12], a trivial dependence of time lag on frequency would account for it [10]. If the experimentally determined variations [13] for composite propellants should be the general characteristics, a trivial modification will also do. There are other possibilities of presenting the burning rate response function phenomenologically, provided that experimental information on the behavior of burning rate response function becomes available. It is believed that we possess sufficient knowledge qualitatively on combustion processes to construct a sensible phenomenological theory, but it is not believed that we possess sufficient information to permit a theoretical determination of the burning rate response function at the present time. The key to significant progress in the future appears to lie in the hands of experimentalists.

REFERENCES

1. Summerfield, M.: *J. of Am. Rocket Society*, 21, 108, 1951.
2. Crocco, L.: *J. of Am. Rocket Society*, Part 1, 21, 163, 1951; Part 2, 22, 7, 1952.
3. ———— and S.I. Cheng: Theory of Combustion Instability in Liquid Propellant Rocket Motors, *AGARDograph No. 8*, Butterworths Scientific Publications, 1956.
4. Grad, H.: Communication of Pure and Applied Math., 2, 79, 1949.
5. Cheng, S.I.: *Jet Propulsion*, Part 1, 24, 27; Part 2, 25, 102, 1954.
6. Crocco, L.: Tenth Symposium (International) on Combustion, The Combustion Institute, p. 1101, 1966.
7. Levine, R.S.: Ibid, p. 1083, 1966.
8. Bird, J.F., L. Haar, R.W. Hart, and F.T. McClure: *J. of Chemical Physics*, 32:5, 1423, 1960.
9. Green, L.J. and W. Nachbar: *Jet Propulsion*, 28, 769, 1958.
10. Cheng, S.I.: Eighth Symposium (International) on Combustion, Williams and Wilkins Co., p. 81, 1962.
11. Denison, M.R. and E. Baum: *J. of American Rocket Society*, 31, 1112, 1963.
12. Hart, R.W. and F.T. McClure: *J. of Chemical Physics*, 30, 1501, 1959.
13. Horton, M.D. and D.W. Rice: *Combustion and Flame*, 8, 21, 1964.
14. Cheng, S.I.: *Jet Propulsion*, 25, 163, 1955.

15. Angelus, T.A.: Eighth Symposium (International) on Combustion, Williams and Wilkins Co., p. 921, 1962.
16. Price, E.W.: Tenth Symposium (International) on Combustion, The Combustion Institute, p. 1067, 1966.
17. Hart, R.W. and T.F. McClure: Ibid, p. 1047, 1966.
18. Culick, F.E.C.: *AIAA Jour.*, 1, 1097, 1963.
19. Sirignano, W.A. and L. Crocco: *AIAA Jour.*, 2,7, 1964.

Part Seven

*Advanced Concepts and
Mission Applications*

An Advanced Space Propulsion Concept

Sin-I Cheng, Professor
Department of Aerospace and Mechanical Sciences
Princeton University

[16-1] INTRODUCTION

[16-1.1] General Consideration for Propulsion in Space

The propulsion system in a vehicle is to provide thrust (or force) for overcoming the resistance to or the inertia of the motion of a vehicle. In the high vacuum environment of outer space, there is no dissipative resistance, and thrust is required primarily to overcome inertia or potential barrier. A self-contained propulsion system on board the vehicle can produce thrust only through the reaction of the time rate of ejection of momentum from the vehicle, $T = \dot{m}V$, where T is the reactive thrust (dynes), $\dot{m}$ is the mass efflux rate (gm/sec.), and V is the velocity (cm/sec.) of the ejected mass relative to the vehicle. The kinetic energy of the mass ejected in unit time is the jet power,

$$P_j \;=\; \frac{1}{2}\,\dot{m}\,(\bar{V} \cdot \bar{V}) \gtrsim \frac{T^2}{2\dot{m}}\,. \tag{16-1}$$

The rate of total energy efflux or the power which the propulsive unit has to supply is necessarily larger than the jet power because the ejected mass must carry with it many different forms of internal energy e, such as ionization, dissociation, etc., that do not contribute to the thrust. The propulsion system must deplete its mass and energy in providing thrust.

The chemical system is unique in that the propellant mass stores in it the energy required for its propulsion. The power or energy requirement of a chemical propulsion system is no extra burden. The storage and handling problems of many a "high energy" propellant often become burdensome. But the most serious limitation of the chemical system lies in the inefficiency of transforming the limited amount of chemical energy per unit mass into propulsive power. Much of the available chemical energy is frozen in the dissociation (and ionization) of the chemical species in the thermal

stage prior to the process of thrust generation. This limitation of dissociation is so severe that even if energy is added from external sources such as electric arc heating to hydrogen as a propellant, the specific impulse (I_{sp}) cannot exceed 1000 seconds. For a reaction type propulsive system, the ratio of initial to final vehicle mass increases exponentially as the ratio of the required total velocity increment of the vehicle to the jet exhaust velocity $(V_e = gI_{sp})$. For most space missions, the total velocity increment required is an order of magnitude larger than the jet velocity offered by any chemical system. Multi-staging of the chemical propulsive system does reduce somewhat the initial to final mass ratio but at the expense of increased mechanical complexities and decreased reliability. Accordingly, the search for space propulsion systems was once interpreted as a search for propulsive devices with high I_{sp} or high jet velocity.

High jet velocity can be achieved by adding energy to the propellant particles directly in the form of collimated motion through a variety of electrostatic or electro-magnetic means rather than in the form of thermal motion. Broadly speaking, such thrust-producing devices requiring the primary energy input in the form of electric energy can be referred to as electric propulsion. A self-contained electric propulsion system must include the power generating unit to provide the electric energy. The provision of propulsive power in electric form will, hence, mean a significant amount ($\gtrsim$ 10 kg/kw) of power plant mass (or weight) per unit electric power to be carried on board the vehicle in addition to the propellant mass for absorbing this energy. In comparison with chemical propulsion systems, the electric propulsion system cannot show any advantage in a given mission until the saving in the propellant mass derived from the higher specific imuplse exceeds the mass of the power plant and the fuel. A meaningful comparison of propulsion systems must consider the power plant along with the thruster.

[16-1.2] Power Supply

Electric energy may be generated from the chemical or nuclear fuel carried on board the vehicle or from solar radiation (or radiant energy from any nearby star). The conversion of chemical energy to electric energy through heat addition as in conventional heat engines is inefficient, while the direct conversion of chemical energy to electrical energy through fuel cells is still in the stage of research. Any advantage that the generation of electric energy from chemical fuel as a space power plant for propulsive purposes is yet to be shown.

Solar energy is supplied from sources outside the vehicle and nuclear fuel is of very low specific fuel mass per unit energy.

The mass of the nuclear or the solar power plant is hence deter-mined by the equipment for power generation, conversion or conditioning. Thus, the plant weight is governed by the power or the rate of electric energy fed into the electric thruster, not by the total energy for propulsive purposes. It is the maximum thrust, not the total impulse, required in a given mission that determines the power plant weight for the electric thrusters. Now

$$P = \frac{P_j}{\eta_p} = \frac{1}{2\eta_p} \, T \cdot I_{sp} \qquad (16\text{-}2)$$

and an electric thruster is to provide thrust at a high jet exhaust velocity or high I_{sp}. Thus, higher I_{sp} is achieved at higher jet power for a given thrust level.

If we take, for the present, a constant propulsive power efficiency η_p, the required power input, P, to the electric thruster will increase linearly with the specific impulse I_{sp}. If the specific weight of the power plant $1/\alpha$ (kg/kw) remains constant, the power plant weight for an electric thruster to deliver a given thrust will increase linearly with I_{sp}. Since the weight of the electric power plant should never exceed the chemical propellant weight required to accomplish the same mission, electric propulsion systems delivering only a few grams of thrust per kilowatt are, hence, power limited. Such high I_{sp}, low thrust devices have to operate for a year or more to gain any advantage over the chemical system. Hence, the reliability and ability of an electric thruster in maintaining its designed performance becomes very important. An electric thruster should operate at an optimum I_{sp} to be competitive. This optimum I_{sp} depends not only on the propulsive efficiency η_p (which may be dependent on I_{sp}) and the selection of the power plant of a given $1/\alpha$, but also on the particular mission for which the comparison is made vis-a-vis chemical rocket and other electric propulsion schemes. As a rough guide, an I_{sp} greater than 10,000 seconds is too high, while an I_{sp} less than 1000 seconds is too low for most space missions.

For nuclear power plants, the weight of the reactor, the nuclear radiation shield and the heat sink radiator for the heat engines are the most significant. With the turbo-generator as the means of converting thermal to electric energy, it does not matter whether the electric power required by the thruster is of the alternating or of the direct current type. It matters little whether the power is to be supplied at 10^2 volts or at 10^4 volts. The specific weight of the nuclear power plants will not be much less than 15 to 20 kg/kw in the near future. To derive electric power from solar energy, the situation is very much different. The structural weight of the collecting surface and/or the solar cell panels for converting the radiation energy into electricity is the important one. Since

the energy flux density of solar radiation is very small, the struc-
ture becomes very bulky. The overall specific weight is again no
less than 15 to 20 kg/kw, although there is no weight associated
with the radiation shield and the radiation heat sink. The electric
energy is supplied as direct current and at voltages substantially
below kilovolts. If the electric thruster requires power supply of
an oscillatory nature or of a d.c. voltage of many kilovolts, it is
necessary to process or "condition" the electric power output,
say, from the solar panels to the kind of power input required by
the thruster. The weight of such "power conditioning" equipment
is a significant part of the specific weight $1/\alpha$ (kg/kw) of the power
plant for electric propulsion systems.

[16-1.3] Propellant Storage and Handling Facilities

With the specific impulse of electric propulsion systems
generally 5 to 10 times that of chemical systems, the propellant
weight will be comparable to the power plant weight. The tons of
propellant to be carried on board the vehicle will present important
problems in its storage and handling.

Gaseous propelant would occupy too big a volume unless it is
stored in cryogenic condition. Cryogenic equipment is heavy and
absorbs significant amount of power. It is doubtful that hydrogen,
however attractive it appears otherwise, will be a practical pro-
pellant for space missions.

Liquid propellant can be conveniently stored in pressurized
tanks. The pressurization is necessary for transferring the liquid
propellant from the storage tank to the thruster in the absence of
gravity; otherwise, pumping facilities would be needed. Propellants,
naturally in a solid state, need to be transformed into molten form
to facilitate the transfer and metering. If the propellant should be
highly reactive, corrosive or easily contaminated, the storage and
handling facilities may present serious problems, especially when
the efficiency of the electric thrusters depends heavily on the
purity of the propellant and may involve significant additional
weight and complexities of the equipment.

Stability of the propellant during storage, which may be of the
order of years for space missions, is another consideration. This
is particularly important for specially prepared propellants such
as colloidal propellants for ion engines. If the thermal environ-
ments during storage, transfer and thrust production are signifi-
cantly different, it is much more important for such specially pre-
pared propellants to maintain the designed property.

The weight of the propellant storage and handling facilities and
of the structure to support them is a significant fraction of the over-
all weight of the propulsion system even if not comparable to total
propellant weight. The additional overall weight reflects, however,

only part of the story. The quality of a propellant to be easily stored, transferred and maintained is of considerable importance although it is difficult to express quantitatively as a single performance parameter. If a thruster should be able to use a commonly available and stable material or even a great variety of them, the significance may be far reaching.

[16-1.4] Electrostatic and Electromagnetic Thrusters

Many different mechanisms of producing thrust electrically have been proposed. The most promising appears to be the ion thrusters [1, 2] and the M.P.D. arc jets [3, 4]. All the electric propulsion systems aim at high I_{sp} and, hence, should operate at high mass utilization efficiency if not at 100%. This means that a high fraction of the propellant escaping from the propulsion system should be accelerated to the desired high jet velocity.

For electrostatic thrusters in which electrostatic field is utilized to accelerate the ionic particles, the propellant should preferably be 100% converted into ions requiring a liberal expenditure of electric energy. The energy spent for generating an ion from the propellant atoms, however, is dissipated in the jet without producing thrust. An easily ionized propellant should then be preferred to lessen the expenditure of electric energy. C_s, the heaviest member of alkali metals, requires the lowest ionization energy of about 4 e.v. per ion and thus is a natural choice; hence, the C_s-ion engine. However, C_s is a highly reactive metal which must be vaporized at high temperature and transferred under high-temperature environment to the ionizer without being contaminated. As a result, it takes more than 400 e.v. to produce a C_s^+ instead of the 4 e.v. ionization energy. Although the ionization energy for Hg is 10 e.v. and the electron bombardment is not as efficient a process as surface ionization, Hg+ can also be produced from Hg in the electron bombardment engine for 4-500 e.v. With 500 e.v. spent to produce an ion, a propulsive efficiency $\eta_p \gtrsim 50\%$ can be acnieved only when the ionic particles are accelerated to a couple of kev. energy, corresponding to $I_{sp} \gtrsim 10^4$ sec. near or above the upper limit of the useful I_{sp} range. To reduce the specific impulse while maintaining the propulsive efficiency, we have to reduce the energy required to produce an ion or to increase the ion mass. The former is under extensive development while the latter, in the form of colloidal particles, is still in the research stage.

Besides being efficient energy-wise, the ionizer should produce, as far as possible, 100% mass utilization, although lowering I_{sp} is not the primary concern. The presence of a small fraction of neutral propellant atoms will undergo significant numbers of charge exchange collisions to scatter the ions while being accelerated and focussed to escape the thruster. Such a scatter of the accelerated

ions leads not only to the loss of thrust (production of low speed ions) but the sputtering erosion of the cathode, accompanied by further deterioration of the focussing mechanism and the overall efficiency of the ionizer and the thruster. To maintain an efficient ionizer and a well-focussed beam for long period operation is the most serious problem of ion engine development. For the same reason, the colloidal ions must be produced as nearly uniform in mass as possible, a requirement that greatly complicates the colloidal ion thruster.

Electromagnetic thrusters do not call for the separation of ions from the electrons and the directed kinetic energy imparted to the ionized species is largely transferred to neutral propellant particles through successive collisions prior to their ejection from the thrusters. The neutral propellant particles are supplied to augment the mass of the jet and must be supplied at a sufficiently large particle density to enable the successful transfer of energy from the charged particles to the neutral particles. This transfer of energy is through the rather inefficient random collision process. The energy spent in ionizing part of the propellant is, however, much less than that required for the electrostatic thrusters. Thus, the propulsive energy efficiency may reach 50% as is reported for the MPD arc jets (magneto-plasma-dynamic). The specific impulse achieved in gaseous MPD arc jets with hydrogen as a propellant ranges from 10^3 to 10^4 sec. as was reported in early laboratory tests. The storage and handling of tons of H_2 in cryogenic condition on board of a space vehicle is, however, not practical. Ammonia NH_3 is an excellent alternative, giving I_{sp} up to 7000 sec. at a propulsive energy efficiency of almost 40% in some laboratory tests. Such optimum early results appear to be significantly altered by the residual gas in the test environment that participates in the acceleration and thrust production process. The thrust derived from the MPD jet in the test appears to be independent of the propellant flow rate (either gaseous or alkali metal vapor) when the propellant flow rate is low and electric power supply is high. Thus, when operated in a hard vacuum like the space environment, both the specific impulse and the propulsive energy efficiency is expected to be significantly below the values indicated above. Nevertheless, the MPD arc jet appears to be the most promising electromagnetic thruster, delivering I_{sp} of a few 10^3 sec. at a specific power consumption of about 1 kw/gm. wt. compared with the ion thruster delivering $\lesssim 10^4$ sec. at a specific power consumption of approximately 1/2 kw/gm. wt. The MPD arc jet does not call for precision control or timing for its successful operation or for any delicate preparation of its gaseous or liquid propellant. The electrodes erosion and the associated cooling problems are serious, but the uncertainty of its performance in vacuum remains the one of the greatest concern.

[16-1.5] Advanced Electric Propulsion Systems for Space Vehicles

A propulsion system is an engineering device for producing thrust for a definite mission. Engineering implies compromises among conflicting requirements to achieve a nearly optimum solution. Rarely, if ever, is the optimum achieved when one aspect of the performance is pushed to the extreme. Thus, a photon rocket with the highest I_{sp}, for example, is not a practical system. What is optimum clearly depends on the nature and magnitude of the mission. As a propulsion system for space vehicles, the overall weight (or volume) of the propulsion system and the reliability of its function must be of primary concern. In view of the fact that space vehicles are power limited and the specific weight of the power plant cannot be substantially decreased, the discussions in previous sections indicate that there is much to be gained if an advanced electric propulsion system for space vehicles should be able to deliver simultaneously (1) an I_{sp} in the range of 1000 to 10,000 sec., (2) a propulsive power efficiency η_p comparable to 50%, and (3) a specific power consumption of a small fraction of a kilowatt of electric power per gram weight thrust. It is important that the thruster operate with the designed efficiency without any precision control or timing, such as the MPD jet, so that the reliability of the system is greatly improved over the ion thruster.

It would be extremely desirable for the propellant of the thruster to be commonly available and employed as structural material, solid crystalline, alloyed or amorphous in its natural state. It would be advantageous for the propellant to be ejected directly from its solid state for the generation of thrust without special treatment or preparation. If we consider the overall mission of space exploration from the ground base, the weight of the equipment for the storage, transfer and preparation of the propellant may be essentially eliminated, and the propellant weight of the space vehicle need not be counted entirely as the payload of the boosters. The spent last booster stage, being almost lifted to the parking orbit in its ferrying operation, can be brought to the parking orbit and salvaged for the propellant of the space vehicle with slight additional expenditure of energy. There would be much room for ingenuity in designing the last booster stage with the space vehicle in mind so as to minimize the salvaging work to be performed in the orbital station. There are admittedly serious technical difficulties of such a maneuver in orbit, but it is certainly feasible in principle. The potential advantage is too significant to be overlooked. If such an electric thruster using structural material as propellant can indeed be conceived and developed, it can offer significant advantages over the existing electric thrusters even if it can offer only a substandard performance such as lower I_{sp} and η_p. In the following section, an attempt to find such a propulsion system is reported. It is, of course, much more attractive

if a system of this kind could offer performance superior to what is outlined above.

[16-2] SPUTTERING, A THRUST GENERATION MECHANISM

[16-2.1] Sputtering Phenomena

The emission of atomic sized particles from a metallic target surface under the impact of energetic neutral or ionic particles is known as "sputtering." The sputtering phenomenon was first observed as the erosion of the cathods in a glow discharge and has been under extensive investigation for over a century. The sputtered particles are neutral, although the incident particles may be neutral or ionic as long as its energy is not more than 50 kev. per particle. For convenience, experiments were usually performed with ionic particles.

Numerous experimental data exist in the literature [5, 6] on the "sputtering yield," *i.e.*, the number of target atoms sputtered per incident ion. Early yield data prior to 1950 tended to be too low due to backward diffusion of the sputtered particles and to the uncertain nature of the incident ion beam in these experiments. Improved experimental techniques have provided more reliable yield data since 1950 and some energy data of the sputtered particles since 1960. It is now established beyond doubt that the average energy $\bar{E}$ carried by each sputtered particle is of the order of tens or even hundreds of electron volts (Fig. 16-1) [5, 6]. The sputtering process is fundamentally different from the purely thermal process of evaporation or sublimation of the target particles after absorbing the incident energy. The specific impulse of these ejected particles after the correction of their angular spread covers the range 500 to 5000 sec. for sputtering targets ranging from gold to graphite. The yield s (number of atoms sputtered per incident ion) of various target materials by 35 kev. Xenon ion is also given in Fig. 16-1.

The mean energy $\bar{E}$ of the sputtered particles is essentially proportional to the logarithm of the incident ion energy, E for a given ion-target material combination (Fig. 16-2). When the incident ion energy E is in the range of 1 to 10 kev., the sputtering yield S is proportional to some fractional power of E. For most materials, the exponent will be approximately one-half (Fig. 16-3).

While the mean energy $\bar{E}$ of sputtered particles decreases slightly with increasing angle of incidence of the ionic particles, the sputtering yield S increases rapidly with increasing angle of incidence.

The sputtered particles are ejected in different directions in the half plane almost according to the cosine distribution at low
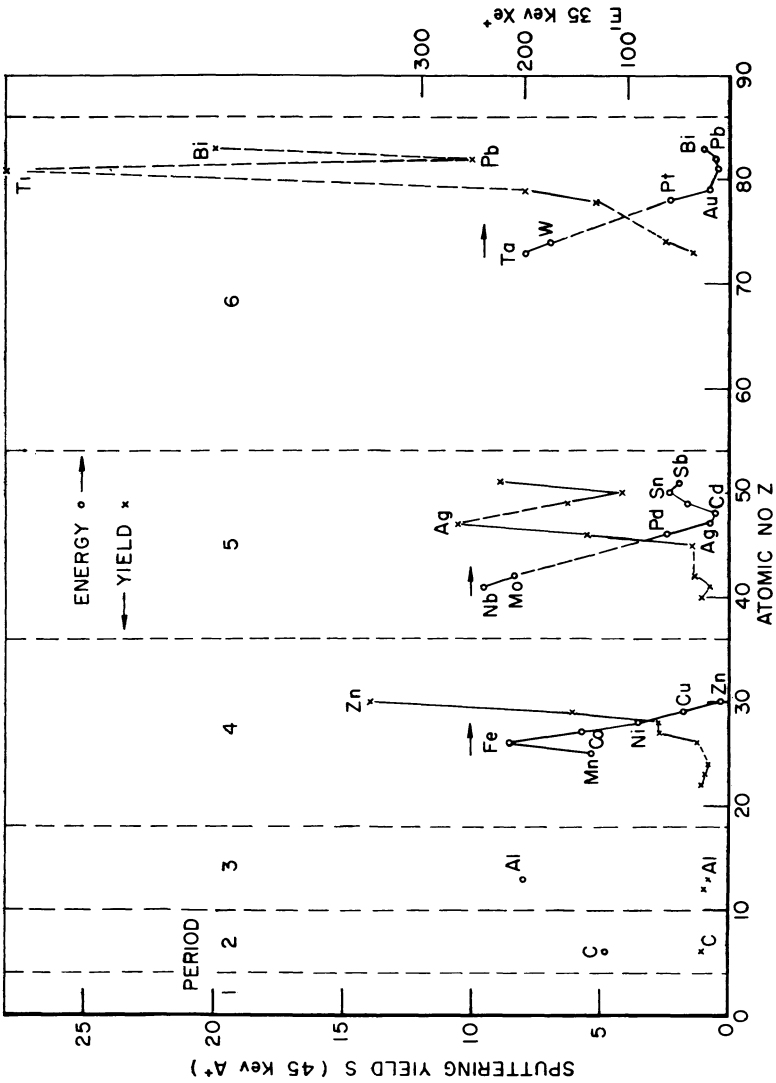
Fig. 16-1 Typical sputtering yield and mean energy data for various metals by 35 kev. Xe^{+}.
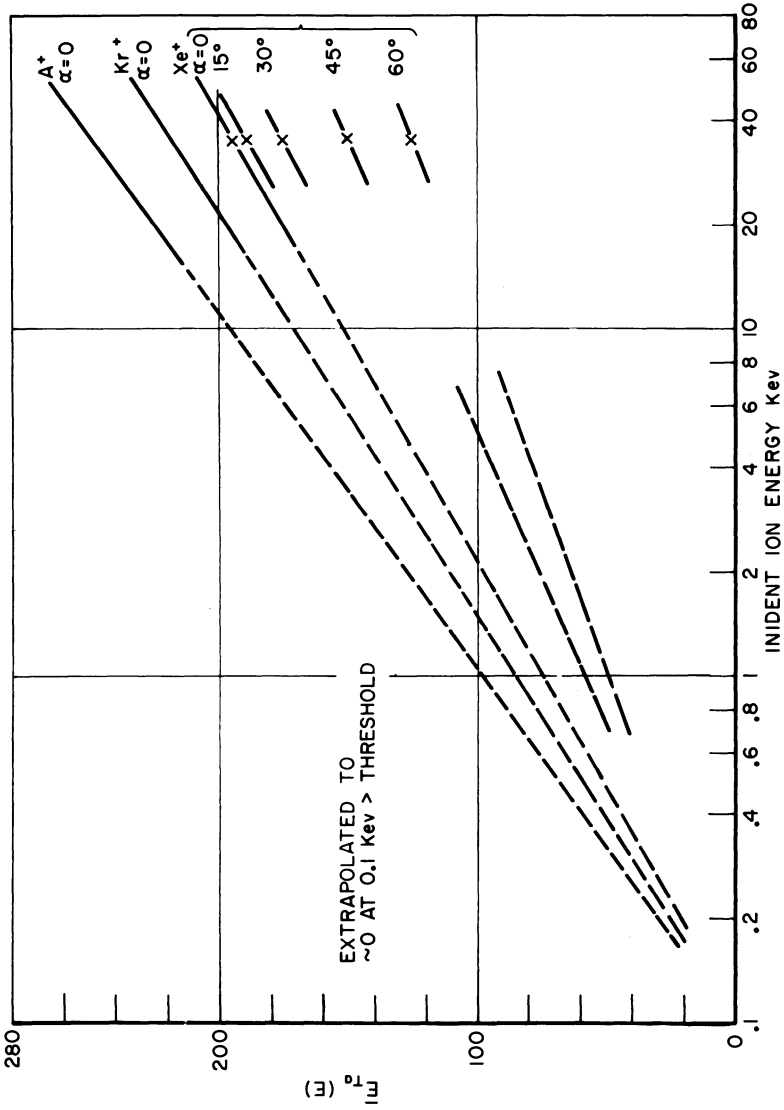
Fig. 16·2 Mean energy data of tantalum target.
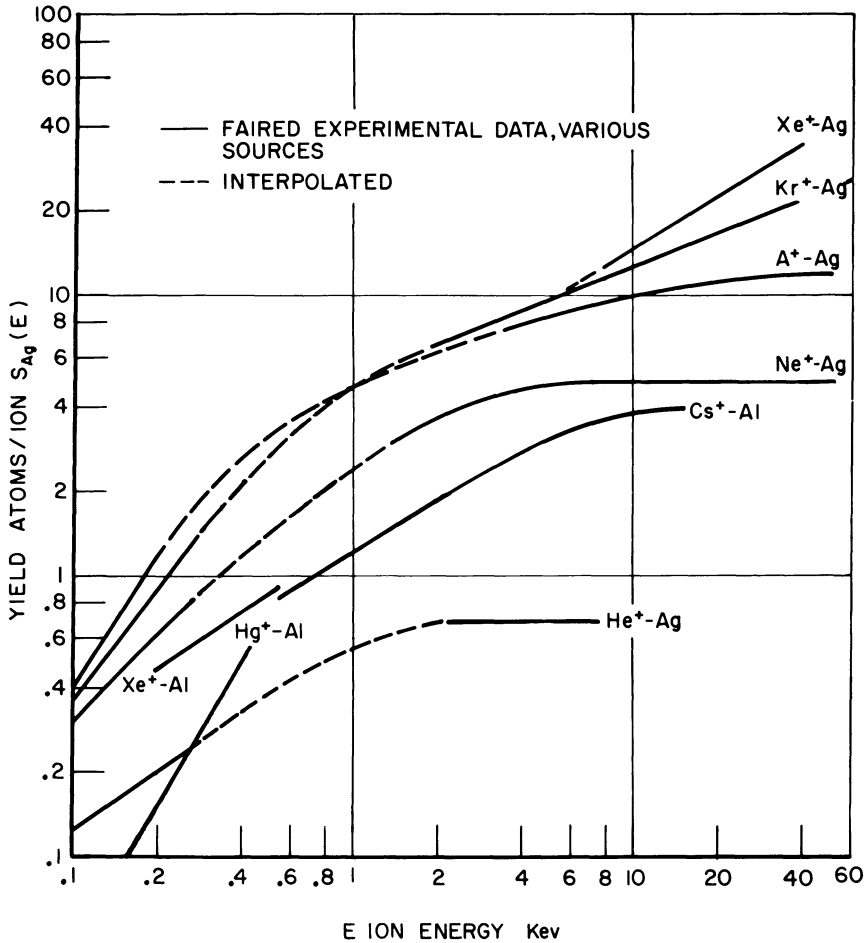
Fig. 16-3 Sputtering yield, S, as functions of incident ion energy E_i for various targets.

energy or to the Gaussian distribution at higher incident ion ener-
gies for polycrystalline targets. Thus, in the evaluation of the
thrust or the specific impulse of the sputtered beam, a multiplying
correction factor for the lack of collimation of the sputtered par-
ticles is about $\pi/4 \cong 0.8$ or larger.

Keeping these qualitative behaviors in mind and with the yield
and energy data of the sputtering process, we can evaluate the per-
formance parameters of interest to propulsion applications. Much
of the thoughts reported in Reference 5 will be reproduced here

briefly. A few subtle and probably crucial points are to be amplified in the following.

[16-2.2] Possible Performance of Sputtering Thrusters

Then experimental values of the yield and energy are adopted (properly extrapolated or interpolated where necessary since properly matched yield and energy data are few), we can obtain a general idea of the possible performance of the sputtering thrusters. The numerical values quoted below are not precise but are given only to reflect the order of magnitudes.

Thrust augmentation through sputtering $(\lambda_{th} > 1)$ will usually be achieved for varieties of material combinations when the incident ion energy E_i is larger than 1 kev. and λ_{th} will reach three to five when $E_i > 10$ kev. before reaching the limiting energy E_c where the sputtering yield apparently becomes saturated. The thrust density as the maximum thrust per mA of incident ion current generally ranges from 10 to 40 dynes/mA.

The specific consumption S.P.C. of electric power input to the thruster (the ion beam power) per unit thrust of the sputtered particles varies from

$$\frac{1}{2} \quad \text{to} \quad \frac{1}{20} \quad \text{watts/dyne} \quad \text{or} \quad \text{kw/gm. wt.}$$

for different material combination and for different levels of incident ion energy E_i. The S.P.C. of a sputtering thruster is not an explicit function of the specific impulse, *i.e.*, different material combinations may give the same I_{sp} but quite different S.P.C. This situation is different from the ion thruster when the incident ion beam of the sputtering thruster is the thrust producing beam. At the power efficiency η_p, we have

$$(\text{S.P.C.})_{\text{ion thruster}} = \frac{g \times I_{sp}}{2 \times 10^7 \times \eta_p} \tag{16-3}$$

typically

$$\frac{1}{3} \text{ watt/dyne} \quad \text{at} \quad I_{sp} = 5,000 \text{ sec.}$$

$$\frac{1}{2} \text{ watt/dyne} \quad \text{at} \quad I_{sp} = 10,000 \text{ sec.}$$

The specific power consumption of the MPD arc jet is, according to test results, one to 1/2 watt/dyne [3] irrespective of the presence of residual gas in the test tank to any significant extent. This figure

of 1 to 1/2 watt/dyne is also consistent with the estimate based on Eq. 23 of Reference 7 when proper values of the arc discharge parameters are substituted. The specific power consumption of the sputtering thrusters with a good many target materials are significantly less than those of ion thrusters and of MPD arc jets. The thrust augmentation of the sputtering process is the principal reason for achieving smaller S.P.C.

The specific impulse of the sputtered particles varies from 500 to 5000 sec. Commonly available target materials of light weight but sputtered with high mean energy are graphite C^{12} and aluminum Al^{27}, giving $I_{sp} \gtrsim 4000$ sec. Iron Fe^{56} and copper Cu^{64} give $\gtrsim 2000$ sec. and $\gtrsim 1000$ sec., respectively. Lead P_b^{207} gives one of the lowest $I_{sp} \sim 500$ sec. These figures are meant to be representative only and the accuracy of the existing experimental data will not permit a more precise statement. As a general trend, the lighter members of each transition series are typically "high energy-low yield" targets, while the heavier members are "low energy-high yield" targets (see Fig. 16-1, for example). It is, however, clear that the sputtering thrusters will deliver I_{sp} in the lower half of the desirable range of 1000 to 10,000 sec. Some exotic materials may give higher I_{sp}, but their use will reduce substantially the benefit discussed in Section 16-1.5. When an alloy of different metals is sputtered, experimental results indicate that each component is sputtered as if it were alone, and the overall sputtering results for the alloy appear to be the weighted average of the corresponding results for each component. A number of stable carbides are very attractive in addition to graphite and aluminum that will give high specific impulse. They may provide essentially a continuous spectrum of I_{sp} to meet the optimum choice for a given mission.

The propulsive power (or energy) efficiency, η_p, of the sputtering thrusters varies from only a few percent to well over 50%. High η_p is generally associated with high energy targets under less than 10 kev. incident ion energy. Since sputtering is traditionally recognized as a rather inefficient process and a high propulsive power efficiency, η_p, is the most important performance parameter of a space thruster, the question of energy efficiency of the sputtering process will be discussed in some detail.

[16-2.3] Energy Efficiency of the Sputtering Process

It will first be demonstrated that the test results of the sputtering of the tantalum sphere by mercury ion at 60° nominal angle of incidence indicated an energy efficiency well above 50%. The sputtering yield, S, is reported by Wehner [8] as $S = 8$ atoms/ion. under 400 v. incident Hg^+. The mean energy data of the sputtered tantalum is shown in Fig. 16-2. The solid portion of each curve

represents five data points with little scatter. Linear extension of these lines seems to converge at the point corresponding to zero $\bar{E}_n$ at 100 e.v. incident ion energy that is significantly above the sputtering threshold of about 20-30 e.v. With 100 e.v. incident ions, we would expect sputtered tantalum to possess at least a few e.v. of energy. The linear interpolation of the tantalum energy data as shown in Fig. 16-2 is thus believed to be on the safe side, *i.e.*, predicting a lower mean energy than what it should be. The ratio of mass of Hg^{200} to Xe^{133} is about the same as the mass ratio of Xe^{133} to Kr^{83}. A corresponding reduction in $\bar{E}_n$ may be expected but is more than offset by the increase of $\bar{E}_n$ since the effective angle of attack is certainly smaller than 60°. Hence, take

$$\bar{E}_{Ta} = 23 \ln \frac{E_i}{100} \text{ e.v.} \qquad (16\text{-}4)$$

according to the $Xe^+ - Ta$ line at 60° incidence. Thus, $\eta_p = S\,(\bar{E}_n/\bar{E}_i)$ will be 65% and 56% at 400 e.v. and 3.6 kev. incident ion, respectively.

Alternatively, if we elect to extrapolate the yield data, we may note that the Xenon ion generally gives higher yield than mercury ion (see Fig. 3, Reference 5), especially when the incident ion energy is less than 10 kev. Thus, the Xe^+ would yield more than 8 atoms/ion from the tantalum sphere and give a propulsive power efficiency, η_p, correspondingly larger than the 65% and 56%, respectively.

The process of data reduction illustrated above contains many uncertainties, and the numbers cannot be taken seriously. It does demonstrate, however, that the sputtering process is not nearly as inefficient as is commonly recognized. Tantalum is not expected to be the only target material to show such high energy efficiencies.

The modern theories of sputtering, although semi-classical in nature, will provide an explanation that such high energy efficiencies are possible where the target atoms are arranged in some regular pattern as all crystals are. Suppose that a displaced target atom moves along the centerline of a row of target atoms at rest to collide with the first atom head-on. A series of head-on collisions would result, leading to the ejection of the last atom in the row with all the other atoms finally at rest. Thus, the energy of the displaced atom is transferred to the ejected or sputtered atom with negligible energy loss. If the displaced atom should approach the first atom in the row within a certain solid angle, the successive collisions between the rows of atoms would become more and more head-on along the centerline of the row of atoms. The energy of the last atom in the line would again be ejected with substantially the same amount of energy as the original displaced atom initiating this sequence of "focussing collisions." This is known as the Silsbee mechanism of momentum focussing [16]. There are many such preferred lines in a crystal lattice along

which atoms are so arranged. The solid angle within which such focussing can take place depends on the interacting potential, the inter-atomic spacing, and the energy of the displaced atoms. There are also other mechanisms of such focussing collisions along different preferred directions. Thus, when a lattice atom at "rest" is collided by some other "randomly moving atom," there is a probability, p_1, that one of the colliding atoms will be deflected to move into the solid angle around one of the many pre-ferred directions to start a focussing sequence of collision and to eject an atom without significant loss of energy. If the displaced atom should fall outside any such solid angles, it would collide with some other neighboring atom with the probability, p_2, of setting this second atom to starting a focussing collision and eventual ejection of a sputtered atom. The process repeats until the energy of the displaced atom is thermalized, *i.e.*, the order of a small fraction of e.v. or comparable to the bond energy be-tween the atomic lattice. When the energy of the incident atom is of the order of kilo-volts, it will undergo tens or even hundreds of collisions before it is thermalized. If, on the average, a mean value of the probability, $\bar{p}$, for initiating focussing collisions is as small as 1%, 50% of its energy will escape with the ejected par-ticles if there is an average of 70 collisions or more. At $\bar{p} \sim 5\%$, only 15 collisions will lead to the ejection of half the incident energy. An energy efficiency well above 50% is not unreasonable. Clearly, definitive yield and energy data are needed to affirm the claim.

[16-3] ANALYSES OF AN ELEMENTARY MISSION WITH DIFFERENT ELECTRIC THRUSTERS

[16-3.1] General Consideration

Comparison of different propulsion systems can only be made for a specific mission, since the mission requirements may be basically different. For example, for station-keeping missions, neither the specific impulse (if above 1000 sec.) nor the pro-pulsive power efficiency matters much. If electric thrusters are to be considered for station-keeping missions, the satellite must be of many years of service life and possess power source and conditioning equipment to perform its natural function as an active satellite. The power required for station-keeping purposes is small and will not cause any appreciable burden on the power system, since the thrust required level is very small. On the other hand, the long operational life of such thrusters will emphasize the reliability and ease of intermittent operations and the storage and handling characteristics of the propellant. The examples

shown [5] for the three year station-keeping mission for a 1500-lb. synchronous satellite clearly illustrated these points.

The major interest in electric thrusters is likely to be primary propulsion systems for space exploration. Launched from a parking orbit around the earth, the space vehicle would need a velocity increment, ΔV, of the order of 60 km/sec. for passing by Jupiter. Much larger velocity increments would be required for missions to go beyond Jupiter. An ion thruster at ~10,000 sec. or a MPD jet thruster delivers $\lesssim 2$ gm/wt thrust per kw electric power. If the electric power is to be supplied by electric power plants of specific weight no less than 20 kg/kw, the thruster could accelerate the dry power plant alone only at ~ 10^{-1} cm/sec^2. It would take about two years (~ 6×10^7 sec.) to impart the 60 km/sec. velocity increment to the dry power plant alone. With propellant and payload, it would take five to ten years to accelerate the vehicle to the required velocity. Since the specific weight of the power plant cannot be substantially reduced in the foreseeable future, it is apparent that a thruster delivering higher specific thrust (thrust/kw), *i.e.,* at lower specific power consumption (S.P.C. = kw/thrust) will be a significant improvement. It is also clear that in specifying a mission for evaluating the relative merits of different thrusters, there should be an upper limit of time period within which the mission should be completed. For the reason just given, existing electric thrusters simply cannot be expected to give a ΔV ~ 60 km/sec. in a period of two years.

A flight time of the order of several years is undesirable not only psychologically but also technically, because it will impose a severe restriction on the reliability of all the components in the system. Thus, for the not so ambitious Mars missions launched from earth's parking orbit, a purely chemical propulsion system is favorably considered. Optimization studies also indicate preference to a two-stage program, *i.e.,* an initial impulsive launching with a chemical booster to be accelerated by an electric thruster after escape from the earth. An electrically propelled single stage is too "long" even for the Mars missions requiring $\Delta V < 30$ km/sec. Without substantial improvement of the specific weight of the power plant or of the S.P.C. of electric thrusters, it is not likely that the velicity increment to be supplied by the electric thruster stage will be much in excess of 30 km/sec. The period of such acceleration will not be appreciably larger than, say, two years. Any missions more ambitious than the Mars exploration will likely be the multistage type. Electric propulsion systems without substantial improvement on S.P.C. can at most be considered one of the multistages for space missions.

For different types of electric thrusters, the S.P.C. depends on the I_{sp} in a different manner. For ion thrusters, S.P.C. increases almost linearly with increasing I_{sp} (*i.e.,* decreasing thrust), while for MPD arc jets, S.P.C. is apparently independent of I_{sp}.

(The effect of entrained residual gas leads to the dramatic increase of I_{sp} but is not likely to increase S.P.C. substantially.) For sputtering thrusters, S.P.C. reaches a minimum at some intermediate value of I_{sp} for a given material combination. For all these thrusters with a given power, larger I_{sp} means smaller propellant mass flux and smaller thrust. To achieve a given velocity increment at smaller thrust, the thruster must operate for a longer period. The total propellant mass, being the product of mass flux rate and the period of operation, will be minimized at some intermediate value of I_{sp}. Such an optimum I_{sp} will clearly be different for different types of thrusters. The comparison of different types of electric thrusters, by assuming that they all operate at the same I_{sp} or at the same S.P.C. or at the same energy efficiency are, therefore, quite irrelevant. We have to make the comparison with each type of thruster operating at its optimum condition for a specific mission. The conclusion drawn in this manner is valid, of course, only for that specific mission. With this in mind, we shall consider in the next section a typical elementary mission of launching a payload w from a parking orbit to produce a velocity increment ΔV during a specified period τ.

[16-3.2] Performance Formula for Electric Thrusters

We shall derive a formula for calculating the ratio of the initial mass M_0 to the payload w of the space vehicle with electric thrusters as the primary propulsion unit to impart a velocity increment ΔV in an interval τ or less. Let

w = the payload of the vehicle
M_f = the initial mass of the fuel or propellant
M_p = the dry mass (or weight) of the propulsive unit
= the sum of the masses of power generation and conversion unit, of power conditioning unit, of the units for propellant storage and handling and of the thruster unit including all the structural weight
M_0 = gross initial mass of the space vehicle launched from the parking orbit
= $w + M_p + M_f$
ΔV = total velocity increment required.

If the propulsive unit delivers thrust T at a constant I_{sp}, Newton's law of motion is easily integrated to the common rocket equation

$$M_0 = (w + M_p) \exp\left(\frac{\Delta V}{g I_{sp}}\right). \tag{16-5}$$

The propellant mass needed to produce the velocity increment ΔV is hence

$$M_f = M_0 - (w + M_p) = (w + M_p) \left[\exp\left(\frac{\Delta V}{gI_{sp}}\right) - 1\right] \qquad (16\text{-}6)$$

Let α be the electric power (kw) delivered by the power conditioning unit to the thruster per unit dry weight of the propulsive unit. Let S.P.C. be the specific power consumption of the thruster, *i.e.*, the electric power input to the thruster per unit thrust delivered by the propulsive unit. Then $M_p \cdot \alpha/\text{S.P.C.}$ is the thrust delivered by the thruster and the time rate of propellant consumption is

$$\frac{dm}{dt} = \dot{m} = \frac{M_p}{gI_{sp}}\frac{\alpha}{\text{S.P.C.}} . \qquad (16\text{-}7)$$

Equation (16-7) implies that the propulsive unit will operate at the maximum power available at all times whenever it is in operation. This assumption is reasonable since the space vehicle is power-limited and the thruster cannot deliver as large a thrust as is desired for shortening the mission time. Hence, the total amount of propellant is

$$M_f = \frac{M_p}{gI_{sp}}\int_0^\tau \frac{\alpha}{\text{S.P.C.}}\,dt = M_p\,\frac{\tau a^*}{gI_{sp}} \qquad (16\text{-}8)$$

where

$$a^* = \frac{1}{\tau}\int_0^\tau \frac{\alpha}{\text{S.P.C.}}\,dt \qquad (16\text{-}9)$$

is the characteristic acceleration of the propulsive unit. $\alpha/\text{S.P.C.} = T/M_p$ is the acceleration of the dry propulsive unit (vehicle mass less payload and propellant mass) if it alone should be acted on by the thrust delivered by the thruster unit. For most electric thrusters, S.P.C. is a constant at a given I_{sp}, and the average valud a^* is the same as the instantaneous value $\alpha/\text{S.P.C.}$

By equating (16-6) with (16-8), we obtain

$$\frac{M_p}{w + M_p} = \frac{\left[\exp\left(\dfrac{\Delta V}{gI_{sp}}\right) - 1\right] \cdot \dfrac{\Delta V}{\tau a^*}}{\dfrac{\Delta V}{gI_{sp}}} = \frac{(e^\mu - 1)}{\mu} \cdot \lambda \qquad (16\text{-}10)$$

where

$$\mu = \frac{\Delta V}{g I_{sp}} \qquad \lambda = \frac{\Delta V}{\tau a^*} = \frac{\Delta V}{\tau} \cdot \frac{\text{S.P.C.}}{\alpha} . \qquad (16\text{-}11)$$

By eliminating M_p from (16-5) and (16-10), we have

$$\frac{M_0}{w} = \frac{e^\mu}{\left[1 - \lambda \left(\frac{e^\mu - 1}{\mu} \right) \right]} \qquad (16\text{-}12)$$

Here μ is the ratio of the velocity increment to the jet exhaust velocity, and λ is the ratio of the time required for accelerating the dry mass of the propulsive unit to produce the required velocity increment to the mission time allowed. Alternatively, λ may be visualized as the ratio of the average vehicle acceleration of the mission $\Delta V/\tau$ to the characteristic acceleration a^* of the dry propulsive unit. Equation (16-12) shows that the initial to payload mass ratio is a function only of these two dimensionless parameters, μ and λ, for any kind of electric thrusters. If Eq. (16-3) is used to evaluate λ, Eq. (16-12) will give the initial mass to payload ratio of the space vehicle with ion thrusters. If S.P.C. is taken to be constant (~ 0.7 watt/dyne according to experimental data [3]), Eq. (16-12) will apply to MPD arc jet thrusters. For sputtering thrusters, λ is evaluated with S.P.C. $= (E_i/10)/(\pi/4) S (2 M_n E_n)^{1/2}$ watt/dyne.

From the physical interpretation of the parameter λ, it is clear that if $\lambda > 1$, the mission as specified cannot be achieved by the thruster. A more restrictive condition is indicated by Eq. (16-12), since the denominator must not vanish or become negative. Hence,

$$\lambda < \frac{\mu}{e^\mu - 1} = \frac{1}{1 + \frac{\mu}{2!} + \frac{\mu^2}{3!} + \cdots} < 1 \qquad (16\text{-}13)$$

is a prerequisite for the mission to be fulfilled at the $I_{sp} = \Delta V/\mu g$. The I_{sp} must not be too large so as to keep the characteristic acceleration a^* of the dry propulsive unit sufficiently larger than the average mission acceleration as is defined by Eq. (16-13).

[16-3.3] Optimization with Electric Thrusters

The optimization problem for a given mission will be defined as the one to achieve minimum initial mass to payload ratio. In general, λ is a function of I_{sp} or μ, because both S.P.C. and α may

be functions of I_{sp}. Thus, the optimum I_{sp} of a given system will, in general, depend on the functional behavior of $\lambda(\mu)$. By equating the derivative of (16-12) with respect to μ to zero, we have

$$\lambda \frac{e^\mu - 1}{\mu} \left[\frac{1}{\mu} \left(1 - \frac{\partial \ln \lambda}{\partial \ln \mu} \right) - \frac{1}{e^\mu - 1} \right] = 1. \qquad (16\text{-}14)$$

Here $-\partial \ln \lambda / \partial \ln \mu = \partial \ln \lambda / \partial \ln I_{sp} = \beta > 0$ for most electric thrust-ers.

For ion thrusters $1 \gtrsim \beta > 0$

MPD arc jet thrusters $1 \gg \beta \gtrsim 0$

Sputtering thrusters $1 \gg \beta \cong 0$ near optimum E_i for a given target material. Note that the square bracket must be greater than unity to conform to the restriction inequality (16-13) in order to get a minimum positive value of M_0/w. Otherwise, the smallest μ should be taken.

For ion thrusters, let us take $\beta = 1$ in the neighborhood of $I_{sp} = 5000$ sec. and $\eta_p = 50\%$. For $1/\alpha = 20$ kg/kw, we find that the optimum I_{sp} for imparting a 30 km/sec. velocity increment in one-and-a-half-hear's time is ~ 5000 sec. This is obtained by solving Eq. (16-13) by trial and error. The corresponding values of $\mu = 0.6$ and $\lambda = 2/3$ give the minimum initial to payload mass ratio $(M_0/w)_{\min} \cong 20$.

For MPD arc jet thrusters with $\beta \ll 1$, we find that the square bracket in (16-20) cannot be greater than unity, even if $\mu \to 0$. Con-sequently, the MPD arc jet should be operated at the highest possible I_{sp} consistent with constant S.P.C. to achieve the smallest M_0/w for the specified mission. With S.P.C. = 1/2 kw/gm. wt. for MPD arc jets, we find again from Eq. (16-11) $\lambda = 2/3$. Thus, if MPD arc jets could deliver $I_{sp} \cong 5000$ sec., the minimum initial to payload weight would be $\cong 20$ but substantially higher if the I_{sp} in vacuum were lower than 5000 sec., even if the S.P.C. of MPD jets operating in vacuum could be maintained at 1/2 kw/gm. wt.

For sputtering engines with tantalum target, the mission cannot be fulfilled since the specific impulse of tantalum target is never substantially above 1000 sec. and the inequality (16-13) cannot be satisfied.

For sputtering engines with iron target Fe^{56}, the mean energy data [9] may be written, according to the logarithmic interpolation corrected for the angle of incidence, as

$$\bar{E}_{Fe} = 37 \frac{1 + \cos \alpha}{2} \ln \frac{E_i}{100} \quad \text{e.v.}$$

The yield data [8] may be taken as $S = 5$ when $\alpha = 45°$ at 400 e.v. Let the sputtering engine operate at 1.6 kev. The I_{sp} of sputtered Fe will be 1770 sec. and the S.P.C. = 1/5 kw/gm. wt. according to

the equation for $\bar{E}_{Fe}$ given above. Then $\mu = 1.7$ and $\lambda = 1/3.75$. The initial to final mass ratio is about 18. It should be noted that the mass of the ions is not included in the calculation. This neglect will not introduce significant error because the incident ion mass lodged inside the target surface will be sputtered at a later instant to provide thrust. Both the specific impulse and the specific power consumption will be reduced with compensating effects so that the result of the initial to final vehicle mass ratio will not be seriously altered. If corrections of the mass of Hg^+ or Ta^+ were introduced in the calculation, the $(M_0/w)_{min}$ might be increased from 18 to 20. The data employed in the calculation are not accurate enough to claim an accuracy to within 10% one way or the other.

The examples given above demonstrate an important point. While the sputtering thruster with iron Fe^{56} target delivers a specific impulse, $I_{sp} \lesssim 2000$ sec., substantially below the optimum I_{sp} of 5000 sec. for the ion thrusters (or the MPD arc jets), the sputtering thruster with Fe^{56} target will accomplish the same mission with substantially the same initial to final vehicle mass ratio. The reduced S.P.C. compensates for more than a proportional decrease of I_{sp}.

Let us consider a more ambitious mission of Jupiter pass-by requiring 60 km/sec. velocity increment, or twice the 30 km/sec. considered in the example given above; we expect to accomplish the mission in twice the time, or three years. If we repeat the calculation just given, we find that for the ion thrusters,

$$\text{Optimum} \quad \mu \cong 1 \text{ with } I_{sp} = 6000 \text{ sec.}$$
$$\lambda \cong 0.4$$
$$\text{and minimum } (M_0/w) \cong 8.7.$$

(These values are somewhat higher than those reported in Reference 5, where the thruster propulsive efficiency was taken to be 100%.) Note that the minimum M_0/w for the 60 km/sec. mission is less than that for the 30 km/sec. mission when the mission time τ is proportionately increased from one-and-a-half years to three years to maintain the same average acceleration, $\Delta V/\tau$. This is due to the saving in propellant, for such a long mission overbalances the increase in power plant weight to operate at a higher I_{sp}. The importance of the time limit in accomplishing a given mission is now clearly demonstrated. Such ambitious missions are only marginally feasible for sputtering engines with C or Al as target in a single stage operation [5]. However, in Section 16-3.1, it is indicated that electric thruster stage requiring ΔV in excess of 30 km/sec. is not likely. Hence, the sputtering engine, even with iron target, is attractive in comparison with ion thrusters and MPD arc jet thrusters from a performance point of view alone. Since the electric thruster stage is generally near the end of a multi-stage thrust program, the added feature that

sputtering thrusters offer the possibility of using the structural material of the spent tankage of previous thrust stages will become really significant from the system point of view.

[16-4] SUMMARY AND CONCLUDING REMARKS

We have explored various aspects that are significantly the general characteristics of all types of electric propulsion systems. All electric propulsion systems are power-limited devices with high specific impulse but low thrust. In order to save enough propellant over the chemical system to compensate for the power plant weight to be carried on board the vehicle, the velocity increment of the mission must be large. With the low thrust, the required period of acceleration becomes very long. The severe requirements of reliability and other undesirable aspects associated with stretching a single exploration program to five or even ten years often put the electric propulsion system in an unfavorable light when compared with chemical systems. With these in mind, any advanced concept of electric propulsion should preferably be able to reduce substantially the specific power consumption so as to derive more thrust from limited power on board and to bring about the required ΔV in a shorter period of time. The emphasis of advanced concepts is certainly not higher I_{sp} and doubtfully higher power efficiency. The electrostatic propulsion, *i.e.*, the ion thruster, cannot provide low S.P.C. at low I_{sp}, since its propulsive power efficiency rapidly decreases when I_{sp} becomes less than 5000 seconds. The MPD arc jet thrusters offer little prospects of improving the specific power consumption. The apparent high I_{sp} does not offer much help, even if the effect of entrained gas in test chambers were discounted.

Sputtering of metallic targets by incident ionic high energy particles provides a means of obtaining higher thrust per unit beam power, *i.e.*, lower S.P.C. at reasonably high specific impulse of the sputtered particles. Thus, sputtering may be looked upon as a thrust augmentation process. Based upon interpolated experimental data of sputtering processes, it is demonstrated that a sputtering engine with an iron target operating at 1.6 kev. will give 30 km/sec. velocity increment in one-and-a-half years with possibly a lower initial to final vehicle mass ratio than the ion thrusters operated at an optimum I_{sp} of 5000 sec. or the MPD arc jet at the $I_{sp} \simeq 5000$ sec. If the velocity increment is smaller or the time of acceleration allowed is smaller, the sputtering thruster with an iron target will show a significant advantage.

In addition, the sputtering concept offers the unique possibility that the propellant for an electric thruster can be salvaged from the spent tankage of the previous booster stages. In view of the multi-stage operation of any space exploration program, the

potential savings of using the spent tankage as propellant is highly significant.

Admittedly, the data used for evaluating the sputtering thrusters with Fe target or tantalum target given above are not very reliable. The important future work with respect to developing the sputtering concept is to establish a reliable set of accurate data to verify the calculations reported herein. Neither iron nor tantalum may be expected to be the highest performing target material. If a careful set of data of graphite or aluminum or some other material should become available, and, if either or both of them and others should prove to offer better performance than iron, the horizon of electric propulsion systems in space exploration might be considerably widened.

REFERENCES

1. Stuhlinger, Ernest: Ion Propulsion for Space Flight, New York, McGraw-Hill, 1964 (and other references by the same author).
2. Ernstene, M.P.: Progress and Prospects of Electrical Propulsion, Review article, AIAA Third Annual Meeting, Boston, Nov.—Dec. 1966.
3. John, R.R. and S. Bennett: Recent Advances in Electrothermal and Hybrid Electrothermal-Electromagnetic Propulsion, Fourth Symposium on Advanced Propulsion Concepts, Palo Alto, 1965.
4. ———, *et.al.*: Arc Jet Technology Research and Development, Final Report through Dec. 1965, *RAD-TR-65-37*, AVCO Corp., Wilmington, Mass., and *NASA CR-54687* (a comprehensive review).
5. Cheng, S.I.: Sputtering as an Advanced Concept of Space Propulsion, *Astronautica Acta*, July–August 1966.
6. Kaminsky, M.: Atomic and Ionic Impact Phenomena on Metal Surfaces, Struktur und Eigenshaften Der Materie XXV, Springer-Verlag and Academic Press, 1965, Chap. 10.
7. Cheng, S.I.: Glow Discharge as an Advanced Propulsion Device, *J. of Am. Rocket Soc.*, December 1962.
8. Wehner, G.K.: Influence of Angle of Incidence on Sputtering Yields, *J. of Applied Physics*, 30, 1762, 1959.
9. Kopitzki, K. and H.E. Stier: Mittelere Kinetische Energie der bei der Kathodenzerstäubung von Metallen ausgesandten Partikel, *Z. Naturforschung*, 17a, 1962.

Zero g Propulsion Problems*

John F. McCarthy, Jr.
Vice President,
Research, Engineering, and Test
Space Division
North American Rockwell Corporation

[17-1] INTRODUCTION

In preceding chapters, the analysis, design and, to some extent, the fabrication of a wide spectrum of propulsion devices have been considered, devices ranging from the more familiar high-thrust jet propulsion engines to advanced electrical propulsion systems with high specific impulse. Attention has been directed to the detailed design of the engines (thrust chambers), to meet specified performance requirements through trade-off analyses of parameters such as specific impulse, thrust nozzle performance, propellant mass flow, etc. Under such emphasis, it is generally and appropriately assumed that the propellants or working fluids are instantly available when required for engine ignition and operation. This assumption is particularly valid for solid-propellant rockets in which the burning of the grain is readily controlled and the propellant is always predictably contained. For hybrid or pure liquid-propulsion systems, however, this predictable containment of the liquid propellant is not always readily possible. For example, when the system is operated in the weightless state of a zero-gravity environment, the liquid may migrate from the tank bottom. In partially filled tanks, moreover, the propellant may be subjected to perturbations such as a change of g-field due to engine cutoff, vehicle attitude changes, astronaut motions, and limit-cycle oscillations. The resultant motion of the propellant could displace the fluid from the tank outlet so that the propellant would not be available for engine start. It thus becomes apparent, from an operational point of view, that a basic requirement of any propulsion system utilizing liquid propellant is the assurance of the immediate availability of a single-phase propellant (free of bubbles) at the tank outlet for proper engine ignition. The major portion of this chapter

will be devoted to the examination of liquid behavior in zero g and of various means of controlling the position (containment) of the propellant within the tank to satisfy the engine restart requirement.

Because of the relative complexity of the subject and the voluminous amount of material to be covered, Fig. 17-1 gives a diagrammatic flow of the specific topics that will be presented in the chapter. The discussion begins with the basic definitions and the major problems associated with liquid-propulsion systems operating in a zero-g environment. The simple case of hydrostatics is then considered from a theoretical approach, and the equilibrium configuration of a liquid-gas-solid combination is predicted by using the minimum-energy principle. For the more complex case of hydrodynamics, only limited analytical approaches can be made to solve the dynamic problems. As a consequence, a semi-empirical approach is taken, and emphasis is placed on describing the techniques and procedures for deriving applicable design data. The discussion is continued through consideration of propellant slosh due to perturbations arising from vehicle attitude change and engine cutoff. These disturbances upset the equilibrium condition, introducing propellant motion so that control of propellant position is required. Three types of position control are discussed: active systems (*e.g.,* bellows), semiactive systems (*e.g.,* thrusting for propellant settling), and passive systems (*e.g.,* capillary barrier). Specific experiments and theoretical developments are itemized in the block on modeling and test. Because available theoretical approaches are limited, dimensional analysis utilizing the pi theorem is used to scale the models and the g-field for the various tests. Where possible, utilizing dimensional analysis techniques, the models are designed so that tests can be performed at 1 g. When required, vertical drops and aircraft flying zero-g (parabolic) trajectories are used to simulate the zero-g environment. The test results are correlated with dimensionless parameters, such as the Bond, Froude, Weber, and Reynolds numbers, and design information is derived. A short discussion of propellant gauging is included, and the chapter is closed with several conclusions.

[17-2] BASIC DEFINITIONS

In the course of the chapter, a number of physical concepts and terminologies will be presented. There are, however, a few basic definitions that are fundamental to the understanding of the chapter and that require early introduction. Among these are the meaning of zero gravity, liquid-container contact angle, surface tension, surface energy, and the principle of minimum energy.
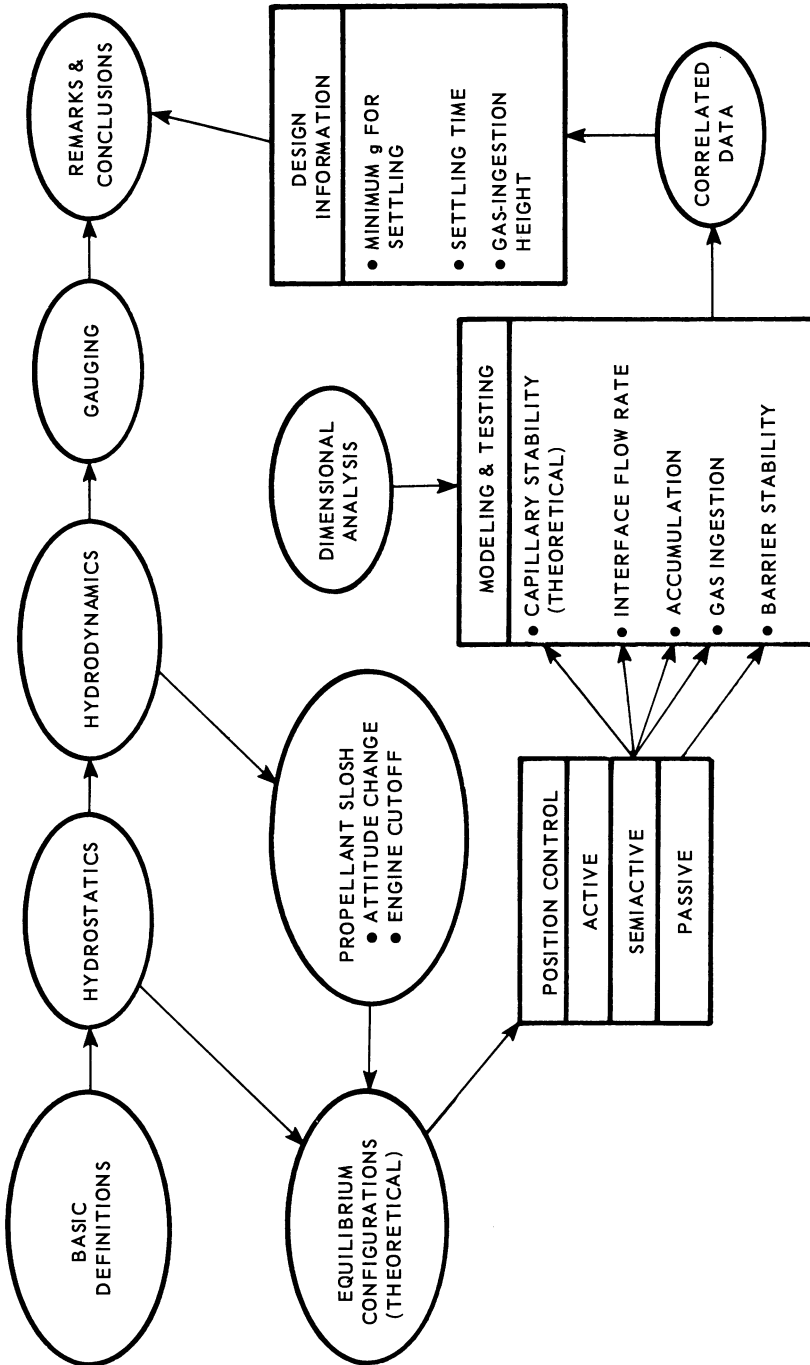
Fig. 17-1 Scope of chapter.

[17-2.1] Zero Gravity

Newton's law of gravitation states that every body in the universe attracts every other body with a force that is directly proportional to the product of the masses and inversely proportional to the square of the distance between their centers. thus,

$$F_g = G\frac{mM}{r^2} = mg \qquad (17\text{-}1)$$

where

F_g = gravitational force of attraction
G = universal gravitational constant
m = mass of smaller body
M = mass of larger body
r = distance between the centers of masses m and M
$g := GM/r^2$ = acceleration due to gravity associated with mass M.

For example, if M is the mass of the earth and r is the radius of the earth, the gravitational acceleration at the surface of the earth is 32.17 ft./sec.^{2}.

Newton's second law of motion (the law of momentum) states that the force is directly proportional to the time rate of change of linear momentum. For the case of constant mass, the force is simply equal to the mass times the acceleration. The total force, however, can be broken into two components: one due to gravitational attraction, and the other due to an externally applied force which may be a simple reactionary force. Consequently, the acceleration of a body can be expressed as a direct function of both the gravitational and externally applied forces:

$$F = ma = F_g + F_e \qquad (17\text{-}2)$$

$$a = \frac{F_g + F_e}{m} = g + \frac{F_e}{m} \qquad (17\text{-}3)$$

where

F = force
F_e = applied external force
a = acceleration.

Zero gravity, as it will be defined in the chapter, can now be explained with the aid of Fig. 17-2. Consider the following three situations: (1) Static: the net unbalanced force on the vehicle is zero, and the case if merely one where the reactionary force just balances the gravitational force. (2) Acceleration: here the external
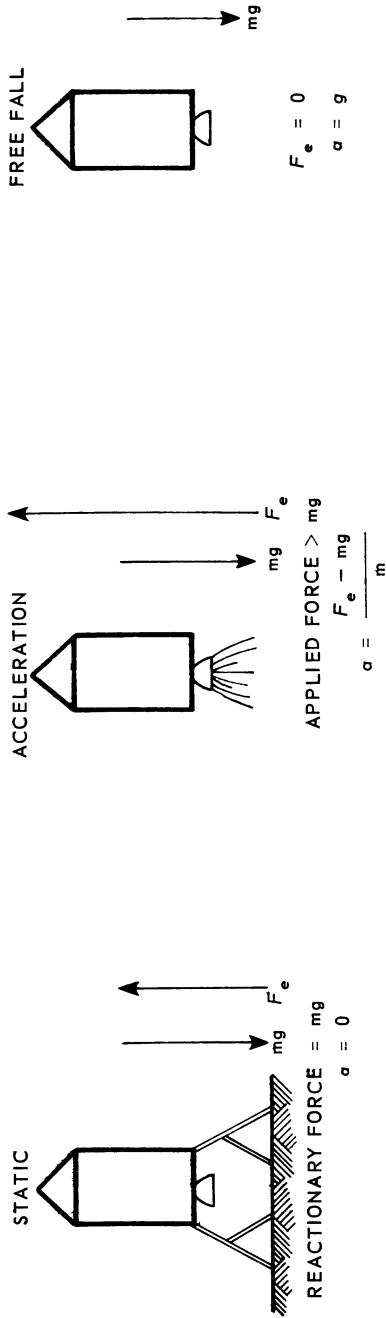
Fig. 17-2 Zero gravity.

force is due to the propulsion system. The net unbalanced force causes the vehicle to accelerate in the direction of the thrusting. (3) Free fall: the only force in this case is that due to gravity, and the vehicle free-falls (weightless state) with an acceleration equal to the acceleration due to gravity. For the purpose of this chapter, the body will be defined as being in zero g when it is in free fall, *i.e.*, when the net unbalanced external force acting on the body is zero, and the body is accelerating with an acceleration equal to g. It is important to note that zero g does not mean the *absence* of gravity.

[17-2.2] Engineering Considerations of Zero-g Environment

In moving from the environment of earth gravity to that of zero g, engineering considerations of fluid behavior take on different perspectives and emphasis. Unlike the familiar cases in which gravitational and inertial effects are the predominant influences on fluid behavior, in zero g the environmental intermolecular forces become important, and the macroscopic consideration of these forces on fluid behavior is required. Intermolecular forces seldom play an important role in the fluid mechanics of 1-g environment except in isolated problems such as the medical thermometer.

One effect of intermolecular forces is the contact angle θ, which is illustrated in Fig. 17-3. The vertex of the contact angle is at the point of intersection between the meniscus and the container and is measured through the liquid between their respective tangent lines at the point of intersection. The magnitude of the contact angle is a function of the liquid-gas-solid combination; however, it will be shown that, for any given combination, the contact angle is invariant with changes in gravity.
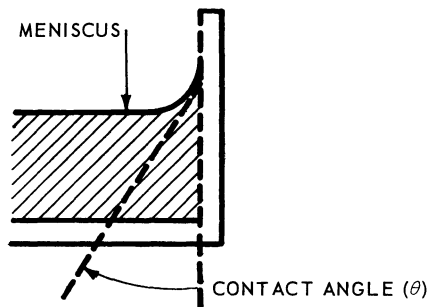

Fig. 17-3 Contact angle.

The meaning of surface tension can be illustrated by a simple experiment. Submerge a U-shaped wire in the liquid and apply a force to lift the wire out of the water so that a film of liquid is attached to and draped over the wire (Fig. 17-4). For an equilibrium condition, the liquid film exerts a force equal and opposite to the applied force. Since each side of the film exerts a force equal to the surface tension σ times the length of the wire l, the total force is $F = 2\sigma l$. Therefore, by measuring the magnitude of the applied force and dividing by twice the length of the wire, the surface tension of a liquid can be determined.
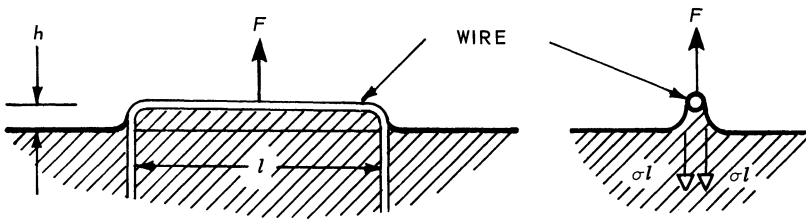
Fig. 17-4 Surface tension.

It can be seen from Fig. 17-4 that the force required to lift the wire out of the liquid to a height, h, performs work equal to force times distance. When the applied force and the opposing force arising from surface tension are equal, the system is in static equilibrium and has potential energy. The stored potential energy is contained in the film of liquid. If the applied force is removed, the film, in regaining its original undisplaced condition, can do the amount of work equal to the applied force the distance h. The concept of surface energy can thus be viewed as stored potential energy with the ability to do work like a stretched elastic membrane, such as an inflated balloon. For the simple experiment described above, the surface energy per unit area γ is equal to the work divided by the area of the film:

$$\gamma = \frac{Fh}{2\,lh}.$$
(17-4)

Note from the equation that the height cancels so that the dimension of the surface energy per unit area is force divided by length, which is dimensionally the same as that for surface tension.

In a closed container partially filled with liquid, surface energies exist at the solid-vapor interface, liquid-solid interface, and liquid-vapor interface (Fig. 17-5). In addition, the liquid can have kinetic and potential energies. For hydrostatic considerations, however, the kinetic energy is zero, and the system contains only potential energies. Surface energy is a form of potential energy.

In the following sections, the stable configurations of the liquid-vapor interface will be determined by using the principle of minimum energy. This principle states that the meniscus of the liquid will attain a shape so that the sum of the surface energies and potential energies is a minimum. In zero gravity, for example, the potential energy disappears, and the three interfaces can be thought of as three stretched membranes, all contracting or expanding in such a way that the resulting stable configuration will have minimum energy. As will be proven subsequently, if a bubble exists in the liquid in zero g and is stable, its shape is spherical.

[17-3] HYDROSTATICS

The concept of surface energies having been defined, it is instructional and a desirable first step to predict theoretically, using the minimum-energy principle, the equilibrium configuration of fluids in a partially filled closed container under the environment of zero g. The mathematical development [1] is based on hydrostatics and will serve as the foundation for the subsequent detailed discussion of hydrodynamics in zero g. For clarity, emphasis is placed on presenting the basic steps in the development, while avoiding the associated detailed mathematical manipulations.

[17-3.1] The Variational Problem

Consider Fig. 17-5. The container, partially filled with a liquid, is a body of revolution of surface area A. Cylindrical coordinates having an arbitrary origin in the liquid are used, where the y axis is the axis of symmetry and the r axis is perpendicular to the y axis. The third coordinate, ϕ, is not shown in this figure. The problem to be solved can be stated as follows: given $y = x(r)$, which denotes the solid-vapor interface, and $y = x_1(r)$, which denotes the liquid-solid interface, what is $y = y(r)$, which denotes the liquid-vapor interface when the system is in static equilibrium in a zero-g environment? A necessary step

Fig. 17-5 Coordinates and interfaces.
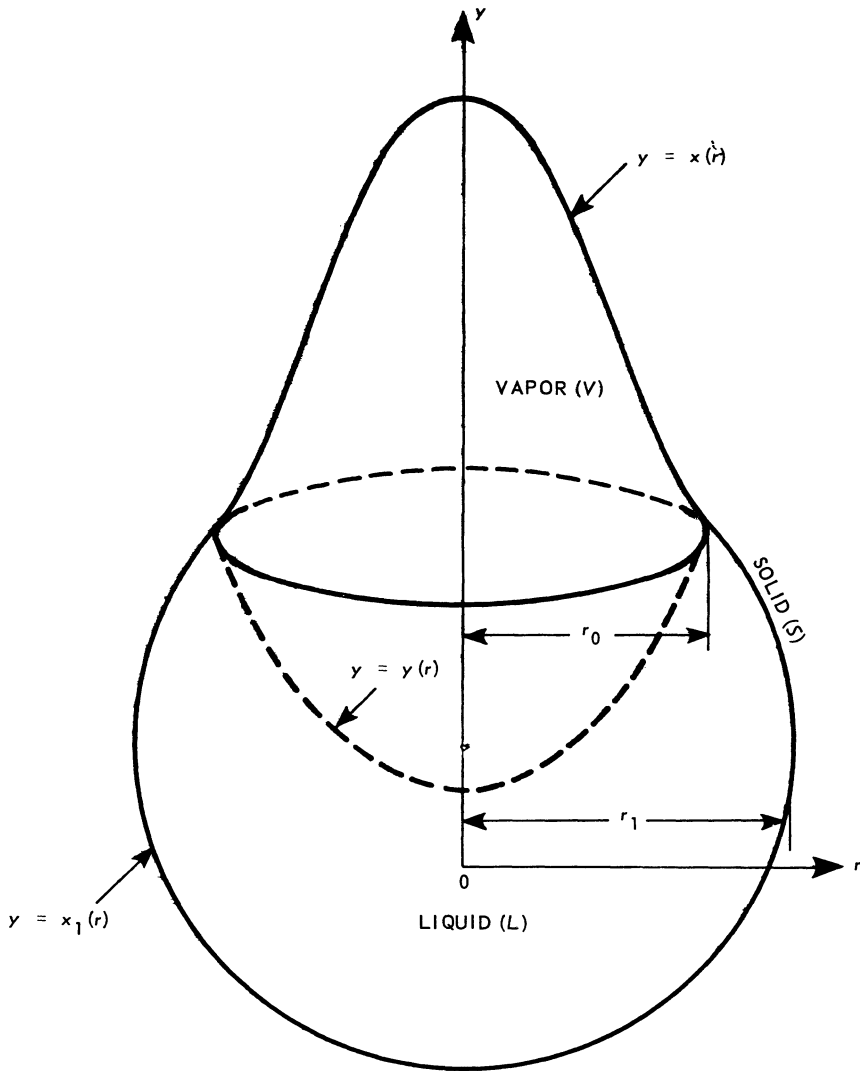
in the mathematical process is to derive an expression for the total surface energy of the system. The surface energy per unit area for the vapor-solid, liquid-solid, and liquid-vapor interfaces can be symbolically represented, respectively, as γ_{VS}, γ_{LS}, and γ_{LV}. From elementary calculus, the corresponding surface areas of the three interfaces can be expressed as

$$A_{VS} = 2\pi \int_0^{r_0} \sqrt{1 + \left(\frac{dx}{dr}\right)^2} \, r \, dr \qquad (17\text{-}5)$$

$$A_{LS} = 2\pi \int_0^{r_0} \sqrt{1 + \left(\frac{dx_1}{dr}\right)^2} \, r \, dr = A - A_{VS} \qquad (17\text{-}6)$$

$$A_{LV} = 2\pi \int_0^{r_0} \sqrt{1 + \left(\frac{dy}{dr}\right)^2} \, r \, dr \qquad . \qquad (17\text{-}7)$$

The surface energies for each of the three interfaces can be determined by multiplying the area of a given interface with the corresponding surface energy per unit area. The summation of these three products will then be equal to the total surface energy, *i.e.*,

$$\text{S.E.} = \gamma_{VS} A_{VS} + \gamma_{LS} A_{LS} + \gamma_{LV} A_{LV} \qquad . \qquad (17\text{-}8)$$

Although potential energy other than surface energy does not exist in a zero-g environment, the potential-energy terms will be retained and set equal to zero only when g is zero, in order to develop the problem completely. By taking $\bar{y}$ as an arbitrary reference level (see Fig. 17-6), the potential energy of the liquid can be expressed mathematically by considering an incremental volume, then multiplying this delta volume by the liquid density ρ, gravity g, and height h above $\bar{y}$. For the liquid under consideration, its volume is divided into volume P_1 (a cylindrical column) and P_2 (the remainder of the liquid). The division of the liquid into volumes P_1 and P_2 is made because volume P_1 is bounded by $y = y(r)$, and volume P_2 is bounded by $y = x_1(r)$. The potential energy expressions for regions P_1 and P_2 are:

$$PE_1 = g\rho \int_0^{r_0} \int_0^{2\pi} \int_{\bar{y}}^y h \, dh \, r \, d\phi \, dr \qquad (17\text{-}9)$$

$$= \pi g\rho \int_0^{r_0} (y^2 - \bar{y}^2) \, r \, dr \qquad (17\text{-}10)$$

$$PE_2 = g\rho \int_{r_0}^{r_1} \int_0^{2\pi} \int_{\bar{y}}^{x_1} h \, dh \, r \, d\phi \, dr \qquad (17\text{-}11)$$

$$= \pi g\rho \int_{r_0}^{r_1} \left(x_1^2 - \bar{y}^2\right) r \, dr \qquad . \qquad (17\text{-}12)$$

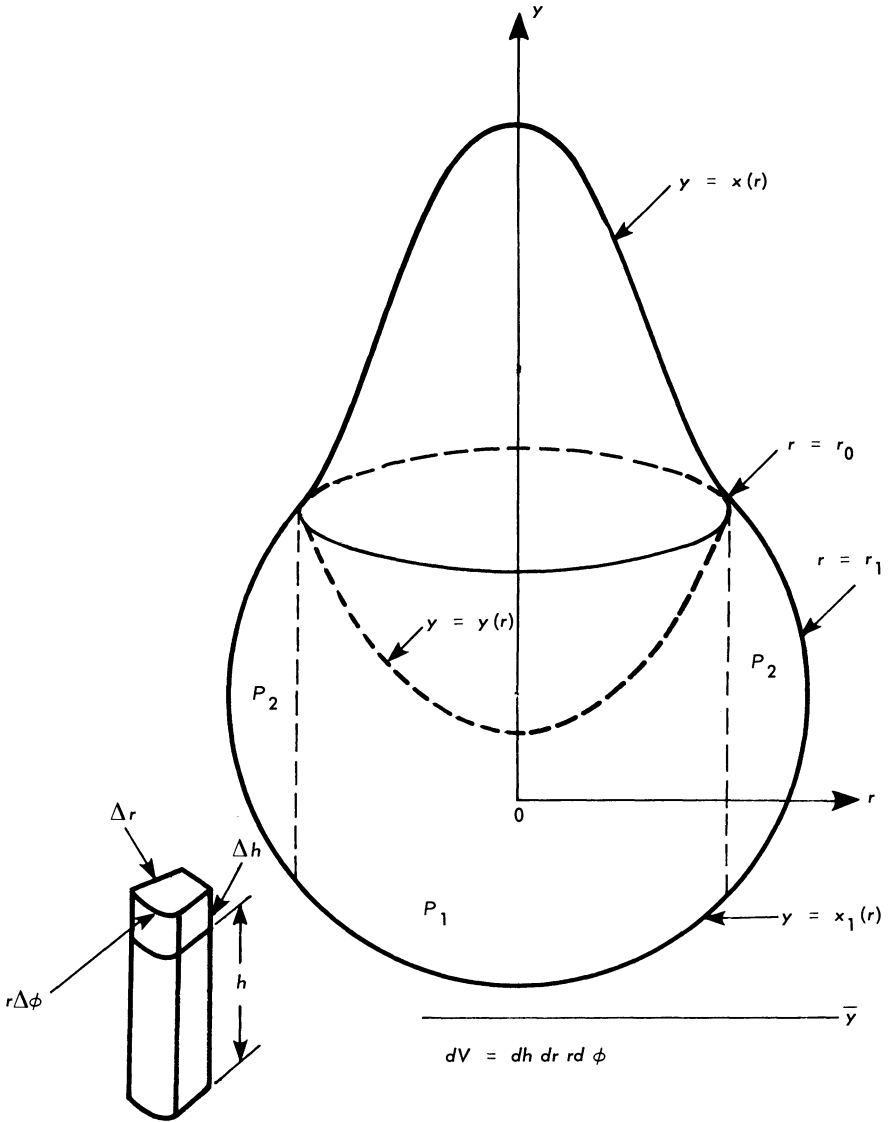The total potential energy is simply the sum of PE_1 and PE_2.

Fig. 17-6 Coordinates for potential energy.

The equations for the surface energies and potential energies having been derived, the total energy in the system can be expressed as

$$2 \pi \gamma_{VL} \int_0^{r_0} \sqrt{1 + \left(\frac{dy}{dr}\right)^2} \; r \, dr + 2 \pi \, (\gamma_{VS} - \gamma_{LS}) \int_0^{r_0} \sqrt{1 + \left(\frac{dx}{dr}\right)^2} \; r \, dr$$

$$+ 2 \pi \gamma_{LS} A + \pi g \rho \int_0^{r_0} \left(y^2 - x_1^2\right) r \, dr + \pi g \rho \int_0^{r_1} \left(x_1^2 - \bar{y}^2\right) r \, dr = \text{minimum.} \tag{17-13}$$

The minimum–energy principle dictates that the total energy must be equal to a minimum. This equation is amenable to solution by the methods of the calculus of variations. Note that the third and fifth terms of the total–energy equation are constants (the upper limit of integration, r_1 in the fifth term, is the maximum diameter of the container, a constant, and the function x_1 does not vary). These constant terms drop out in the variational process and do not contribute to the final solution.

[17-3.2] Solutions for the Variational Problem

The following substitution is made prior to minimizing the total–energy equation:

$$\gamma_{VS} - \gamma_{SL} = \omega \, \gamma_{LV} \tag{17-14}$$

where

ω = parameter.

The magnitude of this parameter, to be determined subsequently, will be instrumental in deriving the equilibrium liquid-solid contact angle.

Two equations of importance result from the variational process: (1) the characteristic equation and (2) the equation representing the terminal condition at point r_0 (r_0 is the common root of $y = x[r]$ and $y = y[r]$, which were defined earlier). These equations are:

Characteristic equation

$$\frac{d}{dr} \left(\frac{r \dfrac{dy}{dr}}{\sqrt{1 + \left(\dfrac{dy}{dr}\right)^2}} \right) = \frac{g \rho r y}{\sigma} + \lambda r \tag{17-15}$$

where

λ = Lagrange multiplier.

Terminal condition (at r_0.)

$$\frac{dy}{dr} = \frac{-\dfrac{dx}{dr} \pm \omega\sqrt{1-\omega^2}\left[1 + \left(\dfrac{dx}{dr}\right)^2\right]}{(1-\omega^2)\left(\dfrac{dx}{dr}\right)^2 - \omega^2} \; . \qquad (17\text{-}16)$$

Before proceeding with the solution of these two equations, it is necessary to introduce the constraint that the volume of the vapor remains constant. The mathematical expression for this constraint is

$$2\pi \int_0^{r_0} (x - y)\, r\, dr = \beta V \qquad (17\text{-}17)$$

where

β = volume of vapor/volume of container
V = volume of container.

Consider now the solution of the characteristic equation, Eq. (17-15). Integration of the characteristic equation yields a solution involving the term λ, a Lagrange multiplier. By substituting this solution into the equation defined by the problem constraint, Eq. (17-17), and solving, the value of the Lagrange multiplier can be determined. This solution for conditions of zero g and no contact angle yields the following expression for the liquid-vapor interface:

$$(y - \bar{y})^2 + r^2 = \left[\left(\frac{3\beta V}{4\pi}\right)^{\frac{1}{3}}\right]^2 . \qquad (17\text{-}18)$$

It can be readily seen that Eq. (17-18) is a circle. Since this circle generates, by revolution, the interfacial surface, it can be concluded that the equilibrium liquid-vapor interface is spherical.

Inspection of the equation for the terminal condition, Eq. (17-16), shows that ω^2 must be less than or equal to unity to avoid imaginary roots. Because the cosine of an angle varies between minus one and plus one, a mathematical substitution can be made in Eq. (17-16) by arbitrarily setting $\omega = \cos\theta$. The approach is to then solve
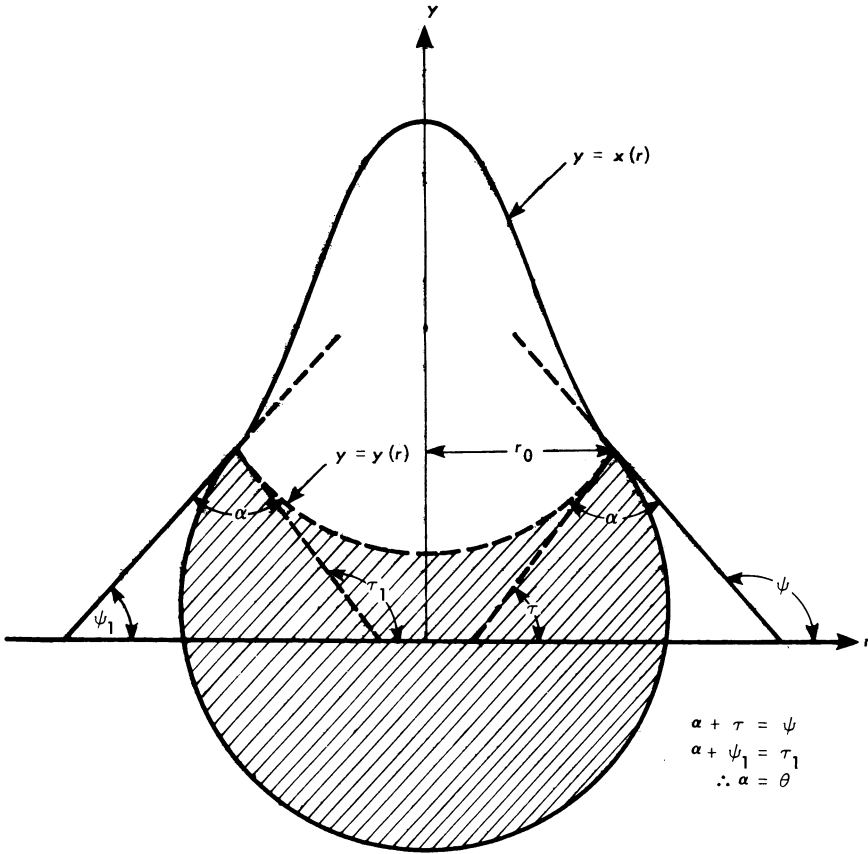
Fig. 17-7 Angular relationships.

Eq. (17-16) in terms of the angle θ and then to determine its physical significance. By constructing the various angles indicated in Fig. 17-7 and substituting into the equation, the following solutions can be obtained:

$$\tan \tau = \tan (\psi - \theta) \quad (+) \tag{17-19}$$

$$\tan \tau_1 = \tan (\psi_1 + \theta) \quad (-) \tag{17-20}$$

The plus sign refers to the positive root of the equation, and the negative sign refers to the negative root. Examination of the interrelationship of the angles τ, τ_1, ψ, ψ_1, α, and θ shows that α must be equal to θ. It is concluded, therefore, that θ physically is the contact angle, and since the expressions for the solution of the equation are independent of gravity, it is further concluded that the contact angle is independent of gravity.

The key conclusions drawn from the hydrostatic analysis using the minimum-energy principle are: (1) that the contact angle of a given liquid-solid combination is constant and invariant with changes in gravitation independent of g, and (2) that if a stable bubble exists in zero g, its shape is spherical. For a nonspherical container, it can be deduced from these conclusions that in going from an environment of one g to that of zero g, the commonly known flat meniscus of liquid-solid combinations whose contact angles are not 90 degrees would be curved (part of a sphere), with the contact angle preserved in each case (Fig. 17-8). For a 90-degree contact angle, the meniscus is still flat, but it could be interpreted that the radius of curvature for the meniscus is infinite. Figure 17-8 illustrates the static equilibrium shapes of the meniscus for different liquid-solid combinations in one-g and zero-g environments. The meniscus is concave for a liquid-solid combination that wets and convex for a combination that does not wet. A point of interest is that water against clean glass forms a contact angle of approximately zero degrees, while water against graphite yields a contact angle of about 90 degrees. Almost all propellants in metal containers have contact angles close to zero. The influence of the gas on contact angle in a liquid-gas-solid combination is negligible, but if two different liquids are in contact with a solid, the contact angle is a function of both liquids and the solid

[17- 4] STATIC CONFIGURATIONS IN ZERO g

Some possible static configurations that could exist in zero g for partially filled, closed containers are illustrated in Fig. 17-9. For a spherical container, the permissible shapes are dependent on contact angle, which may vary considerably depending upon the nature of the liquid-solid combination. Note that a wetting liquid implies that the contact angle is less than 90 degrees. The situation of a contact angle of approximately zero is considered unique because the vapor bubble is stable and will not "burst" if it comes into contact with the wall. For example, a vapor bubble for a liquid that normally makes a contact angle of 45 degrees with its container would, upon touching the wall, immediately begin to deform; it would then form a portion of a bubble with a contact angle of 45 degrees at its intersection with the wall. The corresponding unique condition for a nonwetting liquid would occur at a contact angle of about 180 degrees. For the type of configuration shown in the center of the three spherical containers, the liquid-vapor interface is stable for all contact angles greater than zero but less than 180 degrees.
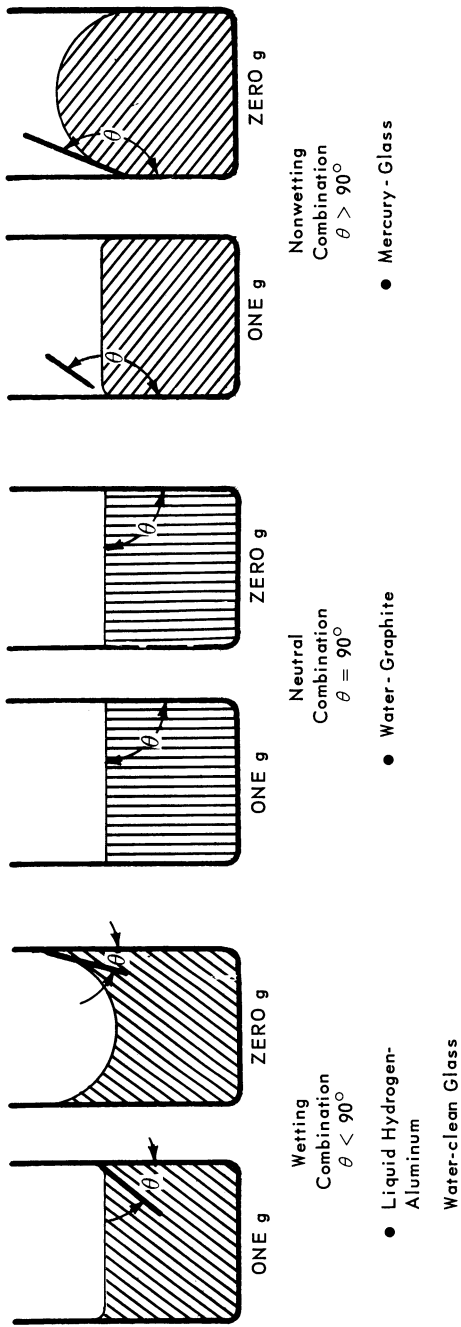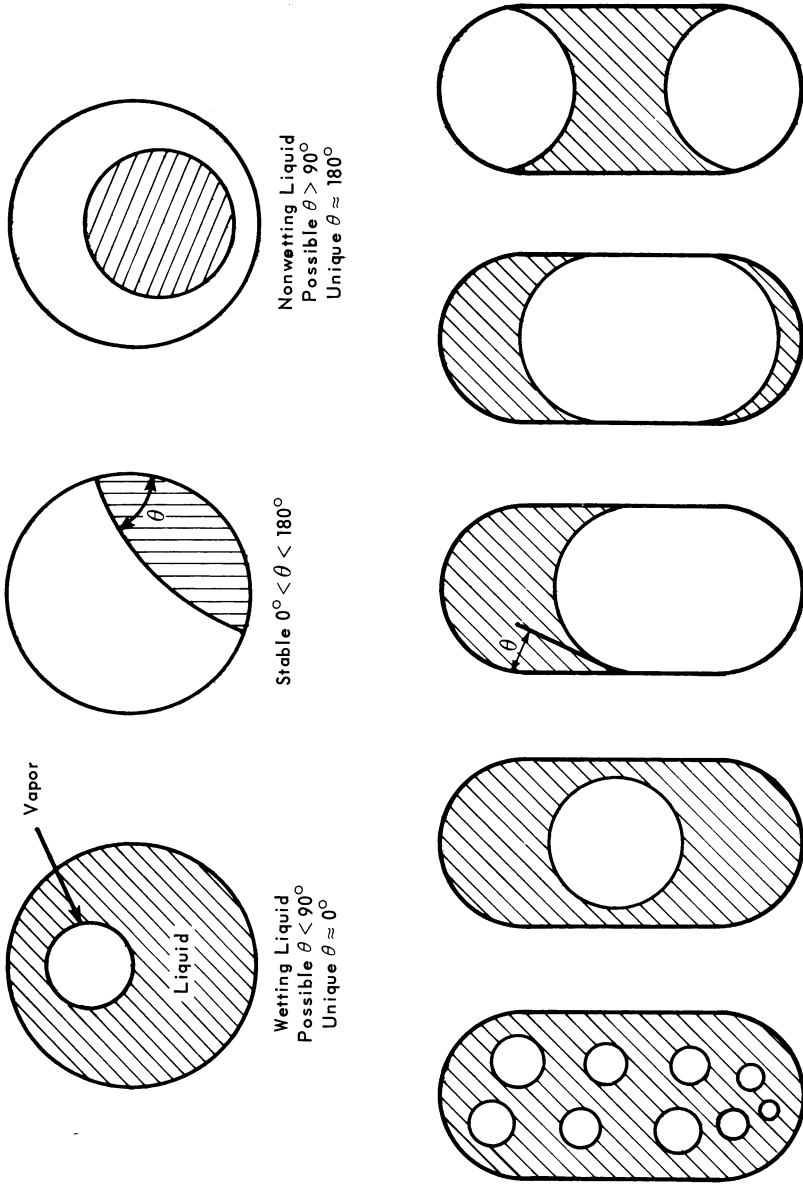
Fig. 17-8 Comparison of meniscus shapes.

Fig. 17-9 Static configurations in zero g.

Five specific configurations are shown in Fig. 17-9 for a cylindrical tank with spherical ends. The liquid can have many bubbles or a single large bubble (the minimum–energy condition); it can collect in one end, collect in both ends, or collect in the center of the tank. While the liquid–at–center configuration is not likely for short tanks, it is the expected configuration for extremely long tanks or for a pipe containing both liquid and gas. A number of experiments have been described [2] which verify many of these zero–g interface shapes.

The contact angle for most propellant–solid combinations is near zero. Therefore, in subsequent sections dealing with space-craft tankage problems, the contact angle will be assumed to be approximately zero.

[17-5] HYDRODYNAMICS

In the foregoing sections, hydrostatic considerations were dis-cussed which relate to the behavior of propellants in a weightless or zero–g environment. It was shown that intermolecular or capillary forces predominate and explicitly determine the possible stable configurations which the liquid and gas can take. With this background, it is interesting to consider the more complex dynamic behavior of propellant that results from various disturbances. It will be shown, for example, that translation or rotation of a spacecraft, such as that shown in Fig. 17-10, may result in re-location of the propellant. The uncertainty of propellant location leads to the problem of determining methods for propellant con-trol. Propellant-location control may be accomplished by devices which prevent the dislocation of the liquid or by schemes for re-locating the propellant after a dislocation has occurred. During drainage of the propellant from a tank under a low-gravity field or during a small vehicle thrust that creates an apparent gravity field, the liquid surface may distort, resulting in ingestion of gas into the outlet line.

In general, the available analytic methods for solving these hydrodynamic problems have not been adequate, and extensive testing has been required to provide the necessary design informa-tion. Therefore, the dimensional analysis, test procedure, and results of test programs for some of these problem areas will be the basis for the discussions which follow. The tests from which those results were obtained were conducted at North American Rockwell Corporation's Space Division. Following is a brief de-scription of the test facilities and of the methods used to achieve "laboratory" zero-g test conditions.

Figure 17-11 illustrates the drop tower test assembly used by the Space Division of North American Rockwell Corporation. It consists of a drag shield and a test package. When the entire
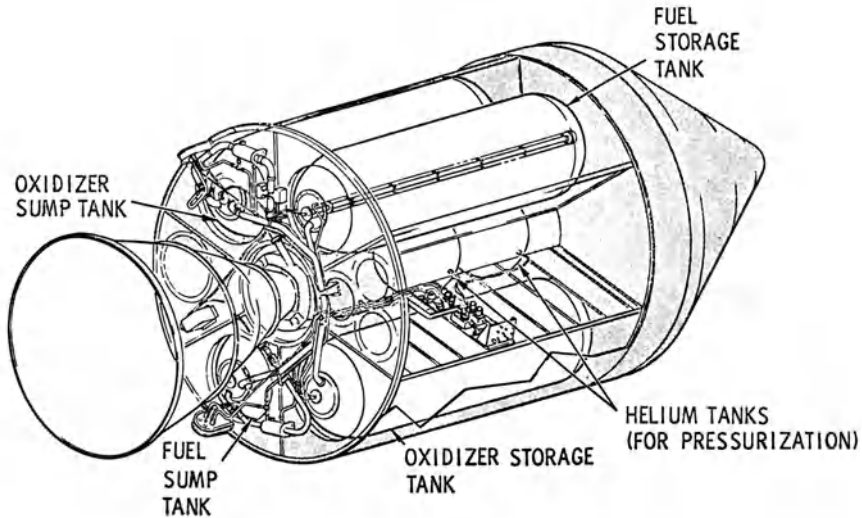
Fig. 17-10 Tankage of service propulsion system for apollo spacecraft.

assembly is dropped, the hook pulls free, and the test package falls inside the drag shield at a low velocity relative to the shield. This arrangement permits the drag shield to isolate the test package from aerodynamic drag. Provision is made within the test package for rotating the test model about various centers with respect to the model center. A program timer controls the starting and stopping of the rotation according to a predetermined schedule. Approximately two seconds of essentially free-fall environment can be obtained with a height of 64 feet.

Another method of obtaining a zero-g environment is to fly an aircraft in a trajectory so that its horizontal velocity is constant and its vertical acceleration is equal to the local acceleration due to gravity. Test durations of as high as 30 seconds, at very low g, have been achieved in KC-135 aircraft flying such trajectories out of Wright-Patterson Air Force Base, Ohio. This airborne test facility was used for several of the test programs discussed in this chapter.

[17-5.1] Propellant Slosh at Zero g

When a partially filled propellant tank is rotated, as in Fig. 17-12, the liquid will tend to resist both rotation and translation and will generally be displace, relative to the tank, from its initial location. The actual resultant distortion of the liquid interface is dependent on several factors, particularly on tank shape and center of rotation. Idealized cases are shown here.
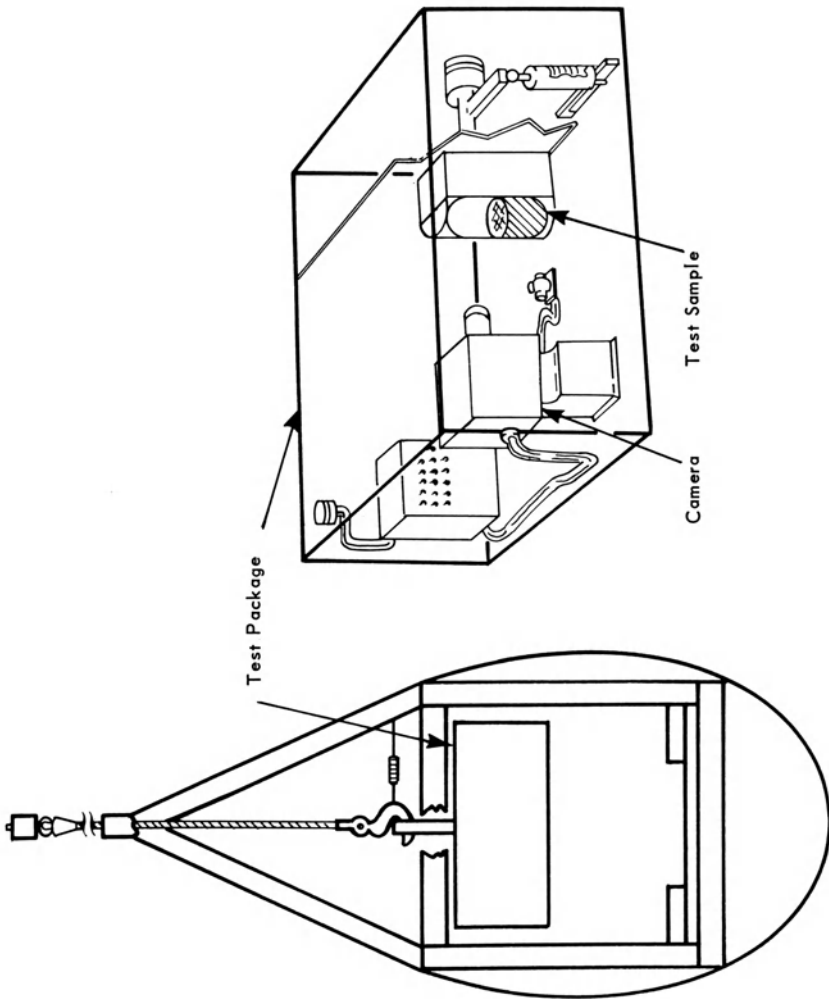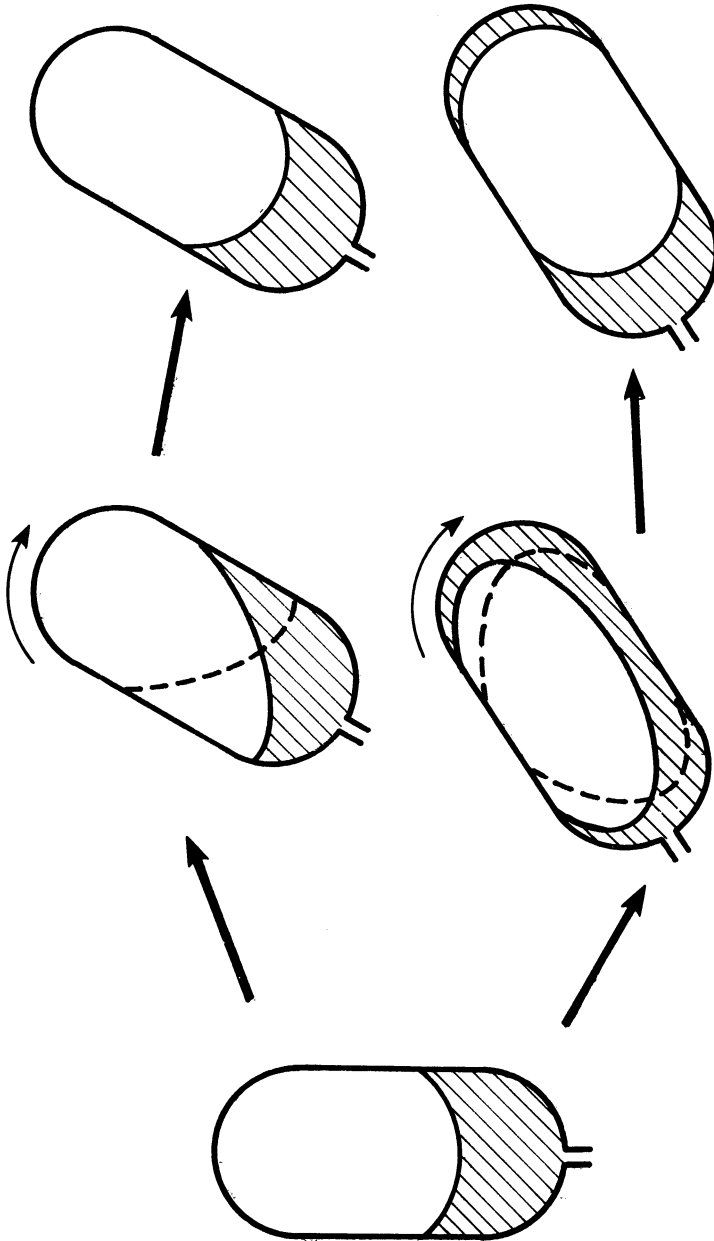
Fig. 17-11 Drop tower test assembly.

Fig. 17-12 Zero-g propellant slosh due to change of vehicle attitude.

The liquid–gas interface is now different from the static equilibrium configuration, and surface forces will act to restore the interface to its original shape. If viscous damping is not too great, an over-shoot of the surface shape will occur and periodic oscillation will result. If the initial disturbance causes liquid to flow into the opposite end of the tank, the liquid will tend to separate and finally come to rest in both ends.

The angular frequency of the liquid oscillation can be estimated from the following expression:

$$\omega = \left[\left(3.68 \frac{g}{D} + K \frac{\sigma}{\rho D^3} \right) \tanh 3.68 \frac{h}{D} \right]^{\frac{1}{2}} \qquad (17\text{--}21)$$

where

   ω = angular frequency of oscillation
   D = tank diameter
   h = height of liquid in tank
   K = dimensionless constant.

A value for K of 49.8 is obtained from linearized potential theory, which assumes small–amplitude displacement from an initially hemispherical interface is allowed. This equation is derived for a tank with a flat bottom. When the height h of liquid in the tank is greater than about one–half the tank diameter, the hyperbolic tangent approaches unity, and the effect of the tank bottom be-comes negligible. For the system shown in Fig. 17–10, for zero g Eq. (17–21) gives

$$0.014 < \omega < 0.0287 \text{ rad/sec.}$$

$$219 < \text{period} < 450 \text{ sec.}$$

depending on the amount of propellant or fuel in the tanks and the value of K used.

During boost or operation of the main propulsion system, accel-eration, or apparent gravity, is high. Under this relatively high-g period, propellant sloshing is likely to occur due to normal per-turbations, such as oscillations caused by the flight control system. Since the energy level of propellant slosh is proportional to g for a fixed tank size and wave amplitude, it is generally large com-pared with the zero-g slosh mode discussed previously, even though the amplitude is much smaller. This mode of propellant slosh could cause problems in the control of vehicle attitude.

In the course of this high-g sloshing, the slosh energy alternates between potential and kinetic forms. When the wave crests and is

at its maximum amplitude, the liquid motion is essentially stopped, and the energy is in potential form. When the wave height is zero, as is represented by a flat liquid surface, the liquid motion is at maximum velocity, and the slosh energy is in kinetic form. When the propulsion system thrust is terminated, the vehicle is at once in a low-g environment. If the propellant slosh wave is primarily in its kinetic form at the time of engine cutoff, the energy will persist, resulting in a large-amplitude distortion of the liquid surface.

Drop tower tests have been conducted to investigate this mode of liquid motion, and a typical test result is shown in Fig. 17-13. The wave front progresses in the direction it was moving at the time of transition from high g to free fall and continues around the
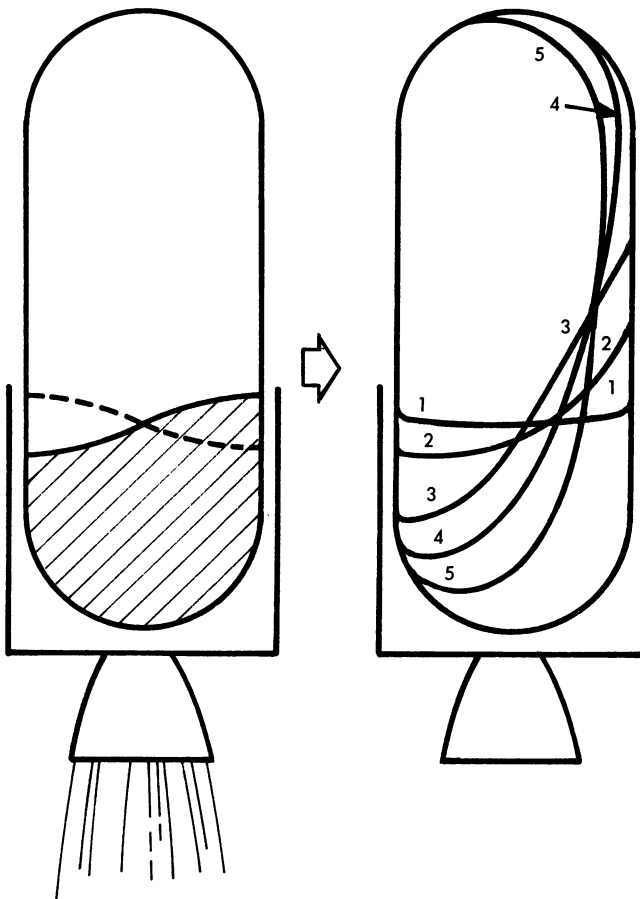

Fig. 17-13 Propellant motion at engine cutoff.

tank until the leading edge of the circulating liquid flows into the liquid which may have remained at the bottom of the tank. Unfortunately, the test duration of approximately two seconds has been too short to permit determination of the final configuration of the fluid.

[17-5.2] Propellant-Position Control

It has been shown that vehicle attitude change can result in dislocation of propellant from its original position in the tank. The residual kinetic energy arising from slosh during thrusting also results in large-amplitude propellant motion. In addition, translation, docking jolts, and aerodynamic drag may act to move the propellant out of its original location. It is concluded, therefore, that a means must be provided for controlling propellant position if the propulsion system requires that liquid be provided to the engine for start-up. (Recent innovations in the design of liquid-fueled rockets may eliminate this requirement. In this case, the rocket operates in "idle mode" and provides a low thrust level while the propellant settles. During this idle-mode period, any mixture of liquid and gas, or only gas, will suffice.)

For convenience, the various propellant-position control systems have been classified into three groups: active, semiactive, and passive. Active systems (Fig. 17-14a), such as bladders, pistons, or bellows, are variable-volume devices which accommodate changes in volume as the propellant quantity varies. Accordingly, for such positive expulsion devices there is no liquid-gas interface, and uncontrolled behavior in low gravity is nonexistent.

For semiactive systems, two approaches are discussed: (1) propellant settling, using external thrusters to create artificial gravity and (2) dielectrophoresis, which depends on electric-body forces to control the position of the propellant. Propellant settling will be considered in detail in Section 17-6.

The dielectrophoretic principle is applicable only to dielectric propellants, *i.e.*, nonconducting propellants. In general, storable propellants are not dielectric. When a dielectric particle is placed in an electrostatic field, as in Fig. 17-14b, charges will be separated within the particle due to electrostatic induction. When the field is uniform, forces due to these charges interacting with the field cancel one another, and no net force results. When the field is divergent, however, there is a component of force in the direction of increasing field strength, and the propellant flow is directed toward the region of highest field strength. On the basis of research which has been reported [4], this concept appears attractive for use with cryogenic propellants such as liquid hydrogen and liquid oxygen.
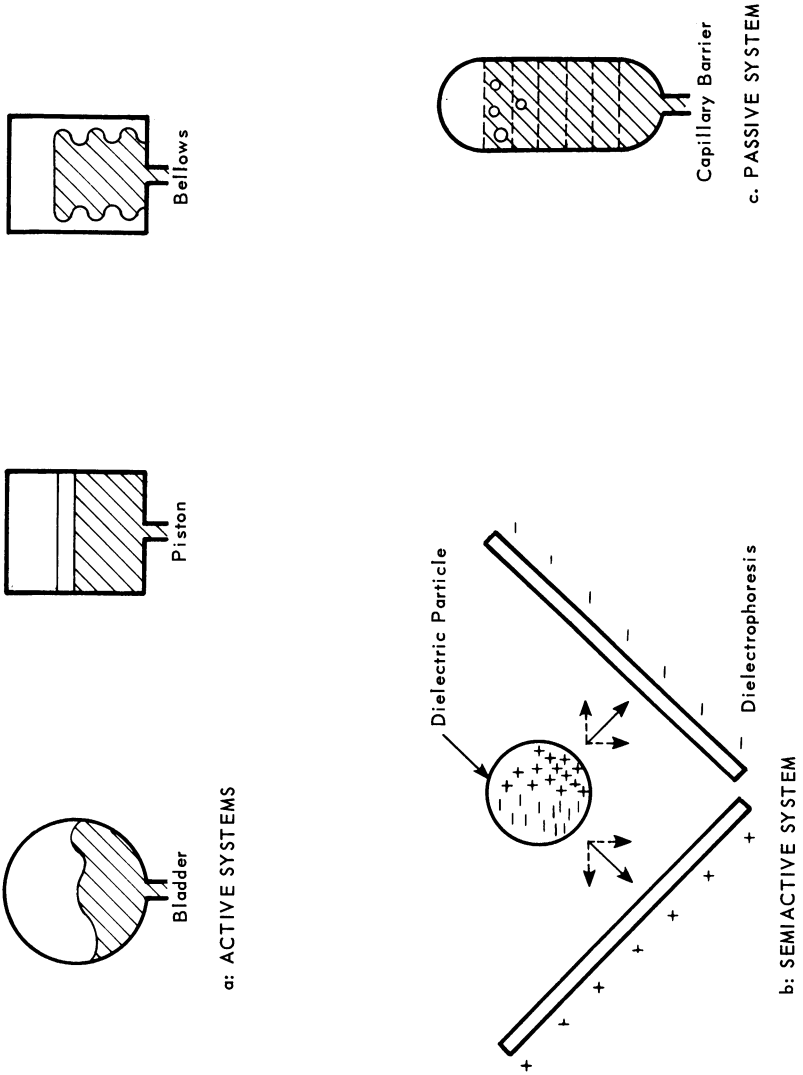
Fig. 17-14 Propellant position control concepts: (a) active systems; (b) semi-active system; (c) passive system.

The importance of capillary or intermolecular forces in the zero-g environment suggests the use of these forces to provide a passive system for control of propellant position. Such a system is based on the concept of the capillary barrier, several of which may be installed as partitions in the tank to prevent the displacement of propellant (Fig. 17-14c). These barriers, which may be woven screens or perforated plates, act, through capillary forces, to prevent liquid migration. Barrier systems will be discussed in more detail in Section 17-7. However, it is desirable at this time to develop the concept of capillary pressure (pressure across the gas-liquid interface) because of its fundamental importance to understanding the discussion that follows. The equation for the pressure difference, due to surface tension, across a curved gas-liquid interface will be developed.

Consider the elemental curved surface $ds \times ds$ constructed about the intersection of the perpendicular lines l_1 and l_2 on the surface, as shown in Fig. 17-15a. R_1 and R_2 are the radii of curvature of l_1 and l_2 at the point of intersection and over the entire element when ds is made arbitrarily small. The tangential force acting on each edge of the surface element is equal to the surface tension σ times ds. The force acting in the direction of the line l_1 is projected onto the plane containing the z axis and the line l_1, as shown in Fig. 17-15b. The force ds is resolved into horizontal and vertical components, with the horizontal components canceling one another. The net downward component of this surface tension force is $2F_1 = 2\sigma \, ds \sin a_1$. A similar analysis for the forces acting on the other two sides of the element shows the net downward force to be $2F_2 = 2\sigma \, ds \sin a_2$. Since the surface element is arbitrarily small, the angles a_1 and a_2 are small and the sine of the angles can be replaced by $ds/2R_1$ and $ds/2R_2$. By dividing the sum of the inward forces by the area of the element, the differential pressure across the interface is obtained:

$$\Delta P = \sigma \left(\frac{1}{R_1} + \frac{1}{R_2} \right). \tag{17-22}$$

The concept of propellant settling by thrusting is illustrated in Fig. 17-16. The thrusting simply accelerates the vehicle and, in so doing, provides artificial gravity. The small auxiliary propulsion system used to generate this thrust must be supplied from a propellant tankage system using bladders or other means for controlling liquid at zero g. Design information of interest includes the settling time and the minimum thrust required to effect settling. Factors of importance to the problem include the initial position of the liquid, fluid properties, tank geometry, and the quality, or minimum bubble content, of the propellant required for engine restart.

For evaluating the concept of propellant settling by use of thrust-induced artificial gravity, the configuration shown in

b: PROJECTION ON PLANE
   THROUGH l_1, R_1, AND
   NORMAL

a: ELEMENTAL SURFACE
   AREA
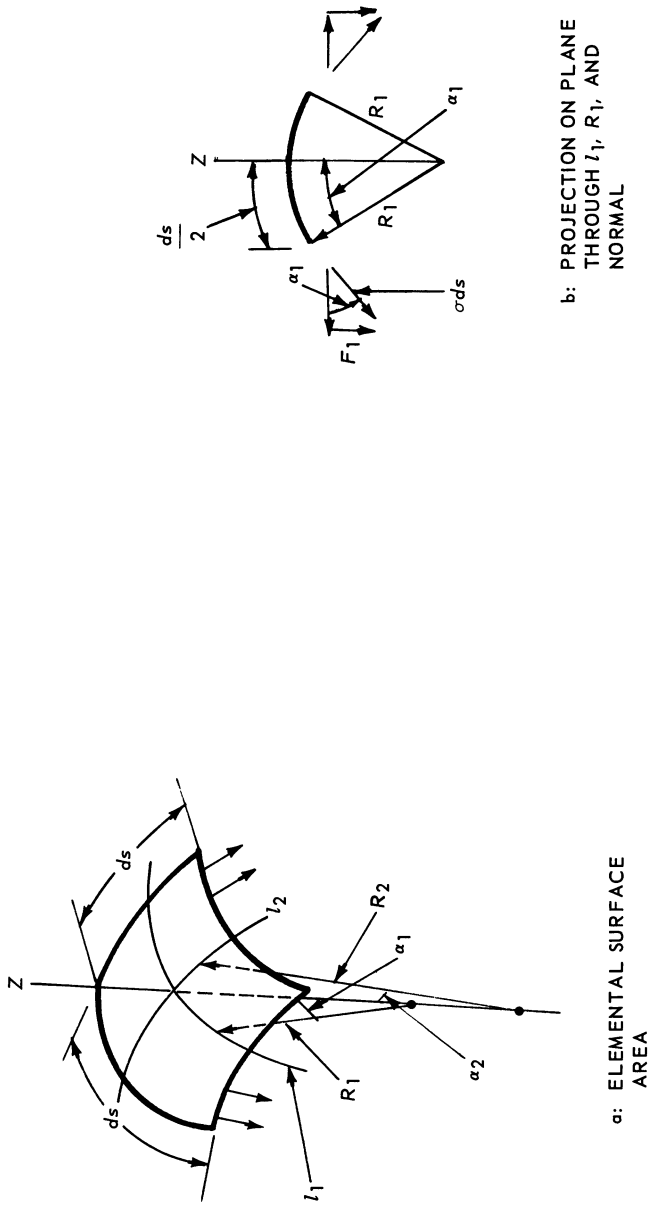
Fig. 17-15   Capillary pressure differential; (a) elemental surface area; (b) projection on plane through l_1, R_1 and normal.
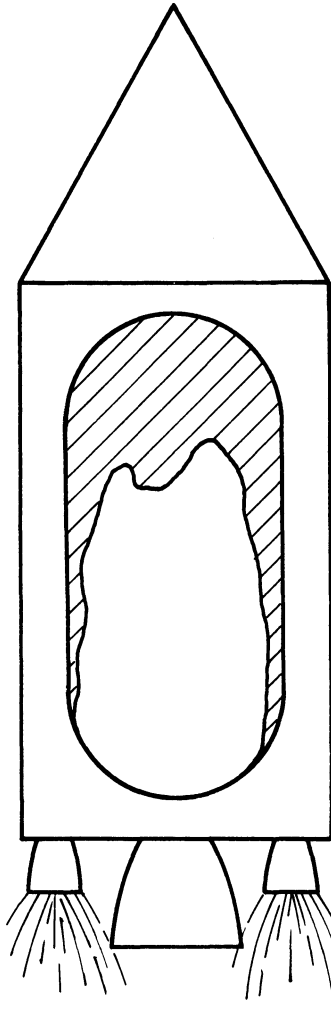
Fig. 17-16. Propellant settling by thrusting.

Fig. 17-17a is assumed. This worst-case condition is not expected to occur frequently, but it cannot at present be eliminated as a possible initial condition. The settling problem can be divided into three parts. The first part is to determine the minimum thrust, or settling acceleration, required to overcome the capillary stability (discussed in the following section) and initiate settling. The second requirement is to determine the manner and rate at which the liquid flows from the top of the tank into the bottom, or outlet end, of the tank. This mode of the settling operation is shown in Fig. 17-17b.

c: ACCUMULATION

b: FLOW FROM
TOP TOWARD
OUTLET REGION

a: ASSUMED
INITIAL
CONFIGURATION

Fig. 17-17 Propellant-settling modes; (a) assumed initial configuration; (b) flow from top toward outlet region; (c) accumulation.

As expected, the liquid does not immediately come to rest after it has reached the bottom of the tank; it may rebound and splash, as indicated in Fig. 17-17c. The third problem, then, is to determine the time required for the propellant to become sufficiently stilled and bubble-free to ensure engine restart.

[17-5.3] Capillary Stability

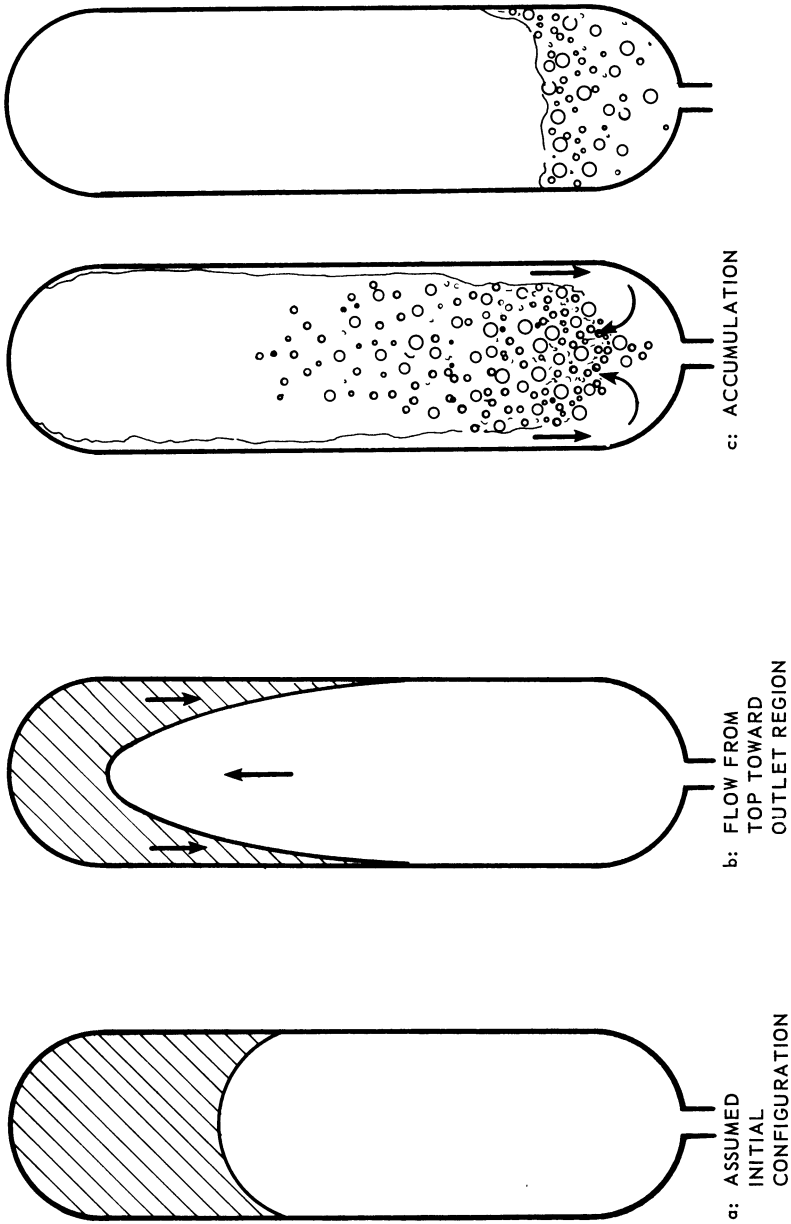If liquid is positioned at the top of a closed cylinder in a gravity field, it may remain at the top even though gravity acts to pull it downward. This can be easily verified by observing water in a soda straw that is closed at the top. The liquid is supported by the gas pressure, *i.e.*, a hydrostatic pressure difference develops through the liquid, and the force due to this pressure difference just equals the weight of the liquid. Examination of the liquid surface at the open end of the straw would show that the meniscus has also attained a static equilibrium. Consequently, an additional less obvious requirement for stability is that the liquid-gas interface be stabilized by the surface tension. The critical condition for this interfacial stability will now be derived for the important case where the contact angle is zero.

Consider Fig. 17-18. The origin of the coordinate system is at the level of contact of the interface with the tank wall and may move as required to conserve the volume of the liquid. R_1 and R_2 are the radii of curvature at any point on the interface. As developed earlier, the pressure in the liquid at any point on the interface is given by the capillary pressure equation,

$$\left(P_L\right)_y = P_G - \sigma\left(\frac{1}{R_1} + \frac{1}{R_2}\right)_y \tag{17-23}$$

where the subscripts L, G, and y refer to liquid, gas, and position at y coordinate, respectively. If the liquid is in static equilibrium, this pressure can also be obtained from hydrostatic considerations and is given by

$$\left(P_L\right)_y = \left(P_L\right)_{y=0} - \rho g y. \tag{17-24}$$

Substituting the capillary equation for the pressure at $y = 0$ Eq. (17-24), in the hydrostatic equation, Eq. (17-23), and then equating the above expressions for P_L, gives the following:

$$\left(\frac{1}{R_1} + \frac{1}{R_2}\right)_y - \left(\frac{1}{R_1} + \frac{1}{R_2}\right)_{y=0} = \frac{\rho g y}{\sigma}. \tag{17-25}$$
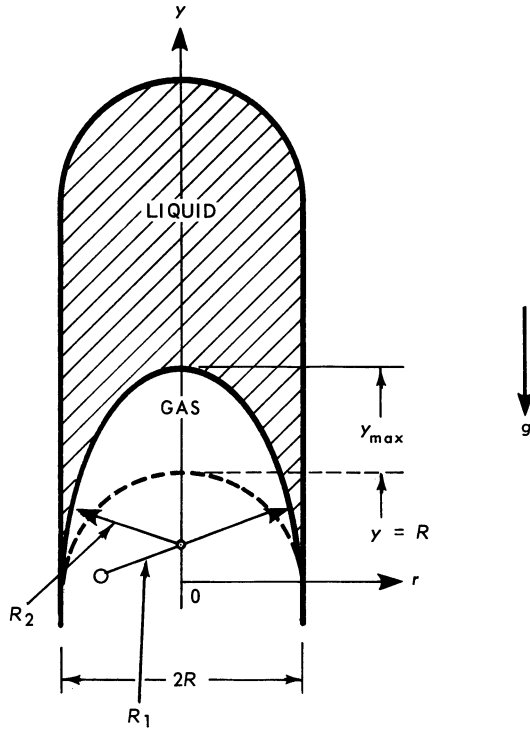
Fig. 17-18 Capillary stability.

The problem is to determine the condition at which instability occurs, or the condition beyond which this equation cannot satisfy the boundary conditions of the problem. As the right-hand part of Eq. (17-25) is increased, *e.g.*, by increasing g and holding y, ρ, and σ constant, the left-hand part must also increase. It can be shown that the left-hand side will reach a maximum for $y = y_{max}$ when the second term, $(1/R_1 + 1/R_2)$ at $y = 0$, becomes a minimum. R_2 is equal to the cylinder radius at $y = 0$ because the contact angle is zero, or the slope is infinite. Therefore, this quantity becomes a minimum when R_1 approaches infinity at $y = 0$. Substituting $R_2 = R$ and $R_1 = \infty$ at $y = 0$ gives the condition for critical stability:

$$\left(\frac{1}{R_1} + \frac{1}{R_2} - \frac{1}{R} \right)_y = \frac{\rho g y}{\sigma} . \qquad (17\text{-}26)$$

This equation can be rewritten in dimensionless form by making the following substitutions:

$$R_1' = \frac{R_1}{R}, \quad R_2' = \frac{R_2}{R}, \quad y' = \frac{y}{R}, \quad r' = \frac{r}{R} \qquad (17\text{--}27)$$

$$\left(\frac{1}{R_1'} + \frac{1}{R_2'} - 1\right)_{y'} = \frac{\rho g R^2}{\sigma} y' = (Bo)\, y' \qquad (17\text{--}28)$$

where

$$Bo = \text{Bond number} = \frac{\rho g R^2}{\sigma}.$$

Of course, for $y = 0$ the gas–liquid interface is spherical (Section 17–3.3).

The Bond number, a ratio of gravity forces to surface-tension forces, plays a very important role in all problems of capillary hydrostatics and low-g propellant behavior. A simple example of a problem involving capillary hydrostatics is that of the rise of liquid in a capillary tube, as shown in Fig. 17–19. The equation for this problem is formulated by equating the weight of the elevated column of liquid to the capillary or surface-tension force by which it is supported. Thus

$$\rho g L_1 \frac{\pi L_2^2}{4} = \sigma \pi L_2 \cos \theta. \qquad (17\text{--}29)$$

Nondimensionalization of this equation gives a Bond number whose value is equal to four times the cosine of the contact angle. The form of the Bond number obtained is

$$Bo = \frac{\rho g L_1 L_2}{\sigma}. \qquad (17\text{--}30)$$

Equation (17–30) is the more general form of the Bond number. The dimension L_1 will be recognized as a hydrostatic length term, and L_2 is a length related to the distance over which the capillary force acts. It should also be noted that the density of the gas was neglected. To be rigorously correct, the density difference between liquid and gas should be used, giving

$$Bo = \frac{(\rho_L - \rho_G)\, g L_1 L_2}{\sigma}. \qquad (17\text{--}31)$$

For many propulsion problems, the terms L_1 and L_2 will be geometrically related, and the Bond number can be expressed in terms
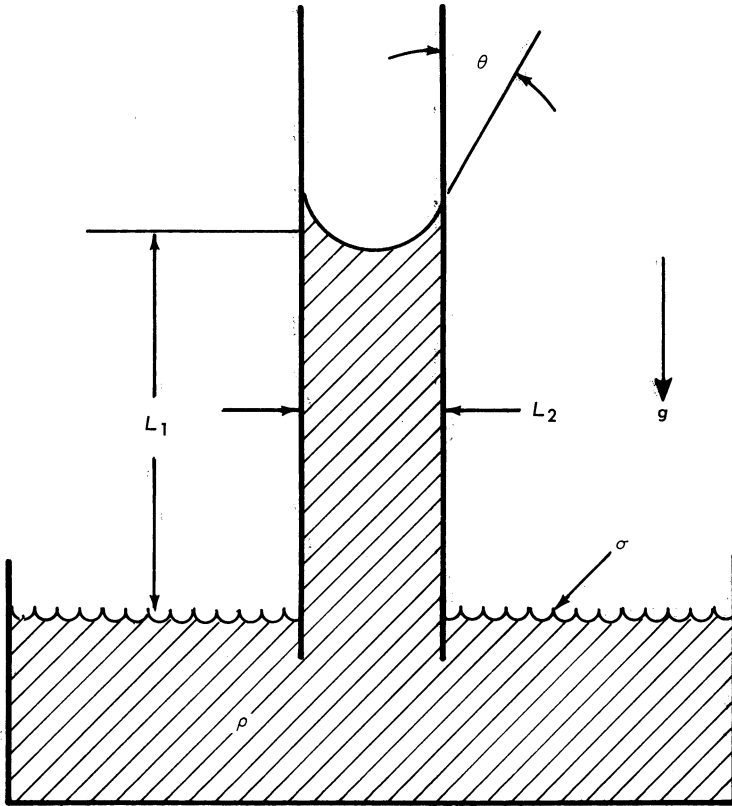
Fig. 17-19 Capillary rise.

of a characteristic length which may be arbitrarily chosen as some significant dimension of the system, such as tank radius. Thus

$$Bo = \frac{(\rho_L - \rho_G)\, g\, L^2}{\sigma}. \tag{17-32}$$

Returning to Eq. (17-28) and expressing the radii of curvature in terms of the derivatives of $y = f(r)$ provides the differential form of the equation:

$$\frac{\dfrac{d^2 y'}{dr'^2}}{\left[1 + \left(\dfrac{dy'}{dr'}\right)^2\right]^{3/2}} + \frac{\dfrac{dy'}{dr'}}{r'\left[1 + \left(\dfrac{dy'}{dr'}\right)^2\right]^{1/2}} - 1 = (Bo)\, y'. \tag{17-33}$$

The boundary conditions are as follows:

$$\text{At}\quad y' = 0, R_1' = \infty\left(\frac{d^2 r'}{dr'^2} = 0\right), r' = 1, \frac{dy'}{dr'} = \infty \quad (17\text{-}34)$$

$$\text{At}\quad r' = 0, \frac{dy'}{dr'} = 0. \quad (17\text{-}35)$$

A solution of this nonlinear differential equation that satisfies the boundary conditions exists for only a unique value of the Bond number. Numerical solution of the equation has shown this value to be 0.84 [5]. (It was first solved in 1883 for droplets.) Thus, where the contact angle is zero, the interface is stable as long as the Bond number is below the critical value of 0.84. This result has been verified experimentally [6, 7].

The critical value of 0.84 for the Bond number allows the determination of the critical acceleration required for liquid to flow to the bottom of a tank. For the configuration shown in Fig. 17-10, it is approximately 10^{-5}g which can be obtained by a force less than 1 pound. For large vehicles, the critical acceleration is very small; for small vehicles, it may be important, since g increases as R decreases for a constant Bond number. The concept of a critical Bond number is valid for other problems, such as bubbles in a pipe or a mercury thermometer. However, the critical value of the Bond number for the latter is not 0.84 because the contact angle is not zero. This critical value is valid for an alcohol–glass thermometer, however, because the contact angle is close to zero.

[17-6] DIMENSIONAL ANALYSIS, MODELING, AND TEST

In this section, the methods of dimensional analysis are used to derive the dimensionless parameters of interest in determining laboratory tests for studying the hydrodynamics of propellant settling by thrusting. Specific discussions include scale–model tests at 1 g and reduced g to examine the gas interface rise, scale model test at 1 g to investigate propellant accumulation at the bottom of the tank, and scale model test at 1 g to study the problem of gas ingestion.

[17-6.1] Gas Interface Velocity

Since it has been shown that vehicle disturbances can result in relocation of the liquid propellant, the worst-case configuration is assumed for this analysis. This configuration, with all the

propellant located at the end of the tank opposite the outlet, is shown in Fig. 17-17a. A propellant-settling maneuver is assumed to be necessary to relocate the propellant to the outlet, and the requirement for minimum acceleration has been determined in terms of the critical Bond number required to overcome capillary stability. It is now necessary to investigate the fluid mechanics of the settling propellant, with the objective of determining the settling time. Initially, the flow from the top of the tank into the lower part of the tank will be considered without regard to the behavior of the liquid as it reaches the bottom.

The problem to be solved is somewhat complex, involving the flow of liquid with a free surface. The condition on this free surface is subject to the influence of surface tension and the contact angle. It is expedient, therefore, to proceed with an experimental investigation, since there is no great likelihood of obtaining an analytical solution with reasonable effort.

The classical Buckingham pi theorem is used to determine the dimensionless parameters of interest. As shown in Fig. 17-20, there are six variables of interest, which can be expressed in terms of three dimensions: mass M, length L, and time T. The pi theorem states that the number of independent dimensionless parameters is equal to the number of variables minus the number of dimensions, or, in this case, three. The variables and dimensions are listed below:

VARIABLES	σ	g	ρ	D	V_I	μ
DIMENSIONS	$\dfrac{M}{T^2}$	$\dfrac{L}{T^2}$	$\dfrac{M}{L^3}$	L	$\dfrac{L}{T}$	$\dfrac{M}{LT}$

where

V_I = velocity of interface rise
μ = viscosity of liquid.

The procedure for determining the dimensionless parameters is as follows: the first dimensionless group, π_1, is written by selecting a number of the variables equal to the number of dimensions plus one, so that all the dimensions (M, L, T) are included. Each of the variables is set to an unknown power. Thus

$$\pi_1 = \sigma^\alpha g^\beta \rho^\gamma D^\delta. \qquad (17\text{-}36)$$

The dimensionless parameter is now rewritten in terms of the basic dimensions and is set equal to a dimensionless constant:

$$\left(\frac{M}{T^2}\right)^{\alpha}\left(\frac{L}{T^2}\right)^{\beta}\left(\frac{M}{L^3}\right)^{\gamma}(L)^{\delta} = 1. \tag{17-37}$$

Equations are written for each of the dimensions, equating the power of that dimension across the equal sign. One of the exponents is arbitrarily set equal to a constant, and the equations are solved simultaneously for the other exponents. It can be seen that the first dimensionless parameter is the Bond number:

$$M; \ \alpha + \gamma = 0 \tag{17-38}$$

$$L; \ \beta - 3\gamma + \delta = 0 \qquad \text{For arbitrary } \beta = 1, \tag{17-39}$$

simultaneous solution yields

$$T; \ -2\alpha - 2\beta = 0$$

$$\alpha = -1, \gamma = 1, \delta = 2 \tag{17-40}$$

$$\pi_1 = \frac{g\rho D^2}{\sigma} = \text{Bond number} \tag{17-41}$$
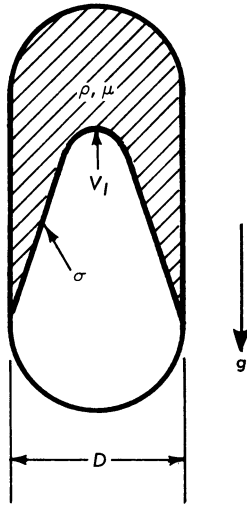
Fig. 17-20 Variables in the analysis of gas interface rise.

This procedure is repeated to determine the remaining dimensionless parameters. For each subsequent step, one variable is removed and another is added in a systematic manner, so that each variable is removed only after all others present when it was added have been removed. Systematic grouping of variables is accomplished by adding the new variable to the right and removing the one on the left, keeping the order of the others constant:

$$\pi_2 = g^a \rho^b D^c V_I{}^d \frac{V_I}{\sqrt{Dg}} = \text{Froude number} \tag{17-42}$$

$$\pi_3 = \rho^{\bar{a}} D^{\bar{b}} V_I^{\bar{c}} \mu^{\bar{d}} \frac{\rho D V_I}{\mu} = \text{Reynolds number.} \qquad (17\text{--}43)$$

If the Froude number is selected as the result parameter, the desired correlation is

$$\frac{V_I}{\sqrt{Dg}} = f\left(\frac{g \rho D^2}{\sigma}, \frac{\rho D V_I}{\mu}\right). \qquad (17\text{--}44)$$

As might be expected, the results from this procedure are somewhat dependent on the original arrangement of the variables. Consequently, a knowledge of the important dimensionless parameters used in fluid mechanics is helpful in ensuring that meaningful results will be obtained.

Figure 17-21 [8] gives the results of tests which determined the steady-state velocity of the interface rising in a cylinder such as illustrated in Fig. 17-20. The test data points indicated by open symbols were obtained in tests at the standard earth-gravity condition, while those indicated by solid symbols were obtained in drop tower tests that simulated 0.01 to 0.08 standard gravity.

It can be seen that the Froude number is a constant when the Bond number is greater than 10. Below this value there is a dependence on the Bond number, indicating that surface tension acts to restrict the flow. The data are correlated by the expression,

$$\frac{V_I}{\sqrt{g \dfrac{D}{2}}} = 0.48 \left[1 - \left(\frac{0.84}{Bo}\right)^{Bo/4.7}\right]. \qquad (17\text{--}45)$$

From this it can be seen that the velocity becomes zero when the Bond number equals 0.84. This is the critical value of the Bond number for zero contact angle (Section 17-5), below which the interface is stabilized by surface tension.

It is of particular interest to note the excellent agreement of the data obtained at 1 g with that obtained at conditions of reduced gravity. From the point of view of proponents of dimensional analysis, such agreement is expected and is therefore, not astounding. However, very few tests have been conducted which actually vary the magnitude of the gravity term to verify the predictions arising from dimensional analysis.

Figure 17-21 and the data correlation above do not indicate any dependence of the interface velocity or Froude number on viscous effects. To account for these effects, Eq. (17-45) must be multiplied by the correction factor (CF) given in Fig. 17-22 [5, 9], *i.e.,*

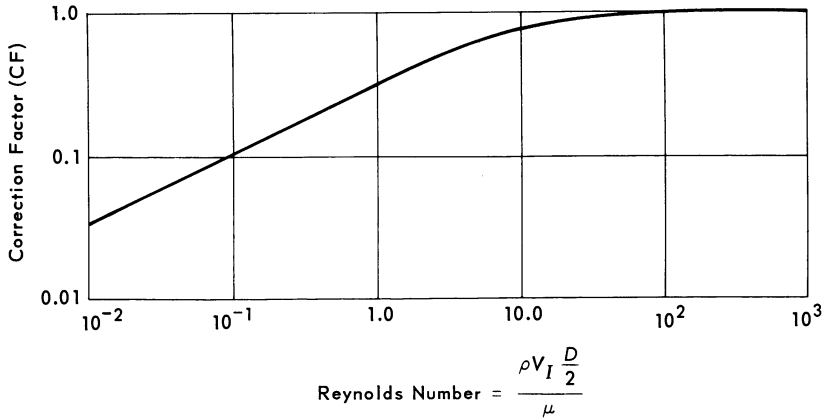Fig. 17-21 Correlation of test results.
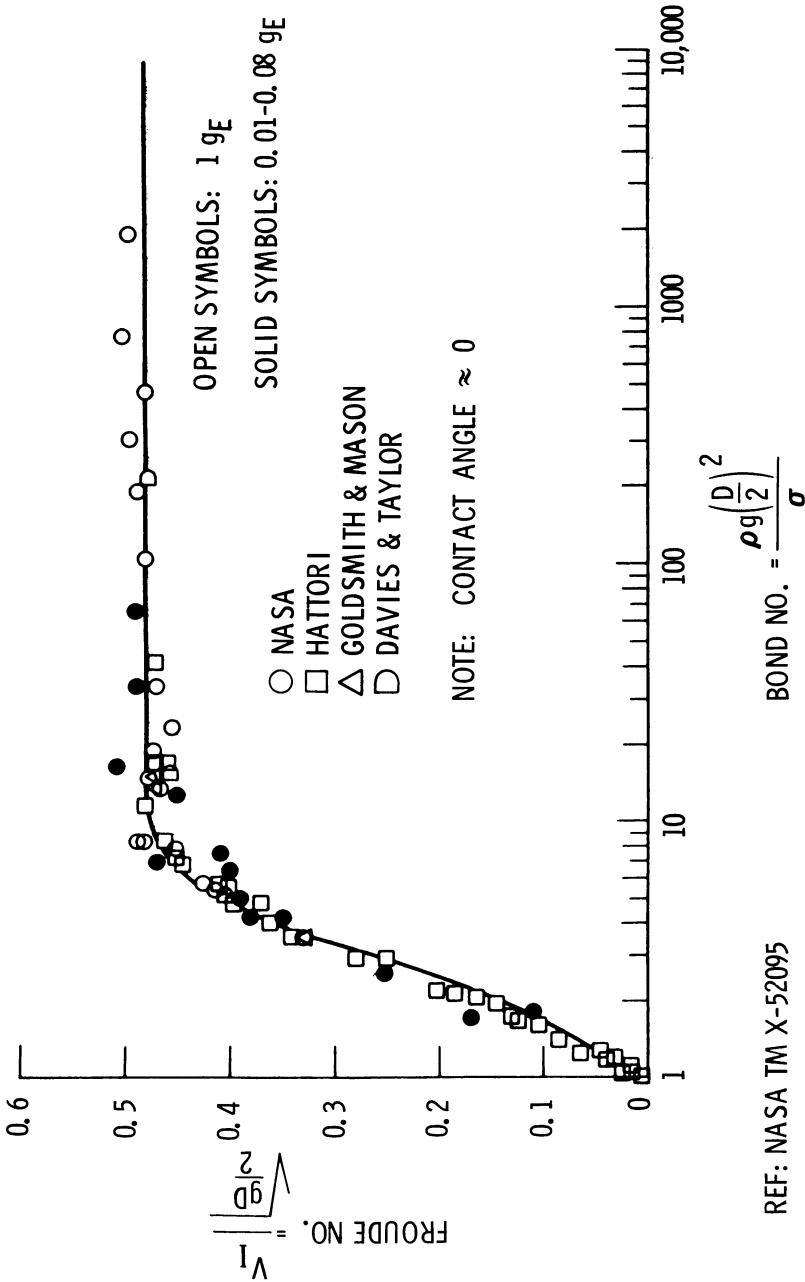
REF: NASA TM X-52095

Fig. 17-22 Effect of Reynolds number.

$$\frac{V_I}{\sqrt{g\,\dfrac{D}{2}}} \;=\; CF_{(Re)}\left[0.48\left\{1-\left(\frac{0.84}{Bo}\right)^{Bo/4.7}\right\}\right]. \qquad (17\text{-}46)$$

When the Reynolds number is greater than 50, the correction factor is approximately 1, indicating there is no effect of viscosity on the interface velocity. Inasmuch as the Reynolds number for typical space vehicle tank sizes and propellant properties will usually be much greater than 50, no correction of the interface-rise velocity need be made because of viscous effects. However, this correlation is useful for interpreting data obtained with very small models where the Reynolds number may be small. Since in practical problems the Bond number is also expected to be greater than 10, the Froude number can be assumed to be a constant value of 0.48 (from Fig. 17-21) in estimating the interface-rise velocity.

Note that the interface velocity is used as the characteristic result parameter for the test correlation, since this velocity can be readily measured. To use the volumetric flow rate as the characteristic result parameter would be a poor choice, because the flow rate varies with the distance from the interface (and consequently with time) and is not readily measurable.

Figure 17-23 helps to illustrate the significance of the gas interface-velocity correlation as it applies to a spacecraft situation. Initially, the propellant is assumed to be at the upper end of the tank, and the vehicle is accelerated at 0.01 g (0.322 ft/sec.^{2}) in order to settle the propellant at the outlet end. For all common propellants and tank sizes, it can be readily verified that the Bond number is greater than 10, and the Reynolds number is greater
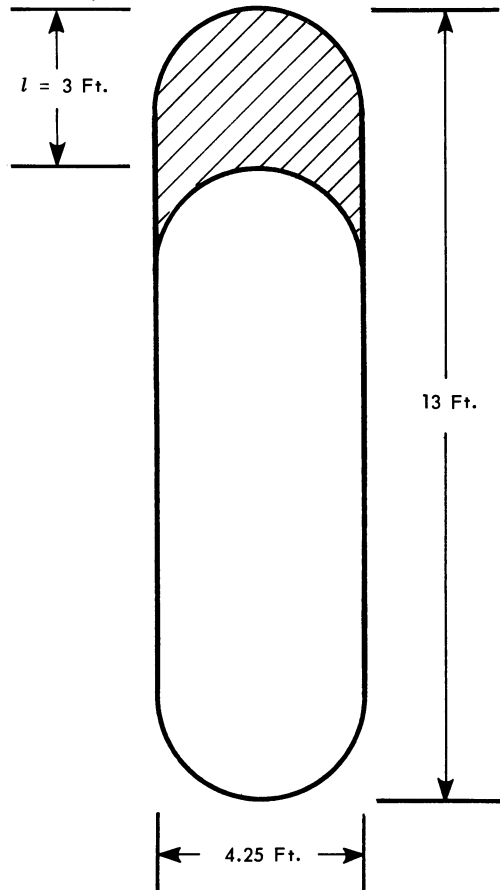
Fig. 17-23 Initial configuration of propellant in tank.

than 50. Therefore, the time required for the interface to penetrate through the 3 feet of liquid is determined as follows:

$$t = \frac{l}{V_I} = \frac{l}{0.48 \sqrt{g \dfrac{D}{2}}} = 7.5 \text{ sec.} \tag{17-47}$$

This result gives the time required for gas to reach the top of the tank, but it does not give the settling time required for propellant to accumulate at the tank outlet. Nevertheless, the interface-velocity correlation will be used later in determining the time required for accumulation. This time must be known before the total fuel required for settling can be calculated.

[17 - 6.2] Propellant Accumulation

For practical spacecraft conditions, viscous effects have been found to be unimportant in determining the interface-rise velocity. However, since the kinetic energy gained by the liquid in flowing from the top to the bottom of the tank must be dissipated through viscous damping, it is questionable whether the small scale-model tests used to determine the interface-rise characteristics could also be used to measure the settling time and to study the nature and rate of liquid accumulation at the bottom of the tank. Consequently, a separate test program was undertaken to determine the time required for accumulation.

Dimensional analysis was used in planning tests for determining the characteristics and duration of this accumulation process. From a Buckingham pi analysis of the problem as formulated in Fig. 17-24, the following eight dimensionless groups are obtained:

h/D = geometric ratio

V_L/D^3 = volumetric ratio (V_L = volume of liquid)

V_A^2/gh = Froude number (V_A = velocity of liquid flowing into tank bottom)

δ/D = geometric ratio, stream thickness/diameter

$t/\sqrt{h/g}$ = time ratio

$\rho\, ghD/\sigma$ = Bond number

$\rho D \sqrt{gh}/\mu$ = Reynolds number

β = arbitrary parameter indicating the degree of accumulation, *e.g.*, percent of bubble content, or height of bubble-free liquid/tank diameter.

The first four groups are preserved by geometric scaling. The time ratio derived from the Froude number is of considerable importance, because the desired result seeks a correlation of the degree of assumulation versus time. The Bond number and Reynolds number are parameters which must be scaled to simulate the space vehicle and may be varied parametrically to determine their importance.

The thickness of the flowing film δ, as determined from the interface-rise tests, varies with the distance from the interface front and, consequently, with time. The volumetric flow rate is scaled in a manner so that geometric similarity of the flow, *i.e.*, the ratio δ/D is approximately preserved. The following expression

11 Parameters
3 Dimensions
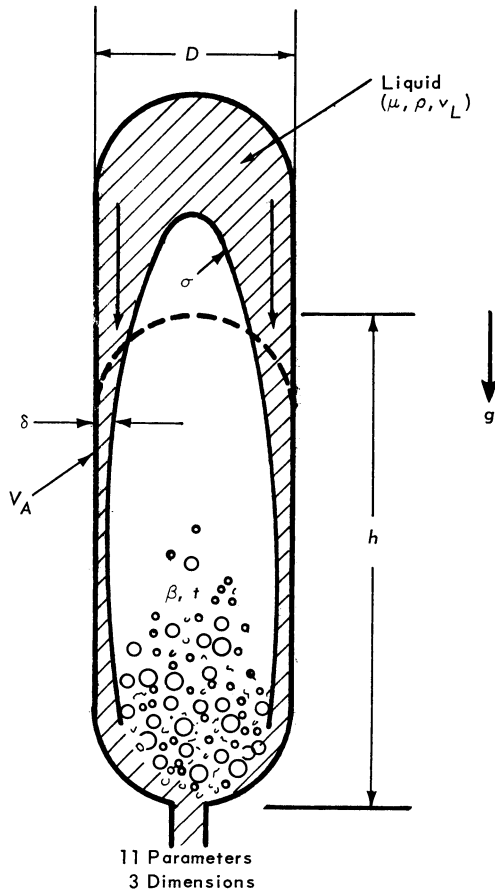
Fig. 17-24 Variables in the analysis of propellant accumulation.

for the volumetric flow rate Q past a given level y_1 is derived in Appendix B (refer to Fig. 17-25 for nomenclature):

$$Q = \pi \left(\frac{D}{2}\right)^2 V_I \left[1 - \frac{0.48 \, f \, (Bo) \sqrt{\dfrac{D}{2}}}{\sqrt{\dfrac{D}{2} \, 0.48 \, f \, (Bo)^2 + 2L}}\right] \qquad (17\text{-}48)$$

where

$$V_I = 0.48 \, f \, (Bo) \sqrt{\frac{gD}{2}} \qquad (17\text{-}49)$$
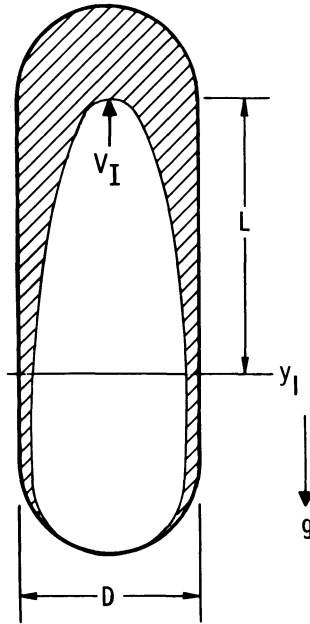
Fig. 17-25 Determination of liquid volumetric flow rate.

and

$$f(Bo) = 1 - \left(\frac{0.84}{Bo}\right)^{Bo/4.7} \qquad (17\text{-}50)$$

The configuration for the propellant accumulation tests is illustrated in Fig. 17-26 [10]. The test apparatus consists principally of a model tank and a reservoir. The latter is essentially a tank with a bottom of fine-mesh screen and is closed at the top except for a high-capacity vent valve. When filled with liquid and the valve is closed, the reservoir retains the liquid by the capillary-stabilizing action of the screen; when the valve is opened, the liquid flows through the screen, which offers very little resistance. A baffle diverts the flow and controls the flow rate, and a pipe passing through the center of the reservoir vents the gas displaced during the test.

Prior to a test, liquid is loaded into the reservoir, which is positioned to the desired height above the tank bottom. At the beginning of the test, the liquid is made to flow from the reservoir to the bottom of the tank in a manner and rate similar to that expected had the flow resulted directly from a rise of the liquid-vapor interface. The behavior of the liquid during accumulation is recorded photographically.
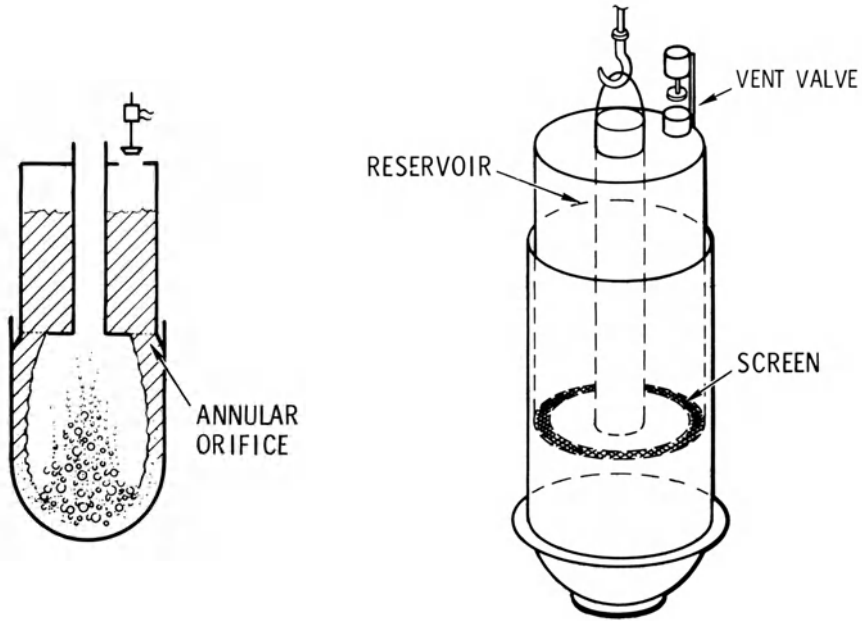
Fig. 17-26 Apparatus for accumulation tests.

Figure 17-27 shows the results of a typical accumulation test. Since the first four dimensionless parameters given earlier in the section are held constant, the desired correlation is

$$\beta = f\left(\frac{t}{\sqrt{\frac{h}{g}}}, \frac{\rho \, ghD}{\sigma}, \frac{\rho D \sqrt{gh}}{\mu}\right). \tag{17-51}$$

In this test, the values of the Bond and Reynolds numbers are as follows:

$$Bo = \frac{\rho \, ghD}{\sigma} \approx 3 \times 10^4 \tag{17-52}$$

$$Re = \frac{\rho D \sqrt{gh}}{\sigma} \approx 1 \times 10^6 . \tag{17-53}$$

The fill condition is given by

$$\frac{V_L}{D^3} \approx 0.5. \tag{17-54}$$
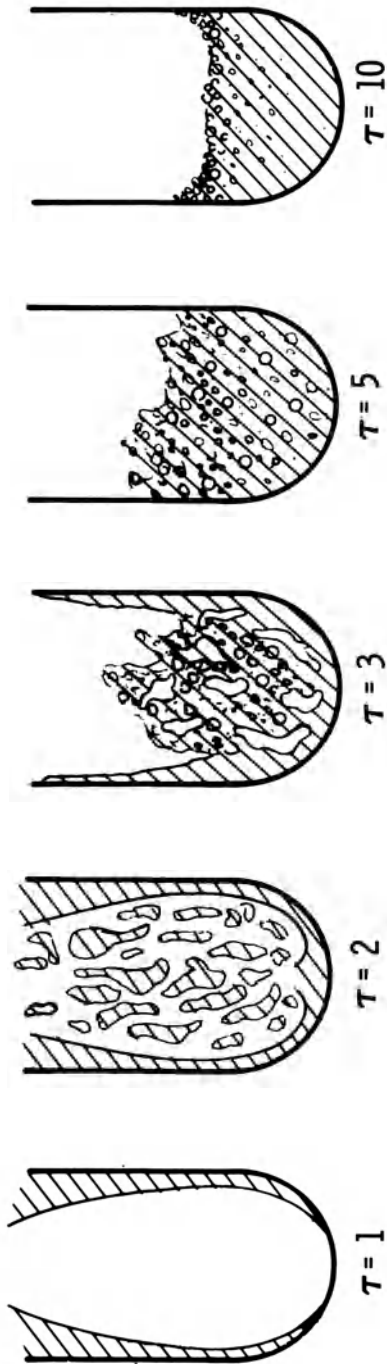
Fig. 17 - 27 Typical result of accumulation test.

For convenience, the dimensionless time unit τ is defined as the number of free-fall periods. Thus

$$\tau = \frac{t}{\sqrt{\dfrac{2h}{g}}} \tag{17-55}$$

As shown in Fig. 17-27, the liquid first reaches the bottom of the tank in one dimensionless unit of time. At $\tau = 2$, the liquid is violently rebounding but has not begun to collect. At $\tau = 3$, the liquid is partially collected but may contain large pockets of gas. Between $\tau = 3$ and $\tau = 5$ the liquid becomes contiguous but has trapped a large amount of gas which breaks into bubbles. The liquid is still very turbulent at this time, and bubbles may be carried from the surface to the outlet area. By $\tau = 10$, the liquid is clear at the bottom, with a few bubbles possible remaining at the liquid surface.

To assess the significance of the results, assume that the quality of the propellant indicated by $\tau = 5$ is acceptable for engine restart. Then, for the problem illustrated in Fig. 17-23,

$$t = \tau \sqrt{\frac{2h}{g}} = 5 \sqrt{\frac{2 \times 10}{0.01 \times 32.2}} = 39 \text{ sec.} \tag{17-56}$$

This application of the test results assumes that the test was scaled properly to simulate the example. For the storable oxidizer in the tank in Fig. 17-23, nitrogen tetroxide, the actual Reynolds number is found to be about 1.7×10^6, 1.7 times the test Reynolds number; the Bond number is about 1.8×10^4, about 0.6 that of the test. (Water was used as the test liquid because of its relatively high surface tension.) Exact duplication of all dimensionless parameters is usually not possible in actual design applications, and as in wind-tunnel testing, experience and judgment must be used in interpreting and extrapolating results. In the case cited here, because the test Bond number is greater and the test Reynolds number is less than that in flight, the surface-tension effect is less and the viscosity effect is greater than that in flight. Therefore, it might be expected that in the test the number of bubbles is greater, their size is smaller, and they rise more slowly than in flight.

In considering the design of an auxiliary propulsion system for propellant settling, parameters of interest include the amount of propellant needed and the time required for settling. Since the time rate of propellant expenditure $\dot{W}_p$ times the specific impulse I_{sp} is equal to force, it follows that the propellant expended as a function of time is Mg/I_{sp}, where M is the total mass of the vehicle.

From the preceding dimensional analysis and accumulation tests, it has been shown that the settling time is given by

$$t = \tau \sqrt{\frac{2h}{g}} \qquad (17\text{-}57)$$

where τ is the dimensionless settling time required to achieve a required degree of settling for engine start and is a function of the quantity of propellant remaining, the Bond number, and the Reynolds number. If the dependence of τ on the Bond and Reynolds numbers is neglected for the moment and a constant minimum value of τ for any given fill condition is assumed, the weight of propellant that must be expended is

$$W_p = \frac{Mg}{I_{sp}} t = \frac{Mg}{I_{sp}} \tau \sqrt{\frac{2h}{g}} = \frac{M \tau \sqrt{2h}}{I_{sp}} \sqrt{g} \ . \qquad (17\text{-}58)$$

Thus, the quantity of propellant required for settling is directly proportional to $\sqrt{g}$. It will be recalled that the flow of liquid from the top of the tank, as indicated by the interface-rise velocity, becomes restricted by surface-tension effects when the Bond number (in this case $[\rho g (D/2)^2/\sigma]$) is less than 10. Consequently, the proportionality of Eq. (17-58) is valid only for a Bond number greater than 10. From Eq. (17-58), in order to expend the least amount of propellant for settling, the lowest possible thrust value (settling acceleration) should be used, provided capillary restriction does not occur $(Bo \overset{\sim}{>} 10)$. This result is significant in the design of auxiliary thrust systems.

In the above discussion, it has been assumed that the dimensionless settling time is independent of the Bond number and the Reynolds number. In optimizing the propulsion system used for propellant settling by reducing its thrust, the magnitude of the Bond and Reynolds numbers will be reduced. Since surface tension and viscosity occur in the respective denominators of these dimensionless ratios, reducing the settling acceleration has the effect of increasing the importance of these liquid properties. When bubbles form, the surface area is increased, resulting in an increase of surface energy. Increasing the surface tension acts to reduce the number of bubbles formed; increasing the importance of viscosity is equivalent to increasing the damping force acting to still the settling liquid. Therefore, as the acceleration is reduced, the formation of bubbles may decrease and damping of the kinetic energy of the liquid may increase. Either of these effects may speed the accumulation process or reduce the value of τ required to achieve acceptable settling. Thus, the above conclusion that $W_p \propto \sqrt{g}$ may be conservative because the required dimensionless settling time is dependent on g.

It can be concluded that an optimum system would result when the auxiliary settling thrusters are sized to give a Bond number of about 10. However, it should be emphasized that the test result given above is only typical, and the settling characteristics and time required must be determined as a function of tank size and geometry, internal hardware, propellants, and settling acceleration. The test procedure and scaling described are recommended for general application.

[17-6.3] Gas Ingestion

When a tank is drained in a gravity field, the liquid surface tends to distort as the surface nears the outlet due to the inertial effects arising from the acceleration of the liquid into the outlet. At the condition of earth gravity, this distortion is usually small because of the leveling forces of gravity. In a low-g environment, however, the distortion may be great enough to cause ingestion of gas into the engine feed line while a considerable amount of liquid remains in the tank. (This interface distortion is not to be confused with the familiar vortex phenomenon which occurs because of rotation of the liquid. Vortexing may also be present in the low-g environment and must be considered separately.)

A test program was conducted [11] to investigate this phenomenon. Tests were again scaled according to the principles of dimensional analysis. In terms of the nomenclature of Fig. 17-28, the following dimensionless groups are found to be of possible significance:

D/d = tank diameter/outlet diameter

V^2/gD = Froude number, where V is the velocity of the interbefore distortion occurs

$VD\rho/\mu$ = Reynolds number

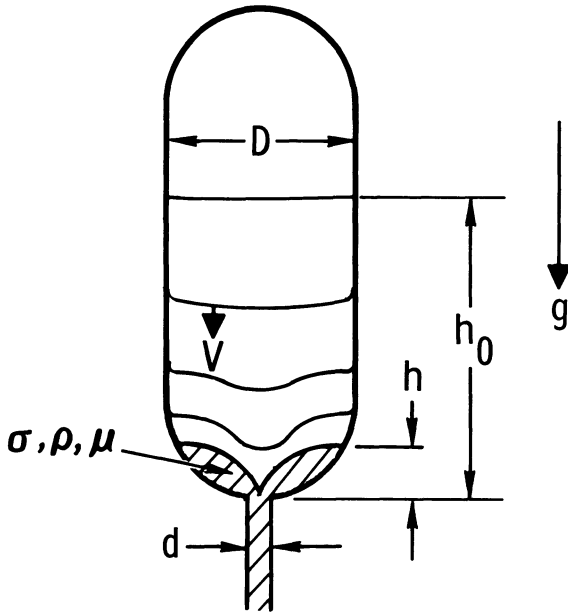$\rho g D^2/\sigma$ = Bond number

h_0/D = initial height/diameter

h/D = gas-ingestion height/tank diameter.

If the ratio h/D is selected as the result parameter, the desired correlation should include the above parameters in the following form:

$$\frac{h}{D} = f\left(\frac{D}{d}, \frac{V^2}{gD}, \frac{VD\rho}{\mu}, \frac{\rho g D^2}{\sigma}, \frac{h_0}{D}\right). \qquad (17\text{-}59)$$

9 PARAMETERS
3 DIMENSIONS

Fig. 17-28 Variables in the analysis of gas ingestion.

Note that the parameters containing g are neither zero nor infinity for the restart period, when a small thrust is being applied for propellant settling. It is feasible, therefore, to conduct tests at any value of g as long as the dimensionless groups can be scaled. Accordingly, the test program was conducted at standard earth-gravity conditions.

Tests to determine the nature and magnitude of gas ingestion were conducted with geometrically scaled models of 1/2-, 1-, 2-, and 4-inch diameters. It was necessary to use small models in order to obtain Froude number simulation at 1 g of expected space-craft conditions. Tests were conducted by filling the model to the desired height h_0, as shown in Fig. 17-29, then increasing the pressure to a predetermined value. The high-speed motion-picture camera was started, and the outflow valve was opened, allowing the tank to drain. Gas-ingestion heights were determined from an analysis of the film.

Excellent correlation of test data was obtained for models with a flat bottom, as shown in Fig. 17-30. The line drawn through
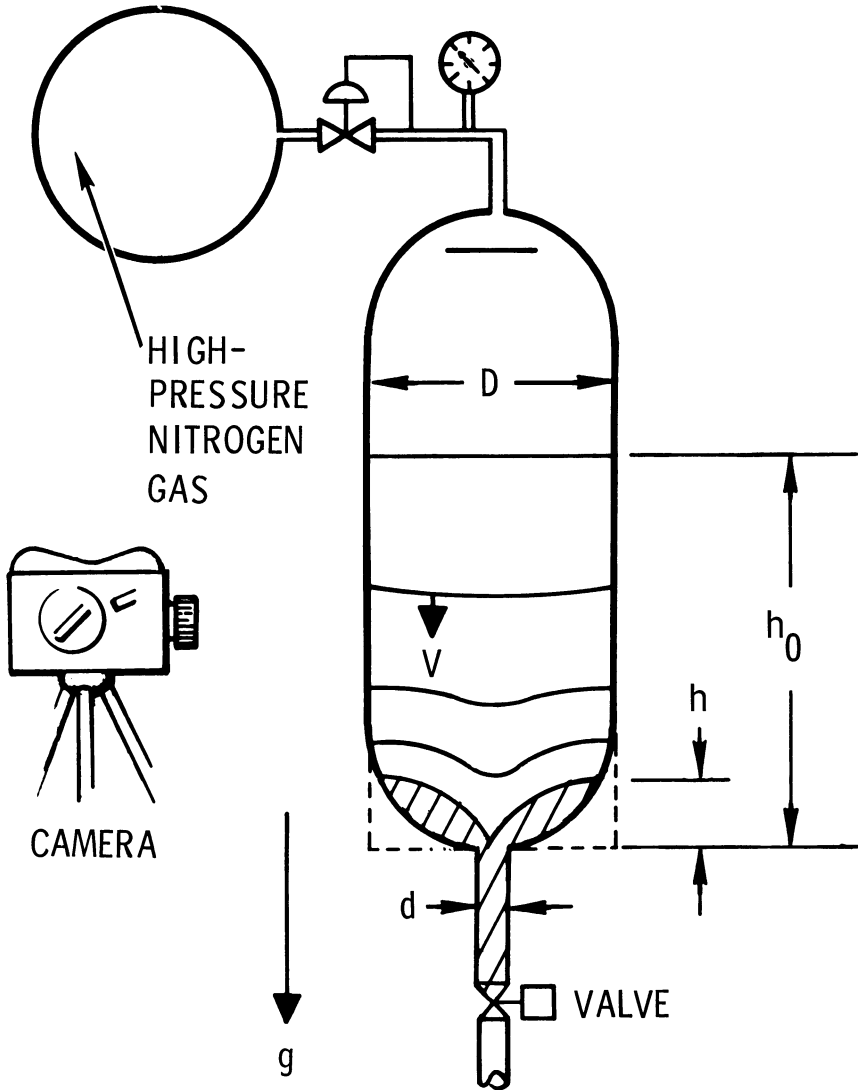
Fig. 17-29 Configuration for gas-ingestion tests.

the data is the empirical function:

$$\frac{h}{D} = 0.43 \, \tanh\left[1.3\left(\frac{V^2}{gd}\right)^{0.29}\right].$$

(17-60)

SYMBOL	D (INCHES)	$\frac{D}{d}$	FLUID
⊡	2	20.0	WATER
⊙	2	10.0	WATER
▷	2	3.2	WATER
◇	2	20.0	HEXANE
◁	2	3.2	HEXANE
■	1	16.7	WATER
●	1	10.0	WATER
▶	1	3.2	WATER

INGESTION HEIGHT, h/D

DIMENSIONLESS GAS-

FROUDE NUMBER, V^2/gd

Fig. 17 - 30 Correlation of results of gas-ingestion tests.

The quantity V^2/gd will be recognized as a form of the Froude number. For very large values of V^2/gd, the dimensionless gas-ingestion height h/D is constant. The data shown in Fig. 17-30 were obtained with 1- and 2-inch-diameter flat-bottom models. Where optical distortion was not excessive, data obtained from hemispherical-bottom tanks of 1-, 2-, and 4-inch diameters agreed reasonably well with the data in Fig. 17-30. However, these points were omitted from the correlation because optical distortion errors were quite large for the smaller values of h/D.

Tests were also conducted with smaller models (to decrease the Bond number) and with viscous liquids (glycerol and glycerol-w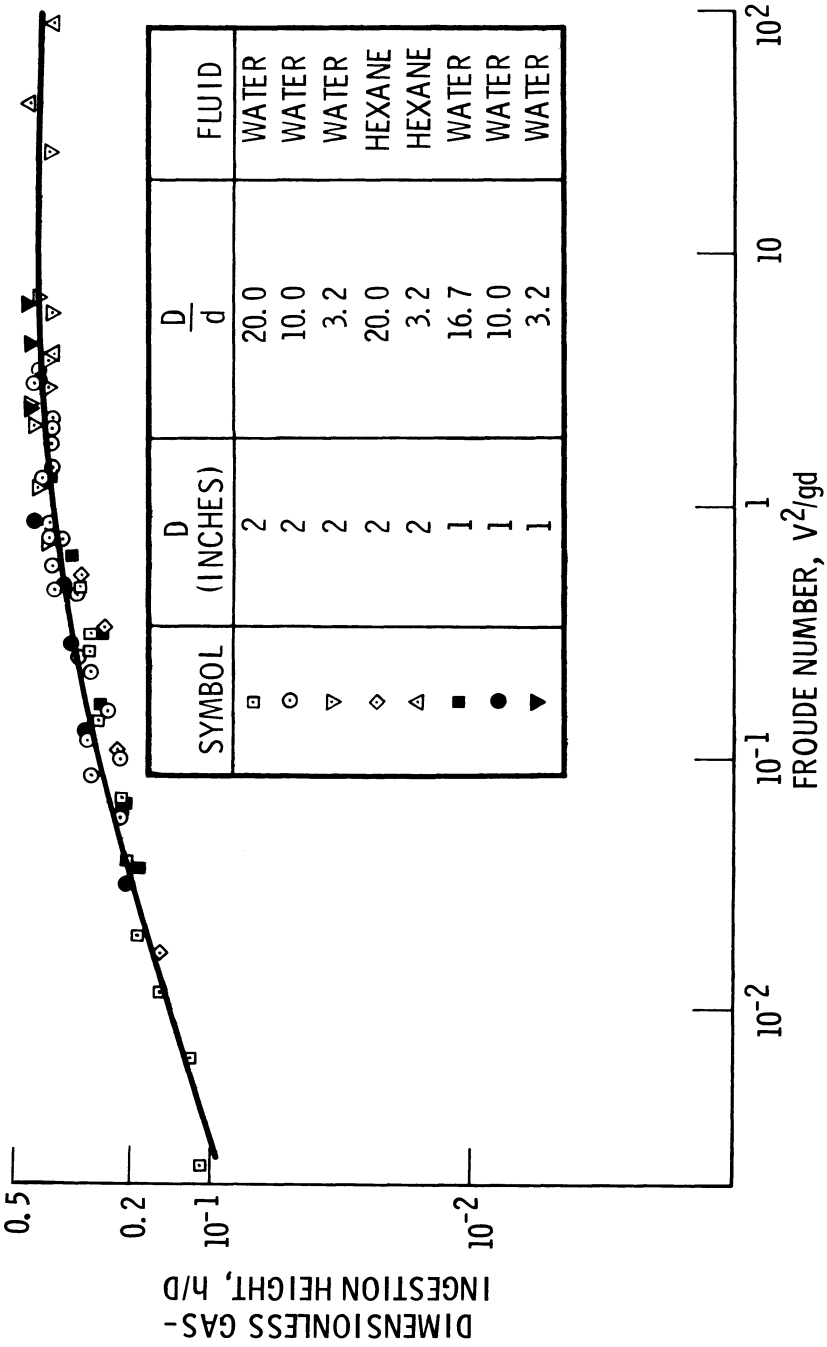ater mixtures) to determine the dependence of the gas-ingestion height on the Bond and Reynolds numbers. It was found that there was no dependence on the Bond number and therefore no surface-tension effects when the Bond number was greater than 100. No effect was found for the ratio of initial height to tank diameter, h_0/D.

[17-6.4] Analytical Considerations of Gas Ingestion

It is interesting to point out possible theoretical approaches to the gas-ingestion problem and a few significant results. Of course, the problem has not been solved exactly, but some headway can be gained by making various gross assumptions. For example, if the liquid is assumed to be inviscid, incompressible, and initially irrotational, the governing equations can be readily written in terms of the potential function ϕ. Based on the geometry and nomenclature of Fig. 17-31, these equations are as follows:

Laplace's equation for axisymmetric condition in cylindrical coordinates

$$\nabla^2 \phi(r, y, t) = \frac{\partial^2 \phi}{\partial r^2} + \frac{1}{r}\frac{\partial \phi}{\partial r} + \frac{\partial^2 \phi}{\partial y^2} = 0 \qquad (17\text{-}61)$$

where

ϕ = velocity potential

Boundary conditions

(1) $\dfrac{\partial \phi}{\partial n} = 0$ at wall $\qquad\qquad\qquad\qquad (17\text{-}62)$

where

n = normal direction to the wall

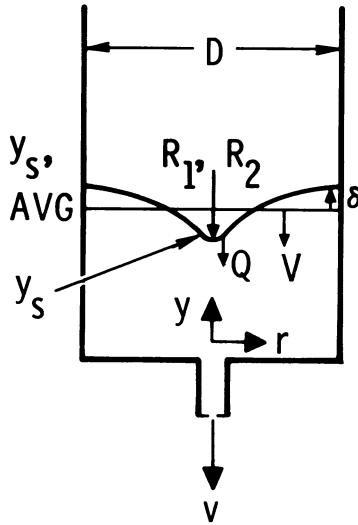(2) $\dfrac{\partial \phi}{\partial y} = v$ at outlet $\qquad\qquad\qquad\qquad (17\text{-}63)$

Fig. 17-31 Theoretical Formulation of gas-ingestion problem.

where

v = outlet velocity

$$(3)\quad \frac{\partial \phi}{\partial t} - \frac{1}{2} Q^2 - g\,\delta + \frac{\sigma}{\rho}\left(\frac{1}{R_1} + \frac{1}{R_2}\right) = C(t) \quad \text{at free surface} \quad (17\text{-}64)$$

where

Q = velocity at any point
$C(t)$ = constant that may change with time but not with position
R_1, R_2 = orthogonal radii of curvature at any point on the interface.

Boundary condition 3 is the integrated form of Bernouli's equation for unsteady, incompressible flow and is nonlinear. It is the forcing function in the problem. To the author's knowledge, no solution for this problem that retains the nonlinear terms has been obtained. Linearized solutions have been obtained but they are only of academic value, since the only case of practical interest (h_{max} in Fig. 17-28) is highly nonlinear.

When the third boundary condition or surface condition is non-dimensionalized by the substitutions

$$Q' = \frac{Q}{V}, \quad \delta' = \frac{\delta}{D}, \quad R'_{1,2} = \frac{R_{1,2}}{D}, \quad \phi' = \frac{\phi}{V^2\sqrt{\dfrac{D}{g}}}, \quad t' = \frac{t}{\sqrt{\dfrac{D}{g}}}$$

$$(17\text{-}65)$$

where

V = average velocity of the interface

the Froude and Bond numbers result as parameters in Eq. (17-64):

$$\frac{\partial \phi'}{\partial t'} - \frac{1}{2}Q'^2 - \frac{\delta'}{\left(\dfrac{V^2}{gD}\right)} + \frac{\left(\dfrac{1}{R'_1} + \dfrac{1}{R'_2}\right)}{\left(\dfrac{V^2}{gD}\right)\left(\dfrac{\rho g D^2}{\sigma}\right)} = C'(t'). \qquad (17\text{-}66)$$

<center>Froude   Froude   Bond</center>

Since these parameters appear in the denominator, their influence approaches zero when their values are very high. This diminishing influence was noted from the test results, where the gas-ingestion height became asymptotic to a constant value for high values of the Froude number. Similarly, no Bond number effect was noted for Bond numbers above 100.

Solutions are available for the flow of liquid from a tank with an outlet constriction when the free-surface condition is omitted [11]. Figure 17-32a illustrates the streamlines and representative velocities for such a solution. If an imaginary interface is defined at a considerable distance from the outlet and the progress of this interface is followed as it moves toward the outlet, distortion will occur. Figure 17-32b shows such a quasi-steady-state solution and can be imagined to be ingestion of a second liquid during feed-out of the first liquid. It was found for the ratio $D/d = 10$ that the height of the interface at the wall when the surface entered the outlet was equal to 0.34 of the tank diameter. This is a lower value than the constant of 0.43 obtained from the experimental results for large values of the Froude number.

[17-7] CAPILLARY BARRIERS

It was shown earlier (Section 17-5.2) that a pressure differential exists across a curved liquid-gas interface due to the effects of surface tension. Such pressure differential can be utilized in a passive control system to position liquid propellant at the outlet end of the tank, by partitioning the tank into two or more compartments through the use of capillary barriers (Fig. 17-33). The capillary barrier may be a woven screen, perforated plate, or porous membrane. Its important property is that a curved interface or bubble will be formed as gas begins to pass through any small opening which is initially wet. Under the low-g conditions, the pressure differential thus created across the liquid-gas interface

a: STREAMLINES AND VELOCITIES FOR STEADY–STATE FLOW

b: LIQUID SURFACE CONFIGURATIONS
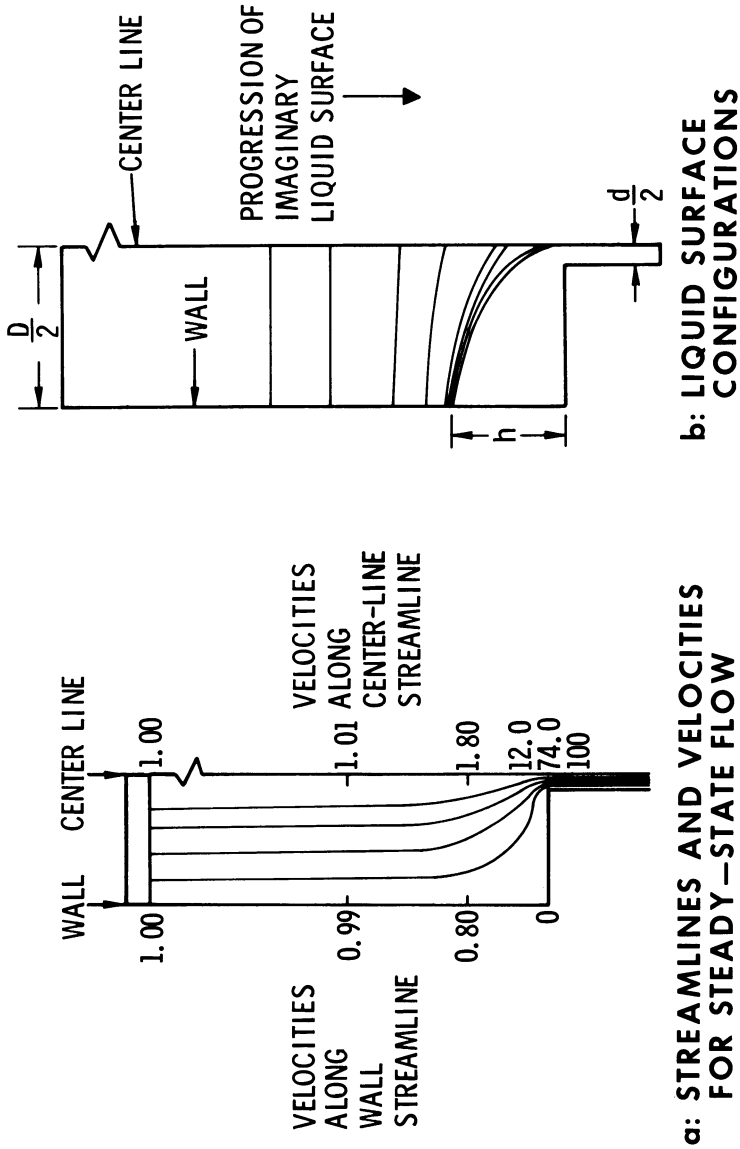
Fig. 17‑32 Solution for gas ingestion without free‑surface condition ($D/d = 10$); (a) streamlines and velocities for steady‑flow; (b) liquid surface configurations.
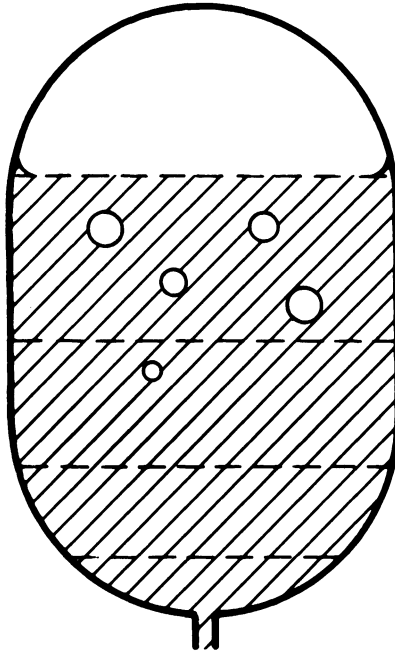
Fig. 17-33 Capillary-barrier positioning.

will prevent the passage of the gas into the liquid; consequently, displacement of liquid from the outlet compartment is prevented. Although the interchange of liquid and gas that would occur during spacecraft coast is prevented, this barrier offers little resistance to the flow of propellant during engine operation.

[17-7.1] Static Stability

The first step in determining design parameters for capillary barriers is to consider criteria for static stability. Figure 17-34 illustrates the principle by which a capillary barrier may position liquid in an adverse g-field. The pressure differential across any liquid-gas interface due to the presence of a barrier is a function
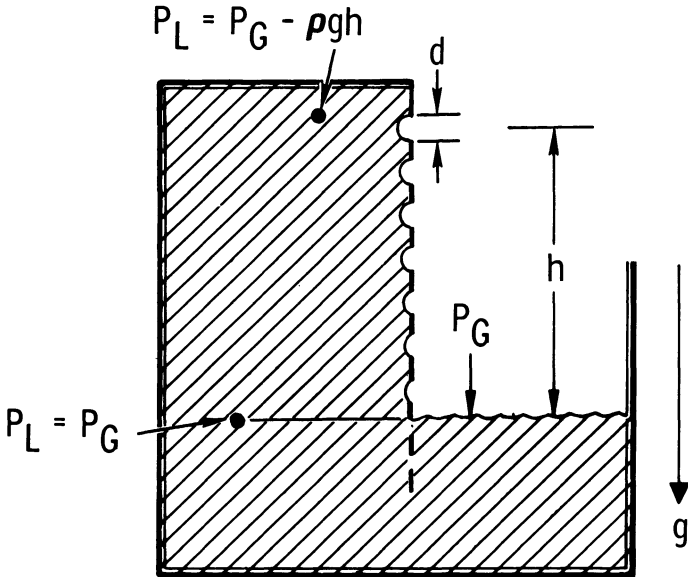
Fig. 17-34 Capillary barrier in static equilibrium.

of the interface curvature and is given by the capillary pressure equation, Eq. (17-22):

$$\Delta P = \sigma \left(\frac{1}{R_1} + \frac{1}{R_2} \right).$$ (17-67)

From hydrostatic considerations, the pressure of the liquid at any point is given by

$$P_L = P_G - \rho g h.$$ (17-68)

For static equilibrium, the capillary pressure difference at the uppermost opening must exactly equal the difference in pressure between gas and liquid at that point. Thus,

$$\sigma \left(\frac{1}{R_1} + \frac{1}{R_2} \right) = \rho g h.$$ (17-69)

For a circular opening, the curvature of the interface reaches a maximum and, consequently, the pressure differential reaches a maximum when the radius of curvature of the interface equals the radius of the opening:

$$\Delta P_{(max)} = \frac{2\sigma}{\left(\dfrac{d}{2} \right)} = \frac{4\sigma}{d}.$$ (17-70)

For noncircular openings, the maximum pressure differential can usually be expressed by

$$\Delta P_{(max)} = \frac{\sigma \times \text{perimeter}}{\text{area}} . \tag{17-71}$$

As the free surface is approached (Fig. 17-34), the radius of curvature of the interface increases from the minimum value associated with maximum pressure differential to infinity at the free surface. The static stability criterion for a barrier with circular openings is $\rho g h \leq 4 \sigma/d$. When this expression is nondimensionalized into a Bond number, the stability criterion becomes

$$\text{Bond number} = \frac{\rho g h d}{\sigma} \leq 4. \tag{17-72}$$

The above discussion assumes that the liquid wets the barrier. If the liquid-solid contact angle is 90 degrees (Fig. 17-8), the barrier resists passage of both liquid and gas. If the contact angle should approach 180 degrees, there would be no resistance to passage of the gas. In the practical case of rocket propellants having a contact angle that approaches zero, the barrier offers resistance to gas only.

[17-7.2] Dynamic Stability

When a tank with a capillary-barrier partition is suddenly disturbed, and an acceleration component along the barrier results, there will be a motion of the liquid with respect to the tank during the period when the curved gas-liquid interface is developing. Therefore, the pressure across the curved interface required to prevent the passage of gas will include (1) that required to arrest the motion of the liquid and (2) the instantaneous hydrostatic pressure due to the acceleration. On the other hand, it is possible for the disturbance to be such that only the momentum of the liquid acts to cause gas to penetrate the barrier. The barrier is said to be stable if gas penetration is prevented. Thus, the liquid will remain positioned within the compartment after an infinite number of disturbances, provided the disturbances do not cause instability.

A spacecraft perturbation that may act to cause instability of a capillary-barrier results from normal pitch or yaw attitude corrections. To evaluate this condition, a test program was conducted on the stability of capillary-barrier partitions in cylindrical tanks being subjected to angular disturbances [12]. Two disturbance modes were considered: angular acceleration and angular velocity. Angular, rather than linear disturbances, are important in spacecraft design.

The angular acceleration mode of disturbance refers to the presence of acceleration at the time the capillary interface is

acting to arrest the motion of the liquid relative to the barrier. This type of loading of the barrier is likely to occur when the liquid-gas interface is initially formed at the barrier, as shown in Fig. 17-35. This initial condition does not require that the remaining propellant be exactly sufficient to fill the compartment below the barrier; rather, it implies that the liquid above the barrier has for some reason been relocated away from it. If instability does not occur, the tank displacement will be very small (on the order of the opening diameter) when the relative liquid motion is arrested by the capillary action. Normally, the torque used to rotate the vehicle will be applied in a short pulse, but the pulse is likely to continue throughout this small displacement.

Based on the nomenclature of Fig. 17-35, the dimensionless parameters of interest found in the dimensional analysis are as follows:

h/D = height of protected compartment/tank diameter

L/D = distance between barrier and center of rotation/tank diameter

d/D = opening diameter/tank diameter

$\rho\ddot{\theta}LDd/\sigma$ = rotational Bond number, where $\ddot{\theta}L$ is the local acceleration

$\rho g D^2/\sigma$ = ambient Bond number

Op = openness ratio of barrier, *i.e.*, ratio of open area to total area

$\rho\dot{\theta}LD/\mu$ = Reynolds number

$\rho\dot{\theta}^2L^2D/\sigma$ = Weber number

Σ = stability criterion, *i.e.*, stable or unstable.

For the zero- or low-g spacecraft condition, the ambient Bond number is approximately zero. It is necessary, therefore, that tests be conducted in a low-g environment. The desired correlation is:

$$\Sigma = f\left(\frac{\rho\ddot{\theta}LDd}{\sigma},\ Op,\ \frac{h}{D},\ \frac{L}{D},\ \frac{d}{D},\ \frac{\rho\dot{\theta}LD}{\mu},\ \frac{\rho\dot{\theta}^2L^2D}{\sigma}\right),\quad (17\text{-}73)$$

$$\text{when}\quad \frac{\rho g D^2}{\sigma} \approx 0\ .$$

To attain a very low-g condition, tests were conducted in a drop tower and in KC-135 aircraft. Test variables included model size,
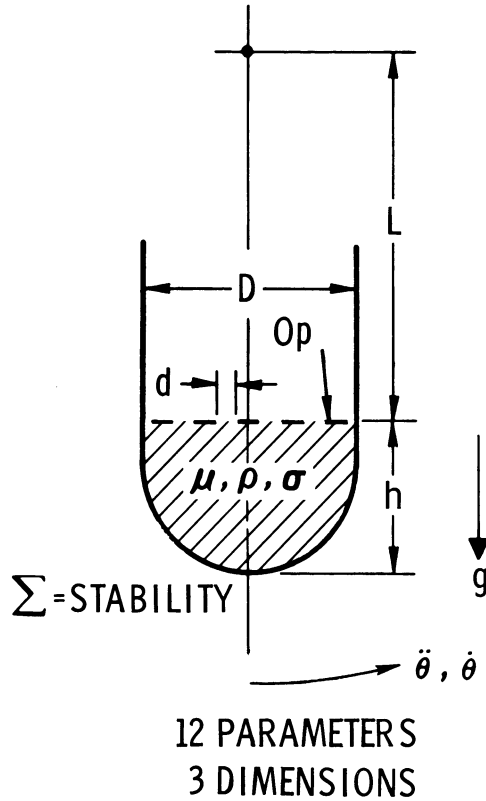
12 PARAMETERS

3 DIMENSIONS

Fig. 17-35 Variables for barrier dynamic stability analysis: angular acceleration distur-
bance mode.

liquid properties, magnitude of angular acceleration, location of
barrier and axis of rotation, and opening size and openness ratio
of the barrier. Diameters of the models were 3 and 5 inches; the
openness ratio of the barrier varied from 0.1 to 0.46 inch; diam-
eter of the openings ranged from 0.020 to 0.060 inch.

The test model, with barrier installed, was filled to the barrier
level. After the low-g condition had been established, the model
tank was rotated using a fairly constant torque. Instrumentation
consisted of a 16-mm high-speed motion-picture camera. Figure
17-36 shows the test arrangement.

The test results obtained are insufficient for determining the
functional dependence of barrier stability on the various dimen-
sionless parameters. Figure 17-37 shows the test data in terms
of stability versus the rotational Bond number. Test conditions
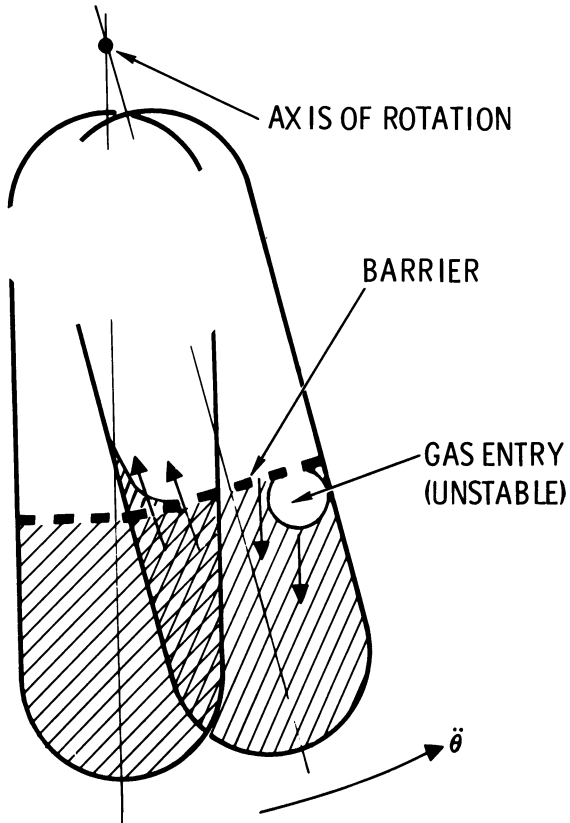represented are as follows:

Fig. 17-36 Configuration for barrier dynamic stability tests: angular acceleration.

$$\frac{\rho g D^2}{\sigma} \approx 0$$

$$0.4 < \frac{h}{D} < 0.85$$

$$1.0 < \frac{L}{D} < 2.0$$

$$0.1 < Op < 0.46.$$

The kinematic viscosity μ/ρ was kept small in the tests to minimize the effects of viscosity.
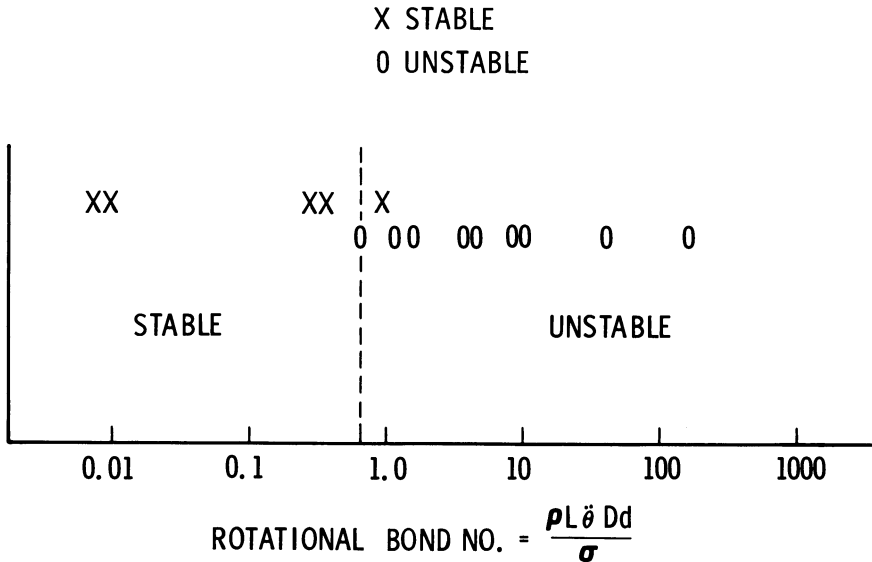
Fig. 17-37 Results of barrier dynamic stability tests: angular acceleration.

From these test results and limited analysis, it is believed that the rotational Bond number, h/D, and L/D are the significant parameters. The rotational Bond number can be compared directly with the static Bond number by equating $\ddot{\theta}L$ with g. It appears obvious from Fig. 17-37 that the barrier is considerably less stable under dynamic disturbances than is indicated by the critical Bond number of 4 obtained in the steady-state analysis.

A different type of dynamic behavior results when a significant quantity of liquid is positioned just above the barrier at the time of rotation. In this case, the tank attains a steady angular velocity before the liquid-gas interface approaches the barrier. Angular acceleration is approximately zero, and only the momentum of the liquid beneath the barrier now acts to cause instability, drawing gas into the compartment below the barrier. This disturbance mode is referred to as angular velocity.

Tests were also conducted to determine the stability characteristics of capillary barriers during this type of disturbance [12]. Dimensional analysis was again employed to determine the dimensionless parameters of interest. Based on the nomenclature given in Fig. 17-38, these parameters are as follows:

h/D = geometric ratio: depth of liquid beneath barrier/tank diameter

L/D = distance between axis of rotation and barrier/tank diameter

d/D = opening diameter/tank diameter

$\rho\dot{\theta}^2 D^3/\sigma$ = rotational Weber number

$\rho g D^2/\sigma$ = ambient Bond number

Op = openness ratio of barrier, *i.e.*, ratio of open area to total area

$\rho\dot{\theta} L D/\mu$ = Reynolds number

h_0/D = initial level/tank diameter

Σ = stability criterion.

In this case, a rotational Weber number is obtained instead of a rotational Bond number. The choice of this form of the Weber number is based on analytical results, which will be discussed subsequently.
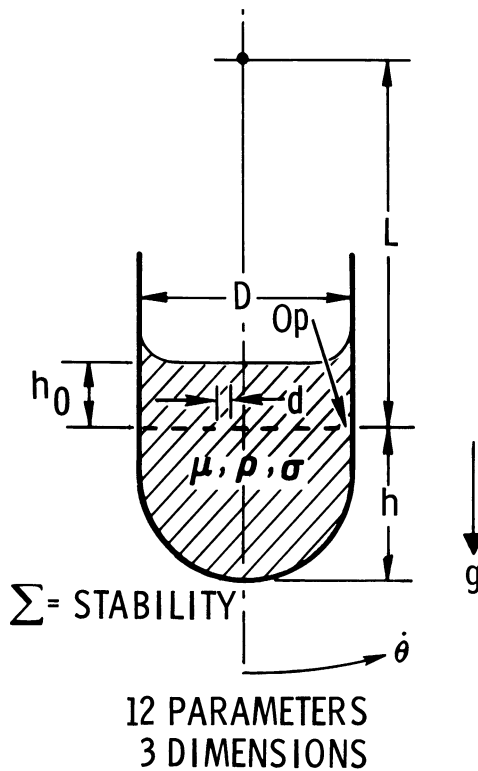
Fig. 17-38 Variables for barrier dynamic stability analysis: angular velocity disturbance mode.

An ambient Bond number again results, indicating that the test must be performed at near zero gravity. The functional relationships can be written as follows:

$$\sum = f\left(\frac{\rho\dot{\theta}^2 D^3}{\sigma},\ Op,\ \frac{\rho\dot{\theta}LD}{\mu},\ \frac{h}{D},\ \frac{L}{D},\ \frac{d}{D},\ \frac{h_0}{D}\right),\ \text{when}\ \frac{\rho g D^2}{\sigma} = 0.$$

(17-74)

Figure 17-39 illustrates a typical test configuration, showing the initial level of the liquid-gas interface and its subsequent motion. The acceleration has terminated before the interface reaches the barrier. If instability occurs, it results from the momentum of the liquid below the barrier, as illustrated.

Fig. 17-39 Configuration for barrier dynamic stability tests: angular velocity.

The tests, which were similar to those for angular acceleration, were conducted at near zero g in a drop tower and KC-135 aircraft. The duration of the angular acceleration was kept short, approximating an impulsive disturbance.

Results of the test program [12] are shown in Fig. 17-40. Data points are plotted as stable and unstable on a graph showing openness ratio versus a normalized Weber 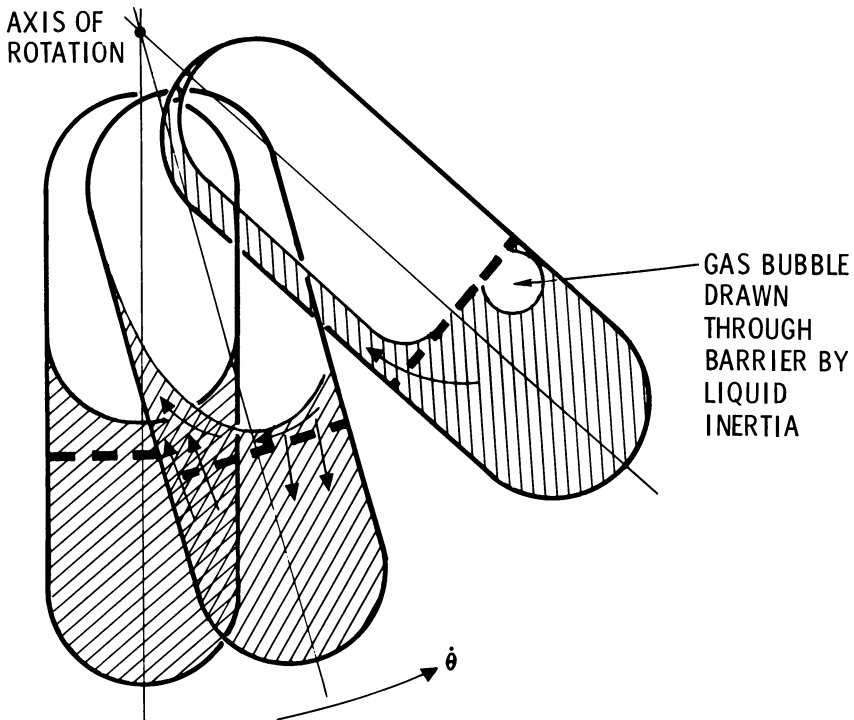number. The normalized Weber number is found by dividing the test Weber number, $\rho \dot{\theta}^2 R^3/\sigma$, by an analytically determined critical Weber number for a barrier with no blockage, i.e., $Op \to 1$. Values for We_c are given as a function of L/R and h/R (Fig. 17-41). In Fig. 17-41, the parameter h/R is important only for small values, which suggests that the shape of the tank bottom is important only when h/R is small.

Since the inertial effect of the liquid in motion acts to overcome the surface-tension forces, the Weber number, a ratio of inertial to surface forces, is expected to be important. The openness ratio is important, as it is related to the blockage of the barrier and, consequently, to the flow velocity which develops below the barrier. The geometric ratios h/D and L/D have been determined to be important from theory, and their effects are incorporated into the normalization procedure for the Weber number.

The ambient Bond number was kept approximately at zero to simulate the spacecraft environment. Theory indicates that the diameter of the barrier opening is not important, and no diameter effect was found in the test results when the hole diameter was varied by a factor of three. To avoid viscous effects, the rotational Reynolds number was kept large in the tests. Since blockage acts to reduce the energy beneath the barrier, the greater the amount of liquid which must flow through the barrier, the greater would be the expected energy dissipation and thus the damping. Therefore, the ratio h_0/D was kept small to obtain the worst-case condition, but large enough to obtain zero rotational acceleration for a finite angular velocity.

In attacking the problem theoretically, use was made of dimensional analysis. It is expected that the Weber number and the ratios h/R and L/R will be important parameters in the determination of barrier stability for the angular velocity disturbance. In Fig. 17-41 are the results of an analysis which was conducted in conjunction with the above test program to evaluate the importance of these parameters.

The problem assumes a barrier with negligible blockage $(Op \to 1)$ that partitions a circular cylinder with a flat bottom. The zero-blockage condition does not imply that the openings are excessively large, and a woven screen with infinitely small wires, compared with their spacing, would approximate this requirement. The procedure for determining the value of the critical Weber number is as follows. First, using the inviscid potential-flow theory, the flow field resulting from tank rotation is determined, ignoring entirely the presence of the barrier. Second, a flow field is determined for the liquid below the barrier, assuming total blockage. It is hypothesized that the first flow field represents
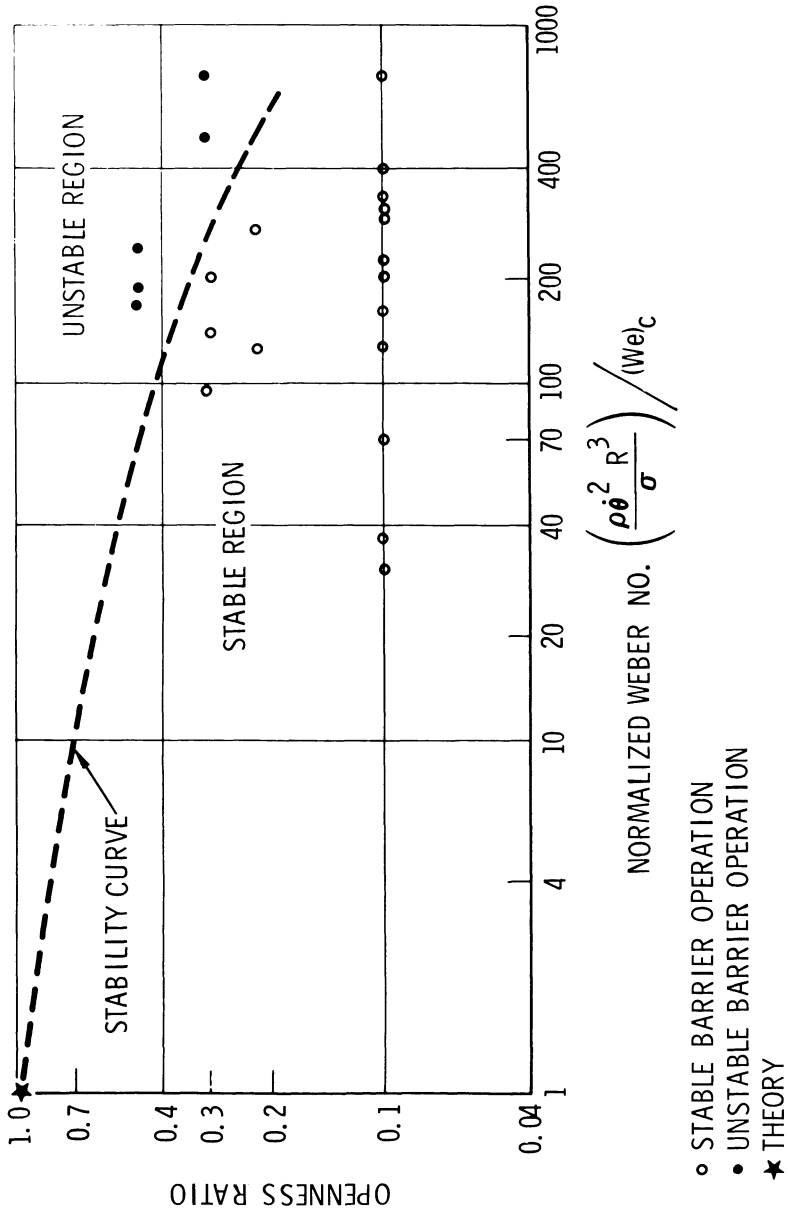
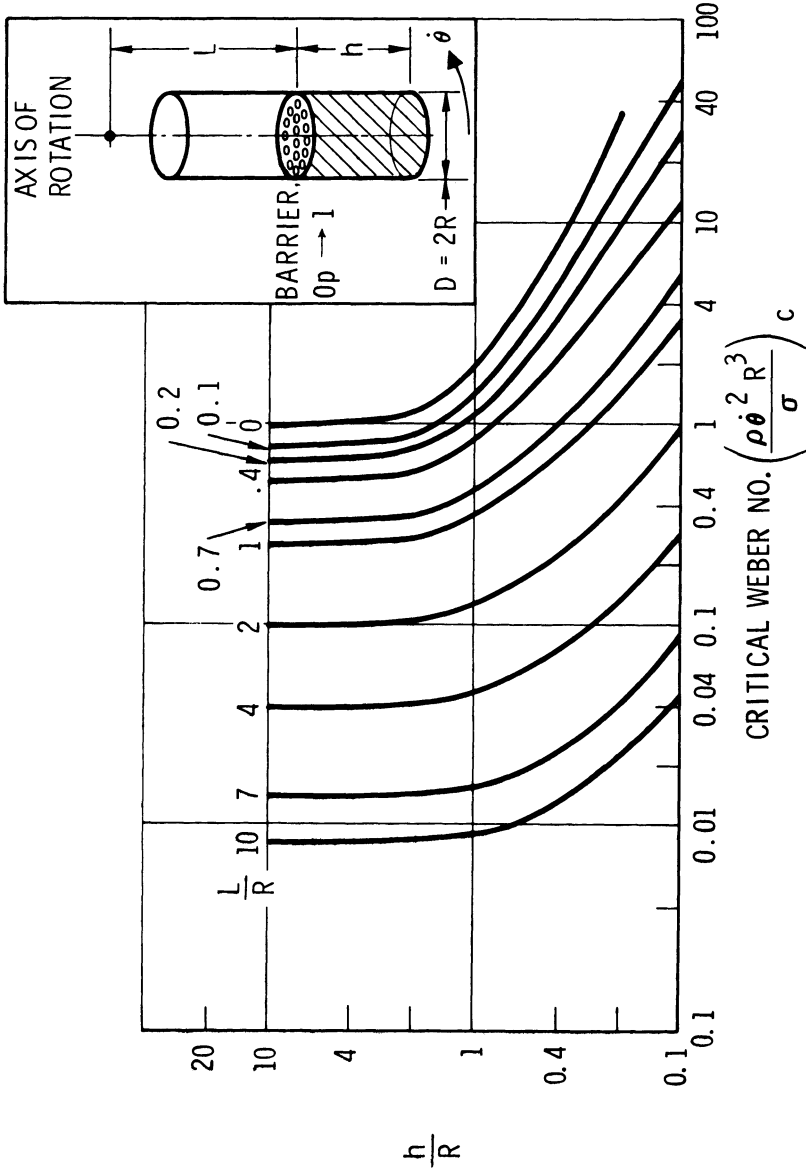Fig. 17 - 40 Results of barrier dynamic stability tests: angular velocity.

Fig. 17-41 Solution for critical Weber number (openness ratio of 1).

the liquid motion before any capillary pressure is developed at the barrier, and the second represents the flow after capillary forces have directed the flow to prevent the passage of gas. Then, assuming a barrier opening near the edge, the change in the value of the flow potential ϕ from the first to the second condition can be equated with the action of the capillary pressure to modify the flow potential, *i.e.*,

$$\phi_2 - \phi_1 = \int_1^2 \frac{P_c}{\rho} \, dt \tag{17-75}$$

where P_c is the pressure across the barrier and varies with the development of the gas-liquid interface. This equation will be recognized as a simplification of the integrated unsteady Bernoulli equation. The final expression for the critical Weber number is as follows:

$$We_c = \left[\left(\frac{l}{R} + 4 \sum_{n=1}^{\infty} \frac{\tanh\left(\frac{\xi_n h}{2R}\right)}{\xi_n \left(\xi_n^2 - 1\right)} \right) \left(1 - 2 \sum_{n=1}^{\infty} \frac{1}{\left(\xi_n^2 - 1\right)\cos h\left(\frac{\xi_n h}{R}\right)} \right) \right.$$

$$\left. + \frac{l}{R} \sum_{n=1}^{\infty} \frac{\xi_n J_1 \left(0.95 \, \xi_n\right)}{\left(\xi_n^2 - 1\right) J_1 \left(\xi_n\right)} \left[\tanh\left(\frac{\xi_n h}{R}\right) \cos h \left(.05 \, \xi_n\right) - \sin h \left(.05 \, \xi_n\right) \right] \right\}^{-1}$$

$$\tag{17-76}$$

where

ξ = the nth root of the equation $\dfrac{d}{dr} J_1 \left(\dfrac{\xi r}{R}\right)\Bigg|_{r = R} = 0$

J_1 = the Bessel function of the first kind and of the order 1.

It is of interest to note that this result is independent of opening size. It was necessary, however, to assume that the capillary pressure was sufficiently great, or the opening size sufficiently small, to dominate the velocity-squared term, which was then eliminated from the Bernoulli equation.

In addition to the stability considerations just reviewed, a few comments are in order for the application of capillary barriers. While it is desirable to design each barrier to be stable for the expected spacecraft conditions, the use of multiple barriers to provide redundancy will greatly minimize the effect of unexpected

disturbances. A number of tests have been conducted to determine the improvement in performance of multiple-barrier configurations over a single barrier. The results indicate that system reliability is greatly enhanced by the use of a multiple-partition configuration.

To control propellant position in the main propulsion system, it may be possible to design a barrier that will be purged of bubbles accumulated during engine operation by barrier tilting, as in a conical configuration. Bubbles which may have accumulated below the barrier will be collected and purged through when the hydrostatic pressure of the collected bubble is high enough to overcome the resisting capillary pressure. The size of the openings and tilt angle must be such that the barrier is unstable during engine firing but stable during coast.

Although the requirements for controlling propellant slosh have not been discussed in this chapter, it is sufficient to say that capillary multiple-barrier installations will effectively control slosh. It should also be noted that the compartment nearest the tank outlet should be designed so that it remains filled, up to and including the last restart. For redundancy, it is desirable that at least the last two barriers have a combined volume less than that required to store propellant for the last restart.

Since the capillary barrier is usually fabricated from metal and requires no moving parts, it offers an advantage over non-metallic devices in being readily sterilizable. During propellant loading, the screens must be kept dry to prevent accumulation of bubbles. In a particular design, before the final configuration is chosen, many factors must be considered, such as weight, complexity, mounting provisions, and operational requirements.

[17-8] ZERO g PROPELLANT GAUGING

An interesting problem arising from the random location of propellant in a tank is propellant gauging. Conventional gauging systems depend on the predictability of the location and configuration of the liquid in the tank and are generally not applicable to a zero-g environment. Five concepts are discussed in the following paragraphs for determining propellant quantity under zero-g conditions.

Capacitance gauging systems are commonly used to measure dielectric liquid quantity. Such systems are inherently position-sensitive, but, by the use of a large number of electrodes that measure the capacitance across various cross sections of the tank (Fig. 17-42), an accurate determination of quantity can be made. Almost all storable propellants are conductors; liquid oxygen and liquid hydrogen are good dielectrics.

A similar scheme, which is applicable to all propellants, is based on nuclear principles. A large number of radiation sources
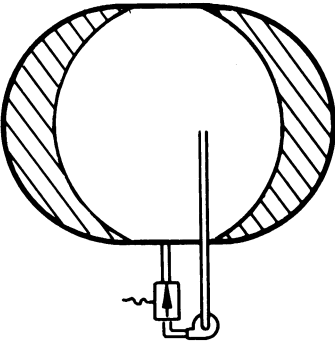
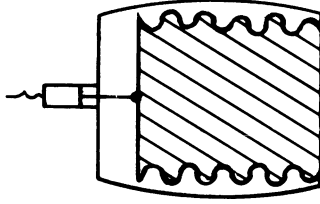Fig. 17 - 44 Zero-g gauging system using radioactive tracer gas.

Fig. 17 - 46 Quantity gauging using position transducer with bellows.
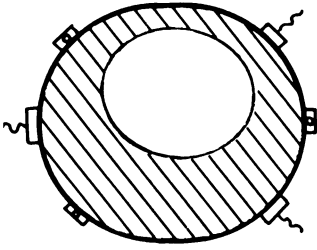

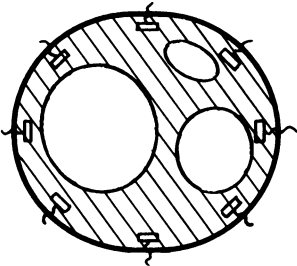Fig. 17 - 43 Radiation gauging system using multiple sources and detectors.

Fig. 17 - 42 Gauging concept using multiple-capacitance measurements for dielectric propellants.
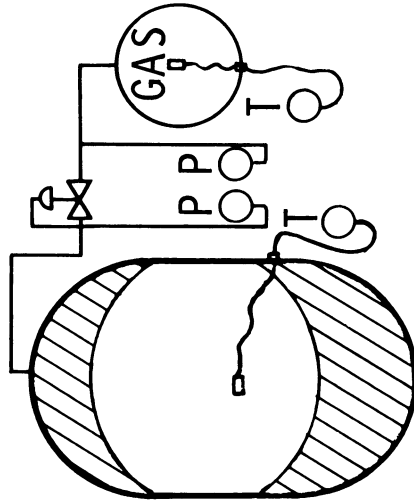

Fig. 17 - 45 PVT (pressure, volume, temperature) gauging concept.

are positioned around the tank (Fig. 17-43), and radiation detectors are placed opposite the sources to measure the absorption of the nuclear energy by the propellant. A properly characterized summation of the readings of the sensors can be used to determine propellant quantity. Again, sensitivity to position is inherent, but it is minimized by the averaging of many measurements.

Another method that uses radioactivity is based on the dilution of a radioactive tracer gas (Fig. 17-44). A known quantity of this gas is loaded into the propellant tank, and a sampling system measures the concentration of this gas in the tank ullage volume. As the propellant quantity decreases, the ullage volume increases, and the tracer gas is diluted. The quantity of propellant remaining can be computed from the measured concentration of the tracer gas. This system is inherently insensitive to liquid position.

A simple scheme for determining propellant quantity is based on the ideal gas law and is referred to as a PVT (pressure, volume, temperature) system (Fig. 17-45). With this system, it is assumed that the total mass of the pressurant gas is conserved. By measuring the pressure and temperature of the gas in the pressurant tank, the volume of which is known, the corresponding mass of the gas can be determined. Subtracting this value of the mass from the total mass of the pressurant gives the amount of pressurant in the propellant tank. By measuring the pressure and temperature of the gas in the propellant, its mass being known, the volume of the gas can be determined. Finally, subtracting this volume from the tank volume, which is known, provides the volume of the propellant remaining. Accuracy can be improved by accounting for the vapor pressure of the liquid. This system is also inherently insensitive to liquid position. It has been used in both the Gemini and Apollo spacecraft.

When propellant is contained in a variable-volume bellows, its volume becomes a function of the position of the bellows. By incorporating a position detector and readout device (Fig. 17-46), a very simple gauging system is obtained. However, this system is relatively heavy.

Of the five methods discussed, three measure liquid quantity and two measure gas quantity. The liquid-gauging sytems, except the bellows method, require multiple measurements and averaging of results, presenting a reliability problem. The primary problem of gas-gauging systems is that leakage of gas strongly affects the results and is an unknown factor during flight.

[17-9] SUMMARY AND CONCLUSIONS

The hydrostatics of a zero-g environment are amenable to theoretical treatment, and fairly rigorous solutions are available. It can be shown, using the minimum-energy principle, that the

contact angle of a given liquid–solid combination is constant and independent of gravity and that, if a bubble exists in zero g, its shape is spherical. For most propellants in metal containers, it can be assumed that the contact angle is zero, considerably simplifying analysis.

Unfortunately, practical hydrodynamics problems are not submissive to theory. Many of the practical problems of propellant management in a weightless environment must be solved empirically. Even in areas where analytical solutions are possible, the results must be checked against experimental data to verify the accuracy of the analytical approach. Some modes of propellant behavior at low gravity can be adequately investigated with tests at earth-gravity conditions, *e.g.*, propellant settling and gas ingestion. Indeed, in many cases, the reduction of model size requires an increase of the applied thrust or g, with the result that the test is better scaled at 1 g than at a very low-g environment. Accordingly, experimental procedures and results have been emphasized in this discussion, with particular attention given the use of dimensional analysis in planning meaningful tests.

Limited data are presented for predicting propellant slosh precipitated by spacecraft attitude change or engine cutoff. The problem of propellant slosh leads to a discussion of controlling propellant position. While several approaches are mentioned, only two have been used in actual spacecraft design: propellant settling using external thrusters to create artificial gravity and passive systems employing capillary barriers.

The problem of propellant settling by auxiliary thrusting can be conveniently divided into three parts. The first task is to determine the minimum thrust, or settling acceleration, to overcome capillary stability and initiate settling. The second requirement is to determine the manner and rate at which the liquid flows from the top of the tank into the outlet end. The third part of the problem is to determine the time required for the propellant to become sufficiently stilled and bubble-free to ensure engine restart.

For the case where the contact angle is zero, the interface is statically stable as long as the Bond number is below the critical value of 0.84. For the dynamic problems, the techniques of dimensional analysis are used to design meaningful experiments. Correlation of test results gives necessary design information in the form of the dimensionless parameters: Bond number, Froude number, and Reynolds number. When the Bond number is greater than 10 and the Reynolds number greater than 50, the Froude number can be assumed to be the constant value of 0.48 for estimating the interface-rise velocity. Propellant accumulation can be predicted by defining the number of dimensionless time units or number of free-fall periods required for settling. Experiments show that a conservative value of five dimensionless time units can be used for design purposes. In order to expend the least

amount of propellant for settling, the lowest possible value of thrust (settling acceleration) should be used, provided capillary restriction does not occur (Bond number greater than 10). This result is significant in the design of auxiliary thrust systems and cannot be predicted intuitively.

A correlating problem associated with propellant settling by thrusting is gas ingestion. Again, design information must be obtained experimentally, although some theoretical results are available. Both theory and experiment indicate that with sufficiently large values for the Froude and Bond numbers, their influence on the gas-ingestion height approaches zero. Experiment indicates that for large values of Froude and Bond numbers, typical of spacecraft applications, the dimensionless gas-ingestion height is 0.43.

The second, or passive, approach to propellant settling involving capillary barriers is again attacked by theory and experiment for both the static and dynamic conditions. Theory indicates that static stability exists when the Bond number is equal to or less than 4 for liquid-solid combinations where the contact angle is zero. Two dynamic-stability modes were considered experimentally: disturbances precipitated by angular acceleration and by angular velocity. The angular-acceleration mode of disturbance refers to the presence of acceleration at the time the capillary interface is acting to arrest the mode of the liquid relative to the barrier. The angular-velocity disturbances mode occurs when a significant quantity of liquid is positioned just above the barrier at the time of rotation; the tank attains a steady angular velocity before the gas-liquid interface approaches the barrier. Stability regions are defined again as a function of dimensionless parameters from limited experimental data. For the dynamic cases, the effective Bond number at which instability occurs is reduced considerably below the value of 4 associated with static stability.

The correlation and significance of key dimensionless ratios for the many tests performed are shown in Table 17-1. Of the Bond, Weber, and Froude numbers, only two are independent; the third can be obtained as a product or ratio of the other two. The Bond number is the controlling parameter for capillary problems. The Weber number, the ratio of inertial forces to capillary forces, is important in the angular-velocity mode of capillary propellant stability. The Froude number, which relates inertial forces to gravity forces, is important in propellant settling and gas ingestion. The Reynolds number is a measure of the relative importance of viscous effects. This parameter is particularly important in the accumulation aspects of the propellant-settling problem when thrusters are used to provide artificial gravity.

Although limited information has been obtained by suitable application of theory and experiment, many aspects of the behavior of propellants in a zero-g environment are not well understood. In this chapter, the problem of predicting that behavior has been

Table 17-1 Importance of Dimensionless Parameters

Problem	Parameters			
	Bond No. $\dfrac{\rho g L^2}{\sigma}$	Weber No. $\dfrac{\rho V^2 L}{\sigma}$	Froude No. $\dfrac{V^2}{gL}$	Reynolds No. $\dfrac{\rho VL}{\mu}$
Static Configurations	Significant		0	0
Capillary Stability	Significant		0	0
Gas Interface Velocity	Significant		Significant	Minor
Accumulation (Settling)	Significant		Significant	Significant
Gas Ingestion	Minor		Significant	Minor
Barrier Stability (Static)	Significant		0	0
Barrier Stability (Angular Acceleration)	Significant*	Minor		Uncertain
Barrier Stability (Angular Velocity)	0	Significant**		Uncertain

*Rotational Bond Number, $\dfrac{\rho \ddot{\theta} LD\, d}{\sigma}$.

**Rotational Weber Number, $\dfrac{\rho \dot{\theta}^2 D^3}{\sigma}$.

Note: Weber and Froude Numbers are independent.

attacked from the standpoint of applicability to practical design problems, specifically to summarize what is known in this field and to provide the designer with some useful tools. However, the field is very fertile for new approaches, expecially in the theoretical area. Propellants in a zero-g environment provide an unusual coupling of intermolecular and inertial forces, and the basic understanding of fluid mechanics can be significantly improved by advances in this area.

[17-10] APPENDIX A. DERIVATION OF SLOSH FREQUENCY

The equation of motion for incompressible inviscid flow in the partially filled cylindrical container shown in Fig. 17-47 can be expressed in terms of the velocity potential ϕ as

$$\nabla^2 \phi = 0$$

or for the cylindrical coordinate system used here:

$$\left[\frac{1}{r}\,\frac{\partial}{\partial r}\left(r\,\frac{\partial \phi}{\partial r}\right)\right] + \left(\frac{1}{r^2}\,\frac{\partial^2 \phi}{\partial \theta^2}\right) + \left(\frac{\partial^2 \phi}{\partial Z^2}\right) = 0. \qquad (17\text{-}77)$$
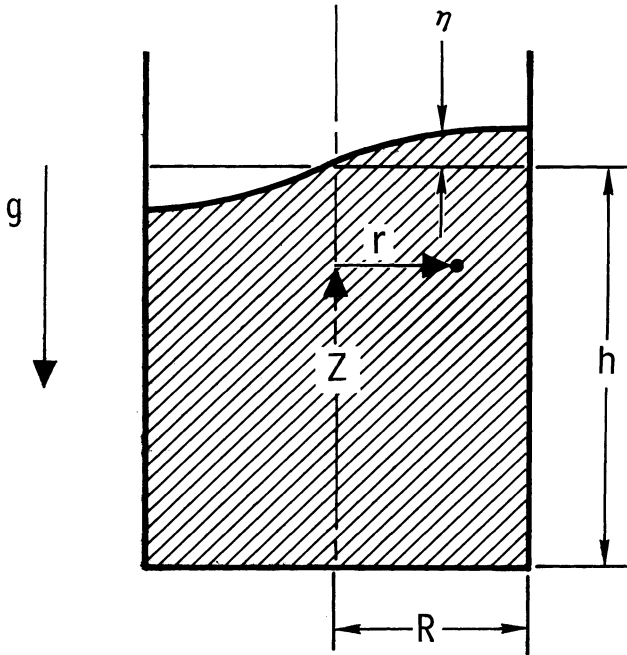
Fig. 17-47 Geometry for analysis of slosh frequency.

It should be remembered that

$$\overline{u} = \overline{\nabla} \phi$$

where $\overset{>}{u}$ is the velocity at any point.

The boundary condition on the cylindrical surface $r = R$ and on the tank bottom $Z = 0$ is that the velocity perpendicular to the wall must be zero. Hence

$$u_r = \frac{\partial \phi}{\partial r} = 0 \quad \text{at} \quad r = R$$

$$u_Z = \frac{\partial \phi}{\partial Z} = 0 \quad \text{at} \quad Z = 0$$

(17-78)

where u_r is the radial component of $\overset{>}{u}$ and u_Z is the axial of $\overset{>}{u}$.

Two conditions must be satisfied *on the free surface* $\eta \{r, \theta, t\}$. The first of these is the kinematic condition that any point on the surface moves with the surface. Thus

$$\frac{\partial \eta}{\partial t} + u_r \frac{\partial \eta}{\partial r} + \frac{u_\theta}{r} \frac{\partial \eta}{\partial \theta} = u_{\text{surface}} .$$

(17-79a)

The second condition is Bernoulli's equation for unsteady flow for a surface on which surface-tension effects are important. This condition may be expressed as

$$\frac{\partial \phi}{\partial t} + \frac{1}{2}\left(\overline{\nabla} \phi \cdot \overline{\nabla} \phi\right) + \frac{P - P_a}{\rho} + g\eta = 0 \qquad (17\text{-}79\text{b})$$

where the terms are to be evaluated at the surface.

These equations can be simplified for the special case of small-amplitude disturbances. The relationship between the ambient pressure P_a and the pressure in the liquid at the surface P is given by

$$P - P_a = \sigma \left\{ \left[\frac{1}{r}\frac{\partial}{\partial r}\left(r\frac{\partial \eta}{\partial r}\right)\right] + \left(\frac{1}{r^2}\frac{\partial^2 \eta}{\partial \theta^2}\right)\right\}. \qquad (17\text{-}80)$$

The terms in the bracket are approximations of the reciprocals of the local radii of curvature for the surface $\eta\{r, \theta, t\}$ and are correct when the displacement approaches zero. In addition, when $\eta \ll h$, it can be shown that Eqs. (17-79a) and (17-79b) reduce to

$$\frac{\partial \eta}{\partial t} = \frac{\partial \phi}{\partial Z} \qquad (17\text{-}81)$$

$$\frac{\partial \phi}{\partial t} = -g\eta + \frac{\sigma}{\rho}\left\{ \left[\frac{1}{r}\frac{\partial}{\partial r}\left(r\frac{\partial \eta}{\partial r}\right)\right] + \left(\frac{1}{r^2}\frac{\partial^2 \eta}{\partial \theta^2}\right)\right\} \qquad (17\text{-}82)$$

where the terms are to be evaluated at the surface, and Eq. (17-80) has been used to eliminate the pressure change across the surface layer. The surface displacement can be eliminated from Eqs. (17-81) and (17-82) in the following manner. Take $\partial/\partial Z$ of Eq. (17-81) and $\partial/\partial t$ of Eq. (17-82) and eliminate all terms in η. This gives

$$\frac{\partial^2 \phi}{\partial t^2} = -g\frac{\partial \phi}{\partial t} + \frac{\sigma}{\rho}\frac{\partial}{\partial Z}\left[\frac{1}{r}\frac{\partial}{\partial r}\left(r\frac{\partial \phi}{\partial r}\right) + \frac{1}{r^2}\frac{\partial^2 \phi}{\partial \theta^2}\right].$$

When Eq. (17-77) is used to eliminate the terms in the bracket, the resultant equation becomes

$$\frac{\partial^2 \phi}{\partial t^2} = -g\frac{\partial \phi}{\partial Z} - \frac{\sigma}{\rho}\frac{\partial^3 \phi}{\partial Z^3} \qquad \text{at} \qquad Z = h. \qquad (17\text{-}83)$$

This equation can be satisfied at h rather than at $\eta + h$ because of our assumption that $\eta \ll h$.

Solutions to Eq. (17-77), subject to boundary conditions imposed on Eq. (17-78) and (17-83), can be found by a straightforward

application of the technique of separation of variables, and a particular solution is

$$\phi = e^{iwt} \ \Phi \{r, \theta, Z\} \tag{17-84}$$

where

$$\Phi = \cos h \left\{ \alpha_0 \frac{Z}{h} \right\} \sin \theta \cdot J_1 \left\{ \alpha_0 \frac{r}{R} \right\}. \tag{17-85}$$

Here ξ_1 is fixed by the condition that

$$\left. \frac{\partial J_1}{\partial r} \right|_{r=R} = 0 \tag{17-86}$$

and J_1 is the Bessel function of the first kind of order 1. Eqs. (17-84), (17-85), and (17-86) satisfy Eq. (17-77) and conditions imposed on Eq. (17-78). In order to satisfy Eq. (17-83), ω must take on a particular value which is the natural frequency of the system. It is found by substituting Eq. (17-84) into Eq. (17-83) and is given by

$$\omega^2 = \alpha_0 \left(\frac{g}{R} \right) \tan h \left\{ \alpha_0 \frac{h}{R} \right\} \left[1 + \frac{\alpha_0^2}{\left(\frac{\rho g R^2}{\sigma} \right)} \right] \tag{17-87}$$

For the form picked in Eqs. (17-84) and (17-85), the value of ω given in Eq. (17-87) corresponds to the frequency of the first mode of the slosh wave. Note that α_0 is a constant given by the condition in Eq. (17-86) and is about 1.84. If $h > R$, the hyperbolic tangent term approaches unity, and Eq. (17-87) simplifies to

$$\omega = \sqrt{\alpha_0} \sqrt{\frac{g}{R}} \left[1 + \frac{\alpha_0^2}{\left(\frac{\rho g R^2}{\sigma} \right)} \right]. \tag{17-88}$$

Thus, the natural angular frequency of slosh is fixed by acceleration g and radius of the tank R and further modified by surface

tension, the bracketed term. This term will change the frequency by less than five percent as long as

$$\beta \equiv \left(\frac{\rho g R^2}{\sigma}\right) > 40. \qquad (17\text{-}89)$$

[17-11] APPENDIX B. DERIVATION OF FLOW RATE DURING PROPELLANT SETTLING

When liquid is accumulated at one end of a cylindrical container, such as a propellant tank, and an acceleration is applied to move the liquid to the other end of the tank, as in a spacecraft settling maneuver, the liquid will flow along the tank walls. The steady-state velocity of the interface motion V_I [8] is

$$V_I = 0.48 \sqrt{\frac{gD}{2}} \; f(Bo) \qquad (17\text{-}90)$$

where

$$f(B) = 1 - \left(\frac{0.84}{Bo}\right)^{\frac{Bo}{4.7}} = \text{Bond number function}$$

and

$$Bo = \frac{\rho g \left(\frac{D}{2}\right)^2}{\sigma}.$$

The volumetric flow rate Q past any level y_1 varies with that level's distance L from the nose of the interface (Fig. 17-48). This flow rate can be derived from the interface velocity if the following assumptions are made [13]:

(1) All liquid below the interface nose y_2 moves in the y direction according to the free-fall equation $V = gt$. For any particle, $t = 0$ when that particle is at the level of the nose of the interface.

(2) Horizontal velocities can be neglected.

Both assumptions are equivalent to a simplification of the flow that takes place in the vicinity of the nose of the interface. The result of this simplification is to give the instantaneous flow rate at some level other than at L below the interface. The error in L is thought

to be less than one radius, and the calculated flow rate will occur below the level at which the calculations are based.
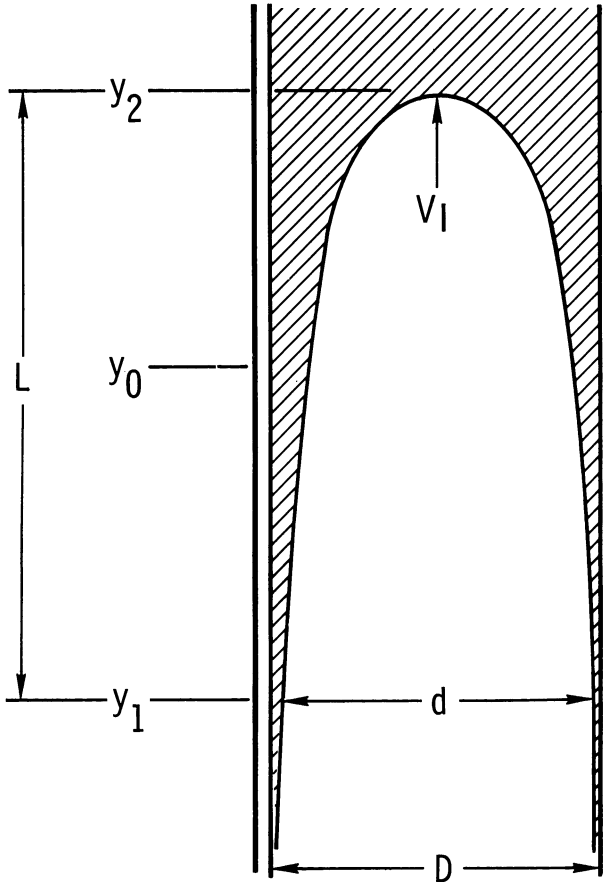

Fig. 17-48 Geometry for analysis of flow rate.

The derivation proceeds as follows, with dimensions as shown in Fig. 17-48:

$$y_0 = \text{level of the interface at} \quad t = 0$$

$$y_0 - y_1 = \frac{1}{2} gt^2 \tag{17-91}$$

$$y_2 - y_0 = V_I t \tag{17-92}$$

$$L = (y_0 - y_1) + (y_2 - y_0) = \frac{1}{2} g t^2 + V_I t \qquad (17\text{-}93a)$$

$$\frac{1}{2} g t^2 + V_I t - L = 0 \qquad (17\text{-}93b)$$

$$t = \frac{\left(- V_I + \sqrt{V_I^2 + 2gL}\right)}{g} \qquad (17\text{-}94)$$

(The other solution $(-\sqrt{\ })$ results in a negative time.)
If V_L = velocity of the liquid at y_1, by the free-fall assumption,

$$V_L = g t = -V_I + \sqrt{V_I^2 + 2gL} \qquad (17\text{-}95)$$

A continuity equation can be written as follows, assuming that the gas is moving at a constant velocity V_I:

$$\frac{1}{4} \pi d^2 V_I = \frac{1}{4} \pi (D^2 - d^2) V_L \qquad (17\text{-}96)$$

$$V_I d^2 = V_L D^2 - V_L d^2 \qquad (17\text{-}97)$$

$$d^2 = \frac{V_L}{V_I + V_L} D^2 . \qquad (17\text{-}98)$$

The volumetric flow rate Q can be written

$$Q = V_L A_L \qquad (17\text{-}99)$$

where A_L is the cross-sectional area of liquid at y_1. Thus

$$A_L = \frac{1}{4} \pi (D^2 - d^2). \qquad (17\text{-}100)$$

Substituting Eq. (17-98) into Eq. (17-100) gives

$$A_L = \pi \left(\frac{D}{2}\right)^2 \left(1 - \frac{V_L}{V_I + V_L}\right) \qquad (17\text{-}101)$$

and substituting Eqs. (17-95) and (17-101) into Eq. (17-99) gives

$$Q = \pi \left(\frac{D}{2}\right)^2 \left(1 - \frac{\sqrt{V_I^2 + 2gL} - V_1}{\sqrt{V_I^2 + 2gL}}\right) \left(\sqrt{V_I^2 + 2gL} - V_I\right) \qquad (17\text{-}102)$$

$$Q = \pi \left(\frac{D}{2}\right)^2 V_I \left(1 - \frac{V_I}{\sqrt{V_I{}^2 + 2gL}}\right) \qquad (17\text{-}103)$$

or, substituting for the interface velocity in the fraction and eliminating g gives

$$Q = \pi \left(\frac{D}{2}\right)^2 V_I \left[1 - \frac{0.48\, f(Bo)\, \dfrac{D}{2}}{\sqrt{\dfrac{D}{2}\left[0.48\, f(Bo)\right]^2 + 2L}}\right] \qquad (17\text{-}104)$$

SYMBOLS AND ABBREVIATIONS

a	Acceleration
A	Surface area of container
A_L	Cross-sectional area of liquid
$a, \bar{a}$	Exponents in Buckingham's pi development
$b, \bar{b}$	Exponents in Buckingham's pi development
Bo	Bond number
$c, \bar{c}$	Exponents in Buckingham's pi development
$C(t)$	Constant in Bernoulli's equation, which may change with time but not with position
CF	Reynolds number correction factor
$d, \bar{d}$	Exponents in Buckingham's pi development
d	Outlet diameter
	Diameter of gas–liquid interface
	Opening diameter of capillary barrier
D	Tank diameter
F	Force
F_e	Applied external force
F_g	Gravitational force of attraction
F_1, F_2	Force due to surface tension
g	Acceleration due to gravity or acceleration due to externally applied force
G	Universal gravitational constant
h	Height
	Gas-ingestion height
h_0	Initial height
i	Imaginary coefficient $(\sqrt{-1})$
I_{sp}	Specific impulse
J_1	Bessel function of the first kind and of order 1
K	Dimensionless constant
l	Length or distance
l_1, l_2	Lines on surface element

L	Length or distance
L_1, L_2	Hydrostatic and capillary length terms in capillary rise problem
m	Mass of smaller of two bodies
M	Mass: basic unit; of larger of two bodies; of space vehicle
n	Direction normal to wall
Op	Openness ratio
P	Pressure
ΔP	Differential pressure
P_1, P_2	Regions within liquid
P_a	Ambient pressure
$P.E.$	Potential energy
PVT	Pressure, volume, temperature
Q	Volumetric flow rate
	Velocity
r	Distance between two masses
	Radial coordinate in cylindrical coordinate system
r_0, r_1	Radii defined in Fig. 17-6
R	Tank radius
R_1, R_2	Radii of curvature
s	Distance
$S.E.$	Surface energy
T, t	Time
u	Velocity
u_r	Radial velocity
u_Z	Axial velocity
v	Outlet velocity
V	Volume
	Velocity
V_I	Interface velocity
V_A	Velocity of liquid
We	Weber number
$\dot{W}_p$	Flow rate of propellant to rocket engine
x, x_1	Functions designating surfaces
y	Function designating surface
y	Axial coordinate in cylindrical coordinate system
$\bar{y}$	Arbitrary reference level
y_0, y_1, y_2	Vertical location of specific points
Z	Vertical coordinate

SUBSCRIPTS AND SUPERSCRIPTS

C	Critical
	Capillary
G	Gas
L	Liquid

LS	Liquid–Solid
LV	Liquid–Vapor
n	Index of Series
VS	Vapor–Solid
( )'	Dimensionless

GREEK LETTERS

$\alpha,\ \alpha_1,\ \alpha_2$	Angles
α	Exponent in Buckingham's pi development
β	Volume ratio, vapor/container
	Degree of settling (arbitrary scale)
	Exponent in Buckingham's pi development
γ	Surface energy per unit area
	Exponent in Buckingham's pi development
δ	Thickness of flowing liquid stream
	Displacement of surface from average height
	Exponent in Buckingham's pi development
η	Wave amplitude
θ	Angular coordinate in cylindrical coordinate system
	Contact angle
	Angular position of tank
λ	Lagrange multiplier
μ	Viscosity
ξ_n	nth root of equation $\left. \dfrac{d}{dr}\, J_1\!\left(\dfrac{\xi r}{R}\right) \right|_{r=0} = 0$
π	Dimensionless parameter in Buckingham's pi development
ρ	Liquid density or difference in density between liquid and gas
σ	Surface tension
Σ	Stability criterion
$\tau,\ \tau_1$	Angles
	Dimensionless time
ϕ	Angular cylindrical coordinate
	Velocity potential
$\Phi(r,\ \theta,\ Z)$	Potential function
$\psi,\ \psi_1$	Angles
ω	Angular frequency
	The quantity $\dfrac{\gamma_{VS} - \gamma_{LS}}{\gamma\, L_V}$

REFERENCES

1. Li, Ta C.: Hydrostatics in various gravitational fields, *J. Chemistry and Physics*, 36:9, May 1, 1962, pp. 2369, 2375.
2. Petrash, D.A., R.F. Zappa and E.W. Otto: Experimental Study of the Effects of Weightlessness on the Configuration of Mercury and Alcohol in Spherical Tanks *TN D-1197*, NASA, 1962.
3. Satterlee, H.M. and W.C. Reynolds: The Dynamics of the Free Liquid Surface in Cylindrical Containers Under Strong Capillary and Weak Gravity Conditions *Technical Report LG-2*, Stanford University, May 1, 1964.
4. Reynolds, J.M. and M. Hurwitz: Electrohydrodynamic Propellant management systems for cryogenic upper stages, *AIAA Paper No. 66-922*, presented at AIAA Third Annual Meeting, Boston, November 29, 1966.
5. Gluck, D.F. and J.P. Gille: Fluid mechanics of zero-g propellant transfer in spacecraft propulsion systems, *Transactions of the A.S.M.E., J. Engineering for Industry*, Vol. 87, Series B, No. 1, February 1965.
6. Masica, W.J., D.A. Petrash, and E.W. Otto: Hydrostatic Stability of the Liquid-Vapor Interface in a Gravitational Field *TN D-2267*, NASA, 1964.
7. Masica, W.J., J.D. Derdul, and D.A. Petrash: Hydrostatic Stability of the Liquid-Vapor Interface in a Low-Acceleration Field *TN D-2444*, NASA, 1964.
8. Masica, W.J. and J.A. Salzman: An Experimental Investigation of the Dynamic Behavior of the Liquid-Vapor Interface Under Adverse Low-Gravitational Conditions *TM X-52095*, NASA, 1965.
9. Zukoski, E.E.: Influence of viscosity, surface tension, and inclination angle on motion of long bubbles in closed tubes, *J. Fluid Mechanics*, Vol. 25, Part 4, 1966, pp. 821-837.
10. O'Brien, J.P.: Test report, one 'g' tests to determine the characteristics of retention screens, high 'g' slosh tests, *North American Aviation Space Division LM 311-6009*, July 1966.
11. Gluck, D.F., J.P. Gille, D.J. Simkin, and E.E. Zukoski: Distortion of a free surface during tank discharge, *J. Spacecraft and Rockets*, 3:11, November 1966, pp. 1961, 1962.
12. Gluck, D.F. *et al.*: Hydrodynamic Stability of Capillary Barriers for Spacecraft Propellant Position Control *SID 66-1087*, North American Aviation Space Division, August 1966.
13. Gille, J.P.: North American Aviation, Inc., *Internal Letter #190-030-FSA65-036*, May 18, 1965.

Propulsion Systems—Comparison and Evaluation for Space Missions

K. A. Ehricke
Assistant Division Director,
Astrionics Autonetics Division,
North American Aviation, Inc.

[18-1] GOALS

Specification of the goals revolves around the three basic aspects of quality, schedule and cost; quality and schedule are determined, to a large degree, by mission requirement and vehicle/propulsion capabilities; cost refers to initial investment (nonrecurring) outlays. Figure 18-1 shows the principal steps in the comparative analysis, where PS stands for propulsion system.

The basic and complex attributes usually of importance in comparing propulsion systems are listed in Tables 18-1 and 18-2, respectively, where the vehicle mass groups referred to in Table 18-2 are defined in Table 18-3. The tie-up of basic and complex quality attributes are shown in the logic diagram, Fig. 18-2. These quality attributes are part of the criteria for the evaluation process. The complete list of these criteria is presented in Table 18-2. Numerical values attached to some or all of them constitute the goals against which the competing systems can be evaluated.

[18-2] PROPULSION-VEHICLE-MISSION INTEGRATION

Basic and complex attributes are defined in Section 18-1, together with a definition of vehicle mass groups and the principal relations between these parameters. On the basis of the terms defined in Figs. 18-1 and 18-2, the mass ratio of a stage i is defined as

$$\mu_i = \frac{m_A}{m_B} = \frac{1}{1 - \Lambda} = \exp\left(\frac{\Delta v}{g I_{sp}}\right) = \exp\left(\frac{\tau}{I_{sp}}\right) \qquad (13\text{-}1)$$
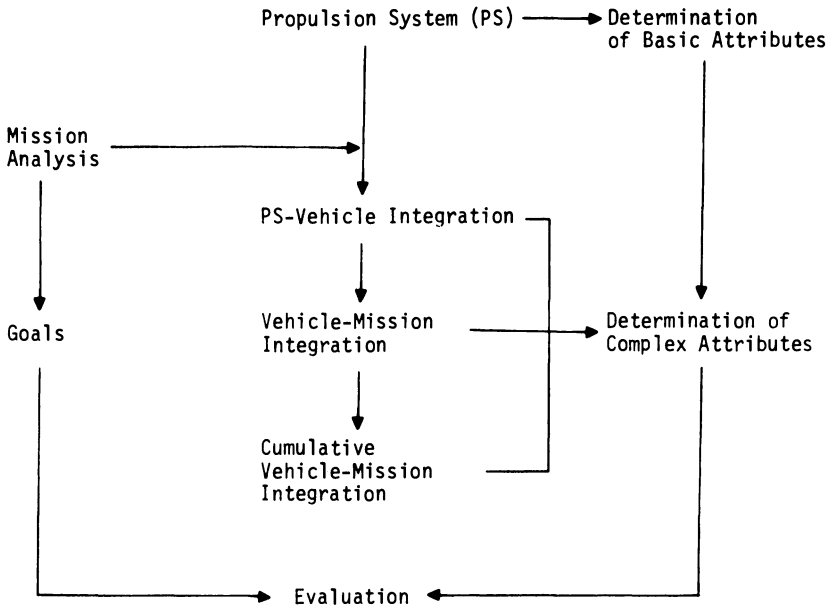
Fig. 18-1 Principal steps in comparative analysis.

Table 18-1   Basic Attributes

Specific Impulse, I_{sp} (sec)

Thrust, F (lb$_F$)

Thrust-Dependent Scaling Coefficient, K_f (lb/lb$_F$)

Electric Power Dependent Scaling Coefficient, α (lb/ekw)

Propellant-Dependent Scaling Coefficient, K_p (lb/lb$_p$)

Propellant Density, d_p (mass/volume)

Propellant Procurement Cost, k_p ($/lb$_p$)

Inert Mass Procurement Cost, k_i ($/lb$_i$)

lb$_F$ = pound of thrust

lb$_p$ = pound of propellant = lb$_{30}$ for 1-stage vehicle

lb$_i$ = pound of inert weight = lb$_{20}$ for 1-stage vehicle

where $r = \Delta v/g$ defines a velocity equivalent term which is convenient because it has the same dimension as the specific impulse.

Based on the interdependence of velocity factor r/I_{sp}, mass ratio μ, mass fraction x, gross (pay) load fraction Λ, propellant fraction λ, propellant mass factor p, and inert mass factor i, a number of charts can be constructed which conveniently correlate these propulsion system, vehicle and mission parameters and permit rapid establishment of trends.
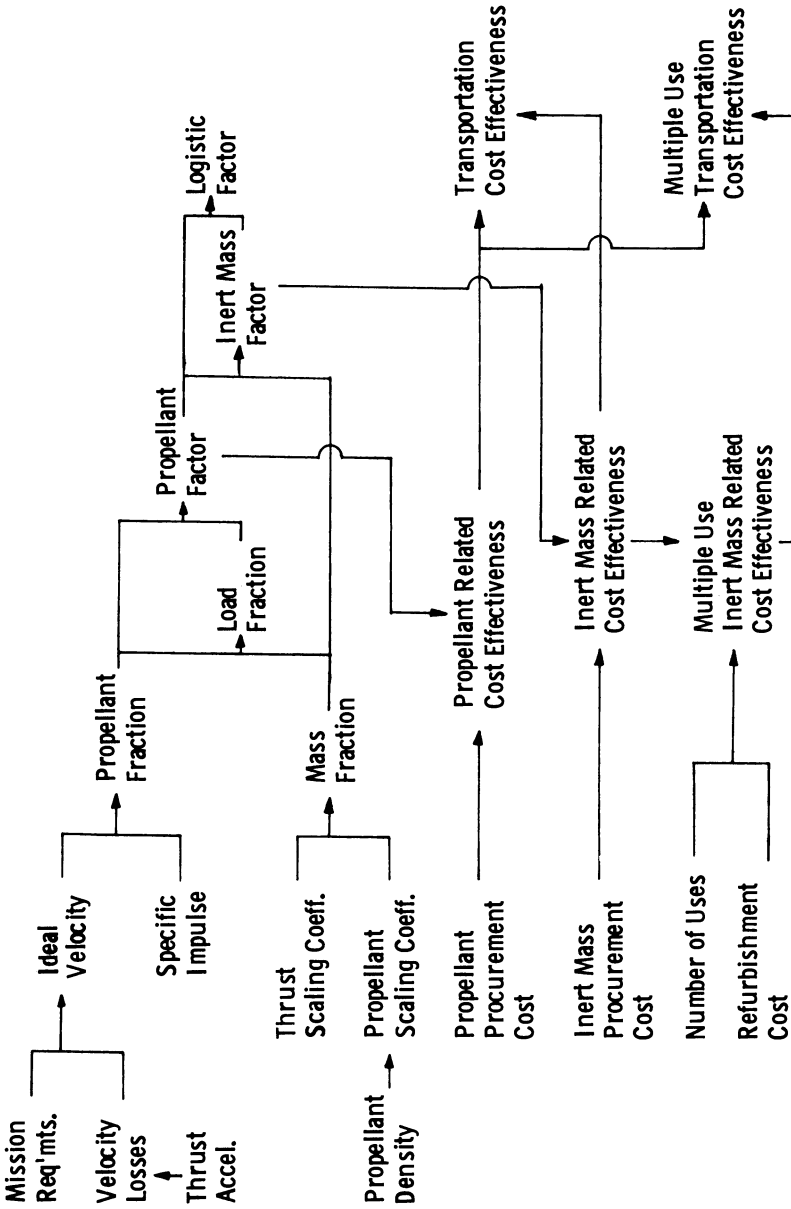
Fig. 18 - 2 Logic diagram interrelating basic and complex quality attributes.

Table 18-2 Complex Attributes

Propellant fraction, Λ	$= 1 - \exp(-\tau/I_{sp})\,(\mathrm{lb}_p/\mathrm{lb}_A)$
Mass fraction, x	$= (1 + K_p + K_i)^{-1}[\mathrm{lb}_p/(\mathrm{lb}_p + \mathrm{lb}_i]$
	$= (1 + K_p + K_f n_0/\Lambda)^{-1}$
	$= [1 + K_p + \alpha(P/F)n_0/\Lambda]^{-1}$ for electrical spacecraft $(P/F = $ electrical power per $\mathrm{lb}_F)$

Gross load fraction, λ $= 1 - \dfrac{\Lambda}{x}\,(\mathrm{lb}_{10}/\mathrm{lb}_A)$

Propellant mass factor, p $= \dfrac{\Lambda}{\lambda} = \dfrac{x}{(x/\Lambda) - 1}\,(\mathrm{lb}_p/\mathrm{lb}_{10})$

Inert mass factor, $i = p\left(\dfrac{1}{x} - 1\right)$ $= \dfrac{1 - x}{(x/\Lambda) - 1}\,(\mathrm{lb}_i/\mathrm{lb}_{10})$

Logistic factor, L $= p + i\,(\mathrm{lb}/\mathrm{lb}_{10})$

Propellant related cost effectiveness, $c_p = p\,k_p\,(\$/\mathrm{lb}_{10})$

Inert mass related cost effectiveness, $c_i = i\,k_i\,(\$/\mathrm{lb}_{10})$

Transportation cost effectiveness, $c_{10} = c_p + c_i\,(\$/\mathrm{lb}_{10})$

Destination load cost effectiveness, $c_{11} = \dfrac{c_{10} + k_{12}\lambda_{12} + k_{13}\lambda_{13}}{\sigma_{11}}\,(\$/\mathrm{lb}_{11})$

$k_{12} = $ operational load procurement cost $(\$/\mathrm{lb}_{12})$

$k_{13} = $ intransit load procurement cost $(\$/\mathrm{lb}_{13})$

The above values of c_i, c_{10}, and c_{11} are for single-use cases (i.e. "or"). For multiple uses ($+$ or $*$):

Number of uses: N

Refurbishment cost between uses: δ (in fractions of c_i)

Multiple use inert mass related cost effectiveness: $c_i^{*,+} = c_i\left(\dfrac{1}{N} + \delta^{*,+}\right)$

Multiple use transportation cost effectiveness, $c_{10} = c_p + c_i^{*,+}$

$c_i^{*,+} = $ either c_i^{*} or c_i^{+}; the value of δ must correspondingly be δ^{*} or δ^{+}, with δ^{+} including replacement of the non-reused hardware as well as refurbishment of the reusable hardware.

Table 18-3   Definition of Vehicle Mass Groups

	Absolute Designation (m or w)	Designation in Fraction of:		
		Initial Mass of Vehicle	Gross Load Mass	Destination Load Mass
10 Gross Load (Gross Payload)	m_{10}	λ	1.0	ω
11 Destination load	m_{11}	λ_{11}	σ_{11}	1.0
12 Operational load	m_{12}	λ_{12}	σ_{12}	ω_{12}
13 Intransit load	m_{13}	λ_{13}	σ_{13}	ω_{13}
20 Inert Mass	m_{20}	b	i	j
21 Thrust dependent	m_{21}	b_{21}	i_{21}	j_{21}
22 Propellant dependent	m_{22}	b_{22}	i_{22}	j_{22}
23 Other	m_{23}	b_{23}	i_{23}	j_{23}
30 Propellant Mass	m_{30}	Λ	p	q
31 Fuel	m_{31}	Λ_{31}	p_{31}	q_{31}
32 Oxidizer	m_{32}	Λ_{32}	p_{32}	q_{32}
33 Expellant	m_{33}	Λ_{33}	p_{33}	q_{33}
34 Auxiliary Fluids	m_{34}	Λ_{34}	p_{34}	q_{34}

Single Stage: Net Mass $m_N = m_{20} + m_{30}$; Initial mass: $m_A = m_N + m_{10}$; Burn-out mass: $m_B = m_{20} + m_{10}$ $b = m_{20}/m_A$; $\Lambda = m_{30}/m_A$; $b + \Lambda + \lambda_{10} = 1.0$; $i = m_{20}/m_{10}$; $p = m_{30}/m_{10}$; $j = i\omega$ $q = p\omega$

Multi-Stage: $m_{A1} = m_{N1} + m_{N2} + \cdots + m_{10}$; $m_{A2} = m_{N2} + m_{N3} + \cdots + m_{10}$; $\lambda_1 = m_{A2} =$
(Stages 1, 2, $m_{N2} + m_{n3} + \cdots + m_{10}$ $b_{tot} = (m_{20,1} + m_{20,2} + \cdots)/m_{A1}$; $\Lambda_{tot} = (m_{30,1} +$
3 ...) $m_{30,2} + \cdots)/m_{A1}$; $i_{tot} = i_1 + i_2 + \cdots$; $p_{tot} = p_1 + p_2 + \cdots$

Figure 18-3 shows a universal vehicle-mission integration chart which correlates μ, τ/I_{sp}, x and λ. Two of these values must be known to enter the chart, *e.g.*, τ/I_{sp} and x. Moving from a given value of τ/I_{sp} down to intersection with the τ/I_{sp} versus μ curve and turning left to the coordinate gives μ. Turning left or right to the point of intersection with the given x-curve, and turning from there down to the abscissa gives λ.

Given combinations of vehicles and propulsion systems (PS) are characterized by a more or less wide range of mass fractions and specific impulses. By specifying τ, each point on the τ/I_{sp} versus μ curve assumes a specific I_{sp} value. Knowing the characteristic upper and lower I_{sp} value for the PS and the characteristic upper and lower x value for the vehicle's propulsion module, one can define an area in the universal vehicle-mission integration chart which characterizes the particular vehicle-PS combination. An example is shown in Fig. 18-4 for $\tau = 930$ sec., corresponding to $\Delta v = 30,000$ ft/sec. The I_{sp} values to which discrete points on the τ/I_{sp} versus μ curve now correspond are shown. These
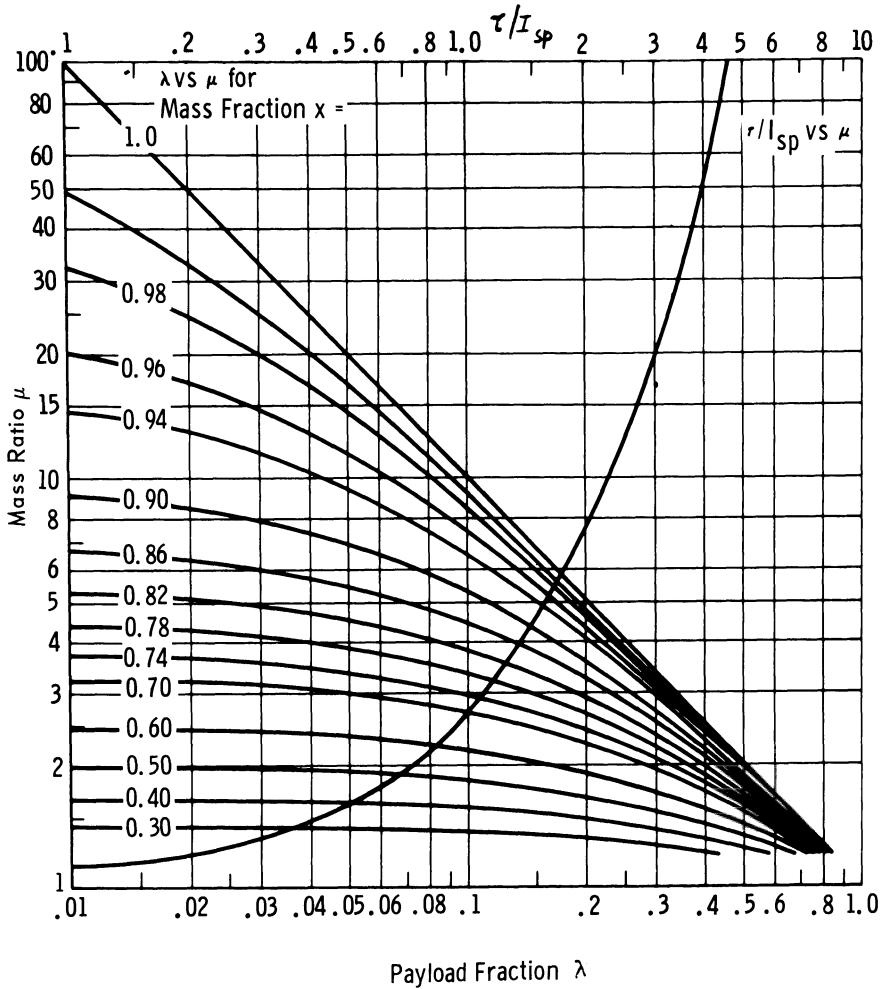
Fig. 18-3 Universal vehicle/mission integration chart.

values correspond to a number of vehicle-PS combination below:

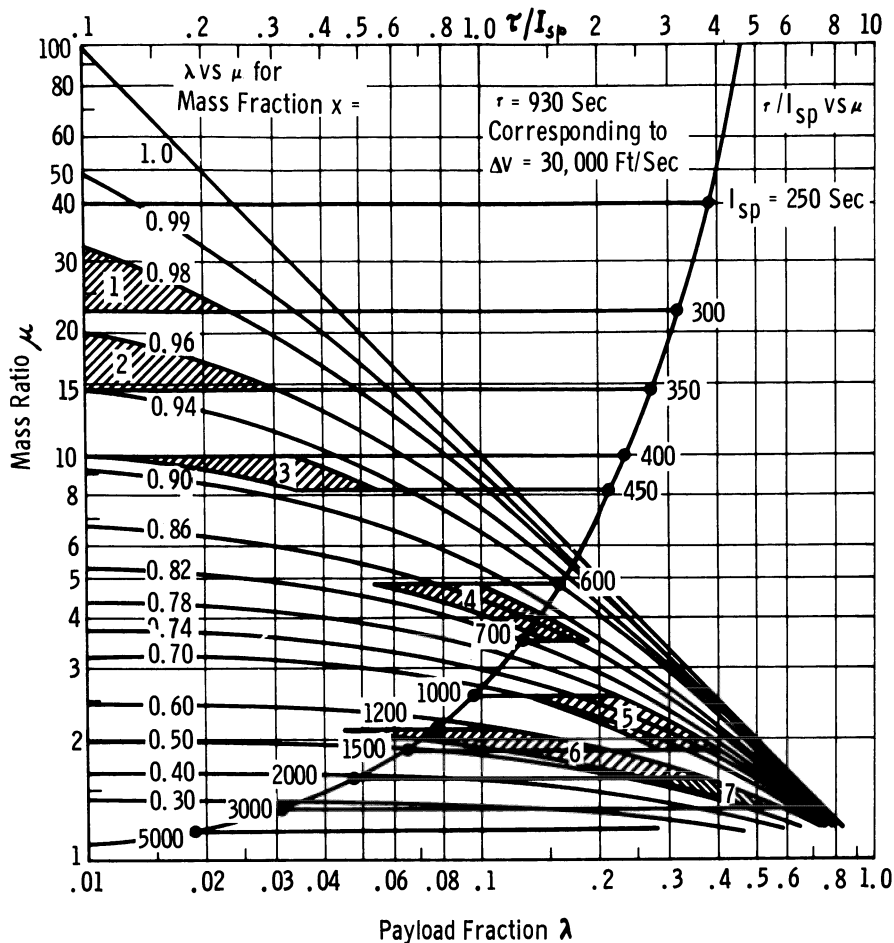|		I_{sp} = 250–300 sec.;	$x \lesssim 0.98$
1.	Solid propellants	I_{sp} = 250–300 sec.;	$x \lesssim 0.98$
2.	Solid propellants	300–350 sec.;	0.96
3.	O_2/H_2	400–450 sec.;	0.91–0.93
4.	SCR	600–700 sec.;	0.84–0.88
5.	GCR (Rocket)	1000–1500 sec.;	0.70–0.78
6.	Airbreathing (Chemical)	1200–2000 sec.;	0.55–0.60
7.	Nuclear Pulse	2000–3000 sec.;	0.50–0.60

Fig. 18-4 Universal vehicle/mission integration chart.

The above data are based on an Earth-to-orbit mission concept, regardless of whether the particular PS is considered suitable for, or capable of, carrying out the mission. They are used here to illustrate the method. The payload fractions indicated by areas 1 through 7 pertain to a one-stage vehicle. For a two-stage vehicle, assuming each stage has to provide a velocity increment of 0.5τ, *i.e.*, 15,000 ft/sec., one can use the same chart by moving down the τ/I_{sp} versus μ curve to a point twice the specific impulse assumed for the one-stage version. Moving from there to the given x-line and then down yields the new λ value per stage. The new overall λ value is then the product of λ values for the two stages. Simply cutting τ in half may be too arbitrary, since generally the ideal velocity of a

stage, hence, τ_{id}, should be roughly equal to its exhaust velocity, or I_{sp}, for the best performance. If one wants to divide τ in various proportions among two or more stages, it may be more advantageous to revert from a τ-value to τ/I_{sp} and the more general chart of Fig. 18-3.

In order to simplify the conversion of Δv to τ/I_{sp}, Fig. 18-5 correlates mission velocity and specific impulse via $\tau/I_{sp} = 1.0$. From this line, τ/I_{sp} for values other than 1.0 can easily be inferred. Ranges of specific impulses and mission velocities are shown for propulsion systems and missions, respectively.

Figure 18-6 correlates propellant mass fraction Λ to the velocity factor. Therefore, through τ/I_{sp}, one can rapidly correlate Λ and the parameters in Fig. 18-3.

Figures 18-7 and 18-8 show a universal transportation effectiveness chart by plotting inert mass factor i and propellant mass factor p as function of mass fraction and velocity factor, respectively. These two mass factors are defined as the amount of inert mass per unit mass of gross (pay) load and the amount of propellant mass per unit mass of gross (pay) load required to carry out a given mission. In the case of a shuttle vehicle, it is $i \sim 0$, except for replacements during refurbishment. With the aid of these charts, the logistic factor $L = p + i$ can readily be found. L, p and i are important not only in connection with a given transport vehicle itself, but they may be even more important for a supply operation. For example, high values of p and i for an inter-orbital space vehicle (ISV) raise the logistic requirements for the ELV which has to deliver larger quantities of the material into orbit. This is especially important if geocentric, cislunar or heliocentric shuttle operations are to be supported from Earth or orbit. So long as these transportation costs per unit mass of ELV payload are much higher than the cost of either hardware or propellant for the shuttle, the orbital procurement costs for either are similar. This is in contrast to ground operations where propellant costs usually are much lower than hardware costs. High specific impulse of the shuttle PS eventually, therefore, becomes more important than high mass fraction of the shuttle, because only high I_{sp} can effectively reduce the propellant supply except if x-values are very low. But in that case, I_{sp} is usually very high, *i.e.*, τ/I_{sp} if very low.

For purposes of correlating p and i with gross load fraction λ, Fig. 18-9 shows the variation of λ with τ/I_{sp} for a number of mass fractions. L and λ are key parameters, both containing p as well as i, since $L = p + i$ and also $L = (1 - \lambda)/\lambda$.

For separately powered propulsion systems in which energy is converted in a separate system, the amount of power inducted into the thrust generating system is fixed or limited. The thrust generating system can use this power in two ways: to increase the rate of expellant ejection and to reduce the specific impulse, or vice versa. In analyzing such systems, it is useful to replace
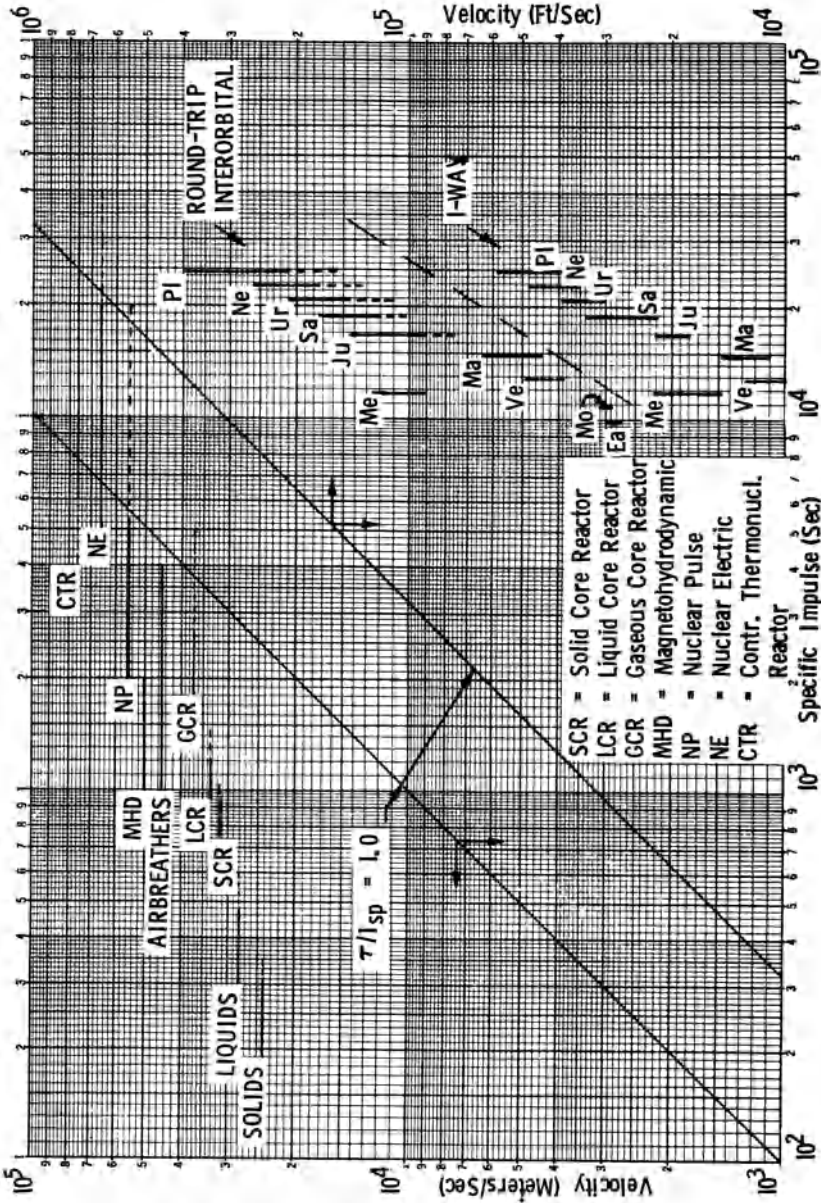
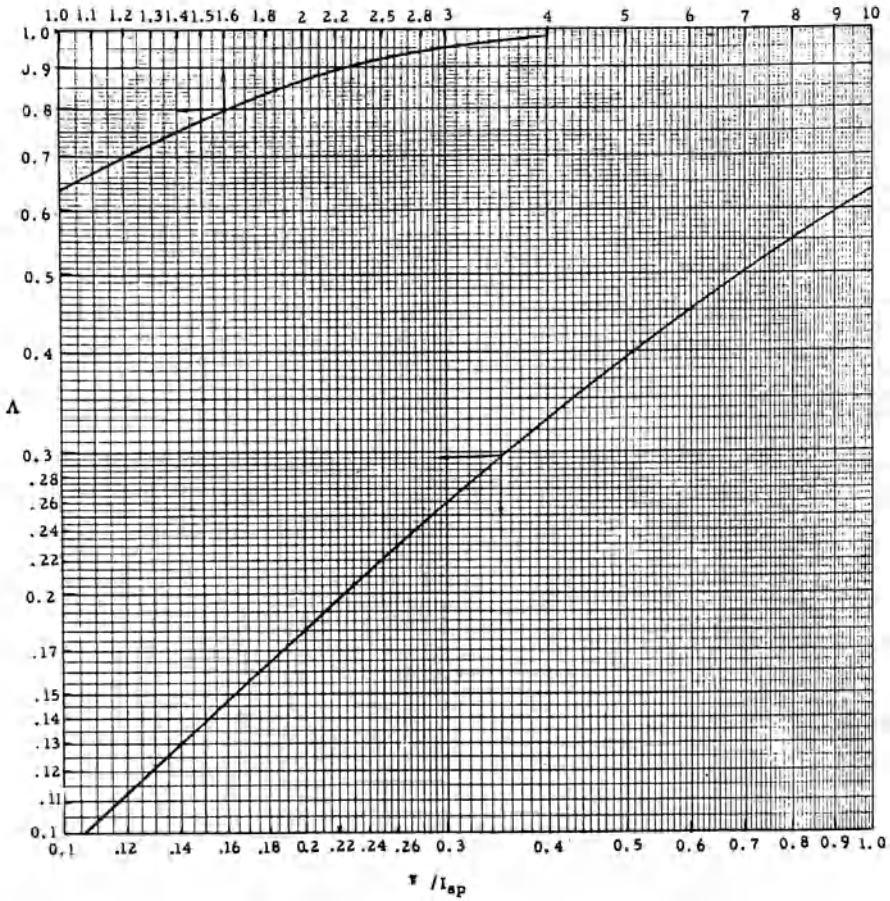Fig. 18-5 Correlation of mission velocity and specific impulse via τ/I_{sp}.

Fig. 18-6 Propellant fraction Λ versus τ/I_{sp}.

mission velocity by the energy per unit mass of the space vehicle. The instantaneous thrust acceleration, in terms of exhaust velocity and mass flow, can be expressed in the form

$$f = ng^* = \frac{\dot{m}}{m} v_e.$$ (18-2)

The kinetic energy of a small mass quantity δm in the exhaust jet is $(-\delta m) v_e^2/2$, and if m is the expended mass per second, $\dot{m}$, the jet power is

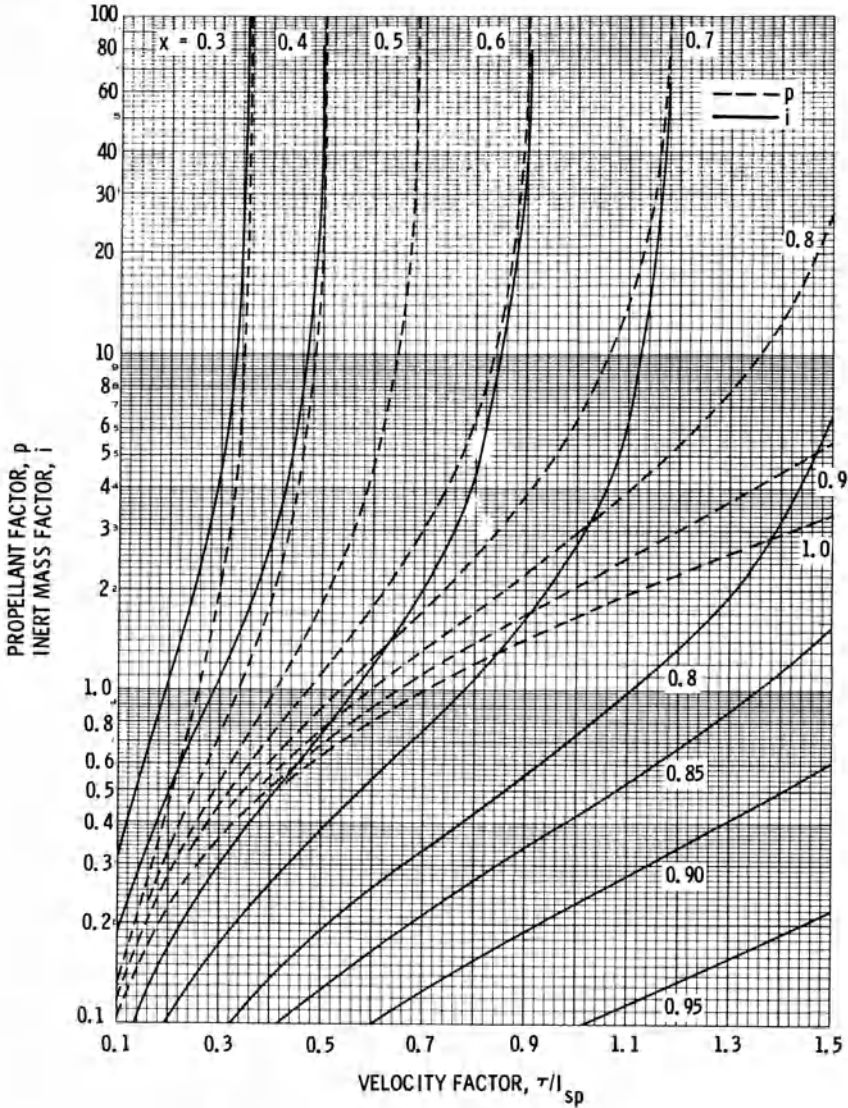$$P_j = \frac{\dot{m}}{2} v_e^2.$$ (18-3)

Fig. 18-7 Propellant factor and inert mass factor versus velocity factor.

Therewith one has

$$\frac{f^2}{2P_j} = \frac{\left(\dfrac{\dot{m}}{m}\right)^2 v_e{}^2}{-\dot{m}v_2{}^2} = -\frac{\dot{m}}{m^2} = \frac{d}{dt}\frac{1}{m} \, . \qquad (18\text{--}4)$$
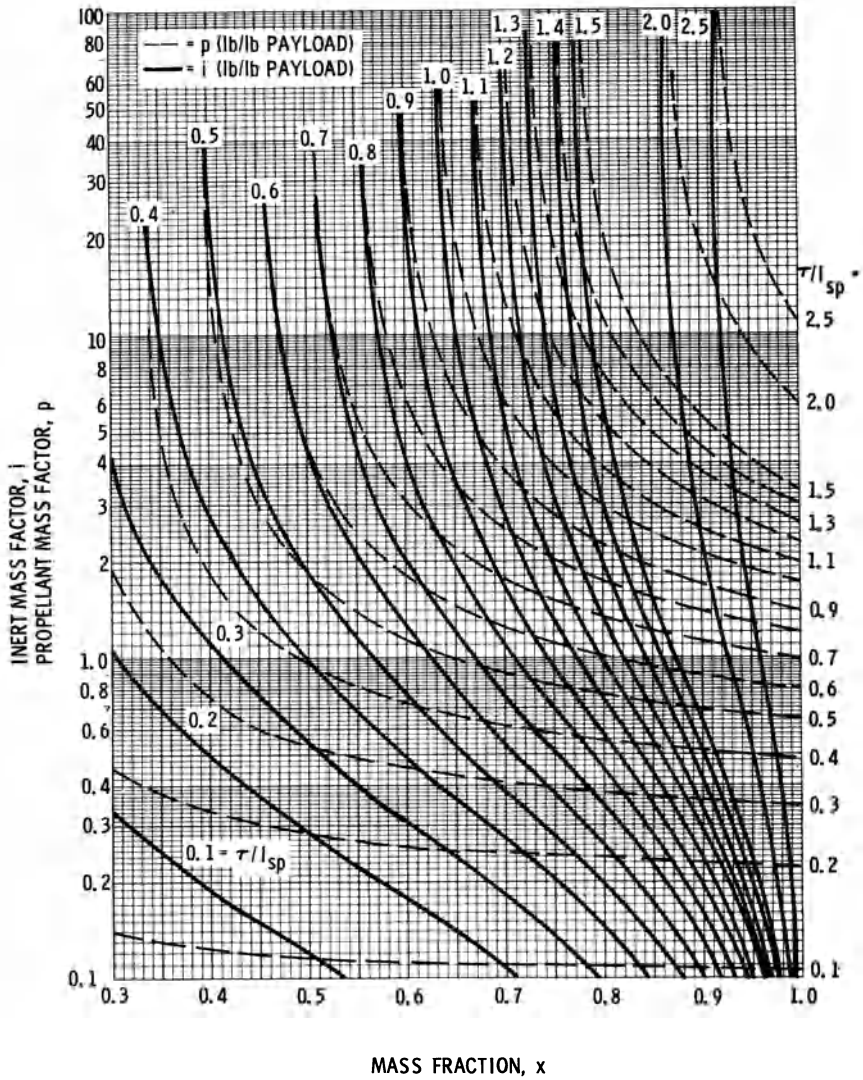
Fig. 18-8 Propellant factor and inert mass factor versus mass fraction.

Integrating this equation to obtain the vehicle mass as function of time,

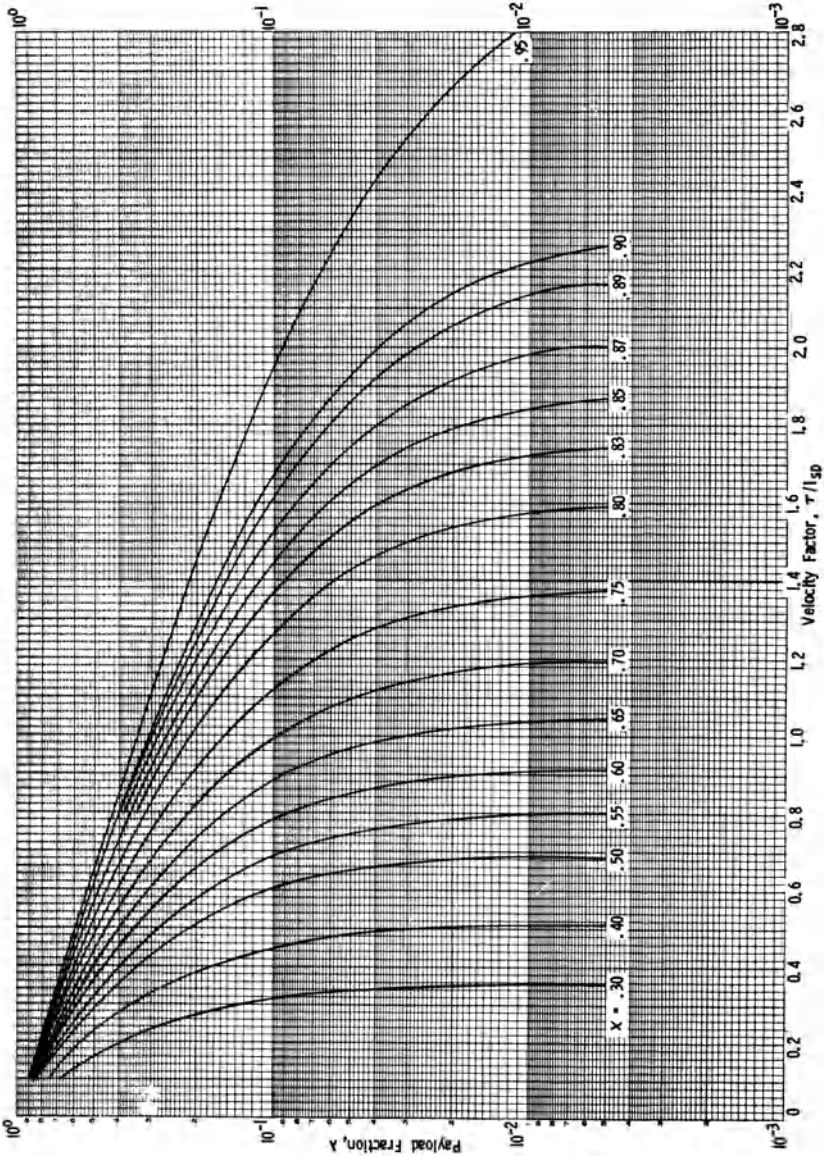$$\frac{1}{m(t)} = \frac{1}{m_A} + \int_0^t \frac{f^2}{2P_j} \, dt. \qquad (18\text{--}5)$$

Fig. 18-9 Variation of λ with τ/I_{sp}.

The jet power P_j is related to the electrical input power P into the thrust generation system by the relation

$$P_j = \epsilon P \qquad (18\text{-}6)$$

where ϵ is the thrust conversion efficiency, defined as the ratio of power in the exhaust jet to electrical power delivered to the thrust units. The ratio of all power-dependent propulsion system component weights W_p to the electrical power P produced at the source is defined as

$$\alpha = \frac{W_p}{P} = \frac{W_p}{\left(\dfrac{P_j}{\epsilon}\right)} \quad (\text{unit mass}/\text{kw}_e). \qquad (18\text{-}7)$$

One can derive the mass ratio required for a powered flight period t from Eq. (18-5)

$$\frac{1}{m_B} - \frac{1}{m_A} = \frac{1}{2P_j} \int f^2\, dt \qquad (18\text{-}8)$$

where m_A is the initial vehicle mass, m_B the vehicle mass after all propellant mass $m_p = m_A - m_B$ is consumed. After some rearrangements, one obtains from Eq. (18-8), for the powered flight time T_F in which the propellant is consumed,

$$\mu = \frac{m_A}{m_B} = \frac{m_A}{2P_j}\,\frac{m_A}{m_p} \int_0^{T_F} f^2\, dt. \qquad (18\text{-}9)$$

Since $\alpha/\epsilon = m_p/P_j$, one can replace P_j in Eq. (18-9) by $m_p\epsilon/\alpha$, where m_p is the mass of all power-dependent propulsion system components. Considering that $m_A/m_p = 1/\Lambda$ and $\Lambda = (\mu - 1)\mu$, the relation for the mass ratio can be expressed in the form

$$\mu = 1 + \frac{1}{2}\,\frac{\alpha}{\epsilon}\,\frac{m_A}{m_p} \int_0^{T_F} f^2\, dt. \qquad (18\text{-}10)$$

The mass ratio is seen to be proportional to the $\int f^2\, dt$. The ideal velocity is

$$v_{id} = \int_0^{t_l} f\,\frac{dt}{v_e} \qquad (18\text{-}11)$$

and the mass ratio of directly powered rockets is, for constant v_e,

$$\mu \;=\; \exp \frac{1}{v_e} \int_0^{t_1} f \, \frac{dt}{v_e} \, . \qquad\qquad (18\text{-}12)$$

In Eq. (18-10), if α is expressed in units of kg/kw and $f^2 \, dt$ in $m^2/\text{sec.}^3$, the second term on the right-hand side of Eq. (18-10) must be multiplied by $1/a$, where $a = 2g^* \, 102 = 2.9.81 \cdot 102 = 2000$. The equation for the propellant fraction, considering that $\mu = 1/(1 - \Lambda)$ and $m_B/m_p = 1 + m_\lambda/m_p$, is

$$\Lambda \;=\; 1 + \frac{m_\lambda}{m_p} \, \frac{1}{2000} \, \frac{\alpha}{\epsilon} \int_0^{T_F} f^2 \, dt. \qquad\qquad (18\text{-}13)$$

This implies that $m_B = m_p + m_\lambda$, i.e., that the mass m_p includes the mass of the thrusters. The overall "dry" propulsion system mass of an electric drive consists of power source, power conversion equipment which converts thermal energy from solar radiation or from a nuclear reactor to electrical power, power conditioning equipment, and thrust generating equipment (thrusters). Of these main components, the first three are power-dependent masses. However, the thrusters represent only a few percent of this mass and therefore are included here in order to avoid unnecessarily complex equations for present purposes.

In order to compute the principal data of (the separately powered) data of electric propulsion systems, we will consider systems which are nuclear powered, i.e., have a constant power source independent of heliocentric distance. The objective is to determine λ, i, p and L. As implied by previous definition of m_p, the initial mass of the electric spacecraft consists of three main components:

$$m_A \;=\; \text{load mass, } m_\lambda \text{ + power-dependent mass, } m_p \text{ +} \qquad (18\text{-}14)$$
$$\text{propellant mass, } m_p$$

or

$$m_A \;=\; m_\lambda + \frac{\alpha}{\epsilon} \, \frac{Fg^* I_{sp}}{2000} + \frac{FT_F}{g^* I_{sp}} \qquad\qquad (18\text{-}15)$$

where $g^* = 9.81 \, m/\text{sec.}^2 = 32.2 \, \text{ft/sec.}^2$, F is the thrust, and T_F the powered flight time. The procedure to compute λ, i, p and L is as follows:

1. Select m_λ/m_p, α/ϵ (kg/kw$_e$) and $\int f^2 \, dt$ $(m^2/\text{sec.}^3)$.

Then compute the following:

2. Λ as given by Eq. (18-13)

3. $\mu = 1/(1 - \Lambda)$
4. $m_p/m_B = \mu\Lambda$
5. $m_p/m_p = 1/[\mu\Lambda(1 + m_\lambda/m_p)]$
6. $x = 1/(1 + m_p/m_p)$
7. $\lambda = 1 - \Lambda/x$
8. $i = (1 - \lambda\mu)/\lambda\mu$
9. $p = \Lambda/\mu$
10. $L = i + p$

Results of such computation are shown in Figs. 18–10 and 18–11, in which λ and p are shown as function of m_λ/m_p with $f^2 dt$ as parameter for the case of $\alpha/\epsilon = \text{kg/kw}_e$ $1\text{kg}m/\text{kw}_e$. It is seen that λ is a maximum for a given m_λ/m_p at a given $f^2 dt$. If λ is a maximum, then according to Eq. (18–14) the sum of power-dependent mass and propellant mass must be a minimum. Figure 18–11 shows that p, hence the propellant mass per unit mass of m_λ is a minimum. Equation (18–15) shows that with increasing I_{sp} the power-dependent mass increases while the propellant mass decreases. At some point between the extremes, the sum of these two masses should be a minimum, hence m_λ a maximum. Differentiation of Eq. (18–15) with respect to I_{sp} yields relation (18–16) for the I_{sp} at which the total initial vehicle mass is a minimum for a given m_λ, hence λ is a maximum,

$$\frac{\alpha}{\epsilon} \frac{g^*F}{2000} I_{sp} = \frac{F}{g^*I_{sp}} T_F \qquad (18\text{–}16)$$

i.e., the power-dependent and the propellant masses are equal. This result is based on a given set of constant F and T_F, since the above differentiation is with respect to I_{sp} only. Solving for I_{sp} yields for the optimum

$$I_{sp} = \frac{2000}{g^{*2}} \frac{\epsilon}{\alpha} T_F . \qquad (18\text{–}17)$$

Thus, for a given $\int f^2 dt$, one can determine the maximum λ and the associated values of m_λ/m_p and p because

$$\frac{1}{\lambda} + 1 + i + p; \qquad (18\text{–}18)$$

the associated value of i can be determined from Eq. (18–18),

$$i = \frac{1}{\lambda} - (p + 1). \qquad (18\text{–}19)$$

Since i and p are known, numerical specification of m_λ yields m_i and m_p. Estimating a value of I_{sp} (typical near-optimum values are:
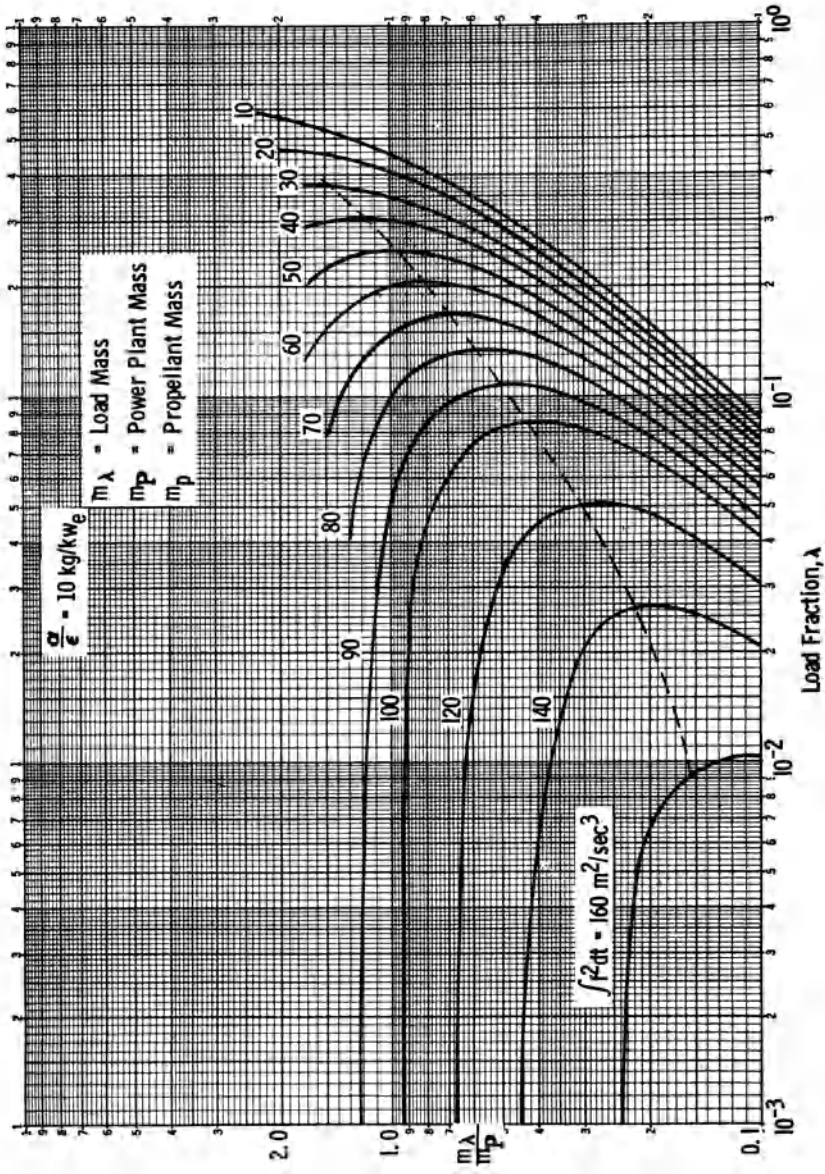
Fig. 18-10 Load fraction (λ) versus m_λ/m_p.

$\frac{\alpha}{\epsilon} = 10 \text{ kg/kw}_e$

m_λ = Load Mass
m_P = Power Plant Mass
m_p = Propellant Mass

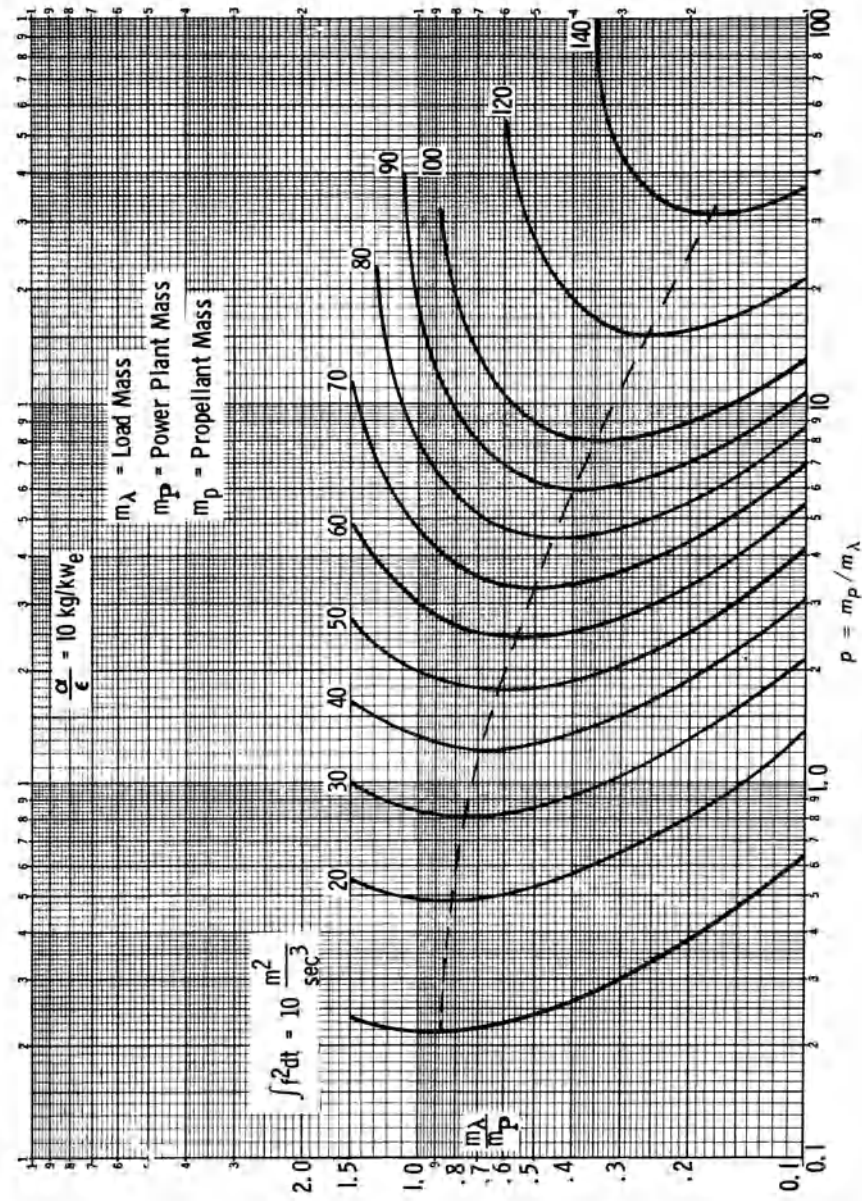$\int f^2 dt = 10 \dfrac{m^2}{sec^3}$

$p = m_p / m_\lambda$

Fig. 18-11 Propellant mass factor (p) versus m_λ / m_p.

for cislunar shuttle $I_{sp} \sim 6000$ sec.; inner solar system round-trip missions $I_{sp} \sim 8000$ sec.; and outer solar system round-trip missions $I_{sp} \sim 10,000$ to 15,000 sec.) and considering that $m_i \equiv m_p$ permits determination of thrust F from

$$m_p \equiv m_i = \frac{\alpha}{\epsilon} \frac{Fg^*I_{sp}}{2000} .$$

Then, knowing F, the powered flight time T_F is computed from the known value of

$$m_p = \frac{FT_F}{g^*I_{sp}} .$$

Compatibility of I_{sp} and T_F for the optimum conditions is then checked by determining I_{sp} from Eq. (18-17), using the previously found T_F. If the I_{sp} value found from Eq. (18-17) differs too much from the one estimated before, another iteration will be necessary.

The jet power P_j (mw$_e$) per kg thrust (kg$_F$) is given by

$$\frac{P_j}{F} \left(\frac{mw_e}{kg_F} \right) = \frac{I_{sp} \text{ (sec.)}}{20,855} \qquad (18\text{-}20)$$

and the electric power output of the power generation systems follows from

$$P = \frac{F}{\epsilon} P_j \text{ (mw}_e). \qquad (18\text{-}21)$$

With charts such as Figs. 18-10 and 18-11, the laborious determination of the maximum λ could be avoided. But each of these charts would be valid only for a given α/ϵ and interpolation between several α/ϵ charts would require cross-plotting. Therefore, machine computations for charts such as Figs. 18-10 and 18-11 were carried out for a wide range of α/ϵ values and the variation of maximum λ and of p with $\int f^2 \, dt$ plotted with α/ϵ as parameter showing the variation of m_λ/m_p along each α/ϵ curve. The results are shown in Figs. 18-12 and 18-13.

It remains to provide a guide for estimating $\int f^2 \, dt$ and α/ϵ. The mission values of $\int f^2 \, dt$ can vary greatly, depending on how, in a two-way mission, the outbound and the return bound leg are flown, or how fast a one-way mission is flown. The computation of $\int f^2 \, dt$ for a given mission is beyond the scope of this discussion. As a rough guide, the following range of values is offered:

Lunar round-trip mission (orbit-to-orbit):
$\int f^2 \, dt = 12 - 30 \ m^2/\text{sec.}^3$; 1-way: $6 - 15 \ m^2/\text{sec.}^3$

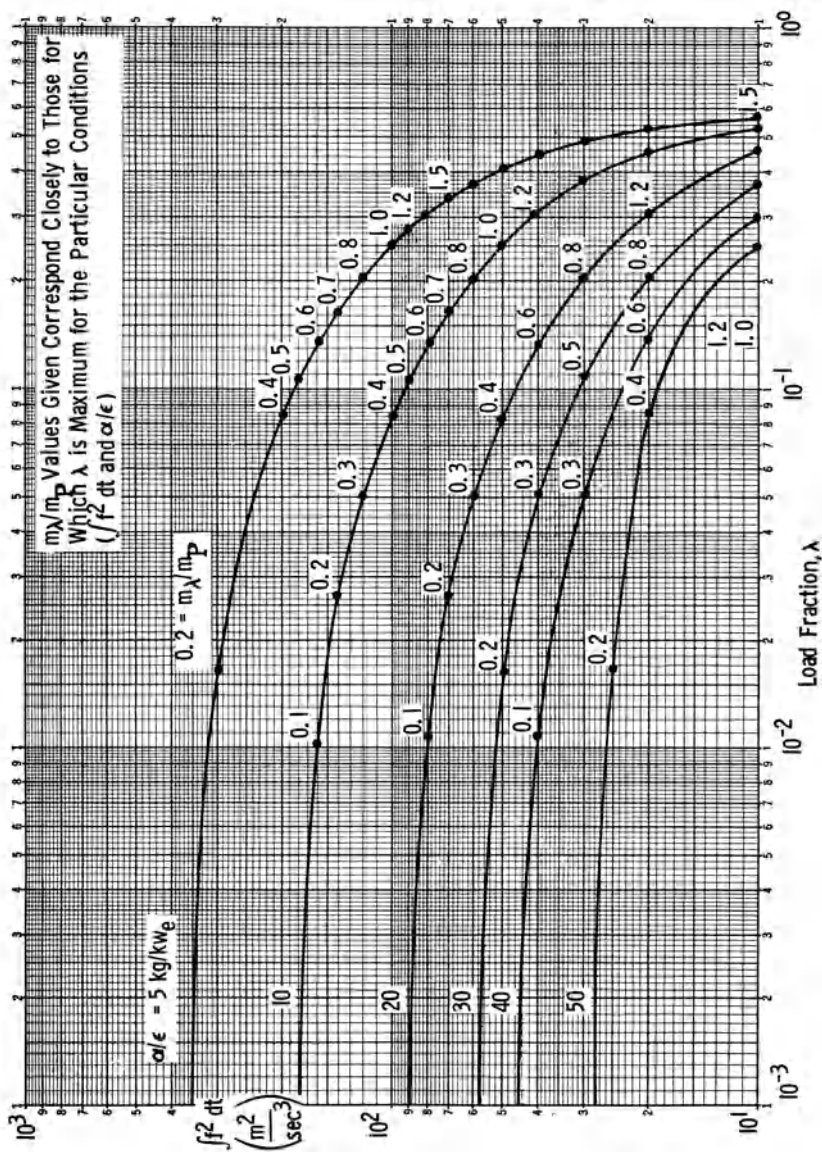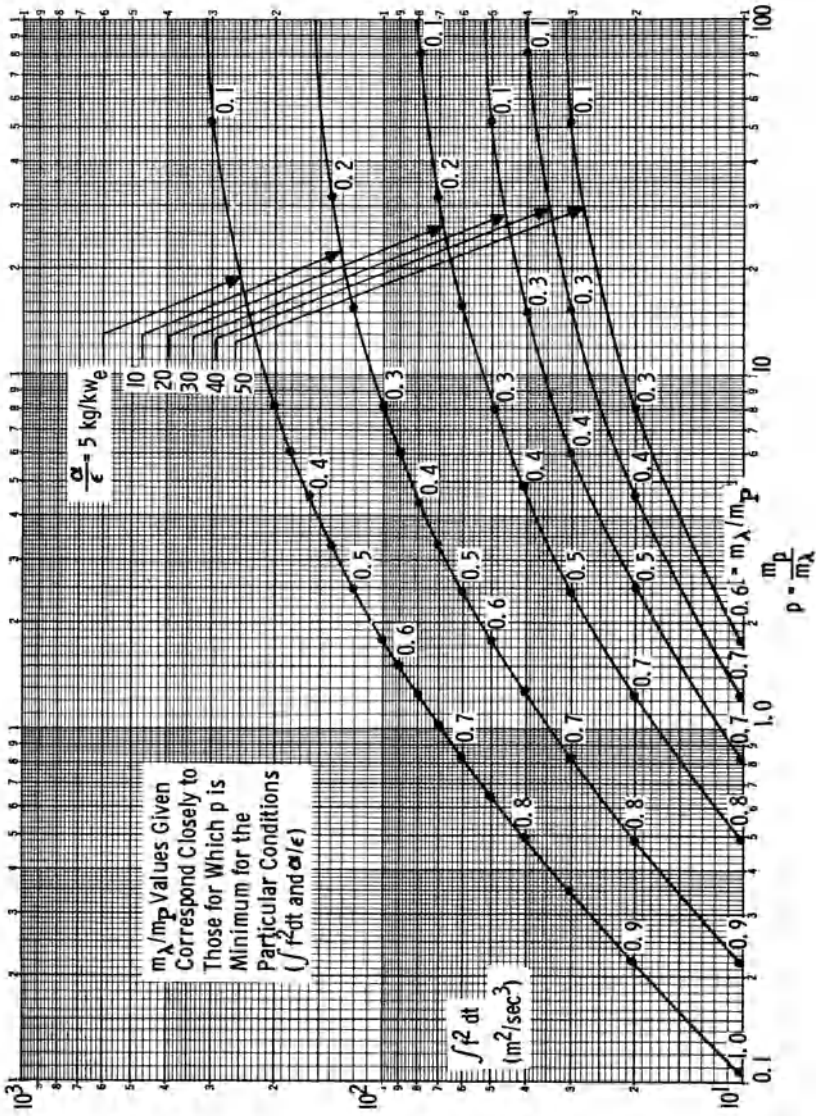**Fig. 18-12** Load fraction (λ) versus $\int f^2\,dt$.

Fig. 18·13 Propellant mass factor (*p*) versus $\int f^2 dt$.

Venus round–trip mission (orbit–to–orbit):
$\int f^2 \, dt = 30 - 60 \ m^2/\sec.^3$; 1-way: $10 - 20 \ m^2/\sec.^3$
Mars round–trip mission (orbit–to–orbit);
$\int f^2 \, dt = 40 - 80 \ m^2/\sec.^3$; 1-way: $15 - 25 \ m^2/\sec.^3$
Jupiter round–trip mission (orbit–to–orbit)
$\int f^2 \, dt = 60 - 120 \ m^2/\sec.^3$; 1-way: $25 - 50 \ m^2/\sec.^3$

[18-3] ELEMENTS OF INTEGRATED TRANSPORTATION SYSTEM COMPARISON (ELV, GISV, CISV AND HISC)

Figure 18-14 compares 13 launch vehicles, encompassing three types in terms of p, i and λ. Abbreviations not explained on the chart are ST = number of stages, EXP = expendable, REUS = reusable, AB = airbreathers. On each vertical line, the upper black dot represents p, the lower black dot indicates i, and the hollow circle is λ.

The logistic factor to be supplied by ELV's for geospace transportation into the synchronous orbit is shown in Table 18-4 for a variety of propulsion systems in one–way and shuttle service. The shuttle service is shown for two mission profiles; namely, with a single–stage GISV and with interorbital rendezvous as shown in Fig. 18-15. Comparison of the third and fifth cases in Table 18-4 shows that the use of interorbital separation and rendezvous can be very effective, especially at somewhat lower mass fractions. This means that this flight profile reduces the sensitivity of the shuttle's logistic supply requirements from Earth surface to reductions in mass fractions as they may occur, for example, during the development of the GISV* or as a result of radiation safety measures during periods of strong solar activity.

Future long–duration manned operations on the Moon and in the solar system must be based on advances in orbital technology and operations, advanced propulsion systems for cislunar and heliocentric interorbital space vehicles (ISV), and an Earth–to–orbit logistic supply capability which is adequate as well as economical. All three factors must be taken into consideration, which is not always done. Solar system operations in the next 20 years or so will be based exclusively on scientific goals. This, in turn, requires coordination of unmanned and manned missions for best effectiveness to the overall program and consideration of the differences in launch vehicle and interorbital vehicle propulsion requirements.

The adequacy of future orbital transportation capability can best be assured by viewing the development of new launch vehicles, and even major improvements of existing launch vehicles, as an integral part of the national space program. The new vehicle(s) should be able to serve as many tasks of space utilization and exploration as possible. The need for a new launch vehicle,

NO.	TYPE	ST.	PROP.	μ[1)	χ[2)
1	EELV	4	S	40	.9
2	EELV	4	S	80	.9
3	EELV	4	S	40	.94
4	EELV	4	S	80	.94
5	EELV	2	O/H	9	.92
6[3)	RELV	2	O/H	9	.88
7[4)	RELV	1	O/H	9	.92
8[4)	RELV	1	O/H	8	.92
9[5)	RAST	2	O/H	9	.78
10[6)	RAST	1	O/H	8	.885
11[6)	RAST	1	O/H	8	.894
12[7)	RAST	1	H; O/H	5	.747
13[8)	RAST	1	H; O/H	2	.536

1) MASS RATIO
2) MASS FRACTION PER STAGE
3) BLUNT BODY RECOVERY OF BOTHSTAGES
4) BLUNT BODY RECOVERY
5) BOTH STAGES LIFTING BODIES
6) ROCKET-POWERED GLIDE VEHICLE
7) TURBORAMJET TO M= 8(HTO)
8) SCRAMLACE

EELV = EXPEND. EARTH LAUNCH VEH.
RELV = REUSABLE ELV
RAST = REUSABLE AERO-SPACE TRANSPORT

● = p
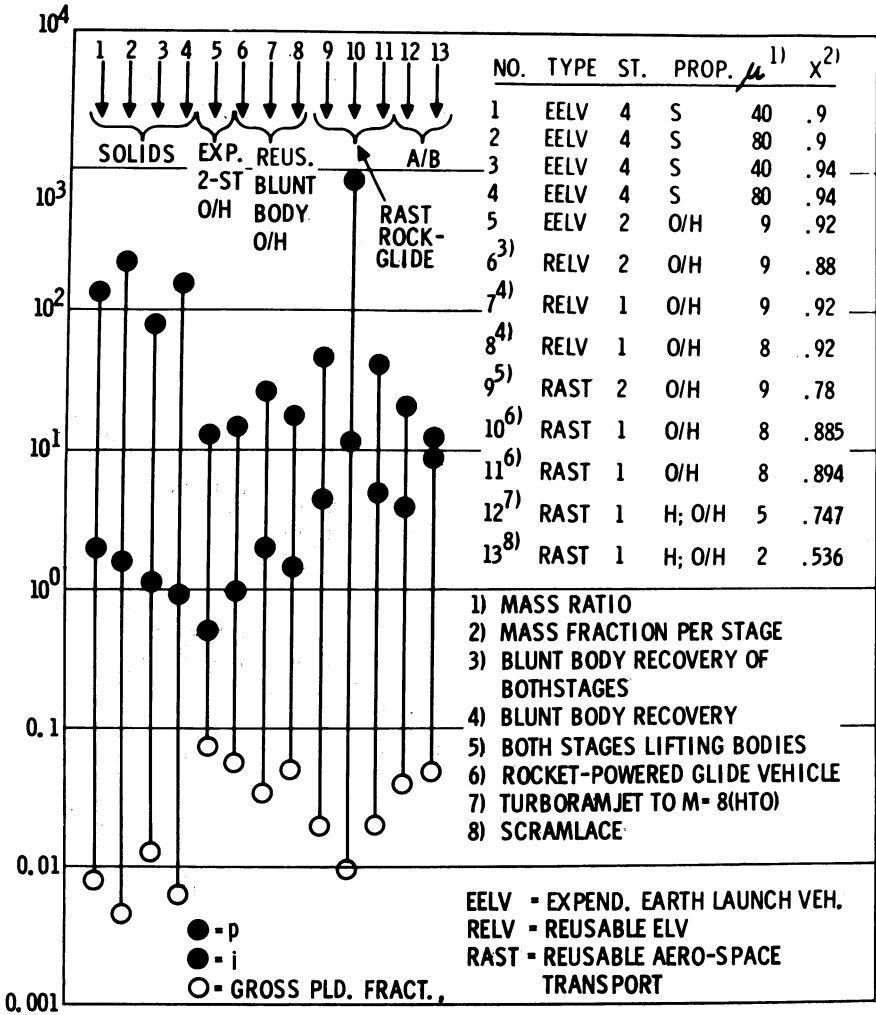● = i
○ = GROSS PLD. FRACT.,

Fig. 18-14 Quality indices of several earth launch vehicles.

therefore, is contingent upon the major program goals of the next 15 to 25 years.

The geospace market on which the worthwhileness of a reusable aerospace transport (RAST) depends, has two main sectors: orbital program activities associated with manned geospace utilization, and orbital launch operations support of deep space missions. The primary payload masses required by the latter exceed the capability of the RAST, but orbital assembly and other support operations need

Table 18-4 Synchronous Orbit Supply Requirements

$\Delta v_i = 8k; \Delta v_2 = 7k; \Delta v_3 = 7k; \Delta v_4 = 8k\ (k = 10^3\ \text{ft/sec.})$

| Mission	Delivery Mode	Stage No.	Propulsion	I_{sp} (Sec.)	Mass Fraction X	Inert Mass Factor i = $\dfrac{\text{Inert Mass}}{\text{Pld. Mass}}$	Propellant Mass Factor p = $\dfrac{\text{Prop. Mass}}{\text{Pld. Mass}}$	Logistic Factor $L = i + p$
Lo-Orb to Sync Orb	1-Way	1	Chemical	450	.80 - .88	1.9 - .16	5.8 - 2.8	7.7 - 3.2
Lo-Orb to Sync Orb	1-Way	1	Nucl. (Metal)	850	.78 - .86	.32 - .16	1.1 - .94	1.4 - 1.1
Lo-Orb Sync Orb	Shuttle Service	1	Chemical	450	.88 - .92	.24 - 1.5	175 - 7.5	199 - 9
Lo-Orb Sync Orb	Shuttle Service	1	Nucl. (Metal)	850	.78 - .86	.78 - .33	2.8 - 2.1	3.6 - 2.4
Lo-Orb Sync Orb	Shuttle Service (Interorb Rendezvous)	2	Chemical	450	.84 - .92	8.4 - 1.5	26.6 - 11.2	35 - 13
		1	Chemical	450	.80 - .88			
Lo-Orb Sync Orb	Shuttle Service (Interorb Rendezvous)	2	Nucl. (Metal)	850	.78 - .86	.94 - .43	3.2 - 2.6	4.1 - 3
		1	Nucl. (Metal)	850	.78 - .86			
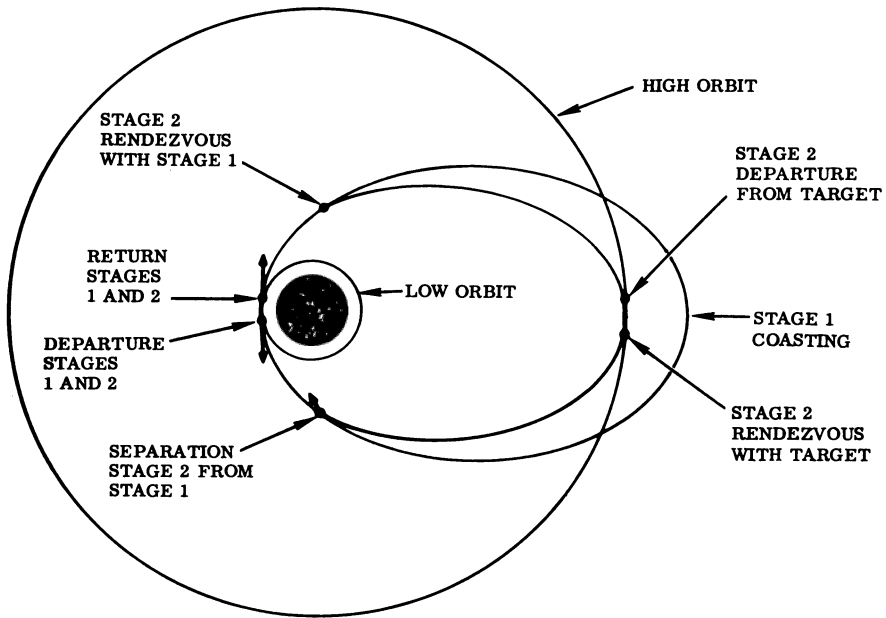
Fig. 18-15 Geospace shuttle service using interorbital rendezvous.

smaller supply loads which are preferably carried either by the RAST or by expendable launch vehicles of comparable payload capability, such as Saturn IB or Titan III. The geospace utilization sector, rather than the other sectors, determine the worthwhile-ness of developing a new launch vehicle of the RAST type for two reasons: (1) Only a broad geospace utilization market requires transport characteristics which are particularly well, or exclusive-ly, satisfied by the RAST, such as the need for accommodating a less selective passenger population (low accelerations), and large footprint and cross-range (lift). (2) Only a broad geospace utiliza-tion market requires sufficiently frequent transport of personnel and medium cargo loads to render reusability at hundreds of missions worthwhile.

   Geospace offers numerous potential applications, indicating the possibility or even probability of a sizable market. If this market potential cannot be verified by orbital experience, or if the space program of the next two or three decades is devoted primarily to unmanned and manned deep space exploration, a RAST most likely could not be justified on the basis of civil and commercial require-ments. This ignores, of course, other aspects not directly trans-latable into amortization dollars but nevertheless important or vital to the Nation. On the other hand, if the geospace market

potential is verified, it can materialize only through the reduction in aerospace transportation cost by an order of magnitude or more. This can be achieved only by prolonged reusability, *i.e.,* a refurbishing cost between flights of between 0.5 and 0.1 percent of the procurement cost (200 to 1000 flights).
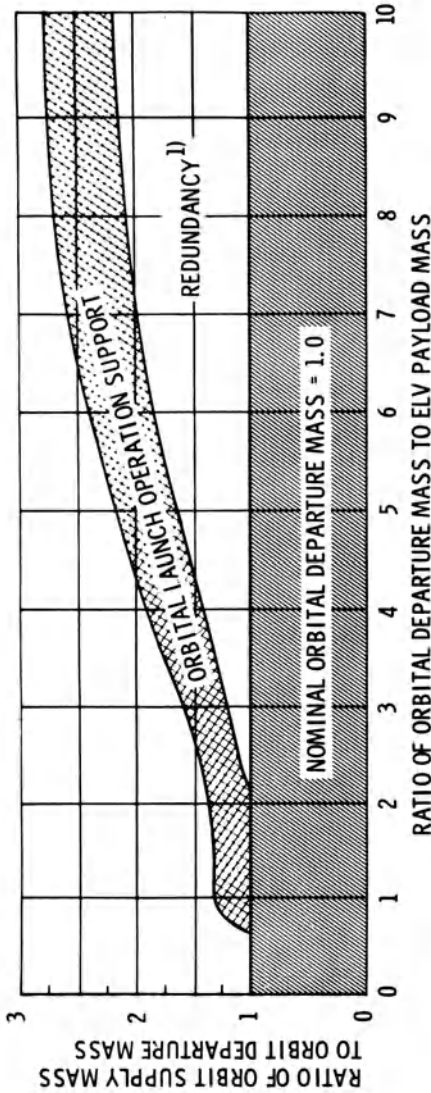
With today's large launch vehicles from Titan to Saturn V, attainable transportation costs range from $800 to $400 per pound of payload delivered into a low-altitude orbit. Even if further increase in vehicle size would reduce the cost effectiveness significantly below $400 per pound, such an approach would only improve the cost effectiveness at the expense of increasing the cost per launch and would be justified only in response to the requirement for increased payload capability, with improved cost effectiveness a derivative benefit.

Accommodation of a less selective passenger population makes an airline-like operation desirable. This can best be assured by using an air-breathing first stage to 8000-12,000 ft/sec. speed (5500-8500 m.p.h.) followed by a rocket-powered stage. The large fuel specific impulse of the airbreather improves the payload fraction by a factor of about 3, compared to an all-rocket system, and it keeps peak acceleration low without excessive gravitational losses.

If an airbreathing first stage is considered, the evolution of a reusable aerospace transport becomes interlaced with the nationally and equally important evolution of high supersonic and hypersonic aircraft of global or intercontinental range. The syntechnical features of these two transportation systems result in an extensive commonality of development problems and, therefore, cost sharing.

Once in existence, the RAST will contribute to the economy of the orbital phase of lunar and planetary missions. For a given type of ISV, the orbital launch operation support requirements tend to grow with the ratio of orbital departure mass of the ISV to payload mass of the launch vehicle because of mating, fueling, maintenance and repair requirements as well as makeup for losses due to leakage or boiloff. The growth rate depends on the state-of-art of orbital operations and on such factors as whether the orbital operation consists mainly of orbital mating of ISV propulsion modules fueled on the ground, or of orbital fueling of modules carried aloft in assembled form, or on whether liquid, especially cryogenic, or solid propellants, as in the nuclear-electric or nuclear pulse, are used. Figure 18-16 shows an example depicting the possible growth rate for the case of liquid hydrogen and a combination of orbital mating and fueling computed for the probabilities shown.

The need for a larger post-Saturn launch vehicle and for rendering this vehicle reusable depends on the detail of the long-range lunar and interplanetary mission objectives. Specifically, the heliocentric mission energy requirements and the anticipated

Fig. 18-16 Orbital launch support requirements.

advances in propulsion system technology for cislunar and helio-centric ISV's determine the desirable payload range of a post-Saturn launch vehicle; the anticipated launch frequency determines whether or not reusability of this vehicle is worthwhile (Fig. 18-17). If the launch frequency does not warrant reusability, the need for more payload capacity can almost certainly be satisfied by a more or less massive uprating of Saturn V. If reusability is warranted, a new post-Saturn launch vehicle is truly needed.
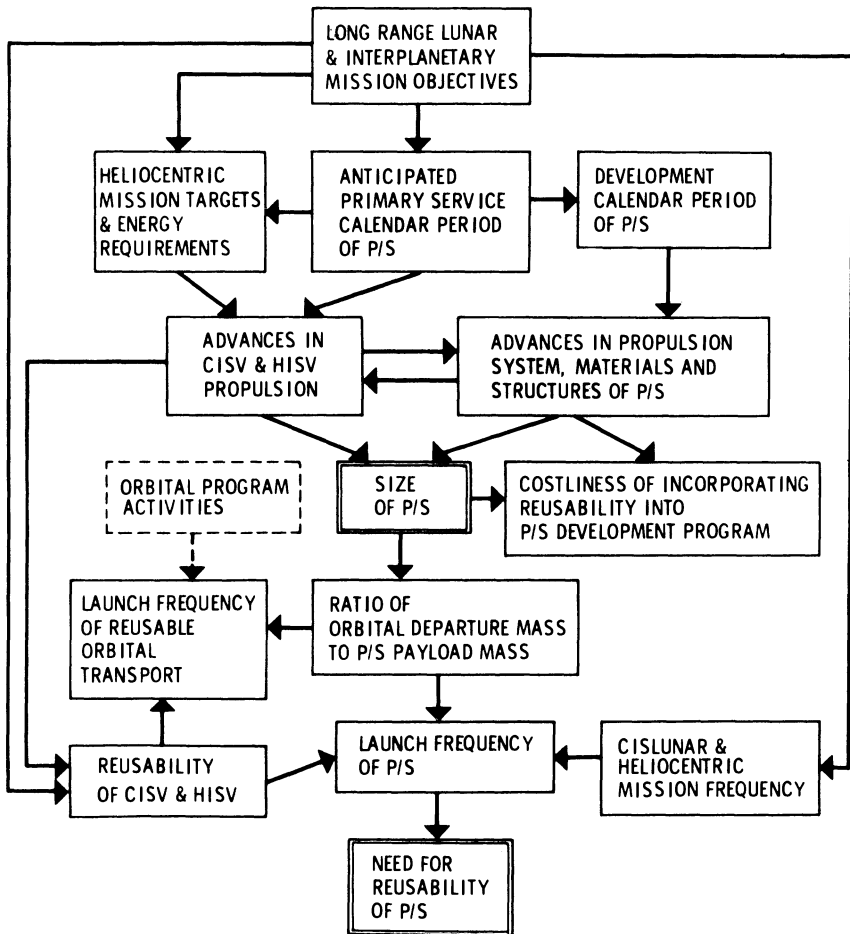
Fig. 18-17 Logic diagram for determining size and need for reusability of post-Saturn launch vehicle.

Figure 18-16, based on deep space vehicles using cryogenic propellants, suggests that the launch vehicle payload mass probably

should not be less than one-third or one-fourth of the orbital de-
parture mass $m_{A,ISV}$ of the individual deep space vehicle, in order
to keep redundancy and orbital launch support masses from be-
coming excessively large. Continued advances in orbital operations
technology may reduce the launch vehicle payload mass to less than
one-fourth of the orbital departure mass. The nomical orbital de-
parture mass per vehicle is equal to the payload mass of the ISV
plus the product of its payload mass $m_{\lambda,ISV}$, times logistic factor.
Therefore, the launch vehicle payload $m_{\lambda,0}$ should approximately
satisfy the general relation

$$m_{\lambda,0} \approx \frac{m_{\lambda,0}}{m_{A,ISV}} \; m_{\lambda,ISV} \, (1 + L)$$

where $m_{\lambda,0}/m_{A,ISV}$ represents the influence of the state-of-art of
orbital technology and operations and L represents the influence
of the level of cislunar and heliocentric propulsion, design and
required mission energy. For one-way lunar surface supply mis-
sions, the logistic factor is 6 to 7, if a three-stage advanced
chemical system is used (Table 18-5). For cislunar shuttle
vehicles, the logistic factors are considerably higher (Table 18-6).
In all cases, a chemical shuttle vehicle between lunar orbit and
surface is stipulated (first line). This means that at least two
stages are involved: lunar lander and cislunar vehicle. If the
latter is a single-stage system, the flight profile is designated
as lunar orbital rendezvous. The effect of an alternative flight
profile on L is also shown, referred to as lunar orbital and cis-
lunar orbital rendezvous shown in Fig. 18-18. It involves a two-
stage cislunar vehicle in which the first stage, for Earth orbital
departure and return, does not orbit the Moon. It enters into
holding orbit A. Stages 2 and 3 enter into lunar capture and
St. 3 descends to the surface. Orbit A is synchronized with
respect to the Moon's orbital motion so that after one month,
Stages 2 and 3 can meet with St. 1 in a cislunar interorbital
rendezvous maneuver. The case shown in Fig. 18-18 exemplifies
a biweekly shuttle service involving two holding orbits. Stages 2
and 3 of vehicle A (whose St. 1 stops in orbit A) rendezvous after
one-half month with St. 1 of vehicle B in holding orbit B. Cor-
respondingly, Stages 2 and 3 of vehicle B meet with St. 1 of vehicle
A. Perturbations of orbits A and B during the holding period are
readily corrected with very little propellant expenditure. Con-
sideration of this expenditure is not included here. Such flight
profile can effectively reduce L (*cf.* cases 2 and 6), but improve-
ments in propulsion of the cislunar vehicle are more effective.
The advent of a gas core reactor or a nuclear-electric driven
Earth orbital departure and return stage can reduce the re-supply
logistic factor to values comparable to the previously mentioned

Table 18-5   Lunar Surface Supply Requirements (One-Way)

$$\Delta v_1 = 11k; \; \Delta v_2 = 7k; \; \Delta v_3 = 6k \; (k = 10^3 \text{ ft/sec.})$$

Mission	Delivery Mode	Stage No.	Propulsion	I_{sp} (Sec.)	Mass Fraction X	Inert Mass Factor i = $\dfrac{\text{Inert Mass}}{\text{Pld. Mass}}$	Propellant Mass Factor p = $\dfrac{\text{Prop. Mass}}{\text{Pld. Mass}}$	Logistic Factor $L = i + p$
Lo-Orb to Lu Surf	1-Way	3	Chemical	450	.84 - .88			
		2	Chemical	450	.85 - .89	.85 - .51	5.9 - 5	6.7 - 5.5
		1	Chemical	450	.88 - .92			
Lo-Orb to Lu Surf	1-Way	3	Chemical	450	.84 - .88			
		2	Chemical	450	.85 - .89	1.0 - .6	3.9 - 3.4	4.9 - 4
		1	Nerva II	800	.74 - .82			

Table 18-6 Lunar Surface Supply Requirements (Shuttle Service)

$\Delta v_1 = 11k; \Delta v_2 = 7k; \Delta v_3 = 7k; \Delta v_4 = 6k; \Delta v_5 = 7k; \Delta v_6 = 11k \ (k = 10^3 \text{ ft/sec.})$

Mission	Delivery Mode	Stage No.	Propulsion	I_{sp} (sec.)	Mass Fraction X	Inert Mass Factor i = $\frac{\text{Inert Mass}}{\text{Pld. Mass}}$	Propellant Mass Factor p = $\frac{\text{Prop. Mass}}{\text{Pld. Mass}}$	Logistic Factor $L = i + p$
Lu-Orb to Lu-Surf	Shuttle Service	3[1]	Chemical	450	.84 - .88	.32 - .23	1.7 - 1.6	2 - 1.8
Lo-Orb to Lu-Surf	Shuttle Service (Lu-Orb Rendezvous)	2	Chemical	450	.84 - .88	12.4 - 3.9	165 - 71	177 - 75
		1	Chemical	450	.93 - .95			
Lo-Orb to Lu-Surf	Shuttle Service (Lu-Orb Rendezvous)	2	Chemical	450	.84 - .88	10.7 - 2.3	43.4 - 16.8	54 - 19
		1	Nerva II	800	.80 - .88			
Lo-Orn to Lu-Surf	Shuttle Service (Lu-Orb Rendezvous)	2	Chemical	450	.84 - .88	5.7 - 1.6	25.2 - 13.7	31 - 15
		1	Nucl. (Metal)	850	.82 - .90			
Lo-Orb to Lu-Surf	Shuttle Service (Lu-Orb Rendezvous)	2[2]	Chemical	450	.84	17.7 - 2.3	19.1 - 5.8	37 - 8
		1	Gas Core	1800	.5 - .7			
Lo-Orb to Lu-Surf	Shuttle Service (Lu-Orb and Cislunar Orbital Rendezvous)	3	Chemical	450	.84 - .88	13.6 - 5.5	97.3 - 61.7	111 - 67
		2	Chemical	450	.87 - .91			
		1	Chemical	450	.88 - .92			
Lo-Orb to Lu-Surf	Shuttle Service (Lu-Orb and Cislunar Orbital Rendezvous)	3	Chemical	450	.84 - .88	13.9 - 5.5	43.7 - 28.7	58 - 34
		2	Chemical	450	.87 - .91			
		1	Nerva II	800	.74 - .82			

[1] The lunar orbit to lunar surface and return shuttle service is included in the values of i, p, and L of the three subsequent cislunar shuttle stage.

[2] This stage corresponds to the lunar orbit surface shuttle service, since the gas core driven vehicle represents a single stage cislunar shuttle.
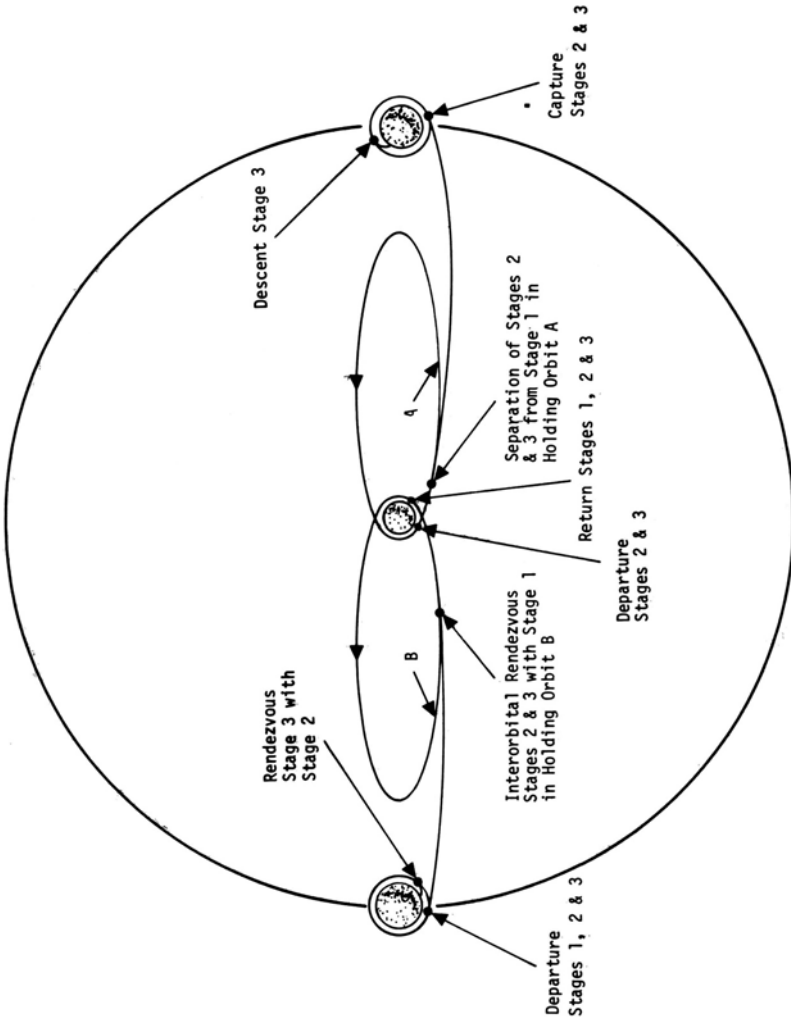
Fig. 18·18 Lunar shuttle service using lunar orbital and cislunar interorbital rendezvous.

one-way delivery values. While advances in specific impulse are a primary requirement, the importance of advances in space structural materials runs a close second in reducing the logistic factor (particularly the propellant mass factor) for cislunar shuttle services. If both advances are pursued vigorously in the 1970's, Saturn V or an uprated version could retain its adequacy until rising mission frequency, if such occurs, eventually renders introduction of a reusable system worthwhile.

The results of the cislunar shuttle transport analysis lead to the conclusion that, prior to introduction of a suitable gas core reactor or nuclear electric drive, a cislunar shuttle service, if any, will be limited to relatively small loads, primarily personnel, to be carried both ways, whereas large supply loads will be delivered by one-way flights. This has a significant effect on the launch vehicle size and launch frequency.

For manned heliocentric missions, orbital departure weights per HISV are shown in Figs. 18-19 and 18-20 for a wide range of propulsion systems and of Earth return conditions. The weights are based on individual vehicle and mission analyses rather than simplified parametric curves. Typical quality indices resulting from these analyses are presented in Figs. 18-21 and 18-22.

The results of the heliocentric transport analysis lead to three primary conclusions.

1) For a realistic planning of all but the most marginal manned planetary missions, the development of at least one multi-thousand-seconds-I_{sp} system is mandatory in order to assure adequate freedom of choice of future manned missions when such choice can be made more knowledgeably than in the next few years and in order to limit the supporting launch vehicle size as well as the extent and complexity of orbital launch support operations.

2) Technologically, the four primary candidates for such development are the advanced gas core reactor ($2500 \leq I_{sp} \leq 3500$ sec.), nuclear pulse ($2500 \leq I_{sp} \leq 10{,}000$ sec.), nuclear electric ($5000 \leq I_{sp} \leq 20{,}000$ sec.), and the controlled thermonuclear reactor (CTR) ($5000 \leq I_{sp} \leq 500{,}000$ sec.). Because of the political and operational liabilities associated with the nuclear pulse, the choice is primarily between the nuclear-electric, the advanced gas core reactor, and the CTR.

3) For the mission range from Mercury to Jupiter, the choice of either system does not affect the launch vehicle size significantly; either type of HISV can be accommodated by post-Saturn (1-$1.5\ \bar{M}$ payload) with one to three launchings per HISV. For missions beyond Jupiter, the CTR becomes increasingly superior.

Once in existence, the reusable aerospace transport (RAST) will contribute to the operational economy of delivering deep space probes into parking orbit. This contribution will increase with the availability of electric propulsion (or equivalent) for deep

Fig. 18-19 Weight summary Mars mission.
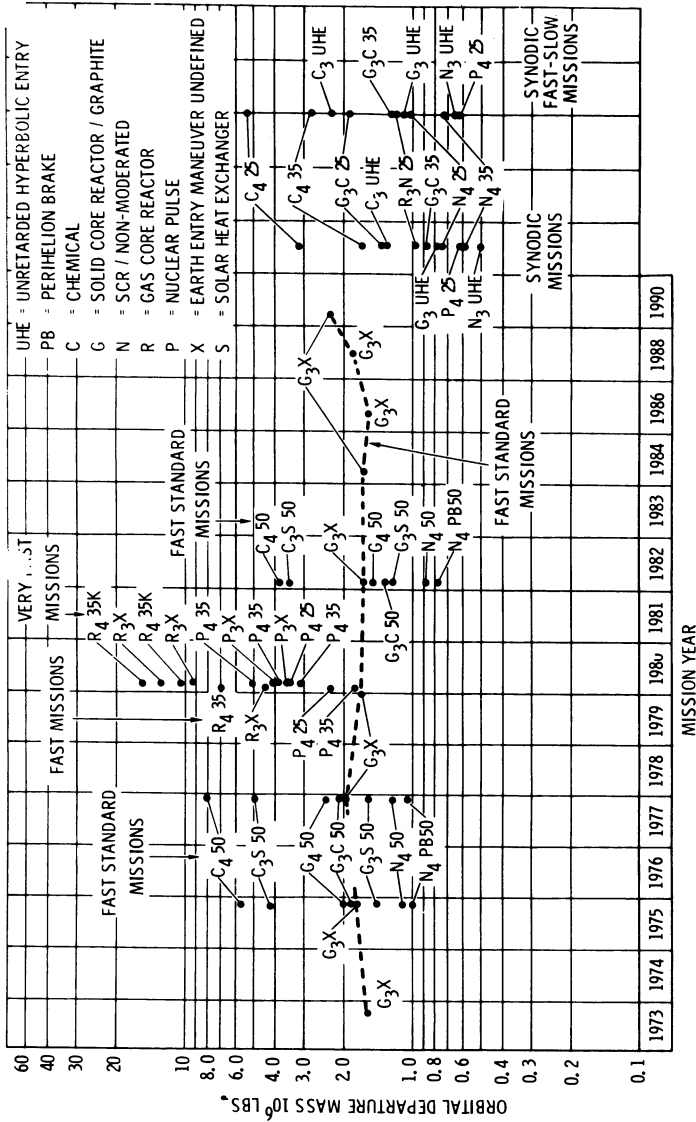
CODE: $C_4 50 = 4$ MANEUVERS, CHEMICAL, 50,000 ft/sec. EARTH RE-ENTRY
$R_4 35 = 4$ MANEUVERS, GAS CORE REACTOR, EARTH CAPTURE AT 35,000 ft/sec. ELONGATED ELLIPSE
$P_4 25 = 4$ MANEUVERS, NUCLEAR PULSE, EARTH CAPTURE CIR. ORBIT AT 25,000 ft/sec.

UHE = UNRETARDED HYPERBOLIC ENTRY
PB = PERIHELION BRAKE
C = CHEMICAL
G = SOLID CORE REACTOR / GRAPHITE
N = SCR / NON-MODERATED
R = GAS CORE REACTOR
P = NUCLEAR PULSE
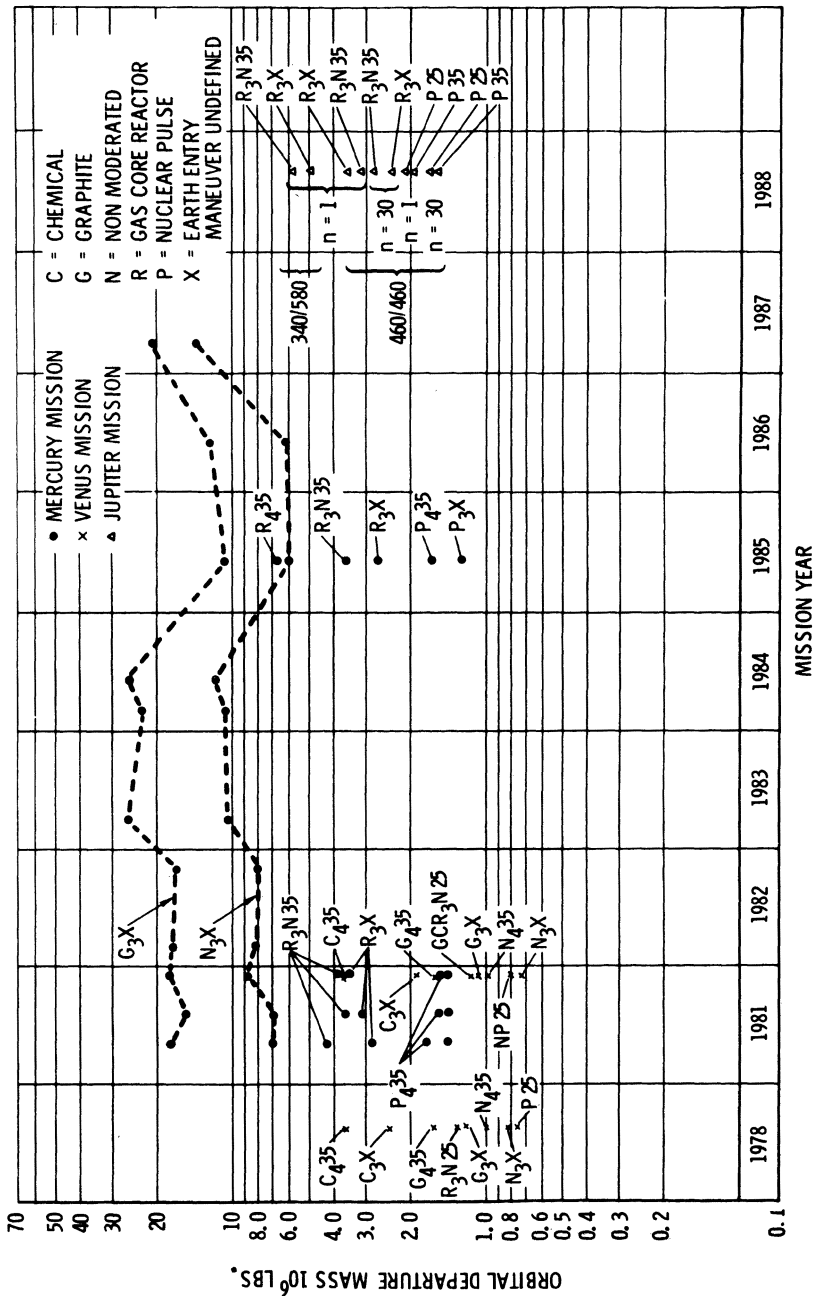X = EARTH ENTRY MANEUVER UNDEFINED
S = SOLAR HEAT EXCHANGER

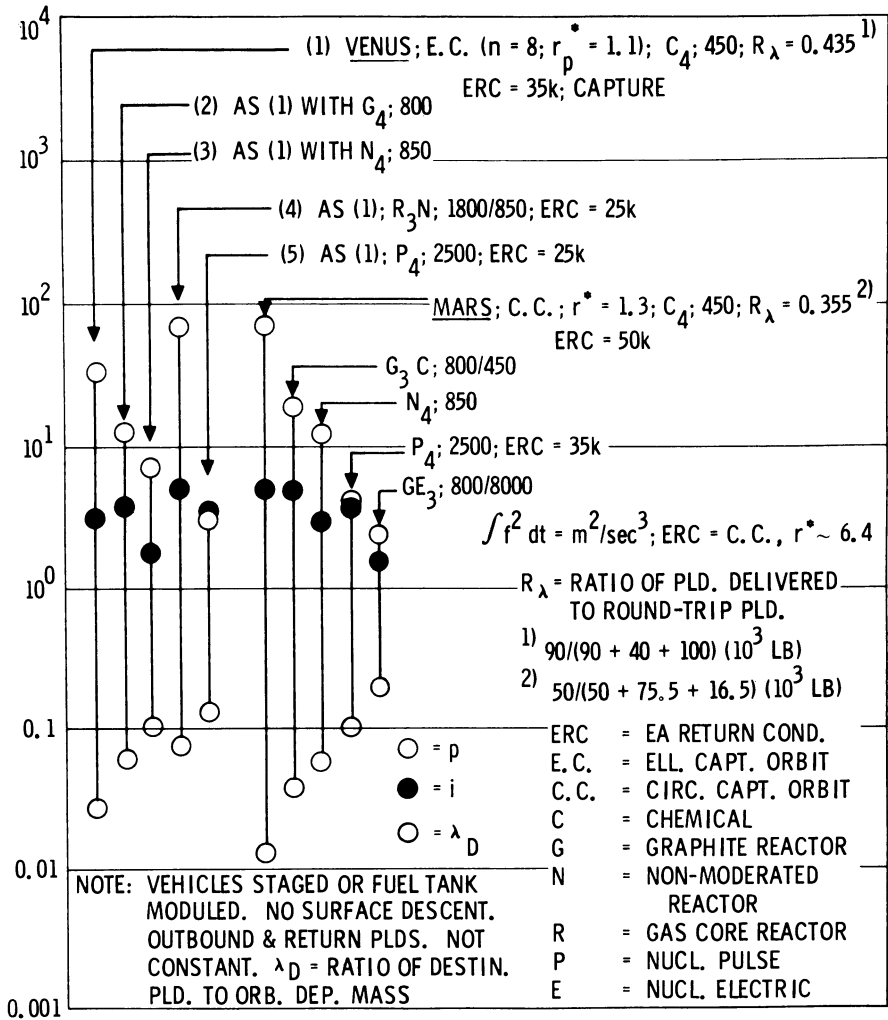Fig. 18-20 Weight summary for Mercury, Venus and Jupiter missions.

Fig. 18-21 Quality indices of heliocentric transports: Venus (1978, 140-20-250) and Mars (1982, 200-50-200).

space probes because attendant reduction of their initial mass will render a greater number of probes compatible with the payload limitations of the RAST.

With the expected cislunar traffic and deep space probe activities in the 1970's and the first half of the 1980's, it appears that Saturn V and uprated/improved Saturn V should be adequate for handling the heavy payload requirements for deep space traffic in conjunction with an orbital operations system which is capable of handling, mating and fueling at least three to four payload packages.
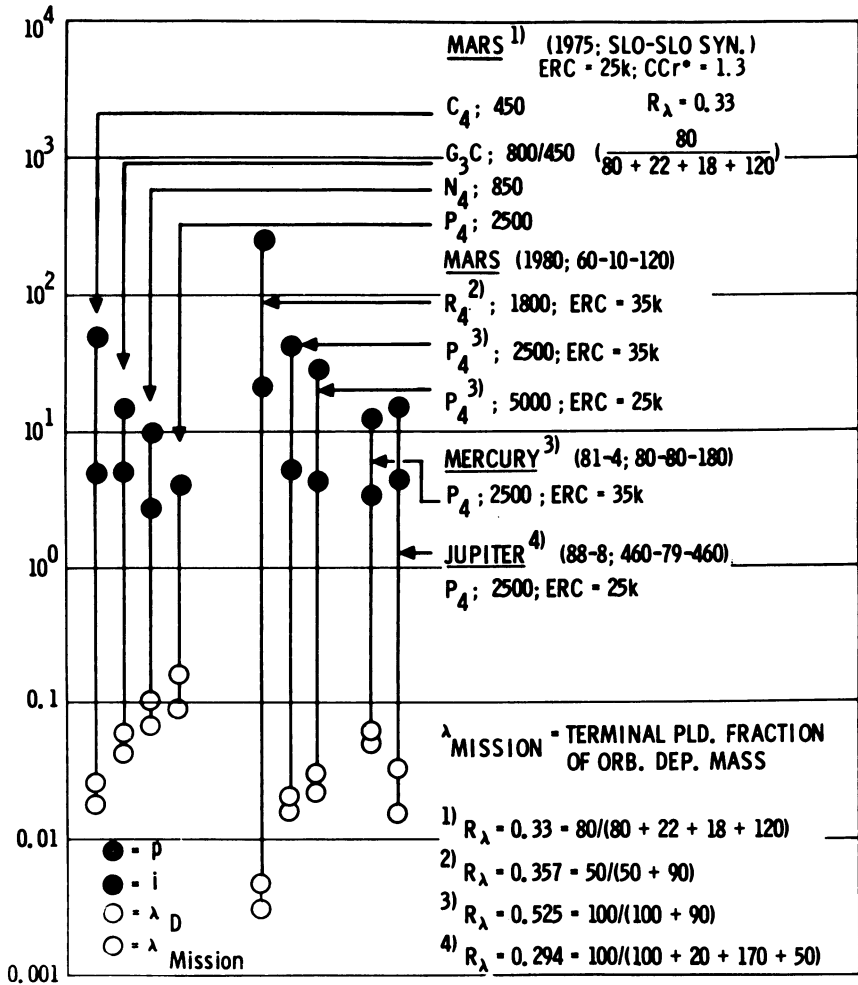
Fig. 18 - 22   Quality indices of heliocentric transports: Mars, Mercury and Jupiter.

The uprated Saturn system (assuming doubling its present payload) in conjunction with the availability of NERVA II can also handle the logistic support services required for a manned capture mission to Venus or to Mars in 1982 or 1984 involving a convoy of one round-trip vehicle and one or two one-way vehicles.

In 1985 to 2000 the payload and energy requirements of planetary missions, manned and unmanned, will probably increase greatly. Under those conditions, a reusable post-Saturn launch vehicle is needed to provide economically the necessary heavy payload logistic support in Earth orbit. With a launch vehicle payload capability

of up to 1.5 $\bar{M}$ lb. and advanced propulsion for the heliocentric vehicles providing specific impulses between 5000 and 20,000 sec., the entire solar system between Mercury and Pluto is accessible to manned vehicles. Permitting a ratio of orbital departure mass to launch vehicle mass of three to four per HISV, the orbital departure mass of the individual vehicle can be as large as 4 to 6 $\bar{M}$ lb.